

Studies of aerosol composition and hygroscopicity

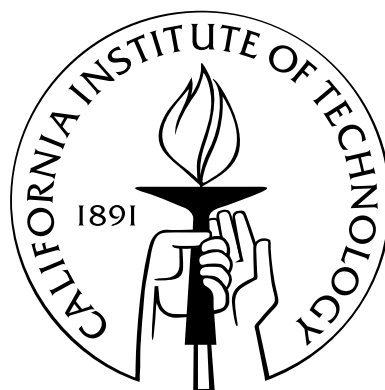
Thesis by

Scott P. Hersey

In Partial Fulfillment of the Requirements

for the Degree of

Doctor of Philosophy



California Institute of Technology

Pasadena, California

2011

(Defended May 24, 2011)

© 2011

Scott P. Hersey

All Rights Reserved

Dedicated to the voiceless poor who carry the weight of our environmental sins on their weary
backs. You matter.

Acknowledgements

Crossroads are times when you look back and observe the country you've traveled through. I look back on my life and see a journey along a road of events and relationships that brought me to exactly this place at exactly this time. Archbishop Desmond Tutu has a philosophy on the essential role that people and relationships play in one's life: "My humanity is bound up in yours, for we can only be human together." The road I've traveled would not have brought me here - made me who I am - without the people I have encountered and the relationships that have left their fingerprints on me.

Mom and dad: you more than anyone else have helped me get to this place. I have enormous gratitude for the importance you placed on my education, and the critical role you played in fostering my independence of thought and my interest in science and the natural world. Thank you for loving me through provision, and for blessing me with the gift of limitless educational opportunities. And to my siblings Ian, Neil, and Wendy: thank you all for teaching me how to be a little brother. You made sure that I learned important lessons in life, like how to get my butt handed to me in a foot race (at age 5... "He needs to learn!"). I know it was a conscious choice for you all to invest in me. Thank you for making that choice.

Two educators stand out as the most influential in all my years leading to grad school. The first is Lucy Duncan, my second grade teacher at Oriole Beach Elementary and avid naturalist. You saw in me a special curiosity about the natural world and you fostered it beautifully. The second was my freshman physics professor at Rice University and the person who gave me my first opportunity to pursue scientific research - Gary Morris. Thank you for the confidence you had in me from day one, trusting me (a lowly sophomore!) to be your colleague in the development and implementation of a major field sampling experiment. Looking back, I realize you must have either been a little insane

or desperate to let me do all that by myself. I got to Caltech because of that experience, and it all started with your faith in me.

I humbly thank John H. Seinfeld for the last 5 years of guidance, advice, mentorship, and support. I admire his wisdom, accomplishments, and expertise in the field, and I respect and hold him in the highest regard as my adviser. Together with co-adviser Rick Flagan, I truly had the dream team of PhD advisers. Now is the time for me to confess that I came to Caltech as much for the legendary Southern California surf as I did for the unparalleled scientific opportunities working under John and Rick. I was disappointed by neither. I was unbelievably lucky to have advisers who not only tolerated my surfing and triathlon endeavors, but even *encouraged* those pursuits. I suppose it helps that I always got my work done before heading to the beach. Well, unless the swell was *really* pumping...

John and Rick are but the cornerstones of a remarkable research group filled with fantastic colleagues. I have an especially large debt of gratitude to my colleague and close friend Armin Sorooshian, who showed me the ropes when I got here and taught me how to be a field scientist. I attribute much of my success in grad school to you, Armin. West side for life. I spent countless hours with Andrew Metcalf, who interestingly recruited me to come to Caltech during my visit weekend and then became my roommate for every trip to the field, conferences, and other random research-related trips. I know I was no Arthur, but hopefully I didn't talk too much in my sleep. My last two years saw me develop a close working relationship with Jill Craven, who I saw mature from an enthusiastic, excited first-year into a seasoned, careful, hard-working, and knowledgeable veteran of the field. And to the rest of the Seinfeld/Flagan crew - Shane Murphy, Arthur Chan, Puneet Chhabra, Christine Loza, Lindsay Yee, Beth Kautzman, Jason Surratt, Man Nin Chan, Sally Ng, Kate Schilling, Zach Lebo, Havalala Pye, Jean Chen, Joey Ensberg, Andi Zuend, Andy Downard, Xerxes Lopez-Yglesias, Jason Gamba, Mandy Grantz, and Tristan Day - thanks for all the conversations and high-fives. And thank you to Yvette Grant, Marcy Fowler, and Anne Hormann for all the chemical orders and shipping arrangements, and for generally keeping things orderly and sane.

As a field scientist, I also had the pleasure of collaborating with a number of exceptional people outside Caltech. I especially thank Fred Brechtel and Andy Corless of BMI, who spent a lot of hours with Armin and I as we got the DASH-SP up and running, and who were always there to support us and help us troubleshoot when something went wrong. Team DASH for life. Nathan Dalleska was crucial in helping me learn the Ion Chromatography systems and give them an overhaul, and he was a great sounding board for my frustrations with the maker of those IC machines. Thanks also to the entire CIRPAS crew, who got our instruments (and us) off the ground and back down safely with top-notch data. Special thanks to Haf Jonsson, the only second-order vegetarian I've ever met (only eats animals who eat vegetables). And thanks so much to Chris McGuire, our pilot with whom I shared lots of laughs, some good waves, a memorable Charlie Bravo flight over the LA basin, and a great friendship. Chris, you had me close to learning how to fly research aircraft. Thanks to the Georgia Tech crew - especially Thanos Nenes, Terry Lathem, and Jack Lin, for all their hard work on CCN data and for helping me understand the intricacies of things like critical diameter and cloud nuclei activation. Thanks also to team ATOFMS from UCSD - Kim Prather, Kaitlyn Suski, and Jack Cahill. You guys have got a great thing going down there, and I hope to work more with you in the future. Say hi to the ocean for me.

My "other" job at Caltech was to serve as a resident associate, or RA, at Dabney house for the last 4 years. As a live-in resource for undergraduates, I saw lots of high and low points in my students' lives, but it was an honor to walk through them all with you guys. Thanks so much to my wonderful RA colleagues and to my bosses Tim Chang, Sue Chiarchiaro, and Geoff Blake. It was a gift to be a part of that team. And through the RA job, I developed excellent working relationships with Lee Coleman, Undergraduate Dean Barbara Green, Vice President for Student Affairs Anneila Sargent, and President Jean-Lou Chameau. Thank you all for your constant support and for valuing the work we do as RAs.

When I look back on my years of grad school, the things I'll remember most are the deep, life-giving relationships I was blessed with here. Many of those friendships were with students from Fuller Seminary, who often made for an odd match (on paper, at least) with the Caltech scientist.

In particular, I am grateful for the brotherhood shared with David Koeker and Kawika Haglund. Thanks for all the waves, music nights, and meals in the garden. And I'm grateful for the friendship of Jeff Hanna and Kakani Young. With Jeff I logged thousands of miles training on the bike, running, and swimming. We went through cycles of loving and hating science together, but those trail runs kept us grounded. You and Kakani are good people.

Of all the amazing experiences and relationships over the last five years, nothing compares to the richness and joy of meeting and falling in love with my future wife, Shelton Oakley. I never in a thousand years could have dreamed that someone as incredible as you existed, and nothing has ever been as exciting as starting life with you. I dream of seeing communities and lives transformed as we partner together and serve with our beautifully complementary gifts and passions, and as we live eloquently and incarnationally through our marriage and family. I love you.

Every journey requires a vehicle and a driver. In the words of Winston Rodney from Burning Spear, "Jah is my driver. Jah is my ride. Jah is the wheels. Jah is the engine. Jah is the radiator. Jah is the water that cools off the engine." Truly God has been everything to me on this journey, bringing me to Caltech, faithfully providing, carrying me through the ups and downs of classes and research, blessing me with relationships through which I grew tremendously, and speaking in life-changing ways every step along the road. And as I leave Caltech, God has given me a vision for how to use my Environmental Science training and passion as part of a holistic restoration of shalom, through both teaching and community development. And he's given me the perfect partner for the journey. We'll be in good hands on that road.

Abstract

Atmospheric aerosols have significant impacts on human health, regional visibility, and the radiative energy balance of Earth, but there remain many uncertainties about their sources and evolution in the atmosphere, as well as the details and magnitude of their impact on climate. This thesis introduces a novel instrument for measuring aerosol hygroscopicity, an important factor in the overall climate impact of aerosols, and presents results from several field campaigns and laboratory experiments aimed at characterizing the chemical composition and hygroscopicity of atmospheric particles.

Aerosol water uptake determines particle size, which thereby determines an aerosol's scattering properties and radiative forcing. The Differential Sizing and Hygroscopicity Spectrometer Probe (DASH-SP) was designed to make rapid measurements of hygroscopicity on timescales short enough for aircraft deployment. Combined with an iterative data processing algorithm, the DASH-SP is demonstrated to accurately measure particle size, growth, and “effective” refractive index for particles from 135 nm to over 1 μm on timescales as short as a few seconds.

The DASH-SP was deployed off the coast of Central California to measure aerosol water uptake in a marine atmosphere impacted by aged anthropogenic emissions. Composition data from an Aerosol Mass Spectrometer (AMS) indicates that organics are uniformly highly oxidized (O:C ratio = 0.92 ± 0.33), and aerosol growth data from the DASH-SP indicates that in such a highly-oxidized environment, growth factor ($\text{GF} = D_{p,wet}/D_{p,dry}$) can be accurately predicted as a simple function of relative humidity (RH) and organic volume fraction.

A major ground-based sampling study was carried out in Pasadena, CA, a receptor site for transported Los Angeles pollution, and was dubbed the Pasadena Aerosol Characterization Observatory (PACO). Results indicate that organics dominate transported Los Angeles aerosols, and that

they are overwhelmingly oxidized in nature. Aerosol species tend to reside in distinct size modes, with inorganics typically found in larger, accumulation-mode aerosol, while semivolatile secondary organic aerosol (SV-OOA) products appear to reside predominantly in a fine mode. Hygroscopicity was found to be a strong function of organic mass fraction (OMF).

The end of PACO sampling coincided with a major forest fire in Los Angeles County. The impact of this fire on the sampling site is explored by comparing water soluble organic carbon (WSOC) and organic mass-to-charge (m/z) markers from the AMS. In the absence of fire influence, WSOC concentrations are primarily driven by concurrent photochemistry and sea breeze transport from source-rich areas. Fire periods are characterized by significant primary production of WSOC and overnight/early morning transport of fire emissions to the sampling site.

Finally, DASH-SP results from the May 2010 CalNex field experiment indicate that aerosol hygroscopicity is determined primarily by the mass fraction of organics and nitrate in the aerosol. Overall hygroscopicity is very similar to that measured during PACO, though organics appear to be less hygroscopic during CalNex - likely because PACO represented transported, aged aerosol, while CalNex flights covered the entirety of the LA basin, including more source-rich areas.

Contents

Acknowledgements	iv
Abstract	viii
1 Introduction	1
2 Rapid Size-Resolved Aerosol Hygroscopic Growth Measurements: Differential Aerosol Sizing and Hygroscopicity Spectrometer Probe (DASH-SP)	5
2.1 Abstract	6
2.2 Introduction	6
2.3 DASH-SP Description	9
2.4 Experimental Methods	13
2.5 Instrument Characterization	13
2.5.1 Size Limits of OPC Detection	13
2.5.2 Time Resolution	14
2.5.3 DASH-SP Accuracy, Precision, and Uncertainties	15
2.5.4 Stability	17
2.6 Data Analysis	18
2.7 Growth Factor Measurements	20
2.7.1 Inorganic Salts	20
2.7.2 Organic Acids	21
2.8 Validation of Iterative Data Processing Code	23

2.9	Field Implementation of DASH-SP	25
2.10	Conclusions	27
3	Aerosol hygroscopicity in the marine atmosphere: a closure study using high-time-resolution, multiple-RH DASH-SP and size-resolved C-ToF-AMS data	46
3.1	Abstract	47
3.2	Introduction	48
3.3	Experimental	49
3.3.1	MASE-II Experiment	49
3.3.2	Aerosol Composition Measurements	50
3.3.3	Hygroscopicity Measurements	51
3.3.4	Hygroscopic Closure	52
3.4	Results	53
3.4.1	Airmass Origin	54
3.4.2	Hygroscopicity Trends	55
3.4.3	Hygroscopic Closure	55
3.4.4	Simplified Parameterization	56
3.5	Discussion	57
3.6	Conclusions	60
4	The Pasadena Aerosol Characterization Observatory (PACO): Chemical and Physical Analysis of the Western Los Angeles Basin Aerosol	78
4.1	Abstract	79
4.2	Introduction	80
4.3	Methods	83
4.3.1	Meteorology	84
4.3.2	Gas-Phase Data	84
4.3.3	Differential Mobility Analyzer	84

4.3.4	Aerosol Mass Spectrometer	84
4.3.5	Positive Matrix Factorization Analysis	85
4.3.6	PILS-IC	86
4.3.7	PILS-TOC	86
4.3.8	Filter Sampling	87
4.3.9	Hygroscopicity	88
4.4	Results and Discussion	89
4.4.1	Atmospheric Conditions	89
4.4.2	Aerosol Composition	90
4.4.3	PMF results	96
4.4.4	Filter Analysis	99
4.4.5	Hygroscopicity	101
4.5	Conclusions	105
4.6	Appendix	135
4.6.1	PMF Analysis	135
5	Impact of a large wildfire on water-soluble organic aerosol in a major urban area: the 2009 Station Fire in Los Angeles County	147
5.1	Abstract	148
5.2	Introduction	149
5.3	Methods	151
5.3.1	Data	151
5.3.2	Fire Development and Influence on the Measurement Site	152
5.4	Results and Discussion	153
5.4.1	PACO Study Background	153
5.4.2	Meteorological Setting and Origin of Air Masses	154
5.4.3	WSOC Production Pathways and Relationship with Ozone	155
5.4.4	Cumulative WSOC Statistics	157

5.4.5	Diurnal WSOC Behavior	158
5.4.6	Relationships Between WSOC, AMS Organic, m/z 44, and m/z 43	160
5.4.7	Case Studies	162
5.5	Conclusions	166
6	Aerosol Hygroscopicity and Composition in the Los Angeles Basin during the 2010 CalNex Experiment	180
6.1	Abstract	181
6.2	Introduction	181
6.3	Methods	183
6.3.1	DASH-SP - Multiple-RH Hygroscopicity	184
6.3.2	AMS - Aerosol Composition	185
6.3.3	CIRPAS Instruments - Microphysics and Meteorology	185
6.4	Aerosol Composition and Microphysics	186
6.5	Hygroscopicity	188
6.6	Conclusions	194
7	Conclusions	210
A	Comprehensive airborne characterization of aerosol from a major bovine source	214
B	Comprehensive Simultaneous Shipboard and Airborne Characterization of Exhaust from a Modern Container Ship at Sea	247
C	On the link between ocean biota emissions, aerosol, and maritime clouds: Airborne, ground, and satellite measurements off the coast of California	263
D	Chemical Composition of Gas- and Aerosol-Phase Products from the Photooxidation of Naphthalene	279

- E** Reactive intermediates revealed in secondary organic aerosol formation from isoprene 302
- F** Constraining the contribution of organic acids and AMS m/z 44 to the organic aerosol budget: On the importance of meteorology, aerosol hygroscopicity, and region 309

List of Tables

2.1	Aerosol hygroscopicity measurement techniques.	36
3.1	Previous marine aerosol hygroscopicity studies.	69
3.2	MASE-II flights.	70
3.3	MASE-II instrument payload.	71
3.4	<i>GF</i> results for below, above, free troposphere (FT), and ship plume measurements.	73
4.1	Previous Los Angeles air quality studies and major findings relative to particulate matter.	132
4.2	PACO sampling regimes (2009).	133
4.3	OC/EC concentrations ($\mu\text{g}/\text{m}^3$) for representative days from each regime.	134
4.4	Mass spectral comparison of several PMF solutions	145
4.5	Time series comparison of several PMF solutions	146
5.1	Statistical summary of the relationship between WSOC ($\mu\text{g C m}^{-3}$) and other chemical and meteorological parameters (measured at Santa Fe Dam). AMS aerosol species concentration units are $\mu\text{g m}^{-3}$	169
6.1	Summary of flights and instrument performance for CIRPAS Twin Otter operations during CalNex.	202

List of Figures

2.1	Schematic of DASH-SP.	37
2.2	Time required as a function of particle number concentration to obtain sufficient pulses for the modal pulse height to be within 1% of the mode that would be obtained when counting at least 10,000 particles at constant particle composition. Also shown is the time needed for the standard deviation to be within 1%, 5%, and 10% of the standard deviation that would be obtained when counting at least 10,000 particles at constant particle composition.	38
2.3	Stability statistics for different species and sizes over a time span of four months. Panel A corresponds to the high-gain OPC setting, and Panel B represents the low-gain setting for dry tests. Panel C represents stability statistics for growth factor during wet studies using the high-gain OPC configuration ($n > 20$ for each salt in the bottom panel).	39
2.4	OPC response as a function of dry particle size for salts of different refractive index. These results are from one OPC for a single set of calibrations performed for each salt. All OPCs show the same general behavior.	40

- 2.5 Data processing procedure from DASH-SP raw pulse height data to growth factors (GFs) for both laboratory-generated aerosol, for which the composition and refractive index (n) of the dry particles are known, and for ambient aerosol, where the composition and refractive index of the dry particles are unknown. The dry pulse height distribution mode is first used to determine the dry particle refractive index, which is used to calculate a volume-weighted wet particle refractive index, taking into account the volume fractions of water and the particle. Iterations are subsequently carried out on the three-dimensional surface shown to converge on a wet particle refractive index. The D_p corresponding to the latter value of refractive index and the wet pulse height distribution mode is subsequently used to calculate growth factor. 41
- 2.6 Experimentally determined growth factor curves for inorganic and organic acid species. Predictions from the Brechtel and Kreidenweis (2000a,b) model are shown for all salts except for glyoxylic acid and potassium chloride, while predictions from the Clegg et al. (1998) model are also shown for ammonium sulfate. The Brechtel and Kreidenweis (2000a,b) model includes the Kelvin term to account for droplet curvature. Error bars reflect uncertainties associated with the RH and sizing (DMA and OPC) measurements. The reported deliquescence RH (DRH) and efflorescence RH (ERH) values are from the following references: Saxena and Hildemann (1997) and Peng et al. (2001) for organic acids, and Seinfeld and Pandis (2006) for the inorganic species. 42
- 2.7 Comparison between two thermodynamic models and DASH-SP data for ammonium sulfate particles. The reported DASH-SP results were calculated by using iterative procedure in Figure 2.5 to process the OPC pulse height data. The RH error bars reflect uncertainties in the RH measurement, while the GF error bars reflect the precision of the measurement after several repetitive trials. 43

- 2.8 Size distributions from wet ammonium sulfate and dry PSL aerosol laboratory tests. Panels A, B, and C correspond to ammonium sulfate tests in which DMA-selected dry particle sizes of 150, 175, and 200 nm, respectively, were exposed to RHs of < 8% (dry), 74%, 85%, and 92%. Each curve is labeled with its calculated growth factor and "effective" refractive index (n), as calculated from the iterative data processing procedure in Figure 2.5. Panel D corresponds to dry PSL size distributions to show that for spherical particles the distributions are narrower than those for salts that may not be perfectly spherical. The size distributions tend to be broader near the minimum and maximum size detection limits of the OPCs. 44
- 2.9 Panel A) Flight tracks during a MASE II flight (July 16, 2007) during which the Twin Otter aircraft sampled emissions from a large cargo ship off the central coast of California. The duration of the ship exhaust plume measurements was approximately 2.5 h. The plane flew at an altitude of 30 m in the ship's plume, before performing multiple cross-wind transects of the plume at the labeled altitudes. Panel B) Water-soluble species concentrations as measured by a PILS onboard the Twin Otter. The four, black vertical lines indicate when the aircraft was immediately behind the ship. Panel C) Growth factors at an RH of 92%. Marker sizes are proportional to the submicrometer particle number concentration (range = 50 - 365,000 cm^{-3}), as determined by a DMA. 45
- 3.1 92% GF values for $D_{em,dry} = 200$ nm particles are shown for below (black) and above (yellow) cloud flight legs. 48-hr HYSPLIT back-trajectories show air mass origin for each flight. Flights 12 and 16 show both suppressed GF values and continental, polluted air mass origin. 72
- 3.2 Below- and above-cloud 92% GF values for $D_{em,dry} = 200$ nm particles as a function of altitude, with lines connecting measurements made on the same 'trip' from bottom to top of cloud. Marker size is proportional to $VF_{organic}$, and ranges from 0.10 to 0.90. 'a' and 'b' designate separate 'trips' during the same flight. 74

3.3	Measured GF values versus volume-weighted predictions. Markers are color-coded with RH, and marker size is proportional to $VF_{organic}$ (ranging from 0.10 to 0.90). The blue line represents 1:1.	75
3.4	Predictions of GF from the simplified parameterization. Markers are color-coded with RH, and marker size is proportional to $VF_{organic}$ (ranging from 0.10 to 0.90). The blue line represents 1:1.	76
3.5	Comparison of growth curves for pure ammonium sulfate, pure hydrophilic organic, and mixed organic/inorganic particles. Ammonium sulfate curves calculated from AIM (Clegg et al., 1998)	77
4.1	Regime I (wind direction marker size proportional to wind speed; max size = 20 km/h).	120
4.2	Regime II (wind direction marker size proportional to wind speed; max size = 20 km/h).	121
4.3	Regime III (wind direction marker size proportional to wind speed; max size = 20 km/h).	122
4.4	Average diurnal DMA number concentrations (cm^{-3}) for regimes I, II, and III.	123
4.5	Bulk AMS diurnal mass averages for regime I, regime II, and regime III. Bottom panel shows size-resolved PToF AMS data for a representative morning and afternoon period in each regime, where morning = 0700-1100 LT and afternoon = 1500-1900 LT.	124
4.6	AMS bulk mass fractions for AM (0700-1100 LT), midday (1100-1500 LT), PM (1500-1900 LT), and night (1900-0700 LT) for regimes I, II, and III.	125
4.7	WSOC magnitude (squares) and % of AMS organic (circles). Black markers represent the average over regime III.	126
4.8	Mass spectra for the three factors identified in PMF analysis (HOA, SV-OOA, and LV-OOA; left) and Pearson's R correlations of those solution mass spectra with previously reported mass spectra (1, 2, 3, 4, 5, 6: Zhang et al., 2005; Lanz et al., 2007; Ulbrich et al., 2009; Bahreini et al., 2005; Alfarra et al., 2004; Ng et al., 2011, respectively).	127
4.9	Mass fraction of total organic accounted for by each PMF factor during regimes I, II, and III.	128

4.10	f_{44} vs. f_{43} for PACO, with color scale corresponding to date. Square markers represent values for HOA, SV-OOA, and LV-OOA factors identified in PACO.	129
4.11	GF at 74, 85, and 92% RH plotted against organic mass fraction, with color scale corresponding to date	130
4.12	κ and critical dry diameter plotted against mass fraction organic, with color scale corresponding to date; lines represent empirical parameterizations from PACO, Central Mexico, and N. American West Coast.	131
4.13	Q/Q_{exp} values for varying number of factors (p values). The circled marker is the presented solution.	137
4.14	Q/Q_{exp} for varying f_{peak} values for $p = 3$. The circled marker is the presented solution.	138
4.15	Sum of the residuals for 1,2, 3, and 4 factor solutions.	139
4.16	Scaled residuals for the 3 factor solution. (seed = 6).	140
4.17	Mass spectral profiles for the 2 factor solution.	141
4.18	Mass spectral profiles for the 4 factor solution.	142
4.19	Time series contributions for the 2-factor solution.	143
4.20	Time series contributions for the 4-factor solution.	144
5.1	Approximate spatial extent of the Station Fire by date (bordered areas). The fire area was estimated using fire maps by “Firefly”, University of Maryland (http://firefly.geog.umd.edu/firemap/). The blue marker in Pasadena represents the measurement site.	170
5.2	Diurnal meteorological parameters (Santa Fe Dam station) and O_3 concentrations. . .	171
5.3	Wind roses for the month of July for South Wilson Avenue and surrounding stations (data from Mesowest, http://mesowest.utah.edu/index.html).	172
5.4	Diurnal averages of aerosol chemistry (m/z 60 shown for the fire period only).	173
5.5	Diurnally averaged ratios of different aerosol measurements.	174

5.6	Summary of the ratios WSOC : organic and m/z 44 : WSOC as functions of m/z 44 : 43 during the (top panels) fire and (bottom panels) the non-fire periods. Symbols are color-coded by time of day, and in the fire panels the symbol sizes are proportional to the tracer for biomass burning m/z 60 (range = 0.03–0.9 $\mu\text{g m}^{-3}$).	175
5.7	Ground station observations of PM _{2.5} , CO and O ₃ for the non-fire (top) and the fire (bottom) period. The four stations (http://www.arb.ca.gov) are shown on the map in Fig. 5.1.	176
5.8	Time series of various measured and derived parameters during selected days outside the fire period. The symbol size for wind direction is proportional to measured wind speed.	177
5.9	Number (top) and volume (bottom) size distributions over the course of (left) 10 July 2009, a day of the non-fire period, and (right) 31 August 2009 in the fire period. . . .	178
5.10	Time series of various measured and derived parameters during the fire period. The symbol size for wind direction is proportional to measured wind speed.	179
6.1	Spatial distribution of the dimensionless ζ , showing the relative abundance of fine particles near source-rich areas. Data are plotted on a Google Earth map layer.	203
6.2	AMS composition ($\mu\text{g}/\text{m}^3$), showing organic (green), sulfate (red), nitrate (blue) and ammonium (orange) concentrations in the Los Angeles Basin. Marker sizes are proportional to species concentration.	204
6.3	Approximate O:C ratio plotted spatially (top) and as a function of longitude (bottom). Dashed line on the bottom plot represents the mission-averaged O:C ratio during the 2009 PACO study in the western Los Angeles Basin (Hersey et al., 2011).	205
6.4	Hygroscopic GF at 74% (bottom) and 92% (top) RH as a function of OMF. Dotted lines are a linear fit of GF data; solid lines are GFs for common inorganic aerosol constituents.	206
6.5	κ hygroscopicity parameter values for the Los Angeles Basin, with color scale and marker size both proportional to κ	207

6.6	κ plotted as a function of OMF, with color scale corresponding to NMF. Lines represent parameterizations from previous studies.	208
6.7	Sensitivity of κ_{org} to κ_{inorg} estimates, with the blue shaded box representing the range of κ_{inorg} commonly assumed in the literature, in the absence of significant NaCl influence.	209

Chapter 1

Introduction

Atmospheric aerosols are very small particles suspended in the air, ranging in diameter from several nanometers to several microns (10^{-9} to 10^{-6} m). For scale, the best ball-point pen money can buy is the Pentel RSVP fine-tip, with a 0.5 mm pin head. If one collected 500 nm particles (actually rather large when it comes to urban aerosol) out of the air, it would be possible to fit one million of these particles on the tip of that pen. These aerosol particles can be particularly efficient at following air streams through the human respiratory system and depositing deep into pulmonary tissues, causing adverse health effects. Additionally, many aerosols are roughly the same diameter as the wavelength of visible light (390-750 nm) and, according to Mie theory, very efficiently and indiscriminately scatter that light, resulting in the hazy conditions referred to in the vernacular as “smog.” Through direct scattering and indirect interactions with clouds, aerosols also result in significant incoming solar radiation being reflected back to space, a so-called “negative forcing” affecting the energy balance of earth.

Aerosols have both natural and anthropogenic sources, and the importance of each has significant regional variation. These fine particles can be directly emitted through combustion (i.e., forest fires and fossil fuel combustion), sea spray (i.e., breaking waves and bubble-bursting), and mechanical processes (i.e., wind-blown dust). Aerosols also result from chemical reactions in the atmosphere, through which gas-phase precursors are oxidized to form lower-volatility species that subsequently condense into the particulate phase, either forming new particles through a process called nucleation or condensing onto pre-existing particles. These secondary processes are especially important in urban areas, where precursor gases are emitted in high concentrations through anthropogenic activities like fossil fuel combustion and industrial processes.

Decades of study have indicated that the majority of aerosol pollution in most urban areas is organic, and that the dominant fraction of organics is secondary in nature. There remains a great deal of uncertainty about the origin and nature of organics in major urban areas, with models systematically underpredicting secondary organic aerosol (SOA). In complex urban areas like the Los Angeles Basin, aerosols undergo significant evolution as they are transported from source-rich to downwind areas, undergoing constant photochemical and aqueous-phase processing in-transit. To

predict the impacts of aerosol pollution in the future and develop effective abatement strategies, it is first necessary to characterize the aerosol in various environments and understand both the sources and evolution of aerosols in real-world conditions.

Aerosol particles grow and shrink with changes in relative humidity (RH), according to thermodynamic equilibrium between water vapor and the chemical constituents of aerosol particles. The intensity of light scattered by aerosols is strongly dependent on the diameter of aerosol particles, such that small increases in aerosol diameter result in significant changes in the radiative properties of aerosol populations. Thus, the relative-humidity-dependent water uptake of aerosols, termed hygroscopicity, is the major factor determining their direct radiative impact. Such sub-saturated hygroscopicity is strongly correlated with the tendency of aerosol particles to serve as cloud condensation nuclei (CCN), interacting with clouds in such a way that their radiative properties are significantly changed. These interactions between aerosols and water vapor were determined to be one of the most significant uncertainties in predicting future climate, as stated in the most recent report from the Intergovernmental Panel on Climate Change (IPCC). It is therefore necessary to study the factors that influence aerosol hygroscopicity in the real world in order to address these uncertainties and better predict and prepare for climate change.

This thesis is a compilation of results from field studies on the North American West Coast, all aimed at characterizing both the chemical composition and hygroscopic nature of aerosols in order to better understand and predict the impact of aerosols on both local communities and on climate. Chapter 2 is a description of a novel instrument (the Differential Aerosol Sizing and Hygroscopicity Spectrometer Probe; DASH-SP) for making multiple-RH hygroscopicity measurements on timescales short enough for aircraft deployment in the field. Chapter 3 presents the first results from aircraft deployment of the DASH-SP, chemical composition data from an Aerosol Mass Spectrometer (AMS) to determine the effect of chemical composition on aerosol hygroscopicity in an anthropogenically-influenced marine environment off the coast of Central California. Chapter 4 represents the results from a major ground-based sampling campaign conducted on the Caltech campus in Pasadena, CA during the summer of 2009, dubbed the Pasadena Aerosol Characterization Observatory (PACO).

A suite of instruments measured chemical composition, microphysical properties, and hygroscopicity during the study, and results indicate the impact of SOA production and transport on aerosol composition, size distributions, and water uptake characteristics. Chapter 5 focuses on measurements of water soluble organic carbon (WSOC) during a period near the end of PACO, when the sampling site was impacted by a major forest fire event. Finally, Chapter 6 presents results from aircraft deployment of the DASH-SP during the CalNex field campaign in May of 2010, exploring the connection between submicron aerosol composition from the AMS and aerosol water uptake characteristics. Finally, the appendix contains a number of field and laboratory studies utilizing data from both the DASH-SP and a Particle-into-Liquid Sampler (PILS).

Chapter 2

Rapid Size-Resolved Aerosol Hygroscopic Growth Measurements: Differential Aerosol Sizing and Hygroscopicity Spectrometer Probe (DASH-SP)*

*Reproduced with permission from “Rapid Size-Resolved Aerosol Hygroscopic Growth Measurements: Differential Aerosol Sizing and Hygroscopicity Spectrometer Probe (DASH-SP)” by A. Sorooshian, S.P. Hersey, F. J. Brechtel, A. Corless, R.C. Flagan, and J.H. Seinfeld, *Aerosol Science and Technology*, 42 (6), 445–464, 2008. Copyright 2008 by the American Association for Aerosol Research.

2.1 Abstract

We report on a new instrument developed to perform rapid, size-resolved aerosol hygroscopicity measurements. The differential aerosol sizing and hygroscopicity spectrometer probe (DASH-SP) employs differential mobility analysis in-concert with multiple humidification and optical sizing steps to determine dry optical size and hygroscopic growth factors for size-selected aerosols simultaneously at three elevated relative humidities. The DASH-SP has been designed especially for aircraft-based measurements, with time resolution as short as a few seconds. The minimum particle diameter detected with 50% efficiency in the optical particle counters (OPCs) is 135 ± 8 nm, while the maximum detectable particle diameter is in excess of 1 μm . An iterative data processing algorithm quantifies growth factors and “effective” refractive indices for humidified particles using an empirically-derived three-dimensional surface (OPC pulse height - refractive index - particle size), based on a calculated value of the “effective” dry particle refractive index. Excellent agreement is obtained between DASH-SP laboratory data and thermodynamic model predictions for growth factor dependence on relative humidity for various inorganic salts. Growth factor data are also presented for several organic acids. Oxalic, malonic, glutaric, and glyoxylic acids grow gradually with increasing relative humidity up to 94%, while succinic and adipic acids show no growth. Airborne measurements of hygroscopic growth factors of ship exhaust aerosol during the 2007 Marine Stratus/Stratocumulus Experiment (MASE II) field campaign off the central coast of California are presented as the first report of the aircraft integration of the DASH-SP.

2.2 Introduction

Uptake of water by atmospheric aerosols is important in a variety of phenomena: light scattering, ability to act as cloud condensation nuclei, and deposition within the human respiratory system. Aerosol hygroscopicity measurements have been made with a variety of systems (Table 2.1). The parameter normally quantified is the diameter growth factor ($GF = D_{p,wet}/D_{p,dry}$). Laboratory growth factor measurements are commonly performed by levitating a particle in an electrodynamic

balance (Cohen et al., 1987; Tang and Munkelwitz, 1993, 1994a,b; Chan et al., 1997; Peng et al., 2001; Peng and Chan, 2001). This method probes single, laboratory-generated particles, directly measuring the mass change in response to humidity variation. The need to directly measure the growth factor of ambient aerosols led to the development of the hygroscopicity tandem differential mobility analyzer (HTDMA, Liu et al., 1978; Sekigawa, 1983; Rader and McMurry, 1986), in which dry particles of a selected size are exposed to a specific relative humidity (RH), after which the wet size is measured by classifying the grown particles with a second DMA, and counting with a condensation particle counter (CPC). Owing to the long duration of time required to measure the size distribution of the grown particles using a DMA, the HTDMA technique is relatively slow. However, both techniques above enable high-precision measurements of the growth factor.

While these methods have produced important insights into the hygroscopic behavior of atmospheric aerosols, the long time required to determine growth factors for different particle sizes and RHs makes them impractical in a number of important measurement scenarios in which the properties of sampled particles vary rapidly, especially during airborne measurements. A number of alternate methods, which are described in detail in Table 2.1, have been employed to probe the hygroscopic properties of the atmospheric aerosol more rapidly than is possible with the HTDMA. Several of these methods probe the entire aerosol as measured at different humidities, using nephelometers to probe ensemble light scattering (Rood et al., 1985; Dougle et al., 1998; Carrico et al., 1998, 2000; Sheridan et al., 2002; Magi and Hobbs, 2003; Kim et al., 2006), or measuring aerosol size distributions with optical particle sizing instruments in parallel (Kotchenruther and Hobbs, 1998; Hegg et al., 2006, 2007; Snider and Petters, 2007), or multiple DMAs operated in parallel (Wang et al., 2003). The use of an optical particle counter (OPC) in place of a DMA detector is not new, as several investigators (Covert et al., 1990; Hering and McMurry, 1991; Brand et al., 1992) used OPC detection of mobility-classified particles to gain insight into the mixing state of atmospheric aerosol and to determine their optical properties. One approach that attempts to provide the resolution of the HTDMA without the response time limitations is to classify particles with a DMA operated at one RH, equilibrate the classified particles at a second RH, and then measure the resulting size

distribution using a fast particle sizer such as an OPC. Kreisberg et al. (2001) classified particles at a high RH, dried the classified particles, and measured the dry particle size using an OPC in an instrument they called the relative humidity-moderated differential mobility optical particle size spectrometer (RH-DMOPSS). The RH-DMOPSS, which is an extension of the DMOPSS design of Stolzenburg et al. (1998), measures shrinkage by drying rather than growth upon humidification like most other hygroscopic growth instruments. The RH-DMOPSS is an improvement upon the HTDMA in that it is faster and can measure a larger range of particle sizes ($0.1 - 1.1 \mu\text{m}$). However, this instrument provides a growth factor at only one RH at any given time.

In this paper, we describe a new instrument that enables simultaneous determination of growth factors at several RHs, and that overcomes the challenges of determining the size of dry particles with unknown composition. The instrument has been designed especially for aircraft-based measurements. The differential aerosol sizing and hygroscopicity spectrometer probe (DASH-SP), developed by Brechtel Manufacturing Inc. (<http://www.brechtel.com/>), employs DMA classification of dry aerosol particles, equilibrates the classified particles to a new RH, and then measures the sizes of the grown particles using an OPC. An iterative data processing algorithm quantifies growth factors and “effective” refractive indices (n) for wet particles based on a calculated “effective” dry particle refractive index; iterations are performed on a three-dimensional surface (pulse height - n - D_p) based on dry particle calibration data from several salts with known refractive indices. By operating four controlled-RH channels in parallel and equipping each of the humidified channels with a separate OPC, hygroscopic growth factors can rapidly be determined at a number of particle sizes without having to incur the time delays required to stabilize a humidification column to a new RH. Depending upon the concentration and size distribution of the aerosol sampled, the growth factors of particles at any selected size within the size resolution of the instrument can be determined in as little as a few seconds.

We present first an overview of the design of the DASH-SP instrument. Results from laboratory characterization tests illustrate the performance of the instrument, including size detection limits, time resolution, stability, accuracy, and inherent uncertainties. The data processing algorithm is

subsequently described, which is used to convert pulse height data to growth factors. Hygroscopicity measurements for various inorganic salts and organic acids are compared to theoretical predictions for growth factor dependence on RH. Finally, airborne field measurements establish that the DASH-SP is capable of measuring growth factors at multiple sizes and RHs with a time resolution as much as two orders of magnitude shorter than that of the HTDMA.

2.3 DASH-SP Description

The DASH-SP, illustrated in Fig. 2.1, couples a single classification DMA system with a set of growth factor measurement systems that are operated in parallel. The modules that comprise the instrument are, in the order in which the aerosol experiences them: (1) an aerosol drier; (2) an aerosol neutralizer; (3) a classification DMA that selects the dry mobility size range for which growth factor measurements are made; (4) a set of parallel aerosol conditioning modules in which the aerosol is brought to equilibrium at controlled RHs; and (5) a detector at the outlet end that determines the total particle concentration leaving the DMA, and the size distributions of the particles after RH equilibration. The aerosol path through the instrument will now be described in detail.

A 0.5 LPM aerosol sample flow first passes through a Nafion drier (described below), and then passes through a ^{210}Po neutralizer that brings the dried particles to a stable, steady-state charge distribution. The aerosol then enters a cylindrical DMA with a 33.9-cm-long classification column, and inner and outer radii of 62.4 mm and 72.3 mm, respectively. The DMA sheath flow rate is 5 LPM. The DMA selects particles in a narrow interval of mobility-equivalent diameters in the 0.1 to 1.0 μm range. The minimum voltage at which particles are classified is 281 V (to select 150 nm diameter particles), so Brownian diffusion does not significantly broaden the DMA transfer function (Flagan, 1999), and the transmission characteristics of the DMA closely approach the ideal, nondiffusion transfer function of Knutson and Whitby (1975). Particles larger than 1 μm can be classified by operating the DMA at lower flowrates, although the fraction of particles that carry multiple charges will become significant, making data analysis more difficult. For the present purposes, we shall limit discussion to measurement of growth factors of particles with dry diameters

of 1 μm or smaller. The classified aerosol leaving the DMA is split into five separate flows. The total concentration of classified particles is determined, without further conditioning of one of the five flows, by measuring the dry, classified particles using an integral TSI Model 3781 water-based condensation particle counter (CPC). The CPC serves as a redundant particle number concentration measurement against which data from the OPCs, to be described below, can be compared.

The remaining four classified aerosol flows are used to measure growth factors. They first pass through a Perma Pure, LLP, Nafion humidifier (Model MD-070-24FS-4) that consists of a Nafion membrane tube that is enclosed in a coaxial tube. The Nafion efficiently transmits water through the membrane, enabling the small aerosol flow through the center tube to equilibrate with the RH of the larger flow between the membrane and the outer shell. The RH of that larger flow is adjusted by mixing of dry air with air that has been saturated with water vapor by passage through a Nafion tube coil that is immersed in a warm water bath. Feedback control using an RH sensor (Model HMP50YCC1A2X, Vaisala) ensures that a constant, predetermined RH is achieved in both the conditioned aerosol flow, and the outer flow. One humidifier is kept dry ($< 8\%$ RH), while the other three are operated at higher and different RHs. The maximum RH is typically below 94% in order to prevent condensation within the instrument, although higher RH can be used for short periods of time.

The aerosol growth factor is measured as a surrogate for particle growth in response to humidity changes in the atmosphere where sufficient time is generally available for the droplets to fully equilibrate with atmospheric water vapor. To simulate the atmospheric response effectively, the time in the conditioning columns must be sufficient to ensure full equilibration. The characteristic time for a droplet to reach thermodynamic equilibrium with water vapor in unsaturated conditions (RH $< 100\%$) is estimated to be on the order of microseconds (Pilinis et al., 1989). The ~ 4 s residence time within each conditioning column is sufficient to ensure equilibration. Moreover, as described below, the outer flow from the Nafion humidifier is used as a sheath flow within the OPC to ensure that the equilibrium is maintained to the point of measurement.

The four conditioned aerosol flows pass directly to dedicated, custom-built OPCs, designed to

detect particles in the 100 nm to 3 μm diameter size range. To ensure that particles pass through the $1.4 \times 10^{-3} \text{ mm}^3$ view volume of the collection optics, the aerosol (0.06 LPM) and a coaxial sheath flow (4 LPM) are focused by acceleration through a nozzle. Laboratory tests have shown that the sheath and aerosol streams do not mix. The view volume of the OPCs is determined by calculating the intersection volume of the cylindrical particle beam and the laser light sheet through which particles pass. The design of the laser light sheet is such that all particles that enter the OPC optical cavity pass through the light. The thickness of the laser light sheet is measured in two ways: 1) projecting the laser against a distant surface and then measuring the projected width with a vernier caliper while using a light meter to define the edges of the light; and 2) by using an oscilloscope to measure the pulse width and, therefore, the transit time of individual particles through the light sheet. The particle velocity is calculated using the known flow rate through the accelerating nozzle. By multiplying the velocity by the transit time, the thickness of the laser light sheet is determined. The two methods for measuring the light sheet thickness agree to within 15% and found a thickness of 0.015 mm. However, the light sheet does not have perfect edges. Therefore, larger particles are observed above the comparator threshold for slightly longer pulse widths.

To minimize size changes during measurements, the OPCs measure scattering of light from single particles as they pass through the laser light sheet originating from the diode laser ($\lambda = 532 \text{ nm}$, World Star Technologies, Model TECGL-30). Scattered light is collected using an elliptical mirror from a wide angle ($+64^\circ/-50^\circ$ in vertical plane and $+/-74^\circ$ in horizontal plane) in the near forward direction to integrate over the Mie resonances, thereby minimizing intensity oscillations that might otherwise lead to ambiguity in size determination. A cone of scattered light ($+/-22^\circ$) emanating from the view volume along the axis of the laser is not collected due to a pass-thru hole in the elliptical mirror that is needed to allow the laser to exit the optical cavity. The mirror focuses the scattered light onto a photomultiplier tube (PMT, Hamamatsu Model H6779-02). RH, temperature (T), flow, and pressure (P) sensors monitor conditions of all flows, both upstream and downstream (except flow) of each OPC.

The DASH-SP employs two data acquisition systems: a high-speed system to acquire the pulse

data produced by the photomultipliers, and a second system to monitor signals from the slower sensors used to record T , RH, DMA size selection, DMA voltage, OPC gain settings, etc. The signal from the PMT is processed through two gain stages, low gain for measurement of particles larger than about 450 nm, and high gain for particles in the $135 < D_p < 450$ nm size range. The instrument automatically selects the appropriate gain stage according to the size expected for that channel. A four-channel high-speed digitizer (National Instruments™, Model PCI-6132) accumulates the logarithmically amplified, detected peak PMT signals from individual particles for count rates up to $2.5 \times 10^6 \text{ s}^{-1}$, corresponding to a concentration of $2.5 \times 10^6 \text{ cm}^{-3}$. Particle coincidence, which occurs when multiple particles are simultaneously in the OPC view volume, is a function of particle number concentration, view volume, and particle size. The coincidence performance of the OPC was validated by simultaneously sampling the same DMA-selected particles with two CPCs and the OPC. One CPC sampled upstream of the OPC, while the second CPC sampled downstream of the OPC. The maximum coincidence error associated with the laboratory and field measurements during this study is 3%, while the 1% particle coincidence concentration limit is approximately 5000 cm^{-3} and 350 cm^{-3} for the smallest (~ 135 nm for high gain) and largest (~ 450 nm for high gain) detectable particles, respectively, in the OPCs.

The DASH-SP can be operated manually or autonomously. In manual operation, the user specifies the RH for each humidifier, the size of particles to be selected by the DMA, and the number of particles to be sized by the OPC for each RH channel. The autonomous mode can step through a number of particle sizes and RHs, measuring a specified number of particles for each D_p /RH combination. Changing the RH on any conditioning column slows the measurements due to the time required for the RH to stabilize after such a change. The typical RH equilibration time needed after a step change in RH from $< 10\%$ to be within $\pm 1\%$ of 74%, 85%, and 92% was determined to be 236 ± 61 s, 372 ± 106 s, and 569 ± 97 s, respectively ($n = 11$); these equilibration times represent an upper limit since smaller changes in RH within these broad ranges would ideally be carried out during experiments.

2.4 Experimental Methods

A series of laboratory experiments were conducted to characterize the DASH-SP while it operated in the manual mode. For all characterization tests described below, test salt aerosols were employed. Salt solutions were prepared by mixing a known amount of salt with Milli-Q water, usually resulting in 0.2% (by mass) solutions. A compressed air source, with a downstream high-efficiency particulate air (HEPA) filter to remove particulate contaminants, supplied flow to a stainless steel, constant-rate atomizer (Liu and Lee, 1975) and sheath air flows for the DMA and OPCs. A dilution flow system was used to maintain atomizer output particle number concentrations below 1000 cm^{-3} at a DMA-selected size.

The DASH-SP was also deployed on the Center for Interdisciplinary Remotely-Piloted Aircraft Studies (CIRPAS) Twin Otter aircraft in the July 2007 Marine Stratus/Stratocumulus Experiment (MASE II) campaign, in which airborne aerosol and cloud measurements were carried out off the central coast of California. For the duration of the field study, the instrument operated in the autonomous mode where the scan sizes and minimum OPC pulse count quantities were pre-programmed. We briefly present data from one particular flight to report the first airborne deployment of the DASH-SP; a more comprehensive analysis of data from this entire campaign will be presented in subsequent work.

2.5 Instrument Characterization

2.5.1 Size Limits of OPC Detection

The range of particle sizes in which characterization experiments are carried out depends on the OPC size detection limits. The optical properties of salts vary, so the size detection limit of the OPCs is a function of the composition of an aerosol sample. By sampling a set of 16 different species (10 inorganic, 6 organic), the minimum particle diameters detected with 50% efficiency in the OPCs were found to be $135 \pm 8 \text{ nm}$ and $234 \pm 16 \text{ nm}$ for high- and low-gain settings, respectively. The variation in OPC response as a function of refractive index is contained within the standard deviations, which

reflect the variability among the ensemble of salts tested. The maximum size that can be detected accurately by the OPC is approximately 450 ± 30 nm with the high-gain setting, and beyond 1 μm with the low-gain setting. However, uncertainties associated with multiply charged particles are enhanced when detecting particles of increasing size, especially near 1 μm . Also, electrical saturation of the OPCs results in enhanced uncertainties starting at $D_p > 450$ nm (high gain) and $D_p > 700$ nm (low gain).

2.5.2 Time Resolution

The time resolution of the instrument is determined by three factors: 1) the transport delays between the point where particles enter the DASH-SP or, for a steady aerosol, where they enter the DMA, and the OPC detectors; 2) delays associated with programmed changes in the sampled particle size; and 3) the time required to obtain statistically significant counts in each OPC channel. A maximum transition time of 17 s is needed when switching between different DMA-selected sizes for normal operating conditions in order to ensure particles of the previous size have exited the system; this addresses the first two factors governing time resolution. The tubing length of each stream from the 5-way splitter (see Fig. 2.1) to each humidification chamber and OPC is equivalent, which results in the same particle transit time in each channel. Tests were performed to estimate the minimum number of particles at a given size required to obtain a response with varying degrees of statistical significance. These tests indicate the length of time the instrument should sample at a given set of operating conditions to obtain representative growth factors. Sample sets of over 10,000 pulses were obtained for a selected particle size for different salts ($D_p = 150 - 404$ nm). Pulses were randomly removed from each data file in a way to determine the variation of the modal pulse height and standard deviation as a function of decreasing counts at a fixed particle size. The ratio of standard deviation to modal pulse height is usually within 10% for pulse numbers ranging from 50 to 10,000. The variation of the modal pulse height is $\pm 1\%$ when comparing pulse counts of over 10,000 to any number of counts down to 50, below which the difference increases relatively quickly. In order for the standard deviation of observed pulse heights to be within 10%, 5%, and 1%

of the original standard deviation calculated for a population of over 10,000 particles, an average of 60, 220, and 530 pulses are required, respectively. Figure 2.2 displays the time required to satisfy these different limits of the original modal pulse height and standard deviation for a wide range of particle number concentrations at a selected dry diameter. For example, for 10 particles cm^{-3} at a DMA-selected size, a minimum of 5 s is needed to be within 1% of the modal pulse height had over 10,000 particles of the same composition been sampled. An additional order of magnitude of time is required to be within 1% of the original standard deviation as compared to 1% of the original mode. As will be shown subsequently, the mode is the critical parameter in quantifying growth factors via the iterative data processing technique. Assuming a pulse height distribution with a distinct and dominant mode (there are often less dominant modes due to multiply-charged particles), the data processing algorithm will determine the correct pulse height distribution mode regardless of the variance in the distribution. Thus, sampling time at a given D_p/RH combination should be reduced to improve time resolution at the expense of variance, which ultimately has no effect on the accuracy of quantified growth factors.

2.5.3 DASH-SP Accuracy, Precision, and Uncertainties

The uncertainty of the DASH-SP measurement of growth factor depends on the uncertainties in the RH and sizing (DMA and OPC) measurements. Critical to the accuracy of the RH measurements is the calibration procedure. One “reference” RH sensor (Model HMP50YCC1A2X, Vaisala) was initially calibrated over six saturated salt solutions within the 8 – 97% RH range. The remaining 12 RH sensors were then calibrated as an ensemble against the “reference” sensor in a temperature-controlled chamber through which a controlled mixture of dry and humid air was circulated. The accuracy of the RH measurements was evaluated by comparing theoretical deliquescence RH (DRH) for multiple salts with measurements. The DRHs of ammonium sulfate, sodium sulfate, and potassium chloride aerosols agreed with literature values (Seinfeld and Pandis 2006) to within $\pm 1.0\%$, while sodium chloride aerosols agreed to within $\pm 1.6\%$. The overall RH measurement uncertainty was calculated by taking the summed root mean square errors of the measured OPC sample and

sheath flow RHs, and combining this with the uncertainty associated with the RH sensors. The overall uncertainty was usually $\pm 1.5\%$, while the RH sensor precision was $\pm 0.7\%$.

Temperature fluctuations and gradients within each of the four humidification chamber-OPC units can lead to uncertainties due to the RH changing. Temperature sensors monitoring the sheath, sample, and exit flows of each OPC exhibited no significant change ($T < 1^\circ \text{C}$) during laboratory scans that lasted as long as ~ 10 min, but temperatures did show a systematic increase ($\Delta T > 1^\circ \text{C}$) over longer periods of time. During aircraft flights lasting 5 h in which the DASH-SP was deployed, the twelve temperature sensors recorded the same level of variation. For example, the twelve sensors during one representative flight exhibited averages between $24.0 - 25.0^\circ \text{C}$ and standard deviations between $3.0 - 3.5^\circ \text{C}$. However, the RH sensors exhibited significantly less variation due to the feedback control of the humidification by the instrument software: the RH standard deviation ranged between $0.1 - 1.8\%$ for OPCs with upstream humidification chambers equilibrated at RHs of 74%, 85%, and 92%. Therefore, the RH variation resulting from temperature fluctuations in the humidification chamber-OPC units is normally within the uncertainty of the RH sensor measurements.

The instrument software calculates the DMA voltage required to classify a selected dry size for the specific geometry and operating parameters (T , P , flow rates) of the DMA. Since the DMA sheath flow rate is usually 10 times larger than the aerosol flow rate and relatively large particles are studied, the width of the sampled electrical mobility window is $\pm 10\%$. DMA performance was frequently evaluated with calibrated PSL particles ranging in diameter between 152 - 1101 nm. Accurate DMA operation is exhibited when the maximum particle concentration is observed at the DMA-selected size that matches the actual size of the PSL particles, rather than a smaller or larger size. The maximum particle concentration was observed to occur at DMA-selected sizes within $\pm 3\%$ of the actual size of the PSL particles tested. It should be noted that the PSL particles studied have a reported size uncertainty ranging from $\pm 1 - 3\%$. The average uncertainty associated with growth factor measurements is calculated to be $\pm 4.3\%$, with an uncertainty as high as 8% at a dry size of 150 nm at lower RHs ($< 80\%$).

Tests were done to check for contamination both in the form of leaks and in the source of Milli-Q

water used in atomizing solutions. When feeding filtered air into the DASH-SP frequently over a period longer than 30 days, no particles were detected by the CPC and fewer than 1 cm^{-3} were detected by the OPC (high gain). Particles detected by the OPC corresponded to sizes below the 50% detection limit of the OPC ($D_p < 135 \text{ nm}$). Pure Milli-Q water was atomized into the DASH-SP system; no particles were detected by the CPC beyond 135 nm, and $< 1 \text{ cm}^{-3}$ were detected by the OPC (high gain). Below 135 nm, background particle concentrations measured by the CPC reached a value as high as 30 cm^{-3} at 5 nm; the OPC response at these lower sizes remained at $< 1 \text{ cm}^{-3}$. No background particle signals were observed using the low-gain OPC configuration for these tests. Since the experiments conducted with salts usually involved OPC number concentrations between $100 - 1000 \text{ cm}^{-3}$ at a specific size, any background particles from the water source and inside the system itself are deemed negligible. Moreover, since no particles larger than 135 nm were observed by the OPC for these tests, contamination is negligible for ambient sampling, as the system is designed to sample at minimum dry D_p exceeding 135 nm (150 nm for this study).

2.5.4 Stability

The stability in dry and wet particle data was studied. For dry data, stability was quantified over a time span of four months by calculating pulse height standard deviation relative to pulse height average for both gain settings and different particle sizes (Fig. 2.3). Above 200 nm, at the high-gain OPC setting, is $< 10\%$, with the species of greatest atmospheric relevance (ammonium sulfate, ammonium nitrate, sodium chloride) being $< 3\%$. For the low-gain setting, is $< 10\%$ at 350 nm and $\leq 5\%$ beyond 350 nm for all species studied. For wet studies, the stability in growth factor at different initial dry sizes and RHs between 30 – 92% was quantified for several species, where was usually $< 3\%$ for all species studied. In summary, the stability of the DASH-SP improves for both dry and wet particles with increasing size above the 50% detection limit of the OPC.

2.6 Data Analysis

Data resulting from the collection of scattered light from individual particles are returned by the OPCs as pulse heights, the amplitudes of which depend on particle size, shape, and refractive index, the latter depending on particle composition. For the purposes of pulse height data interpretation, the following assumptions are made: (1) purely scattering, spherical particles (one exception to the sphericity assumption for growth factor calculations is that a shape factor of 1.08 was assumed for dry sodium chloride particles, thought to be cubic, prior to humidification (Hinds, 1999; Hameri et al., 2000); (2) the DMA-selected particle size corresponds to the mode of the true particle size distribution, and therefore, the mode of the OPC pulse height distribution; and (3) for particles that undergo humidification, the mode of the OPC pulse height distribution represents the true wet particle size. The first assumption is an approximation for ambient particles, but has been commonly made in previous DMA-OPC studies (Stolzenburg et al., 1998; Hand et al., 2000; Ames et al., 2000; Kreisberg et al., 2001; Hand and Kreidenweis, 2002). Growth factors are calculated using the volume-equivalent diameter (D_p), while the DMA classifies particles based on their mobility-equivalent diameter ($D_{p,mob}$), the two diameters of which are only equivalent for spherical particles. Following the methodology of Gysel et al. (2002), employing a shape factor of 1.08 for dry sodium chloride particles results in a value of 0.96 for the ratio $D_p:D_{p,mob}$. This provides a representative indication of the sensitivity of growth factor measurements to particles with one type of shape effect (cubic rather than spherical); without the shape factor correction, growth factors for sodium chloride particles would be underestimated by 4%. The volume of water in particles after humidification is often substantial; the assumption that particles are spherical and scatter, but do not absorb, light is generally valid for those particles for which growth is significant.

Before the pulse height distribution modes can be used to determine the particle size and refractive index, dry particle calibrations must be performed to accumulate sufficient data relating pulse height, particle size, and refractive index. OPC calibrations were carried out for a set of six salts of known refractive index (1.39, 1.47, 1.50, 1.52, 1.54, and 1.60; salts listed in Fig. 2.4) (Weast and Astle, 1987; Lide, 2005) by measuring OPC pulse height response to a range of DMA-selected diam-

eters (150, 175, 200, 225, 250, 300, 350, 375, 404, and 415 nm) without humidification. Figure 2.4 summarizes the OPC response as a function of dry particle size for salts of different refractive index from one set of calibrations. For each OPC, high-order polynomial equations accurately represent the relationship between OPC pulse height and particle dry diameter for different refractive indices ($R^2 > 0.995$), allowing calculation of size from a given refractive index and OPC pulse height:

$$D_{p,dry} = a_5x^5 + a_4x^4 + a_3x^3 + a_2x^2 + a_1x + a_0 \quad (2.1)$$

where x = OPC pulse height and constants $a_0 - a_5$ are determined using calibration data. The relationship between OPC pulse height and refractive index for specific particle dry diameters can be modeled as a cubic polynomial ($R^2 > 0.996$), allowing calculation of refractive index from OPC pulse height at a given dry particle size:

$$\text{Refractive index} = b_3x^3 + b_2x^2 + b_1x + b_0 \quad (2.2)$$

where x = OPC pulse height and constants $b_0 - b_3$ are determined using calibration data. Using Eq. 2, OPC response curves for different dry particle sizes were extrapolated to calculate pulse heights for refractive indices between 1.33 and 1.39 for which calibration salts were not tested (water has a refractive index of 1.33). A three-dimensional surface can now be generated with the following equation, which is derived from multiple regression analysis:

$$\text{Pulse height} = c_5 + c_4D_p + c_3n + c_2D_p^2 + c_1n^2 + c_0D_pn \quad (2.3)$$

where n is refractive index and D_p corresponds to particles in their dry or wet state.

Figure 2.5 summarizes the algorithm used to calculate “effective” refractive index and growth factor from the dry and wet pulse height distribution modes. Initially, the dry pulse height distribution mode is used to iterate on a two-dimensional surface (n vs pulse height, fixed D_p) to determine the dry particle “effective” refractive index. After guessing a value for the wet particle diameter, a volume-weighted refractive index is calculated to account for the refractive index of both water

and the dry particle. Using the wet particle pulse height data, iterations are carried out on the three-dimensional surface to converge on a value for the humidified particle's "effective" refractive index, which is subsequently used to determine the wet particle diameter and growth factor. This iterative process is not possible without a priori knowledge of the dry particle refractive index, which requires one of the four humidification chambers to be operated in the dry state. This algorithm assumes that particles are internally mixed and that particulate matter is completely dissolved in humidified particles.

One exception to the iterative procedure for humidified particles is when testing laboratory-generated aerosols with known dry-particle refractive indices; a thermodynamic model of particle water uptake (Brechtel and Kreidenweis, 2000a,b) can predict the refractive index for a specific salt at a given RH. Only one step is then needed to interpolate on the three-dimensional surface (D_p vs. pulse height, fixed n) to determine the true wet particle size. The modified Köhler model used includes a parameterization for the solution osmotic coefficient that approaches the correct thermodynamic limit as the solution becomes infinitely dilute (Brechtel and Kreidenweis, 2000a,b). Predictions from both this model and the Aerosol Inorganics Model (AIM, Clegg et al., 1998, available online: <http://www.aim.env.uea.ac.uk/aim/aim.html>) are used below for comparison with laboratory data for a number of salts.

2.7 Growth Factor Measurements

2.7.1 Inorganic Salts

Experiments were carried out to determine growth factor values as a function of RH, from 10% to 94%, for different inorganic species (ammonium nitrate, ammonium sulfate, ammonium nitrate, sodium chloride, potassium chloride, and sodium sulfate) and organic acid species (oxalic, glyoxylic, malonic, succinic, glutaric, and adipic acids). The growth factors for these species are either known or can be calculated theoretically to assess the accuracy of the DASH-SP measurements. However, only the inorganics provide a firm comparison between theory and/or laboratory measurements with

those of the DASH-SP since growth factors for organic acids are not as well established as those for inorganic salts.

Figure 2.6 shows the measured hygroscopic growth curves for various inorganic and organic acid species. With the exception of the organic acids and ammonium nitrate, a sharp increase in growth factor is observed at the DRH, providing evidence for the homogeneity of the humidity field experienced by the particles. The measured growth factors of the inorganic species agree well with thermodynamic theory for RH values above the DRH ($\pm 1\%$). For ammonium sulfate at an RH of 92% the discrepancy is $\pm 4\%$ based on the Brechtel and Kreidenweis (2000a,b) model, and $\pm 1\%$ based on the Clegg et al. (1998) model. Growth factor measurements at RH values above the DRH show the following levels of agreement with thermodynamic theory: sodium chloride (1.0% above theory, $\sigma = 2.3\%$, $n > 50$), ammonium sulfate (1.5% above theory, $\sigma = 1.7\%$, $n > 50$), sodium sulfate (2.0% below theory, $\sigma = 2.4\%$, $n > 50$). Ammonium nitrate particles have been shown to remain “wet” at RHs as low as 8% (Dougle et al., 1998; Lightstone et al., 2000), which explains why the observed growth factors exceed unity for RHs below the DRH. Multiple growth factor curves are reported for ammonium nitrate in Fig. 2.6 to show that at sizes near 250 nm, the growth factors increase with higher dry particle sizes.

2.7.2 Organic Acids

In contrast to inorganic species, the hygroscopic properties of organic aerosol species are not as well known. Organic acids are an important component of atmospheric aerosols (Kawamura and Ikushima, 1993; Khwaja, 1995; Chebbi and Carlier, 1996; Saxena and Hildemann, 1996; Kawamura and Sakaguchi, 1999; Kerminen et al., 2000; Yao et al., 2004; Huang et al., 2005; Fisseha et al., 2006; Sorooshian et al., 2007b), the presence of which can affect the hygroscopicity of ambient particles (Saxena et al., 1995; Hansson et al., 1998; Ansari and Pandis, 2000; Cruz and Pandis, 2000; Peng et al., 2001; Peng and Chan, 2001; Prenni et al., 2001, 2003; Wise et al., 2003). Two- to six-carbon dicarboxylic acids are investigated here, in addition to glyoxylic acid, which is a direct precursor to oxalic acid, the most abundant particulate dicarboxylic acid in the atmosphere (Kawamura and

Ikushima, 1993; Kawamura and Sakaguchi, 1999; Kerminen et al., 2000; Poore, 2000; Yao et al., 2004; Crahan et al., 2004; Yu et al., 2005; Huang et al., 2005, 2006; Sorooshian et al., 2006b, 2007a,b).

Oxalic (C_2), malonic (C_3), glyoxylic (C_2), and glutaric (C_5) acids do not exhibit a DRH, but rather grow gradually with increasing RH (Fig. 2.6). This result is consistent with previous studies which showed that organic acids absorb water at all RHs (Saxena and Hildemann, 1997; Dougle et al., 1998). Unlike the other organic acids studied, succinic (C_4) and adipic (C_6) acids exhibited no hygroscopic growth over the RH range studied, which is consistent with the HTDMA results of Prenni et al. (2001). With the exception of glyoxylic acid, previous studies have either measured or calculated DRHs for these organic acids; only malonic (DRH = 74 - 91%) and glutaric (DRH = 84 - 99%) acids exhibit DRHs in the range of RHs tested in this study, while the rest of the organic acids exhibit DRHs exceeding 97% (Saxena and Hildemann, 1997; Peng et al., 2001).

Excluding oxalic and glyoxylic acids, the experimental data in Fig. 2.6 indicate a clear odd-even carbon number effect, where the odd-carbon number organic acids (malonic and glutaric acids) exhibit relatively more hygroscopic growth as compared to the even-carbon number acids (succinic and adipic acids). This behavior is consistent with the literature (Saxena and Hildemann, 1996; Prenni et al., 2001); solubility alternates with the number of carbon atoms in the organic acid molecule up to C_{10} . Oxalic acid is significantly more hygroscopic than succinic and adipic acids, the other two even carbon-number dicarboxylic acids.

Growth factor values for dicarboxylic acids measured in this study tend to be lower than those predicted by the Brechtel and Kreidenweis (2000a,b). The growth factors for malonic acid showed the best agreement with predictions as compared to the other organic acids, with a growth factor that is at most 6% below that predicted. The measured growth factor for glutaric acid was at most 17% below predictions. Malonic and oxalic acids exhibited relatively similar growth factors up to an RH of 92% (1.53 ± 0.07 , 8% below theory, and 1.58 ± 0.07 , 26% below theory, respectively), while glutaric acid showed less growth (1.27 ± 0.05 , 19% below theory). Because thermodynamic parameters are not available for glyoxylic acid, only experimental results are shown; glyoxylic acid exhibits similar hygroscopic behavior when compared to oxalic, malonic, and glutaric acids. Glyoxylic acid has a

measured growth factor of 1.44 ± 0.06 at an RH of 92%.

Five potential explanations for the disagreement between measurements and predictions for the dicarboxylic acid growth factors include: (1) uncertainties in the model parameters used for each dicarboxylic acid (osmotic coefficient, surface tension, solution density); (2) particles did not crystallize during drying prior to size-selection by the DMA and, therefore, do not properly reflect the quantity of solute; (3) particles were non-spherical; (4) volatilization of the organic acids occurred; and (5) the dicarboxylic acid particles exhibit slower water uptake than the inorganic species studied and did not have enough time to reach equilibrium at a given wet RH. The extent to which each of the five aforementioned explanations leads to the discrepancy between predictions and measurements is not known. It is noted that the second, third, and fifth explanations would ideally lead to an underestimate of the growth factor. In particular, there is less known about the morphology of organics as compared to inorganic species, therefore, if the organic acid particles were not spherical or compact, then the experimentally determined growth factors are less than their actual values from a morphology standpoint. The measurements do provide evidence that ambient particles that contain organic acids, specifically oxalic, malonic, glutaric, and glyoxylic acids, experience growth at low RHs ($< 65\%$).

2.8 Validation of Iterative Data Processing Code

In order to assess the validity of the data processing technique for interpreting ambient data, the iterative procedure outlined in Fig. 2.5 was applied to data collected from wet ammonium sulfate experiments to quantify “effective” refractive index and growth factor as a function of RH. The three wet RHs used in the field study subsequently discussed, 74%, 85%, and 92%, were also applied in these wet ammonium sulfate tests ($n > 15$ at each RH). The measurements that have been processed with the iterative code are compared to predictions of the Brechtel and Kreidenweis (2000a,b) and Clegg et al. (1998) models. Figure 2.7 shows that, although the calculated “effective” refractive index at an RH of 74% agrees perfectly with the literature (Weast and Astle, 1987), the DASH-derived average growth factors exceed theory at this RH by as much as 8%. The measured growth

factors at RHs of 85% and 92% lie within one standard deviation of the model predictions, whereas the “effective” refractive indices agree to within 1%. This is a result of the fact that the calculation of growth factor in the iterative data processing code is more sensitive to DMA, OPC, and RH uncertainties as compared to calculation of refractive indices.

Figure 2.8 (A-C) shows examples of the dry and wet size distributions from wet ammonium sulfate data processed with the iterative code. Size distribution data are presented at four RHs (one dry, and three wet RHs) for each of three initial dry sizes (150, 175, and 200 nm). The size distributions for dry particles and those at an RH value of 74% should be identical since ammonium sulfate particles deliquesce at an RH of $79.9 \pm 0.5\%$ (Seinfeld and Pandis 2006). However, the mode diameters of the size distributions at RH = 74% slightly exceed those of the dry size distributions. The dry and RH = 74% size distributions are broader at a dry size of 150 nm than at the two larger sizes; this broadening behavior is normally observed when the particle size is close to the minimum OPC detection limit. There is variation in the growth factors at constant RH, as the range in values at RHs of 74%, 85%, and 92% is 0.04 (average $GF = 1.06$), 0.08 (average $GF = 1.59$), and 0.16 (average $GF = 1.80$), respectively. The differences in growth factor at constant RH for various dry sizes is attributable to uncertainties in the measurements and the iterative data processing procedure, particularly the cubic and high-order polynomial equations. However, all of the growth factors reported in Fig. 2.8 are within 10% of predictions from the Brechtel and Kreidenweis (2000a,b) and Clegg et al. (1998) models.

One would expect narrower size distributions for the dry ammonium sulfate results in Fig. 2.8 since the DMA is selecting one size. To determine whether the broadness of the dry ammonium sulfate size distributions is caused by an instrument issue or by impurities and morphology issues associated with ammonium sulfate particles, dry PSL size distributions were also computed since PSL particles are spherical (Fig. 2.8 D). The PSL size distributions are considerably narrower than those of dry ammonium sulfate particles, suggesting that the latter aerosol likely consisted of non-spherical particles that affect the final optical sizing; particle shape variations can significantly influence their scattering and absorption properties (Chylek et al., 1984; Videen et al., 1997). The

PSL size distributions for particle diameters of 152 nm and 404 nm were slightly broader than distributions at diameters of 199 nm and 300 nm, providing further evidence that the OPCs have somewhat lower size resolution near their minimum and maximum size detection limits. It is unlikely that particle coincidence plays a role in the broadening behavior apparent in Fig. 2.8. If this were the case, the same shape would be observed in the dry PSL distributions for all sizes shown. It is possible, however, that some of the broadening is also due to the particles experiencing a range of RHs.

These results suggest that the iterative procedure is capable of accurately determining refractive indices and providing dry and wet size distributions. Although the distributions may be broader close to the OPC size detection limits, the modes of these distributions can still be used to accurately calculate growth factors.

2.9 Field Implementation of DASH-SP

On July 16, 2007, by prior arrangement, the Twin Otter intercepted and repeatedly sampled the exhaust plume of a large PANAMAX container ship with a 55 MW main engine operating on heavy fuel oil. Figure 2.9A shows the flight tracks during the ship experiment. The aircraft first flew up the plume toward the ship, which was steaming directly into the wind, at an altitude of 30 m; this procedure was repeated three more times. The aircraft also performed several cross-wind transects of the plume at various altitudes in the marine boundary layer (< 250 m), which was clear on this day. Inside the plume, submicrometer particle number concentrations reached as high as $365,000 \text{ cm}^{-3}$, as determined with a differential mobility analyzer with a time resolution of ~ 73 s, whereas the background aerosol concentration outside of the plume was $< 500 \text{ cm}^{-3}$. The plume was ~ 0.4 km wide during the first downwind transect at an altitude of 30 m and it was 2 km wide during the second to last transect at an altitude of 150 m (the plume was not detected in the last transect at 210 m).

Figure 2.9B displays the water-soluble aerosol composition inside the plume as measured every 4.5 min (equivalent to a flown distance of ~ 13.5 km) by a particle-into-liquid sampler (PILS, Brechtel

Manufacturing Inc., Sorooshian et al., 2006a). The water-soluble aerosol mass, which reached values as high $93 \mu\text{g m}^{-3}$ just behind the ship, was composed mainly of sulfate ($96.2\% \pm 4.0\%$ of water-soluble mass; $n = 15$). Other water-soluble components of the aerosol included Na^+ ($1.0\% \pm 2.4\%$), NO_3^- ($1.0\% \pm 0.6\%$), organic acids ($0.6\% \pm 0.3\%$), Cl^- ($0.6\% \pm 0.9\%$), and NH_4^+ ($0.5\% \pm 0.4\%$). The aerosol was highly acidic, as the ammonium-to-sulfate molar ratio was, on average, 0.03. The ratio of water-soluble mass to the DMA-observed volume concentration of the aerosol was $1.13 \text{ g cm}^{-3} \pm 0.30 \text{ g cm}^{-3}$, suggesting that a significant fraction of the aerosol was accounted for by the PILS data, assuming that the ambient aerosol density was close to that of sulfuric acid (1.84 g cm^{-3}). As observed by an Aerodyne time-of-flight aerosol mass spectrometer, the aerosol contained a large proportion of hydrophobic organic species that were not detected by the PILS. It is likely that some of the hydrophobic species were light-absorbing, like soot, which introduces error in the iterative data processing algorithm because of non-zero imaginary components of the refractive index.

DASH-SP data are presented for the following dry diameters: 150, 175, 200, and 250 nm. The instrument was pre-programmed to detect a minimum of 300 pulses in each OPC channel for this flight. For 150 and 175 nm particles, 1 s and 10 s were usually required before all OPCs detected at least 300 pulses inside and outside of the ship plume, respectively. For 200 and 250 nm particles, 10 - 30 s and 10 - 60 s were required inside and outside of the plume, respectively.

The average dry “effective” refractive index of aerosol in the ship plume was determined to be 1.53 ± 0.04 , while the “effective” refractive index in the background aerosol outside of the plume was 1.49 ± 0.04 . It should be noted that the refractive indices of sulfuric acid, ammonium bisulfate, and ammonium sulfate are 1.41, 1.48, and 1.52, respectively (Weast and Astle, 1987; Ames et al., 2000). The time resolution of the DASH-SP is evident in Fig. 2.9C, which shows the spatial distribution of growth factors at an RH of 92%. In the ship plume, the average growth factors at RHs of 74%, 85%, and 92% were 1.11 ± 0.04 , 1.46 ± 0.09 , and 1.53 ± 0.10 , respectively. The corresponding growth factors in the background aerosol were 1.19 ± 0.09 (RH = 74%), 1.54 ± 0.05 (RH = 85%), and 1.63 ± 0.08 (RH = 92%). Therefore, the overall averages suggest that there was a decrease in hygroscopicity inside the ship plume as compared to the background marine aerosol at RHs \geq

74%. There was no significant difference in growth factor as the plane flew closer to the ship in its plume from a downwind distance greater than 30 km. We hypothesize that this occurred because the relative mass fractions of acidic sulfate and hydrocarbon-like organic species did not vary appreciably over the range of timescales of transport between the ship and aircraft. The observed growth factors in the plume are lower than what would be expected for pure sulfuric acid, and this is likely a result of the presence of other species, such as hydrophobic organics, in the particles that reduced the hygroscopicity.

2.10 Conclusions

This study introduces a new instrument, termed the differential aerosol sizing and hygroscopicity spectrometer probe (DASH-SP). In the instrument, a DMA-selected monodisperse aerosol flow is split into five flows, one to each of four OPCs with its own upstream humidification column, and one to a CPC. The DASH-SP has been designed for aircraft operation and other applications where hygroscopic growth observations are required at multiple sizes and RHs with high time resolution. An iterative data processing algorithm calculates growth factors and “effective” refractive indices for humidified particles based on a calculated value of the “effective” dry particle refractive index; iterations are performed on a three-dimensional surface (pulse height – refractive index – D_p) based on dry particle calibration data from several salts with known refractive indices.

Laboratory tests were performed to characterize the instrument’s performance. The minimum particle diameter detected with 50% efficiency in the OPCs is 135 ± 8 nm; particles with diameters > 1 μm are detected by the OPCs using the low-gain setting, subject to increasing uncertainty as a function of growing size due to multiply charged particles and electrical saturation of the OPCs. Estimates for the time required to obtain statistically significant counts in each OPC channel were reported for a wide range of particle number concentrations. The RH uncertainty is $\pm 1.5\%$ with an average uncertainty of $\pm 4.3\%$ for growth factor measurements. Measured DRHs of ammonium sulfate, sodium sulfate, and potassium chloride aerosols agree with literature values to within $\pm 1\%$, while that for sodium chloride aerosols agrees to within $\pm 1.6\%$. A high level of stability exists in

the dry salt calibrations and growth factors for various salts at RHs up to 92%, especially at particle diameters larger than the 50% detection limit of the OPCs.

Excellent agreement exists between growth factor data for several inorganic salts and predictions from a thermodynamic model. Growth factor data for organic acids show that, with the exception of oxalic and glyoxylic acids (both C₂ acids), the organic acids with an odd number of carbons (malonic and glutaric acids) exhibit greater hygroscopic growth than those with an even number (succinic and adipic acids). Succinic and adipic acids exhibit no hygroscopic growth up to an RH of 94%, while the other organic acids show gradual growth starting at low RHs (< 65%). Oxalic acid, the most abundant organic acid in ambient aerosols, exhibits the greatest hygroscopic growth among all of the organic acids studied.

The DASH-SP was successfully deployed in the 2007 Marine Stratus/Stratocumulus Experiment (MASE II) campaign on board the CIRPAS Twin Otter aircraft. Results are presented here for one flight during this study in which the plume from a large container ship was sampled. Growth factors of the exhaust plume aerosol downwind of this ship at RHs of 74%, 85%, and 92% were 1.11 ± 0.04 , 1.46 ± 0.09 , and 1.53 ± 0.10 , respectively. The field data demonstrate that the DASH-SP is capable of providing first-of-a-kind, rapid, simultaneous, size-resolved aerosol hygroscopic growth measurements at multiple RHs. Future work will address the instrument response to non-spherical and light-absorbing particles.

Acknowledgements

Brechtel Manufacturing Inc. acknowledges the support of Dr. Ronald Ferek and the ONR SBIR Program under grant N00014-05-C-0016. This work was also supported by the Office of Naval Research grant N00014-04-1-0118. We appreciate valuable comments and suggestions by Jeff Snider.

Bibliography

- Ames, R., Hand, J., Kreidenweis, S., Day, D., and Malm, W.: Optical measurements of aerosol size distributions in Great Smoky Mountains National Park: dry aerosol characterization, *J. Air Waste Manage.*, 50, 665–676, 2000.
- Ansari, A. and Pandis, S.: Water absorption by secondary organic aerosol and its effect on inorganic aerosol behavior, *Environ. Sci. Technol.*, 34, 71–77, 2000.
- Brand, P., Ruoff, K., and Gebhart, J.: Performance of a mobile aerosol spectrometer for an in situ characterization of environmental aerosols in Frankfurt City, *Atmos. Environ. A.*, 26, 2451–2457, 1992.
- Brechtel, F. and Kreidenweis, S.: Predicting particle critical supersaturation from hygroscopic growth measurements in the humidified TDMA. Part I: Theory and Sensitivity Studies, *J. Atmos. Sci.*, 57, 1854–1871, 2000a.
- Brechtel, F. and Kreidenweis, S.: Predicting particle critical supersaturation from hygroscopic growth measurements in the humidified TDMA. Part II: Laboratory and ambient studies, *J. Atmos. Sci.*, 57, 1872–1887, 2000b.
- Carrico, C., Rood, M., and Ogren, J.: Aerosol light scattering properties at Cape Grim, Tasmania, during the first Aerosol Characterization Experiment (ACE 1), *J. Geophys. Res.*, 103, 16 565, 1998.
- Carrico, C., Rood, M., Ogren, J., Neusüß, C., Wiedensohler, A., and Heintzenberg, J.: Aerosol Optical properties at Sagres, Portugal during ACE-2, *Tellus B*, 52, 694–715, 2000.
- Chan, C., Kwok, C., and Chow, A.: Study of hygroscopic properties of aqueous mixtures of disodium fluorescein and sodium chloride using an electrodynamic balance, *Pharmaceut. Res.*, 14, 1171–1175, 1997.
- Chebbi, A. and Carlier, P.: Carboxylic acids in the troposphere, occurrence, sources, and sinks: A review, *Atmos. Environ.*, 30, 4233–4249, 1996.

- Chylek, P., Ramaswamy, V., and Cheng, R.: Effect of graphitic carbon on the albedo of clouds, *J. Atmos. Sci.*, 41, 3076–3084, 1984.
- Clegg, S., Brimblecombe, P., and Wexler, A.: Thermodynamic Model of the System H^+ - NH_4^+ - Na^+ - SO_4^{2-} - NO_3^- - Cl^- - H_2O at 298.15 K, *J. Phys. Chem. A.*, 102, 2155–2171, 1998.
- Cohen, M., Flagan, R., and Seinfeld, J.: Studies of concentrated electrolyte solutions using the electrodynamic balance. 1. Water activities for single-electrolyte solutions, *J. Phys. Chem.*, 91, 4563–4574, 1987.
- Covert, D., Heintzenberg, J., and Hansson, H.: Electro-optical detection of external mixtures in aerosols, *Aerosol Sci. Tech.*, 12, 446–456, 1990.
- Crahan, K., Hegg, D., Covert, D., and Jonsson, H.: An exploration of aqueous oxalic acid production in the coastal marine atmosphere, *Atmos. Environ.*, 38, 3757–3764, 2004.
- Cruz, C. and Pandis, S.: Deliquescence and Hygroscopic Growth of Mixed Inorganic- Organic Atmospheric Aerosol, *Environ. Sci. Technol.*, 34, 4313–4319, 2000.
- Dougle, P., Veefkind, J., and ten Brink, H.: Crystallisation of mixtures of ammonium nitrate, ammonium sulphate and soot, *J. Aerosol Sci.*, 29, 375–386, 1998.
- Fisseha, R., Dommen, J., Gaeggeler, K., Weingartner, E., Samburova, V., Kalberer, M., and Baltensperger, U.: Online gas and aerosol measurement of water soluble carboxylic acids in Zurich, *J. Geophys. Res.*, 111, D12 316, 2006.
- Flagan, R.: On differential mobility analyzer resolution, *Aerosol Sci. Tech.*, 30, 556–570, 1999.
- Gysel, M., Weingartner, E., and Baltensperger, U.: Hygroscopicity of aerosol particles at low temperatures. 2. Theoretical and experimental hygroscopic properties of laboratory generated aerosols, *Environ. Sci. Technol.*, 36, 63–68, 2002.
- Hameri, K., Vakeva, M., Hansson, H., and Laaksonen, A.: Hygroscopic growth of ultrafine ammonium sulphate aerosol measured using an ultrafine tandem differential mobility analyzer, *J. Geophys. Res.*, 105, 22 231, 2000.

- Hand, J. and Kreidenweis, S.: A new method for retrieving particle refractive index and effective density from aerosol size distribution data, *Aerosol Sci. Tech.*, 36, 1012–1026, 2002.
- Hand, J., Ames, R., Kreidenweis, S., Day, D., and Malm, W.: Estimates of particle hygroscopicity during the Southeastern Aerosol and Visibility Study, *J. Air Waste Manage.*, 50, 677–685, 2000.
- Hansson, H., Rood, M., Koloutsou-Vakakis, S., Hameri, K., Orsini, D., and Wiedensohler, A.: NaCl aerosol particle hygroscopicity dependence on mixing with organic compounds, *J. Atmos. Chem.*, 31, 321–346, 1998.
- Hegg, D., Covert, D., Crahan, K., Jonsson, H., and Liu, Y.: Measurements of aerosol size-resolved hygroscopicity at sub and supermicron sizes, *Geophys. Res. Lett.*, 33, L21 808, 2006.
- Hegg, D., Covert, D., Jonsson, H., and Covert, P.: An Instrument for Measuring Size-Resolved Aerosol Hygroscopicity at both Sub-and Super-Micron Sizes, *Aerosol Sci. Tech.*, 41, 873–883, 2007.
- Hering, S. and McMurry, P.: Optical counter response to monodisperse atmospheric aerosols, *Atmos. Environ. A.*, 25, 463–468, 1991.
- Hinds, W.: *Aerosol technology: properties, behavior, and measurement of airborne particles*, Second Edition, Wiley-Interscience, New York, NY, 1999.
- Huang, X., Hu, M., He, L., and Tang, X.: Chemical characterization of water-soluble organic acids in PM_{2.5} in Beijing, China, *Atmos. Environ.*, 39, 2819–2827, 2005.
- Huang, X., Yu, J., He, L., and Yuan, Z.: Water-soluble organic carbon and oxalate in aerosols at a coastal urban site in China: size distribution characteristics, sources and formation mechanisms, *J. Geophys. Res.*, 111, D22 212, 2006.
- Kawamura, K. and Ikushima, K.: Seasonal changes in the distribution of dicarboxylic acids in the urban atmosphere, *Environ. Sci. Technol.*, 27, 2227–2235, 1993.
- Kawamura, K. and Sakaguchi, F.: Molecular distributions of water soluble dicarboxylic acids in marine aerosols over the Pacific Ocean including tropics, *J. Geophys. Res.*, 104, 3501–3509, 1999.

- Kerminen, V., Ojanen, C., Pakkanen, T., Hillamo, R., Aurela, M., and Merilainen, J.: Low-molecular-weight dicarboxylic acids in an urban and rural atmosphere, *J. Aerosol Sci.*, 31, 349–362, 2000.
- Khawaja, H.: Atmospheric concentrations of carboxylic acids and related compounds at a semiurban site, *Atmos. Environ.*, 29, 127–139, 1995.
- Kim, J., Yoon, S., Jefferson, A., and Kim, S.: Aerosol hygroscopic properties during Asian dust, pollution, and biomass burning episodes at Gosan, Korea in April 2001, *Atmos. Environ.*, 40, 1550–1560, 2006.
- Knutson, E. and Whitby, K.: Aerosol classification by electric mobility: apparatus, theory, and applications, *J. Aerosol Sci.*, 6, 443–451, 1975.
- Kotchenruther, R. and Hobbs, P.: Humidification factors of aerosols from biomass burning in Brazil, *J. Geophys. Res.*, 103, 32 081, 1998.
- Kreisberg, N., Stolzenburg, M., Hering, S., Dick, W., and McMurry, P.: A new method for measuring the dependence of particle size distributions on relative humidity, with application to the Southeastern Aerosol and Visibility Study, *J. Geophys. Res.*, 106, 14 935, 2001.
- Lide, D.: *CRC handbook of Chemistry and Physics*, 86th Edition, CRC press, Florida, 2005.
- Lightstone, J., Onasch, T., Imre, D., and Oatis, S.: Deliquescence, efflorescence, and water activity in ammonium nitrate and mixed ammonium nitrate/succinic acid microparticles, *J. Phys. Chem.*, 104, 9337–9346, 2000.
- Liu, B. and Lee, K.: An aerosol generator of high stability, *Am. Ind. Hyg. Assoc. J.*, 36, 861–865, 1975.
- Liu, B., Pui, D., Whitby, K., Kittelson, D., Kousaka, Y., and McKenzie, R.: The aerosol mobility chromatograph: a new detector for sulfuric acid aerosols, *Atmos. Environ.*, 12, 99–104, 1978.
- Magi, B. and Hobbs, P.: Effects of humidity on aerosols in southern Africa during the biomass burning season, *J. Geophys. Res.*, 108, 8495, 2003.

- Peng, C. and Chan, C.: The water cycles of water-soluble organic salts of atmospheric importance, *Atmos. Environ.*, 35, 1183–1192, 2001.
- Peng, C., Chan, M., and Chan, C.: The hygroscopic properties of dicarboxylic and multifunctional acids: Measurements and UNIFAC predictions, *Environ. Sci. Technol*, 35, 4495–4501, 2001.
- Pilinis, C., Seinfeld, J., and Grosjean, D.: Water content of atmospheric aerosols, *Atmos. Environ.*, 23, 1601–1606, 1989.
- Poore, M.: Oxalic acid in PM_{2.5} particulate matter in California, *J. Air Waste Manage.*, 50, 1874–1875, 2000.
- Prenni, A., DeMott, P., Kreidenweis, S., Sherman, D., Russell, L., and Ming, Y.: The effects of low molecular weight dicarboxylic acids on cloud formation, *J. Phys. Chem. A.*, 105, 11 240–11 248, 2001.
- Prenni, A., DeMott, P., and Kreidenweis, S.: Water uptake of internally mixed particles containing ammonium sulfate and dicarboxylic acids, *Atmos. Environ.*, 37, 4243–4251, 2003.
- Rader, D. and McMurry, P.: Application of the tandem differential mobility analyzer to studies of droplet growth or evaporation, *J. Aerosol Sci.*, 17, 771–787, 1986.
- Rood, M., Larson, T., Covert, D., and Ahlquist, N.: Measurement of laboratory and ambient aerosols with temperature and humidity controlled nephelometry, *Atmos. Environ.*, 19, 1181–1190, 1985.
- Saxena, P. and Hildemann, L.: Water-soluble organics in atmospheric particles: A critical review of the literature and application of thermodynamics to identify candidate compounds, *J. Atmos. Chem.*, 24, 57–109, 1996.
- Saxena, P. and Hildemann, L.: Water absorption by organics: survey of laboratory evidence and evaluation of UNIFAC for estimating water activity, *Environ. Sci. Technol*, 31, 3318–3324, 1997.
- Saxena, P., Hildemann, L., McMurry, P., and Seinfeld, J.: Organics alter hygroscopic behavior of atmospheric particles, *J. Geophys. Res.*, 100, 18 755, 1995.

- Seinfeld, J. and Pandis, S.: Atmospheric Chemistry and Physics: From Air Pollution to Climate Change, Second Edition, Hoboken: Wiley, 2006.
- Sekigawa, K.: Estimation of the volume fraction of water soluble material in submicron aerosols in the atmosphere, *J. Meteorol. Soc. Jpn.*, 61, 359–367, 1983.
- Sheridan, P., Jefferson, A., and Ogren, J.: Spatial variability of submicrometer aerosol radiative properties over the Indian Ocean during INDOEX, *J. Geophys. Res.*, 107, 8011, 2002.
- Snider, J. and Petters, M.: Optical particle counter measurement of marine aerosol hygroscopic growth, *AIP Conf. Proc.*, pp. 1185–1189, 2007.
- Sorooshian, A., Brechtel, F., Weber, R., Corless, A., Flagan, R., and Seinfeld, J.: Modeling and characterization of a particle-into-liquid sampler (PILS), *Aerosol Sci. Tech.*, 40, 396–409, 2006a.
- Sorooshian, A., Varutbangkul, V., Brechtel, F., Ervens, B., Feingold, G., Bahreini, R., Murphy, S., Holloway, J., Atlas, E., Buzorius, G., Jonsson, H., Flagan, R., and Seinfeld, J.: Oxalic acid in clear and cloudy atmospheres: Analysis of data from International Consortium for Atmospheric Research on Transport and Transformation 2004, *J. Geophys. Res.*, 111, doi:10.1029/2005JD006880, 2006b.
- Sorooshian, A., Lu, M., Brechtel, F., Jonsson, H., Feingold, G., Flagan, R., and Seinfeld, J.: On the source of organic acid aerosol layers above clouds, *Environ. Sci. Technol.*, 41, 4647–4654, 2007a.
- Sorooshian, A., Ng, N., Chan, A., Feingold, G., Flagan, R., and Seinfeld, J.: Particulate organic acids and overall water-soluble aerosol composition measurements from the 2006 Gulf of Mexico Atmospheric Composition and Climate Study (GoMACCS), *J. Geophys. Res.*, 112, D13 201, 2007b.
- Stolzenburg, M., Kreisberg, N., and Hering, S.: Atmospheric size distributions measured by differential mobility optical particle size spectrometry, *Aerosol Sci. Tech.*, 29, 402–418, 1998.
- Tang, I. and Munkelwitz, H.: Composition and temperature dependence of the deliquescence properties of hygroscopic aerosols, *Atmos. Environ.*, 27, 467–473, 1993.

- Tang, I. and Munkelwitz, H.: Water activities, densities, and refractive indices of aqueous sulfates and sodium nitrate droplets of atmospheric importance, *J. Geophys. Res.*, 99, 18 801–18 808, 1994a.
- Tang, I. and Munkelwitz, H.: Aerosol phase transformation and growth in the atmosphere, *J. Appl. Meteorol.*, 33, 1994b.
- Videen, G., Pellegrino, P., Ngo, D., Videen, J., and Pinnick, R.: Light-scattering intensity fluctuations in microdroplets containing inclusions, *Appl. Optics*, 36, 6115–6118, 1997.
- Wang, J., Flagan, R., and Seinfeld, J.: A differential mobility analyzer (DMA) system for submicron aerosol measurements at ambient relative humidity, *Aerosol Sci. Tech.*, 37, 46–52, 2003.
- Weast, R. and Astle, M.: *CRC Handbook of Chemistry and Physics*, pp, CRC Press, Florida, 1987.
- Wise, M., Surratt, J., Curtis, D., Shilling, J., and Tolbert, M.: Hygroscopic growth of ammonium sulfate/dicarboxylic acids, *J. Geophys. Res.*, 108, 4638, 2003.
- Yao, X., Fang, M., Chan, C., Ho, K., and Lee, S.: Characterization of dicarboxylic acids in PM_{2.5} in Hong Kong, *Atmos. Environ.*, 38, 963–970, 2004.
- Yu, J., Huang, X., Xu, J., and Hu, M.: When aerosol sulfate goes up, so does oxalate: implication for the formation mechanisms of oxalate, *Environ. Sci. Technol.*, 39, 128–133, 2005.

Table 2.1: Aerosol hygroscopicity measurement techniques.

Aerosol hygroscopicity measurement techniques			
Measurement category	Measurement description	Notes	Studies
Single particle levitation to directly measure mass change in response to humidity variation	Electrodynamic balance	Suitable only for laboratory studies; can study full RH hysteresis behavior	Cohen et al. 1987a, 1987b; Tang and Munkelwitz 1993, 1994a, 1994b; Peng et al. 2001; Peng and Chan 2001
Variation in aerosol light scattering coefficient with changing RH	Humidity-controlled nephelometry: either one or multiple RH-conditioned nephelometers, each typically operated at 3 wavelengths	Growth factor is estimated by the ratio of the humidification factor at a dry RH and an elevated RH	Rood et al. 1985; Carrico et al. 1998, 2000; Kotchenruther and Hobbs 1998; Sheridan et al. 2002; Magi and Hobbs 2003; Malm et al. 2005; Kim et al. 2006
Parallel unit operations to estimate growth factor of total aerosol from size distribution shifts	Comparison of size distributions from two aircraft wing probes: Passive cavity aerosol spectrometer probe (PCASP; dry RH) and forward scattering spectrometer probe (FSSP or F300; ambient RH)	Cannot compare aerosol at one particular size and is limited by the RH at ambient conditions	Kotchenruther and Hobbs 1998; Snider and Petters 2007
	Aerosol hydration spectrometer: Two OPCs in parallel at different RHs (48–53% and 88–92%)	Cannot compare aerosol at one particular size; typically requires 20 min for each sample (maximum = 40 min) (Hegg et al. 2006)	Hegg et al. 2006, 2007
	Dual Automated Classified Aerosol Detector: Two DMAs in parallel at different RHs	Cannot compare aerosol at one particular size	Wang et al. 2003
Unit operations in series to measure growth factor of size-classified aerosol from size distribution shifts	Humidified tandem DMA (HTDMA): Two DMAs in series with a humidification step in between	Usually restricted to sizes less than ~500 nm; limited by one RH at one time; time resolution can be as low as 15 min (Busch et al. 2002)	Sekigawa 1983; McMurry and Stolzenberg 1989; Covert et al. 1991; Zhang et al. 1993; Berg et al. 1998; Covert and Heintzenberg 1993; Swietlicki et al. 1999, 2000; Svenningsson et al. 1992, 1994, 1997; Cocker et al. 2001; Batensperger et al. 2002; Bush et al. 2002; Massling et al. 2003; Gysel et al. 2004; Ferron et al. 2005; Carrico et al. 2005; Gasparini et al. 2006; Akilu et al. 2006; Massling et al. 2007
	Relative humidity-moderated differential mobility optical particle size spectrometer (RH-DMOPSS): high flow DMA followed by an OPC and CPC operating in parallel. DMA and OPC are operated at different RHs; dry aerosol is used to calibrate the OPC continuously during operation	Can study only one wet RH at a time; measures shrinkage upon drying rather than growth upon humidification; initial humid diameters can be as large as 1.1 μm ; time resolution is better than that of the HTDMA	Kreisberg et al. 2001
	Hygroscopic-differential mobility analyzer-aerodynamic particle sizer (H-DMA-APS): DMA followed by a dry APS and a separate RH-conditioned APS	Can study only one wet RH at a time	Massling et al. 2007
	Differential aerosol sizing and hygroscopicity spectrometer probe (DASH-SP): DMA followed by a parallel system of one CPC and four OPCs, each of which has an upstream RH-conditioning module	Can study multiple RHs simultaneously; DMA upper size limit near 1 μm ; OPCs detect particles in excess of 1 μm ; time resolution as short as a few seconds	This study

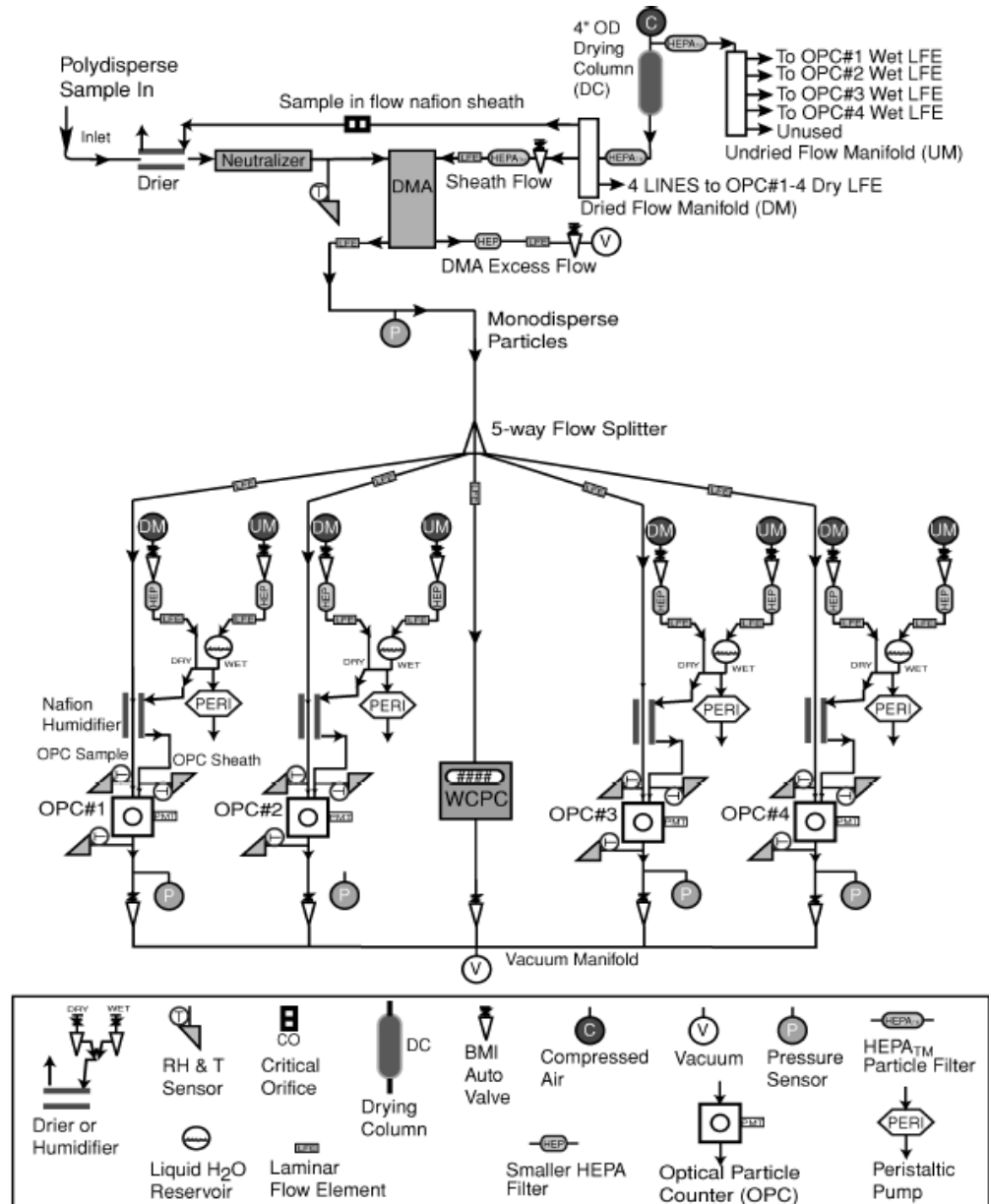


Figure 2.1: Schematic of DASH-SP.

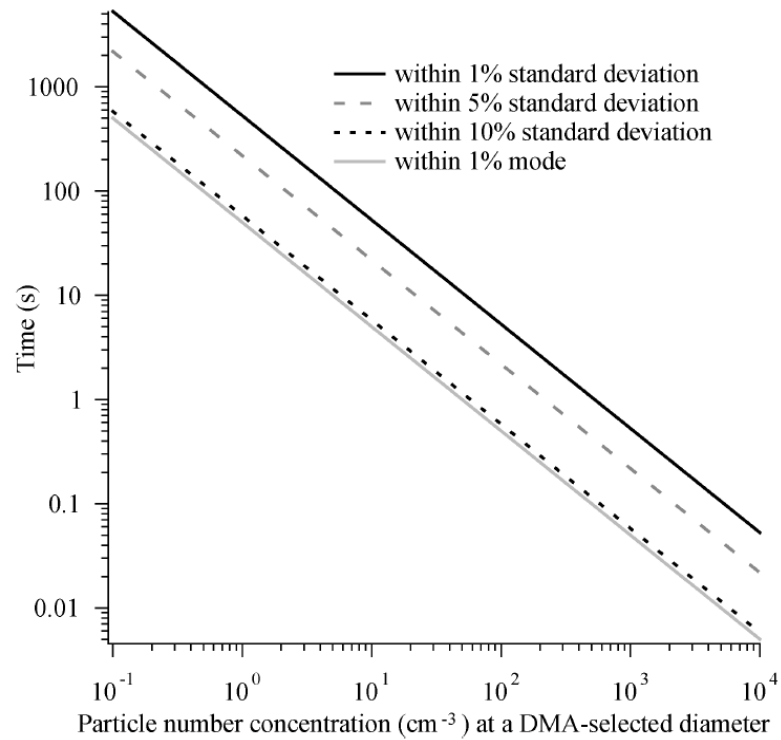


Figure 2.2: Time required as a function of particle number concentration to obtain sufficient pulses for the modal pulse height to be within 1% of the mode that would be obtained when counting at least 10,000 particles at constant particle composition. Also shown is the time needed for the standard deviation to be within 1%, 5%, and 10% of the standard deviation that would be obtained when counting at least 10,000 particles at constant particle composition.

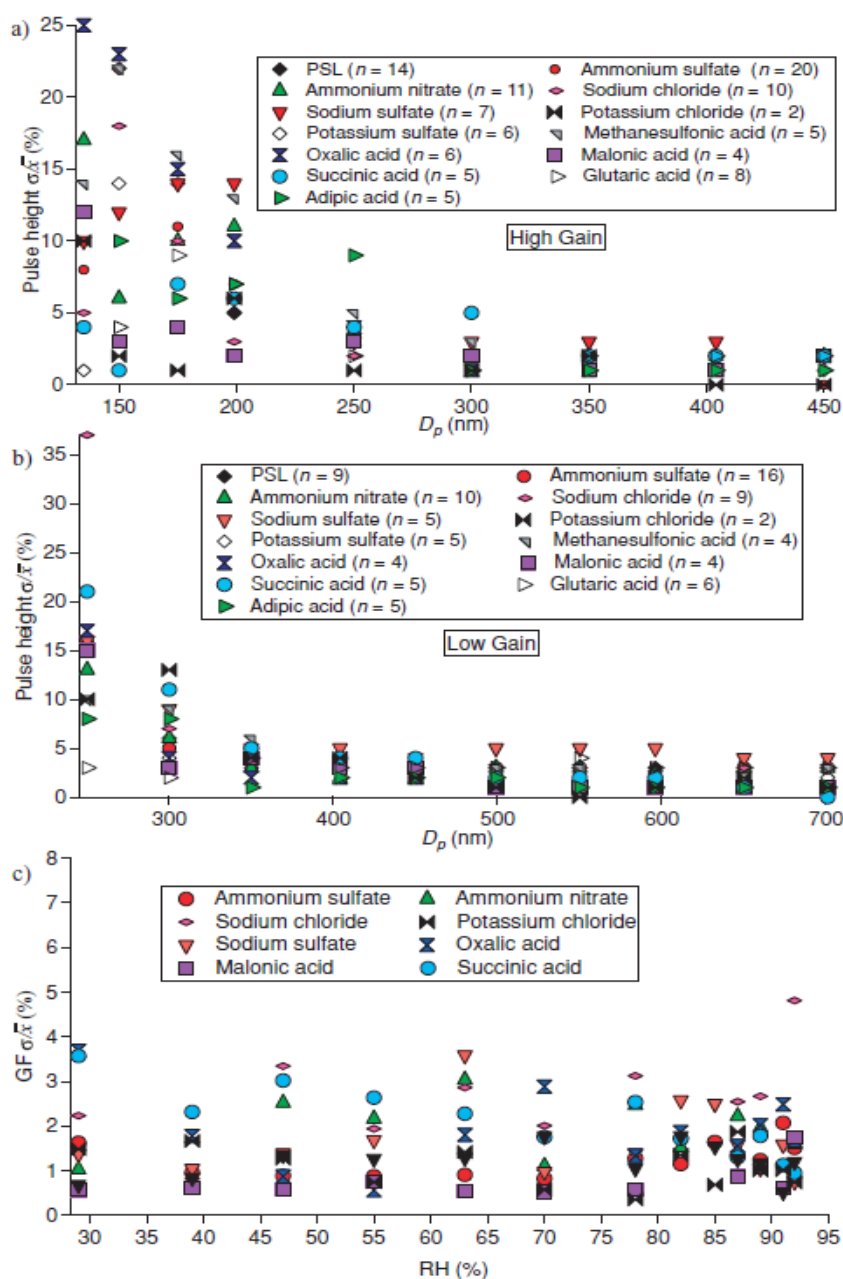


Figure 2.3: Stability statistics for different species and sizes over a time span of four months. Panel A corresponds to the high-gain OPC setting, and Panel B represents the low-gain setting for dry tests. Panel C represents stability statistics for growth factor during wet studies using the high-gain OPC configuration ($n > 20$ for each salt in the bottom panel).

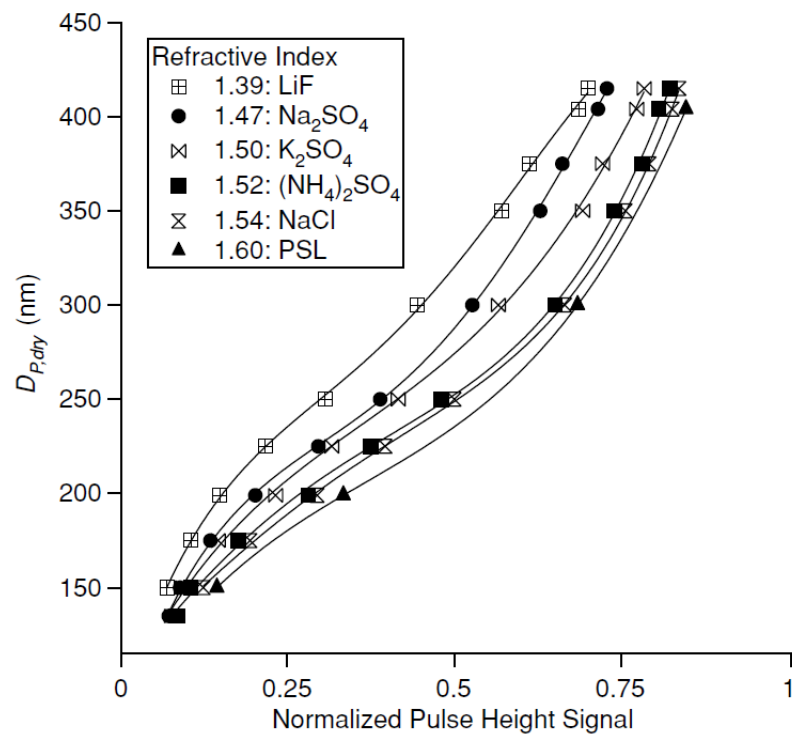


Figure 2.4: OPC response as a function of dry particle size for salts of different refractive index. These results are from one OPC for a single set of calibrations performed for each salt. All OPCs show the same general behavior.

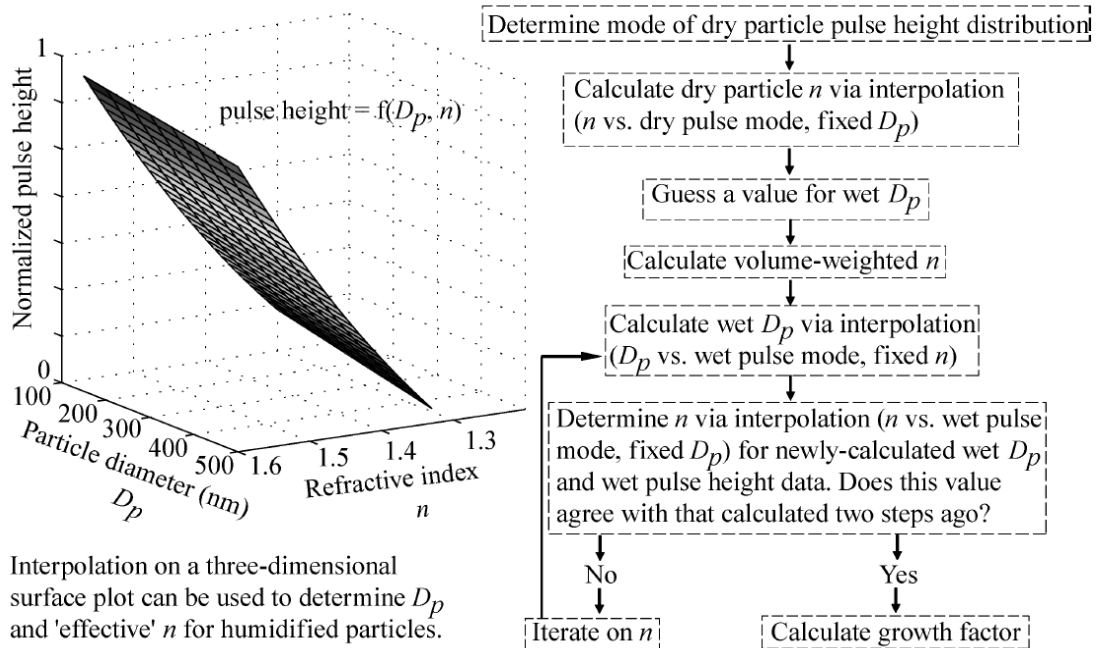


Figure 2.5: Data processing procedure from DASH-SP raw pulse height data to growth factors (GFs) for both laboratory-generated aerosol, for which the composition and refractive index (n) of the dry particles are known, and for ambient aerosol, where the composition and refractive index of the dry particles are unknown. The dry pulse height distribution mode is first used to determine the dry particle refractive index, which is used to calculate a volume-weighted wet particle refractive index, taking into account the volume fractions of water and the particle. Iterations are subsequently carried out on the three-dimensional surface shown to converge on a wet particle refractive index. The D_p corresponding to the latter value of refractive index and the wet pulse height distribution mode is subsequently used to calculate growth factor.

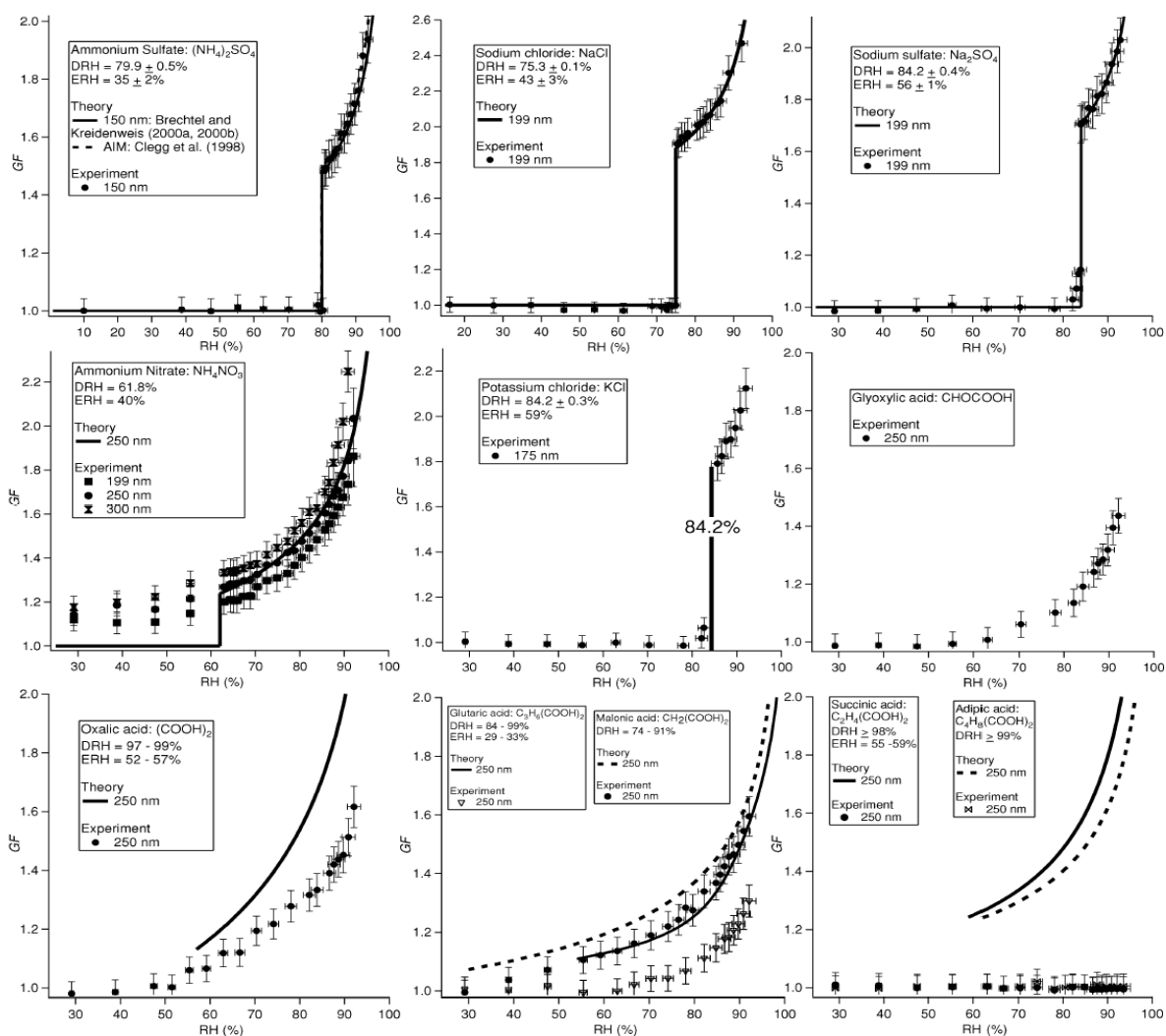


Figure 2.6: Experimentally determined growth factor curves for inorganic and organic acid species. Predictions from the Brechtel and Kreidenweis (2000a,b) model are shown for all salts except for glyoxylic acid and potassium chloride, while predictions from the Clegg et al. (1998) model are also shown for ammonium sulfate. The Brechtel and Kreidenweis (2000a,b) model includes the Kelvin term to account for droplet curvature. Error bars reflect uncertainties associated with the RH and sizing (DMA and OPC) measurements. The reported deliquescence RH (DRH) and efflorescence RH (ERH) values are from the following references: Saxena and Hildemann (1997) and Peng et al. (2001) for organic acids, and Seinfeld and Pandis (2006) for the inorganic species.

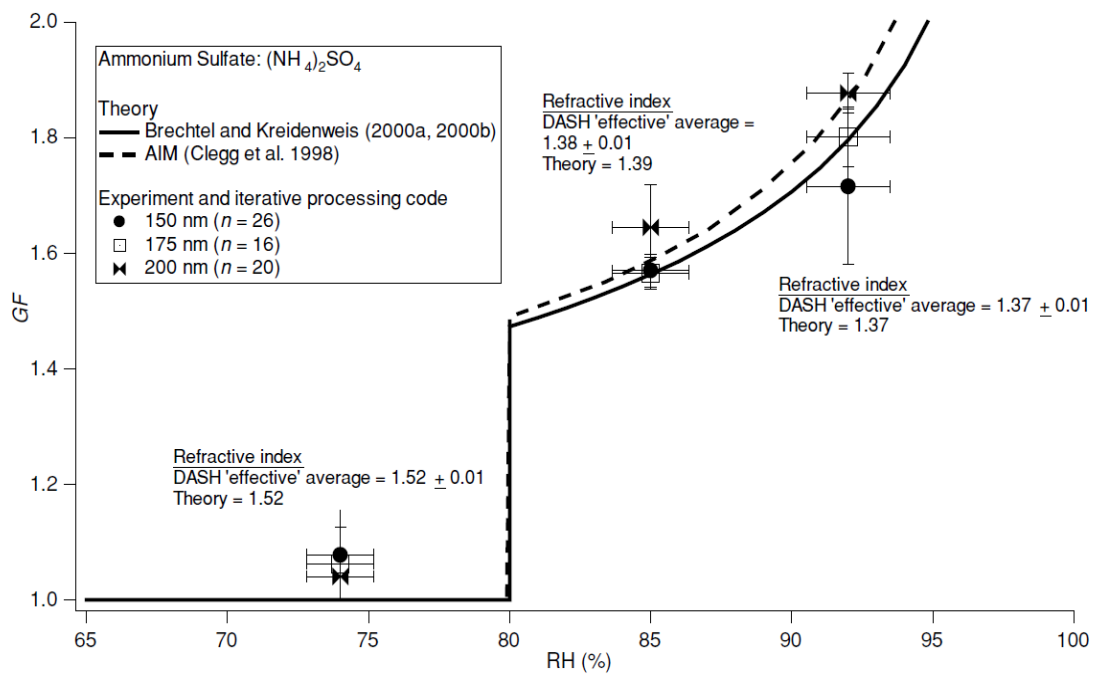


Figure 2.7: Comparison between two thermodynamic models and DASH-SP data for ammonium sulfate particles. The reported DASH-SP results were calculated by using iterative procedure in Figure 2.5 to process the OPC pulse height data. The RH error bars reflect uncertainties in the RH measurement, while the GF error bars reflect the precision of the measurement after several repetitive trials.

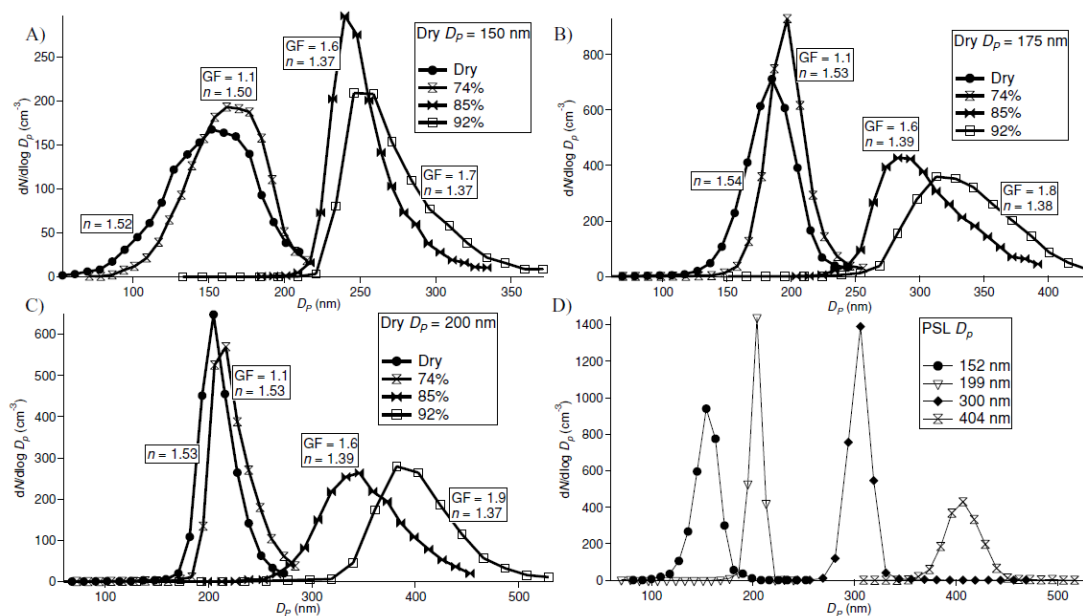


Figure 2.8: Size distributions from wet ammonium sulfate and dry PSL aerosol laboratory tests. Panels A, B, and C correspond to ammonium sulfate tests in which DMA-selected dry particle sizes of 150, 175, and 200 nm, respectively, were exposed to RHs of < 8% (dry), 74%, 85%, and 92%. Each curve is labeled with its calculated growth factor and "effective" refractive index (n), as calculated from the iterative data processing procedure in Figure 2.5. Panel D corresponds to dry PSL size distributions to show that for spherical particles the distributions are narrower than those for salts that may not be perfectly spherical. The size distributions tend to be broader near the minimum and maximum size detection limits of the OPCs.

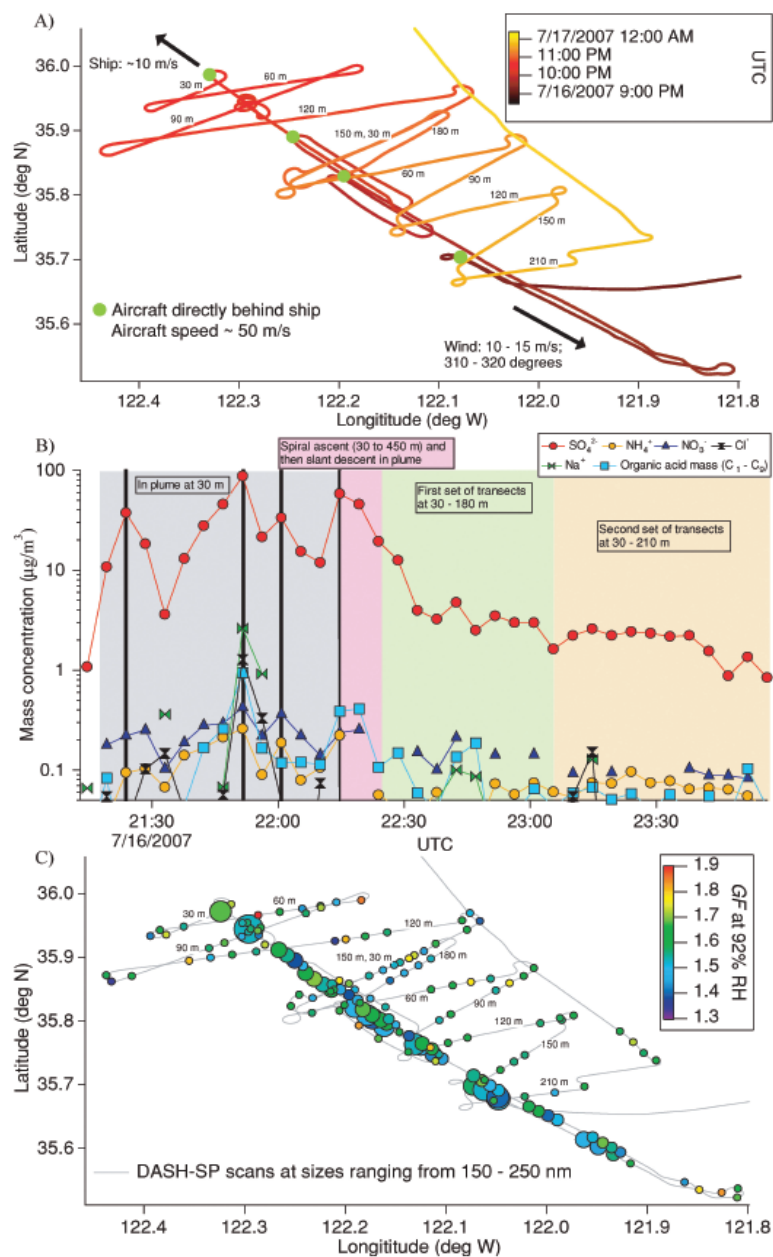


Figure 2.9: Panel A) Flight tracks during a MASE II flight (July 16, 2007) during which the Twin Otter aircraft sampled emissions from a large cargo ship off the central coast of California. The duration of the ship exhaust plume measurements was approximately 2.5 h. The plane flew at an altitude of 30 m in the ship's plume, before performing multiple cross-wind transects of the plume at the labeled altitudes. Panel B) Water-soluble species concentrations as measured by a PILS onboard the Twin Otter. The four, black vertical lines indicate when the aircraft was immediately behind the ship. Panel C) Growth factors at an RH of 92%. Marker sizes are proportional to the submicrometer particle number concentration (range = 50 - 365,000 cm^{-3}), as determined by a DMA.

Chapter 3

Aerosol hygroscopicity in the marine atmosphere: a closure study using high-time-resolution, multiple-RH DASH-SP and size-resolved C-ToF-AMS data*

*Reproduced with permission from “Aerosol hygroscopicity in the marine atmosphere: a closure study using high-time-resolution, multiple-RH DASH-SP and size-resolved C-ToF-AMS data” by Scott P. Hersey, Armin Sorooshian, Shane M. Murphy, Richard C. Flagan, and John H. Seinfeld, *Atmospheric Chemistry and Physics*, 9 (7), 2543-2554, 2009. Copyright 2009 by Authors. This work is licensed under a Creative Commons License.

3.1 Abstract

We have conducted the first airborne hygroscopic growth closure study to utilize data from an Aerodyne compact Time-of-Flight Aerosol Mass Spectrometer (C-ToF-AMS) coupled with size-resolved, multiple-RH, high-time-resolution hygroscopic growth factor (GF) measurements from the differential aerosol sizing and hygroscopicity spectrometer probe (DASH-SP). These data were collected off the coast of Central California during seven of the 16 flights carried out during the MASE-II field campaign in July 2007. Two of the seven flights were conducted in airmasses characterized by continental origin. These flights exhibited elevated organic volume fractions ($V_{F_{organic}} = 0.56 \pm 0.19$, as opposed to 0.39 ± 0.20 for all other flights), corresponding to significantly suppressed GF s at high RH (1.61 ± 0.14 at 92%RH, as compared with 1.91 ± 0.07 for all other flights), more moderate GF suppression at intermediate RH (1.53 ± 0.10 at 85%, compared with 1.58 ± 0.08 for all other flights), and no measurable GF suppression at low RH (1.31 ± 0.06 at 74%, compared with 1.31 ± 0.07 for all other flights). Organic loadings were slightly elevated in above-cloud aerosols, as compared with below-cloud aerosols, and corresponded to a similar trend of significantly suppressed GF at high RH, but more moderate impacts at lower values of RH. A hygroscopic closure based on a volume-weighted mixing rule provided good agreement with DASH-SP measurements ($R^2 = 0.78$). Minimization of root mean square error between observations and predictions indicated mission-averaged organic GF s of 1.22, 1.45, and 1.48 at 74, 85, and 92% RH, respectively. These values agree with previously reported values for water-soluble organics such as dicarboxylic and multifunctional acids, and correspond to a highly oxidized, presumably water-soluble, organic fraction (mission-averaged O:C = 0.92 ± 0.33). Finally, a backward stepwise linear regression revealed that, other than RH, the most important predictor for GF is $V_{F_{organic}}$, indicating that a simple empirical model relating GF , RH, and the relative abundance of organic material can provide accurate predictions ($R^2 = 0.77$) of hygroscopic growth for the California coast.

3.2 Introduction

Atmospheric aerosols change size with fluctuations in relative humidity, with a magnitude dictated by chemical composition. Because this hygroscopic response determines particle size, it influences direct climate forcing attributed to aerosols. Further, subsaturated hygroscopic growth factor ($D_{p,wet}/D_{p,dry}$) is strongly correlated with CCN activity (Prenni et al., 2001). Given the importance of aerosol water uptake on both the direct and indirect light scattering properties of aerosols, incomplete understanding of aerosol hygroscopicity has been identified as a major limitation in estimations of climate forcing (IPCC, 2007).

With a firm foundational understanding of hygroscopic properties of inorganic aerosol constituents, there has been a significant shift in focus toward organic hygroscopicity in the last decade, as a number of theoretical (e.g., Clegg and Seinfeld, 2006; Topping et al., 2005a,b), laboratory (Peng et al., 2001; Choi and Chan, 2002a; Peng and Chan, 2001; Choi and Chan, 2002b; Sjogren et al., 2007; Virkkula et al., 1999; Cruz and Pandis, 2000; Prenni et al., 2001; Cocker et al., 2001a,b; Hameri et al., 2002; Saathoff et al., 2003; Prenni et al., 2003; Petters et al., 2006; Varutbangkul et al., 2006; Sjogren et al., 2007; Prenni et al., 2007; Moore and Raymond, 2008; Rood et al., 1985; Carrico et al., 1998, 2000; Dougle et al., 1998; Magi and Hobbs, 2003; Kim et al., 2006; Kreisberg et al., 2001; Hegg et al., 2006; Massling et al., 2007), and chamber (e.g., Ansari and Pandis, 2000; Cocker et al., 2001a,b; Duplissy et al., 2008) studies have sought to address how the presence of organics affects the water uptake characteristics of atmospheric aerosol. Despite advances in understanding of hygroscopic characteristics of organic-containing particles, measurements of aerosol hygroscopicity in field campaigns have remained relatively sparse.

Closure studies, which attempt to reconcile simultaneously measured hygroscopic and chemical data, link laboratory studies of hygroscopicity, theoretical models for water uptake, and field measurements of aerosol-water interactions. The standard method for predicting hygroscopic growth from composition data is based on volume-weighted water uptake by the individual chemical constituents. While it is usually possible to predict water uptake for the inorganic fraction of atmospheric aerosols, the wealth of organic species in the atmosphere, combined with limited understanding of

organic aerosol hygroscopicity, has led investigators to assign the water uptake of organics as the particle growth not explained by inorganic constituents (e.g., Malm et al., 2005).

An important approach in hygroscopicity closure is to combine ambient measurements of water uptake with simultaneous, detailed chemical measurements from the Aerodyne Aerosol Mass Spectrometer (AMS). One notable ground-based study in an urban atmosphere (Gysel et al., 2007) used chemical data from the AMS to make volume-weighted predictions of hygroscopic growth factor (GF), providing good agreement between predicted and measured hygroscopicity values. Their study represents an improvement in the hygroscopic treatment of organics over prior work, but is limited by both low time resolution and single-RH conditions inherent in HTDMA systems.

The current study presents data obtained during seven flights in the marine atmosphere off the coast of Central California during the second Marine Stratus/Stratocumulus Experiment (MASE-II). The dataset is the first to combine high-time-resolution, size-resolved AMS chemistry with high-time-resolution, size-resolved hygroscopic data at multiple RH values from the Differential Aerosol Sizing and Hygroscopicity Spectrometer Probe (DASH-SP). Hygroscopic studies have previously been carried out in the marine atmosphere (see Table 3.1), but none of those listed utilized either AMS chemical data or hygroscopic data as highly size-, time-, and RH-resolved as those presented here.

3.3 Experimental

3.3.1 MASE-II Experiment

The data presented here were obtained during a series of seven cloud probing flights carried out as part of the second Marine Stratus/Stratocumulus Experiment (MASE-II) field campaign during July 2007. The MASE II experiment was the second of two airborne field campaigns directed toward measurement of aerosol-cloud relationships in marine stratocumulus in the eastern Pacific Ocean. The Marine Stratus/Stratocumulus Experiment (MASE) was carried out in 2005 off the coast of Monterey, California (Lu et al., 2007), and MASE II was undertaken in 2007 in the same region.

Both experiments were carried out in the month of July, when marine stratocumulus are prevalent over the region, and utilized the CIRPAS Twin Otter aircraft. In each campaign, comprehensive airborne measurements were made of aerosol and cloud properties in areas both perturbed and unperturbed by continental emissions. Tables 3.2 and 6.1 list the flights carried out during MASE II and the instrument payload onboard the Twin Otter, respectively. The present study addresses measurements of the hygroscopic properties of marine aerosols during MASE II. Other flights probed emissions from a large bovine source and a large container ship, and these data are presented elsewhere (Sorooshian et al., 2008b; Murphy et al., submitted).

3.3.2 Aerosol Composition Measurements

Non-refractory aerosol chemical species were characterized by the Aerodyne compact Time-of-Flight Aerosol Mass Spectrometer (C-ToF-AMS) (cToF-AMS, Drewnick et al., 2004a,b). Particles with vacuum aerodynamic diameters (D_{va}) $50 \text{ nm} \leq D_{va} \leq 800 \text{ nm}$ are focused by an aerodynamic lens, pass through a 3.5% chopper, and are vaporized at $530 - 600^\circ\text{C}$. The chopper is operated in three modes, to detect background mass spectra, ensemble average mass spectra over all particle sizes, or size-resolved mass spectra. After particle vaporization, molecules are ionized via electron impact, and are pulsed into a time-of-flight mass spectrometer. MASE-II data were collected at unit mass resolution. AMS mass spectra are deconvolved into sulfate, nitrate, ammonium, and organic mass loadings (Allan et al., 2004). O:C ratios are determined by using mass concentration at m/z 44 and a parameterization presented in Aiken et al. (2008).

AMS measurements were averaged to match the time-resolution of hygroscopicity measurements, and particle density was calculated for each flight leg. Because the C-ToF-AMS measures particle vacuum aerodynamic diameter (D_{va}) and the DMA measures electrical mobility diameter (D_{em}), one can determine particle density by comparing the volume distribution from the DMA ($dV/d\log(D_{em})$) to the total mass distribution measured by the C-ToF-AMS ($dM/d\log(D_{em})$) (DeCarlo et al., 2004). If one assumes that the aerosol consists of an internal mixture of spherical particles, the relationship between the two diameters is $\rho_p = (D_{va}/D_m)\rho_o$, where ρ_o is unit density (1 g/cm^3). Under these

assumptions, the ratio of the D_{va} where the mass distribution peaks to the D_{em} where the volume distribution peaks is the density. Reference to the peak of each distribution is given for simplicity, though in practice the ratio that causes the entirety of the two distributions to best align is the final calculated particle density. Organic density is then calculated by using the bulk chemistry from the C-ToF-AMS for a given time period and assuming the particles measured by the DMA are completely dry. The dry densities of all the inorganic components are known and, assuming volume additivity, the density of the organic component can then be estimated. If the inorganic component of the particles measured by the DMA is not completely dry, this procedure will result in an underestimate of the particle density because the D_{em} will be larger than it would have been for a dry particle. Particles entering the C-ToF-AMS are assumed to be dry, and even if they are not completely devoid of water, the presence of small amounts of water causes little change in the vacuum aerodynamic diameter. One important issue concerning C-ToF-AMS data is the collection efficiency of particles within the instrument (Huffman et al., 2005). In this study, C-ToF-AMS mass loadings were confirmed by comparison between the sulfate measurements from the C-ToF-AMS and the Particle Into Liquid Sampler - Ion Chromatograph (PILS-IC, Brechtel Mfg. Inc.) during periods when there were no rapid fluctuations in particulate mass loading. Composition data represent size-resolved AMS chemistry averaged over 10 nm size bins. Since hygroscopicity measurements were carried out for particles of $D_{em,dry}$ equal to 150, 175, and 200 nm.

3.3.3 Hygroscopicity Measurements

Hygroscopicity measurements were carried out with the Differential Aerosol Sizing and Hygroscopicity Spectrometer Probe (DASH-SP, Brechtel Mfg; Sorooshian et al., 2008a). Ambient particles pass through a nafion dryer before receiving a uniform charge distribution in a ^{210}Po neutralizer. A cylindrical, single-classification differential mobility analyzer (DMA) then size selects particles into narrow ranges of mobility-equivalent diameters (D_{em}) between 0.1 and 1.0 μm . The resulting monodisperse aerosol is split into five separate flows. One channel provides a redundant measurement of total particle concentration at the DMA-selected size with a water condensation particle counter

(TSI Model 3831). The remaining four channels consist of parallel nafion humidification chambers (Perma Pure, LLP, Model MD-070-24FS-4), followed by correspondingly humidified custom optical particle counters (OPCs). In the OPC sample volume, particles pass through a focused laser beam ($\lambda = 532$ nm, World Star Technologies, Model TECGL-30) and scatter light in proportion to size (D_p) and refractive index (RI). Forward-scattered light is collected and focused on a photomultiplier tube, and the resulting electrical pulse is recorded by a high-speed data acquisition computer. An iterative data processing algorithm, based on laboratory calibrations with salts of known refractive indices, is used to determine the best fit on a solution surface relating electrical pulse height, size, and refractive index. The hygroscopic growth factor ($GF = D_{p,wet}/D_{p,dry}$) is corrected for the RI change caused by particulate liquid water at elevated RH. Temperature and pressure measurements are continually made at multiple locations in the instrument, and used to ensure that temperature and pressure variability do not impact hygroscopicity measurements. In the current study, hygroscopicity was measured at dry sizes corresponding to D_{em} of 150, 175, and 200 nm. Multiple RH sensors in the nafion tubes and OPCs controlled RHs to dry ($\leq 8\%$), 74%, 85%, and 92%, with RH uncertainty of 1.5%. Low particle loadings inherent in the marine atmosphere required increased on-line collection times at each DMA size step, but usually \leq one minute was sufficient to overcome counting statistic limitations. Overall uncertainty in GF calculations is 4.5%. Assuming particles to be uniform, non-light-absorbing spheres allows the assumption that the intensity of scattered light is a function of only RI and D_p . This assumption also allows calculation of dry, ‘effective’ RI from the known DMA-selected D_p and measured scattered light intensity.

3.3.4 Hygroscopic Closure

A volume-weighted mixing rule was used to perform a hygroscopic closure using AMS and DASH-SP data, under the assumption of independent and additive water uptake by individual constituents in each particle:

$$GF_{mixed}(a_w) = \left(\sum_i \epsilon_i GF_i(a_w)^3 \right)^{1/3} \quad (3.1)$$

where GF_{mixed} is the overall particle GF , a_w is the water activity, GF_i is the hygroscopic growth factor for pure species i , and ϵ_i is the volume fraction of species i . At equilibrium, $a_w = RH$ (Seinfeld and Pandis, 2006). Values for ϵ_i were calculated for the following species, using AMS masses of ammonium (NH_4^+), nitrate (NO_3^-), sulfate (SO_4^{2-}), and total organic: ammonium nitrate (NH_4NO_3), ammonium sulfate ($(NH_4)_2SO_4$), ammonium bisulfate (NH_4HSO_4), sulfuric acid (H_2SO_4), and organic. Partitioning between sulfate species was determined on the basis of the ammonium to sulfate molar ratio ($SR = [NH_4^+]/[SO_4^{2-}]$). When $SR \leq 1$, the sulfate was assumed to be a mixture of H_2SO_4 and NH_4HSO_4 ; when $1 < SR < 2$, sulfate was assumed to be a mixture of NH_4HSO_4 and $(NH_4)_2SO_4$; when $SR \geq 2$, sulfate was assumed to be solely $(NH_4)_2SO_4$. During MASE-II, sulfate was predominantly found to exist as NH_4HSO_4 . $(NH_4)_2SO_4$ is assumed to have a GF of unity at RH equal to 74% since particles are exposed to RH well below its efflorescence point before subsequent rehumidification. The organic fraction was assumed to be hydrophilic, based on evidence of a high degree of organic oxygenation from AMS mass spectra (see Section 3.4.3). Values of GF_i for the organic fraction were calculated as those necessary to minimize the root mean square error in comparing predictions with measured hygroscopicity.

3.4 Results

GF values for seven flights are presented (RF 7, 10, 11, 12, 13, 14, and 16 in Table 3.2). Table 3.4 presents measured GF s at each RH and each $D_{em,dry}$. Typically, multiple measurements were made on each leg, at each size, for each flight. The error reported is \pm one standard deviation in these multiple measurements. When only one measurement was made at a given size in a given leg, it is reported without error. Ship plumes were encountered on flights 10 and 16, as evidenced by brief, significantly elevated particle number concentration. Analysis of GF measurements in these presumptive plumes is not presented in the present work. Aerosol densities were calculated for each leg and used in the analysis below. Mission-averaged densities (averaged over all flight legs) were found to be 1.53 ± 0.19 , 1.56 ± 0.20 , and 1.47 ± 0.15 g/cm³ for below-cloud, above-cloud, and free troposphere legs, respectively. Mission-averaged organic densities were calculated to be 1.20 ± 0.76 ,

1.34 ± 0.46 , and 1.30 ± 0.24 for below-cloud, above-cloud, and free troposphere legs, respectively.

3.4.1 Airmass Origin

Relative to the other flights, RF 12 and 16 exhibited significantly suppressed water uptake at high RH for all dry sizes. During these two flights, 92% GF values for 200 nm $D_{em,dry}$ particles averaged 1.61 ± 0.14 , as compared with 1.91 ± 0.07 for all other flights. These low- GF flights corresponded to significantly elevated total organic, as measured by the AMS. Mass concentration averaged $1.97 \pm 1.71 \mu\text{g}/\text{m}^3$ organic (as opposed to $0.58 \pm 0.63 \mu\text{g}/\text{m}^3$ for all other flights), corresponding to volume fraction organic ($VF_{organic}$) of 0.56 ± 0.19 (as opposed to 0.39 ± 0.20 for all other flights).

Back-trajectory analysis suggests that the MASE-II flights can be categorized by airmass origin as either polluted/continental (flights 12, 16), or non-continentally influenced (flights 7, 10, 11, 13, 14). Figure 3.1 shows 92% GF measurements for 200 nm $D_{em,dry}$ particles, with corresponding 48-hr HYSPLIT (available at <http://www.arl.noaa.gov/ready/hysplit4.html>) back-trajectories identifying airmass origin. Note that the low GF s and high $VF_{organic}$ measured on flights 12 and 16 correspond with airmass origins over the continental United States, while higher GF s and lower $VF_{organic}$ measured on other flights correspond to airmass origins over the clean marine environment. It is interesting to note that trajectories at sea level have marine origins for all flights (including low- GF flights 12 and 16), and that there is a general trend of descending air from aloft over the course of the trajectories. This suggests that mixing of air from aloft is a significant factor in determining marine aerosol characteristics in the marine boundary layer. It is also noteworthy that GF values at low RH were not significantly suppressed, with values of 1.31 ± 0.06 at 74% (compared with 1.31 ± 0.07 for all other flights). GF values at intermediate RH were moderately suppressed in the continental airmasses, measuring 1.53 ± 0.10 at 85% (compared with 1.58 ± 0.08 for all other flights). In other words, the effect of the high- $VF_{organic}$, continental airmass was to significantly suppress GF at high RH, while having no measurable effect on aerosol water uptake at low RH and a moderate impact at intermediate RH. These results, while suggestive of continental airmass influence, should be interpreted in light of the relatively coarse grid resolution of the HYSPLIT

model. In this analysis, small shifts in back-trajectories toward continental origin correlate with significantly suppressed high-RH GF s.

3.4.2 Hygroscopicity Trends

No size-dependent hygroscopicity was observed over the range of measured $D_{em,dry}$, and in addition, no significant size-dependent trends in $VF_{organic}$ were observed. Further, organic-to-sulfate ratios from the AMS showed no significant variation over the size range measured by the DASH-SP. This suggests an internally-mixed aerosol between the sizes of 150 and 200nm.

Figure 3.2 shows below- and corresponding above-cloud 92% GF values for all flights. There exists a ubiquitous trend of higher below-cloud aerosol GF values at high RH when compared with top of cloud hygroscopicity values (1.88 ± 0.14 below cloud, versus 1.78 ± 0.18 above cloud). Marker sizes, proportional to $VF_{organic}$, suggest a trend of higher organic loading above cloud in several flights (0.36 ± 0.15 below cloud, versus 0.43 ± 0.22 above cloud). While variability is rather large in these measurements, the trend of elevated $VF_{organic}$ above-cloud does correspond to suppressed GF at high RH. There is a trend of more moderate GF suppression at intermediate RH in the higher $VF_{organic}$ above-cloud layer (1.53 ± 0.06 above cloud, as compared with 1.58 ± 0.07 below cloud). Unlike the continental-influenced flights, there is evidence of greater suppression of low-RH GF s in above-cloud legs, with 74% GF values of 1.31 ± 0.05 above cloud, compared with 1.36 ± 0.05 below. It appears, then, that the elevated organic loadings typical of above-cloud legs are correlated with GF suppression at high RH, and more moderate GF suppression at lower RHs.

3.4.3 Hygroscopic Closure

A hygroscopic closure was performed, using volume-weighted hygroscopic contributions from each chemical constituent identified by the AMS. O:C ratios for the flights presented were very similar for below-cloud (0.93 ± 0.32), above-cloud (0.91 ± 0.26), and free troposphere (0.92 ± 0.25) legs in both continentally- (0.94 ± 0.30) and marine-influenced (0.91 ± 0.25) flights. This result indicates that the organic component was consistently highly oxidized. With this evidence, the organic fraction was

treated as a bulk, water-soluble constituent and was not divided into soluble and insoluble fractions based on AMS organic mass spectra (Kondo et al., 2007). As described in Section 3.3.4, GF values were calculated for the organic component of the aerosol by minimizing root mean square error when comparing measured GF s with volume-weighted closure predictions. Mission-averaged organic GF s were determined to be 1.22, 1.45, and 1.48 at 74, 85, and 92% RH, respectively. Agreement at 74 and 92% RH is within 2%, compared with the hydrophilic multifunctional and dicarboxylic acids parameterized in Peng et al. 2001, though the 85% organic GF is overpredicted here by 7%. Closure results are presented in Fig. 3.3. Markers in Fig. 3.3 are color-coded according to relative humidity, and marker size is proportional to $VF_{organic}$. The volume-weighted hygroscopic closure utilizing size-resolved AMS chemistry achieves good agreement with the 675 DASH-SP GF measurements, with an R^2 of 0.78. Agreement is better at lower values of RH, owing to smaller GF magnitudes and less overall GF variability.

Aside from the obvious RH dependence of GF values, the clearest trend in Fig. 3.3 is that of larger markers (higher $VF_{organic}$) at low GF transitioning to smaller markers (lower $VF_{organic}$) at high values of GF for the same RH. The clarity and regularity of this trend reveal the importance of the organic fraction in determining GF values.

3.4.4 Simplified Parameterization

To further investigate the relative importance of each parameter in quantifying aerosol water uptake, and to determine the simplest empirical model still capable of accurately predicting GF , a backward stepwise linear regression was performed. The process, which eliminates predictors one-by-one to generate increasingly simplified linear representations of data, started with over 60 predictors, ranging from PILS and AMS chemical parameters to atmospheric data. The result is a two-parameter model that predicts GF as a function of RH and $VF_{organic}$:

$$GF = -0.312 + 0.0233(\text{RH}) - 0.282(VF_{organic}) \quad (3.2)$$

Figure 3.4 demonstrates the accuracy with which this model predicts DASH-SP GF values over the measured range of RH and $VF_{organic}$. It is noteworthy that the R^2 for this model is 0.77, indicating that the simple, two-parameter model explains only 1% less variability than the full volume-weighted chemical closure, which contains significantly more information (i.e. multiple inorganic chemical species and their individual GF s, in addition to organic fraction with its associated GF). It appears as though accurate predictions of particle water uptake in this region can be made simply on the basis of relative humidity and the relative abundance of organics in the aerosol, given a relatively uniform, highly-oxidized organic component internally mixed with predominantly ammonium bisulfate. While this model accurately predicts GF over the range of RH and $VF_{organic}$, and for the O:C ratios measured during MASE-II, it should not be used when RH is outside the range $74\% \leq \text{RH} \leq 92\%$, or where $VF_{organic}$ is less than 0.1 or greater than 0.9.

3.5 Discussion

Comparing mixed organic-inorganic particles with those comprised entirely of inorganic salts, there is a strong RH-dependence in the effect of organics on hygroscopicity (Peng et al., 2001). During the MASE-II field campaign, GF values at 74% RH averaged ~ 1.3 . Organic GF s were calculated to be 1.22 at 74% RH, suggesting that they contributed significantly to overall aerosol water uptake at low RH. GF values at 85% RH averaged ~ 1.6 during the campaign, and so the organic GF of 1.45 calculated for 85% RH suggests that organics played a less significant role, but still influenced water uptake at intermediate RH. An organic GF value of 1.48 was calculated for 92% RH, with DASH-SP 92% GF measurements of ~ 1.8 indicating that organics make little contribution to overall water uptake at high RH.

Inorganic salts exhibit deliquescent behavior as RH is increased. Many organics do not deliquesce or crystallize when RH is increased or decreased, respectively, but instead retain water at RH values well below the RH of deliquescence (RHD) of the inorganic salts with which they often co-exist in ambient particles. As a result, at RH values below the salt RHD, the presence of organics enhances water uptake. Thus, the effect of organics is to contribute significantly to overall water uptake at

low values of RH in mixed organic-inorganic particles. At high RH, on the other hand, organics tend to take up significantly less water than the inorganic constituents with which they co-exist in ambient particles. Therefore, at RH values above the inorganic RHD, organics appear to suppress water uptake relative to that which a pure inorganic particle would exhibit.

Figure 3.5 shows simplified behavior of a pure ammonium sulfate (AS) particle, pure organic acid (OA) particle (as described by Peng et al., 2001), and a mixed organic acid and ammonium sulfate (OA/AS) particle over the range $50\% \leq \text{RH} \leq 94\%$. Note that the mixed OA/AS particle shows smooth growth with RH, as opposed to the deliquescent behavior exhibited by the pure AS particle. The tendency of organics to retain water at low RH causes water uptake behavior for the OA/AS particle to follow that of the descending (i.e. efflorescence) branch of the pure AS growth curve. Since pure OA takes up less water at high RH than does pure AS, the growth curve for the OA/AS particle is suppressed, compared with that of pure AS. The overall result, as predicted by thermodynamic theory, is that the presence of OA leads to enhanced water uptake at low RH and suppressed GF at high RH.

Virkkula et al. (1999) concluded that the most important factor contributing to GF suppression at high RH was the volume fraction of organic present in an aerosol. Others have suggested that the exact chemical identity of the organic constituents is not especially important, and that for an organic component classified as either oxidized or hydrocarbon-like, its relative abundance determines its effect on GF values (McFiggans et al., 2005; Moore and Raymond, 2008). The aerosol measured during MASE-II was comprised of an internally-mixed combination of highly-oxidized organics with predominantly ammonium bisulfate in the size range 150-200nm. Results presented here from a stepwise linear regression on GF data from the marine atmosphere suggest that the single most important factor in predicting GF (aside from RH) is, indeed, $VF_{organic}$. This suggests that an aerosol containing a uniform, highly-oxidized organic component may be sufficiently characterized in global models by a size distribution, RH, and a bulk estimate of the relative abundance of organics.

A brief sensitivity study was undertaken, in order to determine the importance of the $VF_{organic}$ term in predicting water uptake for the marine aerosol encountered during this study. Predictions of

hygroscopic GF based on the assumption of an entirely inorganic aerosol yielded poorer agreement ($R^2 = 0.68$) than the simple parameterization presented in this paper ($R^2 = 0.77$). This suggests that accurate predictions of organic volume fraction are important to predict water uptake for a marine aerosol with a uniformly oxidized organic component.

In most instruments that measure aerosol hygroscopicity, residence times for humidification are on the order of seconds; much longer than the equilibration time for most inorganics with water vapor. Sjogren et al. (2007) noted, however, that particles with high volume fraction organic material may require as long as 40 s to achieve equilibrium with water vapor. If such long times are necessary to achieve equilibrium, hygroscopic measurement methods suitable for the field will tend to overpredict GF at low RH (water vapor does not evaporate completely from the particle during the drying process), while underpredicting GF at high RH (insufficient humidification time is provided for the organic fraction to achieve thermodynamic equilibrium with water vapor). In electrodynamic balance (EDB, (Cohen et al., 1987a,b,c)) studies, suspended particles are subjected to extended exposure to water vapor (minutes to hours), establishing equilibrium. Some organics exhibit extremely high deliquescence relative humidities (DRH) (e.g., oxalic acid), while others exhibit gradual hygroscopic growth at low RH and substantial growth at high RH (e.g., malonic acid) (Peng et al., 2001). It is possible, given the wide range of organic species in the atmosphere and correspondingly wide range of hygroscopic properties associated with those species, and the relatively short humidification times in the DASH-SP and other similar instruments, that the effects attributed to organics may reflect some kinetic instrumental limitations.

Additionally, while particles entering the DASH-SP are dried to well below relative humidity of efflorescence (RHE) for the inorganic salts encountered in the marine atmosphere, it is possible that the presence of organics causes some particles to remain in a supersaturated (with respect to efflorescence) state after drying. The inorganic fraction of such a supersaturated particle would exhibit gradual water uptake with increased relative humidity, even at RH lower than the RHD for the inorganic salt. Assuming deliquescent behavior of the inorganic salt (i.e. the inorganic fraction is crystalline at $RH < RHE$), this enhanced water uptake at low RH would be attributed to solely

the organic fraction, thereby leading to a potential overestimation in the organic GF.

3.6 Conclusions

We report a hygroscopic closure study for the coastal California aerosol, using size-resolved C-ToF-AMS chemical data coupled with highly time-resolved, multiple-RH hygroscopicity measurements from the DASH-SP.

Airmasses originating from continental locations showed elevated organic loading, and correspond to significant GF suppression at high RH. More moderate GF suppression was measured at intermediate RH and no impact was observed at low RH. A comparison of above-cloud with below-cloud aerosol indicated that a slightly organic-enriched layer above cloud corresponded with suppressed GF s at high RH. A volume-weighted hygroscopic closure provided excellent agreement with measured GF s, and mission-averaged organic GF s at 74, 85, and 92% were calculated to be 1.22, 1.45, and 1.48, respectively. These GF values are relatively high when compared with many previous estimations of organic GF , but agree well with values reported for dicarboxylic and multifunctional acids. These high organic GF s are indicative of the highly oxidized state of the aged organic fraction. A simplified parameterization for predicting GF was developed using a stepwise linear regression method. This parameterization is a function of only RH and $VF_{organic}$, and explains only 1% less variability than does the volume-weighted chemical closure. These results may be more broadly applicable to similar coastal conditions, where some aged organics are present in an otherwise marine-influenced atmosphere.

The richness of this hygroscopic/chemical data set underlies the significance of coupling the DASH-SP instrument with the AMS. The improved time resolution available with the DASH-SP eliminates much of the time-averaging of AMS composition data that is otherwise necessary with less highly time-resolved HTDMA hygroscopicity measurements. The importance of simultaneous GF measurements at multiple RH values is demonstrated by a simplified parameterization for predicting GF as a function of RH and $VF_{organic}$; a result potentially important for efficiently representing aerosol-water interactions in global models.

Bibliography

- Aiken, A. C., DeCarlo, P. F., Kroll, J., Worsnop, D., J.A., H., Docherty, K., Ulbrich, I., Mohr, C., Kimmel, J., Sueper, D., Sun, Y., Zhang, Q., Trimborn, A., Northway, M., Ziemann, P., Canagaratna, M., Onasch, T., Alfarra, M., Prevot, A., Dommen, J., Duplissy, J., Metzger, A., Baltensperger, U., and Jimenez, J. L.: O/C and OM/OC Ratios of Primary, Secondary, and Ambient Organic Aerosols with High-Resolution Time-of-Flight Aerosol Mass Spectrometry, *Environ. Sci. Technol.*, 42, 4478–4485, 2008.
- Allan, J., Bower, K., Alfarra, M., Delia, A., Jimenez, J., Middlebrook, A., Drewnick, F., Onasch, T., Canagaratna, M., Jayne, J., and Worsnop, D.: Technical note: Extraction of Chemically Resolved Mass Spectra from Aerodyne Aerosol Mass Spectrometer Data, *J. Aerosol Sci.*, 35, 909–922, 2004.
- Ansari, A. S. and Pandis, S. N.: Water absorption by secondary organic aerosol and its effect on inorganic aerosol behavior, *Environ. Sci. Technol.*, 34, 71–77, 2000.
- Berg, O. H., Swietlicki, E., and Krejci, R.: Hygroscopic growth of aerosol particles in the marine boundary layer over the Pacific and Southern Oceans during the First Aerosol Characterization Experiment (ACE 1), *J. Geophys. Res.*, 103, 16 535–16 545, 1998.
- Carrico, C. M., Rood, M. J., and Ogren, J. A.: Aerosol light scattering properties at Cape Grim, Tasmania, during the First Aerosol Characterization Experiment (ACE 1), *J. Geophys. Res.*, 103, 16 565–16 574, 1998.
- Carrico, C. M., Rood, M. J., Ogren, J. A., Neususs, C., Wiedensohler, A., and Heintzenberg, J.: Aerosol optical properties at Sagres, Portugal during ACE-2, *Tellus Series B-Chemical and Physical Meteorology*, 52, 694–715, 2000.
- Choi, M. Y. and Chan, C. K.: Continuous measurements of the water activities of aqueous droplets of water-soluble organic compounds, *J. Phys. Chem. A*, 106, 4566–4572, 2002a.
- Choi, M. Y. and Chan, C. K.: The effects of organic species on the hygroscopic behaviors of inorganic aerosols, *Environ. Sci. Technol.*, 36, 2422–2428, 2002b.

- Clegg, S. L. and Seinfeld, J. H.: Thermodynamic models of aqueous solutions containing inorganic electrolytes and dicarboxylic acids at 298.15 K. 2. Systems including dissociation equilibria, *J. Phys. Chem. A*, 110, 5718–5734, 2006.
- Clegg, S. L., Brimblecombe, P., and Wexler, A. S.: Thermodynamic model of the system $\text{H}^+\text{-NH}_4^+\text{-SO}_4^{2-}\text{-NO}_3^-\text{-H}_2\text{O}$ at tropospheric temperatures, *J. Phys. Chem. A*, 102, 2137–2154, 1998.
- Cocker, D. R., Clegg, S. L., Flagan, R. C., and Seinfeld, J. H.: The effect of water on gas-particle partitioning of secondary organic aerosol. Part I: alpha-pinene/ozone system, *Atmos. Environ.*, 35, 6049–6072, 2001a.
- Cocker, D. R., Mader, B. T., Kalberer, M., Flagan, R. C., and Seinfeld, J. H.: The effect of water on gas-particle partitioning of secondary organic aerosol: II. m-xylene and 1,3,5-trimethylbenzene photooxidation systems, *Atmos. Environ.*, 35, 6073–6085, 2001b.
- Cohen, M. D., Flagan, R. C., and Seinfeld, J. H.: Studies of concentrated electrolyte-solutions using the electrodynamic balance .1. Water activities for single-electrolyte solutions, *J. Phys. Chem.*, 91, 4563–4574, 1987a.
- Cohen, M. D., Flagan, R. C., and Seinfeld, J. H.: Studies of concentrated electrolyte-solutions using the electrodynamic balance .2. Water activities for mixed-electrolyte solutions, *J. Phys. Chem.*, 91, 4575–4582, 1987b.
- Cohen, M. D., Flagan, R. C., and Seinfeld, J. H.: Studies of concentrated electrolyte-solutions using the electrodynamic balance .3. Solute nucleation, *J. Phys. Chem.*, 91, 4583–4590, 1987c.
- Cruz, C. N. and Pandis, S. N.: Deliquescence and hygroscopic growth of mixed inorganic-organic atmospheric aerosol, *Environ. Sci. Technol.*, 34, 4313–4319, 2000.
- DeCarlo, P., Slowik, J., Worsnop, D., Davidovits, P., and Jimenez, J.: Particle Morphology and Density Characterization by Combined Mobility and Aerodynamic Diameter Measurements. Part 1: Theory, *Aerosol. Sci. Tech.*, 39, 1185–1205, 2004.

- Dougle, P. G., Veefkind, J. P., and ten Brink, H. M.: Crystallisation of mixtures of ammonium nitrate, ammonium sulphate and soot, *J. Aerosol Sci.*, 29, 375–386, 1998.
- Drewnick, F., Jayne, J. T., Canagaratna, M., Worsnop, D. R., and Demerjian, K. L.: Measurement of ambient aerosol composition during the PMTACS-NY 2001 using an aerosol mass spectrometer. Part II: Chemically speciated mass distributions, *Aerosol. Sci. Tech.*, 38, 104–117, suppl. 1, 2004a.
- Drewnick, F., Schwab, J. J., Jayne, J. T., Canagaratna, M., Worsnop, D. R., and Demerjian, K. L.: Measurement of ambient aerosol composition during the PMTACS-NY 2001 using an aerosol mass spectrometer. Part I: Mass concentrations, *Aerosol. Sci. Tech.*, 38, 92–103, suppl. 1, 2004b.
- Duplissy, J., Gysel, M., Alfarra, M. R., Dommen, J., Metzger, A., Prevot, A. S. H., Weingartner, E., Laaksonen, A., Raatikainen, T., Good, N., Turner, S. F., McFiggans, G., and Baltensperger, U.: Cloud forming potential of secondary organic aerosol under near atmospheric conditions, *Geophys. Res. Lett.*, 35, L03818, doi:10.1029/2007GL031075, 2008.
- Gasso, S., Hegg, D. A., Covert, D. S., Collins, D., Noone, K. J., Ostrom, E., Schmid, B., Russell, P. B., Livingston, J. M., Durkee, P. A., and Jonsson, H.: Influence of humidity on the aerosol scattering coefficient and its effect on the upwelling radiance during ACE-2, *Tellus Series B-Chemical and Physical Meteorology*, 52, 546–567, 2000.
- Gysel, M., Crosier, J., Topping, D. O., Whitehead, J. D., Bower, K. N., Cubison, M. J., Williams, P. I., Flynn, M. J., McFiggans, G. B., and Coe, H.: Closure study between chemical composition and hygroscopic growth of aerosol particles during TORCH2, *Atmos. Chem. Phys.*, 7, 6131–6144, 2007.
- Hameri, K., Charlson, R., and Hansson, H. C.: Hygroscopic properties of mixed ammonium sulfate and carboxylic acids particles, *AIChE J.*, 48, 1309–1316, 2002.
- Hegg, D. A., Covert, D. S., Rood, M. J., and Hobbs, P. V.: Measurements of aerosol optical properties in marine air, *J. Geophys. Res.*, 101, 12893–12903, 1996.

- Hegg, D. A., Covert, D. S., Crahan, K., and Jonssen, H.: The dependence of aerosol light-scattering on RH over the Pacific Ocean, *Geophys. Res. Lett.*, 29, 60–4, 2002.
- Hegg, D. A., Covert, D. S., Crahan, K. K., Jonsson, H. H., and Liu, Y.: Measurements of aerosol size-resolved hygroscopicity at sub and supermicron sizes, *Geophys. Res. Lett.*, 33, L21 808, doi:10.1029/2006GL026747, 2006.
- Huffman, J., Jayne, J., Drewnick, F., Aiken, A., Onasch, T., Worsnop, D., and Jimenez, J.: Design, modeling, optimization, and experimental tests of a particle beam width probe for the aerodyne aerosol mass spectrometer, *J. Aerosol Sci.*, 38, 1143–1163, 2005.
- IPCC: Climate Change 2007: The Physical Science Basis. Contribution of Working Group I to the Fourth Assessment Report of the Intergovernmental Panel on Climate Change, Cambridge University Press, Cambridge, United Kingdom and New York, NY, USA, 2007.
- Kaku, K. C., Hegg, D. A., Covert, D. S., Santarpia, J. L., Jonsson, H., Buzorius, G., and Collins, D. R.: Organics in the Northeastern Pacific and their impacts on aerosol hygroscopicity in the subsaturated and supersaturated regimes, *Atmospheric Chemistry and Physics*, 6, 4101–4115, 2006.
- Kasten, F.: Visibility forecast in phase of pre-condensation, *Tellus*, 21, 631–635, 1969.
- Kim, J., Yoon, S. C., Jefferson, A., and Kim, S. W.: Aerosol hygroscopic properties during Asian dust, pollution, and biomass burning episodes at Gosan, Korea in April 2001, *Atmos. Environ.*, 40, 1550–1560, 2006.
- Kondo, Y., Miyazaki, Y., Takegawa, N., Miyakawa, T., Weber, R. J., Jimenez, J. L., Zhang, Q., and Worsnop, D. R.: Oxygenated and water-soluble organic aerosols in Tokyo, *J. Geophys. Res.*, 112, D01 203, doi:10.1029/2006JD007056, 2007.
- Kotchenruther, R. A., Hobbs, P. V., and Hegg, D. A.: Humidification factors for atmospheric aerosols off the mid-Atlantic coast of the United States, *J. Geophys. Res.*, 104, 2239–2251, 1999.

- Kreisberg, N. M., Stolzenburg, M. R., Hering, S. V., Dick, W. D., and McMurry, P. H.: A new method for measuring the dependence of particle size distributions on relative humidity, with application to the Southeastern Aerosol and Visibility Study, *J. Geophys. Res.*, 106, 14 935–14 949, 2001.
- Lu, M. L., Conant, W. C., Jonsson, H. H., Varutbangkul, V., Flagan, R. C., and Seinfeld, J. H.: The Marine Stratus/Stratocumulus Experiment (MASE): Aerosol-cloud relationships in marine stratocumulus, *J. Geophys. Res.*, 112, D10 209, doi:10.1029/2006JD007985, 2007.
- Magi, B. I. and Hobbs, P. V.: Effects of humidity on aerosols in southern Africa during the biomass burning season, *J. Geophys. Res.*, 108, 8495, doi:10.1029/2002JD002144, 2003.
- Malm, W. C., Day, D. E., Kreidenweis, S. M., Collett, J. L., Carrico, C., McMeeking, G., and Lee, T.: Hygroscopic properties of an organic-laden aerosol, *Atmos. Environ.*, 39, 4969–4982, 2005.
- Massling, A., Wiedensohler, A., Busch, B., Neususs, C., Quinn, P., Bates, T., and Covert, D.: Hygroscopic properties of different aerosol types over the Atlantic and Indian Oceans, *Atmospheric Chemistry and Physics*, 3, 1377–1397, 2003.
- Massling, A., Leinert, S., Wiedensohler, A., and Covert, D.: Hygroscopic growth of sub-micrometer and one-micrometer aerosol particles measured during ACE-Asia, *Atmos. Chem. Phys.*, 7, 3249–3259, 2007.
- McFiggans, G., Alfarra, M. R., Allan, J., Bower, K., Coe, H., Cubison, M., Topping, D., Williams, P., Decesari, S., Facchini, C., and Fuzzi, S.: Simplification of the representation of the organic component of atmospheric particulates, *Faraday Discussions*, 130, 341–362, 2005.
- Moore, R. H. and Raymond, T. M.: HTDMA analysis of multicomponent dicarboxylic acid aerosols with comparison to UNIFAC and ZSR, *J. Geophys. Res.*, 113, D04 206, doi:10.1029/2007JD008660, 2008.
- Murphy, S., Agrawal, H., Sorooshian, A., Padaro, L., Gates, H., Hersey, S., Welch, W., Jung, H., Miller, J., Cocker, D., Nenes, A., Jonsson, H., Flagan, R., and Seinfeld, J.: Comprehensive

- Simultaneous Shipboard and Airborne Characterization of Exhaust from a Modern Container Ship at Sea, *Environ. Sci. Technol.*, submitted.
- Peng, C., Chan, M. N., and Chan, C. K.: The hygroscopic properties of dicarboxylic and multifunctional acids: Measurements and UNIFAC predictions, *Environ. Sci. Technol.*, 35, 4495–4501, 2001.
- Peng, C. G. and Chan, C. K.: The water cycles of water-soluble organic salts of atmospheric importance, *Atmos. Environ.*, 35, 1183–1192, 2001.
- Petters, M. D., Kreidenweis, S. M., Snider, J. R., Koehler, K. A., Wang, Q., Prenni, A. J., and Demott, P. J.: Cloud droplet activation of polymerized organic aerosol, *Tellus Series B-Chemical and Physical Meteorology*, 58, 196–205, 2006.
- Prenni, A. J., DeMott, P. J., Kreidenweis, S. M., Sherman, D. E., Russell, L. M., and Ming, Y.: The effects of low molecular weight dicarboxylic acids on cloud formation, *J. Phys. Chem. A*, 105, 11 240–11 248, 2001.
- Prenni, A. J., De Mott, P. J., and Kreidenweis, S. M.: Water uptake of internally mixed particles containing ammonium sulfate and dicarboxylic acids, *Atmos. Environ.*, 37, 4243–4251, 2003.
- Prenni, A. J., Petters, M. D., Kreidenweis, S. M., DeMott, P. J., and Ziemann, P. J.: Cloud droplet activation of secondary organic aerosol, *J. Geophys. Res.*, 112, D10 223, 2007.
- Rood, M. J., Larson, T. V., Covert, D. S., and Ahlquist, N. C.: Measurement of laboratory and ambient aerosols with temperature and humidity controlled nephelometry, *Atmos. Environ.*, 19, 1181–1190, 1985.
- Saathoff, H., Naumann, K. H., Schnaiter, M., Schock, W., Mohler, O., Schurath, U., Weingartner, E., Gysel, M., and Baltensperger, U.: Coating of soot and $(\text{NH}_4)_2\text{SO}_4$ particles by ozonolysis products of alpha-pinene, *J. Aerosol Sci.*, 34, 1297–1321, 2003.
- Seinfeld, J. and Pandis, S.: *Atmospheric Chemistry and Physics*, Second Edition, Wiley-Interscience, New York, NY, USA, 2006.

- Sjogren, S., Gysel, M., Weingartner, E., Baltensperger, U., Cubison, M. J., Coe, H., Zardini, A. A., Marcolli, C., Krieger, U. K., and Peter, T.: Hygroscopic growth and water uptake kinetics of two-phase aerosol particles consisting of ammonium sulfate, adipic and humic acid mixtures, *J. Aerosol Sci.*, 38, 157–171, 2007.
- Sorooshian, A., Hersey, S., Brechtel, F., Corless, A., Flagan, R., and Seinfeld, J.: Rapid, Size-Resolved Aerosol Hygroscopic Growth Measurements: Differential Aerosol Sizing and Hygroscopicity Spectrometer Probe (DASH-SP), *Aerosol. Sci. Tech.*, 42, 445–464, 2008a.
- Sorooshian, A., Murphy, S., Hersey, S., Gates, H., Padaro, L., Nenes, A., Brechtel, F., Jonsson, H., Flagan, R., and Seinfeld, J.: Comprehensive airborne characterization of aerosol from a major bovine source, *Atmos. Chem. Phys.*, 8, 5489–5520, 2008b.
- Swietlicki, E., Zhou, J. C., Covert, D. S., Hameri, K., Busch, B., Vakeva, M., Dusek, U., Berg, O. H., Wiedensohler, A., Aalto, P., Makela, J., Martinsson, B. G., Papaspiropoulos, G., Mentes, B., Frank, G., and Stratmann, F.: Hygroscopic properties of aerosol particles in the northeastern Atlantic during ACE-2, *Tellus Series B-Chemical and Physical Meteorology*, 52, 201–227, 2000.
- Tomlinson, J. M., Li, R. J., and Collins, D. R.: Physical and chemical properties of the aerosol within the southeastern Pacific marine boundary layer, *J. Geophys. Res.*, 112, 1–13, 2007.
- Topping, D. O., McFiggans, G. B., and Coe, H.: A curved multi-component aerosol hygroscopicity model framework: Part 1 - Inorganic compounds, *Atmos. Chem. Phys.*, 5, 1205–1222, 2005a.
- Topping, D. O., McFiggans, G. B., and Coe, H.: A curved multi-component aerosol hygroscopicity model framework: Part 2 - Including organic compounds, *Atmos. Chem. Phys.*, 5, 1223–1242, 2005b.
- Vakeva, M., Hameri, K., and Aalto, P. P.: Hygroscopic properties of nucleation mode and Aitken mode particles during nucleation bursts and in background air, *J. Geophys. Res.*, 107, PAR9–1–11, 2002.

- Varutbangkul, V., Brechtel, F. J., Bahreini, R., Ng, N. L., Keywood, M. D., Kroll, J. H., Flagan, R. C., Seinfeld, J. H., Lee, A., and Goldstein, A. H.: Hygroscopicity of secondary organic aerosols formed by oxidation of cycloalkenes, monoterpenes, sesquiterpenes, and related compounds, *Atmos. Chem. Phys.*, 6, 2367–2388, 2006.
- Virkkula, A., Van Dingenen, R., Raes, F., and Hjorth, J.: Hygroscopic properties of aerosol formed by oxidation of limonene, alpha-pinene, and beta-pinene, *J. Geophys. Res.*, 104, 3569–3579, 1999.
- Zhou, J. C., Swietlicki, E., Berg, O. H., Aalto, P. P., Hameri, K., Nilsson, E. D., and Leck, C.: Hygroscopic properties of aerosol particles over the central Arctic Ocean during summer, *J. Geophys. Res.*, 106, 32 111–32 123, 2001.

Table 3.1: Previous marine aerosol hygroscopicity studies.

Investigators	Year	Study Area	Reported GFs
Hegg	1996	Eastern Pacific	1.4 – 2.0
Berg	1998	Pacific and Southern Oceans	1.56 – 1.78
Kotchenruther	1999	Mid-Atlantic	1.81 – 2.3 [†]
Gasso	2000	Eastern Atlantic	$\gamma = 0.51 - 0.75^{\ddagger}$
Swietlicki	2000	Northeastern Atlantic	1.6 – 1.8
Zhou	2001	Arctic Ocean	1.4 – 1.9
Hegg	2002	Eastern Pacific	$\gamma = 0.2 - 0.7^{\ddagger}$
Vakeva	2002	Northeastern Atlantic	1.3 – 1.4*
Massling	2003	Atlantic and Indian Oceans	1.6 – 2.0
Hegg	2006	Eastern Pacific	1.3 – 1.5
Kaku	2006	Eastern Pacific	1.2 – 1.7
Tomlinson	2007	Southeastern Pacific	1.3 – 1.7*

[†] Ratio of light scattering coefficient at 80% RH to 30% RH

[‡] γ from the expression $b_{sp}(RH)/b_{sp}(RH_0) = ((1 - RH/100)/(1 - RH_0/100))^{-\gamma}$ (Kasten, 1969)

* Aitken mode particles

* 85% RH

Table 3.2: MASE-II flights.

Flight Number (RF)	Date	Type of Flight
1	10-Jul-07	Cloud/aerosol interactions
2	11-Jul-07	Cloud/aerosol interactions
3	12-Jul-07	Bovine source probe
4	14-Jul-07	Cloud/aerosol interactions
5	15-Jul-07	Cloud/aerosol interactions
6	16-Jul-07	Coordinated ship plume probe
7	21-Jul-07	Cloud/aerosol interactions
8	22-Jul-07	Cloud/aerosol interactions
9	23-Jul-07	Cloud/aerosol interactions
10	24-Jul-07	Cloud/aerosol interactions
11	25-Jul-07	Cloud/aerosol interactions
12	26-Jul-07	Cloud/aerosol interactions
13	28-Jul-07	Cloud/aerosol interactions
14	29-Jul-07	Cloud/aerosol interactions
15	30-Jul-07	Bovine source probe
16	31-Jul-07	Cloud/aerosol interactions

Table 3.3: MASE-II instrument payload.

Parameter	Instrument	Time Resolution	Detection Limit	Size Range
Particle Number Concentration	Condensation Particle Counter (TSI CPC 3010)	1 s	$0-10\,000\text{ cm}^{-3}$	$D_p \geq 10\text{ nm}$
Particle Number Concentration (including ultrafine)	Condensation Particle Counter (TSI CPC 3025)	1 s	$0-100\,000\text{ cm}^{-3}$	$D_p \geq 3\text{ nm}$
Aerosol Size Distribution	Scanning differential mobility analyzer (Dual Automated Classified Aerosol Detector, DACAD)	73 s	N/A	10–700 nm
Aerosol Size Distribution	Passive Cavity Aerosol Spectrometer Probe (PCASP)	1 s	N/A	0.1–2.6 μm
Separation of Cloud Droplets From Interstitial Aerosol	Counterflow Virtual Impactor	N/A	N/A	N/A
Cloud Droplet Size Distribution	Phase Doppler Interferometer (PDI)	1 s	N/A	4–200 μm
Cloud and Drizzle Drop Size Distribution	Forward Scattering Spectrometer Probe (FSSP)	1 s	N/A	1–46 μm
Cloud Droplet Liquid Water Content	Light Diffraction (Gerber PVM-100 probe)	1 s	N/A	5–50 nm
Aerosol Bulk Ionic Composition and Soluble Organic Composition	Particle-Into-Liquid Sampler (PILS)	5 min	$0.02-0.28\text{ }\mu\text{g}/\text{m}^3$	1 μm
Aerosol Bulk Composition (non-refractory species)	Aerodyne compact Time-of-Flight Aerosol Mass Spectrometer (C-ToF-AMS)	1 s or 15 s	$\leq 0.25\text{ g}/\text{m}^3$	$40\text{ nm} \leq D_{p,va} \leq 1\text{ }\mu\text{m}$
Aerosol Hygroscopicity	Differential Aerosol Sizing and Hygroscopicity Spectrometer Probe (DASH-SP)	15–100 s	N/A	$150\text{ nm} \leq D_p \leq 1\text{ }\mu\text{m}$
Soot Absorption	Photoacoustic Absorption Spectrometer (PAS)	1 s	1 Mm^{-1}	10 nm–5 μm
Soot Absorption	Particle Soot Absorption Photometer (PSAP)	$\geq 1\text{ s}$	N/A	N/A

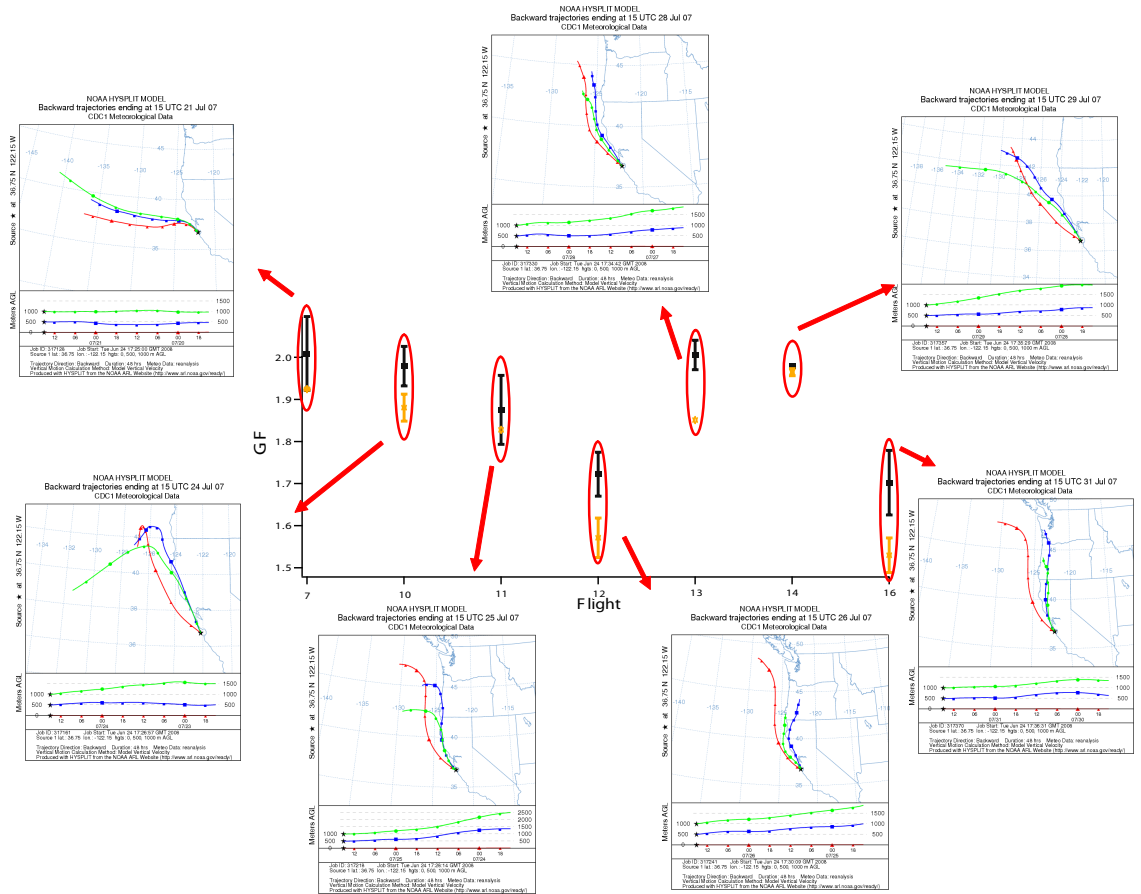


Figure 3.1: 92% GF values for $D_{em,dry} = 200$ nm particles are shown for below (black) and above (yellow) cloud flight legs. 48-hr HYSPLIT back-trajectories show airmass origin for each flight. Flights 12 and 16 show both suppressed GF values and continental, polluted airmass origin.

Table 3.4: *GF* results for below, above, free troposphere (FT), and ship plume measurements.

150 nm												
Flight	Below			Above			FT			Ship Plume		
	74%	85%	92%	74%	85%	92%	74%	85%	92%	74%	85%	92%
7	1.40±0.04	1.57±0.03	1.82±0.05	1.26±0.06	1.55±0.04	1.78±0.01	1.40±0.03	1.55±0.03	1.84±0.04			
10	1.42±0.04	1.60±0.06	1.80±0.04	1.37±0.10	1.57±0.04	1.71±0.11	1.42±0.03	1.56±0.04	1.70±0.07	1.42±0.04	1.62±0.03	1.78±0.04
11	1.44±0.05	1.61±0.06	1.80±0.07	1.40±0.07	1.51±0.02	1.64±0.05	1.38±0.07	1.52±0.06	1.65±0.10			
12	1.38±0.03	1.58±0.03	1.63±0.04	1.34±0.04	1.51±0.03	1.55±0.01	1.38±0.02	1.60±0.01	1.63±0.01			
13	1.39±0.01	1.61±0.05	1.82±0.02	1.35±0.01	1.61±0.03	1.75±0.05	1.27±0.05	1.49±0.07	1.61±0.08			
14	1.36±0.05	1.65±0.21	1.82±0.14	1.39±0.02	1.62±0.01	1.87±0.09	1.37±0.03	1.60±0.03	1.77±0.06			
16	1.41±0.02	1.58±0.05	1.64±0.08	1.33±0.03	1.52±0.03	1.54±0.03	1.29±0.04	1.49±0.07	1.52±0.06	1.38±0.02	1.59±0.02	1.61±0.04

175 nm												
Flight	Below			Above			FT			Ship Plume		
	74%	85%	92%	74%	85%	92%	74%	85%	92%	74%	85%	92%
7	1.36±0.06	1.54±0.02	1.95±0.03	1.28±0.04	1.53±0.03	1.91±0.06	1.24±0.08	1.52±0.03	1.87±0.10			
10	1.41±0.06	1.59±0.05	1.93±0.02	1.34±0.05	1.51±0.01	1.83±0.06	1.33±0.02	1.60±0.03	1.89±0.05	1.34±0.02	1.55±0.05	1.88±0.06
11	1.31±0.08	1.48±0.07	1.82±0.09	1.31±0.03	1.44±0.09	1.77±0.03	1.33±0.04	1.53±0.12	1.77±0.23			
12	1.33±0.02	1.55±0.04	1.63±0.08	1.26±0.06	1.48±0.08	1.51±0.07	1.35±0.02	1.57±0.01	1.60±0.01			
13	1.34±0.03	1.58±0.04	2.00±0.05	1.3	1.55	1.78	1.24±0.05	1.44±0.06	1.63±0.10			
14	1.34±0.01	1.63±0.02	2.03±0.01	1.32±0.02	1.58±0.02	1.91±0.05	1.33±0.02	1.50±0.08	1.79±0.22			
16	1.35±0.04	1.54±0.03	1.62±0.06	1.28±0.02	1.43±0.04	1.45±0.04	1.24±0.04	1.38±0.06	1.40±0.10	1.33±0.03	1.52±0.04	1.55±0.03

200 nm												
Flight	Below			Above			FT			Ship Plume		
	74%	85%	92%	74%	85%	92%	74%	85%	92%	74%	85%	92%
7	1.37±0.04	1.57±0.03	1.98±0.03	1.22±0.06	1.56±0.05	1.92±0.01	1.21±0.01	1.54±0.08	1.91±0.04			
10	1.41±0.09	1.72±0.09	2.01±0.05	1.33±0.02	1.57±0.07	1.87±0.04	1.35±0.01	1.63±0.06	1.93±0.06	1.33±0.04	1.66±0.06	1.95±0.05
11	1.25±0.11	1.45±0.17	1.86±0.07	1.26	1.47	1.83	1.36±0.16	1.56±0.15	1.89±0.20			
12	1.33±0.03	1.64±0.03	1.73±0.05	1.29±0.03	1.48±0.10	1.55±0.12	1.37±0.05	1.64±0.05	1.69±0.04			
13	1.36±0.05	1.68±0.05	2.01±0.04	1.3	1.61	1.85	1.21±0.08	1.45±0.07	1.78±0.12			
14	1.42±0.11	1.65±0.05	1.98±0.10	1.31±0.05	1.60±0.03	1.96±0.01	1.35±0.09	1.59±0.10	1.89±0.11			
16	1.35±0.02	1.59±0.05	1.77±0.08	1.26±0.02	1.45±0.08	1.53±0.10	1.23±0.06	1.40±0.10	1.40±0.11	1.33±0.03	1.62±0.04	1.66±0.06

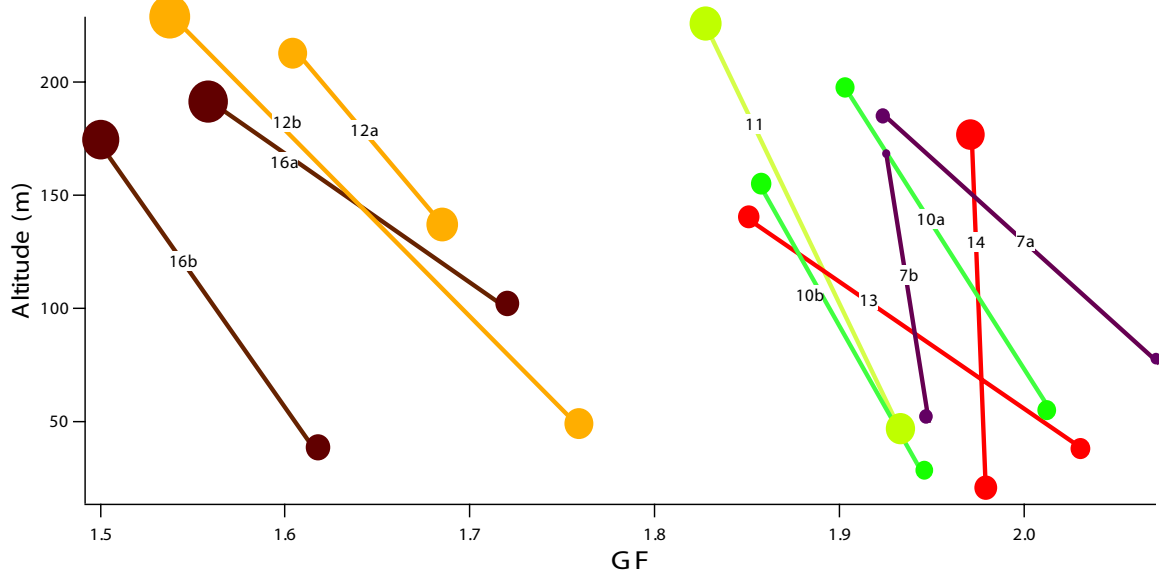


Figure 3.2: Below- and above-cloud 92% GF values for $D_{em,dry}$ 200 nm particles as a function of altitude, with lines connecting measurements made on the same ‘trip’ from bottom to top of cloud. Marker size is proportional to $V_{organic}$, and ranges from 0.10 to 0.90. ‘a’ and ‘b’ designate separate ‘trips’ during the same flight.

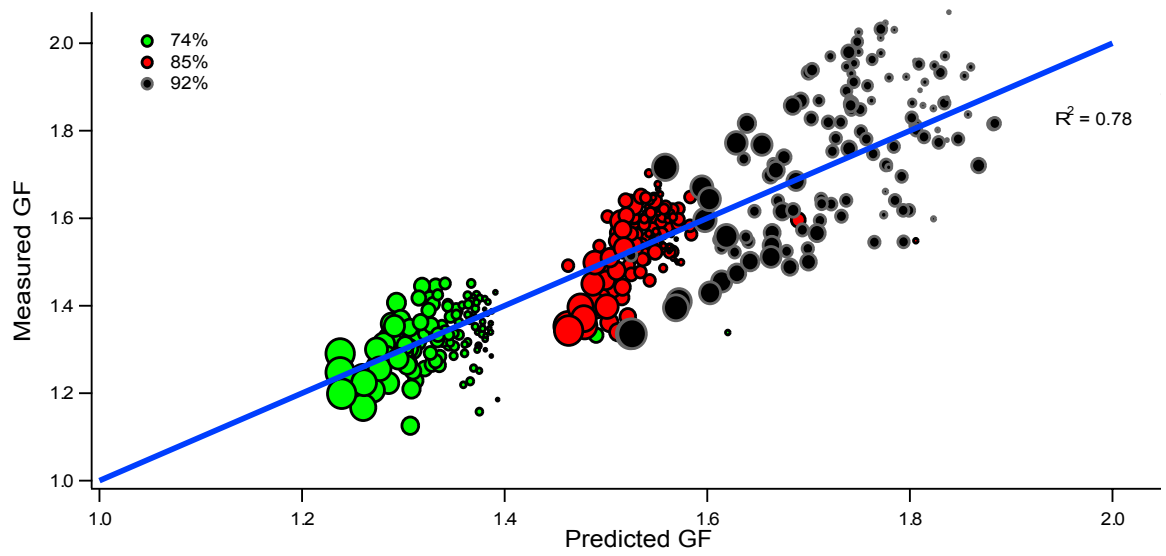


Figure 3.3: Measured GF values versus volume-weighted predictions. Markers are color-coded with RH, and marker size is proportional to $V_{Organic}$ (ranging from 0.10 to 0.90). The blue line represents 1:1.

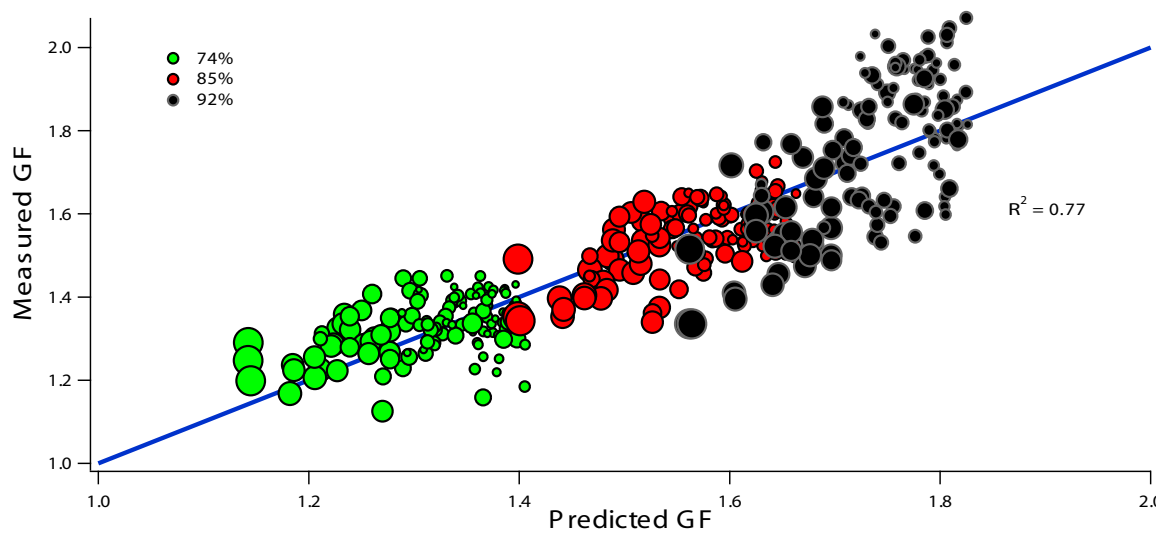


Figure 3.4: Predictions of GF from the simplified parameterization. Markers are color-coded with RH, and marker size is proportional to $V_{Organic}$ (ranging from 0.10 to 0.90). The blue line represents 1:1.

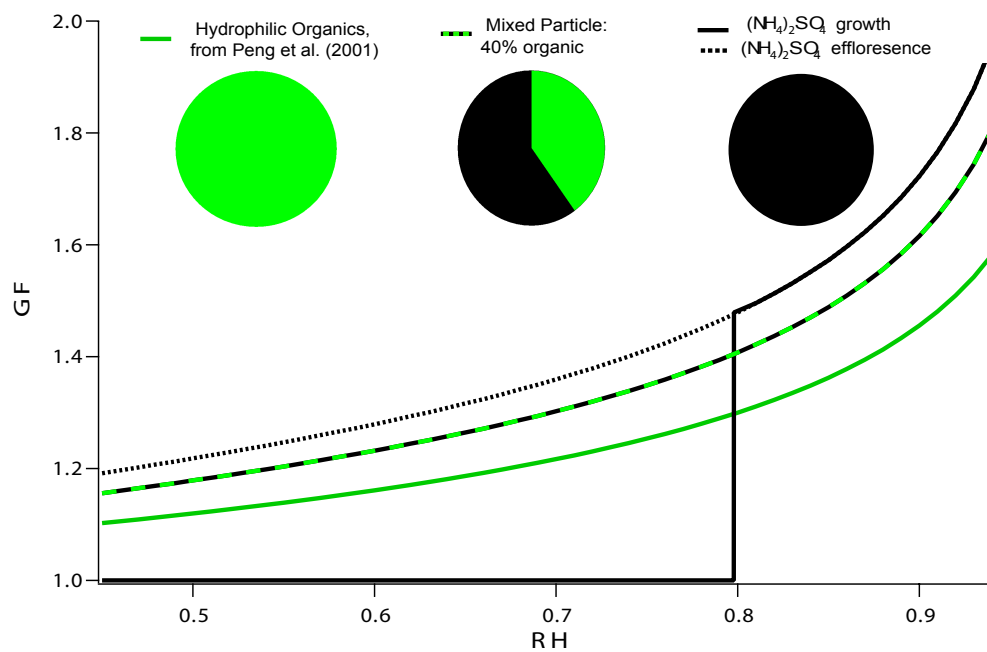


Figure 3.5: Comparison of growth curves for pure ammonium sulfate, pure hydrophilic organic, and mixed organic/inorganic particles. Ammonium sulfate curves calculated from AIM (Clegg et al., 1998)

Chapter 4

The Pasadena Aerosol Characterization Observatory (PACO): Chemical and Physical Analysis of the Western Los Angeles Basin Aerosol*

*Reproduced with permission from “The Pasadena Aerosol Characterization Observatory (PACO): Chemical and Physical Analysis of the Western Los Angeles Basin Aerosol” by S.P. Hersey, J.S. Craven, K.A. Schilling, A.R. Metcalf, M.N. Chan, Richard C. Flagan, and John H. Seinfeld, *Atmospheric Chemistry and Physics Discussions*, 11, 5867–5933, doi:10.5194/acpd-11-5867-2011, 2011. Copyright 2011 by Authors. This work is licensed under a Creative Commons License.

4.1 Abstract

The Pasadena Aerosol Characterization Observatory (PACO) represents the first major aerosol characterization experiment centered in the Western Los Angeles Basin. The sampling site, located on the campus of the California Institute of Technology in Pasadena, was positioned to sample a continuous afternoon influx of transported urban aerosol with a photochemical age of 1-2 h and generally free from major local contributions. Sampling spanned 5 months during the summer of 2009, which were broken into 3 regimes on the basis of distinct meteorological conditions. Regime I was characterized by a series of low pressure systems, resulting in high humidity and rainy periods with clean conditions. Regime II typified early summer meteorology, with significant morning marine layers and warm, sunny afternoons. Regime III was characterized by hot, dry conditions with little marine layer influence.

Organic aerosol (OA) is the most significant constituent of Los Angeles aerosol (42, 43, and 55% of total submicron mass in regimes I, II, and III, respectively), and that the overall oxidation state remains relatively constant on timescales of days to weeks ($O:C = 0.44 \pm 0.08$, 0.55 ± 0.05 , and 0.48 ± 0.08 during regimes I, II, and III, respectively), with no difference in O:C between morning and afternoon periods. Periods characterized by significant morning marine layer influence followed by photochemically favorable afternoons displayed significantly higher aerosol mass and O:C ratio, suggesting that aqueous processes may be important in the generation of secondary aerosol and oxidized organic aerosol (OOA) in Los Angeles.

Water soluble organic mass (WSOM) reaches maxima near 1400-1500 local time (LT), but the percentage of AMS organic mass contributed by WSOM remains relatively constant throughout the day. Sulfate and nitrate reside predominantly in accumulation mode aerosol, while afternoon SOA production coincides with the appearance of a distinct fine mode dominated by organics. Particulate NH_4NO_3 and $(NH_4)_2SO_4$ appear to be NH_3 -limited in regimes I and II, but a significant excess of particulate NH_4^+ in the hot, dry regime III suggests significantly less marine SO_4^{2-} and the presence of organic amines.

Positive Matrix Factorization (PMF) analysis of C-ToF-AMS data resolved three factors, corre-

sponding to a hydrocarbon-like OA (HOA), semivolatile OOA (SV-OOA), and low-volatility OOA (LV-OOA). HOA appears to be a periodic plume source, while SV-OOA exhibits a strong diurnal pattern correlating with ozone. Peaks in SV-OOA concentration correspond to peaks in DMA number concentration and the appearance of a fine organic mode. LV-OOA appears to be an aged accumulation mode constituent that may be associated with aqueous-phase processing, correlating strongly with sulfate and representing the dominant background organic component.

Filter analysis revealed a complex mixture of species during periods dominated by SV-OOA and LV-OOA, with LV-OOA periods characterized by shorter-chain dicarboxylic acids (higher O:C ratio), as well as appreciable amounts of nitrate- and sulfate- substituted organics. Phthalic acid was ubiquitous in filter samples, suggesting that PAH photochemistry may be an important SOA pathway in Los Angeles.

Water uptake characteristics indicate that hygroscopicity is largely controlled by organic mass fraction (OMF). The hygroscopicity parameter κ averaged 0.31 ± 0.08 , approaching 0.5 at low OMF and 0.1 at high OMF, with increasing OMF suppressing hygroscopic growth and increasing critical dry diameter for CCN activation (D_d). An experiment-averaged κ_{org} of 0.14 was calculated, indicating that the highly-oxidized organic fraction of aerosol in Los Angeles is appreciably more hygroscopic than previously reported in urban areas.

Finally, PACO provides context for results forthcoming from the CalNex field campaign, which involved ground sampling in Pasadena during the spring and summer of 2010.

4.2 Introduction

Over half the world's population lives in urban areas, and that fraction is expected to increase in coming decades (Bremner et al., 2009). There have been a number of recent coordinated studies focused on characterizing particulate air quality in major urban areas, such as Pittsburgh, PA (Pittsburgh Air Quality Study, PAQS; e.g., Pekney et al., 2006; Bein et al., 2006; Wittig et al., 2004; Cabada et al., 2004; Modey et al., 2004), Los Angeles, CA [(Southern California Air Quality Study, SCAQS; e.g., Eldering et al., 1994; Watson et al., 1994; Chow et al., 1994; Turpin and Huntzicker,

1991), (Southern California Ozone Study 1997, SCOS97-NARSTO; e.g., Croes and Fujita, 2003; Liu et al., 2000; Pastor et al., 2003; Hughes et al., 2002; Liu et al., 2000), and (Secondary Organic Aerosol in Riverside, SOAR ; e.g., Docherty et al., 2008; Eatough et al., 2008; Denkenberger et al., 2007)), Mexico City, Mexico (Megacity Initiative: Local and Global Research Observations, MILAGRO; e.g., DeCarlo et al., 2008; Stone et al., 2008; Aiken et al., 2009), and Beijing, China (Campaign of Air Quality Research in Beijing, CAREBEIJING; e.g., Matsui et al., 2009; Yue et al., 2009; van Pinxteren et al., 2009).

The Los Angeles metropolitan area, with a population of over 17 million people, has long been considered a laboratory for air quality. Once the quintessential example of classic photochemical smog, the Los Angeles area has, as a result of decades of aggressive emission controls, reached a point where 8-h U.S. National Ambient Air Quality Standard ozone exceedances have decreased from over 200 days/year in the 1980s to 120 in 2008 (AQMD, 2010). Nonetheless, this area remains one in which particulate matter levels continue to regularly exceed air quality standards, with annual $PM_{2.5}$ averages exceeding the national standard every year from 2000-2008 in Los Angeles County (CARB, 2010).

The Los Angeles basin is generally characterized as source-rich in its western area, with prevailing west and southwest winds transporting emissions downwind toward the east and northeast (Lu and Turco, 1995). Three major coordinated studies have been undertaken to characterize Los Angeles air quality, in addition to ongoing work to describe facets of Los Angeles aerosol (Table 4.1). The majority of previous studies in the Los Angeles basin have been centered in the downwind, eastern part of the basin, roughly 60 km east of downtown Los Angeles. The aerosol in this region is predominantly aged, with local contributions as well.

A major source of gaseous and particulate pollution in the Los Angeles area is mobile source emissions. The Los Angeles aerosol undergoes dramatic evolution from nighttime/morning periods to the photochemically active afternoon, characterized by changes in both its microphysical properties and composition. Overall, the submicron aerosol is dominated by organic aerosol (OA), which is predominantly secondary in origin (SOA), and nitrate (Docherty et al., 2008), with smaller amounts

of sulfate and a minor chloride contribution. Sulfate is primarily the result of marine sources, both natural biota and shipping-related sulfur emissions (Watson et al., 1994).

The Pasadena Aerosol Characterization Observatory experiment (PACO) was conducted from May-August 2009 in Pasadena, CA, in the north-central portion of the Los Angeles basin, 16 km NW of downtown Los Angeles. Aerosol physics, composition, and hygroscopicity were measured during 54 days that spanned three distinct regimes of the annual meteorological cycle. A major forest fire occurred at the end of the sampling period, starting on 26-Aug and consuming over 160,000 acres of the Angeles National Forest before containment on 16-Oct. Named the “Station Fire,” its southernmost extent was roughly 8 km from the sampling site, and emissions from the fire impacted the sampling site with periodic heavy smoke, soot, and ash. Results from PACO sampling during the Station Fire will be presented in subsequent work.

PACO represents the first prolonged experiment aimed at characterizing the aerosol near the source-rich western/central part of the Los Angeles basin; comparisons with previous studies in downwind areas will help determine the rate of aerosol generation from Los Angeles sources, as well as the nature of aerosol transformations with downwind transport. Further, the PACO study was well-positioned to precede the 2010 CalNex field campaign (<http://www.esrl.noaa.gov/csd/calnex/>).

This paper presents an overview of the PACO experiment. Aerosol number and volume distributions measured by a differential mobility analyzer (DMA) exhibit distinct diurnal patterns, and composition data from an Aerodyne Compact-Time-of-Flight Aerosol Mass Spectrometer (C-ToF AMS) indicate that these patterns are associated largely with the production of semivolatile oxidized organic species during photochemically active daytime periods. AMS-based Positive Matrix Factorization (PMF) results indicate that the character of OA in Los Angeles is overwhelmingly oxidized and secondary, and the high time resolution data allow for investigation of the daily evolution of OA components. Ultra Performance Liquid Chromatography/Electrospray Ionization Time-of-Flight High-Resolution Mass Spectrometry (UPLC/ESI-TOFMS) analysis of high-volume filter samples provides further evidence for diurnal changes in the character of OA, while thermal-optical analysis of low-volume, denuded filter samples reveals the magnitude of organic and elemental carbon

in morning versus afternoon sampling periods. A particle-into-liquid sampler with offline ion chromatography analysis (PILS-IC) provides quantitative water-soluble inorganic ion composition during PACO, while a PILS coupled with online total organic carbon analysis (PILS-TOC) measured total water soluble organic carbon measurements during the third regime. Finally, trends in aerosol hygroscopicity indicate the degree to which changes in the magnitude and character of OA affect particle water uptake. PACO results are compared with previous aerosol characterization experiments in the Los Angeles basin, with major differences attributed to regional variations in both source profiles and degree of aging.

4.3 Methods

Sampling was conducted on the Caltech campus in Pasadena, at 34.138° N, 118.124° W. Caltech is located in the western portion of the Los Angeles basin, 8 km south of the San Gabriel Mountains and 16 km NE of downtown Los Angeles in the San Gabriel Valley. The 210 freeway is located 1.5 km north of the site, with heavy traffic between the hours of 0800 and 0900, and then again between 1500 and 1900. Prevailing daytime winds are from the W or SW, minimizing the impact of primary emissions from the 210 freeway at the sampling site, but overnight NW winds occasionally bring freeway emissions to Caltech. Other than this periodic impact from local primary emissions, the Pasadena aerosol is representative of urban background particulate pollution from near the source-rich downtown area of the Los Angeles basin.

PACO sampling took place between May and August of 2009, spanning the transition from spring to summer meteorological regimes. PACO was separated into three distinct analysis periods on the basis of meteorology, as summarized in Table 4.2.

With the exception of a high-volume filter sampler located outdoors on the roof, instruments sampled from inlets connected to a main sampling line drawing in ambient air at a 16 liters per minute (L/min) laminar flow rate. Sample flow to each instrument was supplemented with pumps to be isokinetic with flow in the main sampling line, and sample lines were designed to draw from the center of flow through the main line. Ambient air was dried by nafion driers upstream of each

instrument.

4.3.1 Meteorology

Hourly meteorological data were downloaded from the Remote Automatic Weather Stations (RAWS) archive from the Western Regional Climate Center at the Desert Research Institute (DRI, Reno, Nevada). Data are from the Santa Fe Dam station, approximately 16 km east of the sampling site in the San Gabriel Valley, and are available online: <http://www.raws.dri.edu/cgi-bin/rawMAIN.pl?caCSFD>.

4.3.2 Gas-Phase Data

Hourly O_3 , NO_x , and CO data were obtained from the California Air Resources Board's Pasadena (South Wilson) monitoring site located on the Caltech campus. Data are available online at <http://www.arb.ca.gov/adam/hourly/hourly1.php>.

4.3.3 Differential Mobility Analyzer

Particle size distribution measurements were performed with a cylindrical scanning differential mobility analyzer (TSI Model 3081) upstream from a condensation particle counter (TSI Model 3760). A logarithmic scan from a mobility diameter of 15 nm to 815 nm was completed every 237 s. The sheath and excess flows of 2.5 L/min were used, with a 10:1 flow rate ratio of sheath-to-aerosol.

4.3.4 Aerosol Mass Spectrometer

An Aerodyne compact time-of-flight aerosol mass spectrometer (C-ToF-AMS; Drewnick et al., 2005; Canagaratna et al., 2007) measured aerosol composition and size information for 54 days during PACO. The AMS collects sub-micron particles via an aerodynamic lens into a particle sizing chamber, after which particles are vaporized and ionized by a heater and filament assembly. Aerosol fragments are then orthogonally extracted into an ion time-of-flight chamber where they are detected and interpreted as mass spectra. Adjustments to the AMS fragmentation table were made regularly, based on 21 filter sample periods over the course of PACO (Allan et al., 2004b). Additionally,

thirteen ionization efficiency calibrations were made using ammonium nitrate solutions. The AMS sulfate measurement was compared to sulfate concentrations from the PILS-IC, resulting in an AMS collection efficiency (CE) of 0.5. This CE is in agreement with previous ambient studies (Huffman et al., 2005; Drewnick et al., 2003; Allan et al., 2004a). AMS data were processed with the ToF-AMS Analysis Toolkit in Igor Pro 6 (Wavemetrics, Lake Oswego, OR).

4.3.5 Positive Matrix Factorization Analysis

The dominant fraction of aerosol is organic in most urban areas (Zhang et al., 2007). OA comprises a multitude of compounds, such that characterization by identification of each component is not currently possible (Schauer et al 1996). Positive Matrix Factorization (PMF) has been used to deconvolve AMS mass spectra in order to identify classes of organic compounds that constitute OA (Paatero and Tapper, 1994; Paatero, 1997; Ulbrich et al., 2009). PMF solutions represent linear, positive combinations of mass spectra that describe variability in data, and AMS-based PMF results from most sites resolve factors whose mass spectra have characteristics of hydrocarbon-like OA (HOA) and oxygenated OA (OOA), with other factors such as biomass burning OA (BBOA) occurring in some areas (Zhang et al., 2007). OOA can often be further deconvolved into low-volatility OOA (LV-OOA) and semivolatile OOA (SV-OOA), broadly representing aged, transported, and highly oxidized OA and fresher, local, and less oxidized OA, respectively (Ng et al., 2010). AMS measurements, in conjunction with PMF analysis, allow for investigation of the diurnal evolution of OA and rapid changes in OA occurring during photochemically intense periods. Further, the combination of PMF solutions with analysis of the relative abundance of mass-to-charge (m/z) ratios 43 and 44 can be used as an aerosol aging diagnostic that allows comparison between locations (Ng et al., 2010).

For the PACO dataset, bulk AMS organic aerosol was prepared and then processed using the PMF2.exe algorithm (Paatero and Tapper, 1994). Solutions from the PMF algorithm were compared to meteorological variables and chemical tracers, as well as previously published mass spectra, using the PMF Evaluation Tool (PET Ulbrich et al., 2009). The strategic procedure for probing the PMF

solution space is provided in the Supplemental Information.

4.3.6 PILS-IC

A Particle-into-Liquid Sampler coupled with off-line Ion Chromatography (PILS-IC, Sorooshian et al., 2006) sampled during 4-h periods (0700 - 1100 and 1500 - 1900), providing quantitative measurements of inorganic and organic ions. The PILS samples ambient air through a 1 μm cut size impactor and three denuders (URG and Sunset Laboratory) designed to remove inorganic and organic gases that might bias aerosol measurements. Sampled air is then exposed to high water supersaturation in a steam chamber, where particles grow sufficiently large to be collected by inertial impaction before being delivered to vials held on a rotating carousel. Samples were collected every 30 min, and were stored at 2° C until analysis by a dual IC system (Dionex ICS-2000). PILS-IC data from PACO are used primarily to determine collection efficiency corrections for the AMS.

4.3.7 PILS-TOC

Water-soluble organic carbon (WSOC) was quantified during 12-hr periods (0700 - 1900 LT) using a PILS (Brechtel Manufacturing Inc.) coupled to a Sievers Model 800 Total Organic Carbon (TOC) Analyzer (PILS-TOC). Details of this technique are described in detail by Sullivan et al. (2004; 2006). Briefly, particles smaller than 2.5 μm in diameter are sampled by the PILS and passed immediately through an organic carbon denuder (Sunset Laboratory Inc.) to remove organic vapors. Particles are grown into droplets, collected by inertial impaction, and delivered to a TOC analyzer for quantification of WSOC, with data reported every 6 minutes. To account for dilution of the PILS liquid wash flow to the TOC analyzer owing to collected drops and condensation on the PILS droplet impactor, a constant dilution factor of 1.15 is assumed. This factor is based on measurements with an independent PILS system coupled to ion chromatography, a technique that can more precisely quantify the dilution factor. The reported WSOC levels are the difference between the measured and background concentrations. Contamination in the MQ water was the main component of the background levels, which were assumed to be constant between periodic background measurements.

The overall measurement uncertainty is estimated to be approximately 10%. The PILS-TOC was employed during the final, photochemically active regime of PACO, from 10-July to 04-Aug.

4.3.8 Filter Sampling

Both high- and low-volume filter samples were collected during 4-hr sampling periods (0700 - 1100 and 1500 - 1900 LT). High-volume (1250 L/min) samples were collected with a Tisch TE-6001 sampler fitted with a PM_{2.5} fractionator, using Whatman Quartz Microfibre Filters (cat. #1851-865). Low volume (15.9 L/min) samples were collected on 47 mm PALL Life Sciences Pallflex membrane filters, downstream from a Sunset Laboratory parallel-plate carbon filter denuder. Sampling was carried out according to the IMPROVE_A protocol, except that oven limitations forced filters to be pre-baked at 300° C before sampling. Despite the lower pre-baking temperature, subsequent analysis of pre-baked filters revealed ≤ 0.01 μg of organic carbon (OC) and elemental carbon (EC). After sampling, filters were wrapped in two layers of aluminum foil and stored at -20° C until analysis.

Low- and high- volume samples were analyzed for OC and EC via thermal-optical analysis (TOA) with a Sunset OC-EC TOA analyzer, following the IMPROVE_A temperature and calibration protocols. High volume quartz filters were also analyzed by Ultra Performance Liquid Chromatography/Electrospray Ionization Time-of-Flight High-Resolution Mass Spectrometry (UPLC/ESI-TOFMS). One-eighth of each filter was extracted with high-purity methanol under ultrasonication for 45 min. Filter extracts were filtered through a PALL Life Sciences Acrodisc CR 25-mm syringe filter (PTFE membrane, 0.2-mm pore size) into a scintillation vial. The filtered extracts were blown dry under a gentle nitrogen stream at ambient temperature. The residue was reconstituted with 50:50 v/v methanol with 0.1% acetic acid and water. Blank filters were extracted and treated in the same manner as the field samples. Extracts were analyzed by a Waters ACQUITY ultra performance liquid chromatography (UPLC) system, coupled with a Waters LCT Premier TOF mass spectrometer equipped with an electrospray ionization (ESI) source, allowing for accurate mass measurements (i.e., determination of molecular formulas) to be obtained for each observed ion. Extracts were analyzed by UPLC/ESI TOFMS operated in both negative and positive ion modes. Details of operation

protocols, including column information and chromatographic method for the UPLC/ESI-TOFMS are given by Surratt et al. (2008).

4.3.9 Hygroscopicity

Hygroscopicity measurements were carried out with the Differential Aerosol Sizing and Hygroscopicity Spectrometer Probe (DASH-SP, Brechtel Mfg), which is described by Sorooshian et al. (2008). Briefly, ambient particles pass through a nafion dryer before size-selection by a cylindrical, single-classification differential mobility analyzer (DMA). The resulting monodisperse aerosol is split into five separate flows - one providing a redundant measurement of total particle concentration at the DMA-selected size with a water condensation particle counter (TSI Model 3831), and the remaining four channels consisting of parallel nafion humidification chambers (Perma Pure, LLP, Model MD-070-24FS-4), followed by correspondingly humidified custom optical particle counters (OPCs). In the OPC sample volume, particles pass through a focused laser beam ($\lambda = 532$ nm, World Star Technologies, Model TECGL-30) and scatter light in proportion to size (D_p) and refractive index (RI). Forward-scattered light is collected and focused on a photomultiplier tube, and the resulting electrical pulse is recorded by a high-speed data acquisition computer. An iterative data processing algorithm, based on laboratory calibrations with salts of known refractive indices, is used to determine the best fit on a solution surface relating electrical pulse height, size, and refractive index. The hygroscopic growth factor ($GF = D_{p,wet}/D_{p,dry}$) is corrected for the RI change caused by particulate liquid water at elevated RH.

In the current study, the DASH-SP sampled for 4-hr periods (0700 - 1100 and 1500 - 1900 LT). Hygroscopicity was measured at dry sizes corresponding to $D_{p,em}$ of 150, 175, 200, and 225 nm. Multiple RH sensors in the nafion tubes and OPCs controlled RHs to dry ($\leq 8\%$), 74%, 85%, and 92%, with RH uncertainty of 1.5%. Because calculated RI varied little during sampling periods, GF calculations were made with a single RI for each sampling period, representing the average RI calculated for the entire period. The error introduced by this assumption is small, as light scattering in the DASH is far more sensitive to size than RI. Overall uncertainty in GF calculations is calculated

to be 4.5%.

4.4 Results and Discussion

4.4.1 Atmospheric Conditions

Figures 4.1, 4.2, and 4.3 are a compilation of meteorological data, as well as gas- and aerosol-phase composition for regimes I, II, and III, respectively. Wind speed and direction display distinct diurnal patterns, with stagnant or very light winds from the N/NE in the overnight to early morning hours (2000 - 0600 LT) changing direction to come from the W/SW shortly after sunrise (0600-0700 LT). Between 0600 and 1600, wind speed increases from 3-4 km/h to 13-15 km/h out of the W/SW before decreasing back to very light or stagnant out of the N/NE by 2000 LT. One effect of these wind patterns is to allow local emissions to build up in the Los Angeles basin during the nighttime and early morning hours, leading to significant carryover of aged aerosol in the background Los Angeles air, as proposed by Blumenthal et al. (1978). When sea breezes develop, fresh emissions in source-rich areas are gradually transported from the western Los Angeles Basin toward downwind areas in the E/NE. Situated 16 km from downtown Los Angeles, Pasadena can be considered as a receptor site that first receives transported pollution between 1000 and 1100 LT, after roughly 4-5 hr of transport. During the afternoon hours (1300-1800 LT), the sampling site receives a steady influx of air from the W/SW with photochemical age of 1-2 h. There are no significant freeways or point sources of particulate pollution in close W/SW proximity to the sampling site, and so it is expected that air sampled during PACO is representative of transported urban air in Los Angeles. A major freeway with significant diesel and gasoline mobile sources is located 1.5 km to the north of the sampling site, and so overnight N/NE winds may have periodically impacted the site with primary particulate emissions. Daytime variation in gas- and aerosol-phase composition is expected to result from three sources: 1. temporal changes in emissions from source-rich areas, 2. diurnal variations in the intensity of photochemistry, and 3. the age of transported pollution.

A clear diurnal trend is observed in RH and solar radiation, with RH increasing to near 100%

on most nights and remaining at or near saturation until sunrise. The incidence of nighttime and morning marine cloudcover was common during regimes I and II, while regime III was typically drier, with clear nighttime skies more common. Periods of more significant marine layer influence are indicated by longer periods of saturated RH and more gradual decrease in RH (and slower increase in solar radiation) after sunrise. Regime I has been classified as “springtime meteorology” due to the impact of several low pressure systems in Southern California, bringing periodic drizzle and leading to several days of cloudcover and significantly diminished solar radiation (i.e. 06-June to 12-June). Daytime RH rarely fell below 50% during regime I. Regime II exhibited the strongest summertime marine layer influence, with heavy cloudcover persisting until late morning (1000 to 1200 LT) nearly every day before making way for sunny, hazy afternoons with daytime RH between 25 and 40%. Regime III observed the least marine layer influence, with many mornings of clear skies and daytime RH typically between 10 and 30%. Despite differences in meteorology, the diurnal wind patterns described above were robust, with stagnant morning winds giving way to afternoon sea breezes and pollutant transport from the W/SW.

Gas-phase data give a sense of the atmospheric chemical environment during sampling. O_3 exhibits a strong diurnal pattern correlated with solar radiation and serves as a tracer for photochemical activity. During periods of relatively dry atmospheric conditions, the O_3 concentration peak increases in magnitude over subsequent days (see 17 to 19-July and 27-July to 2-August in regime III), suggesting that either pollutants accumulate or photochemical activity increases during periods of consistent, stable atmospheric conditions, resulting in photochemical episodes. CO and NO_x display more random behavior, exhibiting periodic peaks in concentration indicative of plumes of fresher emissions.

4.4.2 Aerosol Composition

OC and EC mass concentrations, in addition to OC:EC ratios from representative days in each regime, are presented in Table 4.3. OC is higher in afternoon periods when compared with mornings in each regime (27, 18, and 4% higher in regimes I, II, and III, respectively), while EC is lower

during afternoons (7, 35, and 22% lower in regimes I, II, and III, respectively). Further, OC:EC ratios are significantly higher during afternoon periods. These diurnal trends in OC are expected, given the importance of photochemical SOA production, and the percentage increase in OC mass between morning and afternoon periods is similar to that observed by the AMS (15, 17, and 10% higher in regime I, II, and III, respectively). Discrepancies may arise due to the different size ranges measured by the AMS and filter sampling (upper limits of measurement are 1.0 and 2.5 μm for the AMS and filters, respectively), in addition to potential volatilization of semivolatile organics relating to the thermo-optical OC/EC analysis technique. The modest increase in OC between morning and afternoon periods during the photochemically intense regime III may indicate that significant OC existed in the background aerosol during this period. The decrease in EC observed between morning and afternoon periods suggests that primary organics are a more significant portion of the Los Angeles aerosol in the mornings, and the relatively low concentrations of EC suggest that the dominant source of organic aerosol in Los Angeles is secondary.

DMA data are presented in panel 8 of Fig. 4.1, 4.2, and 4.3. Diurnal patterns are evident in both DMA volume and number in all regimes. DMA volume tends to reach a maximum in the mid-to-late morning (1000, 1100, 800 LT in regime I, II, and III, respectively), when RH is still high and particles have presumably undergone cloud processing. The early maxima in regime III underscore the absence of significant marine layer influence persisting into the late morning. On average, DMA number concentration reaches a maximum between 1400 and 1500 LT during each regime, roughly 3 h after transported pollution is expected to first arrive at the sampling site (Fig. 4.4). This indicates that increases in fine particle mass at the PACO sampling site are not the result of transport alone, but also affected by photochemical production in transported, polluted air from source-rich areas. There was no significant difference in wind patterns between regimes, so the slightly earlier peak in DMA number in regime II suggests that marine moisture and aqueous-phase processes (most prevalent in regime II) may hasten secondary aerosol production. Fig. 4.4 indicates that appreciable concentrations of fine particles (< 100 nm) are present in late nights and early mornings (particularly in regimes II and III), possibly comprised of fresh emissions, nighttime-

generated NO_3^- , or fine particle carryover residing in a shallow mixed layer.

The third and fourth panels of Fig. 4.1, 4.2, and 4.3 show time traces of bulk AMS aerosol mass concentration and mass fraction, respectively, while the sixth panel shows a time trace of approximate O:C ratio, based on Aiken et al. (2008), as well as WSOC concentration from the PILS-TOC (regime III). Organics dominated the aerosol sampled during PACO, and except for short episodes in regime I, the approximate O:C ratio remained relatively constant during each regime (0.44 ± 0.08 , 0.55 ± 0.05 , and 0.48 ± 0.08 during regimes I, II, and III, respectively). Organic aerosol in regime II appears to be more oxidized than I and III, suggesting that the marine moisture and presumed aqueous processing may enhance the rate of organic oxidation in Los Angeles. From bulk AMS time traces it is evident that organics increase in both magnitude and mass fraction each afternoon, particularly during the more photochemically active regimes II and III. It is noteworthy that there are no distinct trends in approximate O:C between mornings and afternoons (morning approximate O:C = 0.44 ± 0.08 , 0.54 ± 0.08 , and 0.49 ± 0.07 for regimes I, II, and III, respectively, while afternoon approximate O:C = 0.44 ± 0.08 , 0.53 ± 0.06 , 0.50 ± 0.08 for regimes I, II, and III, respectively). This suggests that there is little change in overall oxidation state of Los Angeles aerosol, even on timescales of weeks. It is unlikely that all organics are uniformly oxidized at all times in Los Angeles, but rather that there exists a continuum of OA oxidation, with more reduced and more oxidized ends of that continuum maintaining a relatively constant ratio for extended periods of time.

Trends in aerosol mass fraction are presented in Fig. 4.6. Organics dominate the Los Angeles submicron aerosol, contributing 42, 43, and 55% of aerosol mass in regimes I, II, and III, respectively. Diurnal trends are evident in Fig. 4.6, with organic mass fraction increasing significantly from morning (0700-1100 LT) to midday (1100-1500 LT) to afternoon (1500-1900 LT) in each regime. Sulfate is a significant component in marine/moisture-influenced regimes I and II, and is a more minor in regime III, suggesting that cloud processing and marine influence may be an important source of sulfate in Los Angeles aerosol. Nitrate contributes equal mass fractions in each regime, with a minimum in the afternoon and a maximum in the morning. Ammonium contributes a

remarkably constant mass fraction to the aerosol, despite significantly less inorganic sulfate in regime III, suggesting an ammonium surplus for aerosol sampled in regime III. The significant peak in AMS masses during the early morning of 5-July (regime II) corresponds to a total submicron mass of over $200 \mu\text{g}/\text{m}^3$, and resulted from a myriad of fireworks displays in the area surrounding the sampling site. This plume has been removed from further analysis.

Diurnal trends in bulk composition are highlighted in the top panel of Fig. 4.5. It is noteworthy that during the significantly marine - layer- impacted regime II, bulk organic, sulfate, nitrate, and ammonium masses are all enhanced. This suggests that aqueous processing associated with marine layer influence may be an important factor in generating aerosol mass in Los Angeles. Typically, organics increase in magnitude to a maximum near 1400-1500 LT in each regime, corresponding to a maximum in ozone, solar radiation, and DMA number - evidence of photochemical SOA production. Sulfate exhibits slight enhancements during periods of peak photochemical activity in all three regimes, but as suggested by Kleeman et al. (1999), it appears to be predominantly a background marine species. Nitrate mass is highest in the nighttime and morning periods, likely resulting from ozone- NO_x production of HNO_3 at night and HO_x - NO_x production of HNO_3 after rush hour in the mornings. As mentioned in Sect. 4.4.1, there were periods of high O_3 observed during PACO, and during several of these periods there also appeared to be significantly elevated levels of aerosol nitrate during nighttime sampling (e.g. 30-July to 3-Aug). Further, morning peaks in aerosol nitrate varied significantly in magnitude, suggesting that there may be significant variation in the amount of gas-phase HNO_3 production from day to day. Ammonium mass generally follows the combined trends of SO_4^{2-} and NO_3^- , but appears to be in excess in regime III. Defining an ammonium ratio as:

$$\frac{(\text{moles of } \text{NH}_4^+ \text{ measured by AMS})}{(\text{moles of } \text{NH}_4^+ \text{ required to neutralize } \text{SO}_4^{2-} \text{ and } \text{NO}_3^-)}, \quad (4.1)$$

aerosol sampled in regimes I and II was found to be generally neutralized (average ammonium ratio = 0.96 ± 0.21 and 0.94 ± 0.17 for regimes I and II, respectively), while aerosol from regime III was characterized by significant ammonium excess (ammonium ratio = 1.28 ± 0.30). These results

suggest that aerosol phase NH_4NO_3 was ammonia-limited during regimes I and II, but ammonia may have been in excess during regime III. Investigating molar ratios of inorganic species, it is apparent that the role of SO_4^{2-} is significantly diminished in regime III, corresponding to the absence of marine layer influence. The ratio of NO_3^- to NH_4^+ remains relatively constant across regimes (0.32, 0.29, and 0.34 in regimes I, II, and III, respectively), while the ratio of SO_4^{2-} to NH_4^+ exhibits a marked decrease in regime III (0.42, 0.41, and 0.24 in regimes I, II, and III, respectively). The AMS has difficulty distinguishing whether NH , NH_2 , and NH_3^+ (m/z 15, 16, and 17, respectively) are contributed by inorganics or organic amines. It is hypothesized that ammonium is chiefly inorganic during the moister, marine-layer-influenced regimes I and II, serving primarily to neutralize SO_4^{2-} and NO_3^- , while there may be significant amounts of organic amines in the absence of marine layer influence during regime III. It is also possible that these organic amines are present in all regimes, which would imply that inorganic SO_4^{2-} and NO_3^- are not fully neutralized by NH_4^+ during regimes I and II.

The bottom panel of Fig. 4.5 shows size-resolved PToF AMS composition for a representative morning and afternoon period in each regime, with 09-Jun, 19-Jun, and 19-July representing regimes I, II, and III respectively. Size-resolved data indicate that aerosol in regime I is typically internally-mixed, with the mode centered at $\sim 400\text{-}500$ nm. Afternoon PToF data from regime I indicate that photochemical organic production typically results in organics condensing on existing accumulation mode aerosol. Regime II is characterized by significantly higher aerosol mass and more complex size distributions. While there is a significant internally-mixed accumulation mode present and centered at $\sim 600\text{-}700$ nm, there is also significant aerosol mass at sizes smaller than 300 nm in both morning and afternoon sampling periods, though the mass at smaller sizes does not comprise a distinct mode. Afternoon PToF data from regime II indicate that a fine mode appears coincident with photochemistry, suggesting that fine mode aerosol is predominately comprised of secondary species. Nitrate, sulfate, and ammonium are generally confined to accumulation mode aerosol in regime II. Regime III PToF data reveal an aerosol that is dominated by organics at all sizes and is distinctly bimodal. In addition to an internally mixed accumulation mode centered at $\sim 500\text{-}$

600 nm, distributions from regime III also reveal a significant fine mode centered at ~ 100 -200 nm. The accumulation mode tends to be comprised of sulfate, nitrate, and ammonium (in addition to organics) in the morning periods, with less nitrate in afternoons. Afternoon PToF data from regime III, like those from regime II, reveal fine-mode aerosol growth resulting from production of secondary organic species. Numerous studies have shown that the critical species for new particle formation in the atmosphere is H_2SO_4 . The extent to which the observed fine mode aerosol might have originated from the nucleation of gas-phase species during PACO is unclear. However, given the relatively large amount of pre-existing aerosol surface area, as well as the relatively low concentration of SO_2 , the precursor to H_2SO_4 , it is unlikely that new particle formation by nucleation is an important process in Los Angeles. Instead, the growth of fine-mode organics is proposed to occur by condensation of SOA on existing ultrafine primary aerosol. This tentative conclusion is contrasted with results from Pittsburgh, in which Stanier et al. (2004) found new particle formation to be an important process, strongly correlated with SO_2 concentrations. Whether condensing on nucleated sulfate or existing ultrafine primary aerosol, growth of fine mode particles in Los Angeles is predominantly due to SOA.

Figure 4.7 shows the hourly average for WSOC mass (top panel, representing WSOC organic mass) and % of AMS organic accounted for by WSOC (bottom panel) for regime III. A factor of 1.8 was used to convert water soluble carbon (WSOC) mass to water soluble organic mass (WSOM), within the range of factors presented by Turpin et al. (2001), and matching the factor used by Docherty et al. (2008) for aerosol in the Los Angeles Basin. Averaged hourly data reveal a trend in WSOM, increasing from a minimum in the late evening and early morning to a maximum at 1500 LT, corresponding to maxima in O_3 concentration, solar radiation, AMS organic, and DMA number concentration. This suggests that photochemical production of SOA in air transported from source-rich areas is a significant source of WSOM in the Los Angeles basin. While there is a diurnal trend in WSOM, the fraction of AMS organic accounted for by WSOM is relatively constant at 0.44 ± 0.16 during regime III, with a slight enhancement between 1500 and 1900 LT. This suggests that while significant WSOM is photochemically generated during the course of a day, water soluble organics comprise a relatively constant percentage of organic aerosol in Los Angeles. WSOC has

been found to correlate well with oxidation state of organic aerosol (e.g., Kondo et al., 2007). Given the relatively constant approximate O:C ratio observed in regime III and steady afternoon influx of polluted air on the order of 1-2 hr old, the constant WSOM:AMS organic ratio is not unexpected.

4.4.3 PMF results

AMS data from PACO were combined into a single continuous dataset for analysis by the PMF method. PMF produced several non-unique solutions that were compared with known mass spectra and external time traces in order to choose final solutions. Figure 4.8 presents a summary of PMF factors, while panel 6 of Fig. 4.1, 4.2, and 4.3 represents time traces for PMF factors for regimes I, II, and III, respectively.

Three factors were resolved from the PMF method, and comparisons with previously published spectra indicate that they correspond to a hydrocarbon-like organic aerosol (HOA) and semivolatile- and low-volatility-oxygenated organic aerosol (SV-OOA and LV-OOA, respectively). The HOA factor is closely correlated with previously published spectra from periods dominated by reduced, primary organics (Zhang et al., 2005; Lanz et al., 2007; Ulbrich et al., 2009), and has significant signal at m/z 41 and 57. The LV-OOA factor is closely correlated with previously-published OOA-1 factors and OOA-like factors observed in highly oxidizing environments (Zhang et al., 2005; Lanz et al., 2007; Ulbrich et al., 2009; Alfarra et al., 2004). The SV-OOA factor is also correlated with previously-published OOA factors, but has a higher degree of correlation with previously-published factors expected to represent less-aged, less-oxidized, semivolatile oxygenated organic aerosol, or SV-OOA (Zhang et al., 2005; Lanz et al., 2007; Ulbrich et al., 2009; Bahreini et al., 2005; Alfarra et al., 2004). The LV-OOA factor has a larger ratio of m/z 44 to m/z 43, an indication of a more aged, oxidized organic component (Ng et al., 2010). The SV-OOA factor, on the other hand, has a smaller m/z 44 to m/z 43 ratio. PACO PMF factors correlated closely with “standard” HOA, SV-OOA, and LV-OOA factors reported by Ng et al. (2011), based on an average of results from 15 sites.

As seen in Fig. 4.1, 4.2, and 4.3, the HOA factor has the character of a periodic plume source, with

low background concentrations punctuated by sudden, significant increases in concentration that remain high for several hours at a time. These increases in HOA concentration occurred primarily during regime I and are typically correlated with or just following peaks in CO concentration (panel 3 in Fig. 4.1, 4.2, and 4.3), though the low time- and concentration-resolution of CO measurements made statistical analysis difficult. HOA is typically associated with primary organic aerosol (POA) (e.g., Ulbrich et al., 2009; Ng et al., 2010), and the only significant local source of POA is expected to be the 210 freeway, 1.5 km north of the sampling site. There appears to be a trend of HOA plumes coinciding with or immediately following periods of light winds out of the N, which suggests that the HOA-like factor may represent primary freeway emissions. It is unclear why this HOA factor does not appear during every period of light winds out of the N. Low correlation between the HOA factor and ozone ($Pr = 0.39$) suggests that HOA production is not a photochemical process, and low correlations with inorganic AMS traces ($Pr = 0.18, 0.15, 0.21,$ and 0.02 for sulfate, nitrate, ammonium, and chloride, respectively) suggest that HOA production is independent of formation of inorganic aerosol, and that HOA may comprise an externally mixed mode, separate from the accumulation mode aerosol that is typically comprised of inorganic constituents.

The more dominant LV-OOA factor is most significantly correlated with inorganic AMS traces ($Pr = 0.75, 0.46, 0.65,$ and 0.46 for sulfate, nitrate, ammonium, and chloride, respectively). As discussed in Sect. 4.4.2, inorganics are most prevalent in accumulation mode aerosol (rather than fine mode), and their loadings appear to be associated with significant marine layer influence in the Los Angeles Basin (e.g., regimes I and II). The high degree of correlation between LV-OOA and inorganic constituents suggests that the LV-OOA factor represents an organic component that typically resides in accumulation mode aerosol and may be associated with marine layer/cloud processing influence. The correlation between LV-OOA and ozone is relatively low ($Pr = 0.39$), indicative of an aged background organic species, as opposed to a rapidly-produced photochemical product that exhibits a distinct diurnal trend. Examining time traces for LV-OOA in Fig. 4.1, 4.2, and 4.3 reveals that the LV-OOA factor exhibits relatively high background levels in the mornings and at night, while periodically showing moderate increases in magnitude during midday periods of photochemistry.

These periodic photochemical trends in LV-OOA correspond to periods of intense photochemistry (e.g., 18-19-July), characterized by midday ozone concentrations near 80-100 ppb. This suggests that while LV-OOA appears to be the major constituent of the aged background aerosol discussed in Sect. 4.4.2, it can be photochemically produced on relatively short timescales during periods of intense photochemical activity. Its strong correlation with SO_4^{2-} , consistent presence during humid overnight and morning hours, coincidence with accumulation mode aerosol, and greater prevalence in moisture-impacted regimes I and II suggest that there may be significant aqueous processing sources for LV-OOA in Los Angeles.

Figures 4.1, 4.2, and 4.3 show a regular diurnal trend in SV-OOA, with overnight minima increasing to maximum concentrations daily at approximately 1400-1500 LT, close to maxima in solar radiation, AMS organic, and DMA number concentration. The SV-OOA factor exhibits a reasonable degree of correlation with ozone ($\text{Pr} = 0.53$), suggesting that semivolatile organics are products of local photochemical oxidation of VOCs. Correlations with inorganic traces are lower than those for LV-OOA ($\text{Pr} = 0.42, 0.31, 0.45,$ and 0.19 for sulfate, nitrate, ammonium, and chloride, respectively). As discussed in Sect. 4.4.2, aerosol size distributions exhibit significant enhancements in fine mode aerosol in afternoon periods, with the fine mode comprised almost entirely of organics (particularly in regimes II and III). Further, SV-OOA correlates strongly with DMA number concentration ($\text{Pr} = 0.62$, versus 0.00 and 0.33 for HOA and LV-OOA, respectively). The regular, significant enhancements in SV-OOA during peak photochemical periods, high correlation with DMA number concentration combined with lower correlations with inorganics (which typically comprise accumulation mode aerosol), and the regular appearance of fine organic modes during afternoons suggests that the SV-OOA factor is comprised of early-generation photochemical products that are chiefly responsible for the growth of fine-mode aerosol in the afternoons. Based on wind patterns discussed in Sect. 4.4.1, SV-OOA is proposed to consist of secondary organic products on the order of 1-2 hr old.

Ng et al. (2011) applied a simple method for making real-time estimates of OA components, based on an empirical scaling factor that relates HOA and OOA (further segregated as SV-OOA and

LV-OOA) to signal at fragments m/z 57 and m/z 44. HOA is estimated by $b \times (C_{57} - 0.1 \times C_{44})$, where b for PACO was found to be 13.96, compared with 13.4 (range = 8.5-19.2) for Ng et al. (2011). PACO OOA (combined SV-OOA and LV-OOA) is estimated by $c \times C_{44}$, where c was found to be 8.05 for PACO, compared with 6.6 (range = 2.9-9.0) by Ng et al. (2011). The PACO SV-OOA and LV-OOA factors are estimated by $3.30 \times C_{44}$ and $4.75 \times C_{44}$, respectively.

Figure 4.9 shows the mass fraction of organic accounted for by each organic component during each regime. OA in Los Angeles is overwhelmingly oxidized in nature, with LV- and SV-OOA combined contributing 77, 92, and 86% of OA during regimes I, II, and III, respectively. HOA contributed the largest fraction to OA during regime I, in large part due to episodically high HOA concentrations during May and early June. HOA is a minor factor during regimes II and III. SV-OOA is a major constituent of OA during periods of photochemistry, with the hot, dry, photochemically intense regime III seeing the most significant contribution of SV-OOA to OA. LV-OOA dominates in regimes I and II, which were both periods of significant marine/moisture influence and cloud processing.

4.4.4 Filter Analysis

PMF factors are mathematical solutions that return constant mass spectra that are combined linearly to describe variability in AMS data, and it is important to compare PMF results to physical, independent characterizations of OA. For PACO, UPLC-ESI-(+ and -)-TOF-MS analysis of high-volume filter samples was performed on 9 selected filters representing periods of high HOA, SV-OOA, and LV-OOA concentrations, in order to distinguish chemical profiles associated with the PMF factors. Periods distinguished as “high SV- and LV-OOA” were chosen such that those species were the single, dominant component of OA. PACO filter sampling did not include any periods in which HOA was the isolated, dominant species, as periods distinguished as “high HOA” were also impacted by high background levels of LV-OOA.

Functional groups of interest in UPLC-ESI-(+)-TOF-MS analysis were basic nitrogen groups (i.e. amines, imines) as well as oxygen-containing moieties (i.e. carbonyls, alcohols, ethers). The

complexity of the samples made complete speciation by this technique difficult, but it was possible to identify the majority of the base peaks. Non-oxygenated nitrogenous compounds likely to be amines were detected in significant concentrations and with some variety of carbon chain-length (C8-C16) in the high HOA + LV-OOA periods, as well as during morning periods in which background LV-OOA dominated the organic fraction. This suggests that amines may be an important class of organic compounds in aged, background Los Angeles aerosol. The most prominent class of compounds in all filters was oxygenated organic species, with increased variety of oxygenated species during periods of significant photochemical organic production.

UPLC-ESI(-)-TOF-MS offered better mass spectral resolution and more complete identification of base peaks than (+) - mode, allowing for more complete chemical profiles. Phthalic acid is ubiquitous in appreciable quantities in the extractable fraction of Los Angeles OA. Phthalic acid has been identified as a significant product of poly-aromatic hydrocarbon (PAH) photochemistry (Kautzman et al., 2010), so this result suggests that PAHs may be a significant class of precursor VOCs to OA in Los Angeles. The high HOA + LV-OOA samples were characterized by appreciable quantities of nitrogen- and sulfur-containing organics (> 10% of the extractable, identifiable fraction), which is unique to periods in which both HOA and LV-OOA were high in magnitude. Carboxylic acids were significant during both SV- and LV-OOA periods (> 15% of extractable, identifiable fraction), though the carboxylic acids identified during SV-OOA periods tended to be longer-chain (C7-C10, as opposed to C4-C9 for LV-OOA periods). Additionally, aerosol in LV-OOA periods tended to have a more complex chemical profile, with no single class of compounds dominating the extractable fraction identified by UPLC. This suggests that while the SV- and LV-OOA periods contain many of the same chemical compounds, LV-OOA tends to be characterized by smaller organic acids (higher O:C ratio), as well as a more complex profile of organonitrates, organosulfates, and oxidized acids.

As explained in Ulbrich et al. (2009), aerosol partitioning with a bilinear PMF model is inherently limited in fitting a dynamic organic component. With a dataset as large as that represented by PACO, it is not unexpected that the organic component undergoes numerous and significant changes over the course of a single regime. Thus, two unique, constant mass spectra used to describe

variability in a bilinear model may be more accurately viewed as two points on a continuum of volatility, rather than two distinct components of differing volatility. This hypothesis is supported by the commonality of compound classes identified by UPLC analysis for SV- and LV-OOA periods. The continuum of oxygenation is further illustrated in Fig. 4.10, a plot of m/z 44 (CO_2^+) versus m/z 43 (mostly $\text{C}_2\text{H}_3\text{O}^+$) proposed by Ng et al. (2010) as a mass spectral diagnostic for the age of organic aerosol. It is hypothesized that LV-OOA components tend to have a higher ratio of m/z 44 to m/z 43 and represent a lower-volatility, more-aged organic component with a higher degree of oxidation. Results from PACO indicate that the organic component of Los Angeles aerosol produces a continuum of f_{44} values during each regime and that the most aged organic fraction may actually be comprised of fewer small diacids and a predominance of longer-chain, oxidized monoacids, complex amines, and nitrate- and sulfate- containing organics. It is concluded that for the Los Angeles aerosol, a bilinear PMF model, with mass spectra assumed to be constant over an entire regime, is helpful in qualitatively assessing the degree of aging of the organic component, but represents a broad simplification of a dynamic organic fraction of aerosol.

4.4.5 Hygroscopicity

The intensity of scattered light is a strong function of particle diameter (D_p), and since aerosol water uptake largely determines particle size, it is a major variable determining the interaction of particles with radiation. Urban aerosol tends to be dominated by organic material, which is often hydrophobic, leading to overall growth factors (GFs, $D_{p,wet}/D_{p,dry}$) that are smaller than those for pure inorganic aerosol. At RH above the deliquescence RH of common inorganic aerosol constituents, the comparatively low hygroscopicity of organics tends to result in an inverse correlation between organic mass fraction and overall aerosol hygroscopicity (Shinozuka et al., 2009; Quinn et al., 2005; Hersey et al., 2009).

Because urban aerosol is, in part, an external mixture of organic and inorganic components, hygroscopic behavior is often complex, with several GF modes observed (e.g., Cocker et al., 2001; Massling et al., 2005; Swietlicki et al., 2008; Massling et al., 2009; Meier et al., 2009; Tiitta et al., 2010;

Rose et al., 2010). The optical sizing method utilized by the DASH-SP provides rapid measurements on timescales suitable for aircraft studies, but does not allow resolution of more than two modes (a nonhygroscopic and hygroscopic mode). During PACO, two modes were typically distinguishable: a nonhygroscopic mode ($1 < GF < 1.15$ at 92% RH) identified during morning sampling ($\leq 30\%$ of aerosol), decreasing to very minor significance in the afternoon, in addition to a dominant hygroscopic mode that will be the focus of the rest of this section. This suggests that aerosol sampled in the morning included an appreciable fraction of nonhygroscopic particles, with afternoon photochemistry and SOA production resulting in an aerosol of more uniform, unimodal hygroscopicity. Since it was not possible to resolve multiple growth modes, GF data represent the overall subsaturated water uptake behavior for hygroscopic particles.

The DASH-SP measured GF at dry particle sizes of 150, 175, 200, and 225 nm. There was no statistically significant difference between GF at these dry sizes, and so data were averaged to give GFs representative for particles between 150 and 225 nm dry diameter. Particles sampled during morning periods (0700-1100 LT) were significantly more hygroscopic at 74 and 92% than those sampled during afternoon periods (1500-1900 LT); morning GF averaged 1.14 ± 0.13 , 1.37 ± 0.10 , and 1.97 ± 0.45 at 74, 85, and 92 % RH, respectively, while afternoon GF averaged 1.06 ± 0.04 , 1.37 ± 0.07 , and 1.74 ± 0.20 at 74, 85, and 92 % RH, respectively. Suppressed GF at 74 and 92% during afternoon sampling but constant GF at 85% suggests that the hygroscopic growth curve (GF vs. RH) for morning-sampled aerosol is one with a higher GF at lower RHs, combined with a steep ascending section at $RH > 85\%$, suggestive of a predominantly inorganic aerosol with a small hygroscopic organic component and little nonhygroscopic aerosol.

These GF values are significantly higher than those measured during the 1987 SCAQS study in the eastern Los Angeles Basin (1.23 ± 0.08 for 200 nm particles at $90 \pm 3\%$ RH; (Zhang and McMurray, 1993)), and are more consistent with the most hygroscopic mode measured in Pasadena in 1999 (1.6 at 89% RH; (Cocker et al., 2001)).

Figure 4.11 shows GF at 74, 85, and 92% plotted against organic mass fraction, with markers colored by sampling date and time. PACO data show a clear trend of suppressed GF with increasing

organic mass fraction (Pr = -0.56, -0.78, -0.71 for 74, 85, and 92%, respectively). The lowest GFs and highest values of organic mass fraction occur late in PACO, during the dry and photochemically intense regime III characterized by significant photochemical production of SV-OOA.

An increasingly popular representation of aerosol hygroscopicity is the κ parameter, developed by Petters and Kreidenweis (2007). As outlined in Shinozuka et al. (2009), one can use size-resolved GF data at sub-saturated RH to solve the equation:

$$S(D) = \frac{D^3 - D_d^3}{D^3 - D_d^3(1 - \kappa)} \exp \left[\frac{4\sigma M_w}{RT\rho_w D} \right] \quad (4.2)$$

for κ , where S is the saturation ratio over an aqueous droplet (0.74, 0.85, or 0.92), D and D_d are the humidified and dry diameters, respectively, σ is the surface tension at the interface of air and pure water (0.072 J m^{-2}), M_w is the molecular weight of water (18 g mol^{-1}), R is the gas constant ($8.3 \text{ J mol}^{-1}\text{K}^{-1}$), T is the temperature (298 K), and ρ_w is the density of water (1 g cm^{-3}). Because the effect of organics on surface tension is not explicitly accounted for in this model, the κ here may be regarded an "effective hygroscopicity parameter," which includes both solute-induced water activity changes and surface tension effects (Petters and Kreidenweis, 2007; Rose et al., 2010).

Using the calculated κ values, one may estimate critical dry diameter (D_d), or the diameter above which aerosol particles activate as cloud condensation nuclei (CCN) at a given supersaturation (S_c), using the following equations:

$$\kappa = \frac{4A^3}{27D_d^3 \ln^2 S_c}, \quad (4.3)$$

where:

$$A = \frac{4\sigma M_w}{RT\rho_w}. \quad (4.4)$$

Following Shinozuka et al. (2009) and assuming S_c of 0.2%, the relationship between κ and D_d becomes:

$$D_d = \kappa^{(-1/3)} \cdot 70 \text{ nm} \quad (4.5)$$

Values of κ and critical dry diameter at 0.2% supersaturation were calculated based on GFs at 85% RH and dry particle diameter of 200 nm. Uncertainties are estimated to be 25%, based on sizing uncertainties in the DASH-SP and RH variation in the instrument (Sorooshian et al., 2008). Figure 4.12 shows κ (left axis) and critical dry diameter (right axis; D_d) plotted against organic mass fraction, colored by time and date. Kappa values range from 0.15 to 0.51, with an average of 0.31 ± 0.08 , while critical diameters ranged from 87 to 131 nm, with an average of 105 ± 10 nm. As with GF data, there is a clear trend of decreasing κ and increasing critical dry diameter with increasing organic mass fraction, with the lowest hygroscopicity and CCN activity occurring during regime III. Earlier periods characterized by more marine influence and higher RH exhibited more hygroscopic behavior. At low values of organic mass fraction, κ approaches that of nitrate and sulfate salts (0.53-0.67), while approaching 0.1 at high organic fraction. Results from PACO suggest that organics are moderately hygroscopic, with κ values.

Shinozuka et al. (2009) presented parameterizations for calculating κ as a function of organic mass fraction for 100 nm $D_{p,dry}$ aerosol in Central Mexico and the North American West Coast ($\kappa = 0.34 - 0.20 \cdot \text{OMF}$ and $\kappa = 0.47 - 0.43 \cdot \text{OMF}$, respectively, where OMF is organic mass fraction), and these parameterizations are shown in Fig. 4.12. Overall, aerosol sampled during PACO are more hygroscopic at a given OMF than those presented in Shinozuka et al. (2009), and are parameterized as $\kappa = 0.50 - 0.29 \cdot \text{OMF}$. This suggests that the organic fraction measured by Shinozuka et al. (2009) inhibits hygroscopicity significantly more than in Los Angeles. It is possible that the organics measured in Central Mexico and off the N. American West Coast exhibit more surface-active behavior, inhibiting hygroscopic activity, or that those organics are predominantly nonhygroscopic.

In order to further investigate the hygroscopicity of organics, κ calculations were combined with AMS data giving mass fractions of individual aerosol species in order to estimate a κ value for organics, κ_{org} . If the overall hygroscopicity parameter, κ is given by:

$$\kappa = \sum_{i=1}^n \kappa_i \cdot \chi_i, \quad (4.6)$$

where n is the number of chemical constituents, i , with mole fraction χ_i and hygroscopicity parameter κ_i , then the organic hygroscopicity parameter, κ_{org} can be estimated by:

$$\kappa_{org} = \frac{\kappa - \sum_{i=1}^{n_{inorg}} \kappa_i \cdot \chi_i}{\chi_{org}}, \quad (4.7)$$

where n_{inorg} is the number of inorganic constituents, i , with hygroscopicity parameter κ_i and mole fraction χ_i , and χ_{org} is the mole fraction of organics in the aerosol. Previous publications have assumed κ_{org} of 0.1 for “hygroscopic” organics, and 0 for “nonhygroscopic” organics (Dusek et al., 2010; Wang et al., 2010; Wex et al., 2010). Assuming κ_i for inorganics to be 0.6 and κ_i for sea salt to be 1.3 (Wex et al., 2010), Eq. 6.9 gives κ_{org} of 0.16 for urban background aerosol transported to the PACO sampling site. Assuming κ_i for inorganics to be 0.7 (Dusek et al., 2010) gives κ_{org} of 0.12. Taking a median κ_{org} of 0.14, it is clear that the organics measured during PACO are significantly more hygroscopic than those previously measured in urban areas. This is not unexpected, given the consistently high O:C ratios of organics and the dominance of SV-OOA and LV-OOA during all three regimes of PACO. Further, the PACO sampling site is relatively free from the influence of local sources of primary aerosol, which would have the effect of reducing κ_{org} . Given that organics dominate aerosol in most urban areas, it is potentially significant to find that organics in an important urban center such as Los Angeles would have a value of κ_{org} appreciably higher than previously calculated for urban aerosol.

4.5 Conclusions

A major ambient sampling experiment was conducted at a site in Pasadena, CA positioned to sample a constant afternoon influx of transported Los Angeles pollution with a photochemical age of roughly 1-2 h and generally free from the influence of local point sources. Sampling spanned 4

months during the summer of 2009, and was characterized by three distinct meteorological regimes: a “springtime” period characterized by clean conditions coincident with low pressure systems (regime I), a typical early-summer period characterized by significant morning marine layer followed by warm, photochemically active afternoons (regime II), and a late-summer period characterized by little marine layer influence, hot and dry conditions, and elevated photochemical activity (regime III).

Chemical analysis of aerosol revealed that OC dominates particulate carbon in Los Angeles (OC:EC average of 8.04), and is enhanced relative to EC by an average of 47% in the afternoon, suggesting significant SOA production. High RH during marine-layer-influenced morning sampling periods resulted in hygroscopic growth of aerosol particles and high aerosol volume, while drier afternoon periods saw less hygroscopic growth but increased aerosol number and volume due to proposed SOA production. Maxima in aerosol volume occurred in the mid-late morning, reflecting a balance between RH-induced hygroscopic growth and SOA production. Maxima in aerosol number tended to occur near 1400-1500 LT, indicating that daytime photochemistry tended to generate a fine aerosol mode.

Organics are the most significant constituent of transported Los Angeles aerosol, contributing an average of 42, 43, and 55% of total submicron mass in regimes I, II, and III, respectively. Interestingly, there was no significant difference between morning and afternoon O:C ratios, suggesting that the constant influx of 1-2 hr old aerosol results in an overall organic oxidation state at the sampling site varying little despite significant SOA production. Regime II, characterized by significant morning marine layer influence followed by photochemically active afternoons, displayed significantly higher aerosol mass and higher average O:C ratio, suggesting that aqueous processes may be important in the generation of secondary aerosol and OOA in Los Angeles. Afternoons during regime II and III are characterized by the appearance of a fine organic mode, suggesting that SOA may be responsible for growth of fine particles. It is unclear whether these fine particles are the result of sulfate nucleation and subsequent SOA growth or SOA condensation on existing primary aerosol.

Water soluble organic mass (WSOM) reaches maxima near 1400-1500 LT, coincident with mark-

ers for photochemistry and suggesting significant SOA contribution to WSOM. Sulfate is predominantly an accumulation mode constituent, and its magnitude appears to depend on the degree of marine influence. Nitrate is similarly a predominantly accumulation mode species, reaching maxima after morning rush hour periods. Nighttime nitrate production is observed during periods in which maximum ozone levels indicated significant photochemical events. An ammonium ratio, defined as the moles of ammonium measured divided by the moles of ammonium required to neutralize sulfate and nitrate as $(\text{NH}_4)_2\text{SO}_4$ and NH_4NO_3 , respectively, revealed that ammonium limits particulate NH_4NO_3 in regimes I and II. An ammonium ratio of 1.28 ± 0.30 in regime III suggests that ammonium was in excess and that organic amines may have been an important constituent of submicron aerosol during this hot, dry, photochemically intense sampling period with reduced marine sulfate influence.

PMF analysis of C-ToF-AMS data resolved three factors, corresponding to HOA, SV-OOA, and LV-OOA, and correlating well with the “standard” factors presented in Ng et al. (2011). The HOA factor appears to be a periodic plume source, generally appearing during or shortly after peaks in CO concentration. SV-OOA displays a strong diurnal pattern, correlating strongly with ozone and the appearance of a fine mode (< 100 nm) in the aerosol size distribution, suggesting that these SOA products are generated on timescales of 1-2 h and tend to comprise a fine aerosol mode. LV-OOA is correlated with inorganic nitrate and sulfate and appears to be an aged carryover organic component that resides in accumulation mode aerosol, but may be generated on short timescales (1-2 h) under extremely oxidizing conditions. Its prevalence during humid overnight and morning hours and enhanced importance in moisture-influenced regimes I and II suggest that there may be significant aqueous-phase sources for LV-OOA. Overall the organic fraction of Los Angeles aerosol is overwhelmingly oxidized, with LV- and SV-OOA contributing 77, 92, and 86% of OA in regimes I, II, and III, respectively.

Filter analysis by both (+) and (-) mode UPLC-ESI-TOF-MS reveals a complex mixture of organic compounds dominated by oxygenated species. Long (C8-C16), non-oxygenated nitrogenous compounds likely to be amines are detected during periods impacted by high concentrations of

background LV-OOA, suggesting that amines may be an important constituent of aged organic aerosol in Los Angeles. Phthalic acid represents a ubiquitous, appreciable fraction of extractable OA, suggesting that PAH photochemistry may be an important pathway for SOA production in Los Angeles. Organo-nitro-sulfate species are observed during periods when aerosol appears to be a mixture of aged background species and freshly emitted particles. Carboxylic acids appear to be major contributors to both SV- and LV-OOA, with LV-OOA tending to be associated with shorter (C4-C9) carboxylic acids and thereby higher O:C ratio.

The organic fraction of transported Los Angeles aerosol is dynamic and undergoes numerous and significant changes on timescales of days to weeks, despite exhibiting consistency in the overall degree of oxidation. Many compounds are common to periods identified as distinct by PMF analysis, and PACO data suggest that Los Angeles OA is best described as a complex, dynamic mixture of compounds that represent a continuum of oxidation. Thus, a bilinear PMF model that assumes constant mass spectra representative of classes of OA is a useful tool in qualitatively assessing the degree of OA aging and oxidation, but is a dramatic simplification representing a complex organic fraction.

Finally, aerosol water uptake characteristics measured by the DASH-SP indicate that a bimodal distribution becomes more unimodal during periods of photochemical SOA production. The degree of hygroscopicity of the main hygroscopic mode is highly anti-correlated with organic mass fraction, as indicated by decreasing GF and κ , as well as increasing critical diameter with increased organic fraction. Values for κ averaged 0.31 ± 0.08 , approaching 0.5 at low OMF and 0.1 at high OMF. It appears that organics in Los Angeles inhibit hygroscopicity less than those measured in Central Mexico and off the N. American West Coast, potentially owing to less surface-active behavior or an organic fraction comprised of more water soluble species. Indeed, κ_{org} was found to be 0.14 for PACO, which is appreciably higher than previously reported in urban aerosol.

PACO represents the first major aerosol characterization in the Western Los Angeles Basin, and comparison with SOAR will help identify spatial variation in Los Angeles aerosol and determine the nature of aerosol evolution as it is transported from source-rich (western) to downwind (eastern)

parts of Los Angeles. Further, its timing will serve to contextualize and compare forthcoming results from the CalNex field campaign, part of which involved ground sampling at the PACO site.

Acknowledgements

Funding was provided by the Electric Power Research Institute. The authors would like to thank Jason Surratt for his helpful comments and direction. We would also like to thank Eric Edgerton and the SEARCH network for guidance on high-volume filter sampling and for the use of a sampler during PACO.

Bibliography

- Aiken, A. C., DeCarlo, P. F., , Kroll, J., Worsnop, D., J.A., H., Docherty, K., Ulbrich, I., Mohr, C., Kimmel, J., Sueper, D., Sun, Y., Zhang, Q., Trimborn, A., Northway, M., Ziemann, P., Canagaratna, M., Onstach, T., Alfarra, M., Prevot, A., Dommen, J., Duplissy, J., Metzger, A., Baltensperger, U., and Jimenez, J. L.: O/C and OM/OC Ratios of Primary, Secondary, and Ambient Organic Aerosols with High-Resolution Time-of-Flight Aerosol Mass Spectrometry, *Environ. Sci. Technol.*, 42, 4478–4485, 2008.
- Aiken, A. C., Salcedo, D., Cubison, M. J., Huffman, J. A., DeCarlo, P. F., Ulbrich, I. M., Docherty, K. S., Sueper, D., Kimmel, J. R., Worsnop, D. R., Trimborn, A., Northway, M., Stone, E. A., Schauer, J. J., Volkamer, R. M., Fortner, E., de Foy, B., Wang, J., Laskin, A., Shutthanandan, V., Zheng, J., Zhang, R., Gaffney, J., Marley, N. A., Paredes-Miranda, G., Arnott, W. P., Molina, L. T., Sosa, G., and Jimenez, J. L.: Mexico City aerosol analysis during MILAGRO using high resolution aerosol mass spectrometry at the urban supersite (T0) - Part 1: Fine particle composition and organic source apportionment, *Atmos. Chem. Phys.*, 9, 6633–6653, 2009.
- Alfarra, M., Coe, H., Allan, J., Bower, K., Boudries, H., Canagaratna, M., Jimenez, J., Jayne, J., Garforth, A., Li, S., et al.: Characterization of urban and rural organic particulate in the Lower

- Fraser Valley using two Aerodyne Aerosol Mass Spectrometers, *Atmos. Environ.*, 38, 5745–5758, 2004.
- Allan, J., Bower, K., Coe, H., Boudries, H., Jayne, J., Canagaratna, M., Millet, D., Goldstein, A., Quinn, P., Weber, R., and Worsnop, D.: Submicron aerosol composition at Trinidad Head, California, during ITCT 2K2: Its relationship with gas phase volatile organic carbon and assessment of instrument performance, *J. Geophys. Res. Atmos.*, 109, D23S24, doi:10.1029/2003JD004208, 2004a.
- Allan, J., Delia, A., Coe, H., Bower, K., Alfarra, M., Jimenez, J., Middlebrook, A., Drewnick, F., Onasch, T., Canagaratna, M., Jayne, J., and Worsnop, D.: A generalised method for the extraction of chemically resolved mass spectra from aerodyne aerosol mass spectrometer data, *J. Aerosol Sci.*, 35, 909–922, doi:10.1016/j.jaerosci.2004.02.007, 2004b.
- AQMD: Historic Ozone Air Quality Trends, available at <http://www.aqmd.gov/smog/o3trend.html>, 2010.
- Bahreini, R., Keywood, M., Ng, N., Varutbangkul, V., Gao, S., Flagan, R., Seinfeld, J., Worsnop, D., and Jimenez, J.: Measurements of secondary organic aerosol from oxidation of cycloalkenes, terpenes, and m-xylene using an Aerodyne aerosol mass spectrometer, *Environ. Sci. Technol.*, 39, 5674–5688, 2005.
- Bein, K. J., Zhao, Y. J., Pekney, N. J., Davidson, C. I., Johnston, M. V., and Wexler, A. S.: Identification of sources of atmospheric PM at the Pittsburgh Supersite - Part II: Quantitative comparisons of single particle, particle number, and particle mass measurements, *Atmos. Environ.*, 40, S424–S444, 2006.
- Blumenthal, D., White, W., and Smith, T.: Anatomy of a Los Angeles smog episode: Pollutant transport in the daytime sea breeze regime, *Atmos. Environ.*, 12, 893–907, 1978.
- Bremner, J., Haub, C., Lee, M., Mather, M., , and Zuehlke, E.: World Population Highlights: Key Findings From PRB's 2009 World Population Data Sheet, Population Reference Bureau, 2009.

- Cabada, J. C., Rees, S., Takahama, S., Khlystov, A., Pandis, S. N., Davidson, C. I., and Robinson, A. L.: Mass size distributions and size resolved chemical composition of fine particulate matter at the Pittsburgh supersite, *Atmos. Environ.*, **38**, 3127–3141, 2004.
- Canagaratna, M., Jayne, J., Jimenez, J., Allan, J., Alfarra, M., Zhang, Q., Onasch, T., Drewnick, F., Coe, H., Middlebrook, A., et al.: Chemical and microphysical characterization of ambient aerosols with the aerodyne aerosol mass spectrometer, *Mass Spectrom. Rev.*, **26**, 185–222, 2007.
- CARB: iADAM Air Quality Data Statistics, Available at <http://www.arb.ca.gov/adam/>, California Air Resources Board, 2010.
- Chow, J. C., Fujita, E. M., Watson, J. G., Lu, Z. Q., Lawson, D. R., and Asbaugh, L. L.: Evaluation of Filter-Based Aerosol Measurements during the 1987 Southern California Air-Quality Study, *Environmental Monitoring and Assessment*, **30**, 49–80, 1994.
- Cocker, D. R., Whitlock, N. E., Flagan, R. C., and Seinfeld, J. H.: Hygroscopic properties of Pasadena, California aerosol, *Aerosol Sci. Technol.*, **35**, 637–647, 2001.
- Croes, B. E. and Fujita, E. M.: Overview of the 1997 Southern California Ozone Study (SCOS97-NARSTO), *Atmos. Environ.*, **37**, S3–S26, 2003.
- DeCarlo, P., Kimmel, J., Trimborn, A., Northway, M., Jayne, J., Aiken, A., Gonin, M., Fuhrer, K., Horvath, T., Docherty, K., et al.: Field-deployable, high-resolution, time-of-flight aerosol mass spectrometer, *Anal. Chem.*, **78**, 8281–8289, 2006.
- DeCarlo, P. F., Dunlea, E. J., Kimmel, J. R., Aiken, A. C., Sueper, D., Crouse, J., Wennberg, P. O., Emmons, L., Shinozuka, Y., Clarke, A., Zhou, J., Tomlinson, J., Collins, D. R., Knapp, D., Weinheimer, A. J., Montzka, D. D., Campos, T., and Jimenez, J. L.: Fast airborne aerosol size and chemistry measurements above Mexico City and Central Mexico during the MILAGRO campaign, *Atmos. Chem. Phys.*, **8**, 4027–4048, 2008.
- Denkenberger, K. A., Moffet, R. C., Holecek, J. C., Rebotier, T. P., and Prather, K. A.: Real-

- time, single-particle measurements of oligomers in aged ambient aerosol particles, *Environ. Sci. Technol.*, 41, 5439–5446, 2007.
- Docherty, K. S., Stone, E. A., Ulbrich, I. M., DeCarlo, P. F., Snyder, D. C., Schauer, J. J., Peltier, R. E., Weber, R. J., Murphy, S. M., Seinfeld, J. H., Grover, B. D., Eatough, D. J., and Jimenez, J. L.: Apportionment of Primary and Secondary Organic Aerosols in Southern California during the 2005 Study of Organic Aerosols in Riverside (SOAR-1), *Environ. Sci. Technol.*, 42, 7655–7662, 2008.
- Drewnick, F., Schwab, J., Högrefe, O., Peters, S., Husain, L., Diamond, D., Weber, R., and Demerjian, K.: Intercomparison and evaluation of four semi-continuous PM_{2.5} sulfate instruments, *Atmos. Environ.*, 37, 3335–3350, doi:10.1016/S1352-2310(03)00351-0, 2003.
- Drewnick, F., Hings, S., DeCarlo, P., Jayne, J., Gonin, M., Fuhrer, K., Weimer, S., Jimenez, J., Demerjian, K., Borrmann, S., and Worsnop, D.: A new time-of-flight aerosol mass spectrometer (TOF-AMS) - Instrument description and first field deployment, *Aerosol Sci. Tech.*, 39, 637–658, doi:10.1080/02786820500182040, 2005.
- Dusek, U., Frank, G., Curtius, J., Drewnick, F., Schneider, J., Kürten, A., Rose, D., Andreae, M., Borrmann, S., and Pöschl, U.: Enhanced organic mass fraction and decreased hygroscopicity of cloud condensation nuclei (CCN) during new particle formation events, *Geophys. Res. Lett.*, 37, 2010.
- Eatough, D. J., Grover, B. D., Woolwine, W. R., Eatough, N. L., Long, R., and Farber, R.: Source apportionment of 1 h semi-continuous data during the 2005 Study of Organic Aerosols in Riverside (SOAR) using positive matrix factorization, *Atmos. Environ.*, 42, 2706–2719, 2008.
- Eldering, A., Cass, G. R., and Moon, K. C.: An Air Monitoring Network Using Continuous Particle-Size Distribution Monitors - Connecting Pollutant Properties to Visibility Via Mie Scattering Calculations, *Atmos. Environ.*, 28, 2733–2749, 1994.
- Hersey, S. P., Sorooshian, A., Murphy, S. M., Flagan, R. C., and Seinfeld, J. H.: Aerosol hygroscopic-

- ity in the marine atmosphere: a closure study using high-time-resolution, multiple-RH DASH-SP and size-resolved C-ToF-AMS data, *Atmos. Chem. Phys.*, 9, 2543–2554, 2009.
- Huffman, J., Jayne, J., Drewnick, F., Aiken, A., Onasch, T., Worsnop, D., and Jimenez, J.: Design, modeling, optimization, and experimental tests of a particle beam width probe for the aerodyne aerosol mass spectrometer, *Aerosol Sci. Technol.*, 39, 1143–1163, doi:10.1080/02786820500423782, 2005.
- Hughes, L. S., Allen, J. O., Salmon, L. G., Mayo, P. R., Johnson, R. J., and Cass, G. R.: Evolution of nitrogen species air pollutants along trajectories crossing the Los Angeles area, *Environ. Sci. Technol.*, 36, 3928–3935, 2002.
- Kautzman, K. E., Surratt, J. D., Chan, M. N., Chan, A. W. H., Hersey, S. P., Chhabra, P. S., Dalleska, N. F., Wennberg, P. O., Flagan, R. C., and Seinfeld, J. H.: Chemical Composition of Gas- and Aerosol-Phase Products from the Photooxidation of Naphthalene, *J. Phys. Chem. A*, 114, 913–934, 2010.
- Kleeman, M., Hughes, L., Allen, J., and Cass, G.: Source contributions to the size and composition distribution of atmospheric particles: Southern California in September 1996, *Environ. Sci. Technol.*, 33, 4331–4341, 1999.
- Kondo, Y., Miyazaki, Y., Takegawa, N., Miyakawa, T., Weber, R. J., Jimenez, J. L., Zhang, Q., and Worsnop, D. R.: Oxygenated and water-soluble organic aerosols in Tokyo, *J. Geophys. Res.*, 112, D01 203, doi:10.1029/2006JD007056, 2007.
- Lanz, V., Alfarra, M., Baltensperger, U., Buchmann, B., Hueglin, C., and Prévôt, A.: Source apportionment of submicron organic aerosols at an urban site by factor analytical modelling of aerosol mass spectra, *Atmos. Chem. Phys.*, 7, 1503–1522, 2007.
- Liu, D. Y., Prather, K. A., and Hering, S. V.: Variations in the size and chemical composition of nitrate-containing particles in Riverside, CA, *Aerosol Sci. Technol.*, 33, 71–86, 2000.

- Lu, R. and Turco, R.: Air pollutant transport in a coastal environment–II. Three-dimensional simulations over Los Angeles basin, *Atmos. Environ.*, 29, 1499–1518, 1995.
- Massling, A., Stock, M., and Wiedensohler, A.: Diurnal, weekly, and seasonal variation of hygroscopic properties of submicrometer urban aerosol particles, *Atmos. Environ.*, 39, 3911–3922, 2005.
- Massling, A., Stock, M., Wehner, B., Wu, Z. J., Hu, M., Brüggemann, E., Gnauk, T., Herrmann, H., and Wiedensohler, A.: Size segregated water uptake of the urban submicrometer aerosol in Beijing, *Atmos. Environ.*, 43, 1578–1589, 2009.
- Matsui, H., Koike, M., Kondo, Y., Takegawa, N., Kita, K., Miyazaki, Y., Hu, M., Chang, S. Y., Blake, D. R., Fast, J. D., Zaveri, R. A., Streets, D. G., Zhang, Q., and Zhu, T.: Spatial and temporal variations of aerosols around Beijing in summer 2006: Model evaluation and source apportionment, *J. Geophys. Res. Atmos.*, 114, –, 2009.
- Meier, J., Wehner, B., Massling, A., Birmili, W., Nowak, A., Gnauk, T., Brüggemann, E., Herrmann, H., Min, H., and Wiedensohler, A.: Hygroscopic growth of urban aerosol particles in Beijing(China) during wintertime: a comparison of three experimental methods, *Atmos. Chem. Phys.*, 9, 6865–6880, 2009.
- Modey, W. K., Eatough, D. J., Anderson, R. R., Martello, D. V., Takahama, S., Lucas, L. J., and Davidson, C. I.: Ambient fine particulate concentrations and chemical composition at two sampling sites in metropolitan Pittsburgh: a 2001 intensive summer study, *Atmos. Environ.*, 38, 3165–3178, 2004.
- Na, K., Sawant, A., Song, C., and Cocker, D.: Primary and secondary carbonaceous species in the atmosphere of Western Riverside County, California, *Atmos. Environ.*, 38, 1345–1355, 2004.
- Ng, N. L., Canagaratna, M. R., Zhang, Q., Jimenez, J. L., Tian, J., Ulbrich, I. M., Kroll, J. H., Docherty, K. S., Chhabra, P. S., Bahreini, R., Murphy, S. M., Seinfeld, J. H., Hildebrandt, L., Donahue, N. M., DeCarlo, P. F., Lanz, V. A., Prevot, A. S. H., Dinar, E., Rudich, Y., and

- Worsnop, D. R.: Organic aerosol components observed in Northern Hemispheric datasets from Aerosol Mass Spectrometry, *Atmos. Chem. Phys.*, 10, 4625–4641, 2010.
- Ng, N. L., Canagaratna, M. R., Jimenez, J. L., Zhang, Q., Ulbrich, I. M., and Worsnop, D. R.: Real-Time Methods for Estimating Organic Component Mass Concentrations from Aerosol Mass Spectrometer Data, *Environ. Sci. Technol.*, 45, 910–916, URL <http://pubs.acs.org/doi/abs/10.1021/es102951k>, 2011.
- Paatero, P.: A weighted non-negative least squares algorithm for three-way ‘PARAFAC’ factor analysis, *Chemom. Intell. Lab. Syst.*, 38, 223–242, 1997.
- Paatero, P. and Tapper, U.: Positive Matrix Factorization - a Nonnegative Factor Model with Optimal Utilization of Error-Estimates of Data Values, *Environmetrics*, 5, 111–126, 1994.
- Pastor, S. H., Allen, J. O., Hughes, L. S., Bhave, P., Cass, G. R., and Prather, K. A.: Ambient single particle analysis in Riverside, California by aerosol time-of-flight mass spectrometry during the SCOS97-NARSTO, *Atmos. Environ.*, 37, S239–S258, 2003.
- Pekney, N. J., Davidson, C. I., Bein, K. J., Wexler, A. S., and Johnston, M. V.: Identification of sources of atmospheric PM at the Pittsburgh Supersite, Part I: Single particle analysis and filter-based positive matrix factorization, *Atmos. Environ.*, 40, S411–S423, 2006.
- Petters, M. D. and Kreidenweis, S. M.: A single parameter representation of hygroscopic growth and cloud condensation nucleus activity, *Atmos. Chem. Phys.*, 7, 1961–1971, 2007.
- Quinn, P., Bates, T., Baynard, T., Clarke, A., Onasch, T., Wang, W., Rood, M., Andrews, E., Allan, J., Carrico, C., et al.: Impact of particulate organic matter on the relative humidity dependence of light scattering: A simplified parameterization, *Geophys. Res. Lett.*, 32, 22, 2005.
- Rose, D., Nowak, A., Achtert, P., Wiedensohler, A., Hu, M., Shao, M., Zhang, Y., Andreae, M., and Pöschl, U.: Cloud condensation nuclei in polluted air and biomass burning smoke near the megacity Guangzhou, China- Part 1: Size-resolved measurements and implications for the modeling of aerosol particle hygroscopicity and CCN activity, *Atmos. Chem. Phys.*, 10, 3365–3383, 2010.

- Sawant, A., Na, K., Zhu, X., Cocker, K., Butt, S., Song, C., and Cocker III, D.: Characterization of PM_{2.5} and selected gas-phase compounds at multiple indoor and outdoor sites in Mira Loma, California, *Atmos. Environ.*, **38**, 6269–6278, 2004.
- Shinozuka, Y., Clarke, A., DeCarlo, P., Jimenez, J., Dunlea, E., Roberts, G., Tomlinson, J., Collins, D., Howell, S., Kapustin, V., et al.: Aerosol optical properties relevant to regional remote sensing of CCN activity and links to their organic mass fraction: airborne observations over Central Mexico and the US West Coast during MILAGRO/INTEX-B, *Atmos. Chem. Phys.*, **9**, 6727–6742, 2009.
- Sorooshian, A., Brechtel, F., Weber, R., Corless, A., Flagan, R., and Seinfeld, J.: Modeling and characterization of a particle-into-liquid sampler (PILS), *Aerosol Sci. Technol.*, **40**, 396–409, 2006.
- Sorooshian, A., Hersey, S., Brechtel, F., Corless, A., Flagan, R., and Seinfeld, J.: Rapid, size-resolved aerosol hygroscopic growth measurements: Differential aerosol sizing and hygroscopicity spectrometer probe (DASH-SP), *Aerosol Sci. Technol.*, **42**, 445–464, 2008.
- Stanier, C., Khlystov, A., and Pandis, S.: Nucleation Events During the Pittsburgh Air Quality Study: Description and Relation to Key Meteorological, Gas Phase, and Aerosol Parameters Special Issue of Aerosol Science and Technology on Findings from the Fine Particulate Matter Supersites Program, *Aerosol Sci. Technol.*, **38**, 253–264, 2004.
- Stone, E. A., Snyder, D. C., Sheesley, R. J., Sullivan, A. P., Weber, R. J., and Schauer, J. J.: Source apportionment of fine organic aerosol in Mexico City during the MILAGRO experiment 2006, *Atmos. Chem. Phys.*, **8**, 1249–1259, 2008.
- Sullivan, A., Weber, R., Clements, A., Turner, J., Bae, M., and Schauer, J.: A method for on-line measurement of water-soluble organic carbon in ambient aerosol particles: Results from an urban site, *Geophys. Res. Lett.*, **31**, 2004.
- Sullivan, A., Peltier, R., Brock, C., De Gouw, J., Holloway, J., Warneke, C., Wollny, A., and Weber, R.: Airborne measurements of carbonaceous aerosol soluble in water over northeastern United

- States: Method development and an investigation into water-soluble organic carbon sources, *J. Geophys. Res.*, 111, 1–14, 2006.
- Surratt, J., Gomez-Gonzalez, Y., Chan, A., Vermeulen, R., Shahgholi, M., Kleindienst, T., Edney, E., Offenberg, J., Lewandowski, M., Jaoui, M., et al.: Organosulfate formation in biogenic secondary organic aerosol, *J. Phys. Chem. A*, 112, 8345–8378, 2008.
- Swietlicki, E., Hansson, H., Hameri, K., Svenningsson, B., Massling, A., McFiggans, G., McMurry, P., Petaja, T., Tunved, P., Gysel, M., et al.: Hygroscopic properties of submicrometer atmospheric aerosol particles measured with H-TDMA instruments in various environmentsA review, *Tellus B*, 60, 432–469, 2008.
- Tiitta, P., Miettinen, P., Vaattovaara, P., Joutsensaari, J., Pet, T., Virtanen, A., Raatikainen, T., Aalto, P., Portin, H., Romakkaniemi, S., et al.: Roadside aerosol study using hygroscopic, organic and volatility TDMA: Characterization and mixing state, *Atmos. Environ.*, 44, 976–986, 2010.
- Turpin, B. and Lim, H.-J.: Species Contributions to PM_{2.5} Mass Concentrations: Revisiting Common Assumptions for Estimating Organic Mass, *Aerosol Sci. Technol.*, 35, 602–610, 2001.
- Turpin, B. J. and Huntzicker, J. J.: Secondary Formation of Organic Aerosol in the Los-Angeles Basin - a Descriptive Analysis of Organic and Elemental Carbon Concentrations, *Atmos. Environ. Part A*, 25, 207–215, 1991.
- Ulbrich, I. M., Canagaratna, M. R., Zhang, Q., Worsnop, D. R., and Jimenez, J. L.: Interpretation of organic components from Positive Matrix Factorization of aerosol mass spectrometric data, *Atmos. Chem. Phys.*, 9, 2891–2918, 2009.
- van Pinxteren, D., Brüggemann, E., Gnauk, T., Iinuma, Y., Müller, K., Nowak, A., Achtert, P., Wiedensohler, A., and Herrmann, H.: Size- and time-resolved chemical particle characterization during CAREBeijing-2006: Different pollution regimes and diurnal profiles, *J. Geophys. Res. Atmos.*, 114, –, 2009.

- Wang, J., Cubison, M., Aiken, A., Jimenez, J., and Collins, D.: The importance of aerosol mixing state and size-resolved composition on CCN concentration and the variation of the importance with atmospheric aging of aerosols, *Atmos. Chem. Phys.*, 10, 7267–7283, 2010.
- Watson, J. G., Chow, J. C., Lu, Z. Q., Fujita, E. M., Lowenthal, D. H., Lawson, D. R., and Ashbaugh, L. L.: Chemical Mass-Balance Source Apportionment of Pm(10) during the Southern California Air-Quality Study, *Aerosol Sci. Technol.*, 21, 1–36, 1994.
- Wex, H., McFiggans, G., Henning, S., and Stratmann, F.: Influence of the external mixing state of atmospheric aerosol on derived CCN number concentrations, *Geophys. Res. Lett.*, 37, L10 805, 2010.
- Wittig, A. E., Anderson, N., Khlystov, A. Y., Pandis, S. N., Davidson, C., and Robinson, A. L.: Pittsburgh air quality study overview, *Atmos. Environ.*, 38, 3107–3125, 2004.
- Yue, D. L., Hu, M., Wu, Z. J., Wang, Z. B., Guo, S., Wehner, B., Nowak, A., Achtert, P., Wiedensohler, A., Jung, J., Kim, Y. J., and Liu, S.: Characteristics of aerosol size distributions and new particle formation in the summer in Beijing, *J. Geophys. Res. Atmos.*, 114, –, 2009.
- Zhang, Q., Alfarra, M., Worsnop, D., Allan, J., Coe, H., Canagaratna, M., and Jimenez, J.: Deconvolution and quantification of hydrocarbon-like and oxygenated organic aerosols based on aerosol mass spectrometry, *Environ. Sci. Technol.*, 39, 4938–4952, 2005.
- Zhang, Q., Jimenez, J. L., Canagaratna, M. R., Allan, J. D., Coe, H., Ulbrich, I., Alfarra, M. R., Takami, A., Middlebrook, A. M., Sun, Y. L., Dzepina, K., Dunlea, E., Docherty, K., DeCarlo, P. F., Salcedo, D., Onasch, T., Jayne, J. T., Miyoshi, T., Shimojo, A., Hatakeyama, S., Takegawa, N., Kondo, Y., Schneider, J., Drewnick, F., Borrmann, S., Weimer, S., Demerjian, K., Williams, P., Bower, K., Bahreini, R., Cottrell, L., Griffin, R. J., Rautiainen, J., Sun, J. Y., Zhang, Y. M., and Worsnop, D. R.: Ubiquity and dominance of oxygenated species in organic aerosols in anthropogenically-influenced Northern Hemisphere midlatitudes, *Geophys. Res. Lett.*, 34, –, 2007.

Zhang, X. and McMurray, S.: Mixing characteristics and water content of submicron aerosols measured in Los Angeles and at the Grand Canyon, *Atmos. Environ. A.*, 27, 1593–1607, 1993.

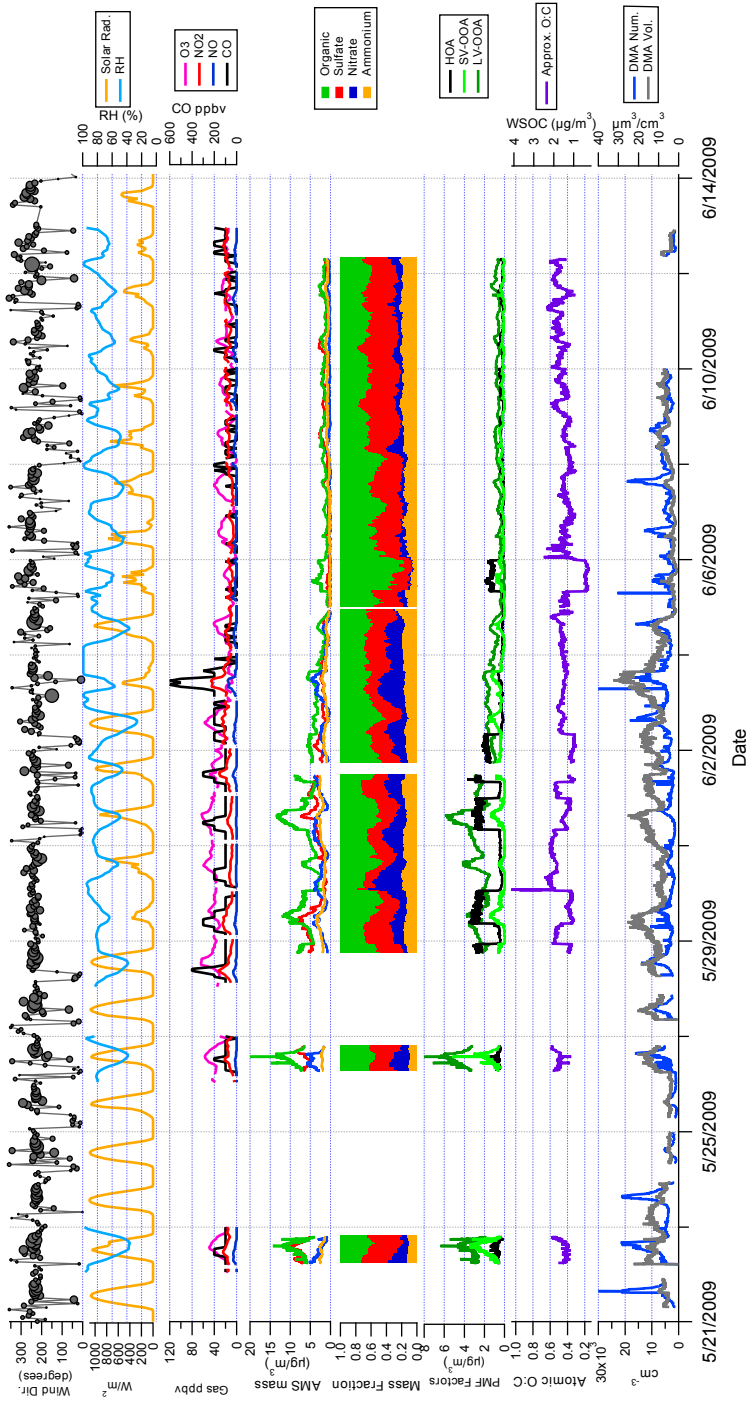


Figure 4.1: Regime I (wind direction marker size proportional to wind speed; max size = 20 km/h).

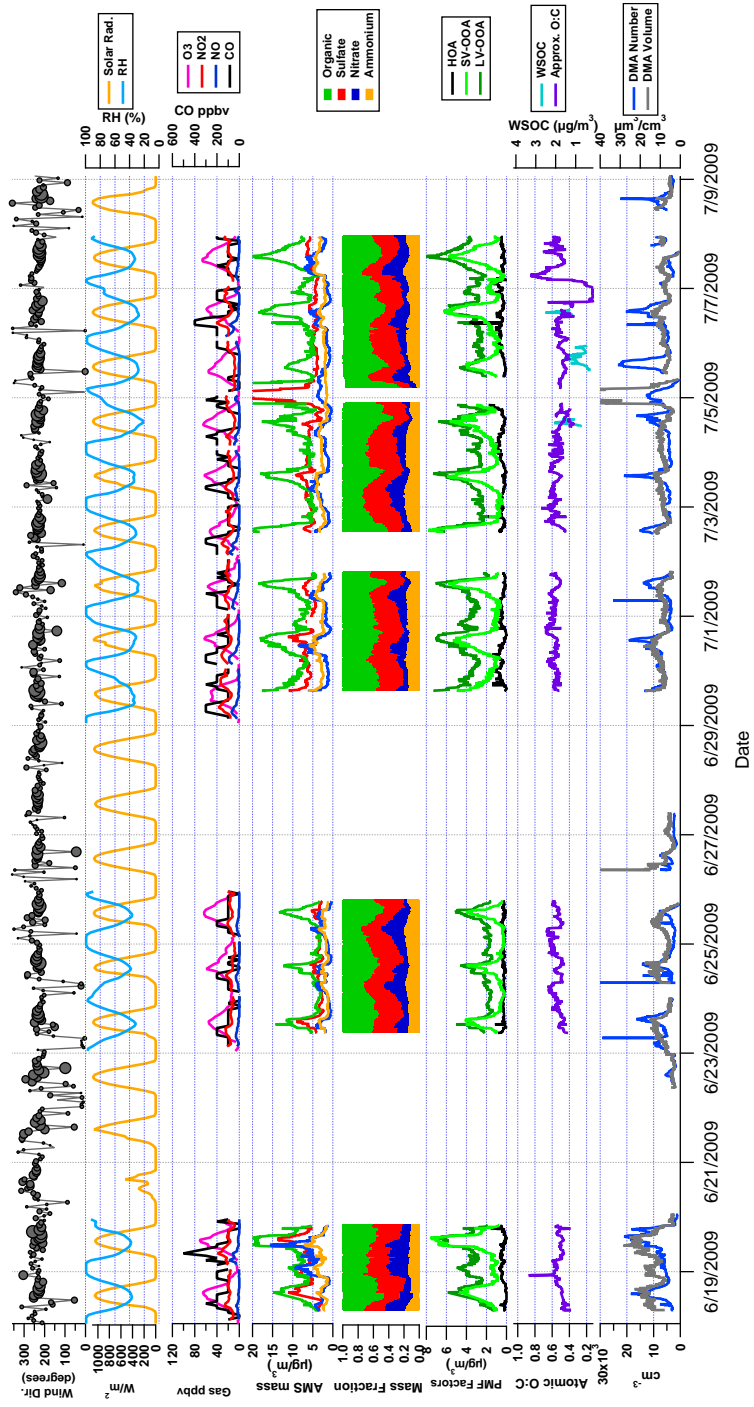


Figure 4.2: Regime II (wind direction marker size proportional to wind speed; max size = 20 km/h).

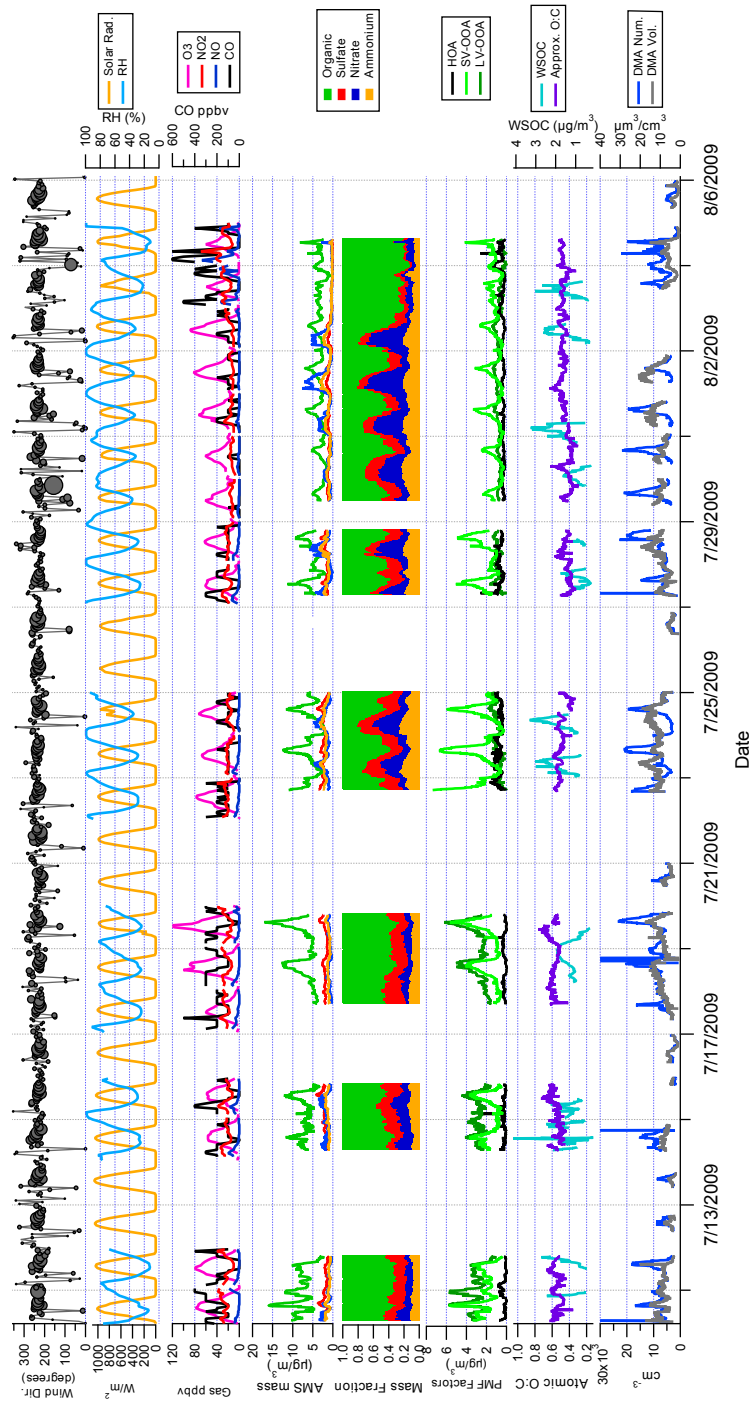


Figure 4.3: Regime III (wind direction marker size proportional to wind speed; max size = 20 km/h).

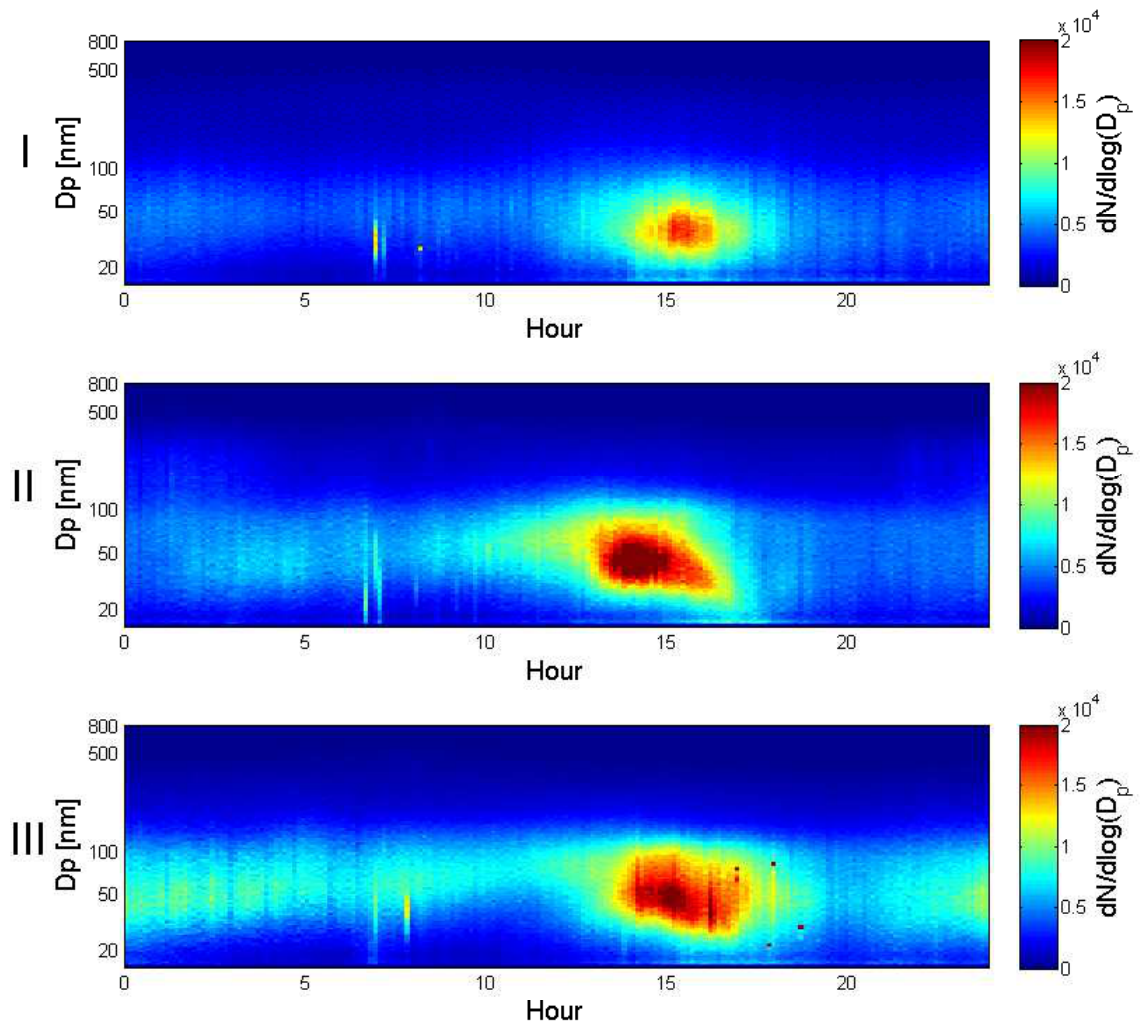


Figure 4.4: Average diurnal DMA number concentrations (cm^{-3}) for regimes I, II, and III.

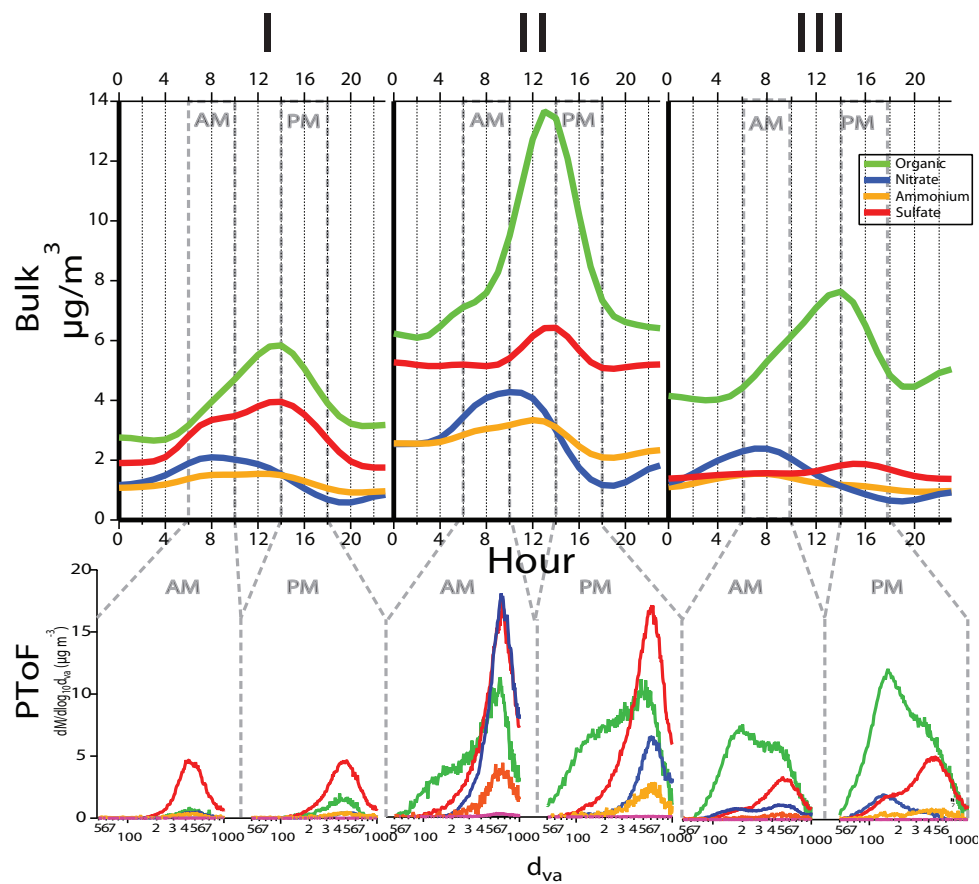


Figure 4.5: Bulk AMS diurnal mass averages for regime I, regime II, and regime III. Bottom panel shows size-resolved PToF AMS data for a representative morning and afternoon period in each regime, where morning = 0700-1100 LT and afternoon = 1500-1900 LT.

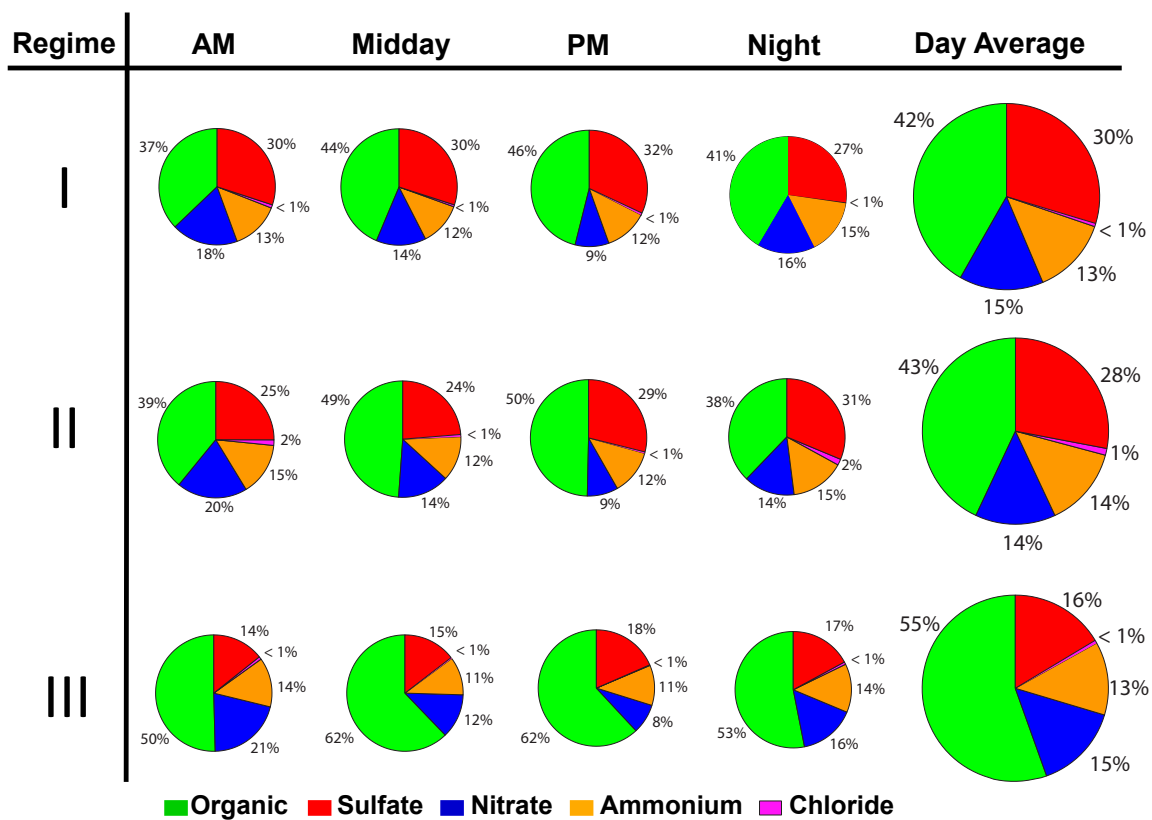


Figure 4.6: AMS bulk mass fractions for AM (0700-1100 LT), midday (1100-1500 LT), PM (1500-1900 LT), and night (1900-0700 LT) for regimes I, II, and III.

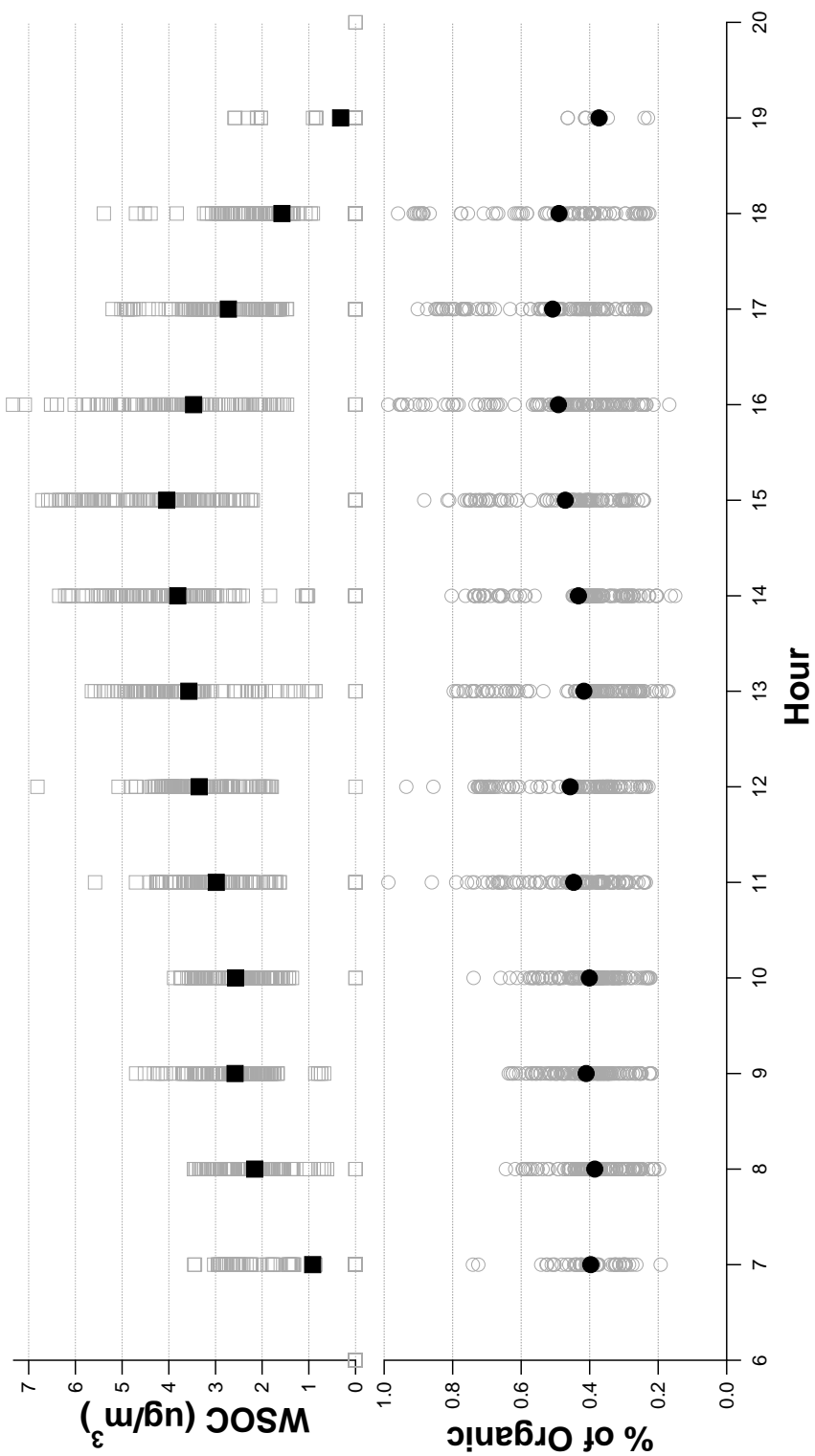


Figure 4.7: WSOC magnitude (squares) and % of AMS organic (circles). Black markers represent the average over regime III.

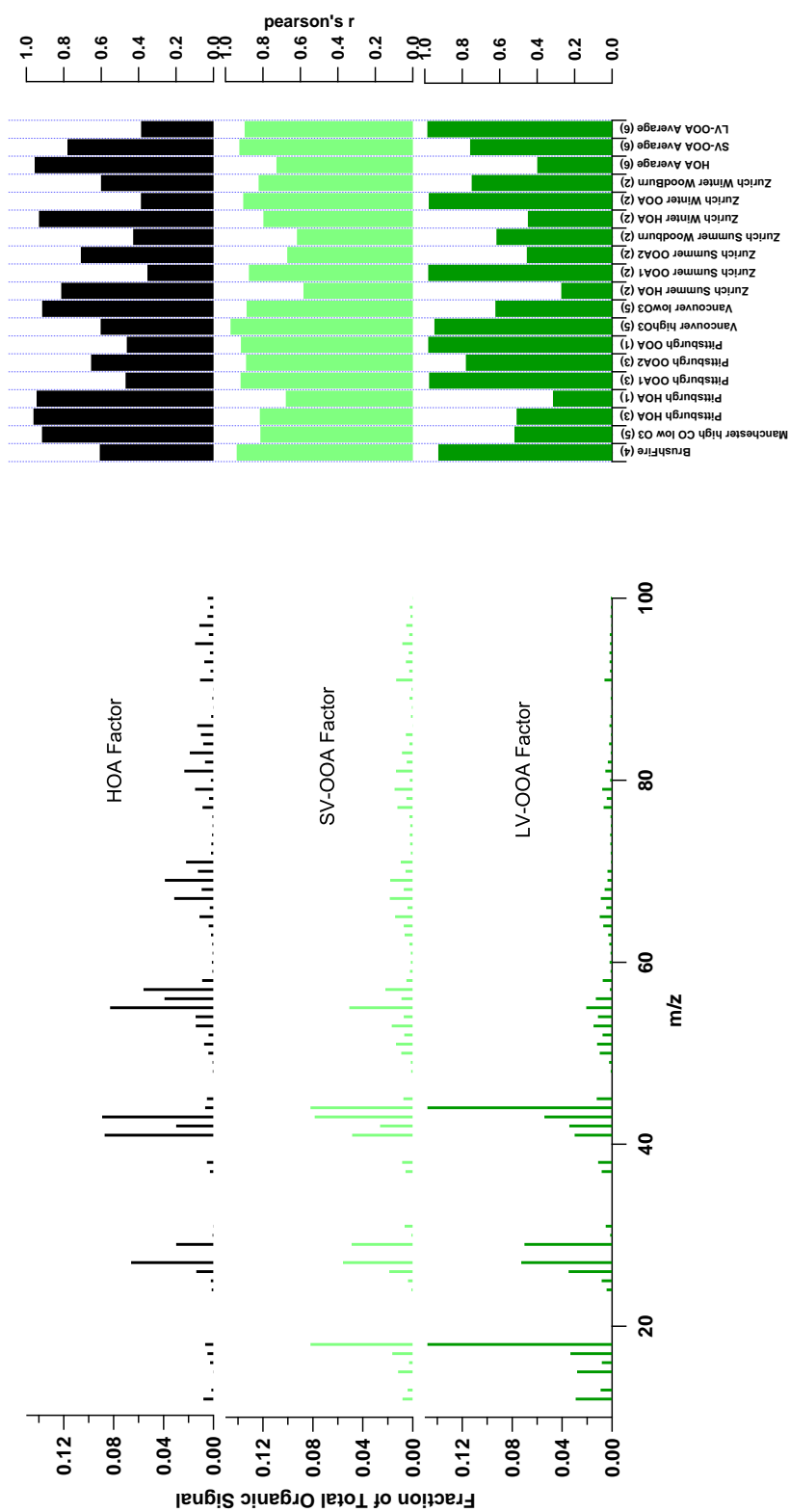


Figure 4.8: Mass spectra for the three factors identified in PMF analysis (HOA, SV-OOA, and LV-OOA; left) and Pearson's R correlations of those solution mass spectra with previously reported mass spectra (1, 2, 3, 4, 5, 6: Zhang et al., 2005; Lanz et al., 2007; Ulbrich et al., 2009; Bahreini et al., 2005; Alfarra et al., 2004; Ng et al., 2011, respectively).

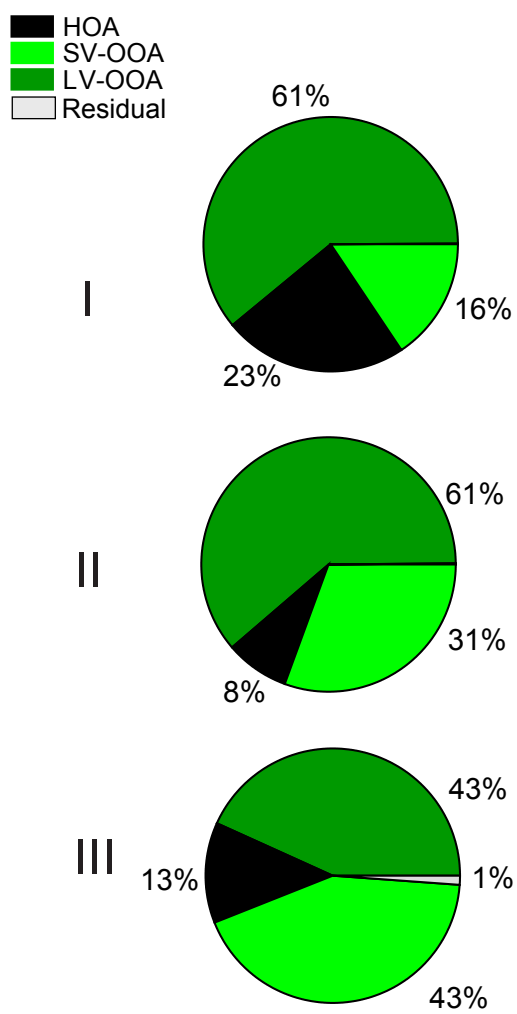


Figure 4.9: Mass fraction of total organic accounted for by each PMF factor during regimes I, II, and III.

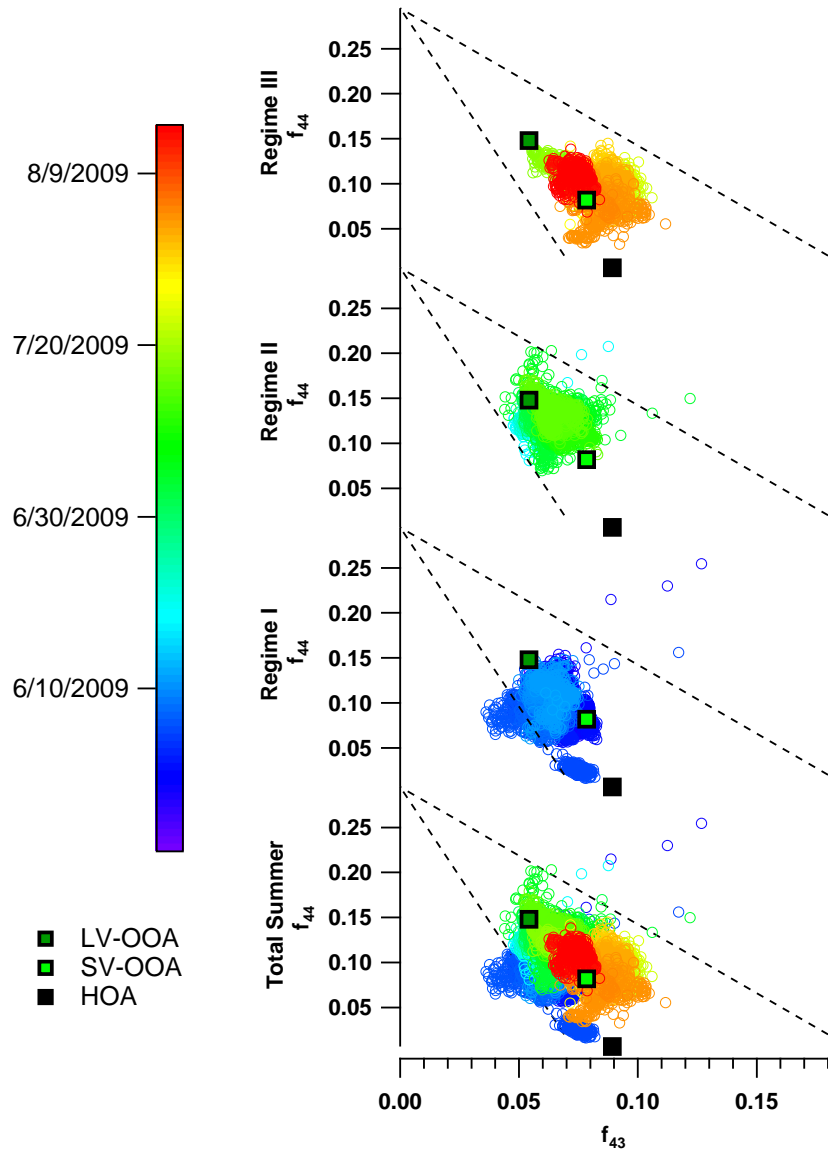


Figure 4.10: f_{44} vs. f_{43} for PACO, with color scale corresponding to date. Square markers represent values for HOA, SV-OOA, and LV-OOA factors identified in PACO.

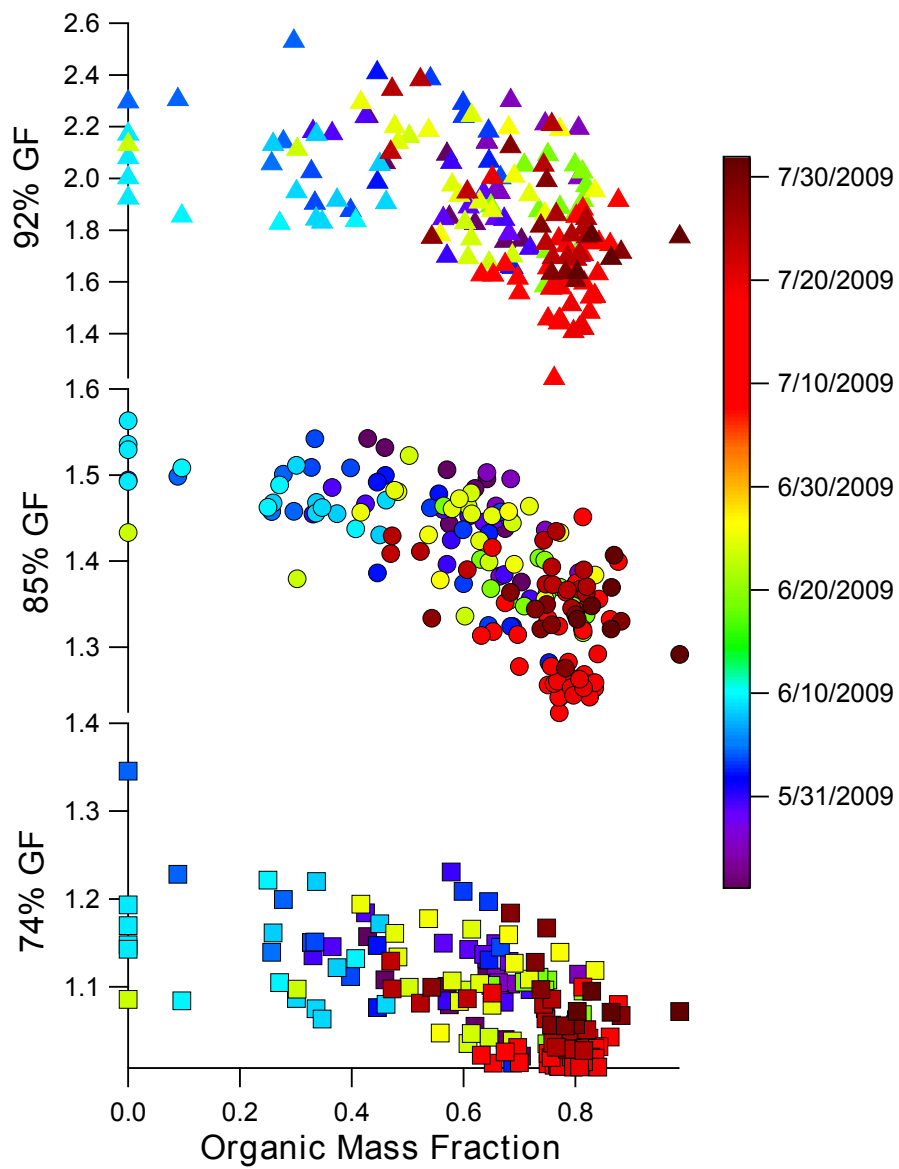


Figure 4.11: GF at 74, 85, and 92% RH plotted against organic mass fraction, with color scale corresponding to date

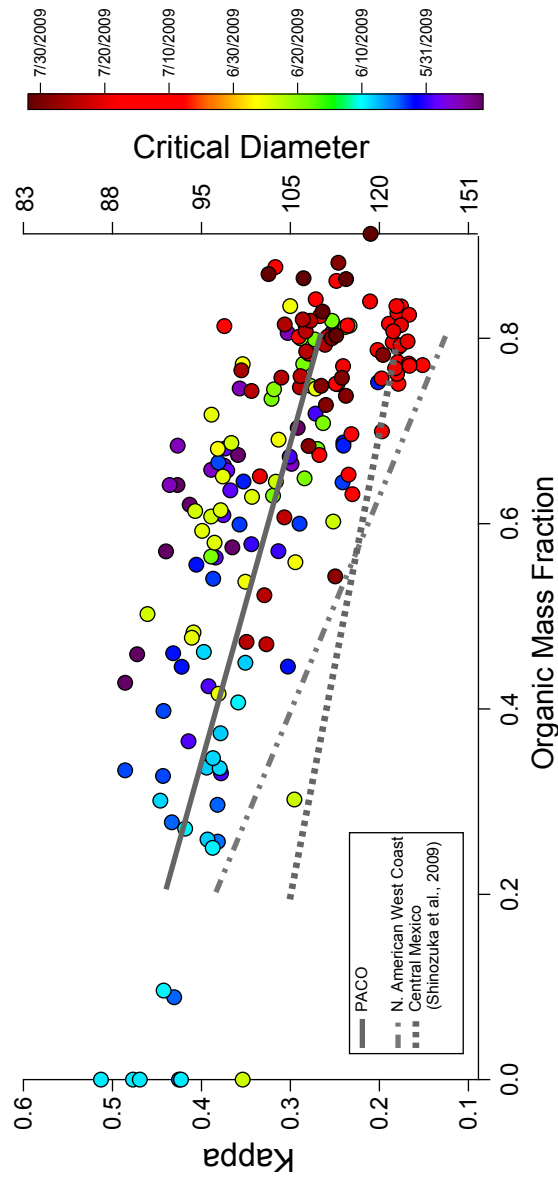


Figure 4.12: κ and critical dry diameter plotted against mass fraction organic, with color scale corresponding to date; lines represent empirical parameterizations from PACO, Central Mexico, and N. American West Coast.

Table 4.1: Previous Los Angeles air quality studies and major findings relative to particulate matter.

Study	Date	Major Aerosol Findings
Southern California Air Quality Study (SCAQS)	Summer-Fall 1987	<ul style="list-style-type: none"> • SOA/OA ~40% in summer afternoon (Turpin and Huntzicker, 1991) • Primary vehicle exhaust is the major aerosol component near PACO sampling site (Watson et al., 1994) • 20-32% of PM₁₀ is SO₄²⁻ and NO₃⁻ (Watson et al., 1994)
Southern California Ozone Study (SCOS97-NARSTO)	Summer 1997	<ul style="list-style-type: none"> • Submicron organic mode evolves during periods of intense photochemistry, coincident with maximum O₃ (Pastor et al., 2003) • NH₄NO₃ and organics added to submicron aerosol with photochemical age (Pastor et al., 2003) • NH₃ sources in eastern basin enhance particulate NH₄NO₃ (Hughes et al., 2002)
Secondary Organic Aerosol in Riverside (SOAR-1, 2)	Aug., Nov. 2005	<ul style="list-style-type: none"> • Significant diurnal changes in organic aerosol, with species more reduced in the morning and more oxidized in the afternoon (DeCarlo et al., 2006) • Oligomers detected in aged, acidic particles (Denkenberger et al., 2007) • SOA/OA = 70-90% at midday and ~45% during morning commute; SOAR average = 74% (Docherty et al., 2008)
Individual Studies	1999, 2001-2002	<ul style="list-style-type: none"> • Complex, multi-modal GF data in Pasadena (Cocker et al., 2001) • SOA > 50% of total PM_{2.5} in eastern basin (Savant et al., 2004; Na et al., 2004)

Table 4.2: PACO sampling regimes (2009).

Regime	Dates	Characteristics
Springtime Meteorology	22-May to 12-June	<ul style="list-style-type: none"> • Basin impacted by a series of low pressure systems • Cutoff low brought rare springtime precipitation and cleaner atmosphere • Persistent cloudcover, unstable atmosphere • Low daytime temperatures, high RH, and limited photochemistry • High visibility with low O₃
Early Summer/Marine Influence	18-Jun to 7-July	<ul style="list-style-type: none"> • Limited impact from low pressure systems • Morning marine layer eroded several hours after sunrise • Higher daytime temperatures, slightly lower RH, and photochemically active afternoons • Hazy afternoons with increased O₃
Photochemically active	10-July to 4-Aug	<ul style="list-style-type: none"> • Semi-permanent high pressure over Southern California • Little marine moisture and infrequent, quickly-eroded marine layer • High daytime temp. (often exceeding 35°C), very low daytime RH ($\leq 15\%$), photochemically active days • Decreased visibility, high afternoon O₃

Table 4.3: OC/EC concentrations ($\mu\text{g}/\text{m}^3$) for representative days from each regime.

Regime	OC		EC		OC:EC	
	AM	PM	AM	PM	AM	PM
I	3.88 ± 0.32	4.92 ± 1.18	0.43 ± 0.02	0.40 ± 0.27	9.1	12.4
II	4.24 ± 0.46	5.01 ± 1.62	0.80 ± 0.31	0.52 ± 0.40	5.3	9.6
III	6.16 ± 1.40	6.41 ± 1.44	0.83 ± 0.47	0.65 ± 0.22	7.4	9.9

4.6 Appendix

4.6.1 PMF Analysis

PMF was initiated using 50 seed values, and then again using a range of f_{peak} values from -1 to 1 varying by 0.1. Figures 4.13 and 4.14 show the Q/Q_{expected} values for the different solutions. The PMF results were sorted by regime, number of factors, and seed (only where it caused the solution to vary) and compared to previously published mass spectra in the AMS online Spectral Database explained in Ulbrich et al. (2009) (Ulbrich, I.M., Lechner, M., and Jimenez, J.L. AMS Spectral Database. URL: <http://cires.colorado.edu/jimenez-group/AMSSd/>). Table 4.4 shows Pearson's r values comparing the PMF mass spectral profile solutions to existing mass spectra. Table 4.5 shows Pearson's r values comparing the PMF time series solutions to gas phase tracers, AMS inorganic tracers, PILS tracers, and WSOC. Figure 4.15 shows total residuals of all masses over time for solutions with different factor numbers. Figure 4.16 shows the scaled residuals at each mass for the presented 3 factor solution. The 2 and 4 factor solution profiles and time series contributions are shown in Figs 4.17-4.20.

The difference in the total residuals was noticeable between the 1 and 2 factor solution and the 2 and 3 factor solution, but negligible between the 3 and 4 factor solution. In the 2 factor solution there is evidence of an HOA-like factor and OOA-like factor from the mass spectral comparison, but when compared to the 3 factor solution, the time series correlations with AMS inorganic and certain gas phase tracers is improved. In the 3 factor case, 3 solutions were explored, and were representative of the 50 possible solutions from the PMF results. Regarding the mass spectral profile, the seed = 6 solution was chosen since it has very strong correlations with the real mass spectra, and each of the profiles are least similar to one another (see the right hand side of Table 4.5) when compared to the two other 3 factor solutions. When considering the time series comparison, the seed = 6 LV-OOA like factor (factor 1) has the highest correlation with the AMS inorganic species. The p-ToF data suggests the organic profile of LV-OOA has similar particle size distributions to the AMS inorganic species (this was investigated in areas of known LV-OOA like factor and low SV-OOA like factor,

since PMF was not performed on pToF data). When the afternoon sun reaches a maximum, there is another, smaller mode that is believed to be SV-OOA, without the strong inorganic signal. Also, the seed = 6 SV-OOA factor correlates best with ozone when compared to the two other solutions. The tracers for HOA were limited in this study since the resolution for the CO and NO_x were poor and the *r* values are very low. However, when comparing the seed = 6 and seed = 1 solutions, the correlations of the HOA-like factor to CO and NO_x are slightly larger. Additionally, the HOA-like factor was compared to *m/z* 57, which is higher for the seed = 6 solutions. The HOA correlations for the seed = 4 solutions are slightly higher than in the seed = 1 and seed = 6 solutions, but this solution is not as strong mass spectrally, and when comparing the tracers for the two other factors. The four factor situation provided two different solutions, representative of the 50 seeds. In addition to the residuals not changing dramatically, in the mass spectral comparison, for both solutions, two of the factors have very similar *r* values (factor 1 and 4 for seed 1 and factor 2 and 4 for seed 4). Also, the time series correlations are worse in the four factor solutions, when compared the the presented 3 factor solution.

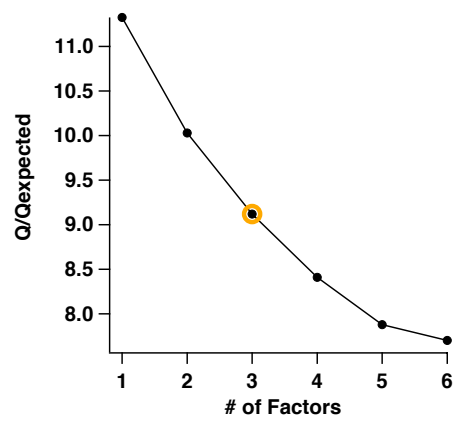


Figure 4.13: Q/Q_{exp} values for varying number of factors (p values). The circled marker is the presented solution.

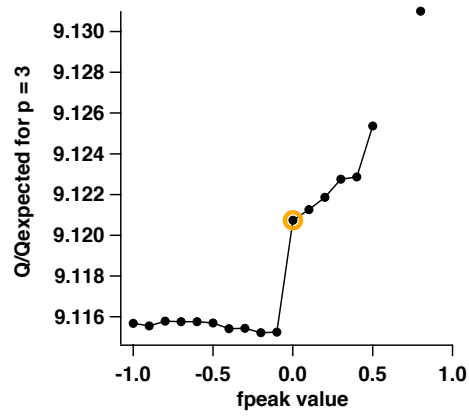


Figure 4.14: Q/Q_{exp} for varying f_{peak} values for $p = 3$. The circled marker is the presented solution.

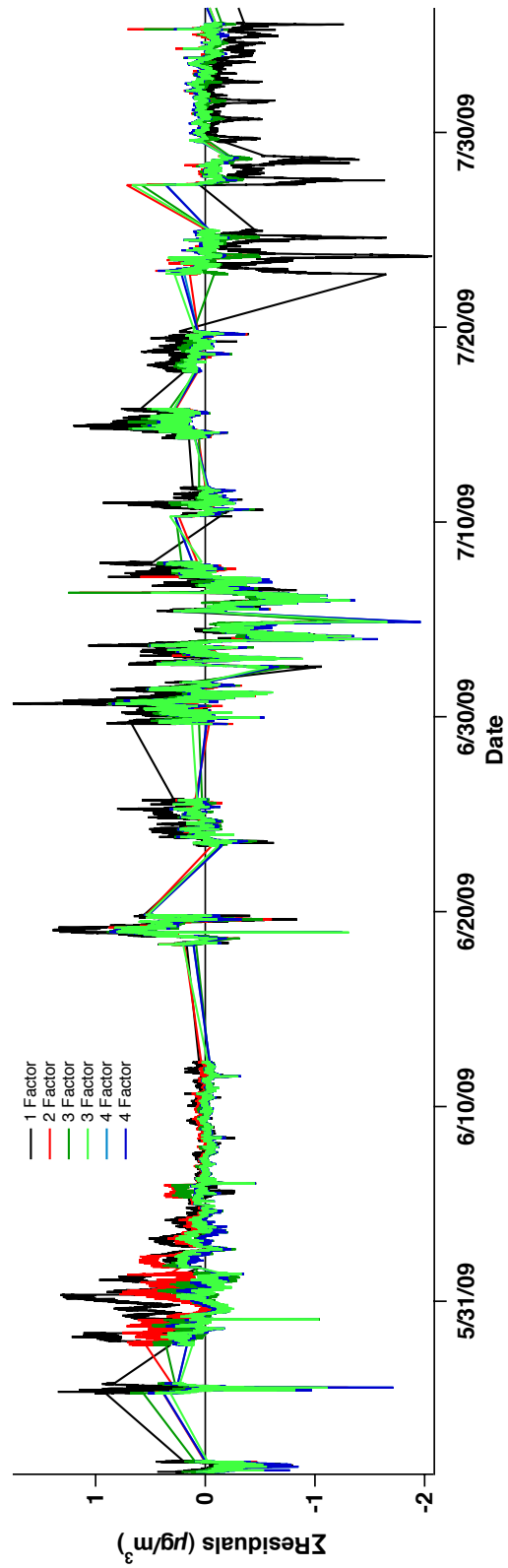


Figure 4.15: Sum of the residuals for 1,2, 3, and 4 factor solutions.

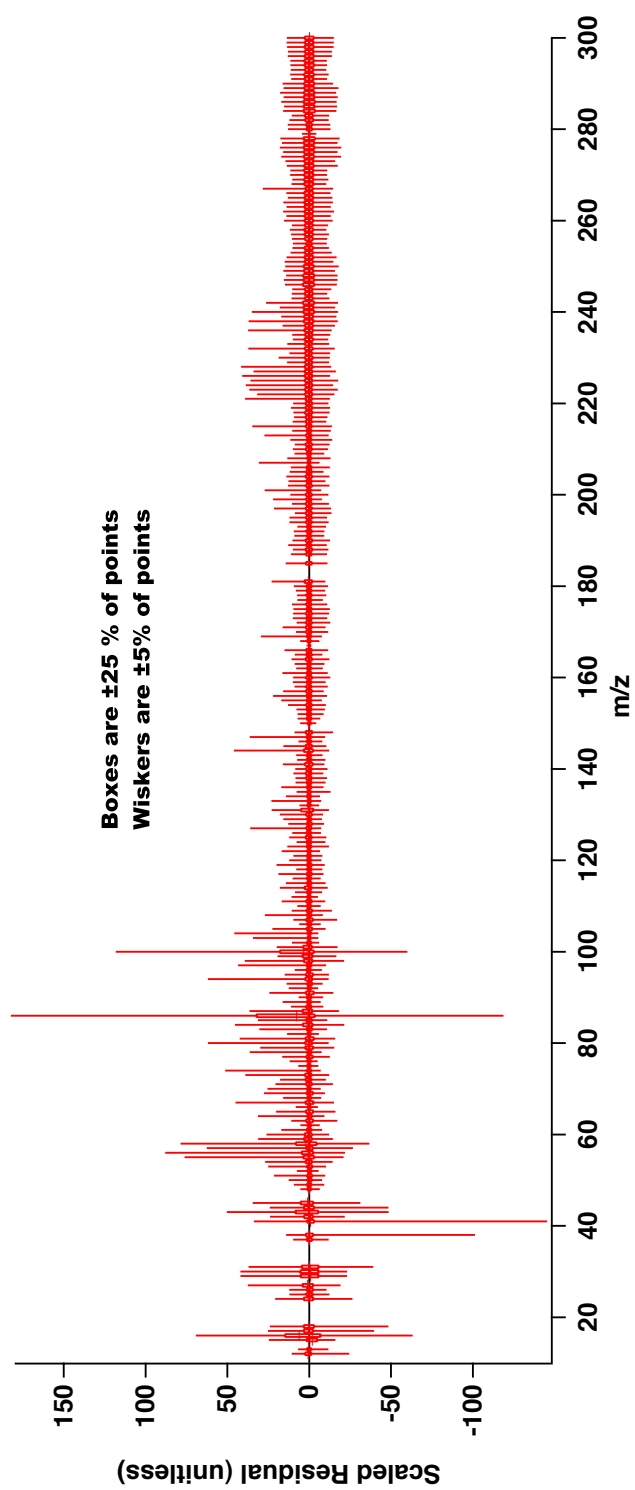


Figure 4.16: Scaled residuals for the 3 factor solution. (seed = 6).

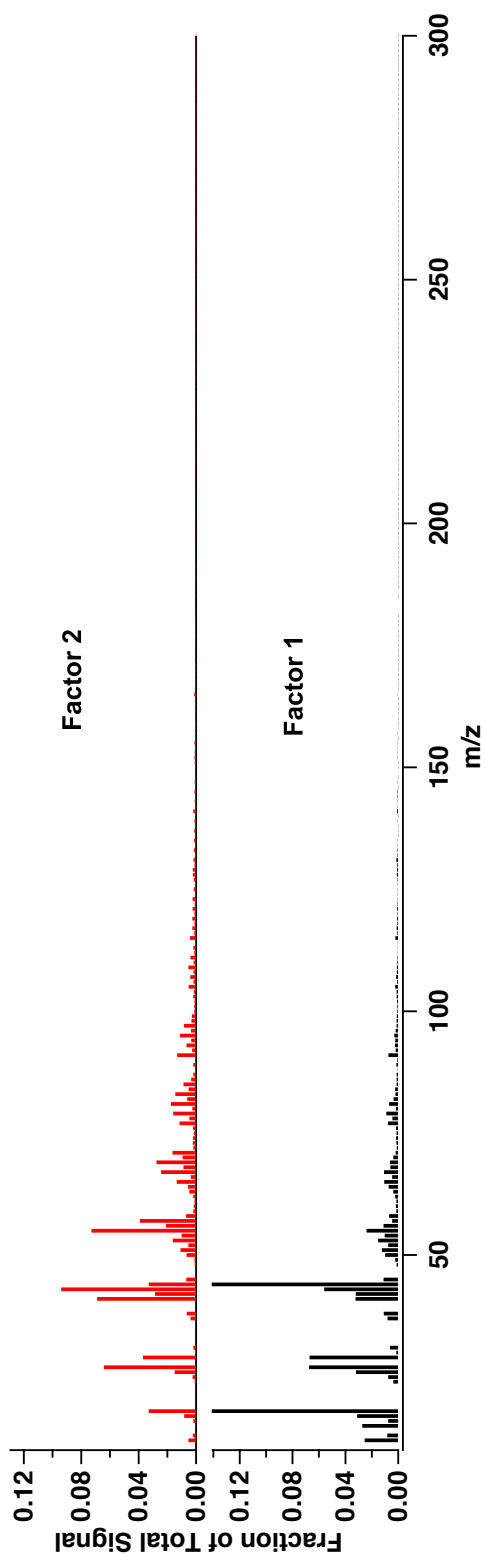


Figure 4.17: Mass spectral profiles for the 2 factor solution.

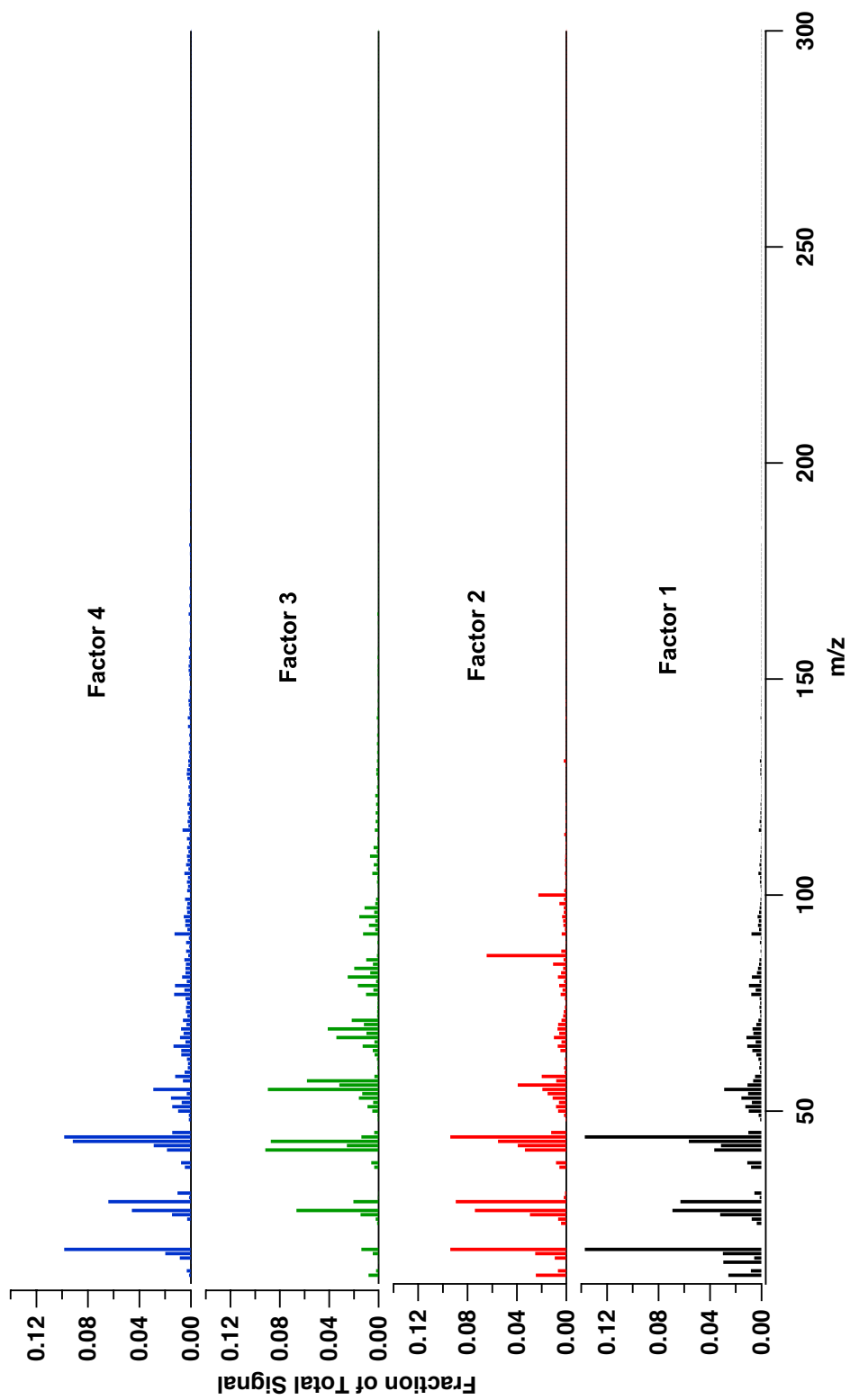


Figure 4.18: Mass spectral profiles for the 4 factor solution.

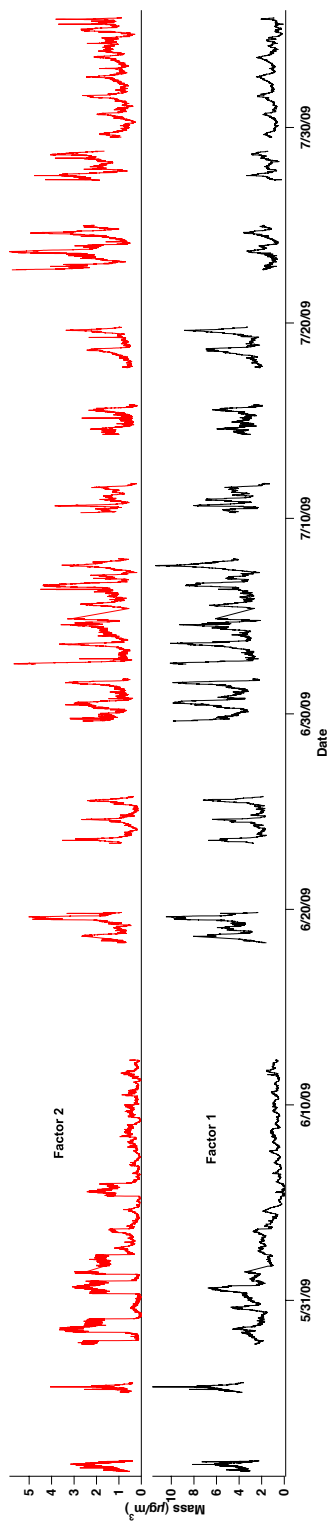


Figure 4.19: Time series contributions for the 2-factor solution.

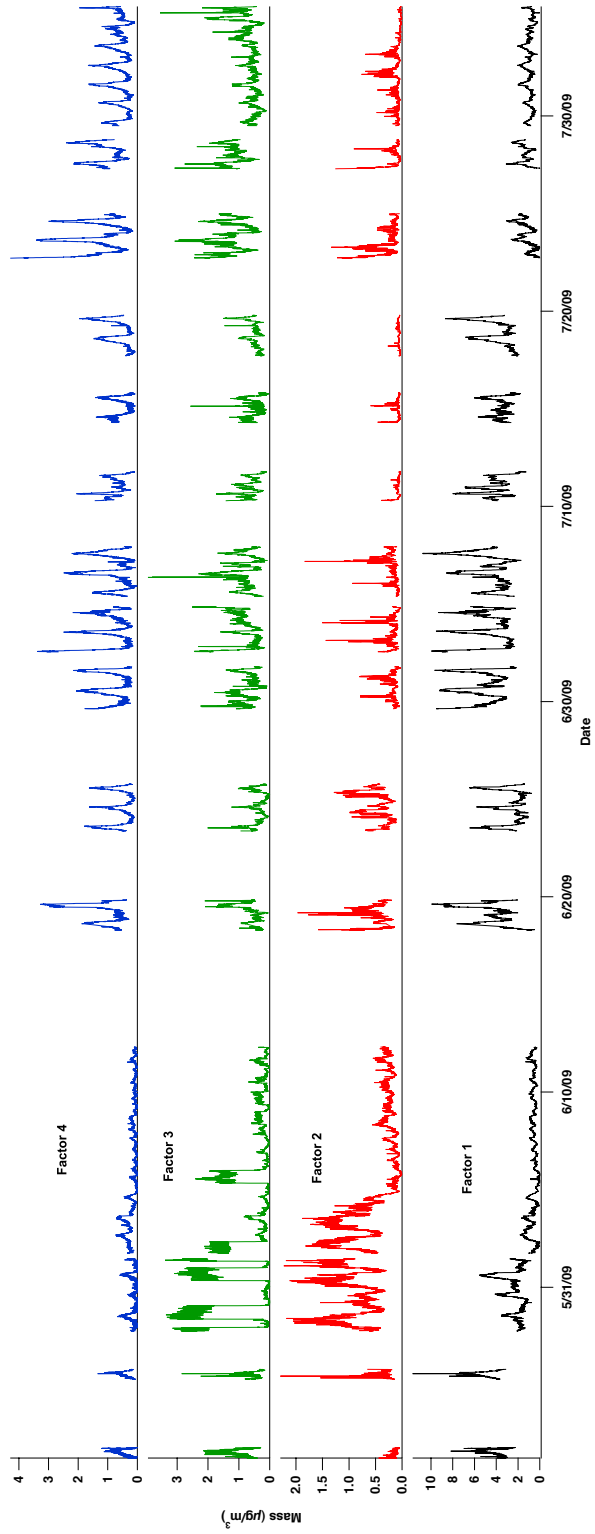


Figure 4.20: Time series contributions for the 4-factor solution.

Table 4.4: Mass spectral comparison of several PMF solutions

		Mass Spectra Comparison																			
Factor Number (p)	Seed																	Factor 1	Factor 2	Factor 3	Factor 4
		Brushfire (4)	Manchester high CO low O3 (5)	Pittsburgh HOA (3)	Pittsburgh HOA(1)	Pittsburgh OOA I (3)	Pittsburgh OOA II (3)	Pittsburgh OOA (1)	Urban Vancouver high O3 (5)	Urban Vancouver low O3 (5)	Zurich Summer HOA (2)	Zurich Summer OOA I (2)	Zurich Summer OOA II (2)	Zurich Summer Wood burning (2)	Zurich Winter HOA (2)	Zurich Winter OOA (2)	Zurich Winter Wood burning (2)				
1	1	0.96	0.68	0.68	0.51	0.97	0.85	0.97	0.99	0.77	0.44	0.95	0.58	0.64	0.66	0.97	0.81				
1	1	0.94	0.55	0.54	0.35	0.98	0.80	0.98	0.96	0.65	0.30	0.98	0.47	0.62	0.50	0.98	0.76		0.64		
2	1	0.77	0.94	0.97	0.91	0.67	0.78	0.66	0.78	0.96	0.78	0.57	0.76	0.51	0.90	0.61	0.73	0.64			
1	1	0.92	0.50	0.49	0.29	0.98	0.77	0.98	0.94	0.60	0.25	0.98	0.44	0.61	0.42	0.98	0.74		0.56	0.56	
2	1	0.74	0.91	0.95	0.88	0.63	0.73	0.62	0.74	0.93	0.76	0.53	0.71	0.51	0.88	0.56	0.69	0.56		0.94	
3	1	0.74	0.95	0.97	0.93	0.63	0.79	0.63	0.76	0.97	0.79	0.54	0.75	0.48	0.92	0.58	0.70	0.56	0.94		
1	4	0.93	0.66	0.66	0.49	0.93	0.79	0.93	0.93	0.73	0.42	0.89	0.56	0.64	0.55	0.92	0.81		0.92	0.57	
2	4	0.92	0.51	0.50	0.30	0.98	0.78	0.98	0.95	0.61	0.26	0.99	0.45	0.61	0.44	0.98	0.74	0.92		0.39	
3	4	0.59	0.93	0.97	0.96	0.46	0.67	0.45	0.61	0.93	0.83	0.35	0.72	0.39	0.95	0.38	0.58	0.57	0.39		
1	6	0.93	0.52	0.51	0.32	0.98	0.78	0.98	0.95	0.62	0.27	0.98	0.46	0.62	0.45	0.98	0.75		0.41	0.90	
2	6	0.61	0.92	0.96	0.95	0.47	0.65	0.46	0.60	0.92	0.81	0.35	0.71	0.43	0.93	0.39	0.60	0.41		0.73	
3	6	0.94	0.81	0.82	0.68	0.92	0.89	0.92	0.97	0.89	0.58	0.88	0.67	0.62	0.80	0.91	0.82	0.90	0.73		
1	1	0.94	0.57	0.56	0.37	0.98	0.81	0.98	0.97	0.67	0.32	0.98	0.49	0.63	0.54	0.98	0.76		0.89	0.49	0.93
2	1	0.90	0.60	0.59	0.43	0.89	0.74	0.89	0.87	0.66	0.37	0.84	0.54	0.65	0.43	0.87	0.80	0.89		0.53	0.86
3	1	0.61	0.92	0.96	0.94	0.48	0.67	0.48	0.63	0.93	0.81	0.38	0.68	0.41	0.94	0.41	0.58	0.49	0.53		0.56
4	1	0.93	0.69	0.66	0.51	0.95	0.86	0.94	0.96	0.75	0.46	0.92	0.62	0.58	0.60	0.95	0.82	0.93	0.86	0.56	
1	4	0.90	0.60	0.59	0.43	0.89	0.74	0.89	0.87	0.66	0.37	0.85	0.54	0.65	0.43	0.88	0.80		0.89	0.53	0.87
2	4	0.94	0.57	0.56	0.37	0.98	0.81	0.98	0.97	0.67	0.32	0.98	0.49	0.63	0.54	0.98	0.76	0.89		0.49	0.93
3	4	0.61	0.92	0.96	0.94	0.48	0.67	0.48	0.63	0.93	0.81	0.38	0.68	0.41	0.94	0.41	0.58	0.53	0.49		0.56
4	4	0.93	0.69	0.66	0.51	0.95	0.87	0.94	0.96	0.76	0.46	0.92	0.63	0.58	0.60	0.95	0.82	0.87	0.93	0.56	

References

- Zhang, Q., et al. ES&T 2005, 39, 4938-4952.
- Lanz, V. A., et al., Atmos. Chem. Phys. 2007, 7, 1503-1522.
- Ulbrich, I.M., et al., Atmos. Chem. and Phys. 2009, 9, 2891-2918.
- Bahreini, R. et al. ES&T 2005, 39, pgs.5674-5688
- Alfarra, R., et al. Atmos. Env. 2004, 38, 5745-5758.

Table 4.5: Time series comparison of several PMF solutions

Factor Number (p)		Gas Phase Tracers			AMS Inorganic Tracers						PILS Tracers						
Seed		Ozone	CO	NOx	SO4	NO3	NH4	ChI	WSOC	org57	NH4	NO3	SO4	Factor 1	Factor 2	Factor 3	Factor 4
1	1	0.51	0.38	0.24	0.66	0.45	0.63	0.35	0.58	0.79	0.70	0.67	0.76				
1	1	0.46	0.33	0.14	0.73	0.45	0.64	0.43	0.53	0.54	0.74	0.69	0.79		0.51		
2	1	0.41	0.34	0.30	0.37	0.31	0.44	0.12	0.30	0.91	0.56	0.56	0.63	0.51			
1	1	0.47	0.33	0.16	0.71	0.44	0.63	0.42	0.56	0.53	0.73	0.68	0.79		-0.02	0.73	
2	1	-0.06	0.15	-0.03	0.23	0.18	0.24	0.06	-0.39	0.61	0.22	0.22	0.20	-0.02		0.00	
3	1	0.51	0.34	0.30	0.43	0.32	0.47	0.18	0.50	0.77	0.60	0.59	0.67	0.73	0.00		
1	4	0.07	0.12	-0.14	0.22	0.29	0.30	0.02	-0.19	0.22	0.10	0.25	0.14		-0.19	-0.02	
2	4	0.47	0.32	0.19	0.66	0.39	0.58	0.40	0.58	0.54	0.71	0.66	0.77	-0.19		0.64	
3	4	0.42	0.35	0.30	0.42	0.31	0.45	0.15	0.36	0.93	0.59	0.58	0.65	-0.02	0.64		
1	6	0.39	0.31	0.09	0.75	0.46	0.65	0.46	0.47	0.49	0.76	0.73	0.81		0.05	0.60	
2	6	0.39	0.17	0.04	0.18	0.15	0.21	0.02	-0.29	0.70	0.16	0.17	0.14	0.05		-0.08	
3	6	0.53	0.31	0.28	0.42	0.31	0.45	0.19	0.56	0.62	0.60	0.58	0.67	0.60	-0.08		
1	1	0.43	0.30	0.15	0.71	0.39	0.58	0.43	0.53	0.52	0.73	0.66	0.79		-0.14	0.26	0.56
2	1	0.01	0.15	-0.07	0.16	0.29	0.26	0.01	-0.22	0.07	0.03	0.20	0.04	-0.14		0.06	-0.18
3	1	0.24	0.29	0.22	0.28	0.19	0.30	0.04	0.16	0.94	0.43	0.43	0.46	0.26	0.06		0.44
4	1	0.51	0.28	0.27	0.31	0.34	0.44	0.13	0.39	0.58	0.57	0.58	0.66	0.56	-0.18	0.44	
1	4	0.01	0.15	-0.07	0.16	0.29	0.26	0.01	-0.23	0.07	0.02	0.20	0.04		-0.15	0.06	-0.18
2	4	0.43	0.30	0.15	0.70	0.39	0.58	0.43	0.54	0.52	0.73	0.66	0.79	-0.15		0.26	0.56
3	4	0.24	0.29	0.22	0.27	0.19	0.30	0.04	0.16	0.94	0.43	0.43	0.46	0.06	0.26		0.43
4	4	0.51	0.28	0.27	0.31	0.34	0.44	0.13	0.39	0.58	0.57	0.58	0.66	-0.18	0.56	0.43	

Chapter 5

Impact of a large wildfire on water-soluble organic aerosol in a major urban area: the 2009 Station Fire in Los Angeles County*

*Reproduced with permission from “Impact of a large wildfire on water-soluble organic aerosol in a major urban area: the 2009 Station Fire in Los Angeles County” by A. Wonaschütz, S.P. Hersey, A. Sorooshian, J.S. Craven, A. R. Metcalf, R.C. Flagan, and J.H. Seinfeld, *Atmospheric Chemistry and Physics Discussions*, 11, 12849–12887, doi:10.5194/acpd-11-5867-2011, 2011. Copyright 2011 by the authors.

5.1 Abstract

Water-soluble organic carbon is a major component of aerosol particles globally. This study examines a field dataset of water-soluble organic aerosol in the Los Angeles Basin, a classic urban setting, under typical conditions and under the influence of a large wildfire (the 2009 Station Fire). The measurements took place between July and September in Pasadena as part of the 2009 Pasadena Aerosol Characterization Observatory (PACO) field campaign. Large differences in the nature of water-soluble organic carbon (WSOC) were observed between periods with and without the influence of the fire. During non-fire periods, WSOC variability was driven most likely by a combination of photochemical production processes and subsequent sea breeze transport, resulting in an average diurnal cycle with a maximum at 15:00 LT (up to $4.9 \mu\text{g C m}^{-3}$). During the Station Fire, smoke plumes advected to the site in the morning hours were characterized by high concentrations of WSOC (up to $41 \mu\text{g C m}^{-3}$) in tight correlation with nitrate and chloride, and with Aerodyne Aerosol Mass Spectrometer (AMS) organic metrics such as the biomass burning tracer m/z 60, and total non-refractory organic mass. These concentrations and correlations and the proximity of the measurement site to the fire suggest that primary production was a key formation mechanism for WSOC. During the afternoons, the sea breeze transported urban pollution and processed residual smoke back to the measurement site, leading to higher afternoon WSOC levels than on non-fire days. Parameters representing higher degrees of oxidation of organics, including the ratios m/z 44 : m/z 57 and m/z 44 : m/z 43, were increased in those air masses. Intercomparisons of relative amounts of WSOC, AMS organic, m/z 44, and m/z 43 are used to examine how the relative abundance of different classes of WSOC species changed as a result of photochemical aging. The fraction of WSOC comprised of acid-oxygenates increased as a function of photochemical aging owing to the conversion of aliphatic and non-acid oxygenated organics to more acid-like organics. Assuming a factor of 1.8 to convert WSOC concentrations to organic mass-equivalent concentrations, the contribution of water-soluble organic species to the organic mass budget (10th–90th percentile values) ranged between 27–72% and 27–68% during fire and non-fire periods, respectively. Therefore, WSOC is a significant contributor to the organic aerosol budget in this urban area. The influence of fires in this basin

greatly enhances the importance of this class of organics, which has implications for the radiative and hygroscopic properties of the regional aerosol.

5.2 Introduction

Globally, roughly one half of atmospheric aerosol mass is organic, a fraction which can be even higher in urban areas. Typically between 40–85% of organic carbon measured in different locations worldwide has been shown to be water-soluble (Ruellan et al., 1999; Graham et al., 2002; Mayol-Bracero et al., 2002; Gao et al., 2003; Jaffrezo et al., 2005; Decesari et al., 2006). Water-soluble organic carbon (WSOC) species are emitted as primary particles, especially during biomass combustion, and produced as a result of reactions in the gas and aqueous phases (Miyazaki et al., 2006; Sullivan et al., 2006; Kondo et al., 2007; Weber et al., 2007; Ervens et al., 2010; Sorooshian et al., 2010; Timonen et al., 2010). Moreover, WSOC has been suggested as a marker for secondary organic aerosol (SOA) in the absence of biomass burning (e.g., Docherty et al., 2008).

The Los Angeles Basin has been the subject of many studies examining the transport and chemical evolution of atmospheric aerosols. Pasadena, the setting of this work, represents an area where particulate pollutant concentrations are governed by meteorology and numerous production and transport processes. The meteorology in the basin is characterized by early morning inversions, which, through increasing surface heating over the course of the morning, give way to a robust midday-afternoon sea breeze. Elevated pollution layers can form by horizontal and vertical displacement of the morning inversion layer and orographic uplift (Lu and Turco, 1995), allowing for aerosol processing in air masses separated from surface pollution sources during the day. These pollution layers can remain aloft during the night and re-entrain the next day through turbulent mixing in a deepening boundary layer, contributing to surface concentrations of aerosols (Husar et al., 1977; Blumenthal et al., 1978).

Organic compounds are a major constituent of the local pollution and are emitted directly as well as produced via secondary processes. Hughes et al. (2000) found increasing relative contributions of organic compounds to increasing mass concentrations of total suspended particulates and fine

particles due to chemical processing along a sea breeze trajectory in the Los Angeles Basin. More recent measurements in the area during a normal summertime period showed that SOA is a major contributor to organic aerosol (Docherty et al., 2008), of which WSOC is an important component (Peltier et al., 2007). Owing to transport processes and spatial gradients in the oxidative capacity of the atmosphere, SOA is expected to contribute more to organic aerosol concentrations at inland areas than at the pollution source regions at the western side of the basin near the coast (Lu and Turco, 1995; Vutukuru et al., 2006).

In the late summer to fall months (August–November), following hot and dry summers, wildfires can be an additional component of the organic aerosol budget in the Los Angeles Basin (Phuleria et al., 2005). The Station Fire, which began on 26 August 2009 in the Angeles National Forest and came as close as 10 km to the PACO field site, was the tenth largest wildfire in modern California history and the largest ever in Los Angeles County, burning an area of more than 600 km² (California Department of Forestry and Fire Protection; http://bof.fire.ca.gov/incidents/incidents_archived). The impact of wildfires on urban aerosol physicochemical properties has been examined in other locations (Lee et al., 2008) but detailed aerosol studies examining the superposition of biomass burning emissions and typical Los Angeles atmospheric conditions are limited. The issue is especially of interest as wildfires in the Southwestern United States have been shown to have become more frequent and longer in duration compared to only a few decades ago and are expected to be a major concern in a future drier and warmer climate (Westerling et al., 2006).

An opportunity to study the nature of WSOC in the Los Angeles Basin in both the presence and absence of a major fire presented itself during the 2009 Pasadena Aerosol Characterization Observatory (PACO) field campaign. The overall campaign is described in detail by Hersey et al. (2011). Here we report an analysis of the nature of particulate WSOC in Pasadena in a three-month period with an aim towards characterizing temporal concentrations, relative relationships with other organic aerosol metrics, sensitivity to meteorology and transport, and impact of the Station Fire. This work also provides a valuable database for comparison with subsequent field datasets collected from the surface and airborne platforms during the 2010 CalNex field campaign

(<http://www.esrl.noaa.gov/csd/calnex/>).

5.3 Methods

5.3.1 Data

During the PACO field study (May–September 2009), ground-based measurements were conducted on the roof of the Keck Building on the campus of the California Institute of Technology (Caltech). The focus of this work is the period from 6 July 2009 to 16 September 2009. WSOC was measured in PM_{2.5} every six minutes with a particle-into-liquid sampler (PILS; Brechtel Mfg. Inc.) coupled to a total organic carbon (TOC) analyzer (Sievers Model 800 Turbo, Boulder, CO). The instrument design and operational details are discussed extensively elsewhere (Sullivan et al., 2006). Briefly, particles smaller than 2.5 μm in diameter are sampled by the PILS and passed immediately through an organic carbon denuder (Sunset Laboratory Inc.) to remove organic vapors. Particles are then grown into droplets, which are collected by inertial impaction, and transported through a 0.5 μm PEEK (polyetheretherketone) liquid filter prior to entering a TOC analyzer for quantification of WSOC. A constant dilution factor of 1.15 is applied to account for dilution of the PILS liquid wash flow to the TOC analyzer owing to collected drops and condensation on the PILS droplet impactor. The reported WSOC levels are the difference between the measured and background concentrations. The overall measurement uncertainty is estimated to be approximately 10%.

Inorganic and non-refractory organic sub-micrometer aerosol measurements were carried out with an Aerodyne Compact Time of Flight Aerosol Mass Spectrometer (C-ToF-AMS) (Drewnick et al., 2005; Murphy et al., 2009) for the non-fire portion of the study and a High-Resolution AMS (HR-AMS) during the Station Fire. AMS data used here include organic markers at specific mass-to-charge ratios (m/z) that serve as proxies for organics with a range of oxidation states: acid-like oxygenated organics (m/z 44 = COO^+), aliphatic and non-acid oxygenated organics (m/z 43 = C_3H_7^+ and $\text{C}_2\text{H}_3\text{O}^+$; m/z 55 = $\text{C}_3\text{H}_3\text{O}^+$), aliphatic organics (m/z 57 = C_4H_9^+), and a biomass burning tracer (m/z 60) (McLafferty and Turecek, 1993; Zhang et al., 2005; Aiken et al., 2008; Ng et al.,

2010; Alfarra et al., 2007). The PILS and AMS chemical measurements were time synchronized, accounting for sampling time delays in the PILS relative to the AMS (Sorooshian et al., 2006). The PILS sampled sub-2.5 μm particles while the AMS measured sub-micrometer particles; therefore, ratios of WSOC to AMS data represent an upper limit.

Particle size distribution measurements were carried out with a cylindrical scanning differential mobility analyzer (DMA; TSI Model 3081) coupled to a condensation particle counter (TSI Model 3760). Thirty-two days of hourly CO, O₃ and PM_{2.5} measurements were obtained from ground sites in Pasadena (South Wilson Avenue), Upland, Burbank, and downtown Los Angeles (North Main Street) (<http://www.arb.ca.gov>) and are used to help interpret the WSOC data. Additional hourly meteorological data were obtained from the Mesowest database (<http://mesowest.utah.edu/index.html>). The stations used include the South Wilson Avenue station on the Caltech campus, the North Main Street station near downtown Los Angeles (~ 12.5 km southwest of measurement site), and the Santa Fe Dam station ~ 15 km east of the measurement site.

5.3.2 Fire Development and Influence on the Measurement Site

The Station Fire burned over several weeks. Its spatial extent and exact location, and thus the influence it exerted on the measurement site, changed over that time period. Figure 5.1 shows the progression of the fire over several days. The fire area was estimated from Moderate Resolution Imaging Spectroradiometer (MODIS) fire maps (<http://firefly.geog.umd.edu/firemap/>). The fire started on 26 August less than 10 km north of the sampling site and grew in areal extent over the next four days. It split into an eastern and a western part on 31 August. The western part quickly decreased in size while moving northward, was reduced to a relatively small remnant ~ 25 km northwest of the site by 2 September, and became unidentifiable by MODIS by 4 September. The eastern part remained sizeable, but moved farther eastward. Notable easterly wind patterns did not occur during the measurement period, making the eastern part of the fire an unlikely direct influence on the measurement site.

The dataset was split into a “fire period” and a “non-fire period” by examining the MODIS fire

maps and using the AMS m/z 60 concentration as a tracer for biomass burning. The “fire period”, consisting of the eight days between 26 August and 2 September, was marked by frequent high spikes in the measured m/z 60 concentration, reaching values up to $1.4 \mu\text{g m}^{-3}$. The mean m/z 60 concentration over the fire period was $0.065 \pm 0.122 \mu\text{g m}^{-3}$. During the remaining measurement days (“non-fire period”) the mean m/z 60 concentration was $0.013 \pm 0.005 \mu\text{g m}^{-3}$. While m/z 60 (and levoglucosan) have been shown to decay with exposure to the hydroxyl radical (Hennigan et al., 2010), the systematically higher levels of this mass spectral marker during the Station Fire make it a robust tool to identify periods with fire influence. CO similarly exhibited contrasting behavior during non-fire and fire periods, with mean concentrations of $0.13 \pm 0.12 \text{ ppm}_v$ and $0.45 \pm 0.50 \text{ ppm}_v$, respectively.

5.4 Results and Discussion

5.4.1 PACO Study Background

Hersey et al. (2011) provide a comprehensive summary of the physical and chemical properties of aerosols sampled at the PACO measurement site over the time period between 10 July and 4 August, which overlaps with the beginning of the period examined in this work. We briefly describe results from that study that are relevant to the interpretation of WSOC measurements during non-fire periods. Organic mass accounted for approximately 55% of the submicrometer AMS aerosol mass. Average organic carbon (OC) concentrations were greater by approximately 4% in the afternoons (15:00–19:00 LT) than in the mornings (07:00–11:00 LT). Conversely, elemental carbon (EC) decreased by approximately 22% from the mornings to the afternoons. Both trends lead to a much increased afternoon OC:EC ratio. It was concluded that production of primary organic carbon was relatively more important in the mornings while secondary production of organic carbon was more dominant in the afternoons. Size-resolved measurements showed that the afternoon submicrometer organic mass was bimodal with one modal vacuum aerodynamic diameter centered around 100–200 nm and another around 500–600 nm. Positive matrix factorization analysis showed

that low-volatility and semi-volatile oxidized organic aerosol (LV-OOA and SV-OOA) accounted for 86% of organic aerosol, suggestive of a large contribution by an oxidized organic fraction. The following sections will examine the nature and character of the WSOC fraction of the aerosol, which coincides with this highly oxidized organic fraction.

5.4.2 Meteorological Setting and Origin of Air Masses

Weather conditions were warm and dry during the entire WSOC measurement period (Fig. 5.2). Ambient temperatures ranged from 15° to ~ 40 °C. Relative humidity (RH) usually dropped below 40% during the day but reached 100% in the early morning hours of many days. Temperatures averaged several degrees higher during the Station Fire period, while RH was around 20% lower, helping to sustain the duration and spread of the fire. Air mass back-trajectories calculated with the NOAA HYSPLIT model (Draxler and Rolph, 2003) showed that sampled air masses were generally of marine origin with brief continental exposure prior to reaching the sampling site.

As the western edge of the Los Angeles Basin is major source region for pollutants (Lu and Turco, 1995), it is important to identify dominant wind patterns and transport times to Pasadena. Figure 5.3 shows the local wind characteristics at South Wilson Avenue/Caltech Campus and at several surrounding stations. The most common wind directions at all stations are southerly to westerly, a manifestation of the sea breeze. The diurnal development of wind at South Wilson Avenue starts with very calm air at night and in the early mornings. During the late morning hours the wind tends to turn clockwise from the NE through S to the predominant afternoon sea breeze direction from the SW. Wind speeds increase during the development of the sea breeze in the afternoons. Initially stagnant air in the early morning is therefore, over the course of the late morning, expected to be influenced by air masses from more polluted urban areas and ultimately replaced by air masses of largely marine origin with anthropogenic influence, carrying particles with a mix of fresh and aged components. In the mornings, the air is expected to be more influenced by local sources, as well as by accumulated residual pollution from the previous day. The South Wilson Avenue Station measures systematically lower wind speeds than the surrounding stations,

which is likely a localized effect caused by buildings and trees in the immediate surroundings of the site. Wind speeds measured at that site are therefore assumed to represent a lower limit of the areal wind speed. A statistical analysis of wind speeds and directions between 13:00–18:00 LT showed that the most common wind speeds were 4.5 ms^{-1} at North Main Street and 1.3 ms^{-1} at South Wilson Avenue. The most common wind directions were 270° and 225° , respectively. The afternoon transport time of urban pollution from downtown Los Angeles to Pasadena is thus on the order of 1–2 h (13:00–18:00 LT), consistent with the estimate by Hersey et al. (2011) for the period between May and August 2009. Given the most common afternoon wind speed at North Main Street, the transport time of anthropogenically influenced marine air from the coast to Pasadena from a southwesterly direction is approximately two hours.

5.4.3 WSOC Production Pathways and Relationship with Ozone

Identifying the relative importance of primary and secondary production mechanisms of WSOC is difficult given diurnal complexities in aerosol and precursor emissions, transport patterns and dynamic vertical structure of the boundary layer in the basin (Blumenthal et al., 1978; Vutukuru et al., 2006). WSOC concentrations measured on non-fire days may be governed by all or a subset of the following mechanisms: 1. local primary production of WSOC; 2. local secondary production; 3. advection of existing WSOC that was either primarily or secondarily produced; 4. advection of precursor VOCs, with WSOC production occurring during transport; 5. volatilization and subsequent oxidation into SOA of semivolatile primary organic aerosol (POA) (Robinson et al., 2007); and 6. re-entrainment of pollution layers aloft. The Station Fire adds another level of complexity as additional sources of WSOC include direct emission of WSOC and secondary production from precursors emitted in the fire.

Previous work in the study region has shown that the temporal behavior of organic aerosol is closely related to that of O_3 , indicative of photochemical production of SOA (Hersey et al., 2011). In Pasadena, WSOC peaks after O_3 on 16 out of 20 examined days with a typical time lag of 1.5–2.5 h. WSOC peaks occurred simultaneously or slightly before O_3 peaks (0.5 h) on 3 days, and only on one

day did the WSOC peak precede an unusually late O₃ peak by hours. This points to a strong link between overall WSOC concentrations and photochemical processes.

The variability of O₃ concentrations at different ground sites in the Los Angeles basin provides insight into the spatiotemporal behavior of photochemical processes and the photochemical potential at the Pasadena site. O₃ concentrations measured at ground stations in Pasadena (South Wilson Avenue), Burbank, Upland and downtown Los Angeles (North Main Street) were examined for a period of 24 days in July (a subset of those days is shown in Fig. 5.7). In the prevailing sea breeze regime, transport of precursors from downtown Los Angeles (a classic pollutant source location) is expected to influence O₃ concentrations at the measurement site. On 10 out of the examined 24 non-fire days, O₃ peaked in downtown Los Angeles approximately an hour before it did in Pasadena, consistent with the transport times of 1–2 h given most common mid-afternoon (13:00 to 16:00 LT) wind speeds of 1.3 m s⁻¹ in Pasadena and 3.6 m s⁻¹ at downtown Los Angeles. Peak O₃ concentrations in Pasadena were consistently higher (22 out of 24 days) than in downtown Los Angeles, owing to additional time for photochemical processing of O₃ precursors in addition to the expected advection of O₃ itself from upwind locations. The farther downwind site of Upland is characterized by even higher and more delayed O₃ peaks. This observed spatial O₃ behavior and its implications for SOA production are consistent with the findings of Vutukuru et al. (2006) who showed that SOA levels in the basin are higher at inland (e.g., Azusa, Riverside) than at coastal sites. However, on six days (two of which are discussed in the case study below) O₃ reached peak concentrations in Pasadena before it did so in downtown Los Angeles (an average of 1.5 h earlier) and on six other days (one of which is discussed in the case study below), it peaked within the same hour as in downtown Los Angeles. These days were not associated with unusual wind directions or increased wind speeds. Local sources, downward mixing of elevated pollution layers from previous days in a deepening mixed layer, and/or unusually vigorous photochemical activity (as described by Hersey et al., 2011) could explain these “early” O₃ peaks. Therefore, advection of oxidants from downtown Los Angeles on any given day is not necessarily a requirement for photochemical activity in Pasadena.

5.4.4 Cumulative WSOC Statistics

During the non-fire period, the highest WSOC concentration measured was $4.9 \mu\text{g C m}^{-3}$. The observed concentration range is consistent with that of independent measurements in other urban areas (Jaffrezo et al., 2005; Sullivan et al., 2004, 2006; Kondo et al., 2007), including those in nearby Riverside during the summer of 2005 (Peltier et al., 2007). WSOC exhibits a weak correlation with solar radiation ($r^2 = 0.28$) and somewhat higher correlations with O_3 ($r^2 = 0.35$) and T ($r^2 = 0.44$) (Table 5.1). The low correlations with meteorological parameters are likely due to the complexity of the processes governing WSOC levels in Pasadena, including diverse sources, and the superposition of secondary formation and transport processes. The highest correlations between WSOC and AMS aerosol components were found for the following organic markers: m/z 43 ($r^2 = 0.49$), total AMS organic mass ($r^2 = 0.47$), and m/z 55 and 60 ($r^2 = 0.45$). Although m/z 55 and m/z 43 are prominent components in traffic emissions, they are more related to oxygenated organics than the primary hydrocarbon-like organic aerosol (HOA) marker m/z 57 (e.g., Zhang et al., 2005); for example, they are less correlated with NO_x and CO. As a result, the correlation of WSOC with m/z 57 ($r^2 = 0.20$) is the lowest among the correlations with AMS organic markers. WSOC exhibits little to no correlation with the inorganic compounds nitrate (NO_3^-), sulfate (SO_4^{2-}), chloride (Cl^-), and ammonium (NH_4^+) ($r^2 \leq 0.08$).

During the fire period, the range of measured WSOC levels ($0.8\text{--}40.6 \mu\text{g C m}^{-3}$) was consistent with that observed in other measurements with major biomass burning influences: $11\text{--}46 \mu\text{g C m}^{-3}$ (Mayol-Bracero et al., 2002), $2.2\text{--}39.6 \mu\text{g C m}^{-3}$ (Graham et al., 2002), $4.4\text{--}52.6 \mu\text{g C m}^{-3}$ (Decesari et al., 2006), and $0.57\text{--}18.45 \mu\text{g C m}^{-3}$ (Sullivan et al., 2006). The highest WSOC concentration, $40.6 \mu\text{g C m}^{-3}$, was measured in the morning of 30 August. WSOC correlations (r^2) with most organic metrics (i.e. total AMS organic mass and m/z 44, 60, 43, and 55, but not m/z 57) ranged between 0.80 and 0.92 (cf. 0.35 and 0.49 during non-fire periods). The systematically higher correlations during the fire period indicate that there likely was a single dominating factor governing the variability of both organic and WSOC levels; since WSOC was highly correlated with m/z 60 ($r^2 = 0.90$), fire emissions were clearly influential. A high correlation between WSOC and NO_3^- was

observed ($r^2 = 0.79$), followed by WSOC and Cl^- ($r^2 = 0.57$), but correlations with NH_4^+ and SO_4^{2-} ($r^2 \leq 0.18$) were poor. Fresh biomass burning emissions consist mainly of organic carbonaceous components and have been reported to have only minor contributions from inorganic species (Reid et al., 2005; Fuzzi et al., 2007; Grieshop et al., 2009); however, enhanced NO_3^- concentrations have been observed in smoke plumes (Gao et al., 2003; Reid et al., 2005; Peltier et al., 2007). Potassium chloride is also thought to be a common constituent in fire emissions (Posfai et al., 2003; Reid et al., 2005), which can explain the enhanced correlation of WSOC and Cl^- , providing additional support for a primary production mechanism. The correlation of WSOC with O_3 is absent during the fire period, even though O_3 concentrations are influenced by the fire (peak concentrations in the diurnal average of 91.5 ppb_v during the fire vs. 58.5 ppb_v for the non-fire diurnal average; Fig. 5.2). This also indicates that photochemical production is not the dominant process governing the large increases of WSOC concentrations during the fire.

During the fire period, the ratio of WSOC to organic mass ranged from 0.11 to 0.53 $\mu\text{g C}/\mu\text{g}$, with a 10th percentile of 0.15 and a 90th percentile of 0.40. After converting the 10th and 90th percentile values to an equivalent organic mass concentration using a factor of 1.8 (Docherty et al., 2008), water soluble organics are estimated to account for between 27% and 72% (with an average of $47 \pm 15\%$) of the organic mass. The WSOC : organic ratio range during the non-fire period is similar (10th/90th = 0.15/0.38), which after applying the 1.8 conversion factor to WSOC results in a 10th–90th percentile range of 27–68% (average = $45 \pm 16\%$).

5.4.5 Diurnal WSOC Behavior

During the non-fire period, the daytime diurnal average concentration of WSOC (Fig. 5.4) exhibits a maximum around 15:00 LT, coincident with maxima in AMS organic mass, m/z 44 and 43, but after O_3 (13:00) and solar radiation (14:00) (Fig. 5.2). Since wind direction itself has a pronounced diurnal cycle, the afternoon peak in WSOC can be plausibly explained by both photochemical production and/or transport from downtown Los Angeles via the afternoon sea breeze (a complication in explaining diurnal variability of pollutants noted specifically for Pasadena by Blumenthal et al.

(1978). The behavior of m/z 57 provides some insight: while it does show an increase starting at 06:00 and a local peak at 09:00, consistent with local rush hour traffic (confirmed with ground-based CO data, Fig. 5.8), its maximum concentration occurs at 13:00, when local primary emissions are expected to be lower than in the morning. Since all organic metrics including m/z 57 reach their highest concentrations with high temporal coincidence in the early afternoon, it is likely that transport from more polluted areas, specifically downtown Los Angeles, plays a major role. While the contribution of organics to total AMS mass increases from 06:00 to 15:00, WSOC:organic is relatively constant until it begins to increase at 14:00 (Fig. 5.5). The majority of the relative increase of WSOC to organics occurs between 14:00–19:30, during a decrease of total AMS mass, WSOC, and organic m/z markers shown (Fig. 5.4). The advancing sea breeze front is known to produce strong gradients in secondary pollutants (Lu and Turco, 1995). Thus, a likely scenario for the relative increase of WSOC during the decrease of absolute concentrations of most every organic marker is the superposition of secondary production of WSOC by photochemical processing and transport of cleaner and more aged marine air to the site. The ratio m/z 44:57 increases with WSOC:organic, indicative of an increasing oxidized fraction of the organic aerosol.

During the fire period, organics dominated the sub-micrometer aerosol mass, with significantly higher organic mass fractions than in the non-fire period (Fig. 5.5). The contribution of WSOC to organics was systematically elevated from the early morning hours through the late afternoon, with relatively stable and higher ratios between 04:00–12:00 compared to other times. WSOC concentrations peaked in the mornings. Average WSOC concentrations (Fig. 5.4) were higher by a factor of 10 than in the non-fire period at \sim 08:30. Lower wind speeds during the mornings promoted accumulation of smoke, and variable wind directions allowed for smoke from the burning areas to be advected to the sampling site and farther into the basin. The diurnal behavior of the biomass burning tracer m/z 60 matches that of WSOC (with the exception of a sharper decrease from 08:00 to 12:00), providing evidence for the presence of biomass burning aerosols at the measurement site when WSOC increased in concentration. In the afternoon, southwesterly winds directed smoke plumes away from the measurement site, leading to a decrease in measured WSOC concentrations.

The afternoon peak of diurnally-averaged WSOC at 15:00 that was evident during the non-fire period is barely visible given the high WSOC concentrations during earlier parts of the days; nonetheless, the diurnal average WSOC concentration at this time of day exceeds that of the non-fire period by a factor of 1.5. As organic precursors emitted in the fire were likely present in the entire Los Angeles basin after several days of burning, residual and processed smoke are thought to have played an additional role in the usual transport of pollutants by the afternoon sea breeze. The fire period exhibits an earlier rise and higher maximum of the diurnal average O₃ concentrations than the non-fire period, underlining the impact of the fire on the timing and magnitude of photochemical activity. There are large systematic increases in the m/z 44:43 and m/z 44:57 ratios between 09:00–15:00 during the fire (Fig. 5.5), at times when the absolute values of all organic measurements decreased after the major morning peaks (cf. Fig. 5.4). The larger absolute increases of these ratios in the fire compared to non-fire conditions points to a more vigorous conversion of organics towards a more oxidized state at a relatively stable WSOC:organic ratio.

5.4.6 Relationships Between WSOC, AMS Organic, m/z 44, and m/z 43

Since WSOC comprises both hydrophobic and hydrophilic fractions (e.g., Sullivan and Weber, 2006), it is of interest to examine the relative behavior of m/z 44, m/z 43, total AMS organic, and WSOC. Given that the fire constitutes a source of WSOC that is very different from those that are dominant during non-fire days, the chemical nature of the WSOC measured in the morning smoke-plumes is expected to differ from that measured in the afternoons. Morning-to-afternoon ratios (i.e. concentrations at 08:00 LT vs. 14:00 LT) of diurnally-averaged m/z 44, 43, 60, organic, and WSOC concentrations (shown in Fig. 5.4) are examined to explore these potential differences. The smallest morning-to-afternoon ratio for any of these organic metrics was for m/z 44 (1.9), followed by AMS organic (2.4), m/z 43 (2.7), and WSOC (3.3). The morning-to-afternoon ratio for m/z 60 was 9.6, confirming the much larger direct influence of the fire in the morning. Given the different morning-to-afternoon ratios of m/z 44 and 43, it is plausible that the afternoon WSOC contained constituents produced as a result of photochemical processing of smoke, with more of the non-acid

oxygenates having been converted to acid-like oxygenates.

Recent studies have utilized m/z 44 and m/z 43 (Ng et al., 2010; Chhabra et al., 2011) to track the aging of organic aerosols in the atmosphere. Hersey et al. (2011) conducted an analysis of f_{44} (m/z 44:total organic signal) vs. f_{43} (m/z 43:total organic signal) for Los Angeles aerosol, where higher levels of f_{44} relative to f_{43} are thought to indicate a greater degree of organic oxygenation and lower volatility. They observed a high level of consistency in the overall degree of oxidation of the aerosol over a span of several months between May and August of 2009. Ng et al. (2010) suggested an alternative way to conduct a similar type of analysis that can incorporate measurements from instruments other than the AMS (see their Fig. 5.5). They specifically used multiple field datasets to plot f_{44} and the O:C ratio vs. m/z 44:43 and observed that both f_{44} and the O:C ratio increase sharply at the beginning of oxidation and then plateau at larger m/z 44:43 ratios, suggesting the existence of a maximum oxidation state of the aerosol. Figure 5.6 examines the ratios of m/z 44:WSOC and WSOC:organic as functions of the m/z 44:43 ratio for both the fire- and non-fire period. The m/z 44:43 ratios range between 0.6–2.7 (non-fire period) and 1.1–3.1 (fire period). In the mentioned plot in Ng et al. (2010, Fig. 5.5), this is a range in which the O:C ratio and f_{44} are increasing rapidly prior to reaching a plateau. We first note that the product of the quantities displayed on the y -axes in Fig. 5.6 (m/z 44:WSOC \times WSOC:organic) is equivalent to f_{44} , which when examined as a function of m/z 44:43 qualitatively reproduces the curve shown in Ng et al. (2010). During both the fire-and non-fire period, the m/z 44:WSOC ratio grows as a function of m/z 44:43, indicating that the contribution of acid-like oxygenates to WSOC increases as the chemical functionality of the species contributing to m/z 44 and 43 move towards a more oxidized state. This is most clearly illustrated by the data representing the greatest influence by the smoke plume (larger symbols in Fig. 5.6). The early morning fire plumes advected to the measurement site exhibit relatively low values of m/z 44:43. The m/z 44:WSOC ratio increased gradually as a function of m/z 44:43 and time of day, suggesting that conditions associated with transitioning from morning to afternoon hours (higher temperatures, O₃, solar radiation, changing wind direction) promoted processing of organics to contain more oxidized organics and transport of these processed

species back to the sampling site. The WSOC : organic ratio is a less variable function of m/z 44 : 43 than the m/z 44 : WSOC ratio. This is because WSOC consists of species including those represented by m/z 44 and 43. Changes in the chemical functionality of m/z 44 and 43 are thus not necessarily expected to cause variability of WSOC : organic. WSOC : organic ratios most influenced by the fire plume (larger symbols in Fig. 5.6) have a relatively constant value across the observed range of m/z 44 : 43, suggesting that the more noticeable effect of photochemical processing during the day was to transform components of the WSOC into more oxidized forms rather than to produce more WSOC mass.

5.4.7 Case Studies

5.4.7.1 Non-Fire Period (7 July 2009–15 July 2009)

A period of five days between 7 July 2009 and 15 July 2009 is used to study the nature of WSOC during non-fire days more closely (Fig. 5.8). Ground station data for CO, O₃, and PM_{2.5} across the Los Angeles basin for this time period are shown in Fig. 5.7. WSOC concentrations always peaked between 13:00–14:00 LT and usually did so immediately after or simultaneously with O₃. The range of absolute WSOC concentrations was similar from day to day, but there were large differences in the temporal concentration profiles. CO levels were usually lower in Pasadena than at the other sites, indicative of a less pronounced influence of local traffic emissions.

On 7 July (Tuesday), the wind in Pasadena was low from the NW to NE until 10:00, and then increased gradually while turning to a southerly direction. The sea breeze was fully developed by noon. There was remarkable covariance between WSOC, AMS organic, numerous m/z markers (43, 44, 55, 57, 60), and the ratio of WSOC : total AMS mass. Their common behavior features a smooth morning increase followed by an equally smooth afternoon decrease. The WSOC concentration increased from 0.96 $\mu\text{g C m}^{-3}$ at 07:30 to 3.41 $\mu\text{g C m}^{-3}$ at 14:00 before gradually decreasing to 1.44 $\mu\text{g C m}^{-3}$ at 19:00. The ratio of WSOC : organic, which would be expected to increase during photochemical WSOC production, remained relatively stable through the entire day. Transport of pollution was a major factor in influencing the observed increase in WSOC concentration; however, this does not

preclude the possibility that the measured WSOC in Pasadena was secondarily produced upwind or during transport. Hersey et al. (2011) noted that semi-volatile OOA (SV-OOA) was well correlated with O_3 and associated with peaks in DMA number concentration, suggestive of early generation SOA products that are 1–2 h old. This is consistent with our observations on 7 July: a number of metrics for the degree of organic oxidation (e.g. m/z 44:43 and m/z 44:57) began to decrease starting around 11:00–12:00, while O_3 concentrations increased and the sea breeze advected fresh and processed organics to the measurement site. AMS inorganic species did not follow the behavior of the organic species. The afternoon increase in SO_4^{2-} coupled with the decrease of organics can be attributed to the increasing wind speed and influx of marine air.

The importance of wind direction is illustrated on 10 July 2009 (Friday) as WSOC sharply declined in concentration (from 2.05 to 0.48 $\mu\text{g C m}^{-3}$ between 11:40–13:20) and then increased to 3.93 $\mu\text{g C m}^{-3}$ between 14:00 and 16:00. This behavior is qualitatively reflected in all other parameters shown in Fig. 5.8 (with the exception of O_3) and is also visible in the size distribution data as a sudden decrease in both number and volume concentrations over all particle sizes (Fig. 5.9). In the time period of lower concentrations, the wind, previously from S to SE, shifted to a northeasterly direction at a speed of 1.3 m s^{-1} , carrying in a less polluted air mass with lower WSOC concentrations. O_3 concentrations were not impacted by the wind shift, but exhibited a typical smooth diurnal cycle consisting of a gradual increase up to a peak concentration at 14:00, followed by a decrease for the rest of the day. This mismatch between WSOC and O_3 concentration changes indicates that transport rather than local photochemical production dominated WSOC variability in the earlier part of this day. The wind shifted to a southwesterly direction between 14:00 and 16:00, leading to initially increasing WSOC levels and DMA number concentrations, which then decreased due to continuing sea breeze winds and a decrease in photooxidation corresponding to decreased intensity of solar radiation. Similar trends between WSOC and DMA size distribution data were observed on 11 July 2009.

During the last two days of this case study period (Tuesday and Wednesday; 14 and 15 July), the peak WSOC concentration did not lag as far behind maximum O_3 levels as on previous days. Fur-

thermore, on 15 July, WSOC concentrations began to increase in the afternoon before the sea breeze was fully established, indicating that local photochemical production may have played a somewhat more important role than on the other case study days. Later in the day, the advection of cleaner air by the sea breeze reduced concentrations of WSOC and AMS organic species. Thus, photochemical processes are important for overall WSOC production in the basin, but much of the measured variability of WSOC in Pasadena is dominated by transport effects.

5.4.7.2 Station Fire Period (27 August 2009–2 September 2009)

While diurnal average features of the fire days have been discussed, more details about day-to-day variability and daily features of aerosol parameters over a period of seven successive days are shown in Fig. 5.10, with associated basin-wide gas and PM_{2.5} ground station data shown in Fig. 5.7. The impact of the fire on the sampling site was variable, ranging from large increases of every measured quantity on 28, 30 and 31 August, to much lower impacts on 29 August and 1 September. In Fig. 5.10, the connection between wind and smoke influence on aerosol composition is clearly visible: using m/z 60 as a tracer for the smoke plume, it is evident that periods with low wind speeds and wind directions with a northerly component feature the highest smoke concentrations. The fact that measured concentrations of m/z 60 were higher in the morning hours than in the evenings (when wind speeds are equally low) may be due to the boundary layer being most shallow and stagnant conditions having persisted for a number of hours by the morning. On individual days, the dynamic development of the fire itself may play a role as well. Concentrations of m/z 60 decrease immediately as the wind direction shifts and the wind speed picks up in the developing sea breeze.

The ground station data (Fig. 5.7) reflect the impact of the fire on the entire Los Angeles basin: CO, a tracer for combustion processes, reaches its highest values on the mornings of 30 and 31 August, especially in Pasadena and Burbank which, of the four sites, were the closest to the fire. During the nine non-fire days, typical rush hour PM_{2.5} levels in downtown LA ranged from 30 to 50 $\mu\text{g m}^{-3}$, whereas on 30 and 31 August, they reached 149 and 73 $\mu\text{g m}^{-3}$, respectively, showing that the fire had a direct influence on locations farther south and southwest of Pasadena. Thus, even

when the afternoon sea breeze directed the smoke plume away from the site, it still transported aged smoke to the site. O_3 exhibited systematically higher levels at all four stations, especially on 30 and 31 August.

The mornings of 28, 30 and 31 August are particularly impacted by the accumulation of smoke. WSOC shows a very tight correlation with m/z 60, NO_3^- , and Cl^- during the smoke events. Most other organic metrics also vary in lockstep with WSOC with the notable exception of SO_4^{2-} , which exhibited a poor correlation with WSOC and lower levels in the diurnal average than on non-fire days. Reid et al. (2005) note that while SO_4^{2-} is a secondary product of biomass burning, its production requires high relative humidity, a requirement which was not met during the PACO fire period. Given this lack of liquid-phase SO_4^{2-} production, and the low relative humidity observed during the majority of the study period, it is unlikely that liquid-phase processes played a key role in WSOC production (e.g., Hennigan et al., 2008, 2009) during either the fire or the non-fire period. In the afternoons of 28, 30 and 31 August, the temporal behavior of WSOC, m/z 60, and AMS organic metric concentrations became less coordinated. While the developing sea breeze started to direct the smoke away from the site, the residual smoke was subject to photochemical processing, as indicated by the rise in m/z 44:57 and m/z 44:43 and the unusually high O_3 concentrations (176 ppb_v at 14:00 on 30 August and 124 ppb_v at 10:00 on 31 August). Afternoon WSOC concentrations were about a factor of two higher than the non-fire average. Concentrations of m/z 60 were elevated by a factor of two to three above average non-fire concentrations, which is expected given that smoke at that point would have distributed all over the basin, as confirmed by the observed smoke influence in downtown Los Angeles (Fig. 5.7). On 27 and 29 August, the spectacular morning smoke plumes observed on the days discussed above were absent; however, both O_3 and afternoon WSOC concentrations are above the non-fire average (WSOC: 3.8 $\mu\text{g m}^{-3}$ at 15:10 on 29 August and 11.2 $\mu\text{g m}^{-3}$ at 11:50 on 27 August), reflecting contributions of transported aerosols in the sea breeze containing aged smoke and fresh and processed anthropogenic aerosols.

Figure 5.9 shows the development of sub-micrometer number and volume size distributions on 31 August, a day with significant fire influence. It is evident that the smoke event between 02:00

and 12:00 LT is associated with larger particles (modal diameter of about 150 nm) than typically observed during that time on non-fire days (modal diameter of 80 nm) and that most of the volume is concentrated around 230 nm. At 12:00, there was a distinct shift to smaller particles (around 40 nm), which coincided with a decrease in WSOC concentrations (Fig. 5.10). The concentration of these smaller particles subsequently increased and reached a maximum at approximately 15:00, coinciding with an increase in WSOC concentrations owing most likely to photochemical production.

5.5 Conclusions

This work examines a ground-based field dataset of WSOC in conjunction with numerous other aerosol, gas, and meteorological measurements. Two periods governed by the presence and absence of a major wildfire are separately examined with respect to WSOC and the processes governing its temporal variability at a fixed site in Pasadena, California. WSOC is considered a tracer for SOA in the absence of biomass burning due to its highly oxidized nature. The PACO study showed that in the absence of biomass burning, changes in WSOC concentrations in Pasadena are largely driven by the diurnal sea breeze circulation and concurrent photooxidation of the transported airmasses. Initially, in the early afternoon, the sea breeze transports pollutants from the direction of the source-rich downtown Los Angeles area to Pasadena. Chemical processing of those air masses likely occurs while they are on their way and contributes to the temporal WSOC concentration gradient observed at the measurement site, in addition to the influx of WSOC that was already produced at upwind locations. Later in the afternoons, the continuing sea breeze brings in cleaner air masses while photochemical activity decreases with reduced intensity of solar radiation. These processes cause a marked decrease in WSOC, but enhanced WSOC:organic ratios. Given our observations, photochemical processes are important for overall WSOC formation in the Los Angeles basin, but cannot be assumed to dominate the observed variability at a single site. That variability is determined by a combination of transport and secondary formation processes, as well as factors we were unable to quantify, such as the magnitude of residual WSOC levels in upwind areas and in layers aloft that may be mixed into the boundary layer as a result of surface heating and boundary layer deepening over the course

of the day.

During the Station Fire, WSOC concentrations and their contributions to total organic mass were significantly higher than on typical non-fire days. WSOC was produced via both primary and secondary pathways. Close covariance of WSOC with many other measured species (nitrate, chloride, total AMS organic aerosol mass) in smoke events (defined by unusually high m/z 60 concentrations in stagnant/northerly wind conditions) is a good indicator for primary (and potentially sufficiently fast secondary) production of WSOC in the fire emissions. Secondary production of WSOC becomes detectable after the initial morning smoke plumes are directed away from the sampling site and aged smoke from farther upwind makes its way back to the measurement site with the afternoon sea breeze. Increasing m/z 44:57 and m/z 44:43 ratios show the ongoing oxidation of the smoke-influenced air masses once they arrive back at the measurement site with the sea breeze. Unusually high and early O_3 concentration maxima indicate high photochemical activity, which may also lead to some of the increased WSOC concentrations observed outside of the direct smoke plume. Multiphase processes were not a significant source of WSOC owing to low relative humidities during the entire study.

A close examination of the relationship between WSOC, m/z 44, and m/z 43 provided insight into the contribution of various classes of oxygenated species to WSOC as a result of aerosol aging. The ratio of WSOC:organic was a relatively constant function of m/z 44:43 during this study, hinting at a greater complexity of WSOC species than explained by either m/z 44 or 43. The ratio of m/z 44:WSOC increased as a function of m/z 44:43 both during the fire- and the non-fire period, suggesting that non-acid oxygenates were being converted to more acidic oxygenates, thereby enhancing the contribution of the latter to WSOC.

This work has illustrated the complexity of factors governing WSOC levels at a fixed point in the Los Angeles Basin. A follow-up study using aircraft observations in the same region during the 2010 CalNex field campaign will extend the discussion of the relative importance of various factors (e.g. transport, meteorology, diverse sources) in governing concentrations and spatiotemporal variability in WSOC in this metropolitan center and outflow regions.

Acknowledgements

This work was supported by the Electric Power Research Institute. The authors gratefully acknowledge the NOAA Air Resources Laboratory (ARL) for provision of the HYSPLIT transport and dispersion model. Analyses and visualizations used in this study were produced with the Giovanni online data system, developed and maintained by the NASA GES DISC. We also acknowledge NASA for the production of the data used in this research effort.

Bibliography

- Aiken, A. C., Decarlo, P. F., Kroll, J. H., Worsnop, D. R., Huffman, J. A., Docherty, K. S., Ulbrich, I. M., Mohr, C., Kimmel, J. R., Sueper, D., Sun, Y., Zhang, Q., Trimborn, A., Northway, M., Ziemann, P. J., Canagaratna, M. R., Onasch, T. B., Alfarra, M. R., Prevot, A. S. H., Dommen, J., Duplissy, J., Metzger, A., Baltensperger, U., and Jimenez, J. L.: O/C and OM/OC ratios of primary, secondary, and ambient organic aerosols with high-resolution time-of-flight aerosol mass spectrometry, *Environ. Sci. Technol.*, 42, 4478–4485, 2008.
- Alfarra, M. R., Prevot, A. S. H., Szidat, S., Sandradewi, J., Weimer, S., Lanz, V. A., Schreiber, D., Mohr, M., and Baltensperger, U.: Identification of the mass spectral signature of organic aerosols from wood burning emissions, *Environ. Sci. Technol.*, 41, 5770–5777, 2007.
- Blumenthal, D. L., White, W. H., and Smith, T. B.: Anatomy of a Los-Angeles smog episode – pollutant transport in daytime sea breeze regime, *Atmos. Environ.*, 12, 893–907, 1978.
- Chhabra, P. S., Ng, N. L., Canagaratna, M. R., Corrigan, A. L., Russell, L. M., Worsnop, D. R., Flagan, R. C., and Seinfeld, J. H.: Elemental composition and oxidation of chamber organic aerosol, *Atmos. Chem. Phys. Discuss.*, 11, 10305–10342, doi:10.5194/acpd-11-10305-2011, 2011.
- Decesari, S., Fuzzi, S., Facchini, M. C., Mircea, M., Emblico, L., Cavalli, F., Maenhaut, W., Chi, X., Schkolnik, G., Falkovich, A., Rudich, Y., Claeys, M., Pashynska, V., Vas, G., Kourtchev, I., Vermeylen, R., Hoffer, A., Andreae, M. O., Tagliavini, E., Moretti, F., and Artaxo, P.: Characteriza-

- tion of the organic composition of aerosols from Rondônia, Brazil, during the LBA-SMOCC 2002 experiment and its representation through model compounds, *Atmos. Chem. Phys.*, 6, 375–402, doi:10.5194/acp-6-375-2006, 2006.
- Docherty, K. S., Stone, E. A., Ulbrich, I. M., DeCarlo, P. F., Snyder, D. C., Schauer, J. J., Peltier, R. E., Weber, R. J., Murphy, S. M., Seinfeld, J. H., Eatough, D. J., Grover, B. D., and Jimenez, J. L.: Apportionment of primary and secondary organic aerosols in Southern California during the 2005 study of organic aerosols in riverside (SOAR), *Environ. Sci. Technol.*, 42, 7655–7662, 2008.
- Draxler, R. R. and Rolph, G. D.: HYSPLIT (HYbrid Single-Particle Lagrangian Integrated Trajectory) Model access via NOAA ARL READY Website, available at: <http://www.arl.noaa.gov/ready/hysplit4.html>, NOAA Air Resources Laboratory, Silver Spring (last access: August 2010), 2003.
- Drewnick, F., Hings, S. S., DeCarlo, P., Jayne, J. T., Gonin, M., Fuhrer, K., Weimer, S., Jimenez, J. L., Demerjian, K. L., Borrmann, S., and Worsnop, D. R.: A new time-of-flight aerosol mass spectrometer (TOF-AMS) – Instrument description and first field deployment, *Aerosol Sci. Tech.*, 39, 637–658, doi:10.1080/02786820500182040, 2005.
- Ervens, B. and Volkamer, R.: Glyoxal processing by aerosol multiphase chemistry: towards a kinetic modeling framework of secondary organic aerosol formation in aqueous particles, *Atmos. Chem. Phys.*, 10, 8219–8244, doi:10.5194/acp-10-8219-2010, 2010.
- Fuzzi, S., Decesari, S., Facchini, M. C., Cavalli, F., Emblico, L., Mircea, M., Andreae, M. O., Trebs, I., Hoffer, A., Guyon, P., Artaxo, P., Rizzo, L. V., Lara, L. L., Pauliquevis, T., Maenhaut, W., Raes, N., Chi, X. G., Mayol-Bracero, O. L., Soto-Garcia, L. L., Claeys, M., Kourtchev, I., Rissler, J., Swietlicki, E., Tagliavini, E., Schkolnik, G., Falkovich, A. H., Rudich, Y., Fisch, G., and Gatti, L. V.: Overview of the inorganic and organic composition of size-segregated aerosol in Rondonia, Brazil, from the biomass-burning period to the onset of the wet season, *J. Geophys. Res.*, 112, D01201, doi:10.1029/2005jd006741, 2007.

- Gao, S., Hegg, D. A., Hobbs, P. V., Kirchstetter, T. W., Magi, B. I., and Sadilek, M.: Water-soluble organic components in aerosols associated with savanna fires in Southern Africa: identification, evolution, and distribution, *J. Geophys. Res.*, 108, 8491, doi:10.1029/2002JD002324, 2003.
- Graham, B., Mayol-Bracero, O. L., Guyon, P., Roberts, G. C., Decesari, S., Facchini, M. C., Artaxo, P., Maenhaut, W., Koll, P., and Andreae, M. O.: Water-soluble organic compounds in biomass burning aerosols over Amazonia – 1. Characterization by NMR and GC-MS, *J. Geophys. Res.*, 107, 8047, doi:10.1029/2001jd000336, 2002.
- Grieshop, A. P., Logue, J. M., Donahue, N. M., and Robinson, A. L.: Laboratory investigation of photochemical oxidation of organic aerosol from wood fires 1: measurement and simulation of organic aerosol evolution, *Atmos. Chem. Phys.*, 9, 1263–1277, doi:10.5194/acp-9-1263-2009, 2009.
- Hennigan, C. J., Bergin, M. H., Dibb, J. E., and Weber, R. J.: Enhanced secondary organic aerosol formation due to water uptake by fine particles, *Geophys. Res. Lett.*, 35, L18801, doi:10.1029/2008gl035046, 2008.
- Hennigan, C. J., Bergin, M. H., Russell, A. G., Nenes, A., and Weber, R. J.: Gas/particle partitioning of water-soluble organic aerosol in Atlanta, *Atmos. Chem. Phys.*, 9, 3613–3628, doi:10.5194/acp-9-3613-2009, 2009.
- Hennigan, C. J., Sullivan, A. P., Collett Jr., J. L., and Robinson, A. L.: Levoglucosan stability in biomass burning particles exposed to hydroxyl radicals, *Geophys. Res. Lett.*, 37, L09806, doi:10.1029/2010GL043088, 2010.
- Hersey, S. P., Craven, J. S., Schilling, K. A., Metcalf, A. R., Sorooshian, A., Chan, M. N., Flanagan, R. C., and Seinfeld, J. H.: The Pasadena Aerosol Characterization Observatory (PACO): chemical and physical analysis of the Western Los Angeles Basin aerosol, *Atmos. Chem. Phys. Discuss.*, 11, 5867–5933, doi:10.5194/acpd-11-5867-2011, 2011.
- Hughes, L. S., Allen, J. O., Salmon, L. G., Mayo, P. R., Johnson, R. J., and Cass, G. R.: Evolution

- of nitrogen species air pollutants along trajectories crossing the Los Angeles area, *Environ. Sci. Technol.*, **36**, 3928–3935, 2002.
- Husar, R. B., Patterson, D. E., Blumenthal, D. L., White, W. H., and Smith, T. B.: 3-dimensional distribution of air-pollutants in Los-Angeles Basin, *J. Appl. Meteorol.*, **16**, 1089–1096, 1977.
- Jaffrezo, J.-L., Aymoz, G., Delaval, C., and Cozic, J.: Seasonal variations of the water soluble organic carbon mass fraction of aerosol in two valleys of the French Alps, *Atmos. Chem. Phys.*, **5**, 2809–2821, doi:10.5194/acp-5-2809-2005, 2005.
- Kondo, Y., Miyazaki, Y., Takegawa, N., Miyakawa, T., Weber, R. J., Jimenez, J. L., Zhang, Q., and Worsnop, D. R.: Oxygenated and water-soluble organic aerosols in Tokyo, *J. Geophys. Res.*, **D01203**, doi:10.1029/2006jd007056, 2007.
- Lee, S., Kim, H. K., Yan, B., Cobb, C. E., Hennigan, C., Nichols, S., Chamber, M., Edger-ton, E. S., Jansen, J. J., Hu, Y. T., Zheng, M., Weber, R. J., and Russell, A. G.: Diagnosis of aged prescribed burning plumes impacting an urban area, *Environ. Sci. Technol.*, **42**, 1438–1444, doi:10.1021/Es7023059, 2008.
- Lu, R., and Turco, R. P.: Air pollutant transport in a coastal environment. 2. 3-Dimensional simulations over Los-Angeles Basin, *Atmos. Environ.*, **29**, 1499–1518, 1995.
- Mayol-Bracero, O. L., Guyon, P., Graham, B., Roberts, G., Andreae, M. O., Decesari, S., Facchini, M. C., Fuzzi, S., and Artaxo, P.: Water-soluble organic compounds in biomass burning aerosols over Amazonia – 2. Apportionment of the chemical composition and importance of the polyacidic fraction, *J. Geophys. Res.*, **107**, 8091, doi:10.1029/2001jd000522, 2002.
- McLafferty, F. W. and Turecek, F.: *Interpretation of Mass Spectra*, 4th Edn., University Science Books, Mill Valley, California, 1993.
- Miyazaki, Y., Kondo, Y., Takegawa, N., Komazaki, Y., Fukuda, M., Kawamura, K., Mochida, M., Okuzawa, K., and Weber, R. J.: Time-resolved measurements of water-soluble organic carbon in Tokyo, *J. Geophys. Res.*, **111**, D23206, doi:10.1029/2006jd007125, 2006.

- Murphy, S. M., Agrawal, H., Sorooshian, A., Padro, L. T., Gates, H., Hersey, S., Welch, W. A., Jung, H., Miller, J. W., Cocker, D. R., Nenes, A., Jonsson, H. H., Flagan, R. C., and Seinfeld, J. H.: Comprehensive simultaneous shipboard and airborne characterization of exhaust from a modern container ship at sea, *Environ. Sci. Technol.*, 43, 4626–4640, doi:10.1021/Es802413j, 2009.
- Ng, N. L., Canagaratna, M. R., Zhang, Q., Jimenez, J. L., Tian, J., Ulbrich, I. M., Kroll, J. H., Docherty, K. S., Chhabra, P. S., Bahreini, R., Murphy, S. M., Seinfeld, J. H., Hildebrandt, L., Donahue, N. M., DeCarlo, P. F., Lanz, V. A., Prévôt, A. S. H., Dinar, E., Rudich, Y., and Worsnop, D. R.: Organic aerosol components observed in Northern Hemispheric datasets from Aerosol Mass Spectrometry, *Atmos. Chem. Phys.*, 10, 4625–4641, doi:10.5194/acp-10-4625-2010, 2010.
- Peltier, R. E., Weber, R. J., and Sullivan, A. P.: Investigating a liquid-based method for on-line organic carbon detection in atmospheric particles, *Aerosol Sci. Tech.*, 41, 1117–1127, doi:10.1080/02786820701777465, 2007.
- Phuleria, H. C., Fine, P. M., Zhu, Y. F., and Sioutas, C.: Air quality impacts of the October 2003 Southern California wildfires, *J. Geophys. Res.*, 110, D07S20, doi:10.1029/2004jd004626, 2005.
- Posfai, M., Simonics, R., Li, J., Hobbs, P. V., and Buseck, P. R.: Individual aerosol particles from biomass burning in Southern Africa: 1. Composition and size distributions of carbonaceous particles, *J. Geophys. Res.*, 108(D13), 8483, doi:10.1029/2002JD002291, 2003.
- Reid, J. S., Koppmann, R., Eck, T. F., and Eleuterio, D. P.: A review of biomass burning emissions part II: intensive physical properties of biomass burning particles, *Atmos. Chem. Phys.*, 5, 799–825, doi:10.5194/acp-5-799-2005, 2005.
- Robinson, A. L., Donahue, N. M., Shrivastava, M. K., Weitkamp, E. A., Sage, A. M., Grieshop, A. P., Lane, T. E., Pierce, J. R., and Pandis, S. N.: Rethinking organic aerosols: semivolatile emissions and photochemical aging, *Science*, 315, 1259–1262, doi:10.1126/science.1133061, 2007.
- Ruellan, S., Cachier, H., Gaudichet, A., Masclet, P., and Lacaux, J. P.: Airborne aerosols over

- Central Africa during the experiment for regional sources and sinks of oxidants (EXPRESSO), *J. Geophys. Res.*, 104, 30673–30690, 1999.
- Sorooshian, A., Brechtel, F. J., Ma, Y. L., Weber, R. J., Corless, A., Flagan, R. C., and Seinfeld, J. H.: Modeling and characterization of a particle-into-liquid sampler (PILS), *Aerosol Sci. Tech.*, 40, 396–409, doi:10.1080/02786820600632282, 2006.
- Sorooshian, A., Murphy, S. M., Hersey, S., Bahreini, R., Jonsson, H., Flagan, R. C., and Seinfeld, J. H.: Constraining the contribution of organic acids and AMS m/z 44 to the organic aerosol budget: on the importance of meteorology, aerosol hygroscopicity, and region, *Geophys. Res. Lett.*, 37, L21807, doi:10.1029/2010GL044951, 2010.
- Sullivan, A. P. and Weber, R. J.: Chemical characterization of the ambient organic aerosol soluble in water: 1. Isolation of hydrophobic and hydrophilic fractions with a XAD-8 resin, *J. Geophys. Res.*, 111, D05314, doi:10.1029/2005jd006485, 2006.
- Sullivan, A. P., Weber, R. J., Clements, A. L., Turner, J. R., Bae, M. S., and Schauer, J. J.: A method for on-line measurement of water-soluble organic carbon in ambient aerosol particles: results from an urban site, *Geophys. Res. Lett.*, 31, L13105, doi:10.1029/2004gl019681, 2004.
- Sullivan, A. P., Peltier, R. E., Brock, C. A., de Gouw, J. A., Holloway, J. S., Warneke, C., Wollny, A. G., and Weber, R. J.: Airborne measurements of carbonaceous aerosol soluble in water over Northeastern United States: method development and an investigation into water-soluble organic carbon sources, *J. Geophys. Res.*, 111, D23S46, doi:10.1029/2006jd007072, 2006.
- Timonen, H., Aurela, M., Carbone, S., Saarnio, K., Saarikoski, S., Mäkelä, T., Kulmala, M., Kerminen, V. M., Worsnop, D. R., and Hillamo, R.: High time-resolution chemical characterization of the water-soluble fraction of ambient aerosols with PILS-TOC-IC and AMS, *Atmos. Meas. Tech.*, 3, 1063–1074, doi:10.5194/amt-3-1063-2010, 2010.
- Vutukuru, S., Griffin, R. J., and Dabdub, D.: Simulation and analysis of secondary organic

- aerosol dynamics in the South Coast Air Basin of California, *J. Geophys. Res.*, 111, D10S12, doi:10.1029/2005jd006139, 2006.
- Weber, R. J., Sullivan, A. P., Peltier, R. E., Russell, A., Yan, B., Zheng, M., de Gouw, J., Warneke, C., Brock, C., Holloway, J. S., Atlas, E. L., and Edgerton, E.: A study of secondary organic aerosol formation in the anthropogenic-influenced Southeastern United States, *J. Geophys. Res.*, 112, D13302, doi:10.1029/2007jd008408, 2007.
- Westerling, A. L., Hidalgo, H. G., Cayan, D. R., and Swetnam, T. W.: Warming and earlier spring increase Western US forest wildfire activity, *Science*, 313, 940–943, doi:10.1126/science.1128834, 2006.
- Zhang, Q., Alfarra, M. R., Worsnop, D. R., Allan, J. D., Coe, H., Canagaratna, M. R., and Jimenez, J. L.: Deconvolution and quantification of hydrocarbon-like and oxygenated organic aerosols based on aerosol mass spectrometry, *Environ. Sci. Technol.*, 39, 4938–4952, doi:10.1021/Es048568l, 2005.

Table 5.1: Statistical summary of the relationship between WSOC ($\mu\text{g C m}^{-3}$) and other chemical and meteorological parameters (measured at Santa Fe Dam). AMS aerosol species concentration units are $\mu\text{g m}^{-3}$.

		Station Fire				No Fire			
		r^2	Slope	Intercept	n	r^2	Slope	Intercept	n
AMS ($\mu\text{g m}^{-3}$)	Total organic	0.92	-1.05	0.34	1298	0.47	0.14	0.69	1557
	<i>m/z</i> 60	0.90	40.16	1.88	1298	0.45	94.46	0.48	1557
	<i>m/z</i> 44	0.84	3.04	-1.15	1298	0.35	0.95	0.94	1557
	<i>m/z</i> 43	0.84	5.22	-1.45	1298	0.49	2.25	0.51	1557
	<i>m/z</i> 55	0.80	9.47	-1.43	1298	0.45	3.79	0.61	1557
	NO_3^-	0.79	4.30	-1.09	1298	0.00	-0.02	1.75	1557
	Cl^-	0.57	77.39	0.99	1296	0.03	-1.28	1.82	1557
	<i>m/z</i> 57	0.47	1.24	0.60	1298	0.20	6.58	0.96	1557
	NH_4^+	0.18	7.06	0.54	1298	0.00	0.04	1.64	1557
	SO_4^{2-}	0.14	-2.67	7.41	1298	0.08	0.14	1.40	1557
Gas	CO (ppm_v)	0.18	3.66	2.78	151	0.00	0.26	1.69	212
	O₃ (ppb_v)	0.05	0.03	3.35	151	0.35	0.02	0.83	212
	No_x (ppb_v)	-0.01	-0.01	4.77	151	0.03	-0.01	1.94	212
Meteorology	Wind speed (m s⁻¹)	0.07	-	-	144	0.11	-	-	210
	Solar radiation (W m⁻²)	0.00	-	-	148	0.28	-	-	209
	T (C)	0.01	-	-	144	0.44	-	-	209
	RH (%)	0.00	-	-	147	0.14	-	-	209

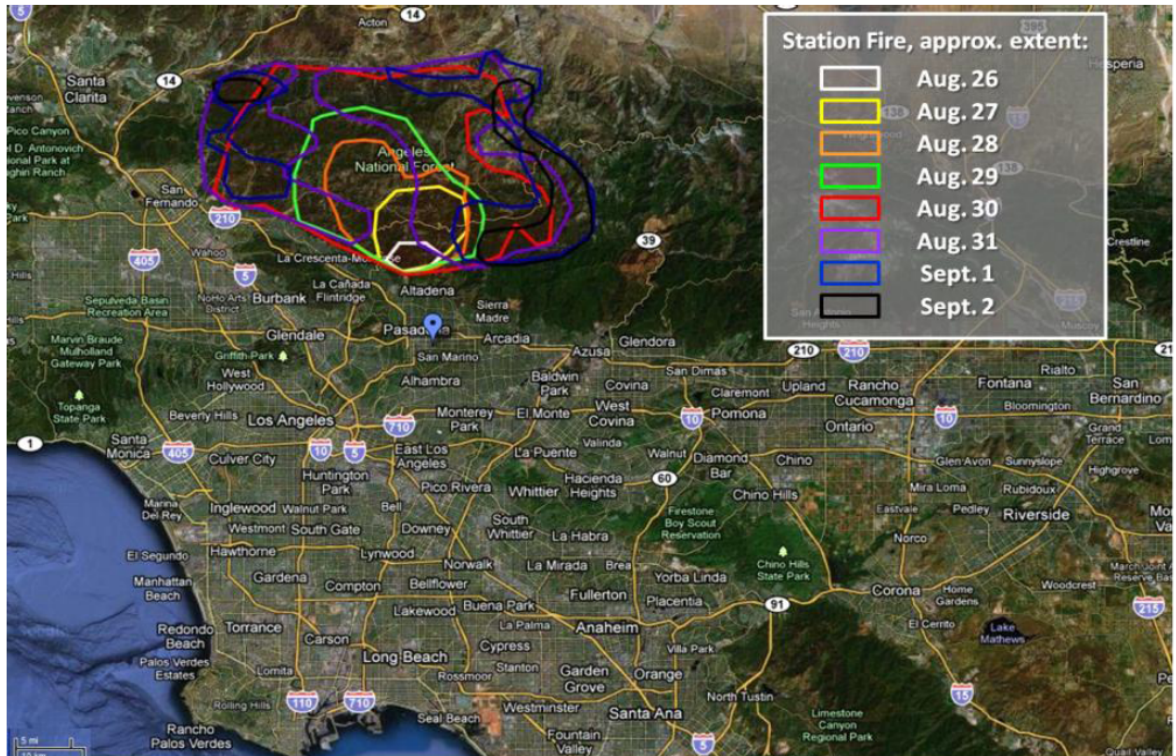


Figure 5.1: Approximate spatial extent of the Station Fire by date (bordered areas). The fire area was estimated using fire maps by “Firefly”, University of Maryland (<http://firefly.geog.umd.edu/firemap/>). The blue marker in Pasadena represents the measurement site.

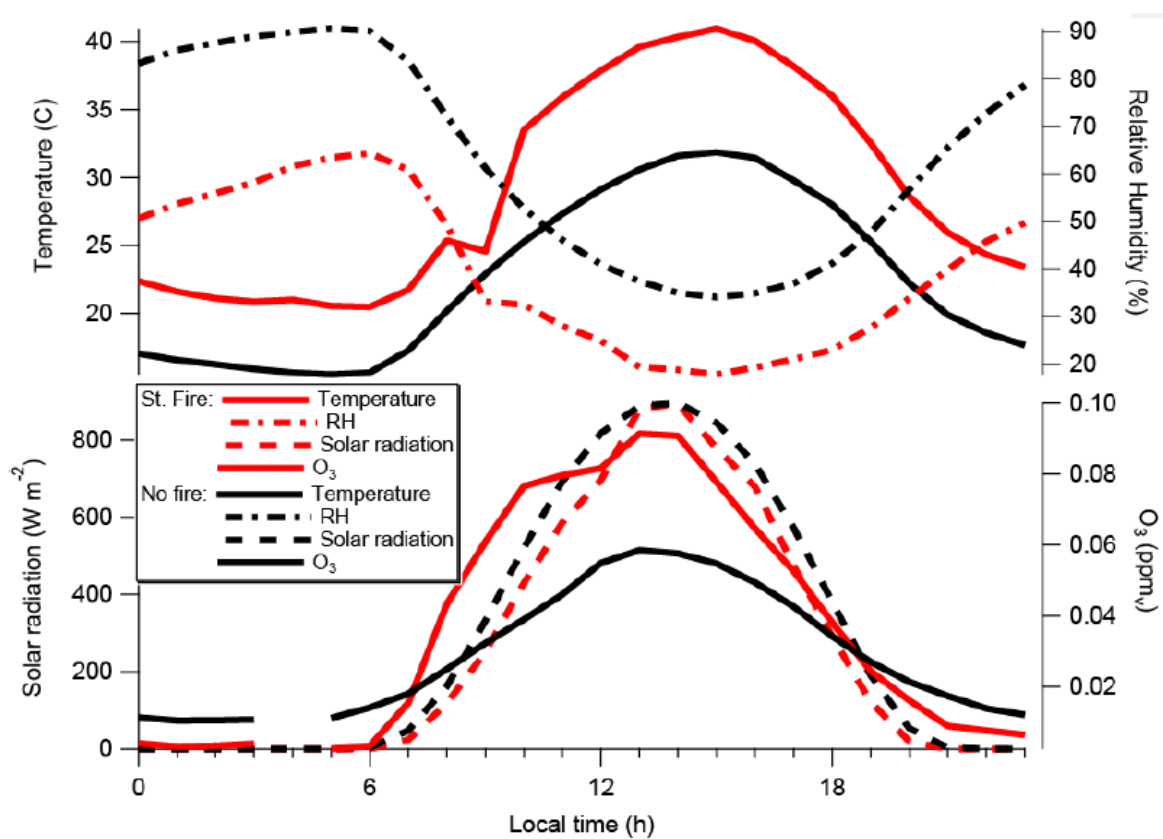


Figure 5.2: Diurnal meteorological parameters (Santa Fe Dam station) and O₃ concentrations.

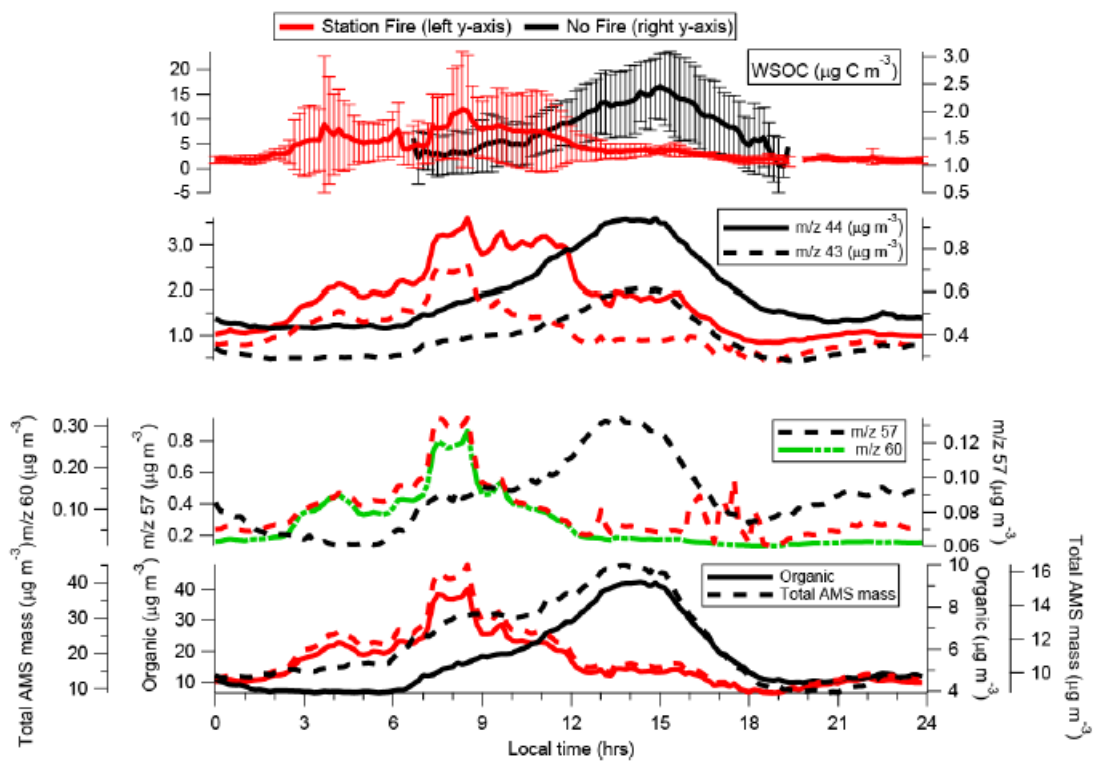


Figure 5.4: Diurnal averages of aerosol chemistry (m/z 60 shown for the fire period only).

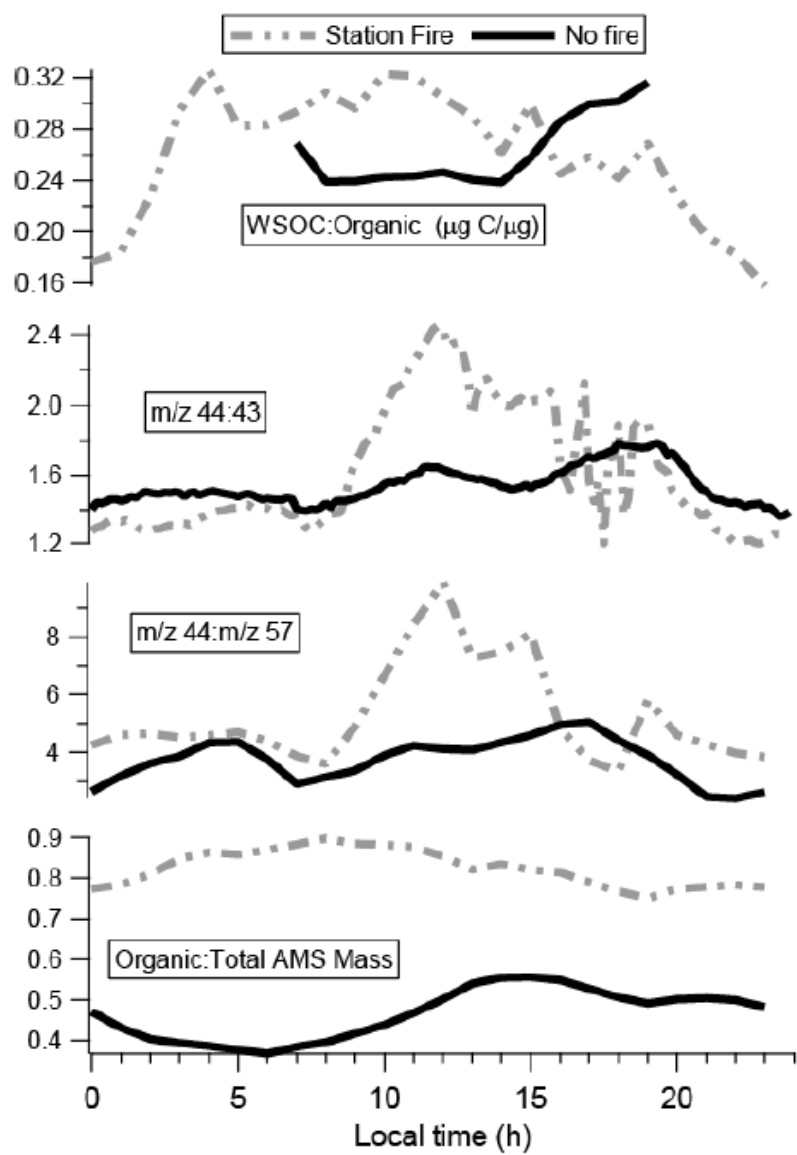


Figure 5.5: Diurnally averaged ratios of different aerosol measurements.

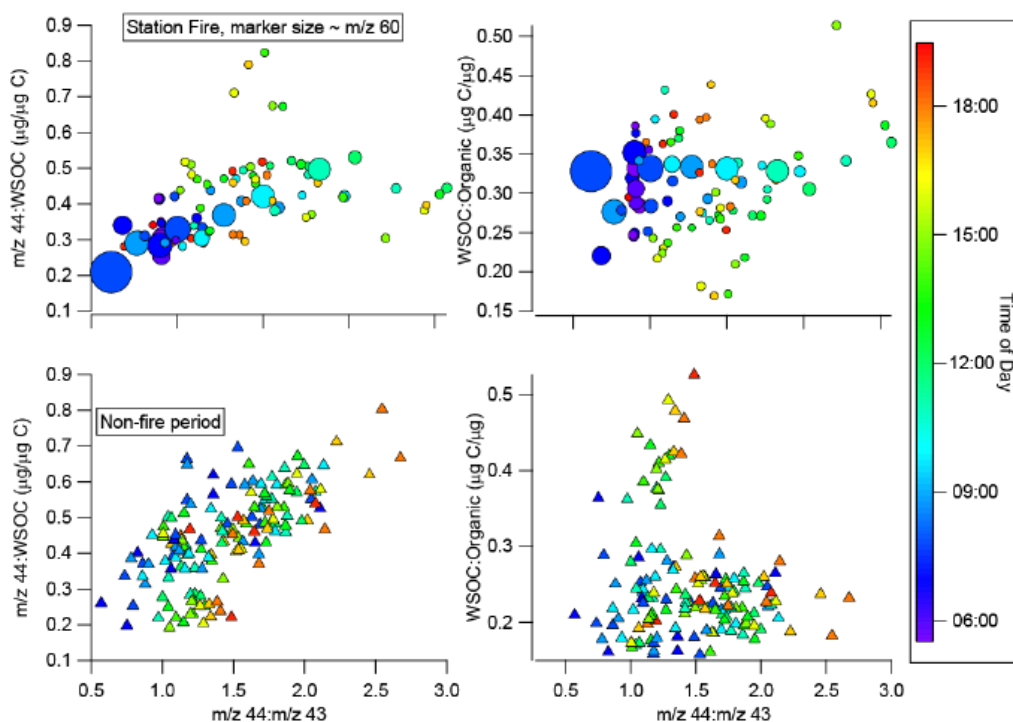


Figure 5.6: Summary of the ratios WSOC: organic and $m/z\ 44:WSOC$ as functions of $m/z\ 44:43$ during the (top panels) fire and (bottom panels) the non-fire periods. Symbols are color-coded by time of day, and in the fire panels the symbol sizes are proportional to the tracer for biomass burning $m/z\ 60$ (range = $0.03\text{--}0.9\ \mu g\ m^{-3}$).

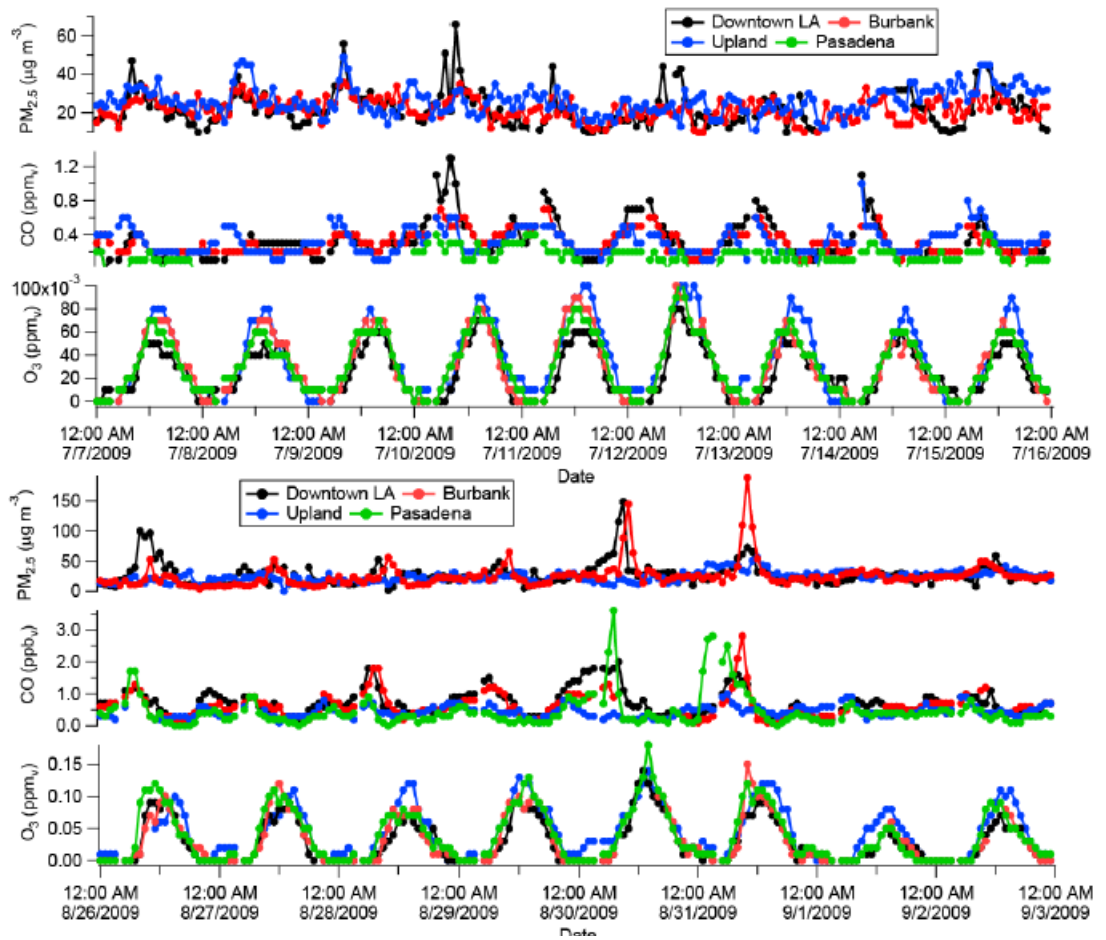


Figure 5.7: Ground station observations of $\text{PM}_{2.5}$, CO and O_3 for the non-fire (top) and the fire (bottom) period. The four stations (<http://www.arb.ca.gov>) are shown on the map in Fig. 5.1.

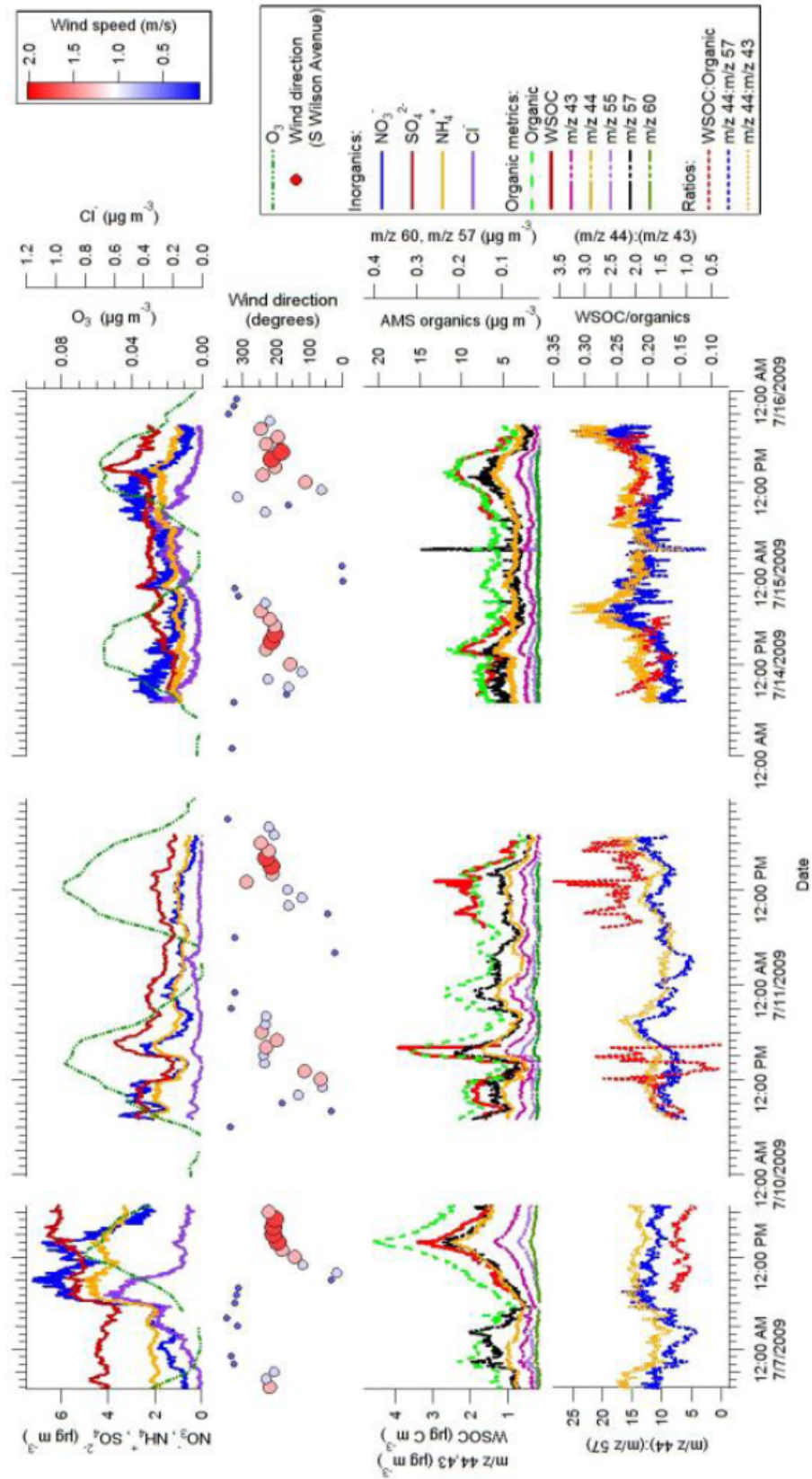


Figure 5.8: Time series of various measured and derived parameters during selected days outside the fire period. The symbol size for wind direction is proportional to measured wind speed.

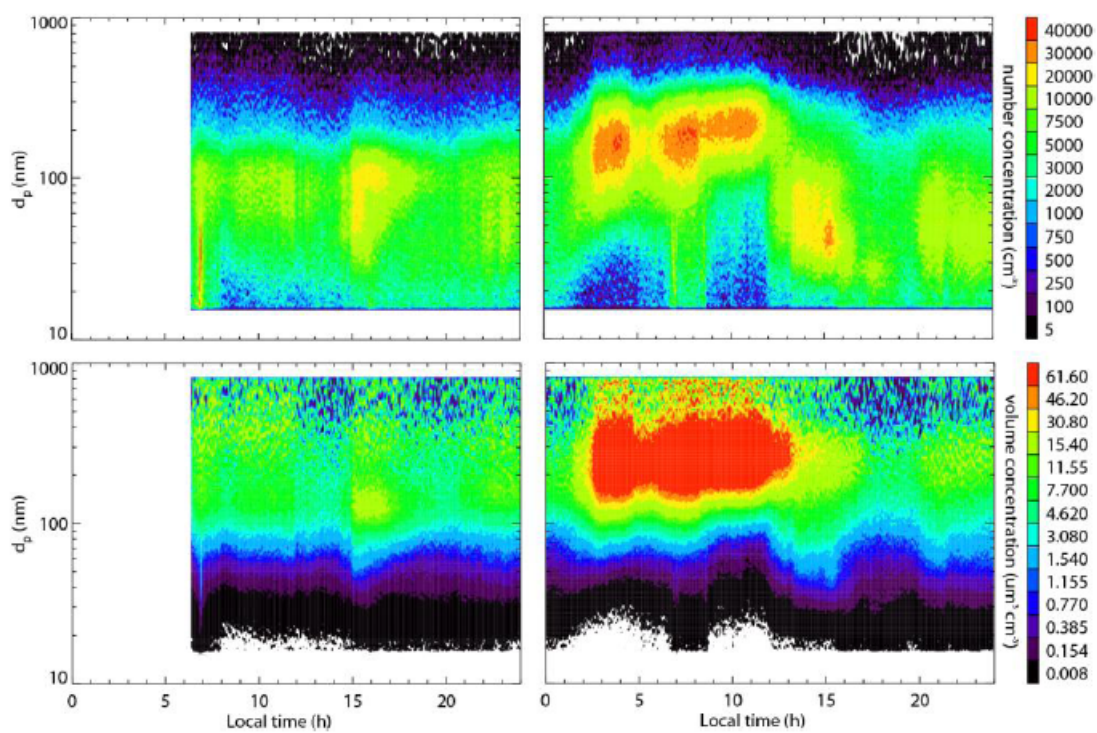


Figure 5.9: Number (top) and volume (bottom) size distributions over the course of (left) 10 July 2009, a day of the non-fire period, and (right) 31 August 2009 in the fire period.

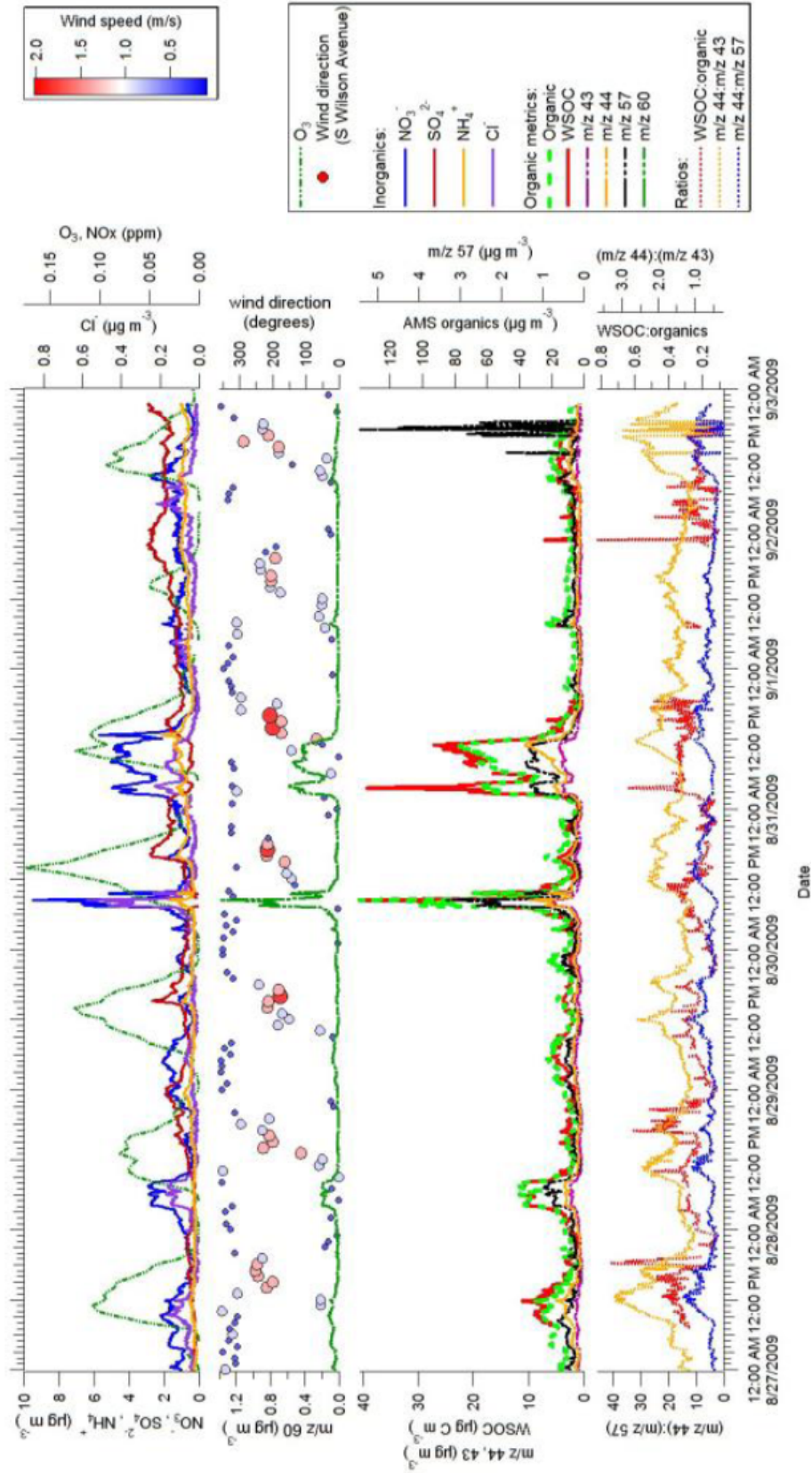


Figure 5.10: Time series of various measured and derived parameters during the fire period. The symbol size for wind direction is proportional to measured wind speed.

Chapter 6

Aerosol Hygroscopicity and Composition in the Los Angeles Basin during the 2010 CalNex Experiment

6.1 Abstract

This work presents the first aircraft study aimed at investigating the links between aerosol composition and hygroscopicity across a major urban area. Data were collected during the CalNex field experiment, which was carried out in the Los Angeles Basin in May 2010. Fine particles in the source-rich western and southwestern region of the basin evolve into accumulation mode particles during transport to the eastern and northeastern portions of the basin. This particle growth corresponds to enhancements in nitrate, ammonium, and organics, in addition to increased O:C ratio of organics.

Hygroscopic growth factor (GF) averaged 1.74 ± 0.29 at 92% RH and 1.20 ± 0.10 at 74% RH during CalNex. Hygroscopic GF displays a strong anti-correlation with organic mass fraction (OMF) at 92% RH, but organics have little effect on hygroscopicity at lower ($< 75\%$) RH. The hygroscopicity parameter κ averaged 0.32 ± 0.17 and critical diameter (D_c) averaged 109 ± 19 nm across the Los Angeles Basin, agreeing well with previous studies in urban environments. CalNex data indicate that the κ parameter is inversely correlated with OMF, with κ displaying a greater degree of sensitivity to OMF than in a 2009 study in which background urban aerosol in the Western Los Angeles Basin was sampled (Hersey et al., 2011). Organic κ (κ_{org}) averaged 0.11 for CalNex, lower than the value of 0.14 found in the 2009 study, and corresponding to a less-oxidized organic component (O:C = 0.31 during CalNex, versus 0.44-0.53 in Hersey et al. (2011)). Overall, organics in Los Angeles appear to be hygroscopic, though their hygroscopicity depends strongly on their degree of oxygenation.

6.2 Introduction

Aerosols represent the largest uncertainty in projections of future climate. When particle diameter is similar to the wavelength of incoming light, Mie scattering reflects a fraction of incoming solar radiation back to space and results in a climate-cooling negative forcing called the direct aerosol effect. The intensity of Mie scattering by aerosols, and thereby the magnitude of the direct aerosol effect, is a strong function of aerosol particle diameter between ~ 0.1 and $2 \mu\text{m}$, such that larger

particles scatter significantly more light and result in a stronger negative forcing. Particle diameter (D_p) is determined in large part by aerosol water content, which in turn is a function of relative humidity (RH) and chemical composition. Further, sub-saturated water uptake is strongly correlated with the tendency of aerosols to serve as cloud condensation nuclei (CCN) (Prenni et al., 2001; Mochida et al., 2006), which affects the reflectivity and lifetime of clouds (IPCC, 2007). Climate predictions require relating aerosol size and composition to RH. Field measurements of sub-saturated water uptake, or hygroscopicity, of aerosols are needed to corroborate the relationships between hygroscopicity and chemical composition that are used in climate models.

Currently over half of the world's population lives in urban centers, and that fraction is increasing steadily (Bremner et al., 2009). Cities are major sources of particulate matter, which can be advected out of the boundary layer and remain aloft in the free troposphere for days to weeks (Jaffe et al., 1999; Liu et al., 2003; Liang et al., 2004), impacting Earth's radiative balance while undergoing intercontinental transport. Given the regional and global importance of urban aerosols, it is necessary that the interaction of urban aerosols with water vapor be well-characterized.

A number of studies have focused on aerosol hygroscopicity in major urban areas. Water uptake is typically complex, with multiple growth modes comprised of hydrophobic, slightly hygroscopic, and hygroscopic modes, with as many as six growth modes observed periodically (Cocker et al., 2001; Massling et al., 2009). Size-dependent hygroscopic properties are often observed, corresponding to distinct composition for Aitken and accumulation mode aerosol (Cubison et al., 2008; Meier et al., 2009). While hygroscopic properties of inorganic species are well-characterized, organics can exhibit hygroscopic behavior ranging from hydrophobic to somewhat hydrophilic (Cubison et al., 2008; Dusek et al., 2010; Wang et al., 2010). Increasing organic mass fraction is generally associated with suppressed water uptake (Mochida et al., 2008; Meier et al., 2009; Pan et al., 2009; Shinozuka et al., 2009). Oxidized, water soluble organic carbon can exhibit RH-dependent effects, with enhanced water uptake at lower RH (below 75%) and suppressed uptake at high RH (above 90%) (Aggarwal et al., 2007; Hersey et al., 2009). Because organics comprise the dominant fraction of most urban aerosols (Zhang et al., 2007), the hygroscopicity of the urban organic fraction plays a key role in the

overall hygroscopic behavior of the aerosol.

The Los Angeles Basin represents the largest urban area in the United States. It is home to a population of over 17 million, the busiest container port in the United States, and myriad industrial, agricultural, and bovine operations. Recent studies of particulate matter in Los Angeles have revealed a dynamic aerosol population that is predominantly organic and appears to undergo evolution from source-rich to downwind areas (Docherty et al., 2008; Hersey et al., 2011). Water uptake of Los Angeles aerosol is complex, with multi-modal growth and an anti-correlation between hygroscopicity and organic mass fraction (Cocker et al., 2001; Cubison et al., 2008; Hersey et al., 2011). Despite advances in the understanding of urban aerosol hygroscopicity, no study has employed aircraft measurements to characterize composition and hygroscopicity over an entire urban center with myriad sources and complex aerosol evolution.

This paper represents the first aircraft study to investigate the links between aerosol composition, aging, and hygroscopicity across an extensive urban area. Data were collected as part of the summer 2010 CalNex field campaign in Los Angeles, CA, onboard the Center for Interdisciplinary Remotely-Piloted Aircraft Studies (CIRPAS) Twin Otter aircraft, which operated with goals of discerning the origin and composition of Los Angeles aerosol, the effect of aging on aerosol composition and oxidation state, sub- and super- saturated hygroscopicity, mixing state, and black carbon (BC) content of the LA aerosol. Here, aerosol mass spectrometer (AMS) data are employed to determine the effects of composition on aerosol hygroscopicity, with special focus on the magnitude and character of the organic fraction. Extensive analysis of the composition and evolution of Los Angeles aerosol will appear in subsequent works.

6.3 Methods

The CalNex field experiment (<http://www.esrl.noaa.gov/csd/calnex/>) was conducted between May and July of 2010, utilizing several aircraft, ship, and ground-based sampling platforms to investigate the atmosphere of the Los Angeles Basin and San Joaquin Valley in Southern California. The Center for Interdisciplinary Remotely-Piloted Aircraft Studies (CIRPAS) Twin Otter aircraft participated in

the experiment from May 4 to May 28, conducting 18 flights in the Los Angeles Basin, basin outflows, and the San Joaquin Valley. Flight times, locations, and instrument performance are summarized in Table 6.1. The Twin Otter was based at the Ontario International Airport (ONT/KONT, 34.056° N, 117.601° W). Typical flight duration on the order of 4 h and covered roughly 700-800 km. Aerosol composition was measured by the Aerosol Time-of-Flight Mass Spectrometer (ATOFMS, UCSD) and an Aerodyne Compact Time-of-Flight Mass Spectrometer (c-ToF-AMS, Caltech), which split time on the aircraft. Analysis here is limited to flights 11, 13, and 15-18, which focused on the Los Angeles basin and its outflows, with the c-ToF-AMS measuring composition. Future analysis will include composition data from the ATOFMS in addition to that from the c-ToF-AMS, and will incorporate analysis of data from the San Joaquin Valley.

6.3.1 DASH-SP - Multiple-RH Hygroscopicity

The Differential Aerosol Sizing and Hygroscopicity Spectrometer Probe (DASH-SP, Brechtel Mfg.) was used to measure subsaturated aerosol water uptake at 74 and 92% RH during CalNex. During CalNex, the DASH-SP was operated as described by Sorooshian et al. (2008), except that the 85% RH humidification channel was not functioning. Briefly, ambient aerosol particles are dried in a nafion dryer before being size-selected in a cylindrical differential mobility analyzer (DMA) to generate a monodisperse aerosol of 150, 175, 200, or 225 nm dry diameter ($D_{p,dry}$) particles. After size-selection, the flow of monodisperse aerosol is split into four separate flows, one providing a redundant measurement of particle number concentration via a condensation particle counter (CPC, TSI Model 3831), with the other three channels consisting of parallel nafion humidification chambers (Perma Pure, LLP, Model MD-070-24FS-4) operated at dry (< 10), 74, and 92% RH, followed by custom built optical particle counters (OPCs). Within the OPCs, particles pass through a focused laser beam ($\lambda = 532$ nm, World Star Technologies, Model TECGL-30), where all forward-scattered light is collected and focused on a photomultiplier tube, and the resulting electrical pulse is recorded by a high-speed data acquisition computer. An iterative data processing algorithm, based on laboratory calibrations with salts of known refractive indices, is used to determine the best fit

on a solution surface relating electrical pulse height, size, and refractive index, thereby accounting for the change in refractive index with particle water uptake. Temperature, pressure, and RH are monitored and controlled at several locations in the DASH-SP, ensuring that variability in these parameters does not impact growth factor measurements. RH was controlled to within 1.5%, and overall uncertainty in GF calculations is 4.5%.

6.3.2 AMS - Aerosol Composition

Chemical composition of submicron non-refractory aerosol was measured with an Aerodyne compact Time-of-Flight Aerosol Mass Spectrometer (C-ToF-AMS) (cToF-AMS, Drewnick et al., 2004a,b). An aerodynamic lens focuses particles with vacuum aerodynamic diameters (D_{va}) $50 \text{ nm} \leq D_{va} \leq 800 \text{ nm}$, which then pass through a 3.5% chopper and are subsequently vaporized at $530 - 600^\circ\text{C}$. The chopper is operated in three modes, detecting background mass spectra, ensemble average mass spectra over all particle sizes, or size-resolved mass spectra. After vaporization, particles are ionized by electron impact and pulsed into a time-of-flight mass spectrometer. Mass spectral deconvolution resolves sulfate, nitrate, ammonium, chloride, and organic mass loadings (Allan et al., 2004), and approximate organic O:C ratios are calculated by using mass concentration at m/z 44 and a parameterization presented in Aiken et al. (2008). During CalNex, both bulk and size-resolved particle time-of-flight (PToF) AMS data were collected. The current analysis utilizes bulk AMS data (ensemble average between $D_{va} = 50$ and 800 nm), encompassing the DASH-SP size range ($D_{em} = 150$ to 225 nm). It is likely that ensemble average bulk composition has some discrepancies when compared with composition within the narrow DASH-SP size range, and future analysis will utilize size-resolved PToF data to explore composition solely within the DASH-SP size range.

6.3.3 CIRPAS Instruments - Microphysics and Meteorology

A suite of instruments onboard the CIRPAS Twin Otter collected microphysical and meteorological data during CalNex. Three condensation particle counters (TSI), each with a different lower size limit (3, 10, and 15 nm), measured total particle number concentration, while a Passive Cavity

Aerosol Spectrometer Probe (PCASP) measured number concentration between 0.1 and 2.6 μm . Meteorological measurements included temperature, dewpoint temperature, RH, mixing ratio of water, specific humidity, wind speed, wind direction, pressure, air density, potential temperature.

6.4 Aerosol Composition and Microphysics

In order to understand trends of hygroscopicity in the Los Angeles basin, it is necessary to begin with a brief description of the microphysical properties and composition of the aerosols. Detailed analysis will follow in subsequent works. The western/central Los Angeles Basin can be generalized as source-rich, with prevailing W/SW winds continuously transporting air toward downwind eastern areas of Los Angeles and Riverside Counties. As air parcels are transported from west to east, particles evolve due to photochemistry, aqueous processing, and inputs of new emissions.

One result of these evolution processes is that particles tend to grow as they age, transforming aerosol populations dominated by fine particles into populations characterized by larger, accumulation-mode particles. This trend is illustrated in Fig. 6.1, which displays ζ , a dimensionless metric for determining the relative abundance of fine to large particles, defined as:

$$\zeta = \log \frac{[\text{UFCPC}]}{[\text{PCASP}]}, \quad (6.1)$$

where [UFCPC] is the number concentration of particles with $D_p > 3 \text{ nm}$ (cm^{-3}) and [PCASP] is the number concentration of particles with $D_p > 200 \text{ nm}$ (cm^{-3}). ζ approaches its maximum near 2.5, at which fine particles dominate over larger particles in number concentration; as ζ approaches zero, particles are predominantly accumulation mode and larger. Viewing ζ on a Google Earth map layer (Fig. 6.1, one observes that fine particles are most prevalent in the southwestern portion of the Twin Otter flight tracks, over the industrial and shipping center of Long Beach. Fine particles also dominate in a corridor along the 91 freeway that is impacted by outflow from the Long Beach area. An abundance of fine particles is also observed 10-12 km from the outflow of Los Angeles air through both the El Cajon and Banning passes, suggesting possible nucleation events in these

outflow areas. In general, larger particles dominate in the E/NE parts of the Los Angeles Basin. CalNex data show that RH is typically 25-50% lower in the eastern portion of the basin than in the west, so it is concluded that this particle growth likely reflects aging processes that result in the condensation of secondary species, as opposed to water uptake by particles.

A summary of AMS aerosol composition is shown in Fig. 6.2. Distinct spatial trends are observed for organics, nitrate, ammonium, and sulfate. Organics comprise, on average, 41% of the submicron aerosol sampled during CalNex, with enhancements in concentration near downtown, in the area northeast of Riverside, and in the narrow El Cajon and Banning passes, through which Los Angeles plumes flow out to the desert. Comparing the organic trace with the ζ plot in Fig. 6.1, it is apparent that while there are significant concentrations of fine particles in the Long Beach area and the outflow along the 91 freeway, there is little organic mass detected by the AMS in these areas. In the 2009 PACO study of urban background aerosols in Pasadena, Hersey et al. (2011) used size-resolved pToF AMS data to show that organics often comprise a fine mode in aerosol size distributions. It is likely that many of the fine particles identified along the 91 freeway corridor by the CPCs are not detected by the AMS, which has a lower detection limit of 50 nm. Both nitrate and ammonium reach maxima in the northeast portion of the basin and in the narrow El Cajon and Banning passes. This likely reflects the impact of appreciable ammonia emissions from dairies in the area near Chino and Riverside in the eastern basin, which drive the formation of particulate NH_4NO_3 . Sulfate is contributed predominantly by marine sources in the Los Angeles Basin (Watson et al., 1994; Hersey et al., 2011), which is reflected in its relatively constant mass concentration across the basin, with slight enhancement near the coast. It appears as though there may be significant point sources of sulfate near the industrial/shipping area of Long Beach. Black carbon (not displayed in Fig. 6.2) shows fairly uniform mass concentrations across the Los Angeles Basin and outflows, and contributes a relatively constant but small (< 4%) mass fraction of the aerosol.

Oxidation state is a major factor determining the hygroscopicity of aerosol organics, with more oxidized, acidic organics tending to be more hygroscopic (Petters and Kreidenweis, 2008). Organics with a higher degree of oxygenation tend to account for the majority of water soluble organic carbon

(WSOC), and accounting for the contribution of WSOC to aerosol mass has been shown to improve predictions of hygroscopicity (Asa-Awuku et al., 2011). Figure 6.3 shows the approximate O:C ratio plotted spatially in the Los Angeles Basin, as well as versus longitude. O:C averaged 0.31 ± 0.08 during CalNex, which is significantly lower than the range of 0.44-0.53 reported during the Pasadena PACO study (Hersey et al., 2011). This suggests that, on average, the organics sampled during CalNex were significantly less oxidized than the urban background sampled in PACO, and therefore are likely to exhibit diminished hygroscopic behavior when compared with results from Hersey et al. (2011). In Fig. 6.3, one can see that organic O:C ratio tends to increase from west to east. Thus, it is expected that organics will tend to be more hygroscopic toward the eastern part of the basin.

6.5 Hygroscopicity

If urban aerosol is present as an external mixture, one expects complex hygroscopic behavior with several growth modes (e.g., Cocker et al., 2001; Massling et al., 2005; Swietlicki et al., 2008; Massling et al., 2009; Meier et al., 2009; Tiitta et al., 2010; Rose et al., 2010). The DASH-SP utilizes an optical sizing method that provides rapid measurements of hygroscopicity suitable for aircraft deployment. Light scattering by particles, on which DASH-SP optical sizing is based, depends on particle size, refractive index, and shape. Two particles of identical size and refractive indices, but slightly different morphology, will appear to be slightly different sizes based on their light scattering signatures. Because atmospheric particles are rarely perfectly spherical, particle size distributions become broadened in optical sizing instruments. Such broadening can mask complexity in multiple hygroscopic growth modes such as those described in Cocker et al. (2001). Given this limitation, the optical sizing employed by the DASH-SP does not allow resolution of more than two hygroscopic modes (a nonhygroscopic and hygroscopic mode). Since it was not possible to resolve multiple growth modes, DASH-SP data represent the overall subsaturated water uptake behavior for hygroscopic particles.

Several metrics exist for quantifying particle water uptake. The hygroscopic growth factor,

$$\text{GF} = \frac{D_{p,wet}}{D_{p,dry}}, \quad (6.2)$$

is the most common metric used in the literature, and provides a simple and intuitive measure of the magnitude of particle growth due to water uptake. During CalNex, the DASH-SP measured GF for dry particle sizes of 150, 175, 200, and 225 nm. There was no statistically significant difference in GF between these sizes, and so data were combined into a representative GF for the dry size range of 150-225 nm.

As discussed in Section 6.2, an inverse correlation typically exists between hygroscopicity at high RH and the relative abundance of organics in urban aerosol, with increased organic mass fraction (OMF) corresponding to suppressed GF (Massling et al., 2005; Mochida et al., 2006; Aggarwal et al., 2007; Cubison et al., 2008; Mochida et al., 2008; Massling et al., 2009; Meier et al., 2009; Pan et al., 2009; Shinozuka et al., 2009; Dusek et al., 2010; Wex et al., 2010). At lower RH, on the other hand, organics tend not to suppress GF, often enhancing hygroscopicity because of their tendency to be associated with water below the deliquescence and efflorescence RH for the inorganics in the aerosol (Aggarwal et al., 2007; Hersey et al., 2009). These trends are displayed in Fig. 6.4, which shows GF at 74% (bottom) and 92% (top) plotted against OMF, with markers color-coded by nitrate mass fraction (NMF). Dotted lines represent a linear fit of the data, while solid lines on the 92% GF plot indicate GFs for common inorganic aerosol constituents. It is evident that at 92% RH, GF measured during CalNex is typically suppressed below the GF of common sulfate and nitrate inorganics, and approaches the GF of pure inorganics at low OMF. A basin-averaged 92% GF of 1.74 ± 0.29 indicates a relatively hygroscopic aerosol, despite the presence of organics, but average hygroscopicity is appreciably less than that of pure inorganic aerosols. These GF values are significantly higher than those measured during the 1987 SCAQS study in the eastern Los Angeles Basin (1.23 ± 0.08 for 200 nm particles at $90 \pm 3\%$ RH; (Zhang and McMurray, 1993), and are more consistent with the most hygroscopic mode measured in Pasadena in 1999 (1.6 at 89% RH; Cocker et al., 2001) and similar to values reported in Hersey et al. (2011) for background urban aerosol sampled in Pasadena during the PACO experiment (1.74 ± 0.20). A small fraction of particles

with OMF between 0.1 and 0.4 have GFs approaching that of nitric acid, which suggests a possible mixture of slightly hygroscopic organics with highly hygroscopic, acidic inorganics. Overall, there is a clear trend of suppressed GF with increasing OMF at 92% RH.

At 74% RH, on the other hand, there appears to be little relationship between OMF and GF. Inorganic constituents such as NH_4NO_3 and $(\text{NH}_4)_2\text{SO}_4$ have a GF of 1 at 74% on the deliquescence curve, while HNO_3 has a GF of 1.68. A basin-averaged 74% GF of 1.2 ± 0.10 suggests that organics do not suppress GF at lower ($< 75\%$) RH, and may even be associated with enhanced water uptake at these RHs. The absence of a clear relationship between OMF and GF at 74% suggests that organics have little effect on particle water uptake at lower ($< 75\%$) RH. These results agree with those from Aggarwal et al. (2007) and Hersey et al. (2009), which both observed RH-dependent effects of organics on hygroscopicity.

An increasingly popular metric for hygroscopicity is the so-called single parameter representation of hygroscopicity, κ , introduced by Petters and Kreidenweis (2007, 2008). κ is related to GF through the relationship:

$$S(D) = \frac{D^3 - D_d^3}{D^3 - D_d^3(1 - \kappa)} \exp \left[\frac{4\sigma M_w}{RT\rho_w D} \right] \quad (6.3)$$

for κ , where S is the saturation ratio over an aqueous droplet (0.74 or 0.92), D and D_d are the humidified and dry diameters, respectively, σ is the surface tension at the interface of air and pure water (0.072 J m^{-2}), M_w is the molecular weight of water (18 g mol^{-1}), R is the gas constant ($8.3 \text{ J mol}^{-1}\text{K}^{-1}$), T is the temperature (298 K), and ρ_w is the density of water (1 g cm^{-3}). Organics have been demonstrated to affect the surface tension of aqueous aerosols, but this effect is not explicitly accounted for in this model. Therefore, the κ parameter should be considered an “effective hygroscopicity parameter,” which includes both solute-induced water activity changes and surface tension effects (Petters and Kreidenweis, 2007; Rose et al., 2010).

With κ values calculated from DASH GF data, it is possible to relate sub-saturated water uptake with supersaturated cloud condensation nuclei (CCN) activity. This relationship is achieved by estimating critical dry diameter (D_d), the diameter above which aerosol particles activate as CCN

at a given supersaturation (S_c), using the following equations:

$$\kappa = \frac{4A^3}{27D_d^3 \ln^2 S_c}, \quad (6.4)$$

where:

$$A = \frac{4\sigma M_w}{RT\rho_w}. \quad (6.5)$$

Following Shinozuka et al. (2009) and assuming S_c of 0.2%, the relationship between κ and D_d becomes:

$$D_d = \kappa^{(-1/3)} \cdot 70 \text{ nm}. \quad (6.6)$$

For CalNex, reported values of κ and critical dry diameter at 0.2% supersaturation represent the average of κ and D_d calculated from DASH-SP GF at 74% and 92% RH. Uncertainties are estimated to be 25%, based on sizing uncertainties in the DASH-SP and RH variation in the instrument (Sorooshian et al., 2008).

Figure 6.5 shows the spatial distribution of κ in the Los Angeles Basin, with marker size and color scale corresponding to κ . The mission-averaged value of κ for CalNex is 0.32 ± 0.17 , agreeing well with a typical urban κ of 0.3 reported in a review by Wex et al. (2010) and 0.31 reported for the Western Los Angeles Basin during PACO (Hersey et al., 2011). The average D_d was 109 ± 19 nm for CalNex, compared with 105 ± 10 nm for PACO. The highest values of κ appear to be in the northeastern basin, where particulate NO_3^- concentrations increase significantly downwind from the sizable ammonia emissions associated with dairies in Chino and Riverside (Sec. 6.4). Particles sampled over the industrial/shipping areas near Long Beach also exhibited enhanced hygroscopic behavior, corresponding to sizable point-sources of sulfate. Aerosol in the corridor between Pasadena and Long Beach also exhibited relatively large κ values, and while this region had sizable organic concentrations, significant sulfate was also present, owing to closer proximity to marine sources. From this brief comparison of spatial distributions of κ and aerosol constituents, it is apparent that

the highest κ values are coincident with enhanced levels of inorganics relative to organics, suggesting that the relative abundance of inorganic aerosol constituents controls aerosol hygroscopicity in Los Angeles.

This trend is also evident in Fig. 6.6, which shows κ and critical diameter plotted against OMF, with color scale corresponding to NMF. The lines on Fig. 6.6 represent parameterizations for κ as a function of OMF for Central Mexico (Shinozuka et al., 2009), the North American West Coast (Shinozuka et al., 2009), the Western Los Angeles Basin (Hersey et al., 2011), and the current CalNex study. Immediately evident from Fig. 6.6 is the inverse relationship between κ and OMF, agreeing with results from other studies of urban hygroscopicity (Mochida et al., 2008; Meier et al., 2009; Shinozuka et al., 2009; Pan et al., 2009). The parameterizations plotted in Fig. 6.6 give insight into the hygroscopic nature of organics sampled in each study, and take the form of a linear regression where:

$$\kappa = \epsilon - \beta \cdot \text{OMF}. \quad (6.7)$$

Shinozuka et al. (2009) characterized aerosol hygroscopicity in Central Mexico and the North American West Coast, developing empirical parameterizations for κ as a function of OMF ($\kappa = 0.34 - 0.20 \cdot \text{OMF}$ and $\kappa = 0.47 - 0.43 \cdot \text{OMF}$, respectively). Following Shinozuka et al. (2009), Hersey et al. (2011) found that hygroscopicity in the Western Los Angeles Basin was parameterized by $\kappa = 0.50 - 0.29 \cdot \text{OMF}$ during the PACO study. For CalNex, κ is parameterized by $\kappa = 0.51 - 0.53 \cdot \text{OMF}$. Comparing CalNex results with those from Hersey et al. (2011), the remarkably similar ϵ values indicate that at low organic loadings, the aerosol sampled in the Western Los Angeles Basin is representative of aerosol hygroscopicity across the entire CalNex sampling area. The β values, on the other hand, are significantly different between the two studies, with the much higher β for CalNex suggesting that organics suppress hygroscopicity significantly more than the organics in the transported background urban aerosol (relatively free from local sources of primary aerosol) sampled during the Hersey et al. (2011) PACO study.

To further investigate the hygroscopic behavior of organics in the Los Angeles Basin, κ values

calculated from DASH-SP data were combined with information on the mass fraction of various organic and inorganic species from the AMS. Assuming linearly additive hygroscopicity and no interaction between aerosol constituents, it is possible to estimate the κ hygroscopicity parameter for organics. If the overall hygroscopicity parameter, κ is given by:

$$\kappa = \sum_{i=1}^n \kappa_i \cdot \chi_i, \quad (6.8)$$

where n is the number of chemical constituents, i , with mole fraction χ_i and hygroscopicity parameter κ_i , then the organic hygroscopicity parameter, κ_{org} can be estimated by:

$$\kappa_{org} = \frac{\kappa - \sum_{i=1}^{n_{inorg}} \kappa_i \cdot \chi_i}{\chi_{org}}, \quad (6.9)$$

where n_{inorg} is the number of inorganic constituents, i , with hygroscopicity parameter κ_i and mole fraction χ_i , and χ_{org} is the mole fraction of organics in the aerosol. Previous publications have assumed κ_{org} of 0.1 for “hygroscopic” organics, and 0 for “nonhygroscopic” organics (Dusek et al., 2010; Wang et al., 2010; Wex et al., 2010), while Hersey et al. (2011) found a median value of 0.14 for the Western Los Angeles Basin. Assuming κ_i for inorganics to be 0.7 (Dusek et al., 2010) and κ_i for sea salt to be 1.3 (Wex et al., 2010), Eq. 6.9 gives κ_{org} of 0.10 for aerosol sampled in the Los Angeles Basin during CalNex. The values of κ_{org} observed during CalNex are on the upper end of hygroscopicity typically assumed for organics, while those estimated in Hersey et al. (2011) are appreciably higher than that previously assumed for urban organics. It is clear that aerosol organics in Los Angeles are hygroscopic, which is an important result when predicting both sub- and super-saturated hygroscopicity of urban aerosol.

From Eq. 6.9, it is evident that κ_{org} is linearly dependent on assumptions of the hygroscopicity of inorganics, κ_{inorg} . A sensitivity study revealed that if the estimation of κ_{inorg} is increased from 0.7 to an extreme of 1.2 ($\kappa_{H_2SO_4}$), estimates of κ_{org} are reduced from 0.10 to 0.02 for CalNex. Figure 6.7 shows the effect of varying κ_{inorg} assumptions on κ_{org} for CalNex, with nonlinearity due to data filtering artifacts. The blue shadowed box indicates the range of κ_{inorg} literature values. Assuming

that sea salt aerosol does not contribute an appreciable fraction of aerosol mass, a good assumption for CalNex, given that chloride mass fraction averaged 0.01, accounting for the range of reasonable κ_{inorg} assumptions, κ_{org} for CalNex is estimated to be between 0.10 and 0.13, with a median value of 0.11.

The lower value of κ_{org} for CalNex, compared with that from the 2009 PACO study (Hersey et al., 2011), is expected. The parameterizations for predicting κ as a function of OMF suggest that aerosol organics measured during CalNex suppress hygroscopicity significantly more than those sampled during PACO, as evidenced by the significantly higher value for β in Eq. 6.7. Comparing the O:C values for the two studies, which are 0.31 ± 0.08 for CalNex, versus 0.44-0.53 during PACO, suggests that the organics sampled in CalNex should be appreciably less hygroscopic, which agrees with the parameterizations discussed above. PACO sampling was conducted at a ground site in Pasadena, representing aerosols with photochemical age on the order of 1-2 hr, with little impact from local primary emissions. During CalNex, on the other hand, flights covered the entire basin, including source-rich areas near downtown Los Angeles and Long Beach, in addition to significant flight time spent over major freeways in the basin. The difference in the effect of organics on κ between CalNex and PACO is apparently due primarily to regional variation in the character of organics and the relative importance of primary emissions, rather than any temporal difference in chemistry between the two studies.

6.6 Conclusions

This study presents the first major aircraft-based investigation of aerosol hygroscopicity across a major urban area. The Los Angeles Basin is characterized as source-rich in the west and southwest, with emissions being transported by prevailing W/SW winds toward downwind receptor sites in the east and northeast. Aerosols evolve during transport, from a population dominated by fine particles to one enhanced in larger, accumulation mode particles. This particle growth is associated with enhancements in both nitrate and organics, which reach maxima in the downwind eastern and northeastern areas of the Los Angeles Basin. Sulfate tends to be at a maximum in the western

basin, owing to closer proximity to its marine source, and in areas near Long Beach, due to industrial and shipping activities. In addition to the northeast basin, organics are also enhanced near downtown Los Angeles and in the immediate outflow from the downtown area in the northwestern basin. Ammonium closely follows nitrate concentrations, with significant enhancements in particulate ammonium downwind from major bovine emissions in the eastern basin. Organic O:C ratio steadily increases toward the eastern basin, indicating that organics become more oxidized as they are transported and aged. Averaged over the entire Los Angeles area, organics are less oxidized than those sampled in the western basin by Hersey et al. (2011) in the 2009 PACO field study, likely owing to the absence of local primary emissions near the PACO sampling site.

Hygroscopic growth factor averaged 1.74 at 92% and 1.16 at 74% during CalNex. Growth factor is significantly suppressed by the presence of organics at high RH (92%), while organics appear to have little effect on water uptake at 74%. Growth factors in CalNex are significantly higher than those reported in previous studies in the Los Angeles Basin, suggesting that emissions controls over the last two decades may have resulted in aerosol containing a smaller fraction of relatively insoluble primary species, and instead exhibiting an organic fraction dominated by oxidized constituents.

Calculations of the hygroscopicity parameter κ reveal that aerosols in Los Angeles are comparably hygroscopic to those in other urban areas, with a basin-averaged κ of 0.32 ± 0.17 . Organics act to suppress κ significantly in the Los Angeles Basin, with κ exhibiting a greater degree of sensitivity to organic mass fraction than in a recent study of aerosols in 1-2 hr old transported pollution during the PACO study in Pasadena (Hersey et al., 2011). Calculations of κ_{org} revealed that organics were significantly less hygroscopic in CalNex than during PACO, with κ_{org} of 0.10 for CalNex, compared with 0.14 for PACO. The organics sampled during CalNex were, on average, less oxidized than those reported by Hersey et al. (2011), indicating that oxidation state is a major factor determining the hygroscopic activity of organics.

While overall κ is similar between the 2009 PACO study and CalNex, κ_{org} was significantly lower in CalNex. One major difference between the two studies is that PACO was conducted at a fixed ground site roughly 10 km from downtown Los Angeles, receiving a steady influx of aerosols aged

by 1-2 hr and generally free from local primary sources, while CalNex represents composition over the entire Los Angeles Basin, including many source-rich areas. Despite the fact that the PACO ground site is relatively near the “source-rich” western part of the basin, significant oxidation was able to occur, transforming the organic fraction into oxidized organics on relatively short timescales. Further, the PACO sampling site allowed for investigation of urban background pollution free from major local emissions of primary aerosols. This result highlights the complex nature of aerosol organics in an urban area such as Los Angeles, where different regions may have appreciably different chemical signatures and hygroscopic properties.

Bibliography

- Aggarwal, S., Mochida, M., Kitamori, Y., and Kawamura, K.: Chemical closure study on hygroscopic properties of urban aerosol particles in Sapporo, Japan, *Environ. Sci. Tech.*, 41, 6920–6925, 2007.
- Aiken, A. C., DeCarlo, P. F., , Kroll, J., Worsnop, D., J.A., H., Docherty, K., Ulbrich, I., Mohr, C., Kimmel, J., Sueper, D., Sun, Y., Zhang, Q., Trimborn, A., Northway, M., Ziemann, P., Canagaratna, M., Onasch, T., Alfarra, M., Prevot, A., Dommen, J., Duplissy, J., Metzger, A., Baltensperger, U., and Jimenez, J. L.: O/C and OM/OC Ratios of Primary, Secondary, and Ambient Organic Aerosols with High-Resolution Time-of-Flight Aerosol Mass Spectrometry, *Environ. Sci. Technol.*, 42, 4478–4485, 2008.
- Albrecht, B.: Aerosols, cloud microphysics, and fractional cloudiness, *Science*, 245, 1227, 1989.
- Allan, J., Delia, A., Coe, H., Bower, K., Alfarra, M., Jimenez, J., Middlebrook, A., Drewnick, F., Onasch, T., Canagaratna, M., Jayne, J., and Worsnop, D.: A generalised method for the extraction of chemically resolved mass spectra from aerodyne aerosol mass spectrometer data, *J. Aerosol Sci.*, 35, 909–922, doi:10.1016/j.jaerosci.2004.02.007, 2004.
- Asa-Awuku, A., Moore, R., Nenes, A., Baherini, R., Holloway, J., Brock, C., Middlebrook, A., Ryerson, T., Jimenez, J., DeCarlo, P., Hecobain, A., Weber, R., Stickel, R., Tanner, D., and

- Huey, L.: Airborne Cloud Condensation Nuclei Measurements during the 2006 Texas Air Quality Study, *J. Geophys. Res.*, *submitted*, 2011.
- Bremner, J., Haub, C., Lee, M., Mather, M., , and Zuehlke, E.: World Population Highlights: Key Findings From PRB's 2009 World Population Data Sheet, Population Reference Bureau, 2009.
- Cocker, D. R., Whitlock, N. E., Flagan, R. C., and Seinfeld, J. H.: Hygroscopic properties of Pasadena, California aerosol, *Aerosol Sci. Technol.*, *35*, 637–647, 2001.
- Cubison, M., Ervens, B., Feingold, G., Docherty, K., Ulbrich, I., Shields, L., Prather, K., Hering, S., and Jimenez, J.: The influence of chemical composition and mixing state of Los Angeles urban aerosol on CCN number and cloud properties, *Atmos. Chem. Phys.*, *8*, 5649–5667, 2008.
- Docherty, K. S., Stone, E. A., Ulbrich, I. M., DeCarlo, P. F., Snyder, D. C., Schauer, J. J., Peltier, R. E., Weber, R. J., Murphy, S. M., Seinfeld, J. H., Grover, B. D., Eatough, D. J., and Jimenez, J. L.: Apportionment of Primary and Secondary Organic Aerosols in Southern California during the 2005 Study of Organic Aerosols in Riverside (SOAR-1), *Environ. Sci. Technol.*, *42*, 7655–7662, 2008.
- Drewnick, F., Jayne, J. T., Canagaratna, M., Worsnop, D. R., and Demerjian, K. L.: Measurement of ambient aerosol composition during the PMTACS-NY 2001 using an aerosol mass spectrometer. Part II: Chemically speciated mass distributions, *Aerosol. Sci. Tech.*, *38*, 104–117, suppl. 1, 2004a.
- Drewnick, F., Schwab, J. J., Jayne, J. T., Canagaratna, M., Worsnop, D. R., and Demerjian, K. L.: Measurement of ambient aerosol composition during the PMTACS-NY 2001 using an aerosol mass spectrometer. Part I: Mass concentrations, *Aerosol. Sci. Tech.*, *38*, 92–103, suppl. 1, 2004b.
- Dusek, U., Frank, G., Curtius, J., Drewnick, F., Schneider, J., Kürten, A., Rose, D., Andreae, M., Borrmann, S., and Pöschl, U.: Enhanced organic mass fraction and decreased hygroscopicity of cloud condensation nuclei (CCN) during new particle formation events, *Geophys. Res. Lett.*, *37*, 2010.

- Hersey, S., Craven, J., Schilling, K., Metcalf, A., Sorooshian, A., Chan, M., Flagan, R., and Seinfeld, J.: The Pasadena Aerosol Characterization Observatory (PACO): chemical and physical analysis of the Western Los Angeles Basin aerosol, *Atmos. Chem. Phys. Disc.*, 11, 2011.
- Hersey, S. P., Sorooshian, A., Murphy, S. M., Flagan, R. C., and Seinfeld, J. H.: Aerosol hygroscopicity in the marine atmosphere: a closure study using high-time-resolution, multiple-RH DASH-SP and size-resolved C-ToF-AMS data, *Atmos. Chem. Phys.*, 9, 2543–2554, 2009.
- Jaffe, D., Anderson, T., Covert, D., Kotchenruther, R., Trost, B., Danielson, J., Simpson, W., Berntsen, T., Karlsdottir, S., Blake, D., et al.: Transport of Asian air pollution to North America, *Geophys. Res. Lett.*, 26, 711–714, 1999.
- Liang, Q., Jaeglé, L., Jaffe, D., Weiss-Penzias, P., Heckman, A., and Snow, J.: Long-range transport of Asian pollution to the northeast Pacific: Seasonal variations and transport pathways of carbon monoxide, *J. Geophys. Res.*, 109, 2004.
- Liu, H., Jacob, D., Bey, I., Yantosca, R., Duncan, B., and Sachse, G.: Transport pathways for Asian pollution outflow over the Pacific: Interannual and seasonal variations, *J. Geophys. Res.*, 108, 2009–2010, 2003.
- Massling, A., Stock, M., and Wiedensohler, A.: Diurnal, weekly, and seasonal variation of hygroscopic properties of submicrometer urban aerosol particles, *Atmos. Environ.*, 39, 3911–3922, 2005.
- Massling, A., Stock, M., Wehner, B., Wu, Z. J., Hu, M., Brüggemann, E., Gnauk, T., Herrmann, H., and Wiedensohler, A.: Size segregated water uptake of the urban submicrometer aerosol in Beijing, *Atmos. Environ.*, 43, 1578–1589, 2009.
- Meier, J., Wehner, B., Massling, A., Birmili, W., Nowak, A., Gnauk, T., Brüggemann, E., Herrmann, H., Min, H., and Wiedensohler, A.: Hygroscopic growth of urban aerosol particles in Beijing(China) during wintertime: a comparison of three experimental methods, *Atmos. Chem. Phys.*, 9, 6865–6880, 2009.

- Mochida, M., Kuwata, M., Miyakawa, T., Takegawa, N., Kawamura, K., and Kondo, Y.: Relationship between hygroscopicity and cloud condensation nuclei activity for urban aerosols in Tokyo, *J. Geophys. Res.*, 111, D23 204, 2006.
- Mochida, M., Miyakawa, T., Takegawa, N., Morino, Y., Kawamura, K., and Kondo, Y.: Significant alteration in the hygroscopic properties of urban aerosol particles by the secondary formation of organics, *Geophys. Res. Lett.*, 35, 2008.
- Pan, X., Yan, P., Tang, J., Ma, J., Wang, Z., Gbaguidi, A., and Sun, Y.: Observational study of influence of aerosol hygroscopic growth on scattering coefficient over rural area near Beijing mega-city, *Atm. Chem. Phys.*, 9, 7519–7530, 2009.
- Petters, M. D. and Kreidenweis, S. M.: A single parameter representation of hygroscopic growth and cloud condensation nucleus activity, *Atmos. Chem. Phys.*, 7, 1961–1971, 2007.
- Petters, M. D. and Kreidenweis, S. M.: A single parameter representation of hygroscopic growth and cloud condensation nucleus activity - Part 2: Including solubility, *Atmos. Chem. Phys.*, 8, 6273–6279, 2008.
- Prenni, A., DeMott, P., Kreidenweis, S., Sherman, D., Russell, L., and Ming, Y.: The effects of low molecular weight dicarboxylic acids on cloud formation, *J. Phys. Chem. A*, 105, 11 240–11 248, 2001.
- Rose, D., Nowak, A., Achtert, P., Wiedensohler, A., Hu, M., Shao, M., Zhang, Y., Andreae, M., and Pöschl, U.: Cloud condensation nuclei in polluted air and biomass burning smoke near the mega-city Guangzhou, China- Part 1: Size-resolved measurements and implications for the modeling of aerosol particle hygroscopicity and CCN activity, *Atmos. Chem. Phys.*, 10, 3365–3383, 2010.
- Shinozuka, Y., Clarke, A., DeCarlo, P., Jimenez, J., Dunlea, E., Roberts, G., Tomlinson, J., Collins, D., Howell, S., Kapustin, V., et al.: Aerosol optical properties relevant to regional remote sensing of CCN activity and links to their organic mass fraction: airborne observations over Central Mexico and the US West Coast during MILAGRO/INTEX-B, *Atmos. Chem. Phys.*, 9, 6727–6742, 2009.

- Sorooshian, A., Hersey, S., Brechtel, F. J., Corless, A., Flagan, R. C., and Seinfeld, J. H.: Rapid, size-resolved aerosol hygroscopic growth measurements: Differential aerosol sizing and hygroscopicity spectrometer probe (DASH-SP), *Aerosol Sci. Technol.*, 42, 445–464, 2008.
- Swietlicki, E., Hansson, H., Hameri, K., Svenningsson, B., Massling, A., McFiggans, G., McMurry, P., Petaja, T., Tunved, P., Gysel, M., et al.: Hygroscopic properties of submicrometer atmospheric aerosol particles measured with H-TDMA instruments in various environments A review, *Tellus B*, 60, 432–469, 2008.
- Tiitta, P., Miettinen, P., Vaattovaara, P., Joutsensaari, J., Pet, T., Virtanen, A., Raatikainen, T., Aalto, P., Portin, H., Romakkaniemi, S., et al.: Roadside aerosol study using hygroscopic, organic and volatility TDMA: Characterization and mixing state, *Atmos. Environ.*, 44, 976–986, 2010.
- Twomey, S.: Pollution and the planetary albedo, *Atmospheric Environment* (1967), 8, 1251–1256, 1974.
- Wang, J., Cubison, M., Aiken, A., Jimenez, J., and Collins, D.: The importance of aerosol mixing state and size-resolved composition on CCN concentration and the variation of the importance with atmospheric aging of aerosols, *Atmos. Chem. Phys.*, 10, 7267–7283, 2010.
- Watson, J. G., Chow, J. C., Lu, Z. Q., Fujita, E. M., Lowenthal, D. H., Lawson, D. R., and Ashbaugh, L. L.: Chemical Mass-Balance Source Apportionment of Pm(10) during the Southern California Air-Quality Study, *Aerosol Sci. Technol.*, 21, 1–36, 1994.
- Wex, H., McFiggans, G., Henning, S., and Stratmann, F.: Influence of the external mixing state of atmospheric aerosol on derived CCN number concentrations, *Geophys. Res. Lett.*, 37, L10 805, 2010.
- Zhang, Q., Jimenez, J., Canagaratna, M., Allan, J., Coe, H., Ulbrich, I., Alfarra, M., Takami, A., Middlebrook, A., Sun, Y., et al.: Ubiquity and dominance of oxygenated species in organic aerosols in anthropogenically-influenced Northern Hemisphere midlatitudes, *Geophys. Res. Lett.*, 34, L13 801, 2007.

Zhang, X. and McMurray, S.: Mixing characteristics and water content of submicron aerosols measured in Los Angeles and at the Grand Canyon, *Atmos. Environ. A.*, 27, 1593–1607, 1993.

Table 6.1: Summary of flights and instrument performance for CIRPAS Twin Otter operations during CalNex.

CalNex Twin Otter Flight and Instrument Performance Summary Table

RF	Flight Date (UTC)	Flight Time (UTC)	General Flight Information		Aerosol Physics and Chemistry										Optical Particle Counters					CIRPAS Misc	
			Mission Type	Flight PI	Coord	DMA	AMS	ATOFMS	WSOC	CCN	DASH	SP2	PASS3	PSAP	CPC1	CPC2	CPC3	PCASP	CAFS	MET	NAV
1	5/4/10	18:01-21:23	LA basin, 1+ loops with missed approaches	Andrew	-	OK	N/A	OK	OK	down	OK	OK	OK	OK	OK	OK	OK	OK	OK	OK	OK
2	5/5/10	18:04-22:10	LA basin, 2 loops with missed approaches	Scott	-	OK	N/A	OK	OK	down	OK	OK	OK	OK	OK	OK	OK	OK	OK	OK	OK
3	5/6/10	18:06-22:39	LA basin, 2 loops without missed approaches	Scott	-	OK	N/A	>30%	OK	OK	OK	OK	OK	OK	OK	OK	OK	OK	OK	OK	OK
4	5/7/10	18:06-21:43	LA basin loops, clean in Banning	Stinn	-	OK	N/A	OK	OK	OK	OK	OK	OK	OK	OK	OK	OK	OK	OK	OK	OK
5	5/7/10	18:09-21:03	LA basin loops, clean in Banning	Stinn	-	OK	N/A	OK	OK	OK	OK	OK	OK	OK	OK	OK	OK	OK	OK	OK	OK
6	5/7/10	17:56-22:08	LA basin, 1 loop + Sallion Sea	Scott	-	OK	N/A	down	OK	OK	OK	OK	OK	OK	OK	OK	OK	OK	OK	OK	OK
7	5/13/10	18:05-21:54	LA basin, 1 loop + Sallion Sea	Scott	-	OK	N/A	OK	OK	OK	OK	OK	OK	OK	OK	OK	OK	OK	OK	OK	OK
8	5/14/10	17:59-22:01	LA basin, 3 loops	Andrew	-	OK	N/A	OK	OK	OK	OK	OK	OK	OK	OK	OK	OK	OK	OK	OK	OK
9	5/15/10	18:13-22:13	LA Basin, 2 loops, N-S tracks	Scott	-	OK	N/A	OK	OK	OK	OK	OK	OK	OK	OK	OK	OK	OK	OK	OK	OK
10	5/15/10	18:59-22:53	LA Basin, 2 loops, just after a front	Andrew	-	OK	N/A	OK	OK	OK	OK	OK	OK	OK	OK	OK	OK	OK	OK	OK	OK
11	5/19/10	18:40-22:45	LA Basin, coordinated flight plan, N-S tracks	Scott	P3, KA	OK	OK	OK	OK	OK	OK	OK	OK	OK	OK	OK	OK	OK	OK	OK	OK
12	5/20/10	18:53-22:58	San Joaquin valley, morning clouds, El Capon pass	Andrew	KA	OK	OK	N/A	OK	OK	OK	OK	OK	OK	OK	OK	OK	OK	OK	OK	OK
13	5/21/10	17:57-22:05	LA Basin, 2 loops, N-S tracks, El Capon & Banning passes	Scott	KA	OK	OK	N/A	OK	OK	OK	OK	OK	OK	OK	OK	OK	OK	OK	OK	OK
14	5/22/10	18:01-22:12	San Joaquin valley, N-S track up to Fresno and back	Andrew	KA	OK	OK	N/A	OK	OK	OK	OK	OK	OK	OK	OK	OK	OK	OK	OK	OK
15	5/24/10	18:01-22:03	LA Basin, with Santa Ana, El Capon pass, and Sallion Sea	Scott	KA	OK	OK	N/A	OK	OK	OK	OK	OK	OK	OK	OK	OK	OK	OK	OK	OK
16	5/25/10	18:27-22:31	LA Basin, with Santa Ana, El Capon pass, and Sallion Sea	Andrew	KA	OK	OK	N/A	OK	OK	OK	OK	OK	OK	OK	OK	OK	OK	OK	OK	OK
17	5/27/10	17:59-21:45	LA Basin, 3 loops	Andrew	-	OK	OK	N/A	OK	OK	OK	OK	OK	OK	OK	OK	OK	OK	OK	OK	OK
18	5/28/10	17:58-22:03	LA Basin, 3 loops, with tanker firecon 91	Scott	-	OK	OK	N/A	OK	OK	OK	OK	OK	OK	OK	OK	OK	OK	OK	OK	OK

Coord. legend:
 KA NASA King Air
 P3 NOAA P3

Status legend:
 OK* SCA mode (seamless flows) not active
 OK* Data not yet analyzed due to a different calibration

Instrument performance legend:
 OK Instrument was on and functioning well during the entire flight
 >30% Instrument was functioning for most of the flight (suffered some loss of data, quantity/quality)
 <50% Instrument was not functioning, or there were other errors resulting in no good data for this flight
 down Instrument was not on board or not turned on during flight
 N/A

Instrument description:	Measurement Description
DMA	Dry particle size distributions from 15 nm to 1 micron
AMS	Sub-micron, non-refractory size-resolved and bulk aerosol composition
ATOFMS	Single-particle composition and size from 70 nm to 1.2 micron
CU-S-TOC	Water-soluble organic carbon (WSOC)
DASH-SP	Cloud droplet activation characteristics
SP2	Growth factors for 180, 175, 200, and 225 nm dry particles at 74 and 92% relative humidity
PASS3	Refractory black carbon number and mass distributions with coating information
PSAP	Absorption and scattering coefficient of aerosol particles
CPC1	Filter-based absorption coefficient
CPC2	Total aerosol number concentration
PCASP	Cloud droplet activation
CAFS	Total aerosol number concentration
Met	Particle size distribution from 120 nm to 2.5 micron
Nav	Aerosol and cloud hydrometeor size distributions from 0.5 to 50 micron and precipitation size distributions from 25 to 1550 micron
	Meteorology data
	Navigation data system (C = C-MGTTS; N = NovalTel; T = TransVector)

Last updated: 4/18/11

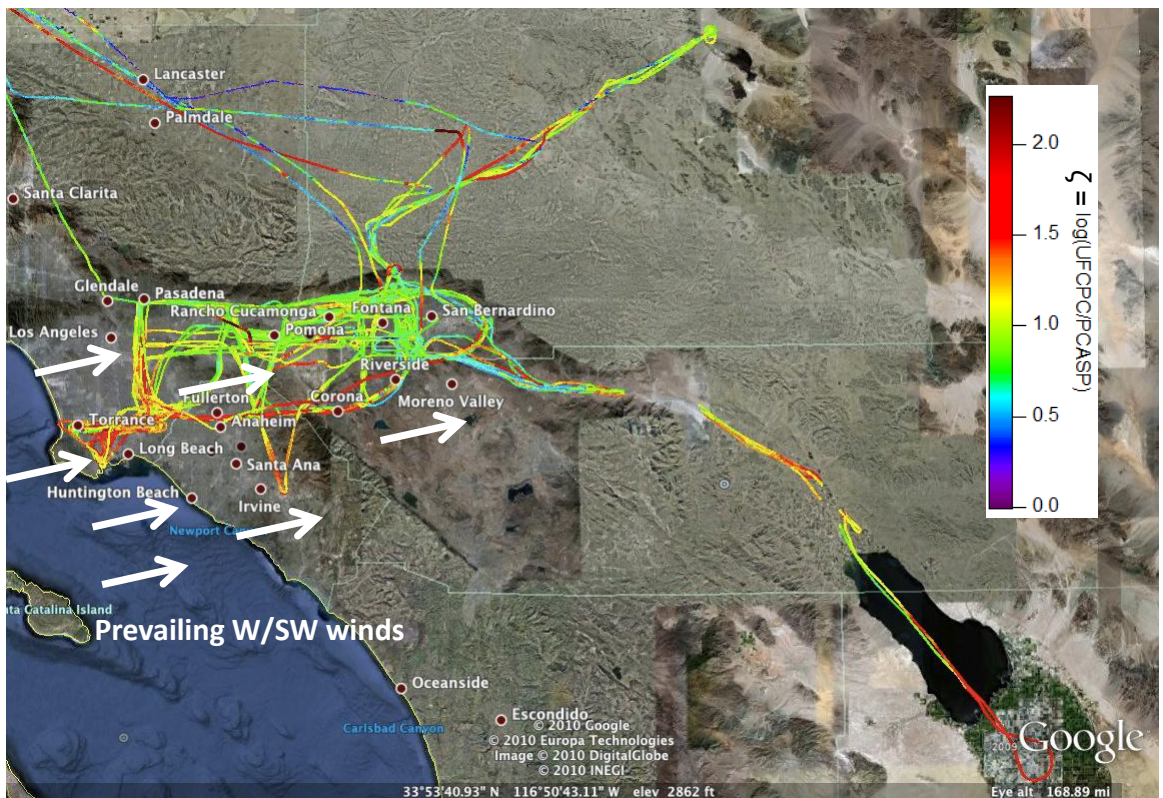


Figure 6.1: Spatial distribution of the dimensionless ζ , showing the relative abundance of fine particles near source-rich areas. Data are plotted on a Google Earth map layer.

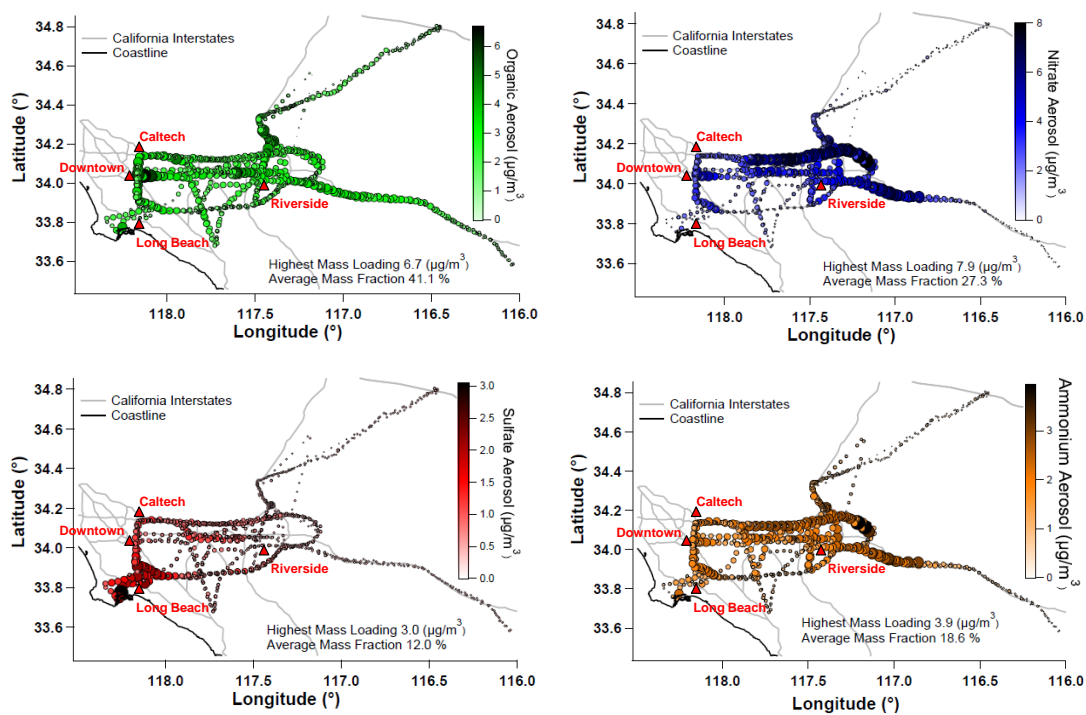


Figure 6.2: AMS composition ($\mu\text{g}/\text{m}^3$), showing organic (green), sulfate (red), nitrate (blue) and ammonium (orange) concentrations in the Los Angeles Basin. Marker sizes are proportional to species concentration.

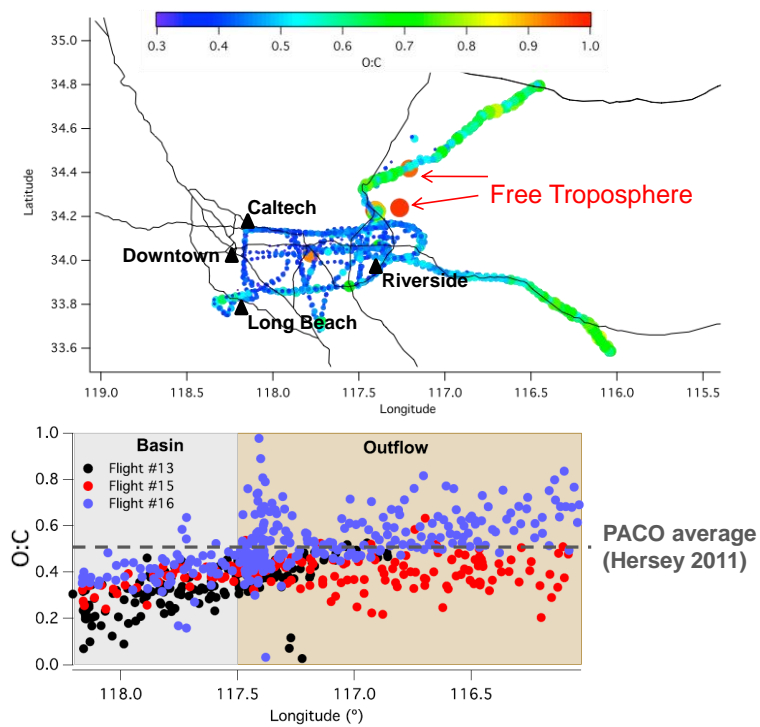


Figure 6.3: Approximate O:C ratio plotted spatially (top) and as a function of longitude (bottom). Dashed line on the bottom plot represents the mission-averaged O:C ratio during the 2009 PACO study in the western Los Angeles Basin (Hersey et al., 2011).

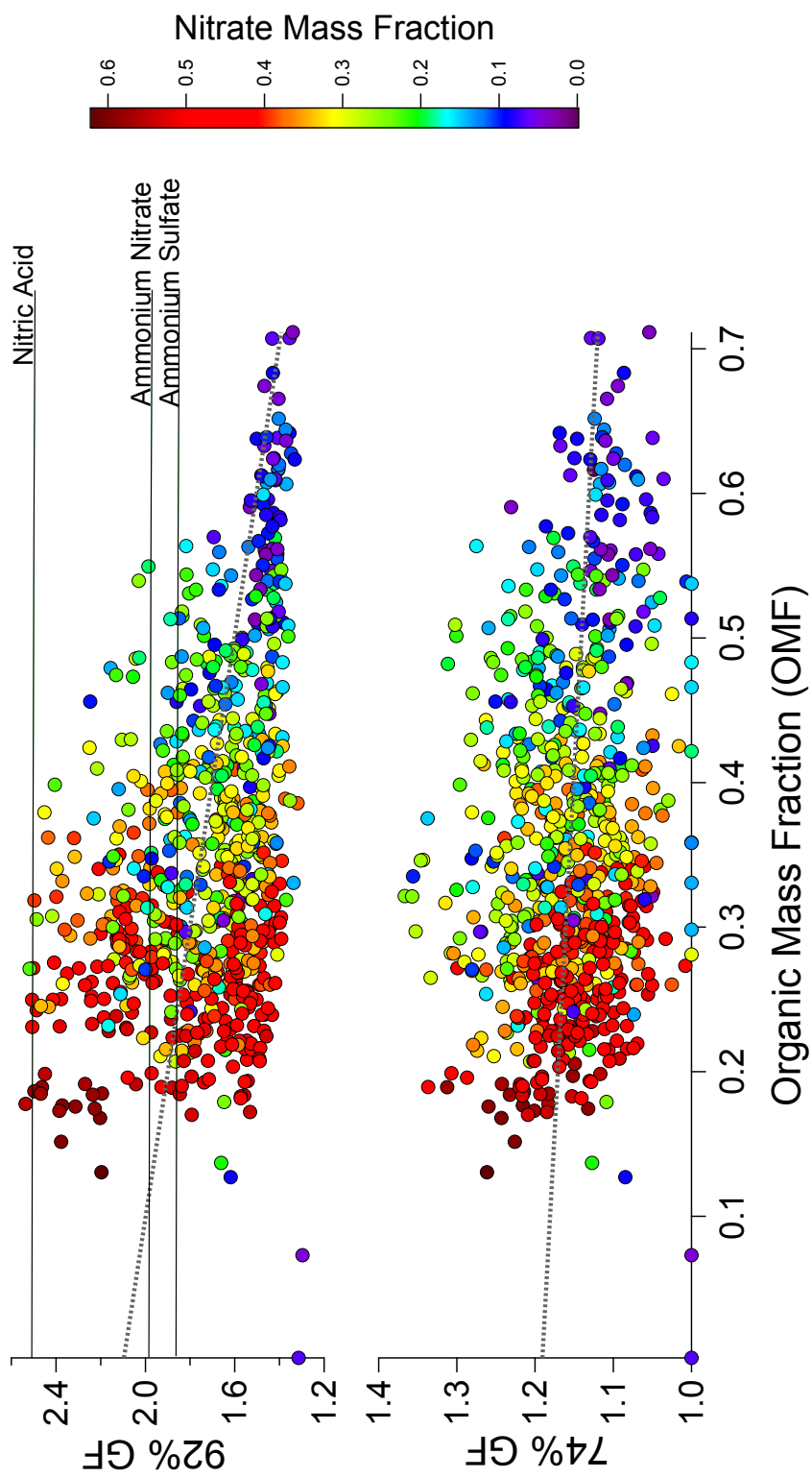


Figure 6.4: Hygroscopic GF at 74% (bottom) and 92% (top) RH as a function of OMF. Dotted lines are a linear fit of OMF. Dotted lines are a linear fit of GF data; solid lines are GFs for common inorganic aerosol constituents.

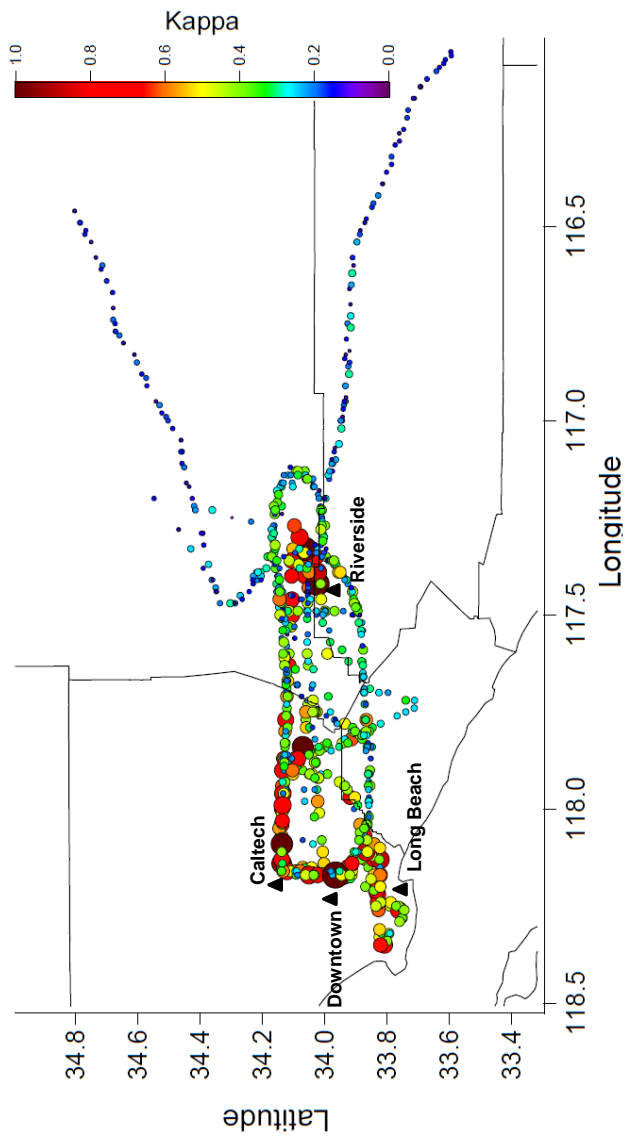


Figure 6.5: κ hygroscopicity parameter values for the Los Angeles Basin, with color scale and marker size both proportional to κ .

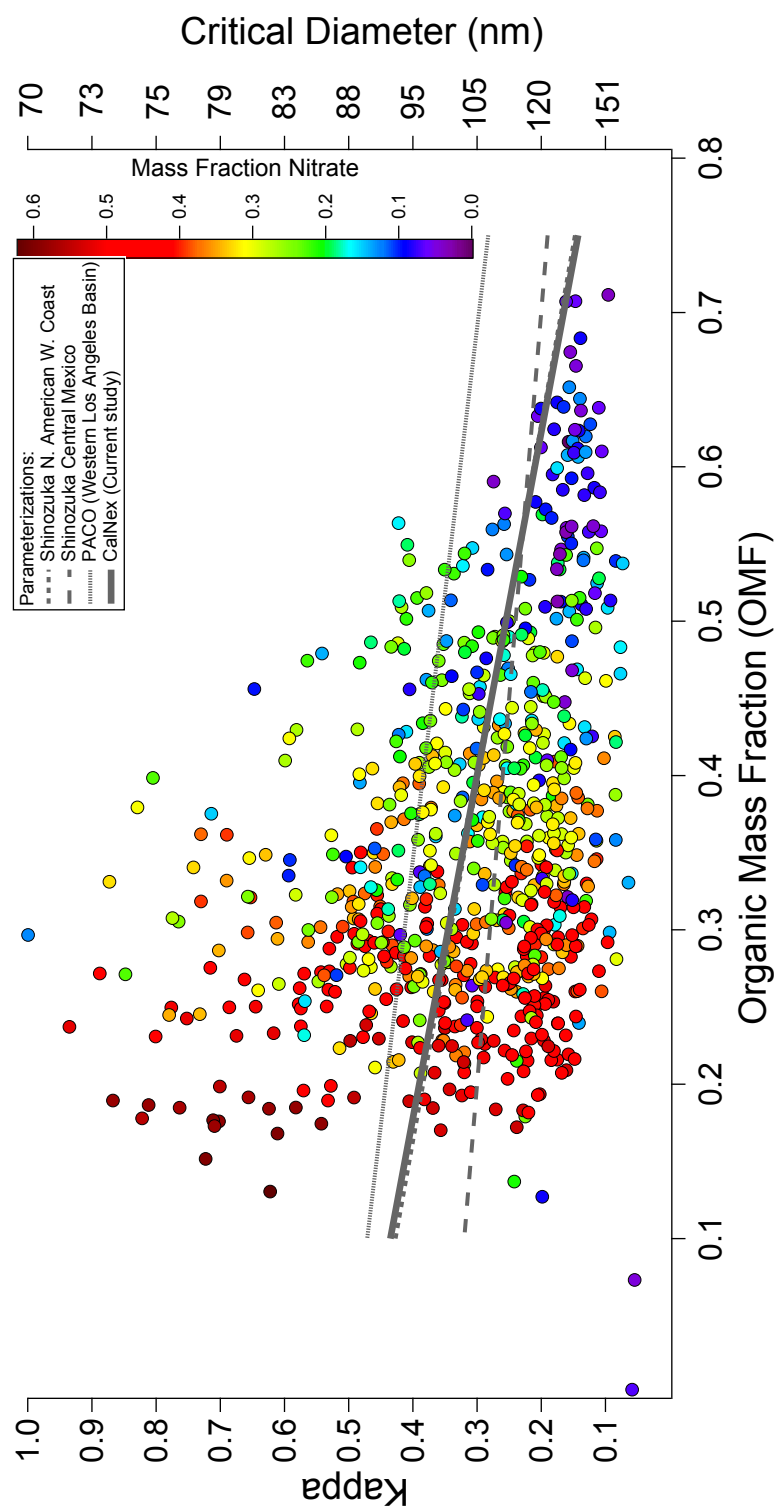


Figure 6.6: κ plotted as a function of OMF, with color scale corresponding to NMF. Lines represent parameterizations from previous studies.

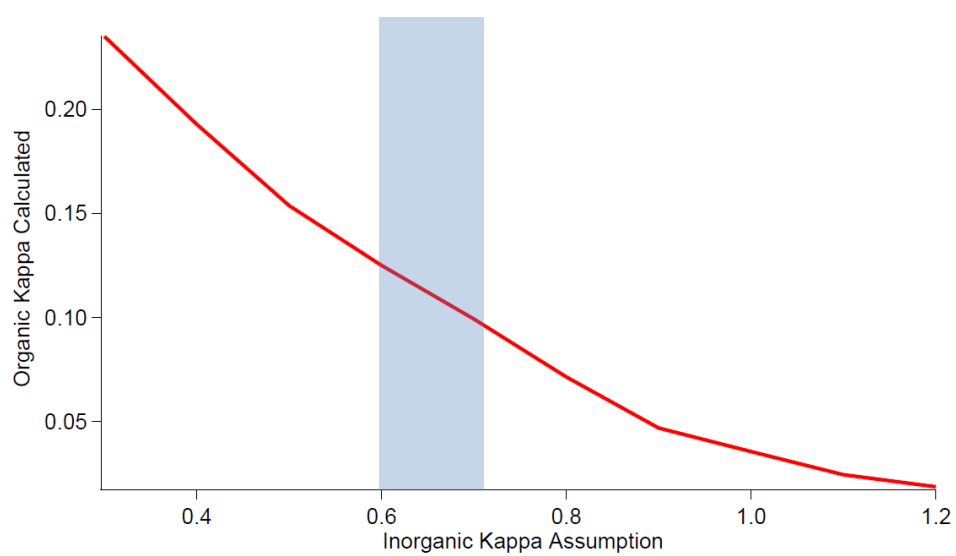


Figure 6.7: Sensitivity of κ_{org} to κ_{inorg} estimates, with the blue shaded box representing the range of κ_{inorg} commonly assumed in the literature, in the absence of significant NaCl influence.

Chapter 7

Conclusions

Atmospheric aerosols are complex in their sources, evolution, and interactions with water vapor in the atmosphere. This thesis presents techniques for measuring aerosol properties, as well as results from a number of field and laboratory studies aimed at addressing uncertainties in the sources, evolution, and water uptake characteristics of aerosols in both marine and urban areas.

Chapter 2 introduces a novel instrument for measuring aerosol hygroscopicity, the most important factor determining size, and therefore direct radiative impact of aerosol particles. The Differential Aerosol Sizing and Hygroscopicity Spectrometer Probe (DASH-SP) combines differential mobility analysis and multiple-RH humidification, followed by rapid optical sizing for particles from 135 nm to over 1 μm . An iterative data processing algorithm calculates both humidified particle diameter and “effective” refractive index by relating electrical pulse height, refractive index, and particle diameter on an empirically-derived 3-dimensional solution surface. Uncertainty in growth factor measurements is demonstrated to be less than 5%, and refractive index calculations agree well with theory.

The DASH-SP was first deployed in the MASE-II aircraft-based field experiment in July 2007, and Chapter 3 summarizes results from that study. Two flights were impacted by continental airmasses, exhibiting elevated organic volume fraction and significantly suppressed growth factor at high RH, but no impact on growth factor at low RH, owing to the characteristics of growth curves for organics. Organics were enhanced in above-cloud sampling legs, and corresponded to a similar trend of significantly suppressed GF at high RH, but little impact at low RH. Organics were found to be uniformly highly oxidized ($\text{O:C} = 0.92 \pm 0.33$ mission average), and the most important factor determining GF was the fraction of organics in the aerosol. A simple empirical model was able to accurately predict GF from just RH and the volume fraction of organics.

Chapter 4 presents results from PACO, a ground-based ambient sampling experiment conducted during the summer of 2009. Sampling took place on the Caltech campus, a site positioned to sample a continuous influx of transported Los Angeles pollution with photochemical age on the order of 1-2 hr in the afternoon, and free from the influence from local primary sources. Sampling spanned three distinct meteorological regimes, with the first characterized by a series of low-pressure systems, the

second by typical marine-layer influenced early-summer meteorology, and the third characterized by hot, dry conditions with little marine influence. Organics comprised the dominant fraction of aerosols in all three regimes, and were significantly more oxidized during the marine-layer-influenced regime II, suggesting that aqueous oxidation processes may be important for producing oxidized organic aerosol in Los Angeles. Inorganic constituents were typically found in accumulation mode aerosol, and afternoon SOA production coincided with the appearance of a fine mode in the aerosol. Positive Matrix Factorization (PMF) analysis of AMS data revealed a reduced hydrocarbon-like, oxidized semivolatile, and oxidized low-volatility organic fractions (HOA, SV-OOA, and LV-OOA, respectively). HOA is typically a minor constituent, and appears to be transported to the sampling site in periodic plumes. SV-OOA shows distinct diurnal trends that correspond to O₃ concentrations, solar radiation, and the appearance of a fine aerosol mode, suggesting that it consists of early-generation SOA products that are locally produced on short timescales. LV-OOA appears to be an aged background species residing in accumulation mode aerosol, and dominates the organic fraction during regimes I and II. Hygroscopicity was found to be a strong function of organic mass fraction (OMF), but organics appear to be more hygroscopic in transported Los Angeles pollution than in previous studies, likely because of their high degree of oxidation.

PACO sampling coincided with a major forest fire event in Los Angeles County, and Chapter 5 explores the impact of forest fires on concentrations of water soluble organic carbon (WSOC). In the absence of forest fire impact, WSOC shows diurnal trends corresponding to seabreeze pollutant transport and concurrent photooxidation. WSOC concentrations were significantly higher under the influence of fire emissions, with concentrations peaking in the overnight to early morning hours, when winds were favorable for transport from the fire. These fire-impacted periods saw strong correlations between WSOC, nitrate and chloride ions, total organic mass, and m/z 60, a biomass burning tracer in the AMS. Examining ratios of AMS markers m/z 43, 44, and 57, as well as WSOC, it appears that WSOC is a complex mixture of acidic and non-acidic oxidized organics, in addition to aliphatic compounds. Results suggest that the species comprising WSOC evolve diurnally as aliphatic and non-acid oxygenated organics give way to more oxidized acid-oxygenates.

Finally, Chapter 6 summarizes DASH-SP results from the May 2010 aircraft-based CalNex campaign. Aerosols evolve as they are transported from source-rich areas of the western and southwestern Los Angeles Basin toward downwind receptor sites in the east and northeast. This evolution corresponds to growth in particle size, enhancements in organics due to SOA condensation, and enhancements in ammonium and nitrate downwind from major ammonia emissions. Aerosol hygroscopicity is a strong function of organic mass fraction (OMF) across the Los Angeles Basin. Basin-averaged organics sampled during CalNex appear to suppress hygroscopicity more significantly than organics sampled during PACO, owing to a greater influence of primary sources during CalNex sampling. Overall hygroscopicity agrees well with results from previous studies in urban areas, and organics in Los Angeles fall on the high end of reported organic hygroscopicity values for urban aerosol.

Appendix A

Comprehensive airborne characterization of aerosol from a major bovine source*

*Reproduced with permission from “Comprehensive airborne characterization of aerosol from a major bovine source” by Sorooshian, A., Murphy, S.M., Hersey S.P., Gates, H., Padro, L.T., Nenes, A., Brechtel, F.J., Jonsson, H., Flagan R.C., and Seinfeld, J.H., *Atmospheric Chemistry and Physics*, 8 (2), 5489–5520, 2008. Copyright 2008 by Authors. This work is licensed under a Creative Commons License.

Comprehensive airborne characterization of aerosol from a major bovine source

A. Sorooshian^{1,*}, S. M. Murphy¹, S. Hersey¹, H. Gates¹, L. T. Padre², A. Nenes^{2,3}, F. J. Brechtel^{1,4}, H. Jonsson⁵, R. C. Flagan¹, and J. H. Seinfeld¹

¹Departments of Environmental Science and Engineering and Chemical Engineering, California Institute of Technology, Pasadena, CA, USA

²School of Chemical and Biomolecular Engineering, Georgia Institute of Technology, Atlanta, GA, USA

³School of Earth and Atmospheric Sciences, Georgia Institute of Technology, Atlanta, GA, USA

⁴Brechtel Manufacturing Inc., Hayward, CA, USA

⁵Center for Interdisciplinary Remotely-Piloted Aircraft Studies, Naval Postgraduate School, Monterey, CA, USA

*now at: Cooperative Inst. for Research in the Atmosphere (CIRA), Colorado State University, Fort Collins, CO, USA

Received: 23 April 2008 – Published in Atmos. Chem. Phys. Discuss.: 3 June 2008

Revised: 12 August 2008 – Accepted: 15 August 2008 – Published: 12 September 2008

Abstract. We report an extensive airborne characterization of aerosol downwind of a massive bovine source in the San Joaquin Valley (California) on two flights during July 2007. The Center for Interdisciplinary Remotely-Piloted Aircraft Studies (CIRPAS) Twin Otter probed chemical composition, particle size distribution, mixing state, sub- and supersaturated water uptake behavior, light scattering properties, and the interrelationship between these parameters and meteorology. Total PM_{1.0} levels and concentrations of organics, nitrate, and ammonium were enhanced in the plume from the source as compared to the background aerosol. Organics dominated the plume aerosol mass (~56–64%), followed either by sulfate or nitrate, and then ammonium. Particulate amines were detected in the plume aerosol by a particle-into-liquid sampler (PILS) and via mass spectral markers in the Aerodyne C-ToF-AMS. Amines were found to be a significant atmospheric base even in the presence of ammonia; particulate amine concentrations are estimated as at least 14–23% of that of ammonium in the plume. Enhanced sub- and supersaturated water uptake and reduced refractive indices were coincident with lower organic mass fractions, higher nitrate mass fractions, and the detection of amines. The likelihood of suppressed droplet growth owing to kinetic limitations from hydrophobic organic material is explored. After removing effects associated with size distribution and mixing state, the normalized activated fraction of cloud condensation nuclei (CCN) increased as a function of the subsaturated

hygroscopic growth factor, with the highest activated fractions being consistent with relatively lower organic mass fractions and higher nitrate mass fractions. Subsaturated hygroscopic growth factors for the organic fraction of the aerosol are estimated based on employing the Zdanovskii-Stokes Robinson (ZSR) mixing rule. Representative values for a parameterization treating particle water uptake in both the sub- and supersaturated regimes are reported for incorporation into atmospheric models.

1 Introduction

Bovine emissions are major sources of methane (CH₄), nitrous oxide (N₂O), and ammonia (NH₃); they are also the dominant anthropogenic source for amines (Schade and Crutzen, 1995). Ammonia is the dominant base in the atmosphere, efficiently neutralizing acidic substances. The main global sources of ammonia are from livestock waste, fertilizer applications, biomass burning, motor vehicle emissions, and coal combustion (Apsimon et al., 1987; Asman and Janssen, 1987; Kleeman et al., 1999; Anderson et al., 2003; Battye et al., 2003). Typical ammonia mixing ratios over continents range between 0.1 and 10 ppb (Edgerton et al., 2007, and references therein), while levels as high as a few ppm have been reported near areas of extensive livestock operations (Rumburg et al., 2006).

The principal inorganic aerosol components involving ammonia are ammonium nitrate and ammonium sulfate. The formation of these inorganic salts depends on temperature, relative humidity (RH), and concentrations of NH₃, nitric



Correspondence to: J. H. Seinfeld
 (seinfeld@caltech.edu)

acid (HNO_3), and sulfur dioxide (SO_2). Ammonium nitrate tends to form after sulfuric acid is completely neutralized. Atmospheric ammonium nitrate generally obeys thermodynamic equilibrium with gaseous nitric acid and ammonia (Stelson et al., 1979; Doyle et al., 1979; Stelson and Seinfeld, 1982a, 1982b; Russell et al., 1983; Hildemann et al., 1984; Zhang et al., 2002; Takahama et al., 2004; Yu et al., 2005), although some studies have pointed out that factors such as mass transport limitations can, at times, result in departures from equilibrium (Wexler and Seinfeld, 1992; Meng and Seinfeld, 1996; Fridlind and Jacobson, 2000; Fridlind et al., 2000). The equilibrium between particulate ammonium nitrate and gaseous nitric acid and ammonia shifts to the gas phase as ambient temperature increases, and RH decreases. Similar to ammonia, amines undergo neutralization reactions with nitric and sulfuric acids to form amine salts (Mozurkewich, 1993; Stelson and Seinfeld, 1982a; Angelino et al., 2001; Murphy et al., 2007). The photooxidation of gas-phase amines has been shown to form aerosol based on recent laboratory experiments (Angelino et al., 2001; Murphy et al., 2007).

Gaseous amines, including methylamine, dimethylamine, trimethylamine, ethylamine, diethylamine, triethylamine, ethanoloamine, *n*-butylamine, amylamine, 1,4-butanediamine, isobutylamine, and isopropylamine, have been identified in emissions from bovine sources (Mosier et al., 1973; Hutchinson et al., 1982; Schade and Crutzen, 1995; Rabaud et al., 2003; Ngwabie et al., 2005). Amine emission rates from animal husbandry sources are typically two to three orders of magnitude lower than those of ammonia (Schade and Crutzen, 1995; Ngwabie et al., 2005). Gaseous amines are also present in vehicular exhaust (Cadle and Mulawa, 1980; Westerholm et al., 1993), the marine atmosphere (Vanneste et al., 1987), biomass burning plumes (Lobert et al., 1991), as well as emissions from decaying organic matter, waste incineration, and sewage treatment plants (Manahan, 2005). Amine salts have sufficiently low vapor pressures to partition to the aerosol phase; moreover, they exhibit greater water-solubility as compared to other particulate organic nitrogen species (Milne and Zika, 1993; Gorzelska et al., 1994; Murphy and Thomson, 1997; Glagolenko and Phares, 1994; Abalos et al., 1999; Angelino et al., 2001; Makela et al., 2001; Tan et al., 2002; Zhang et al., 2002; Zhang and Anastasio, 2003; Maria et al., 2003; Beddows et al., 2004; Denkenberger et al., 2007; Murphy et al., 2007; Sorooshian et al., 2007a).

The availability of a massive, concentrated source of ammonia and amines offers a unique opportunity to probe the response of the resulting aerosol. During July 2007, the Center for Interdisciplinary Remotely Piloted Aircraft Studies (CIRPAS) Twin Otter probed the aerosol downwind of a major cattle feedlot in the San Joaquin Valley in California. The San Joaquin Valley, the major geographical feature in central California, is bordered on its west and east sides by mountain ranges and is characterized by relatively stagnant

air circulation (Fig. 1a). Consequently, this region is one of the largest nonattainment areas for ozone and particulate matter in the United States (Chow et al., 2006). The San Joaquin Valley contains numerous animal husbandry operations, the largest of which is the focus of this study. This feedlot operation covers several hundred acres and contains up to 100 000 head of cattle at any one time. Although gas-phase measurements were not carried out, the presence of ammonia and amines is inferred from established emissions inventories from animal husbandry sources and from measurements of the ammonium and amine content of the aerosol downwind of the plume source.

The goal of the present study is to provide a comprehensive airborne characterization of the aerosol downwind of a major bovine source. First, the aircraft instrument payload and flight path strategy are presented. Detailed measurements were obtained for: meteorology, aerosol size distributions and number concentrations, aerosol composition, mixing state, refractive index, hygroscopic growth factors at three different relative humidities, and cloud condensation nucleus (CCN) behavior. Special attention is given to the sub- and supersaturated water uptake properties of the aerosol, and how these relate to chemical composition. Sub-saturated hygroscopic growth factors for the organic fraction of the aerosol are reported based on a closure analysis employing the Zdanovskii-Stokes Robinson mixing rule. Sub-saturated hygroscopic growth data are then compared to measured supersaturated CCN activity to evaluate the level of consistency between observed water uptake in the two regimes.

2 Experimental methods

The data on which the present study is based were acquired during two clear air flights in the San Joaquin Valley on 12 July 2007 and 30 July 2007. Henceforth, these two flights will be termed flight A (12 July 2007) and flight B (30 July 2007). The aircraft total aerosol inlet, characterized by Hegg et al. (2005), provided sample air to instruments on the aircraft. The instrument payload on the Twin Otter aircraft is described elsewhere (<http://www.cirpas.org>), however, attention is given below to those instruments the data from which will be discussed in detail.

2.1 Aerosol chemical composition (Aerodyne C-ToF-AMS)

Chemical composition measurements for non-refractory aerosol species (sulfate, nitrate, ammonium, and organics) were performed using an Aerodyne compact Time of Flight Aerosol Mass Spectrometer (C-ToF-AMS; Drewnick et al., 2005). At the entrance to the instrument, an aerodynamic lens focuses particles with vacuum aerodynamic diameters between approximately 50 nm and 800 nm through a 3.5%

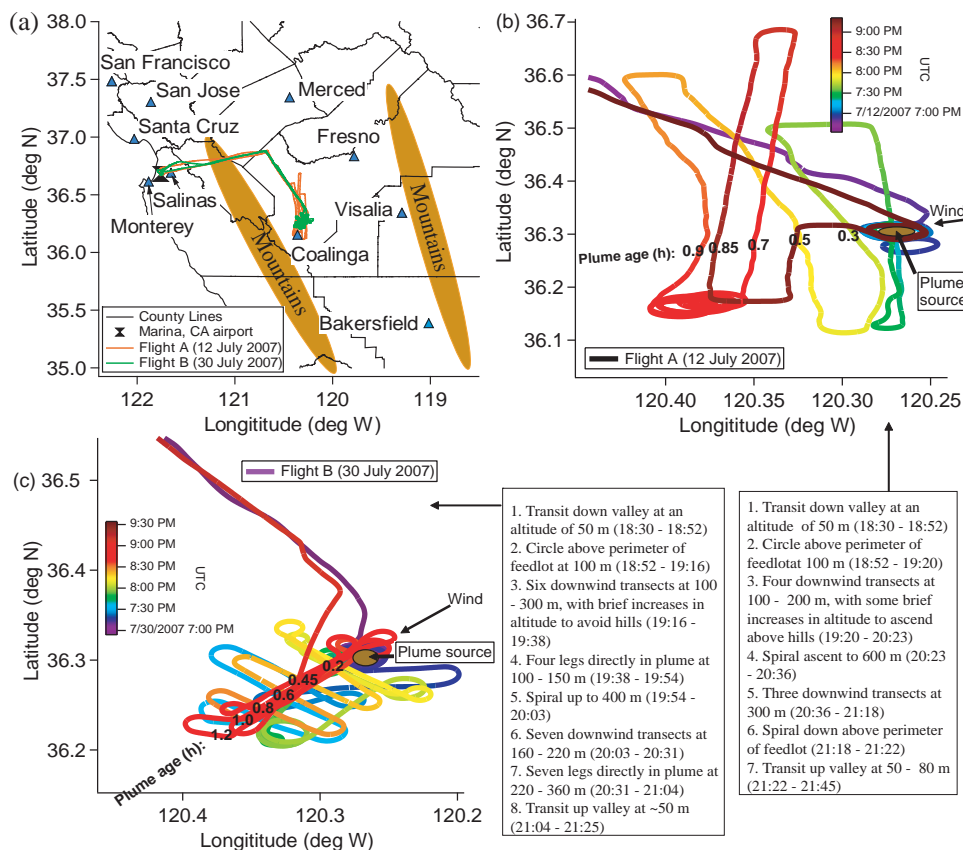


Fig. 1. (a) Complete flight tracks for the two flights in the San Joaquin Valley of California. The shaded mountain areas are meant to provide a relative view of how the San Joaquin Valley is bordered by major topographical features. (b)/(c) Detailed tracks for flights A (12 July 2007) and B (30 July 2007) with a step-by-step description of the aircraft maneuvers. Plume ages were calculated using downwind distance and average wind speed in the vicinity of the feedlot.

chopper and onto a tungsten vaporizer ($\sim 550^\circ\text{C}$) (Murphy et al., 2007). The chopper can be operated in three modes to gather either background mass spectra, ensemble average mass spectra over all particle sizes, or size-resolved mass spectra. Once vaporized, molecules undergo electron impact ionization and travel through a time of flight mass analyzer. The C-ToF-AMS detects the presence of amines in the form of characteristic amine peaks at m/z 30, 56, and 86 (McLafferty and Turecek, 1993; Angelino et al., 2001; Murphy et al., 2007). The detection limit, calculated as three times the standard deviation of the noise for filtered air, is $<0.05 \mu\text{g}/\text{m}^3$ for all species measured.

The C-ToF-AMS can be used to calculate a quantity that will be referred to subsequently as *excess nitrate*. *Excess nitrate* is defined as the nitrate mass, derived from C-ToF-AMS spectra, remaining after both sulfate and nitrate have been fully neutralized by ammonium. A zero or slightly negative value indicates that sufficient ammonia exists to neutralize both sulfate and nitrate, while a positive value indicates that

some nitrate is associated with other cations besides ammonium. C-ToF-AMS calibrations allow an assessment of the error associated with the *excess nitrate* calculation; introducing pure ammonium nitrate into the instrument should result in an *excess nitrate* value of zero. After flight A, calibrations were conducted with monodisperse ammonium nitrate particles ranging from 50 nm to 400 nm and mass concentrations ranging from $1.5 \mu\text{g}/\text{m}^3$ to $7.0 \mu\text{g}/\text{m}^3$, similar to concentrations in flight. Thirty-three calibration points were collected that exhibited an average *excess nitrate* of $0.08 \pm 0.31 \mu\text{g}/\text{m}^3$. Similarly during a calibration on the day of flight B, 350 nm and 400 nm ammonium nitrate particles were introduced into the instrument at levels near $\sim 3 \mu\text{g}/\text{m}^3$, which exceeds the peak nitrate concentration observed during the flight. The average *excess nitrate* was $-0.014 \pm 0.095 \mu\text{g}/\text{m}^3$ ($n=17$). As will be shown, ambient *excess nitrate* concentrations in the plume aerosol significantly exceeded the background values for pure ammonium nitrate.

Nitrate species can be detected by peaks at m/z 30 and 46. A problem innate to C-ToF-AMS unit mass-resolution spectra is differentiating between NO^+ , CH_2O^+ , and C_2H_6^+ , all of which give peaks at m/z 30. If the contribution of organic fragments to the signal at m/z 30 is not correctly accounted for, the mass of nitrate, as inferred from NO^+ , can be overestimated. A relatively conservative approach is to calculate nitrate mass using the peak intensity at m/z 46 (NO_2^+), which rarely corresponds to an organic fragment (McLafferty and Turecek, 1993). Calibration of the instrument with pure ammonium nitrate allows observation of the ratio of the peak intensities at m/z 30 and 46 when NO^+ and NO_2^+ are present without organic interference. During such a calibration conducted after flight A, the peak at m/z 30 was observed to be 2.2 times that at m/z 46. Thus, for this flight, nitrate mass at m/z 30 was calculated to be 2.2 times the mass at m/z 46. Based on calibrations on the day of flight B, the peak at m/z 30 was observed to be 2.8 times that at m/z 46. The two calibrations were seventeen days apart, and instrumental drift is responsible for the difference in the m/z 30:46 ratio between the two days; typical values observed with this instrument range between two and three. The mass remaining at m/z 30 after the nitrate contribution is subtracted is assumed to be organic species, including amines, which often exhibit a major peak here.

2.2 Aerosol chemical composition (PILS)

Water-soluble aerosol chemical composition was measured by a particle-into-liquid sampler (PILS, Brechtel Mfg Inc.; Sorooshian et al., 2006a). In the PILS, submicrometer ambient particles are grown into droplets sufficiently large to be collected by inertial impaction for subsequent chemical analysis. At the entrance to the instrument a series of three denuders (URG and Sunset Laboratories) remove inorganic (basic and acidic) and organic gases that would otherwise bias aerosol measurements. The impacted droplets are delivered to a rotating carousel containing 72 vials, with each vial containing material representing a period of ~ 5 min of flight, or alternatively, a distance of 15 km in flight (aircraft speed ~ 50 m/s). The contents of the vials are subsequently analyzed off-line using a dual ion chromatography (IC) system (ICS-2000, Dionex Inc.) for simultaneous anion and cation analysis.

The PILS-IC instrument uncertainty has been established as $\pm 7\%$, and the detection limit (calculated as air-equivalent concentration of the lowest concentration standard that is distinct from baseline noise in the IC plus three times the standard deviation of this measurement) is $< 0.1 \mu\text{g}/\text{m}^3$ for the inorganic ions (Na^+ , NH_4^+ , K^+ , Mg^{2+} , Ca^{2+} , Cl^- , NO_2^- , NO_3^- , and SO_4^{2-}) and $< 0.01 \mu\text{g}/\text{m}^3$ for the organic acid ions (carboxylic acids with one to nine carbon atoms) (Sorooshian et al., 2007b). The PILS-IC technique has been demonstrated to speciate amines, including ethylamine, diethylamine, triethylamine, methylamine, dimethylamine,

and trimethylamine (Murphy et al., 2007); however, only ethylamine and diethylamine were measured above detection limits ($0.01 \mu\text{g}/\text{m}^3$) in the present study. It should be noted that ammonium and ethylamine co-elute in the IC cation column; however, ethylamine was detected at sufficiently high concentrations for its peak to be distinguishable from that of ammonium. The reported concentrations of ethylamine represent a lower limit due to this co-elution effect. Since acetate, lactate, and glycolate also co-elute, these three species are reported as a collective mass using the calibration equation of acetate; therefore, the contribution of acetate reported is likely an overestimate. As compared to acetate, using the calibration equation of glycolate would reduce the estimates by $< 10\%$.

An important issue during this study was the potential for denuder breakthrough in the PILS because the sampling site represents the most concentrated ambient source of ammonia and amines encountered by this PILS. The denuders have been shown to successfully remove gaseous amine species in laboratory chamber experiments (Murphy et al., 2007); estimated initial mixing ratios for gaseous amines in those experiments ranged between 50–500 ppb, which is expected to represent levels expected in areas of intense animal husbandry. To check for evidence of ammonia breakthrough, the ammonium levels measured by the PILS and C-ToF-AMS, which is not prone to gaseous artifacts, are compared. For the following calculations it is assumed that the C-ToF-AMS collection efficiency for ammonium was constant throughout the flights and was identical to that of sulfate, even though external mixing was evident. The average of the ammonium ratio (PILS:C-ToF-AMS) was 0.90 ± 0.11 during flight A and 0.87 ± 0.21 during flight B. There was no clear enhancement in the ratio of PILS:C-ToF-AMS ammonium levels within the plume either flight. These data suggest that ammonia breakthrough did not lead to a positive artifact in the PILS, and even if so, it was masked by some other effect such as volatilization of ammonium in the PILS or an inaccurate collection efficiency applied to C-ToF-AMS ammonium data. Sorooshian et al. (2006a) showed that approximately 12% of ammonium in laboratory-generated ammonium sulfate particles is lost by volatilization at similar PILS operating conditions as implemented during this study, and the PILS data here are corrected for this 12%. Therefore, it is uncertain as to why the PILS ammonium levels were on average less than those of the C-ToF-AMS.

2.3 Aerosol hygroscopicity and refractive Index (DASH-SP)

A differential aerosol sizing and hygroscopicity spectrometer probe (DASH-SP; Brechtel Mfg Inc.; Sorooshian et al., 2008) was included in the instrument payload on the aircraft. The DASH-SP consists of a single classification differential mobility analyzer (DMA) followed by a set of parallel hygroscopic growth chambers operated at different relative

humidities. A ~ 0.5 LPM aerosol sample flow passes first through a Nafion drier, and then through a ^{210}Po neutralizer that brings the dried particles to a stable, steady-state charge distribution. A cylindrical DMA selects particles in a narrow interval of mobility-equivalent diameters in the 0.1 to $1.0\ \mu\text{m}$ range. The classified aerosol leaving the DMA is split into five separate flows. In one of the five streams, the total concentration of classified particles is determined using an integral TSI Model 3831 water-based condensation particle counter (CPC). The remaining four classified aerosol flows pass through a Nafion humidifier (Perma Pure, LLP, Model MD-070-24FS-4) to achieve thermodynamic equilibrium with water vapor at a constant, predetermined RH. The four conditioned aerosol flows pass directly to dedicated, custom-built OPCs ($\lambda=532\ \text{nm}$, World Star Technologies, Model TECGL-30) designed to size particles in the 100 nm to $3\ \mu\text{m}$ diameter size range. An iterative data processing algorithm quantifies an “effective” aerosol refractive index that is used to calculate hygroscopic growth factors ($\text{GF}=D_{p,\text{wet}}/D_{p,\text{dry}}$) corrected for the refractive-index dependence of the OPC response (Sorooshian et al., 2008). During this study, the DASH-SP provided simultaneous measurements of GFs at different RHs for dry DMA-selected particle diameters between $D_p=150\text{--}200\ \text{nm}$. One humidifier was operated dry ($\text{RH}<8\%$), and the other three were at RHs of 74%, 85%, and 92%. (No data from the $\text{RH}=85\%$ channel were available during flight A.) The uncertainty associated with growth factor measurements is $\sim \pm 4.5\%$, and the uncertainty in the RH is $\pm 1.5\%$.

2.4 Cloud Condensation Nuclei Counter (CCNc)

A continuous flow thermal gradient cloud condensation nuclei counter (CCNc, Droplet Measurement Technologies Inc.; Roberts and Nenes, 2005; Lance et al., 2006) was used to quantify the number of particles that activate at supersaturations ranging from 0.1% to 0.6%. In the instrument a supersaturation is generated in an axisymmetric flow by applying a constant streamwise temperature gradient, using three sets of thermal electric coolers across a wetted column. At the exit of the CCNc column, those particles that activate and grow sufficiently large ($D_p>0.75\ \mu\text{m}$) for detection by an OPC were quantified. The activated fraction is determined as the ratio of the CCN number concentration to the total particle (CN) number concentration.

The CCNc was calibrated numerous times throughout this study and a brief description of the procedure now follows; we refer the reader to Appendix A for a more detailed explanation. Dried ammonium sulfate particles are sent to a DMA (Model 3081L, TSI Inc.) for size selection. The resulting monodisperse aerosol stream is split and sent to both a condensation particle counter (Model 3010, TSI Inc.) and a continuous-flow streamwise thermal gradient chamber (operated at constant flow rate, temperature gradient, and pressure) to measure CN and CCN, respectively. The

level of supersaturation in the instrument is determined from the minimum dry particle diameter, D_{p50} (dry diameter for which the $\text{CCN}/\text{CN}=0.50$), that activates in the instrument. The instrument supersaturation is related to D_{p50} by applying Köhler theory assuming ammonium sulfate has a density of $1760\ \text{kg}/\text{m}^3$, surface tension of water, molar mass of $0.132\ \text{kg}/\text{mol}$, and an effective van't Hoff factor of 2.5; studies have found the latter value to lie between 2 and 2.5 (Gerber et al., 1977; Brechtel and Kreidenweis, 2000; Kumar et al., 2003; Rose et al., 2008).

2.5 Size distributions and particle number concentration

Aerosol size distribution data were obtained by a DMA ($D_p = 10\text{--}800\ \text{nm}$) and an external passive cavity aerosol spectrometer probe ($0.1\text{--}3\ \mu\text{m}$) (PCASP, PMS Inc., modified by DMT Inc.). Particle number concentrations were quantified with two condensation particle counters (CPC Model 3010, TSI Inc., $D_p>10\ \text{nm}$; UFCPC Model 3025, TSI Inc., $D_p>3\ \text{nm}$). When the two CPCs experienced electrical saturation, particle number concentrations from the DMA are reported. The DMA time resolution is 74 s as opposed to 1 s for the CPCs.

2.6 Flight strategy

Complete flight tracks from flights A and B are shown in Fig. 1a. Both flights were intended to resemble each other in the time of the day and flight path. Starting from the Marina, CA airport, the aircraft transited east before descending to 50 m above the surface of the San Joaquin Valley. Then the aircraft flew southeast directly towards the feedlot, approaching to within one kilometer of the feedlot. A close-up of the flight tracks near the plume source with step-by-step details of the flight strategy is shown in Fig. 1b and c. In each flight, the Twin Otter circled above the perimeter of the source several times, performed a spiral ascent to characterize the meteorological profile, performed several downwind transects of the plume at various altitudes below the boundary layer top, flew directly in the plume for several legs (only flight B), and transited northwest back up the valley. Sampling lasted for more than three hours starting just before noon during both flights. The feedlot operation is slightly larger than $3\ \text{km}^2$ in area (~ 800 acres). The feedlot is bordered on the west side by the Interstate 5 roadway, which is a major transportation route and source of vehicular emissions, connecting northern and southern California.

3 Results

3.1 Meteorology

Figures 2 (flight A) and 3 (flight B) display the time evolution of meteorological and particle number concentration data, while Fig. 4 presents vertical profiles. During flight

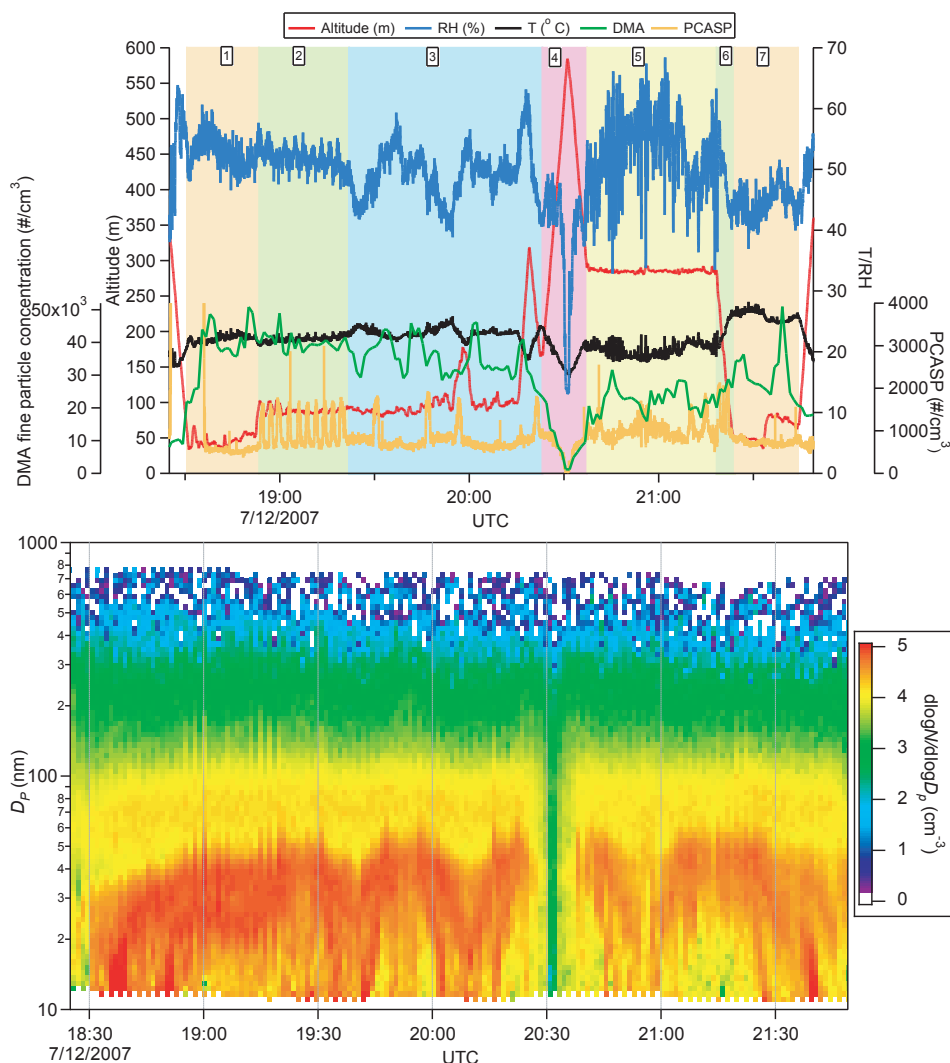


Fig. 2. Upper panel: time series of particle number concentration and meteorological data for flight A. Lower panel: time series of aerosol size distribution. The number labels at the top of each shaded block correspond to the respective flight segment listed in Fig. 1.

B, ambient temperatures ($27.5 \pm 2.4^\circ\text{C}$) were higher and RHs ($25.8 \pm 5.9\%$) were lower than observed in flight A ($21.8 \pm 2.3^\circ\text{C}$; $49.0 \pm 7.8\%$). During both flights, the aircraft performed three vertical profiles of the boundary layer. The temperature inversions were weak ($< 1^\circ\text{C}$), so decreases in RH and particle number concentrations, as quantified by the DMA and PCASP, are used as indicators for inversion layers. The boundary layer exhibited multiple inversions, the highest of which was observed at the end of the flights ($\sim 03:00$ p.m. local time) at ~ 630 m. The depth of the inversion layers increased with time as the surface warmed. The vertical temperature and RH profiles, and the relatively uniform particle concentrations with altitude (Fig. 4) provide evidence for

a vigorously-mixed boundary layer, as was previously observed by Neuman et al. (2003) in the San Joaquin Valley in May 2002.

Five-day back-trajectories, computed using the NOAA HYSPLIT model (Draxler and Rolph, 2003), show that the background air during flight A originated over the Pacific Ocean, whereas the background air during flight B was transported over land from the north (Fig. 5). This suggests that the background aerosol in flight A may have carried the signature of cleaner marine air, while that measured during flight B was more exposed to urban and agricultural emissions.

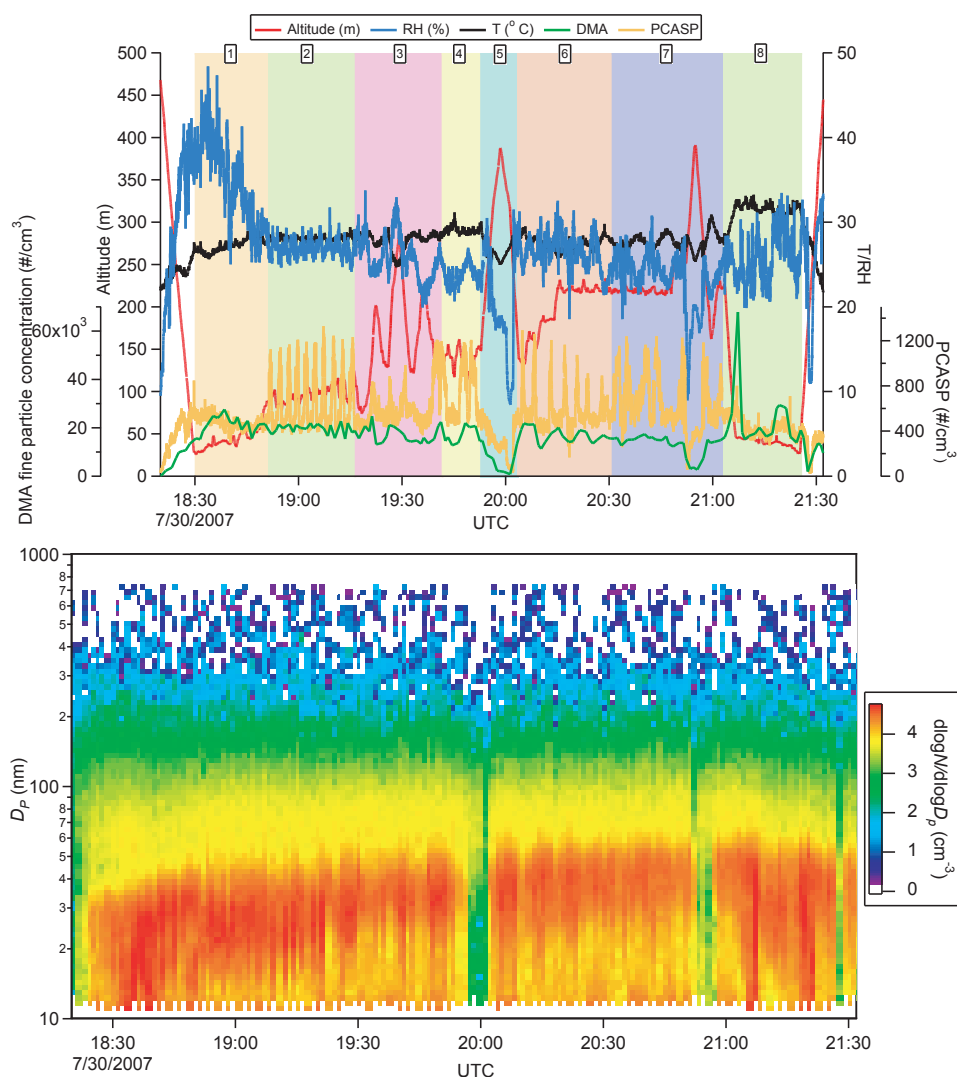


Fig. 3. Upper panel: time series of particle number concentration and meteorological data for flight B. Lower panel: time series of aerosol size distribution. The number labels at the top of each shaded block correspond to the respective flight segment listed in Fig. 1.

3.2 Particle number concentrations and size distributions

Average submicrometer particle number concentrations in the plume were $30\,528 \pm 8987\text{ cm}^{-3}$ (flight A) and $16\,606 \pm 4286\text{ cm}^{-3}$ (flight B) (Table 1). Particle number concentrations in and out of the plume were similar, indicating the absence of significant emissions of particles from the source. (As noted in Sect. 3.3, nitrate enhancement is used to identify the location of the plume.) During the downwind plume transects, number concentrations decreased slightly with increasing altitude until a sharp decrease near the top of the boundary layer to below 300 cm^{-3} (flight A) and 800 cm^{-3} (flight B) at altitudes of 550 m and 400 m, respec-

tively. The ratio of the number concentration of particles with $D_p > 3\text{ nm}$ to the number concentration of particles with $D_p > 10\text{ nm}$ was 1.1 ± 0.1 and 1.2 ± 0.1 for flights A and B, respectively. This ratio showed no difference in and out of the plume and decreased with altitude.

The vertical structure of the PCASP ($D_p = 0.1\text{--}3\text{ }\mu\text{m}$) and CPC number concentrations were similar. Average PCASP concentrations in the plume for flights A and B were 1065 ± 330 and $675 \pm 220\text{ cm}^{-3}$, respectively, indicating that most of the particles were smaller than 100 nm in diameter. The number of 0.1 to 3 μm diameter particles in the plume was enhanced by a factor of 2.5–3 times as much over that in the background aerosol. This is especially evident

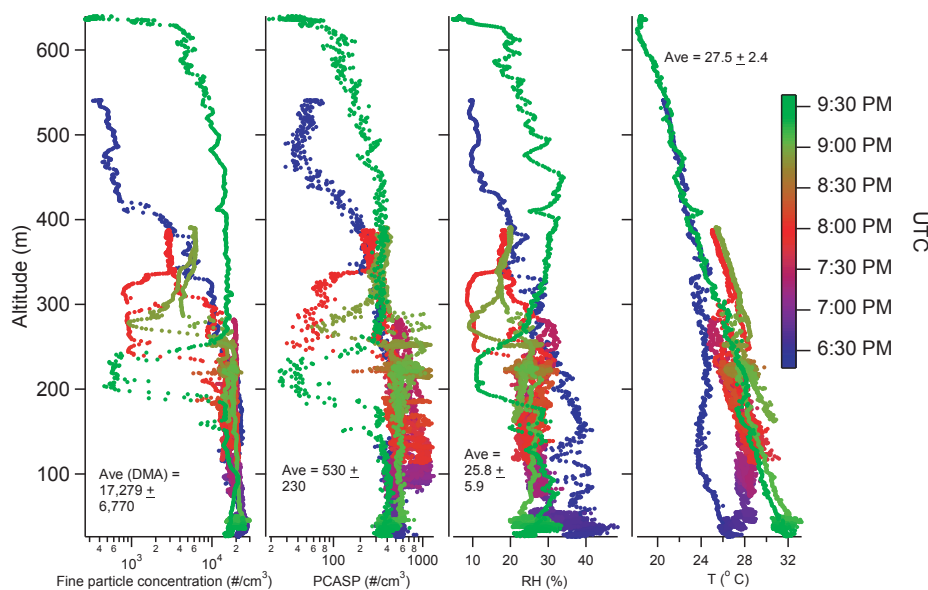


Fig. 4. Vertical profiles of particle number concentration and meteorological data for flights A (upper panel) and B (lower panel). For the submicrometer particle concentration data (CPC 3010), it should be noted that the absolute concentrations are not accurate due to electrical saturation of the instrument; these data are plotted because of the 1 s time resolution of the data. The DMA and CPC 3010 number concentrations were proportional throughout both flights, therefore, the CPC 3010 values are useful for qualitative purposes to identify the mixing layer height. DMA number concentrations indicated are accurate.

Table 1. Summary of in-plume and out-of-plume measurements of composition and particle number and mass concentration.

		Total Mass ($\mu\text{g}/\text{m}^3$)	Organic ($\mu\text{g}/\text{m}^3$)	NO_3^- ($\mu\text{g}/\text{m}^3$)	SO_4^{2-} ($\mu\text{g}/\text{m}^3$)	NH_4^+ ($\mu\text{g}/\text{m}^3$)	Excess NO_3^- ($\mu\text{g}/\text{m}^3$)	$[\text{NH}_4^+:\text{SO}_4^{2-}]$ molar ratio	% Organic	% NO_3^-	% SO_4^{2-}	% NH_4^+	DMA particle concentration (#/cm ³)	(UFCPC 3025:CPC 3010) ^a	cToF- AMS: <i>m/z</i> 57:44	cToF-AMS: <i>m/z</i> 44/Total Organic	O:C atomic ratio ^b	
Flight A	In plume	AVE	10.48	6.48	0.93	2.06	1.02	0.04	2.64	61.9	8.6	19.8	9.7	30 528	1.1	0.07	0.10	0.45
		ST DEV	1.64	0.98	0.40	0.24	0.23	0.50	0.51	2.6	2.4	1.7	1.7	8987	0.0	0.01	0.01	0.02
	Out of plume	AVE	8.01	5.10	0.30	1.81	0.80	-0.16	2.38	63.5	3.7	22.8	10.1	30 778	1.1	0.07	0.10	0.45
		ST DEV	1.48	1.07	0.11	0.31	0.17	0.41	0.47	3.3	1.1	2.6	1.8	11 026	0.0	0.02	0.01	0.02
Flight B	In plume	AVE	4.53	2.46	1.08	0.54	0.44	0.02	4.61	55.5	22.7	12.3	9.6	16606	1.2	0.07	0.11	0.48
		ST DEV	0.87	0.29	0.50	0.10	0.14	0.34	2.25	6.4	7.3	3.0	2.1	4286	0.1	0.02	0.01	0.04
	Out of plume	AVE	2.65	1.73	0.19	0.56	0.19	0.00	1.94	63.1	7.2	23.1	7.0	18 139	1.2	0.09	0.12	0.53
		ST DEV	0.95	0.70	0.12	0.26	0.10	0.21	1.42	11.9	2.4	11.0	3.8	8910	0.1	0.08	0.02	0.09

^a The ratio of the particle number concentration for $D_p > 3$ nm (UFCPC 3025) to that for $D_p > 10$ nm (CPC 3010).

^b The O:C atomic ratio was calculated using the data inventory and slope equation presented by Aiken et al. (2008; Fig. 4b)

by the increase in number concentration ($D_p > 100$ nm) observed when passing through the beginning of the plume over the perimeter of the source (upper panels of Figs. 2 and 3; see the flight segments labeled “2” when the aircraft was circling the perimeter of the plume source); this likely is a result of smaller particles growing into this size range. However, the increase in number concentration for particles with $D_p = 0.1$ – 3 μm was not sufficiently large to result in a significant difference in the submicrometer number concentration ($D_p = 0.01$ – 1 μm) in and out of the plume.

Aerosol number and volume distributions were similar both between the two flights, and in and out of the plume. Multiple modes normally existed in the number and volume distributions. A number concentration mode was generally

present between $D_p = 20$ – 60 nm, with a weaker mode between $D_p = 60$ – 100 nm (lower panels of Figs. 2 and 3). There was also a dominant number concentration mode, which will be referred to as the nucleation mode, at sizes smaller than the detection limit of the DMA (10 nm); this mode is evident from the difference in number concentration measured by the DMA and the UFCPC 3025. Volume concentration modes existed at $D_p = 30$ – 60 nm, $D_p \sim 100$ nm, and frequently at $D_p > 100$ nm. The number and volume distributions in the plume shifted slightly to larger sizes with downwind distance from the plume source.

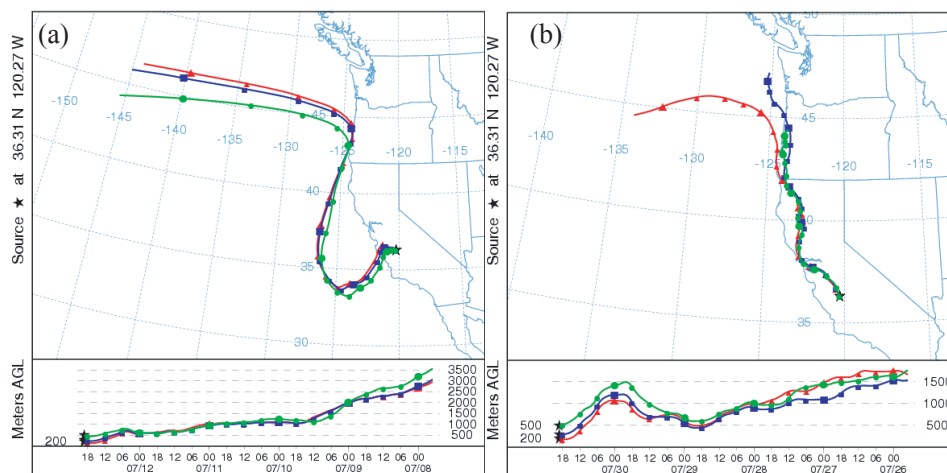


Fig. 5. HYSPLIT five-day backward trajectory analysis for flights A (panel (a)) and B (panel (b)). Six hours of time separate each marker on the trajectories.

3.3 Submicrometer aerosol chemical composition

Figure 6 (time series), Figs. 7 and 8 (spatial distribution), and Fig. 9 (vertical distribution) summarize the submicrometer aerosol composition data, in addition to Table 1, which reports the background and in-plume composition for both flights. The reported total organic mass is non-refractory organic mass that was measured by the C-ToF-AMS. The total aerosol mass is determined as the sum of inorganic mass, as determined by the PILS and C-ToF-AMS, and non-refractory organic mass from the C-ToF-AMS. Nitrate enhancement is used to define the location of the plume. Then, knowing where the plume is, local enhancements in other species concentrations and aerosol properties can be determined. Plume ages are noted on the spatial plots in Fig. 1b and c and were calculated using downwind distance and average wind speed in the vicinity of the source. The highest plume age encountered in flights A and B was 0.9 h and 1.2 h, respectively.

3.3.1 Total aerosol mass and major components

The average total aerosol mass in the boundary layer was $8.85 \pm 1.79 \mu\text{g}/\text{m}^3$ and $3.40 \pm 0.98 \mu\text{g}/\text{m}^3$ during flights A and B, respectively, with significant enhancements in the plume (Table 1). The highest concentrations, $17.07 \mu\text{g}/\text{m}^3$ (flight A) and $6.27 \mu\text{g}/\text{m}^3$ (flight B), occurred in the plume while the lowest concentrations were observed at the highest altitudes when the aircraft performed spiral ascents (flight A = $1.40 \mu\text{g}/\text{m}^3$; flight B = $0.24 \mu\text{g}/\text{m}^3$).

Overall, organic species dominated the total mass. Organics accounted for $61.9\% \pm 2.6\%$ (flight A) and $55.5\% \pm 6.4\%$ (flight B) of the plume aerosol mass, and $63.5\% \pm 3.3\%$ (flight A) and $63.1\% \pm 11.9\%$ (flight B) of the background aerosol mass. The organic mass concentration in the

plume was $6.48 \pm 0.98 \mu\text{g}/\text{m}^3$ (flight A) and $2.46 \pm 0.29 \mu\text{g}/\text{m}^3$ (flight B), and in the background aerosol was $5.10 \pm 1.07 \mu\text{g}/\text{m}^3$ (flight A) and $1.73 \pm 0.70 \mu\text{g}/\text{m}^3$ (flight B). The next largest contributor to the particulate mass was either sulfate or nitrate, depending on the day and aerosol type, followed by either ammonium or nitrate (see Table 1). The ratio of organic mass to inorganic mass in the plume was 1.64 ± 0.19 (flight A) and 1.30 ± 0.39 (flight B), while the ratio in the background aerosol was 1.77 ± 0.29 (flight A) and 1.92 ± 0.68 (flight B). Previous measurements in the San Joaquin Valley have also shown that organic aerosol contributes significantly to the fine particle mass (Chow et al., 1996; Neuman et al., 2003).

3.3.2 Inorganic Aerosol

Within the source plume, the levels of nitrate and ammonium increased significantly above their respective values in the background valley aerosol (Fig. 6–8). The ammonium-to-sulfate molar ratio is an important indicator of the level of partitioning of ammonium nitrate between the gas and aerosol phases. Since this ratio usually exceeded two, ammonia was available to foster partitioning of nitrate to the aerosol phase in the plume. The vertical distribution of nitrate and ammonium exhibited similar trends in each flight, unlike sulfate, which did not increase in concentration at plume altitudes (~ 100 – 300 m) (Fig. 9).

Generally, other inorganic species, including chloride, sodium, potassium, calcium, magnesium, and nitrite, did not contribute significantly ($> 0.1 \mu\text{g}/\text{m}^3$) to the aerosol mass. Many of these species are expected to be found primarily in the coarse particle fraction ($D_p > 1 \mu\text{m}$), owing to their origins in sea salt (Na^+ , Cl^-) and dust and soil (Ca^{2+} ,

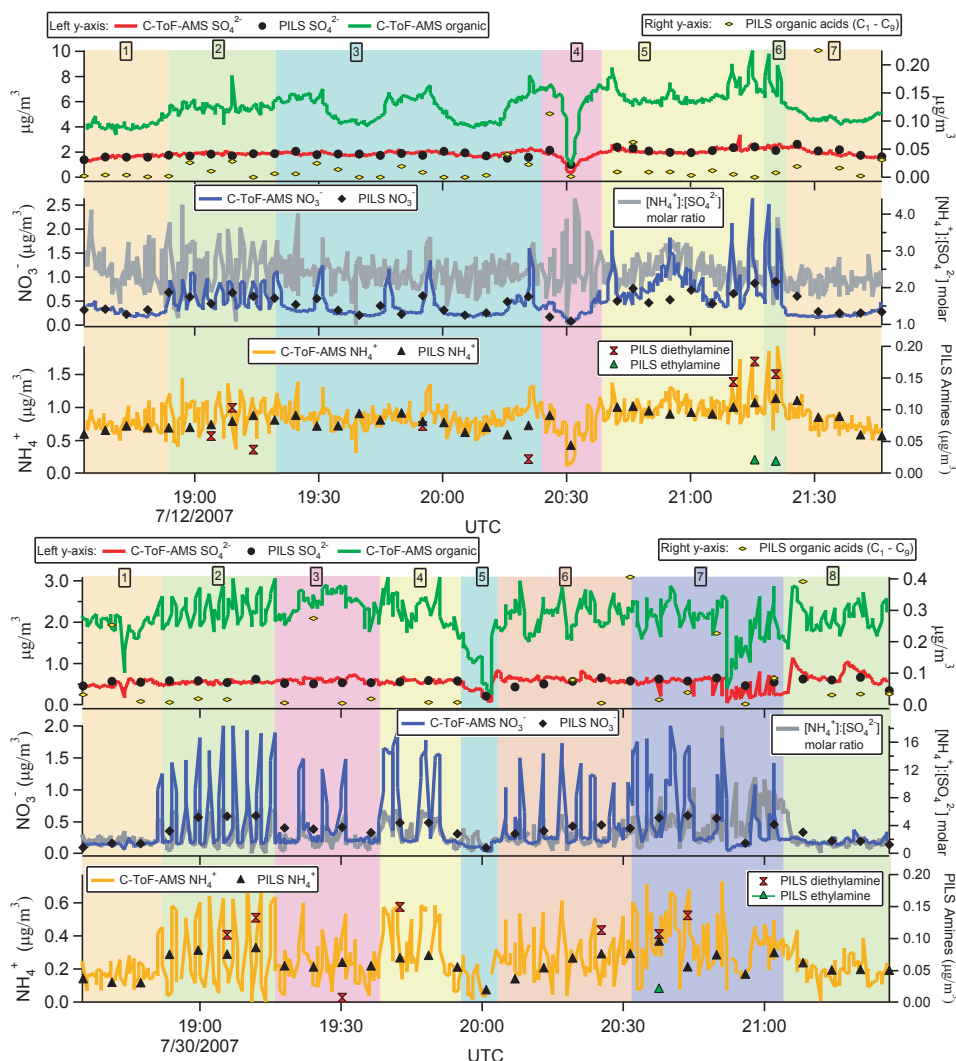


Fig. 6. Time series of PILS water-soluble aerosol composition and C-ToF-AMS composition for flights A (upper panel) and B (lower panel). The number labels for each shaded box correspond to the portion of each flight represented in Fig. 1. The shaded areas representing the plume are characterized by significant increases in organics, ammonium, nitrate, and amines. The ammonium-to-sulfate molar ratio exceeds 2.0 in the plume, allowing nitrate to partition into the aerosol phase. The multiple C-ToF-AMS spikes in the species concentrations cannot be resolved by the PILS since the 5-min time intervals for sample collection average out the quick plume passes with the longer legs outside of the plume. Agreement between the PILS and C-ToF-AMS is most evident for sulfate, since this species was relatively level in concentration during the flights.

Mg^{2+} , Na^+ , K^+). Magnesium, calcium, and potassium concentrations were all below detection limits ($< 0.05 \mu\text{g}/\text{m}^3$). Sodium and chloride were sparsely detected in both flights, usually in the background aerosol during the transits, with concentrations near $\sim 0.1 \mu\text{g}/\text{m}^3$. Nitrite above detection limits was found in only one PILS sample ($0.10 \mu\text{g}/\text{m}^3$) during flight A while circling the feedlot near the beginning of the flight (UT $\sim 19:00$).

3.3.3 Organic Aerosol

The concentration of total organics, as determined by the C-ToF-AMS, in the plume aerosol significantly exceeded those in the background valley aerosol (Fig. 6–8). The vertical distribution of total organic concentrations was somewhat similar to those of nitrate and ammonium, with the exception that there was not as sharp an enhancement in concentration at plume altitudes, as was especially evident in flight B (Fig. 9).

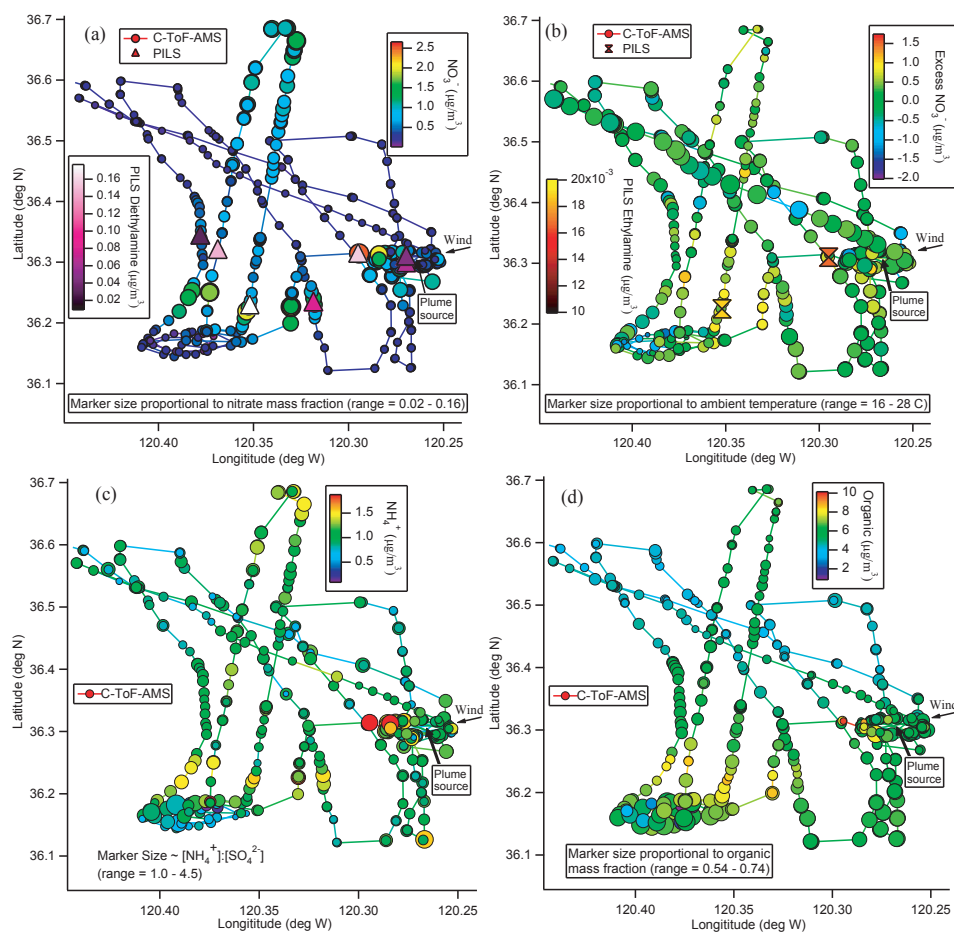


Fig. 7. Spatial distribution of various aerosol species during flight A. (a) C-ToF-AMS nitrate and PILS diethylamine, with marker size proportional to nitrate mass fraction; (b) *Excess nitrate* remaining after both sulfate and nitrate have been neutralized by ammonium (see Sect. 2.1 for further explanation), with marker size proportional to ambient temperature; (c) C-ToF-AMS ammonium, with marker size proportional to the ammonium-to-sulfate molar ratio; (d) C-ToF-AMS organic, with marker size proportional to organic mass fraction. The PILS markers are spatially placed wherever the aircraft was at the midpoint of the time when a particular sample was collected (after being corrected for liquid residence time in the instrument); therefore the amine markers are spatially distinct from the core of the plume (especially the two markers representing the highest plume ages).

Figure 10 shows the representative mass spectra of the organic fragments detected by the C-ToF-AMS in the background valley aerosol, the plume aerosol close to the source, and farther downwind. All non-organic contributions to the mass spectra have been removed using the methodology described in Allan et al. (2004); fragmentation at m/z 30 was further modified as described in Sect. 2.1. Figure 11 indicates that the signal at m/z 30 represents a large fragment for organics, including amines. The chemical signatures of the organic aerosol in the three categories appear to be quite similar. One difference, which is highlighted also in Fig. 10, is that the m/z 30 (common amine marker) peak intensity is enhanced by $\sim 150\%$ at the closest point to the plume source

as compared to background aerosol, and decreases by $\sim 25\%$ at the farthest downwind distance. Figure 11 shows comparisons of the plume aerosol organic mass spectra to the background spectra for both flights. The overall organic aerosol appears to be similar in and out of the plume; however, peak intensities at m/z 30, 56, and 86 are enhanced in plume. These are all peaks in the electron impact mass spectrum of amines, including diethylamine and triethylamine (McLafferty and Turecek, 1993; Angelino et al., 2001; Murphy et al., 2007). A similar analysis for plume organics close to the feedlot and farther downwind reveals no significant difference in most peaks, although the intensity of the m/z 30 peak decreases with increasing plume age; as will be discussed

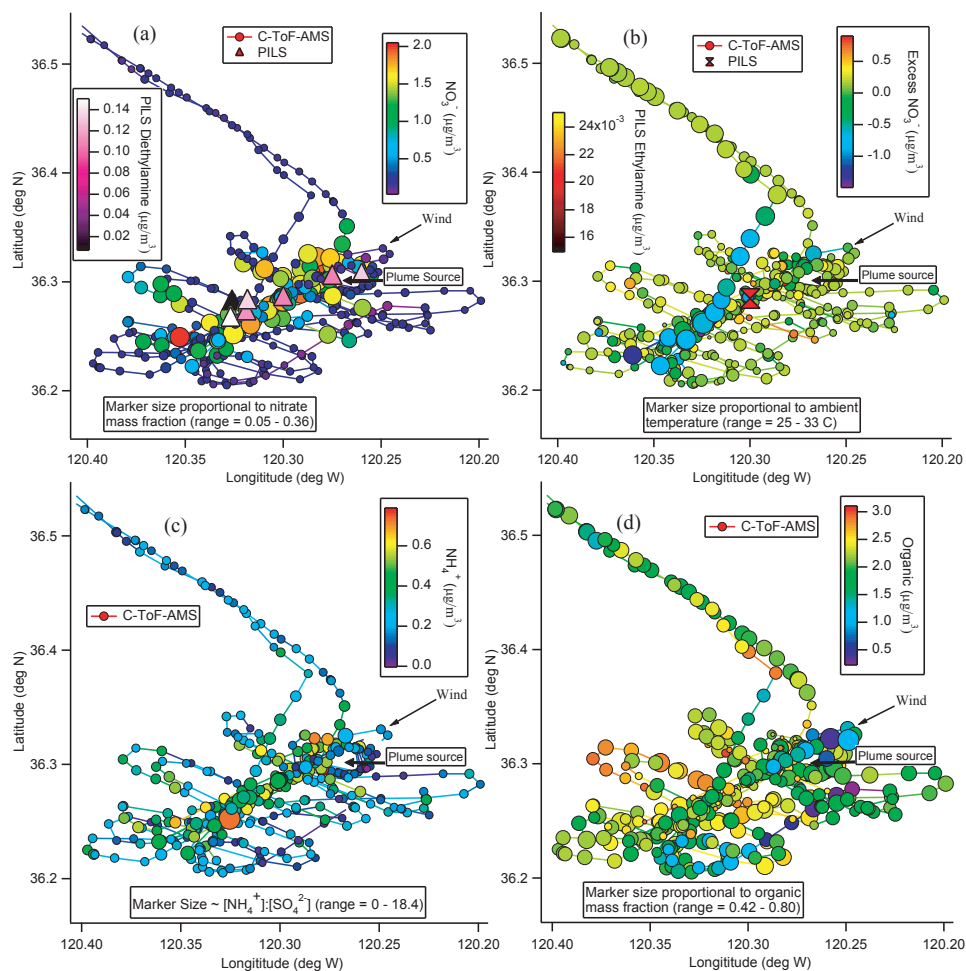


Fig. 8. Spatial distribution of various aerosol species during flight B. (a) C-ToF-AMS nitrate and PILS diethylamine, with marker size proportional to nitrate mass fraction; (b) *Excess nitrate* remaining after both sulfate and nitrate have been neutralized by ammonium (see Sect. 2.1 for further explanation), with marker size proportional to ambient temperature; (c) C-ToF-AMS ammonium, with marker size proportional to the ammonium-to-sulfate molar ratio; (d) C-ToF-AMS organic, with marker size proportional to organic mass fraction. The PILS markers are spatially placed wherever the aircraft was at the midpoint of the time when a particular sample was collected (after being corrected for liquid residence time in the instrument).

subsequently, this is likely attributed to increased partitioning of particulate amines to the gas phase to maintain thermodynamic equilibrium as the plume dilutes with background air. An analysis of the background valley aerosol spectra during the transit portions of the flights indicates that the organic aerosol composition was similar throughout the valley.

Two amines were detected by the PILS, diethylamine and ethylamine; these were found only in the plume (Figs. 6–8). Diethylamine reached higher concentrations (up to $0.18 \mu\text{g}/\text{m}^3$ and 6.0% of the organic mass) and was more abundant farther downwind of the feedlot as compared to ethylamine; diethylamine was observed at plume ages up to 0.9 h (flight A) and 0.7 h (flight B). Ethylamine was detected

by the PILS only in three samples collected during the two flights. It was found immediately downwind of the feedlot up to plume ages of 0.7 h (flight A) and 0.3 h (flight B) at concentrations near $0.02 \mu\text{g}/\text{m}^3$, which corresponds to 0.8% of the total organic mass, as inferred from the C-ToF-AMS data.

The collective organic acid concentration, as determined by the PILS, reached levels of up to $0.23 \mu\text{g}/\text{m}^3$ (flight A) and $0.41 \mu\text{g}/\text{m}^3$ (flight B), accounting for 0.4% ($\pm 0.8\%$) and 0.4% ($\pm 0.6\%$) of the C-ToF-AMS total organic mass during flights A and B, respectively. Oxalate was the most abundant organic acid, followed by succinate, formate, and acetate. The concentration of the organic acids ($\text{C}_1\text{--}\text{C}_9$) were not

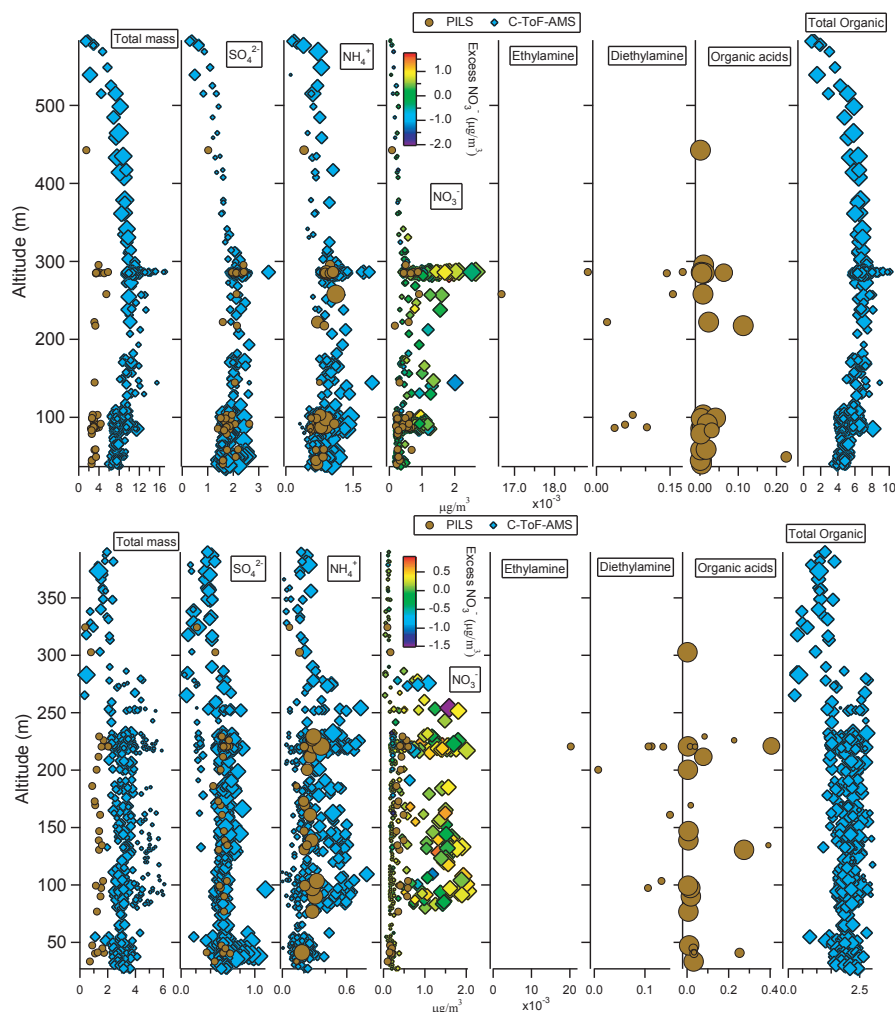


Fig. 9. Vertical distribution of total submicrometer particulate mass and species concentrations from both the PILS and C-ToF-AMS, for flights A (upper panel) and B (lower panel). The C-ToF-AMS marker sizes for “Total mass” are proportional to the organic:inorganic ratio. Marker sizes for the individual C-ToF-AMS species are proportional to the respective mass fraction of that species. Marker sizes for PILS “Organic acids” are proportional to the relative contribution by oxalate. Marker sizes for PILS ammonium are proportional to the ammonium-to-sulfate molar ratio. Total mass, nitrate, ammonium, and organics increase in concentration with increasing altitude up to ~250–300 m, before decreasing in both flights. C-ToF-AMS concentrations exceed those of the PILS for commonly detected species in the plume, especially nitrate and ammonium, since the PILS averages 5-min worth of aerosol composition whereas the C-ToF-AMS has a time resolution of ~20–30 s. Total PILS mass includes inorganics and organic acids, whereas total C-ToF-AMS mass includes inorganics and nonrefractory organic mass.

found to be correlated with those of total organics, amines, or any inorganic species.

3.4 Aerosol mixing state

Figure 12 shows speciated size distributions for the background and in-plume aerosol at various downwind distances for both flights. Organics, nitrate, and sulfate all appear to be externally mixed to some extent. This is especially clear

when examining the plume aerosol at various downwind distances in flight B; the distribution of nitrate aerosol grows in diameter, while the organic distribution shows relatively less growth and the sulfate distribution does not exhibit any corresponding shift in size. Speciated size distributions for the valley aerosol during transit are similar to the background aerosol in the vicinity of the feedlot, indicating chemically similar particles.

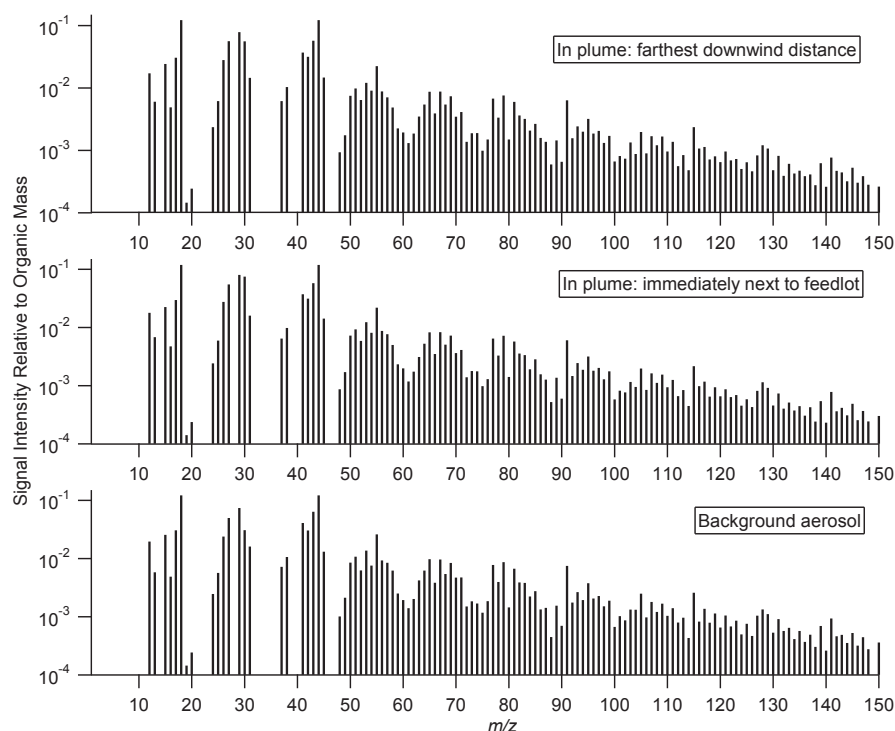


Fig. 10. Aerosol mass spectra from the C-ToF-AMS in the background aerosol and in the plume at various downwind distances from the feedlot for flight B. There is no significant difference in the chemical signature of the aerosol in the three categories shown, with the notable exception of an enhancement in the m/z 30 peak, a common amine marker, at the closest point to the source. The flight A spectra are similar to those presented here.

3.5 Refractive index

The background aerosol exhibited a consistent average dry-particle refractive index of 1.54 ± 0.07 and 1.54 ± 0.04 for flights A and B, respectively (Table 2). Since these values are close to those of ammonium nitrate (1.55) and ammonium sulfate (1.52–1.53) (Weast, 1987; Tang, 1996), which are the dominant inorganic components of the aerosol, assuming a volume-weighted overall refractive index, the organic component refractive index is calculated also to be 1.54. Notably, Zhang et al. (1994) reported a similar refractive index of 1.55 for particulate organic compounds in Grand Canyon aerosol. The overall aerosol refractive indices were slightly lower in the plume, with the lowest values observed closest to the feedlot during the aircraft circling maneuvers (1.48 ± 0.09 and 1.51 ± 0.01 for flights A and B, respectively). Organic species, such as amines, may be responsible for this decrease as the organic mass fraction dominated the total mass; ethylamine and diethylamine have refractive indices of 1.37 and 1.39, respectively (Dean, 1999). Although only two particulate amines were speciated at low concentrations (<4% of total mass), other amine compounds may well have existed in the total organic mass with comparable refractive indices.

3.6 Hygroscopic properties of the aerosol

3.6.1 Subsaturated water uptake

Figures 13 and 14 present the spatial distribution of hygroscopic growth factors at the RHs studied for flights A and B, respectively. Aerosol growth factors ranged from 1.00 to 1.27 at 74% RH, 1.21 to 1.62 at 85% RH, and 1.30 to 2.04 at 92% RH (Table 2), depending on location, altitude, and proximity to the plume source. For reference, growth factors for pure ammonium nitrate ($D_{p,dry}=150$ nm) at RHs of 74%, 85%, and 92% are 1.37, 1.60, and 1.94, respectively (deliquescence RH=61.8%; Brechtel and Kreidenweis, 2000). Growth factors for pure ammonium sulfate ($D_{p,dry}=150$ nm) at RHs of 85% and 92% are 1.56 and 1.80, respectively (deliquescence RH=79.9%; Brechtel and Kreidenweis, 2000). Overall, the plume aerosol exhibited higher hygroscopic growth factors as compared to the background aerosol. Hygroscopic growth factors in the immediate vicinity of the source were usually between 1.75–1.90 at RH=92%.

Hygroscopic growth factors are now related to the mass fractions of the aerosol components. Figure 15 shows the

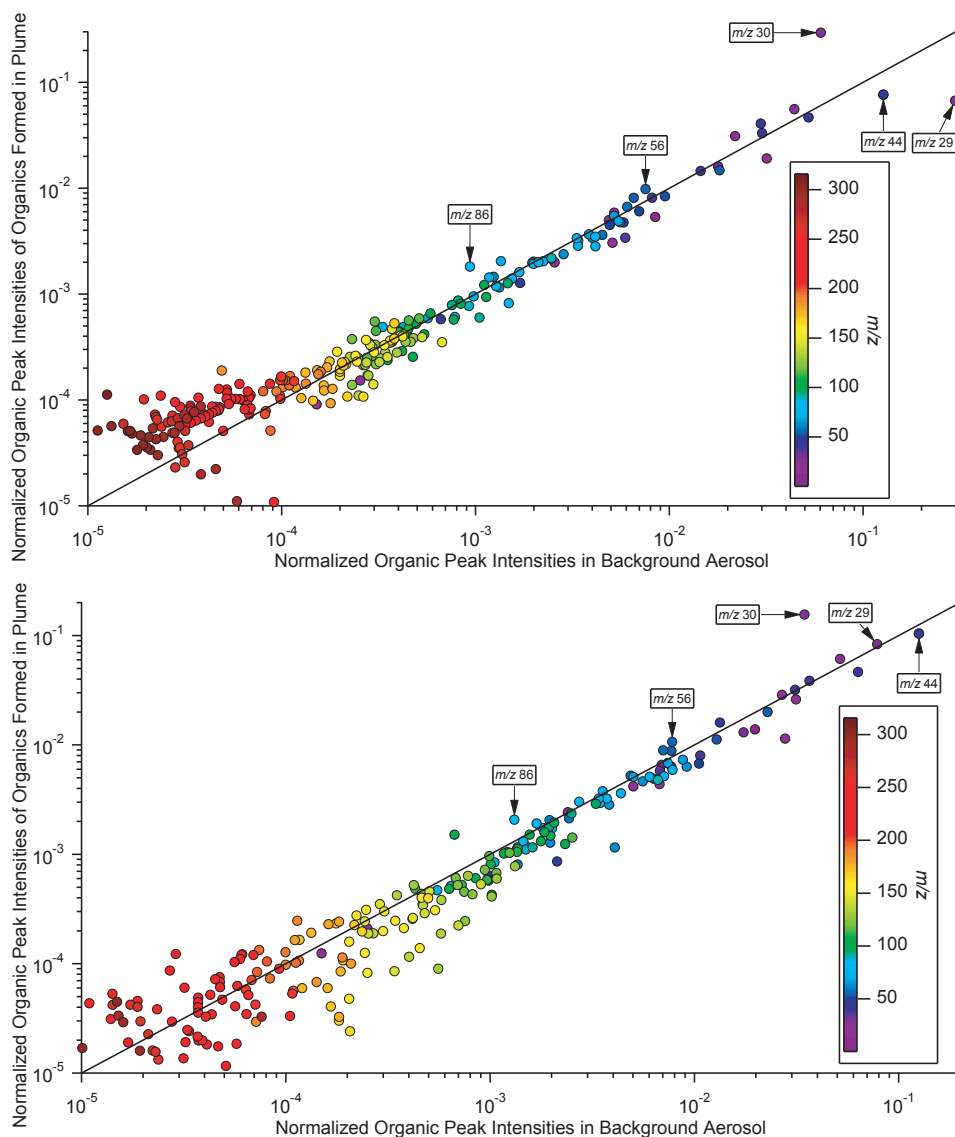


Fig. 11. A comparison of the plume organic mass spectra versus the background aerosol organic mass spectra for flights A (upper panel) and B (lower panel). All non-organic contributions to the mass spectra have been removed by fragmentation calculations described in Sect. 3.3.3. This means that the signal at m/z 30 represents a fragment of organics, including amines. The data on the y-axis were generated by taking the difference in the organic spectra in the plume and out of the plume. The organic aerosol appears to be very similar except this plot shows that there is an increase in peak intensities at m/z 30, 56, and 86, common amine peaks, in the plume. The peak intensity at m/z 44 (and 29 in flight A) is greater in the background aerosol spectra indicating increased oxidation out of the plume as compared to inside the plume.

dependence of growth factors at an RH of 92% on mass fractions of nitrate and organics measured for flight B. (Similar effects occur at the other RHs.) Increasing growth factors coincide with higher nitrate mass fractions. This effect is most evident during flight B, in terms of slope (0.31) and correlation ($r^2=0.43$), partly because of the larger range of

nitrate mass fractions observed. In addition, growth factors exhibited a negative correlation ($r^2=0.46$, slope= -0.28) with organic mass fractions. Less correlation exists between observed growth factors and mass fractions of ammonium and sulfate ($r^2<0.21$). The data show that subsaturated hygroscopicity increases as a function of increasing fraction of

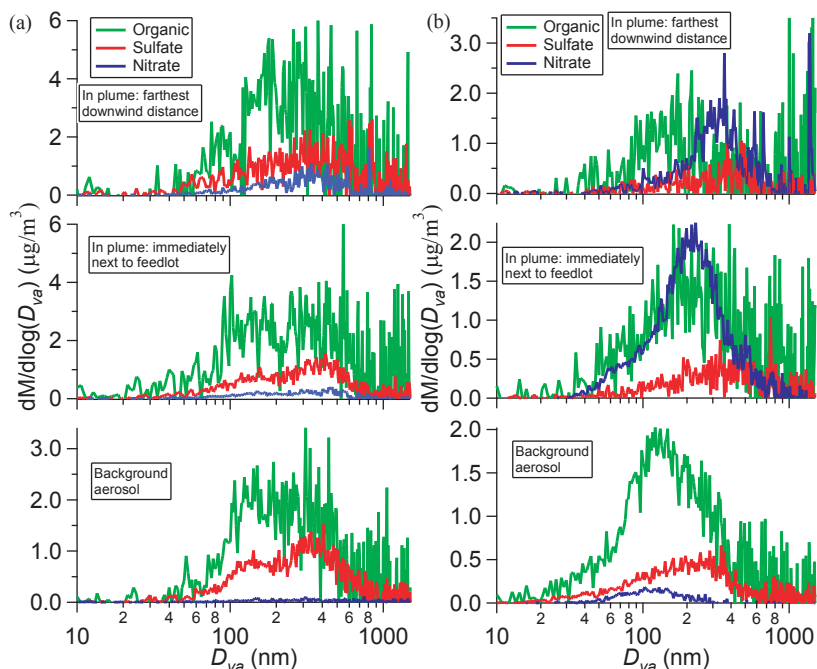


Fig. 12. Speciated size distributions as determined by the C-ToF-AMS for flights A (panel (a)) and B (panel (b)). The x-axis is the vacuum aerodynamic diameter. There is evidence of externally mixed aerosols, evident by the independent shifts of various species as a function of increasing plume age. This is clearest in flight B where nitrate is shown to grow in size with plume age with less growth for organics and no growth for sulfate.

Table 2. DASH-SP hygroscopicity and dry particle refractive index data categorized by the time of flight as shown in Fig. 1. Data at RH=85% are not available for flight A.

		<i>GF</i> (74%)	<i>GF</i> (85%)	<i>GF</i> (92%)	Dry Refractive Index
Flight A	Valley transit	1.10±0.05		1.64±0.17	1.52±0.08
	Circle above plume source	1.16±0.12		1.79±0.22	1.48±0.08
	First set of transects (1–4)	1.07±0.03		1.55±0.19	1.52±0.06
	Transect 1 (plume age=0.3 h)	1.04±0.03		1.59±0.17	1.54±0.04
	Transect 2 (plume age=0.5 h)	1.05±0.03		1.51±0.22	1.56±0.05
	Transect 3 (plume age=1.1 h)	1.08±0.03		1.70±0.18	1.48±0.05
	Transect 4 (plume age=1.5 h)	1.06±0.01		1.74±0.08	1.51±0.01
	Spiral up to 600 m	1.07±0.05		1.47±0.15	1.53±0.10
	Second set of transects (5–7)	1.09±0.04		1.61±0.13	1.54±0.05
	Transect 5 (plume age=1.2 h)	1.06±0.01		1.68±0.06	1.54±0.05
	Transect 6 (plume age=1.3 h)	1.12±0.05		1.60±0.08	1.54±0.05
	Transect 7 (plume age=0.8 h)	1.12±0.01		1.69±0.16	1.54±0.09
	Spiral down above plume source	1.33±0.30		1.80±0.19	1.40±0.10
	Valley transit	1.06±0.02		1.53±0.15	1.56±0.05
Flight B	Valley transit	1.03±0.04	1.35±0.06	1.49±0.07	1.55±0.04
	Circle above plume source	1.10±0.07	1.50±0.10	1.88±0.22	1.51±0.01
	First set of transects (plume age<0.9 h)	1.12±0.05	1.39±0.08	1.65±0.20	1.52±0.01
	Directly in plume (plume age<0.9 h)	1.15±0.06	1.44±0.06	1.86±0.14	1.52±0.01
	Spiral up to 400 m	1.07±0.04	1.37±0.06	1.57±0.07	1.52±0.01
	Second set of transects (plume age<0.9 h)	1.08±0.04	1.39±0.06	1.65±0.17	1.53±0.03
	Directly in plume (plume age<0.9 h)	1.09±0.05	1.40±0.09	1.65±0.16	1.51±0.02
	Valley transit	1.11±0.04	1.39±0.08	1.55±0.11	1.53±0.05

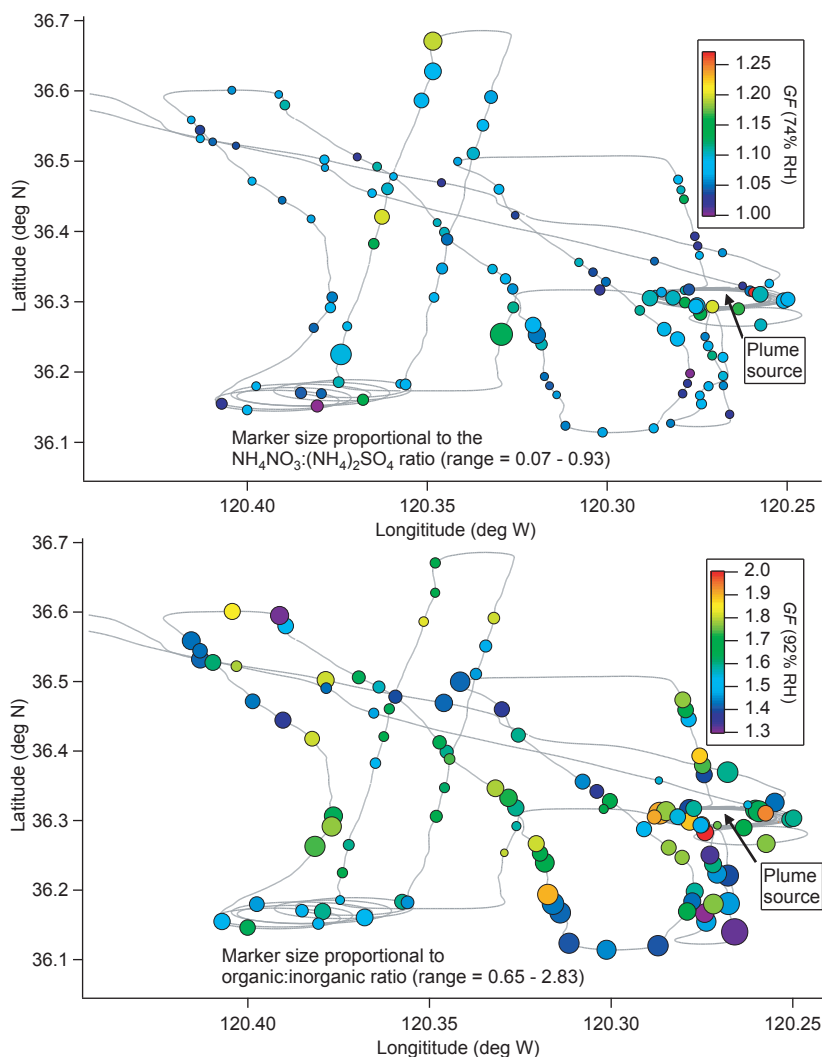


Fig. 13. Growth factor data from flight A at RHs of 74% (upper panel) and 92% (lower panel). The markers represent individual DASH-SP scans at dry diameters between 150 and 200 nm. Marker sizes in upper panel are proportional to the ammonium nitrate:ammonium sulfate ratio, while marker sizes in the lower panel are proportional to the organic:inorganic ratio (inorganic=ammonium sulfate+ammonium nitrate).

ammonium nitrate, a highly hygroscopic salt, and decreasing fraction of organics, the growth factor of which will be explored subsequently.

3.6.2 CCN

The CCN data acquired are summarized in Table 3 and Fig. 16. Owing to the large number of particles with diameters below about 60 nm, in the background atmosphere as well as in the plume, the activated fractions were quite small. An enhancement in activated fraction was observed in the plume, which is consistent with the observed behavior of subsaturated hygroscopic growth factors.

An important issue is the extent to which aerosol composition influences CCN behavior. This can be manifested in two ways: (1) by affecting the critical supersaturation of the particles; and (2) by influencing the growth rate once the particle activates. Figure 17 shows the normalized activation fraction as a function of hygroscopic growth factor for flight B. The normalization is done by computing the activation fraction assuming the CCN are composed of pure ammonium sulfate. The normalization removes any variations due to shifts in the shape of the size distribution. It is noted that, in general, higher supersaturations are required to activate particles composed of less hygroscopic material.

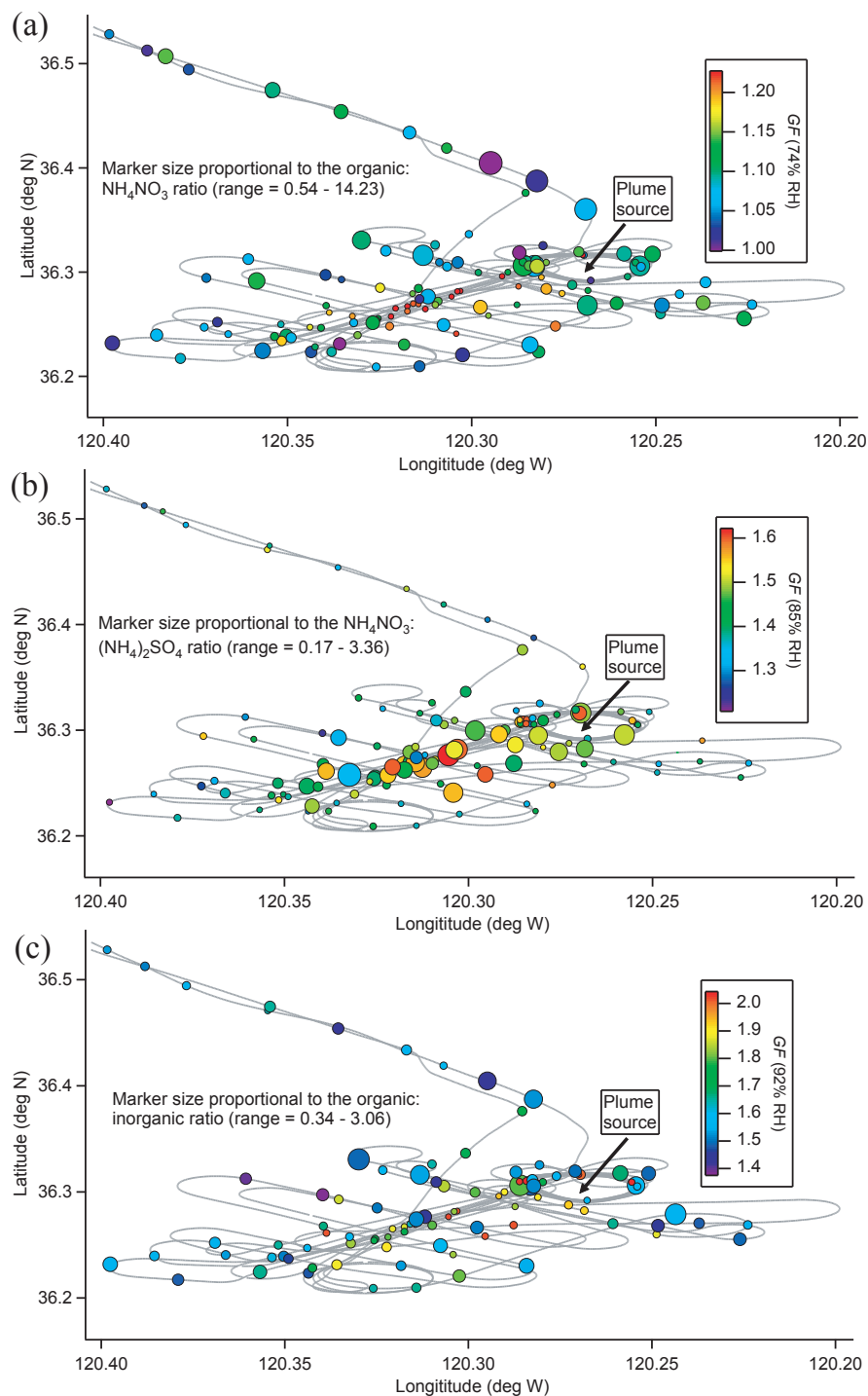


Fig. 14. Growth factor data from flight B at RHs of 74% (a), 85% (b), and 92% (c). The markers represent individual DASH-SP scans at dry diameters between 150 and 200 nm. (a) Marker sizes are proportional to the organic:ammonium nitrate ratio; (b) marker sizes are proportional to the ammonium nitrate:ammonium sulfate ratio; (c) marker sizes are proportional to the organic:inorganic ratio (inorganic=ammonium sulfate+ammonium nitrate).

Table 3. Summary of CCN data for flights A and B.

			CCN (#/cm ³)	Activated fraction								
			SS~0.1%		SS~0.2%		SS~0.3%		SS~0.4–0.45%		SS~0.5%	
Flight A	In plume	AVE	92	0.01	329	0.02	1114	0.06	1882	0.08	2265	0.08
		ST DEV	123	0.01	354	0.02	628	0.05	526	0.04	478	0.02
	Out of plume	AVE	141	0.01	252	0.01	1124	0.05	1641	0.06	1966	0.08
		ST DEV	218	0.01	295	0.01	561	0.03	484	0.02	478	0.02
			SS~0.2%		SS~0.25–0.35%		SS~0.4–0.45%		SS~0.6%			
Flight B	In plume	AVE	855	0.05	1246	0.07	2027	0.11	2436	0.15		
		ST DEV	584	0.03	713	0.04	523	0.03	834	0.05		
	Out of plume	AVE	707	0.04	1073	0.06	1796	0.08	4168	0.14		
		ST DEV	596	0.03	770	0.05	768	0.03	2052	0.04		

Regarding the effect of particle composition on growth rate, consider two particles each having the same critical supersaturation. If the ambient supersaturation exceeds the critical supersaturation, then each particle will activate. The subsequent rate of growth by water condensation depends on the uptake of water molecules. If the two particles have different composition, then the uptake coefficients for water vapor can be different; the particle with the smaller water uptake coefficient will exhibit a slower rate of growth after activation. In a CCN instrument, like the CCNc employed here, the more slowly growing particle may not reach its ultimate size before it exits the growth chamber of the instrument and is detected by the OPC. The growth rate of pure ammonium sulfate particles of the same critical supersaturation as that of the particle in question can be taken as the standard against which particle growth rates can be compared. Since an entire distribution of particles enter the CCNc, with different critical supersaturations (as a result of size and composition), the standard used is ammonium sulfate with a critical supersaturation equal to the supersaturation of the instrument. Based on this standard, if all particles grow as quickly as those composed entirely of ammonium sulfate, all particles will have droplet sizes equal to or larger than the standard. Hence, at a given supersaturation, the presence of droplets with a size less than that of the standard indicates retarded growth. We express this effect in terms of the fraction of droplets less than the standard at the supersaturation of the instrument.

Figure 18 shows the C-ToF-AMS - derived ratio of m/z 57:44 as a function of organic mass fraction. (A larger m/z 57:44 ratio is correlated with the organic material being less oxidized, and hence more hydrophobic.) The color coding of the data points corresponds to the fraction of droplets that have a size (D_i) less than the ammonium sulfate standard (D_{AS}), as described above. The size of the symbols reflects the hygroscopic growth factor at 92% RH. The data indicate that at high organic mass fractions when the particles are composed of less oxidized material, there is a tendency, although weak, towards retardation of growth. The degree of correlation (r^2) between the fraction of droplets

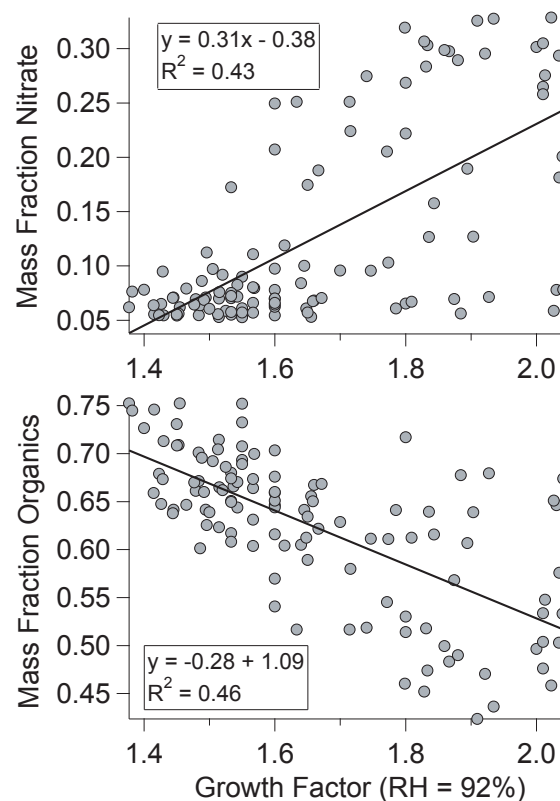


Fig. 15. Relationship between the hygroscopic growth factor at 92% RH and mass fractions of nitrate and organics during flight B. Less correlation exists between the subsaturated hygroscopic growth factors and the mass fractions of ammonium ($r^2=0.19$, slope=0.07) and sulfate ($r^2=0.21$, slope=-0.10).

with (D_i)<(D_{AS}) and various measurements of the organic material are as follows: m/z 57:44 (0.11), organic mass fraction (0.03), product of m/z 57:44 and organic mass fraction

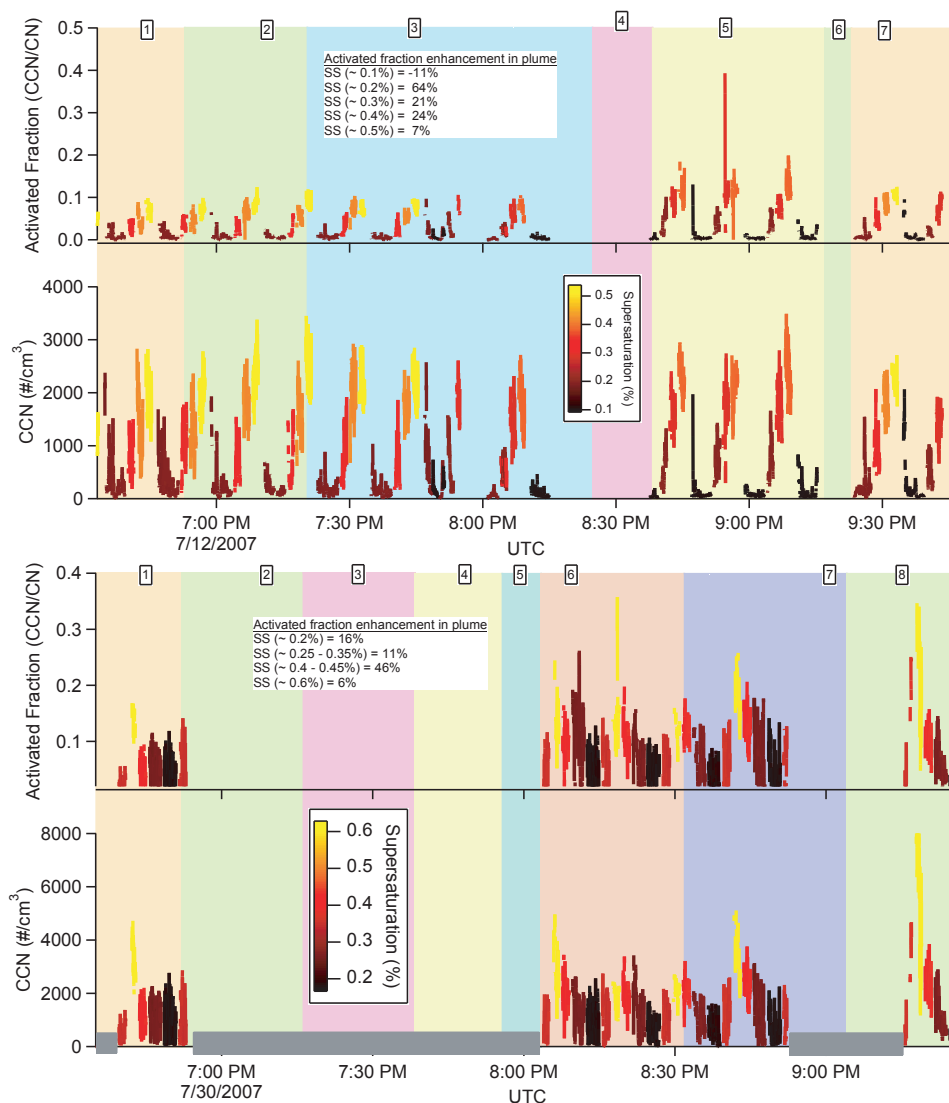


Fig. 16. Time series of activated fraction of aerosol (CCN/CN), and total CCN concentration during flights A (upper panel) and B (lower panel). Data points are color-coded with instrument supersaturation. The shaded gray boxes in the lower panel indicate portions of flight B when the CCNc was operating in an alternative mode and those data are not presented here.

(0.01). The growth factor exhibits a clear anti-correlation with organic mass fraction.

4 Discussion

In this section we explore key findings in this study. The observations reveal significant differences in aerosol properties in and out of the plume, and as a function of plume age. Significant enhancements in nitrate, ammonium, and organic levels in the plume were observed; this coincided with an

increased potential for water uptake in both the sub- and supersaturated regimes. While trends in the data from the two flights were similar, particle number and mass concentrations were larger in flight A. Explanations for this discrepancy will be pursued.

Owing to the range of organic fractions observed, the present study provides an opportunity to evaluate the sensitivity of mixed inorganic/organic particle hygroscopicity to the organic fraction. Subsaturated hygroscopic growth factors are calculated for the organic fraction based on a closure

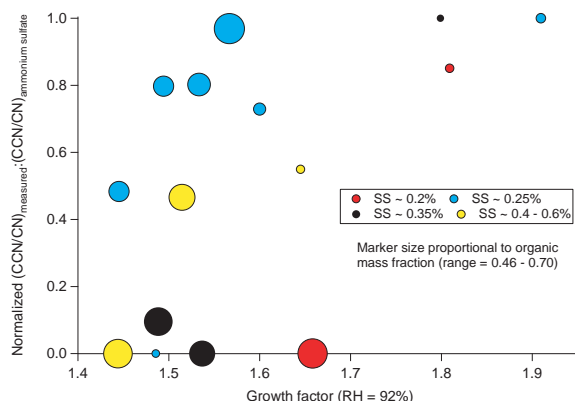


Fig. 17. Normalized CCN activation ratio, $(\text{CCN}/\text{CN})_{\text{measured}}:(\text{CCN}/\text{CN})_{\text{ammonium sulfate}}$, as a function of hygroscopic growth factors for flight B. The effects of size distribution and mixing state have been removed from the data and the calculated activation ratio to isolate the impact of composition on the relationship between water uptake in the sub- and supersaturated regimes (see Sect. 3.6.2).

analysis using the Zdanovskii-Stokes Robinson (ZSR) mixing rule. Measurement of CCN activity in this study also presents an opportunity to assess the consistency of observed supersaturated water uptake with the subsaturated water uptake measurements.

4.1 Enhancements in mass production and water uptake in the plume aerosol

Significant production of ammonium nitrate and organic mass in the plume occurred during both flights. Ammonium nitrate production is expected due to the high ammonia levels and the presumed abundance of nitric acid from the daytime photochemistry. Organic aerosol mass production results from both condensation of semi-volatile organic species and acid-base chemistry of amines, followed by condensation of low-volatility products onto pre-existing aerosols.

Enhanced sub- and supersaturated water uptake coincides with greater fractions of ammonium, nitrate, and amines. Dinar et al. (2008) have shown, for example, that the reactive uptake of ammonia by aerosols containing slightly soluble organics leads to substantial increases in hygroscopic growth and CCN activity. This observation appears to be consistent with the present measurements. Speciated size distributions show that the aerosol is, in part, externally mixed, with different species growing independently during plume aging (Fig. 12). The high organic fractions, particularly during flight A, may have masked the expected and significant growth exhibited by pure ammonium nitrate and ammonium sulfate salts; however, amines, which represent one class of organic species in the plume, are thought to be highly hygroscopic. Aklilu et al. (2006) also suggested that the organic

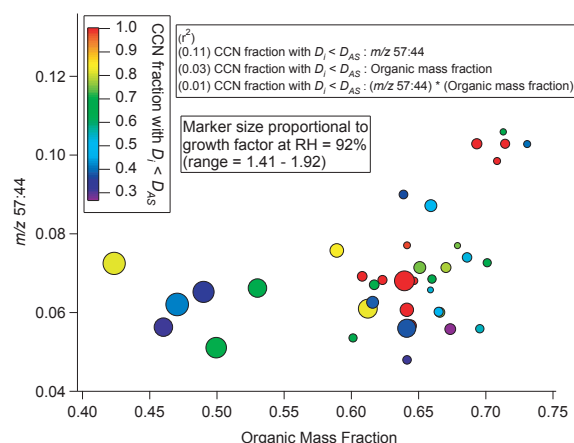


Fig. 18. The relationship between the m/z 57:44 ratio, the organic mass fraction, the CCN fraction with less droplet growth than ammonium sulfate ($D_i < D_{AS}$), and the hygroscopic growth factor at $\text{RH}=92\%$. The CCN fraction with $D_i < D_{AS}$ is a qualitative measure of kinetic limitations to droplet growth. The majority of the markers representing the lowest values of $D_i < D_{AS}$ occur at m/z 57:44 < 0.07, while most of the higher values of $D_i < D_{AS}$ coincide with the highest organic mass fractions (>0.6). The highest growth factors at $\text{RH}=92\%$ occur at the lowest organic mass fractions and m/z 57/44 ratios.

fraction of the aerosol can suppress the growth normally associated with nitrate based on ambient measurements at two rural, urban-influenced sites.

4.2 Amines as an atmospheric base

4.2.1 Is nitric acid or ammonia the limiting reactant?

Previous studies of particulate ammonium nitrate formation in the San Joaquin Valley suggest that the limiting reactant is nitric acid because of abundant ammonia emissions (Blanchard et al., 2000; Pun and Seigneur, 1999). During an aircraft study in the San Joaquin Valley in May 2002, Neuman et al. (2003) reported simultaneous nitric acid depletion and aerosol mass enhancements when the aircraft either encountered large ammonia sources or reached lower temperatures at higher altitudes in the boundary layer. Ammonia is emitted from the ground, whereas nitric acid is efficiently produced photochemically throughout the entire boundary layer, especially during the summer in the daytime San Joaquin Valley atmosphere.

Since gas-phase ammonia and nitric acid were not measured in the present study, observed particulate levels of ammonium, nitrate, sulfate, and amines can help determine the limiting reactant in chemical processing inside the plume. *Excess nitrate* is most abundant within the plume, reaching levels as high as $1.72 \mu\text{g}/\text{m}^3$ (flight A) and $0.89 \mu\text{g}/\text{m}^3$ (flight B). (As defined in Sect. 2.1, *excess nitrate* is the amount

of nitrate remaining after both sulfate and nitrate have been fully neutralized by ammonium.) The greatest *excess nitrate* values coincide with relatively lower ambient temperatures, higher altitudes, the presence of diethylamine and ethylamine, and are correlated with amine markers in the C-ToF-AMS spectra (m/z 56 and 86) (Figs. 7b, 8b and 9). The background aerosol tends to exhibit *excess nitrate* values close to zero, indicating that just enough ammonia was present, on average, to neutralize both sulfate and nitrate. The data suggest either of two conclusions: (1) insufficient ammonia was present to neutralize both sulfate and nitrate within the plume, thereby distinguishing ammonia as the limiting reactant; or (2) sufficient ammonia was present, but a significant amount of nitric acid formed salts preferentially with amines rather than ammonia. The detection of amines by the PILS and the large amount of organic mass, with representative amine markers detected by the C-ToF-AMS, suggests that the second explanation may be more plausible. This is a significant finding in the atmosphere that is consistent with laboratory observations made in photooxidation experiments of aliphatic amines (Angelino et al., 2001; Murphy et al., 2007). The affinity of inorganic acids for amines in the presence of ammonia could possibly have greater implications under conditions of lower temperatures and higher RHs due to increased partitioning of both ammonium nitrate and amine salts into the aerosol phase. However, caution must be taken when extrapolating the current results to other atmospheric conditions such as stronger pollution events, especially during winter stagnation events in the San Joaquin Valley, when a great excess of ammonia can exist over nitric acid.

4.2.2 Sources and character of amines

The formation of particulate amine salts depends on temperature, the identity and concentrations of the amine and acidic species present, and the concentration of ammonia that competes with amines for the acidic species. Once the particulate amine salts are formed, they may revolatilize, undergo subsequent particle-phase reactions including oxidation, or serve as a site for the condensation of other organic compounds. Chamber experiments performed by Murphy et al. (2007) showed that the dominant formation mechanism for amines is that of acid-base reactions (amine+nitric acid) rather than from photooxidation to form non-salt condensable organics. These experiments showed that nitric acid preferentially reacts with amines, depending on the species, rather than ammonia. It is expected that particulate amines should be prevalent close to the source of amine emissions where gaseous amine concentrations are highest. If the temperature dependence of amine salt equilibria resembles that of ammonium nitrate, then amines should partition more favorably to the aerosol phase at lower temperature (higher altitudes) within the plume. Of the six amines studied by Murphy et al. (2007), diethylamine was shown to have the

most favorable equilibrium constant for salt formation in the presence of ammonia, an observation that is consistent with the present field measurements since diethylamine was the most abundant amine detected in the aerosol. The amine salts produced in the laboratory chamber experiments eventually repartitioned back to the gas phase. In the present study, amine concentrations decreased as a function of plume age, as evident in the m/z 30 peak intensity data from the C-ToF-AMS (Fig. 10). The decreasing amine levels in the aerosol phase presumably occur because of two reasons: (1) amine concentrations, like those of ammonium and nitrate, decrease due to dilution as a function of plume age; and (2) amines partition back to the gas phase to maintain thermodynamic equilibrium due to the decreasing gas-phase concentrations owing to dilution.

Diethylamine, measured exclusively in the plume, exhibited a strong and positive correlation with nitrate, ammonium, sulfate, and total organics during flight A ($n=8$, r^2 : nitrate=0.65, ammonium=0.73, sulfate=0.72, organics=0.68), but showed a weaker correlation with the same species during flight B ($n=7$, r^2 : nitrate=0.35, ammonium=0.04, sulfate=0.13, total organics=0.40). The positive correlation between diethylamine and nitrate suggests that nitric acid exhibits an affinity for amines as an atmospheric base, even in the presence of ammonia. Diethylamine concentrations correlated more weakly with sulfate than to nitrate during flight B, possibly because nitric acid levels were higher than those of sulfuric acid causing the formation of particulate amines to proceed only through the amine + HNO_3 acid-base reaction. When diethylamine was detected, its average mass ratio relative to nitrate was 0.31 (flight A) and 0.36 (flight B); relative to sulfate it was 0.16 (flight A) and 0.36 (flight B), and relative to ammonium it was 0.31 (flight A) and 0.17 (flight B).

4.2.3 Total amine mass calculations

One can estimate the total mass of amines present in the plume. This calculation assumes that *excess nitrate* is in a 1:1 molar ratio with amines. Amine mass is then determined by assuming a representative molecular weight for the amine population. We choose to use methylamine and triethylamine as lower and upper limits, respectively, since these species represent the smallest and largest amines that can be speciated using the PILS-IC technique (Murphy et al., 2007); the molecular weight of the two amines detected in this study, ethylamine and diethylamine, fall within the range of those of methylamine and triethylamine.

On the basis of the molecular weight of methylamine (31.1 g/mol), average amine concentrations in the plume are calculated to have been $0.23 \pm 0.13 \mu\text{g}/\text{m}^3$ (4% of total organic mass) (flight A) and $0.06 \pm 0.10 \mu\text{g}/\text{m}^3$ (2% of total organic mass) (flight B), while maximum plume concentrations were $0.86 \mu\text{g}/\text{m}^3$ (13% of total organic mass) (flight A) and $0.44 \mu\text{g}/\text{m}^3$ (19% of total organic mass) (flight B).

B). On the basis of the molecular weight of triethylamine (101.1 g/mol), average amine concentrations are calculated to have been $0.76 \pm 0.43 \mu\text{g}/\text{m}^3$ (12% of total organic mass) (flight A) and $0.20 \pm 0.32 \mu\text{g}/\text{m}^3$ (8% of total organic mass) (flight B), while maximum levels were $2.81 \mu\text{g}/\text{m}^3$ (43% of total organic mass) (flight A) and $1.45 \mu\text{g}/\text{m}^3$ (63% of total organic mass) (flight B). Using the conservative molecular weight of methylamine, amine mass was at least 23% (flight A) and 14% (flight B) of ammonium mass in this plume. In addition, speciated amines (ethylamine and diethylamine via the PILS) accounted for at least 25% (flight A) and 45% (flight B) of the estimated total amine mass (via the *excess nitrate* calculation from the C-ToF-AMS).

4.3 Degree of oxidation and volatility in the Aerosol

In the absence of strong signals in the data representing primary particulate emission sources, the submicrometer aerosol in the sampling region is presumed to originate mainly from secondary production. No obvious signs of primary aerosol vehicular emissions existed based on organic markers in the C-ToF-AMS spectra. The ratio of m/z 57:44 peak intensities from the C-ToF-AMS can provide some insight into the relative ratio of hydrocarbon-like (HOA) and oxygenated organic (OOA) aerosols (Zhang et al., 2005); m/z 57 is representative of hydrocarbon-like structures (typically C_4H_9^+), while m/z 44 (typically CO_2^+ ion) arises only from oxygenated compounds (Alfarra et al., 2004; Cubison et al., 2006). To provide a framework, values of the m/z 57:44 ratio have been observed to range between 1–2 at urban sites in Canada and the UK, less than 0.10 at a rural site in Canada, less than 0.10 above the Eastern Pacific Ocean, and between 0.5–2.0 in the exhaust plume of a container ship (<http://cires.colorado.edu/jimenez-group/AMSSd/>; Alfarra et al., 2004; Ulbrich et al., 2008; Murphy et al., 2008¹). This ratio was $\sim 0.07 \pm 0.01$ during both flights, with no major changes between the plume and background aerosol (Table 1). Based on this ratio, it appears that the aerosol was highly oxygenated with relatively little hydrocarbon-like organic aerosol (HOA). The ratio of the peak intensity between m/z 44 and total organics was, on average, 0.10 ± 0.01 in the plume aerosol and 0.11 ± 0.02 in the background aerosol (Table 1). Peak intensities at m/z 44 (and 29 for flight A) are slightly greater in the background aerosol relative to plume aerosol, indicating a greater degree of oxidation out of the plume than within it (Fig. 11). This is presumably because the background aerosol had aged longer than the fresh emissions in the plume.

¹Murphy, S. M., Agrawal, H., Sorooshian, A., Padró, L. T., Gates, H., Hersey, S., Welch, W. A., Jung, H., Miller, J. W., Cocker III, D. R., Nenes, A., Jonsson, H. H., Flagan, R. C., and Seinfeld, J. H.: Comprehensive simultaneous shipboard and airborne characterization of exhaust from a modern container ship at sea, *Environ. Sci. Technol.*, submitted, 2008.

The O:C atomic ratio, which is indicative of the oxidation state of the organic aerosol (OA), can be derived from the ratio of m/z 44:OA using the data inventory and methodology presented by Aiken et al. (2008). They determined that O:C values range between 0.2 and 0.8 for ambient urban OA, with a diurnal cycle marked by decreases with primary emissions and increases due to photochemical processing and secondary organic aerosol (SOA) production. In the present study, the O:C ratio is typically between 0.45 and 0.50 both in and out of the plume (Table 1); these values are consistent with what would be expected from fresh SOA.

Organic acids represent a pool of organic species that are water-soluble and highly oxidized. In previous aircraft measurements, organic acids ($\text{C}_1 - \text{C}_9$) contributed $3.4 \pm 3.7\%$ to the total PILS mass in an urban atmosphere (Houston, Texas; Sorooshian et al., 2007a) and $3.5 \pm 3.1\%$ in a marine atmosphere (Eastern Pacific Ocean; Sorooshian et al., 2007b). In the present study, organic acids contributed $2.4 \pm 5.5\%$ to the total PILS mass, indicating greater variability and a lower average mass fraction of organic acids than seen in the other field data. Gas-particle partitioning of these water-soluble organic species may have been affected by the high ambient temperatures in the present flights. In addition, the relatively low humidities and lack of clouds prevented organic acid production via aqueous-phase processing during the measurement period (Sorooshian et al., 2006b). Assuming that photochemical reactions efficiently take place in the aqueous phase, the possibility also exists that photochemical processing is less effective in the absence of an aqueous medium. Organic acid concentrations were not correlated with ammonium or nitrate, which represent semi-volatile species, during the present flights. The ammonium nitrate levels varied significantly in the plume, but concentrations of the organic acids were relatively stable. Thus, the data do not allow one to conclude whether volatility or RH was the dominant factor controlling organic acid levels.

4.4 Factors influencing aerosol number/mass concentrations

Particle number and mass concentrations were significantly higher during flight A than in flight B. The presence of nucleation cannot explain this discrepancy, especially in terms of mass concentration (Table 1). The background aerosol concentration in the valley was also higher during flight A than in flight B. Since there are no significant sources of SO_2 in the sampling region, sulfate can be employed as a tracer for accumulated aerosol originating from long-range transport. It should be noted that comparable levels of vehicular emissions could be expected both days as both flights occurred on weekdays. Sulfate concentrations were significantly higher during flight A. The lower temperatures and higher RH during flight A favored partitioning of semi-volatile species, such as ammonium nitrate and organics, to the aerosol phase. The back-trajectory analysis indicates that the sampled air

mass during flight A originated three days previously over the Pacific Ocean, while the air sampled in flight B originated in a more polluted inland area (Fig. 5). We conclude that ventilation of the valley during flight B was more effective than in flight A, reducing aerosol number and mass concentrations.

Over the flight durations, aerosol concentrations were influenced by competition between a growing boundary layer, decreasing RH, and increasing temperatures. Although the aerosol was well-mixed locally in the valley, the timescale for equilibration between the gas and particle phases is shorter than the boundary layer mixing time (Neuman et al., 2003); this may explain fluctuations in the concentrations of aerosol species at various altitudes and distances downwind of the plume source. The topography of the sampling region downwind of the source and general buoyancy in the boundary layer facilitated vertical transport of emissions to lower temperature regions, reducing the dissociation constant of ammonium nitrate aerosol and, presumably, semi-volatile organics (Figs. 7–9). This might explain why the concentrations of organics (diethylamine in particular), nitrate, and ammonium peaked at the highest altitude and farthest downwind distance from the plume source in flight A (Fig. 7 and 9).

4.5 Estimated subsaturated hygroscopic growth factors for the organic fraction

Calculations were carried out to determine the effective growth factor for the organic fraction needed to achieve composition – hygroscopicity closure. Due to its simplicity and frequent application (Cruz and Pandis, 2000; Dick et al., 2000; Choi and Chan, 2002a, 2002b; Prenni et al., 2003; Wise et al., 2003; Clegg et al., 2003; Clegg and Seinfeld, 2004, 2006a, 2006b; Khlystov et al., 2005; Rissler et al., 2005; Aklilu et al., 2006; Svenningsson et al., 2006; Varutbangkul et al., 2006; Gysel et al., 2007; Sjogren et al., 2007; Dinar et al., 2008), the Zdanovskii-Stokes Robinson (ZSR) (Zdanovskii, 1948; Stokes and Robinson, 1966) mixing rule is employed to predict hygroscopic growth factors. This procedure of estimating hygroscopic growth based on specified composition is based on the assumption that water uptake by each individual component of a particle is independent and additive. We use the following form of the ZSR mixing rule (Aklilu et al., 2006; Gysel et al., 2007):

$$GF_{\text{mixed}}(a_w) \approx \left(\sum_i \epsilon_i GF_i(a_w)^3 \right)^{1/3} \quad (1)$$

where GF_{mixed} is the hygroscopic growth factor of the mixed particle, GF_i is the hygroscopic growth factor of pure compound i , a_w is the activity coefficient of water, and ϵ_i is the volume fraction of pure compound i in the dry particle. $a_w = \text{RH}$ in Eq. (1) (Seinfeld and Pandis, 2006). Growth factors for the pure inorganic components were obtained from

the Aerosol Inorganics Model (AIM; <http://mae.ucdavis.edu/~sclegg/aim.html>; Clegg et al., 1998). A growth factor of unity is also assumed for EC, as suggested by Aklilu et al. (2006). Bulk composition data is used to calculate volume fractions in Eq. (1). Although there is evidence for externally-mixed particles in the plume (Fig. 12), assuming an internal mixture for the purposes of calculating volume fractions eliminates uncertainties associated with converting vacuum aerodynamic diameters from the C-ToF-AMS to mobility-equivalent diameters between 150–200 nm for particles of different densities (the measured growth factors are for dry particle mobility-equivalent diameters between 150–200 nm). Therefore, the assumption of an internal mixture is not entirely correct but it will provide for a fairly accurate representation of the composition for the majority of the size distribution.

Assuming an internal mixture, calculating the individual volume fractions requires an estimate of the organic density. If it is assumed that the aerosol is composed of ammonium sulfate (AS), ammonium nitrate (AN), organic carbon (OC), and elemental carbon (EC), then total aerosol density can be expressed as:

$$\rho = x_{OC}\rho_{OC} + x_{AS}\rho_{AS} + x_{AN}\rho_{AN} + x_{EC}\rho_{EC} \quad (2)$$

where x_i are mass fractions and ρ is density of the multi-component particle, as determined by the ratio of the aerosol mass (via the PILS and C-ToF-AMS) to the aerosol volume (via the DMA); in Eq. (2), ρ_{OC} is the unknown quantity that we desire to determine. Elemental carbon was not quantified in the present study; however, based on extensive chemical characterization of San Joaquin Valley PM_{2.5} by Chow et al. (2006), the mass fraction of EC tends to be ~5–10% near the present sampling site. In the absence of a quantitative measure of EC, it is assumed that 5% of the total sub-micrometer mass is composed of EC. It is assumed for the purpose of this calculation that all of the sulfate is neutralized by ammonium, and the remaining ammonium occurs as ammonium nitrate. Densities of 1.725, 1.769, and 1.9 g/cm³ are used for AN, AS, and EC respectively. A wide range of densities are reported for EC (0.625–2.25) g/cm³ (Fuller et al., 1999); here we assume a value of 1.9 g/cm³, similar to that employed by Dillner et al. (2001). From the mass concentrations and respective densities of AN, AS, OC, and EC, the volume fraction of each component can be calculated.

On average, the in-plume organic growth factors needed to match the data (flight A/B) are 1.07/1.02 (74% RH), NA/1.28 (85% RH), and 1.49/1.53 (92% RH) (Fig. 19). The background aerosol organic growth factors (flight A/B) are 1.08/1.03 (74% RH), NA/1.21 (85% RH), and 1.29/1.24 (92% RH). Flight B is characterized by a wider range in the mass fractions of organics, thus this flight presents a better indication of trends in organic growth factor with changing mass fractions. During this flight, inferred organic growth factors increase in the plume as a function of decreasing organic fraction. The lowest organic fractions in flight B

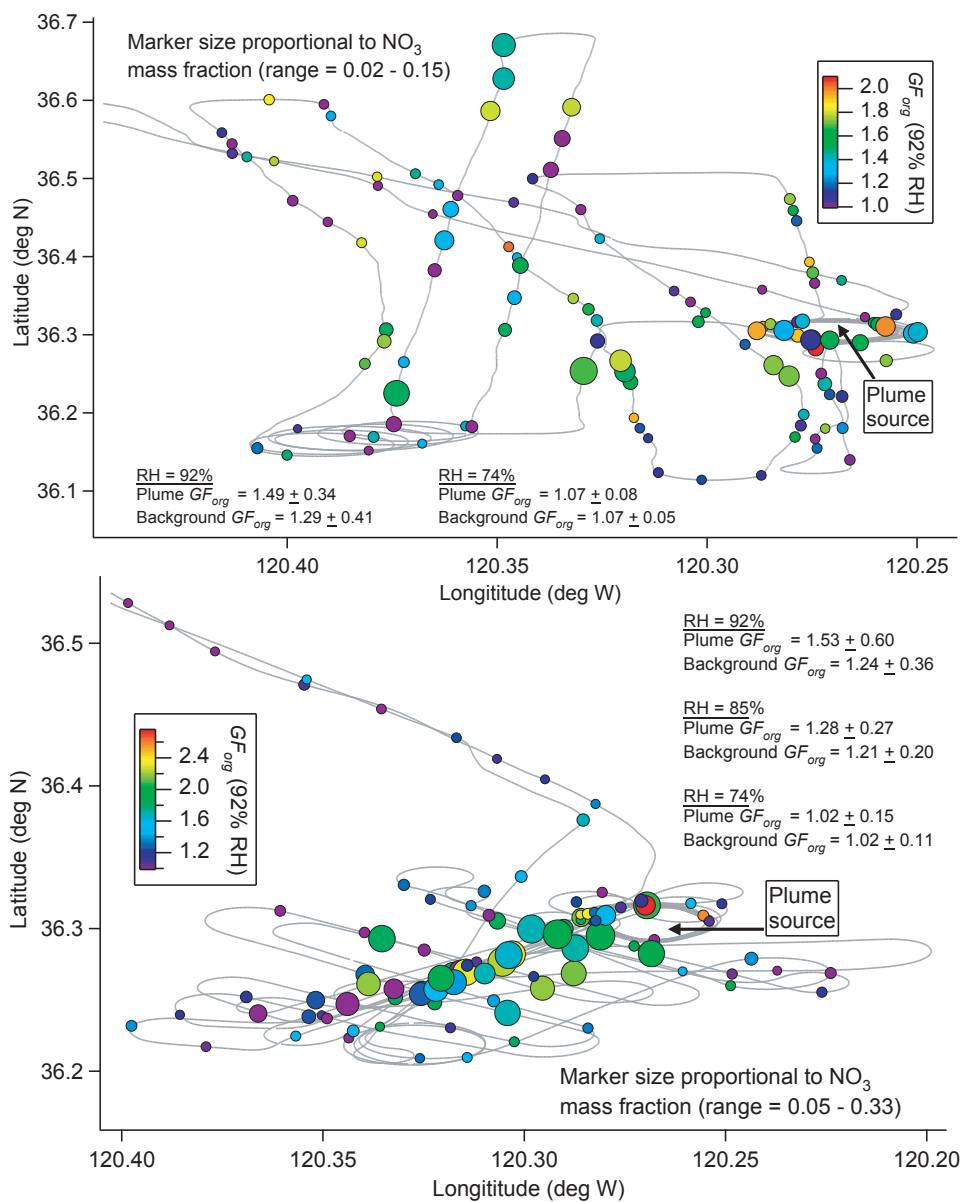


Fig. 19. Spatial distribution of the calculated organic growth factors, using the ZSR mixing rule, for flights A (upper panel) and B (lower panel). Marker sizes are proportional to the mass fraction of nitrate.

coincide with the detection of amines, which likely enhance the hygroscopicity of the organic fraction. There is a significant amount of variation in predicted growth factors at constant organic mass fractions and the absolute values of some of the predicted organic growth factors (<1 and >2) are unrealistic. Possible explanations for the unrealistic organic hygroscopic growth factors include: (1) complex particle morphology; (2) complex interactions between the components

in the particles leading to non-additive water uptake among the individual components; and (3) errors associated with the calculation of the volume fractions and uncertainties in the measurements.

Table 4. Summary of κ values (Petters and Kreidenweis, 2007) for the total aerosol and the organic component of the aerosol, as derived from subsaturated hygroscopic growth factor data at the respective RHs shown. Data at RH=85% are not available for flight A. The organic κ values were calculated using Eq. 7 from Petters and Kreidenweis (2007), CCN-derived values of κ for ammonium sulfate and ammonium nitrate from their Table 1, the total κ value calculated at RH=92%, and measured volume fractions of ammonium nitrate, ammonium sulfate, and organics.

	In plume		Out of plume	
	Flight A	Flight B	Flight A	Flight B
κ_{total} (85%)	NA	0.40±0.12	NA	0.33±0.09
κ_{total} (92%)	0.36±0.12	0.44±0.19	0.29±0.12	0.28±0.10
κ_{organic} (92%)	0.13±0.08	0.14±0.15	0.06±0.07	-0.06±0.23

4.6 Relationship between sub- and supersaturated water uptake

One anticipates a direct correspondence between subsaturated hygroscopic behavior and supersaturated CCN activity. For example, Mochida et al. (2006) explored the relationship between hygroscopicity and CCN activity for urban aerosols using a hygroscopic tandem DMA (HTDMA) coupled in series to a CCNc; enhanced CCN activity coincided with higher subsaturated growth factors. A similar analysis for the present data (Fig. 17) shows that the normalized CCN activation ratio is generally consistent with water uptake in the subsaturated regime. One interesting feature is the tendency towards relatively higher normalized activation ratios at a supersaturation of 0.25%; we do not have a clear explanation for this other than to point out that more data points were available at this supersaturation, and that temporal and spatial factors during these specific measurements may have played a role. Also, higher activated fractions are consistent with smaller markers, which represent lower organic mass fractions and higher nitrate mass fractions. Enhancements in water uptake for aerosols with lower organic content are likely due to increasing dissolution of water-soluble species, including ammonium nitrate and amine salts, and the possible reduction in surface tension by surface-active species. Organics have previously been shown to influence CCN activity by adding solute and suppressing surface tension (Shulman et al., 1996; Facchini et al., 1999; Feingold and Chuang, 2002; Nenes et al., 2002).

Recent work has shown that kinetic limitations, including surface films and slow dissolution of particulate substances, can suppress droplet growth (Asa-Awuku and Nenes, 2007; Ruehl et al., 2008). With few exceptions including solute being physically “trapped” within some type of waxy material, dissolution kinetics is governed by diffusion of solute from the solid “core” at the center of a droplet to the growing droplet. It has been argued that the latter process is slow

enough for compounds with high molecular weights to influence droplet growth kinetics and the Köhler curve (Asa-Awuku and Nenes, 2007; Taraniuk et al., 2007; Moore et al., 2008). According to Fig. 18, droplet growth was at times less than that expected for pure ammonium sulfate. In addition, it is shown to some extent that the droplet growth was suppressed for CCN with relatively greater amounts of hydrophobic organic material. This suggests kinetic limitations may have played a role in suppressing water uptake. This issue will be revisited in subsequent work that will address size-resolved CCN data from this experiment.

4.7 Parameterization for sub- and supersaturated water uptake

To effectively represent the process of water uptake by multicomponent particles in atmospheric models, parameterizations are used. A number of investigators have attempted to introduce parameters to describe water uptake in both the sub- and supersaturated regimes. Expanding upon the earlier work of Fitzgerald et al. (1982), Svenningsson et al. (1992) used a parameter termed to link subsaturated water uptake to cloud and fog activation. Subsequent work introduced closely related parameters for sub- and supersaturated regimes (Kreidenweis et al., 2005; Rissler et al., 2006; Petters and Kreidenweis, 2007). A recently introduced parameter, κ (Petters and Kreidenweis, 2007), can be calculated without knowledge of the particle properties such as density, molecular weight, and surface tension.

Kappa can be determined from either CCN activity data or subsaturated hygroscopic growth data. Since the subsaturated DASH-SP growth factors are measured for size-resolved particles, we use the subsaturated hygroscopicity data to predict the value of κ with the following equation (Petters and Kreidenweis, 2007):

$$\frac{RH}{\exp\left(\frac{A}{D_d GF}\right)} = \frac{GF^3 - 1}{GF^3 - (1 - \kappa)} \quad (3)$$

where $A = (4\sigma_{s/a}M_w)/(RT\rho_w)$, D_d is the dry particle diameter, GF is the growth factor at the corresponding RH, M_w is the molecular weight of water, ρ_w is the density of water, R is the universal gas constant, T is temperature, and $\sigma_{s/a}$ is the surface tension at the air/water interface. The water surface tension of 0.072 J/m² is assumed, as in the analysis of Petters and Kreidenweis (2007). Briefly, κ values of 0.5 to 1.4 represent highly hygroscopic salts such as sodium chloride, values of 0.01 to 0.5 represent slightly to very hygroscopic organics, and a value of 0 represents a non-hygroscopic component (Petters and Kreidenweis, 2007; see Table 1). κ values representative of urban, maritime, continental, and remote areas, as derived by Petters and Kreidenweis (2007) using data from previous ambient studies (Fitzgerald and Hoppel, 1982; Hudson and Da, 1996; Dusek et al., 2006), have been reported to range from 0.1 to 0.94.

Table 4 summarizes the values of κ derived in the present study for both the total aerosol and the organic component of the aerosol. A noticeable enhancement in κ occurs within the plume as compared to the background aerosol, which is consistent with the enhancement in subsaturated growth factors. κ for the total aerosol is enhanced by between 21% and 67% in the plume, with typical values being between 0.36–0.44. The range of κ values, based on DASH-SP data at RHs of 85% and 92%, is 0.11–0.87. The correlation between κ values and the mass fraction of organics is more pronounced for flight B; κ increases as the mass fraction of organics decreases and that of nitrate increases. A clear enhancement in the κ values for the organic fraction of the aerosol is observed in the plume; typical values are between 0.10 and 0.15 inside the plume and near zero for the background aerosol. Representative κ values are assigned to two categories: aerosol from the strong bovine source ($\kappa=0.40$) and aerosol in an agricultural area ($\kappa=0.30$). Values of κ determined here fall within the range of those derived from previous ambient studies.

5 Conclusions

An extensive set of airborne aerosol and meteorological measurements were performed downwind of a massive bovine source in the San Joaquin Valley of California during two flights in July 2007; these include meteorology, particle size distributions, aerosol composition and mixing state, sub- and supersaturated water uptake behavior, aerosol refractive index, and interrelationships between these properties.

Concentrations of total mass, organics, nitrate, and ammonium were elevated within the plume as compared to the background aerosol during both flights. Evidence exists of some degree of external mixing of particles in the plume. Organics constituted the dominant fraction of the total mass in the plume and background aerosol (~56–64%), followed either by sulfate or nitrate, and then ammonium. The O:C atomic ratio of the organic fraction is estimated to have typically been between 0.45 and 0.50 both in and out of the plume. Particulate amines were detected in the plume and are shown to be a significant atmospheric base even in the presence of ammonia; the total amine concentration accounted for at least 23% (flight A) and 14% (flight B) of that of ammonium.

The refractive index of the background aerosol in the valley was on average 1.54, but reductions were observed in the plume, especially in the immediate vicinity of the plume source (flight A ~1.48; flight B ~1.51). Measurements indicate that increasing uptake of ammonia by aerosols, in the form of ammonium nitrate and ammonium sulfate, relative to the organic fraction, results in an enhancement in particle water uptake and a reduction in refractive index. Amine salts are also hypothesized to have contributed to significant hygroscopic growth in the plume. Hygroscopic growth factors

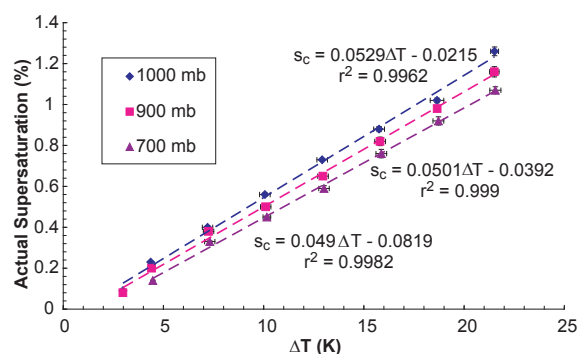


Fig. A1. Critical supersaturation versus delta T calibration for ammonium sulfate aerosol. Calibration was performed at 500 cm³/min at 700, 900, and 1000 mb.

in the immediate vicinity of the source were generally between 1.75–1.90 at RH=92%. Estimated hygroscopic growth factors (RH=92%) for the organic fraction on average were 1.49–1.53 in the plume and 1.24–1.29 in the background aerosol. Kinetic limitations associated with hydrophobic organic species may have possibly suppressed droplet growth, but the tendency is shown to be weak in this study. After removing effects associated with size distribution and mixing state, enhanced CCN activated fractions were generally observed as a function of increasing subsaturated growth factors, with the highest activated fractions being consistent with the lowest organic mass fractions. Representative values (Petters and Kreidenweis, 2007) are assigned to two categories: aerosol from the bovine source ($\kappa=0.40$) and aerosol in an agricultural area ($\kappa=0.30$). There was a clear enhancement in the values of κ representing the organic fraction of the aerosol within the plume, with average values of 0.13 and 0.14 for the two flights.

Appendix A

This appendix details the calibration procedure for the CCNc. The instrument used in this study was calibrated using ammonium sulfate particles classified with a DMA as follows. An aqueous solution of ammonium sulfate was atomized via a collision-type atomizer operated at 4 psig. The droplet stream was passed through multiple diffusional dryers (operating at 5–10% RH), resulting in a polydisperse dry aerosol (with modal diameter ~50 nm), which was sent through a DMA (Model 3081L, TSI Inc.) operated with a sheath-to-aerosol flow ratio of 10:1. The classified aerosol stream was then sent to a CPC (Model 3010, TSI Inc.) and the Continuous-flow Streamwise Thermal Gradient Chamber (CFSTGC) (operated at constant flow rate, temperature gradient, and pressure) to measure the total aerosol concentration and the total activated particles, respectively. The level of supersaturation in the instrument is determined from the

5516

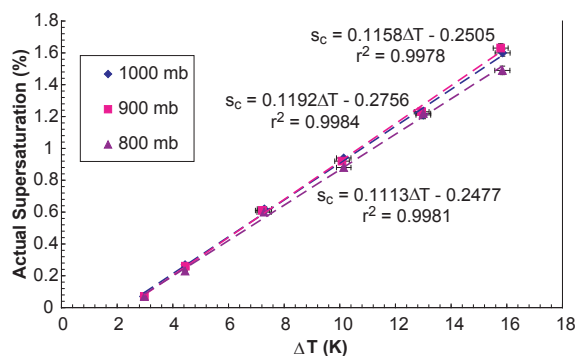


Fig. A2. Critical supersaturation versus delta T calibration for ammonium sulfate aerosol. Calibration was performed at $1000\text{ cm}^3/\text{min}$ at 800, 900, and 1000 mb.

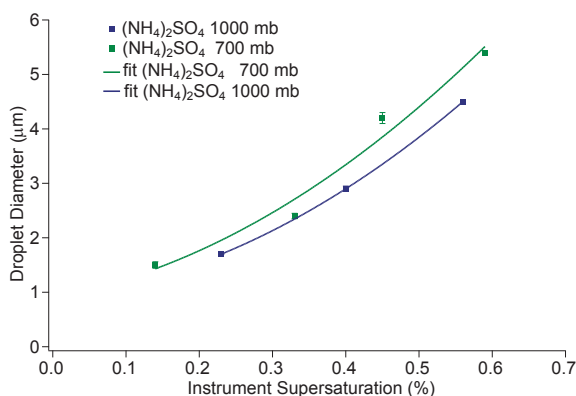


Fig. A3. Growth kinetics plots for aerosol ammonium sulfate aerosol. Calibration was performed at $500\text{ cm}^3/\text{min}$ at 700 and 1000 mb.

minimum dry particle diameter, D_{p50} , that activates in the instrument, found by plotting the ratio of CCN to CN concentration as a function of mobility particle diameter. A sigmoidal fit to the data (neglecting the effects of multiple particle charging, which is minor for the aerosol used) then determines D_{p50} as the dry diameter for which $\text{CCN}/\text{CN}=0.50$. The instrument supersaturation is related to D_{p50} by applying Köhler theory assuming ammonium sulfate has a density of $1760\text{ kg}/\text{m}^3$, surface tension of water, molar mass of $0.132\text{ kg}/\text{mol}$, and an effective van't Hoff factor of 2.5. The standard deviation in the supersaturation was determined from the standard deviation observed in the D_{p50} . The error bars in the temperature difference are 1σ of the observed variation during the calibrations. Droplet diameter of activated CCN at the exit of the growth column is also measured; in this study, the growth rate of ammonium sulfate particles is characterized by the average size of droplets formed from particles with dry diameter equal to D_{p50} .

The instrument was calibrated numerous times throughout the study for supersaturations ranging from 0.1 to 1.4% SS,

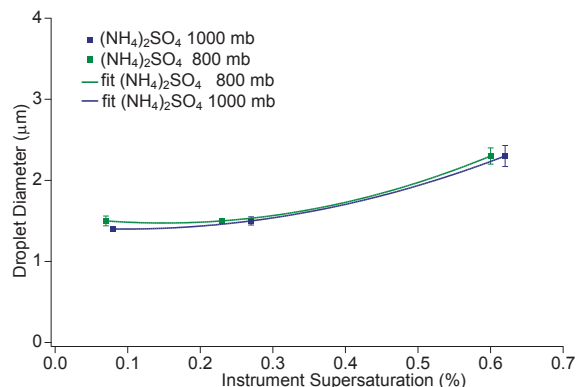


Fig. A4. Growth kinetics plots for aerosol ammonium sulfate aerosol. Calibration was performed at $1000\text{ cm}^3/\text{min}$ at 800 and 1000 mb.

for pressures between 700 and 1000 mb, and for flow rates ranging between 500 and $1000\text{ cm}^3/\text{min}$. The resulting calibration curves are presented in Figs. A1 and A2. The average size of activated droplets, together with 1σ error bars, are shown in Figs. A3 and A4.

The instrument was not operated at constant pressure during flights; instead, the pressure was allowed to vary with altitude. As a result, some transition time is required for the instrument supersaturation to adjust every time altitude changes; the data used in the closure study was filtered for transients resulting from changes in instrument pressure and temperature gradient. The calibration curves are then interpolated with respect to temperature gradient and pressure to determine the in-flight supersaturation.

Acknowledgements. This work was supported, in part, by NOAA grant NA06OAR4310082. A. N. acknowledges support from an NSF CAREER award, NOAA, and NASA. L. T. P. acknowledges support from a NASA Earth System Science Fellowship. The authors gratefully acknowledge the NOAA Air Resources Laboratory (ARL) for provision of the HYSPLIT transport and dispersion model.

Edited by: V. F. McNeill

References

- Abalos, M., Bayona, J. M., and Ventura, F.: Development of a solid-phase microextraction GC-NPD procedure for the determination of free volatile amines in wastewater and sewage-polluted waters, *Anal. Chem.*, 71, 3531–3537, 1999.
- Aiken, A. C., Decarlo, P. F., Kroll, J. H., Worsnop, D. R., Huffman, J. A., Docherty, K. S., Ulbrich, I. M., Mohr, C., Kimmel, J. R., Sueper, D., Sun, Y., Zhang, Q., Trimborn, A., Northway, M., Ziemann, P. J., Canagaratna, M. R., Onasch, T. B., Alfarra, M. R., Prevot, A. S. H., Dommen, J., Duplissy, J., Metzger, A., Baltensperger, U., and Jimenez, J. L.: O/C and OM/OC ratios of primary, secondary, and ambient organic aerosols with

- high-resolution time-of-flight aerosol mass spectrometry, *Environ. Sci. Technol.*, 42, 4478–4485, 2008.
- Aklilu, Y., Mozurkewich, M., Prenni, A. J., Kreidenweis, S. M., Alfarra, M. R., Allan, J. D., Anlauf, K., Brook, J., Leaitch, W. R., Sharma, S., Boudries, H., and Worsnop, D. R.: Hygroscopicity of particles at two rural, urban influenced sites during Pacific 2001: Comparison with estimates of water uptake from particle composition, *Atmos. Environ.*, 40, 2650–2661, 2006.
- Alfarra, M. R., Coe, H., Allan, J. D., Bower, K. N., Boudries, H., Canagaratna, M. R., Jimenez, J. L., Jayne, J. T., Garforth, A. A., Li, S. M., and Worsnop, D. R.: Characterization of urban and rural organic particulate in the lower Fraser valley using two aerodyne aerosol mass spectrometers, *Atmos. Environ.*, 38, 5745–5758, 2004.
- Allan, J. D., Delia, A. E., Coe, H., Bower, K. N., Alfarra, M. R., Jimenez, J. L., Middlebrook, A. M., Drewnick, F., Onasch, T. B., Canagaratna, M. R., Jayne, J. T., and Worsnop, D. R.: A generalised method for the extraction of chemically resolved mass spectra from aerodyne aerosol mass spectrometer data, *J. Aerosol Sci.*, 35, 909–922, 2004.
- Anderson, N., Strader, R., and Davidson, C.: Airborne reduced nitrogen: ammonia emissions from agriculture and other sources, *Environ. Int.*, 29, 277–286, 2003.
- Angelino, S., Suess, D. T., and Prather, K. A.: Formation of aerosol particles from reactions of secondary and tertiary alkylamines: Characterization by aerosol time-of-flight mass spectrometry, *Environ. Sci. Technol.*, 35, 3130–3138, 2001.
- Apsimon, H. M., Kruse, M., and Bell, J. N. B.: Ammonia emissions and their role in acid deposition, *Atmos. Environ.*, 21, 1939–1946, 1987.
- Asa-Awuku, A. and Nenes, A.: Effect of solute dissolution kinetics on cloud droplet formation: Extended Kohler theory, *J. Geophys. Res.*, 112, D22201, doi:10.1029/2005JD006934, 2007.
- Asman, W. A. H. and Janssen, A. J.: A long-range transport model for ammonia and ammonium for Europe, *Atmos. Environ.*, 21, 2099–2119, 1987.
- Battye, W., Aneja, V. P., and Roelle, P. A.: Evaluation and improvement of ammonia emissions inventories, *Atmos. Environ.*, 37, 3873–3883, 2003.
- Beddows, D. C. S., Donovan, R. J., Harrison, R. M., Heal, M. R., Kinnersley, R. P., King, M. D., Nicholson, D. H., and Thompson, K. C.: Correlations in the chemical composition of rural background atmospheric aerosol in the UK determined in real time using time-of-flight mass spectrometry, *J. Environ. Monitor.*, 6, 124–133, 2004.
- Blanchard, C. L., Roth, P. M., Tanenbaum, S. J., Ziman, S. D., and Seinfeld, J. H.: The use of ambient measurements to identify which precursor species limit aerosol nitrate formation, *J. Air Waste Manage.*, 50, 2073–2084, 2000.
- Brechtl, F. J. and Kreidenweis, S. M.: Predicting particle critical supersaturation from hygroscopic growth measurements in the humidified TDMA. part I: Theory and sensitivity studies, *J. Atmos. Sci.*, 57, 1854–1871, 2000.
- Cadle, S. H. and Mulawa, P. A.: Low-molecular weight aliphatic amines in exhaust from catalyst-equipped cars, *Environ. Sci. Technol.*, 14, 718–723, 1980.
- Choi, M. Y. and Chan, C. K.: The effects of organic species on the hygroscopic behaviors of inorganic aerosols, *Environ. Sci. Technol.*, 36, 2422–2428, 2002a.
- Choi, M. Y. and Chan, C. K.: Continuous measurements of the water activities of aqueous droplets of water-soluble organic compounds, *J. Phys. Chem. A*, 106, 4566–4572, 2002b.
- Chow, J. C., Watson, J. G., Lu, Z. Q., Lowenthal, D. H., Frazier, C. A., Solomon, P. A., Thuillier, R. H., and Magliano, K.: Descriptive analysis of PM(2.5) and PM(10) at regionally representative locations during SIVAQS/AUSPEX, *Atmos. Environ.*, 30, 2079–2112, 1996.
- Chow, J. C., Chen, L. W. A., Watson, J. G., Lowenthal, D. H., Magliano, K. A., Turkiewicz, K., and Lehrman, D. E.: PM2.5 chemical composition and spatiotemporal variability during the California Regional PM10/PM2.5 Air Quality Study (CRPAQS), *J. Geophys. Res.*, 111, D10S04, doi:10.1029/2005JD006457, 2006.
- Chuang, P. Y.: Measurement of the timescale of hygroscopic growth for atmospheric aerosols, *J. Geophys. Res.*, 108, 4282, doi:10.1029/2002JD002757, 2003.
- Clegg, S. L., Brimblecombe, P., and Wexler, A. S.: Thermodynamic model of the system H⁺-NH₄⁺-Na⁺-SO₄²⁻-NO₃⁻-Cl⁻-H₂O at 298.15 K, *J. Phys. Chem. A*, 102, 2155–2171, 1998.
- Clegg, S. L., Seinfeld, J. H., and Edney, E. O.: Thermodynamic modelling of aqueous aerosols containing electrolytes and dissolved organic compounds. II. An extended Zdanovskii-Stokes-Robinson approach, *J. Aerosol Sci.*, 34, 667–690, 2003.
- Clegg, S. L. and Seinfeld, J. H.: Improvement of the Zdanovskii-Stokes-Robinson model for mixtures containing solutes of different charge types, *J. Phys. Chem. A*, 108, 1008–1017, 2004.
- Clegg, S. L. and Seinfeld, J. H.: Thermodynamic models of aqueous solutions containing inorganic electrolytes and dicarboxylic acids at 298.15 K. 1. The acids as nondissociating components, *J. Phys. Chem. A*, 110, 5692–5717, 2006a.
- Clegg, S. L. and Seinfeld, J. H.: Thermodynamic models of aqueous solutions containing inorganic electrolytes and dicarboxylic acids at 298.15 K. 2. Systems including dissociation equilibria, *J. Phys. Chem. A*, 110, 5718–5734, 2006b.
- Cruz, C. N. and Pandis, S. N.: Deliquescence and hygroscopic growth of mixed inorganic-organic atmospheric aerosol, *Environ. Sci. Technol.*, 34, 4313–4319, 2000.
- Cubison, M. J., Alfarra, M. R., Allan, J., Bower, K. N., Coe, H., McFiggans, G. B., Whitehead, J. D., Williams, P. I., Zhang, Q., Jimenez, J. L., Hopkins, J., and Lee, J.: The characterisation of pollution aerosol in a changing photochemical environment, *Atmos. Chem. Phys.*, 6, 5573–5588, 2006.
- Dean, J. A.: *Lange's Handbook of Chemistry*, Fifteenth Edition, McGraw-Hill, 1999.
- Denkenberger, K. A., Moffet, R. C., Holecek, J. C., Rebotier, T. P., and Prather, K. A.: Real-time, single-particle measurements of oligomers in aged ambient aerosol particles, *Environ. Sci. Technol.*, 41, 5439–5446, 2007.
- Dick, W. D., Saxena, P., and McMurry, P. H.: Estimation of water uptake by organic compounds in submicron aerosols measured during the Southeastern Aerosol and Visibility Study, *J. Geophys. Res.*, 105, 1471–1479, 2000.
- Dillner, A. M., Stein, C., Larson, S. M., and Hitznerberger, R.: Measuring the mass extinction efficiency of elemental carbon in rural aerosol, *Aerosol Sci. Tech.*, 35, 1009–1021, 2001.
- Dinar, E., Anttila, T., and Rudich, Y.: CCN activity and hygroscopic growth of organic aerosols following reactive uptake of ammonia, *Environ. Sci. Technol.*, 42, 793–799, 2008.

- Doyle, G. J., Tuazon, E. C., Graham, R. A., Mischke, T. M., Winer, A. M., and Pitts, J. N.: Simultaneous concentrations of ammonia and nitric-acid in a polluted atmosphere and their equilibrium relationship to particulate ammonium-nitrate, *Environ. Sci. Technol.*, 13, 1416–1419, 1979.
- Draxler, R. R. and Rolph, G. D.: HYSPLIT (HYbrid Single-Particle Lagrangian Integrated Trajectory) Model access via NOAA ARL READY Website (<http://www.arl.noaa.gov/ready/hysplit4.html>), NOAA Air Resources Laboratory, Silver Spring, MD, 2003.
- Drewnick, F., Hings, S. S., DeCarlo, P., Jayne, J. T., Gonin, M., Fuhrer, K., Weimer, S., Jimenez, J. L., Demerjian, K. L., Borrmann, S., and Worsnop, D. R.: A new time-of-flight aerosol mass spectrometer (tof-ams) – instrument description and first field deployment, *Aerosol Sci. Tech.*, 39, 637–658, 2005.
- Dusek, U., Frank, G. P., Hildebrandt, L., Curtius, J., Schneider, J., Walter, S., Chand, D., Drewnick, F., Hings, S., Jung, D., Borrmann, S., and Andreae, M. O.: Size matters more than chemistry for cloud-nucleating ability of aerosol particles, *Science*, 312, 1375–1378, 2006.
- Edgerton, E. S., Saylor, R. D., Hartsell, B. E., Jansen, J. J., and Hansen, D. A.: Ammonia and ammonium measurements from the southeastern United States, *Atmos. Environ.*, 41, 3339–3351, 2007.
- Facchini, M. C., Mircea, M., Fuzzi, S., and Charlson, R. J.: Cloud albedo enhancement by surface-active organic solutes in growing droplets, *Nature*, 401, 257–259, 1999.
- Feingold, G. and Chuang, P. Y.: Analysis of the influence of film-forming compounds on droplet growth: Implications for cloud microphysical processes and climate, *J. Atmos. Sci.*, 59, 2006–2018, 2002.
- Fitzgerald, J. W., Hoppel, W. A., and Vietti, M. A.: The size and scattering coefficient of urban aerosol-particles at Washington, DC as a function of relative-humidity, *J. Atmos. Sci.*, 39, 1838–1852, 1982.
- Fitzgerald, J. W. and Hoppel, W. A.: Measurement of the relationship between the dry size and critical supersaturation of natural aerosol particles, *J. Hung. Meteorol. Serv.*, 86, 242–248, 1982.
- Fridlind, A. M. and Jacobson, M. Z.: A study of gas-aerosol equilibrium and aerosol pH in the remote marine boundary layer during the First Aerosol Characterization Experiment (ACE 1), *J. Geophys. Res.*, 105, 17 325–17 340, 2000.
- Fridlind, A. M., Jacobson, M. Z., Kerminen, V. M., Hillamo, R. E., Ricard, V., and Jaffrezo, J. L.: Analysis of gas-aerosol partitioning in the Arctic: Comparison of size-resolved equilibrium model results with field data, *J. Geophys. Res.*, 105, 19 891–19 903, 2000.
- Fuller, K. A., Malm, W. C., and Kreidenweis, S. M.: Effects of mixing on extinction by carbonaceous particles, *J. Geophys. Res.*, 104, 15 941–15 954, 1999.
- Gerber, H. E., Hoppel, W. A., and Wojciechowski, T. A.: Experimental verification of the theoretical relationship between size and critical supersaturation of salt nuclei, *J. Atmos. Sci.*, 34, 1836–1841, 1977.
- Glagolenko, S. and Phares, D. J.: Single-particle analysis of ultra-fine aerosol in College Station, Texas, *J. Geophys. Res.*, 109, D18205, doi:10.1029/2004JD004621, 2004.
- Gozelska, K., Talbot, R. W., Klemm, K., Lefer, B., Klemm, O., Gregory, G. L., Anderson, B., and Barrie, L. A.: Chemical composition of the atmospheric aerosol in the troposphere over the Hudson-Bay Lowlands and Quebec-Labrador Regions of Canada, *J. Geophys. Res.*, 99, 1763–1779, 1994.
- Gysel, M., Crosier, J., Topping, D. O., Whitehead, J. D., Bower, K. N., Cubison, M. J., Williams, P. I., Flynn, M. J., McFiggans, G. B., and Coe, H.: Closure study between chemical composition and hygroscopic growth of aerosol particles during TORCH2, *Atmos. Chem. Phys.*, 7, 6131–6144, 2007, <http://www.atmos-chem-phys.net/7/6131/2007/>.
- Hegg, D. A., Covert, D. S., Jonsson, H., and Covert, P. A.: Determination of the transmission efficiency of an aircraft aerosol inlet, *Aerosol Sci. Tech.*, 39, 966–971, 2005.
- Hildemann, L. M., Russell, A. G., and Cass, G. R.: Ammonia and nitric-acid concentrations in equilibrium with atmospheric aerosols – experiment vs theory, *Atmos. Environ.*, 18, 1737–1750, 1984.
- Hudson, J. G. and Da, X. Y.: Volatility and size of cloud condensation nuclei, *J. Geophys. Res.*, 101, 4435–4442, 1996.
- Hutchinson, G. L., Mosier, A. R., and Andre, C. E.: Ammonia and amine emissions from a large cattle feedlot, *J. Environ. Qual.*, 11, 288–293, 1982.
- Khlystov, A., Stanier, C. O., Takahama, S., and Pandis, S. N.: Water content of ambient aerosol during the Pittsburgh air quality study, *J. Geophys. Res.*, 110, D07S10, doi:10.1029/2004JD004651, 2005.
- Kleeman, M. J., Hughes, L. S., Allen, J. O., and Cass, G. R.: Source contributions to the size and composition distribution of atmospheric particles: Southern California in September 1996, *Environ. Sci. Technol.*, 33, 4331–4341, 1999.
- Kreidenweis, S. M., Koehler, K., DeMott, P. J., Prenni, A. J., Carrico, C., and Ervens, B.: Water activity and activation diameters from hygroscopicity data – Part I: Theory and application to inorganic salts, *Atmos. Chem. Phys.*, 5, 1357–1370, 2005, <http://www.atmos-chem-phys.net/5/1357/2005/>.
- Kumar, P. P., Broekhuizen, K., and Abbatt, J. P. D.: Organic acids as cloud condensation nuclei: Laboratory studies of highly soluble and insoluble species, *Atmos. Chem. Phys.*, 3, 509–520, 2003, <http://www.atmos-chem-phys.net/3/509/2003/>.
- Lance, S., Medina, J., Smith, J. N., and Nenes, A.: Mapping the operation of the DMT Continuous Flow CCN counter, *Aerosol Sci. Tech.*, 40, 242–254, 2006.
- Lober, J. M., Scharffe, D. H., Hao, W. M., Kuhlbusch, T. A., Warneck, P., and Crutzen, P. J.: Experimental evaluation of biomass burning emissions: Nitrogen and carbon containing compounds, in: *Global Biomass Burning: Atmospheric, Climate and Biospheric Implications*, edited by: Levine, J. S., MIT Press, Cambridge, MA, 1991.
- Makela, J. M., Yli-Koivisto, S., Hiltunen, V., Seidl, W., Swietlicki, E., Teinila, K., Sillanpaa, M., Koponen, I. K., Paatero, J., Rosman, K., and Hameri, K.: Chemical composition of aerosol during particle formation events in boreal forest, *Tellus B*, 53, 380–393, 2001.
- Manahan, S. E.: *Environmental Chemistry*, Eighth Edition, CRC Press, Boca Raton, Florida, 2005.
- Maria, S. F., Russell, L. M., Turpin, B. J., Porcja, R. J., Campos, T. L., Weber, R. J., and Huebert, B. J.: Source signatures of carbon monoxide and organic functional groups in Asian Pacific Regional Aerosol Characterization Experiment (ACE-Asia) submicron aerosol types, *J. Geophys. Res.*, 108, 8637, doi:10.1029/2003JD003703, 2003.

- McLafferty, F. W. and Turecek, F.: Interpretation of Mass Spectra, Fourth Edition, University Science Books, Mill Valley, California, 1993.
- Meng, Z. Y. and Seinfeld, J. H.: Time scales to achieve atmospheric gas-aerosol equilibrium for volatile species, *Atmos Environ.*, 30, 2889–2900, 1996.
- Milne, P. J. and Zika, R. G.: Amino-acid nitrogen in atmospheric aerosols – occurrence, sources and photochemical modification, *J. Atmos. Chem.*, 16, 361–398, 1993.
- Mochida, M., Kuwata, M., Miyakawa, T., Takegawa, N., Kawamura, K., and Kondo, Y.: Relationship between hygroscopicity and cloud condensation nuclei activity for urban aerosols in Tokyo, *J. Geophys. Res.*, 111, D23204, doi:10.1029/2005JD006980, 2006.
- Moore, R. H., Ingall, E. D., Sorooshian, A., and Nenes, A.: Molar mass, surface tension, and droplet growth kinetics of marine organics from measurements of CCN activity, *Geophys. Res. Lett.*, 35, L07801, doi:10.1029/2008GL033350, 2008.
- Mosier, A. R., Andre, C. E., and Viets, F. G.: Identification of Aliphatic-Amines Volatilized from Cattle Feedyard, *Environ. Sci. Technol.*, 7, 642–644, 1973.
- Mozurkewich, M.: The dissociation-constant of ammonium-nitrate and its dependence on temperature, relative-humidity and particle-size, *Atmos Environ.*, 27, 261–270, 1993.
- Murphy, D. M. and Thomson, D. S.: Chemical composition of single aerosol particles at Idaho Hill: Positive ion measurements, *J. Geophys. Res.*, 102, 6341–6352, 1997.
- Murphy, S. M., Sorooshian, A., Kroll, J. H., Ng, N. L., Chhabra, P., Tong, C., Surratt, J. D., Knipping, E., Flagan, R. C., and Seinfeld, J. H.: Secondary aerosol formation from atmospheric reactions of aliphatic amines, *Atmos. Chem. Phys.*, 7, 2313–2337, 2007, <http://www.atmos-chem-phys.net/7/2313/2007/>.
- Nenes, A., Charlson, R. J., Facchini, M. C., Kulmala, M., Laaksonen, A., and Seinfeld, J. H.: Can chemical effects on cloud droplet number rival the first indirect effect?, *Geophys. Res. Lett.*, 29, 1848, doi:10.1029/2002GL015295, 2002.
- Neuman, J. A., Nowak, J. B., Brock, C. A., Trainer, M., Fehsenfeld, F. C., Holloway, J. S., Hubler, G., Hudson, P. K., Murphy, D. M., Nicks, D. K., Orsini, D., Parrish, D. D., Ryerson, T. B., Sueper, D. T., Sullivan, A., and Weber, R.: Variability in ammonium nitrate formation and nitric acid depletion with altitude and location over California, *J. Geophys. Res.*, 108, 4557, doi:10.1029/2003JD003616, 2003.
- Ngwabie, N. M., Custer, T. G., Schade, G. W., Linke, S., and Hinz, T.: Mixing ratio measurements and flux estimates of volatile organic compounds (VOC) from a cowshed with conventional manure treatment indicate significant emissions to the atmosphere, *Geophys. Res. Abstr.*, 7(01175), 2005.
- Petters, M. D. and Kreidenweis, S. M.: A single parameter representation of hygroscopic growth and cloud condensation nucleus activity, *Atmos. Chem. Phys.*, 7, 1961–1971, 2007, <http://www.atmos-chem-phys.net/7/1961/2007/>.
- Prenni, A. J., De Mott, P. J., and Kreidenweis, S. M.: Water uptake of internally mixed particles containing ammonium sulfate and dicarboxylic acids, *Atmos Environ.*, 37, 4243–4251, 2003.
- Pun, B. K. and Seigneur, C.: Understanding particulate matter formation in the California San Joaquin Valley: conceptual model and data needs, *Atmos. Environ.*, 33, 4865–4875, 1999.
- Rabaud, N. E., Ebeler, S. E., Ashbaugh, L. L., and Flocchini, R. G.: Characterization and quantification of odorous and non-odorous volatile organic compounds near a commercial dairy in California, *Atmos. Environ.*, 37, 933–940, 2003.
- Rissler, J., Pagels, J., Swietlicki, E., Wierzbicka, A., Strand, M., Lillieblad, L., Sanati, M., and Bohgard, M.: Hygroscopic behavior of aerosol particles emitted from biomass fired grate boilers, *Aerosol Sci. Tech.*, 39, 919–930, 2005.
- Rissler, J., Vestin, A., Swietlicki, E., Fisch, G., Zhou, J., Artaxo, P., and Andreae, M. O.: Size distribution and hygroscopic properties of aerosol particles from dry-season biomass burning in Amazonia, *Atmos. Chem. Phys.*, 6, 471–491, 2006, <http://www.atmos-chem-phys.net/6/471/2006/>.
- Roberts, G. C. and Nenes, A.: A continuous-flow streamwise thermal-gradient CCN chamber for atmospheric measurements, *Aerosol Sci. Tech.*, 39, 206–221, 2005.
- Rose, D., Gunthe, S. S., Mikhailov, E., Frank, G. P., Dusek, U., Andreae, M. O., and Poschl, U.: Calibration and measurement uncertainties of a continuous-flow cloud condensation nuclei counter (DMT-CCNC): CCN activation of ammonium sulfate and sodium chloride aerosol particles in theory and experiment, *Atmos. Chem. Phys.*, 8, 1153–1179, 2008, <http://www.atmos-chem-phys.net/8/1153/2008/>.
- Ruehl, C. R., Chuang, P. Y., and Nenes, A.: How quickly do cloud droplets form on atmospheric particles?, *Atmos. Chem. Phys.*, 8, 1043–1055, 2008, <http://www.atmos-chem-phys.net/8/1043/2008/>.
- Rumburg, B., Mount, G. H., Yonge, D., Lamb, B., Westberg, H., Filipy, J., Bays, J., Kincaid, R., and Johnson, K.: Atmospheric flux of ammonia from sprinkler application of dairy waste, *Atmos Environ.*, 40, 7246–7258, 2006.
- Russell, A. G., Mccrae, G. J., and Cass, G. R.: Mathematical modeling of the formation and transport of ammonium-nitrate aerosol, *Atmos. Environ.*, 17, 949–964, 1983.
- Schade, G. W. and Crutzen, P. J.: Emission of aliphatic-amines from animal husbandry and their reactions - potential source of N₂O and HCN, *J. Atmos. Chem.*, 22, 319–346, 1995.
- Seinfeld, J. H. and Pandis, S. N.: Atmospheric Chemistry and Physics, Second Edition, Wiley-Interscience, New York, 2006.
- Shulman, M. L., Jacobson, M. C., Carlson, R. J., Synovec, R. E., and Young, T. E.: Dissolution behavior and surface tension effects of organic compounds in nucleating cloud droplets, *Geophys. Res. Lett.*, 23, 277–280, 1996.
- Sjogren, S., Gysel, M., Weingartner, E., Baltensperger, U., Cubison, M. J., Coe, H., Zardini, A. A., Marcolli, C., Krieger, U. K., and Peter, T.: Hygroscopic growth and water uptake kinetics of two-phase aerosol particles consisting of ammonium sulfate, adipic and humic acid mixtures, *J. Aerosol Sci.*, 38, 157–171, 2007.
- Sorooshian, A., Brechtel, F. J., Ma, Y. L., Weber, R. J., Corless, A., Flagan, R. C., and Seinfeld, J. H.: Modeling and characterization of a particle-into-liquid sampler (PILS), *Aerosol Sci. Tech.*, 40, 396–409, 2006a.
- Sorooshian, A., Varutbangkul, V., Brechtel, F. J., Ervens, B., Feingold, G., Bahreini, R., Murphy, S. M., Holloway, J. S., Atlas, E. L., Buzorius, G., Jonsson, H., Flagan, R. C., and Seinfeld, J. H.: Oxalic acid in clear and cloudy atmospheres: Analysis of data from International Consortium for Atmospheric Research on Transport and Transformation 2004, *J. Geophys. Res.*, 111, D23S45, doi:10.1029/2005JD006880, 2006b.

- Sorooshian, A., Ng, N. L., Chan, A. W. H., Feingold, G., Flagan, R. C., and Seinfeld, J. H.: Particulate organic acids and overall water-soluble aerosol composition measurements from the 2006 Gulf of Mexico Atmospheric Composition and Climate Study (GoMACCS), *J. Geophys. Res.*, 112, D13201, doi:10.1029/2007JD008537, 2007a.
- Sorooshian, A., Lu, M. L., Brechtel, F. J., Jonsson, H., Feingold, G., Flagan, R. C., and Seinfeld, J. H.: On the source of organic acid aerosol layers above clouds, *Environ. Sci. Technol.*, 41, 4647–4654, 2007b.
- Sorooshian, A., S. Hersey, F. J. Brechtel, A. Corless, R. C. Flagan, and Seinfeld, J. H.: Rapid, size-resolved aerosol hygroscopic growth measurements: differential aerosol sizing and hygroscopicity spectrometer probe (DASH-SP), *Aerosol Sci. Tech.*, 42, 445–464, 2008.
- Stelson, A. W., Friedlander, S. K., and Seinfeld, J. H.: Note on the equilibrium relationship between ammonia and nitric-acid and particulate ammonium-nitrate, *Atmos. Environ.*, 13, 369–371, 1979.
- Stelson, A. W. and Seinfeld, J. H.: Relative-humidity and temperature-dependence of the ammonium-nitrate dissociation-constant, *Atmos. Environ.*, 16, 983–992, 1982a.
- Stelson, A. W. and Seinfeld, J. H.: Relative-humidity and Ph-dependence of the vapor-pressure of ammonium-nitrate nitric acid-solutions at 25 degrees C, *Atmos. Environ.*, 16, 993–1000, 1982b.
- Stokes, R. H. and Robinson, R. A.: Interactions in aqueous nonelectrolyte solutions. I. Solute-solvent equilibria, *J. Phys. Chem.*, 70, 2126–2130, 1966.
- Svenningsson, I. B., Hansson, H. C., Wiedensohler, A., Ogren, J. A., Noone, K. J., and Hallberg, A.: Hygroscopic growth of aerosol-particles in the Po Valley, *Tellus B*, 44, 556–569, 1992.
- Svenningsson, B., Rissler, J., Swietlicki, E., Mircea, M., Bilde, M., Facchini, M. C., Decesari, S., Fuzzi, S., Zhou, J., Monster, J., and Rosenorn, T.: Hygroscopic growth and critical supersaturations for mixed aerosol particles of inorganic and organic compounds of atmospheric relevance, *Atmos. Chem. Phys.*, 6, 1937–1952, 2006, <http://www.atmos-chem-phys.net/6/1937/2006/>.
- Takahama, S., Wittig, A. E., Vayenas, D. V., Davidson, C. I., and Pandis, S. N.: Modeling the diurnal variation of nitrate during the Pittsburgh Air Quality Study, *J. Geophys. Res.*, 109, D16S06, doi:10.1029/2003JD004149, 2004.
- Tan, P. V., Evans, G. J., Tsai, J., Owega, S., Fila, M. S., and Malpica, O.: On-line analysis of urban particulate matter focusing on elevated wintertime aerosol concentrations, *Environ. Sci. Technol.*, 36, 3512–3518, 2002.
- Tang, I. N.: Chemical and size effects of hygroscopic aerosols on light scattering coefficients, *J. Geophys. Res.*, 101, 19245–19250, 1996.
- Taraniuk, I., Graber, E. R., Kostinski, A., and Rudich, Y.: Surfactant properties of atmospheric and model humic-like substances (HULIS), *Geophys. Res. Lett.*, 34, L16807, doi:10.1029/2007GL029576, 2007.
- Ulbrich, I. M., Lechner, M., and Jimenez, J. L.: AMS Spectral Database, <http://cires.colorado.edu/jimenez-group/AMSsd/>, 2008.
- Ulbrich, I. M., Canagaratna, M. R., Zhang, Q., Worsnop, D. R., and Jimenez, J. L.: Interpretation of organic components from positive matrix factorization of aerosol mass spectrometric data, *Atmos. Chem. Phys. Discuss.*, 8, 6729–6791, 2008, <http://www.atmos-chem-phys-discuss.net/8/6729/2008/>.
- Vanneste, A., Duce, R. A., and Lee, C.: Methylamines in the marine atmosphere, *Geophys. Res. Lett.*, 14, 711–714, 1987.
- Varutbangkul, V., Brechtel, F. J., Bahreini, R., Ng, N. L., Keywood, M. D., Kroll, J. H., Flagan, R. C., Seinfeld, J. H., Lee, A., and Goldstein, A. H.: Hygroscopicity of secondary organic aerosols formed by oxidation of cycloalkenes, monoterpenes, sesquiterpenes, and related compounds, *Atmos. Chem. Phys.*, 6, 2367–2388, 2006, <http://www.atmos-chem-phys.net/6/2367/2006/>.
- Weast, R. C.: *CRC Handbook of Chemistry and Physics*, Sixty Eighth Edition, CRC Press, Florida, 1987.
- Westerholm, R., Li, H., and Almen, J.: Estimation of aliphatic amine emissions in automobile exhausts, *Chemosphere*, 27, 1381–1384, 1993.
- Wexler, A. S. and Seinfeld, J. H.: Analysis of aerosol ammonium-nitrate - departures from equilibrium during Scaqs, *Atmos. Environ.*, 26, 579–591, 1992.
- Wise, M. E., Surratt, J. D., Curtis, D. B., Shilling, J. E., and Tolbert, M. A.: Hygroscopic growth of ammonium sulfate/dicarboxylic acids, *J. Geophys. Res.*, 108, 4638, doi:10.1029/2003JD003775, 2003.
- Xiong, J. Q., Zhong, M. H., Fang, C. P., Chen, L. C., and Lippmann, M.: Influence of organic films on the hygroscopicity of ultrafine sulfuric acid aerosol, *Environ. Sci. Technol.*, 32, 3536–3541, 1998.
- Yu, S. C., Dennis, R., Roselle, S., Nenes, A., Walker, J., Eder, B., Schere, K., Swall, J., and Robarge, W.: An assessment of the ability of three-dimensional air quality models with current thermodynamic equilibrium models to predict aerosol NO₃-, *J. Geophys. Res.*, 110, D07S13, doi:10.1029/2004JD004718, 2005.
- Zdanovskii, A.: New methods for calculating solubilities of electrolytes in multicomponent systems, *Zh. Fiz. Khim.*, 22, 1475–1485, 1948.
- Zhang, J., Chameides, W. L., Weber, R., Cass, G., Orsini, D., Edgerton, E., Jongejan, P., and Slanina, J.: An evaluation of the thermodynamic equilibrium assumption for fine particulate composition: Nitrate and ammonium during the 1999 Atlanta Supersite Experiment, *J. Geophys. Res.*, 108, 8414, doi:10.1029/2001JD001592, 2002.
- Zhang, X. Q., Turpin, B. J., McMurry, P. H., Hering, S. V., and Stolzenburg, M. R.: Mie theory evaluation of species contributions to 1990 wintertime visibility reduction in the Grand-Canyon, *J. Air Waste Manage.*, 44, 153–162, 1994.
- Zhang, Q., Anastasio, C., and Jimenez-Cruz, M.: Water-soluble organic nitrogen in atmospheric fine particles (PM_{2.5}) from northern California, *J. Geophys. Res.*, 107, 4112, doi:10.1029/2001JD000870, 2002.
- Zhang, Q. and Anastasio, C.: Free and combined amino compounds in atmospheric fine particles (PM_{2.5}) and fog waters from Northern California, *Atmos. Environ.*, 37, 2247–2258, 2003.
- Zhang, Q., Alfarra, M. R., Worsnop, D. R., Allan, J. D., Coe, H., Canagaratna, M. R., and Jimenez, J. L.: Deconvolution and quantification of hydrocarbon-like and oxygenated organic aerosols based on aerosol mass spectrometry, *Environ. Sci. Technol.*, 39, 4938–4952, 2005.

Appendix B

Comprehensive Simultaneous Shipboard and Airborne Characterization of Exhaust from a Modern Container Ship at Sea*

*Reproduced with permission from "Comprehensive Simultaneous Shipboard and Airborne Characterization of Exhaust from a Modern Container Ship at Sea" by Murphy, S.M., Agrawal, H., Sorooshian, A., Padro, L.T., Gates, H., Hersey, S.P., Welch, W.A., Jung, H., Miller, J.W., Cocker, D.R., Nenes, A., Jonsson, H., Flagan R.C., and Seinfeld, J.H., *Environmental Science & Technology*, 43 (13), 4626–4640, 2007. Copyright 2009 by the American Chemical Society.

Research

Comprehensive Simultaneous Shipboard and Airborne Characterization of Exhaust from a Modern Container Ship at Sea

SHANE M. MURPHY,[†]
 HARSHIT AGRAWAL,^{‡,§}
 ARMIN SOROOSHIAN,[†] LUZ T. PADRÓ,^{||}
 HARMONY GATES,[†] SCOTT HERSEY,[†]
 W. A. WELCH,[§] H. JUNG,^{§,||} J. W. MILLER,^{‡,§}
 DAVID R. COCKER III,^{‡,§}
 ATHANASIOS NENES,^{⊥,¶}
 HAFLIDI H. JONSSON,[∇] RICHARD C. FLAGAN,[†]
 AND JOHN H. SEINFELD^{†,*}

Departments of Environmental Science and Engineering and Chemical Engineering, California Institute of Technology, Pasadena, California 91125, Departments of Chemical, Environmental, and Mechanical Engineering, University of California, Riverside, California 92521, College of Engineering-Center for Environmental Research and Technology, 1084 Columbia Avenue, Riverside, California 92507, School of Chemical and Biomolecular Engineering, School of Earth and Atmospheric Sciences, and School of Mechanical Engineering, Georgia Institute of Technology, Atlanta, Georgia 30332, and Center for Interdisciplinary Remotely-Piloted Aircraft Studies, Naval Postgraduate School, Monterey, California 93933

Received August 28, 2008. Revised manuscript received November 29, 2008. Accepted December 9, 2008.

We report the first joint shipboard and airborne study focused on the chemical composition and water-uptake behavior of particulate ship emissions. The study focuses on emissions from the main propulsion engine of a Post-Panamax class container ship cruising off the central coast of California and burning heavy fuel oil. Shipboard sampling included micro-orifice uniform deposit impactors (MOUDI) with subsequent off-line analysis, whereas airborne measurements involved a number of real-time analyzers to characterize the plume aerosol, aged from a few seconds to over an hour. The mass ratio of particulate organic carbon to sulfate at the base of the ship stack was 0.23 ± 0.03 , and increased to 0.30 ± 0.01 in the airborne exhaust plume, with the additional organic mass in the airborne plume being concentrated largely in particles below

100 nm in diameter. The organic to sulfate mass ratio in the exhaust aerosol remained constant during the first hour of plume dilution into the marine boundary layer. The mass spectrum of the organic fraction of the exhaust aerosol strongly resembles that of emissions from other diesel sources and appears to be predominantly hydrocarbon-like organic (HOA) material. Background aerosol which, based on air mass back trajectories, probably consisted of aged ship emissions and marine aerosol, contained a lower organic mass fraction than the fresh plume and had a much more oxidized organic component. A volume-weighted mixing rule is able to accurately predict hygroscopic growth factors in the background aerosol but measured and calculated growth factors do not agree for aerosols in the ship exhaust plume. Calculated CCN concentrations, at supersaturations ranging from 0.1 to 0.33%, agree well with measurements in the ship-exhaust plume. Using size-resolved chemical composition instead of bulk submicrometer composition has little effect on the predicted CCN concentrations because the cutoff diameter for CCN activation is larger than the diameter where the mass fraction of organic aerosol begins to increase significantly. The particle number emission factor estimated from this study is 1.3×10^{16} (kg fuel)⁻¹, with less than 1/10 of the particles having diameters above 100 nm; 24% of particles (>10 nm in diameter) activate into cloud droplets at 0.3% supersaturation.

1. Introduction

Ship exhaust is estimated to represent an appreciable fraction of global NO_x (21 Tg y⁻¹), SO_x (12 Tg y⁻¹), and hydrocarbon emissions (1.96 Tg y⁻¹) (1). Ship emissions are also thought to be a significant contributor to global particulate mass (PM, 1.67 Tg y⁻¹), though emission factors for PM remain highly uncertain (1–3). Particles emitted from ships impact climate through both direct and indirect effects and are often emitted close to populated coastlines where they impact air quality (2, 4, 5). In their 2003 study on the global impact of ship emissions, Corbett and Koehler (6) state that error in the estimated fuel consumption of the world fleet (based on estimates of the number, type, and activity level of vessels in different regions of the world) is the most important uncertainty for every type of ship emission except PM, for which the emission factor itself remains the dominant uncertainty. Relatively little data exist concerning the composition of particles emitted from ships and the ability of those particles to grow by hygroscopic water uptake and act as cloud condensation nuclei (1, 3, 7). While it has been established that fresh particulate emissions from ships consist of sulfuric acid, organics, and soot, estimates of the organic mass fraction vary widely (8–10). Undoubtedly, much of the variation in the particulate composition stems from the type of fuel used, but because heavy fuel oil (HFO) represents over 80% of the fuel consumed by the world fleet, emissions from HFO clearly need to be characterized. Another source of variation in particulate emissions is ship type, though the majority of worldwide emissions are from large cargo or container vessels (6). Finally, engine type and load can significantly influence both particle number and composition, though the amount of time ships spend entering and exiting port with highly varying engine loads is a relatively small fraction of overall operating time.

Emission studies conducted on engine test beds offer obvious advantages in that engine load can be controlled,

* Corresponding author e-mail: seinfeld@caltech.edu.

[†] California Institute of Technology.

[‡] Department of Chemical and Environmental Engineering, University of California, Riverside.

[§] Center for Environmental Research and Technology, University of California, Riverside.

^{||} Department of Mechanical Engineering, University of California, Riverside.

[⊥] School of Chemical and Biomolecular Engineering, Georgia Institute of Technology.

[¶] School of Earth and Atmospheric Sciences, Georgia Institute of Technology.

[∇] Center for Interdisciplinary Remotely-Piloted Aircraft Studies, Naval Postgraduate School.

TABLE 1. Selected Heavy Fuel Oil Properties

product grade	IFO 380
density at 15 °C	988.5 kg/m ³
viscosity at 50 °C	290.6 mm ² /s
sulfur	3.01% m/m
ash	0.05% m/m
vanadium	75 mg/kg
nickel	29 mg/kg

fuel characteristics are precisely known, and testing can be conducted in a stationary, stable environment (8, 11). While these test-bed studies provide important insight into the emission characteristics of different engines at various loads, they need to be evaluated against measured emissions from engines in actual usage at sea. To determine the relationship between test-bed results and in situ emissions, groups have begun to measure emissions inside the stacks of vessels under sail (12, 13). Other groups have used airborne platforms to characterize particulate ship emissions in the marine atmosphere (3, 7, 11). However, when there is limited knowledge of the fuel being used or the operating conditions of the vessel, it is difficult to relate airborne emissions measurements to fuel consumption inventories. Corbett (14) summarized the gap in the current literature as follows, "By directly measuring what the engine emits at the stack with pollution chemistry "seen by the environment" in the aging plume, we may improve large-scale inventories used in chemical transport models."

We report here the first study with simultaneous in-stack and airborne measurements of emissions from a container ship. Shipboard measurements give detailed gas and particle-phase emissions for a wide range of chemical species, while airborne measurements are focused on particulate number, mass, composition, hygroscopic growth, and CCN activity. We evaluate the relationship between shipboard and airborne measurements and explore how these findings impact the characterization of emissions from this important class of ships.

2. Materials and Methods

2.1. Container Ship. The ship, representative of a modern Post-Panamax class container ship (Panamax = maximum size allowed through the Panama Canal), was 347 m long, with a gross tonnage (GT) of 91 690 and a capacity of 8680 TEUs (20-foot equivalent unit). The main propulsion engine (ME) of the vessel was a 2-stroke, slow-speed diesel engine (12k90MC, build: Hitachi MAN B&W 12K90Mk mk 6 (1998)). The engine's rated power and speed are 54840 kW and 94 r/min with a maximum pressure at maximum continuous rating (MCR) of 141 bar. During the study, load was stable with ME running at 57% of maximum power, approximately 31.2 MW, and 81 rpm. The ME operated on heavy fuel oil (HFO); selected properties are in Table 1, and the ME exhaust included a heat recovery section after the on-board sampling section.

2.2. Shipboard Platform Measurements. A detailed description of the shipboard methods for sampling and analysis of gases and particulate matter (PM) is given in Section S1 of the Supporting Information (SI) and briefly described here. In-stack measurements conformed to the requirements of ISO 8178-1 (15). The sampling approach for PM and speciated hydrocarbons involved the use of a partial flow dilution system with single venturi and is shown in SI Figure S1 and described in Agrawal et al. (13). While ISO 8178-1 allows a transfer line of 5 m, no transfer line was used in this study based on previous experience showing significant loss of particulate mass in the transfer line. Concentrations of CO₂ and NO_x were measured in both the raw exhaust

gas and dilution tunnel using the exhaust gas analyzer (EGA). The dilution ratio in the dilution tunnel, determined from either CO₂ or NO_x concentrations, agreed within 5%, as specified in the reference method (15).

Emission measurement of different gases, PM_{2.5} (particulate matter of diameter <2.5 μm) mass, size resolved PM composition, metals, ions, elemental and organic carbon, selected hydrocarbon species, including polycyclic aromatic hydrocarbons (PAHs), carbonyls, and *n*-alkanes, were performed off-line following standard methods (15–19). The SO₂ data are calculated from the sulfur level in the fuel as per ISO 8178-1 (15). Other PM measurements were made with: a MOUDI, a thermophoretic sampler with transmission electron microscopy (TEM) grids (model 3320C-CF, SPI Inc.), and Dekati Mass Monitor (20). TEM grids were analyzed for nonorganic elemental composition using EDS (energy dispersive X-ray spectroscopy).

2.3. Aircraft-Based Measurements. The Center for Interdisciplinary Remotely Piloted Aircraft Studies (CIRPAS) Twin Otter aircraft performed a series of passes through the exhaust plume of the container ship on July 16, 2007. The ship–plane rendezvous occurred in the Pacific Ocean 65 km west of the central California Coast at 122° west longitude and 35° north latitude. The Twin Otter remained in the vicinity of the ship for roughly 2.5 h, characterizing the aerosol properties within the plume and background air. Plume aerosol was measured at ages ranging from a few seconds to over an hour.

2.3.1. Aerosol Number and Volume. Aerosol number concentrations were measured by three independent condensation particle counters (CPCs), two TSI model 3010 counters with a minimum detection diameter of 10 nm and a saturation threshold of 10⁶ particles cm⁻³ and one ultrafine condensation particle counter (TSI model 3025) with a minimum detection diameter of 3 nm and a saturation threshold of 10⁶ particles cm⁻³. In the concentrated exhaust plume just behind the ship, all three CPC's were saturated; when this occurred, number concentration data were obtained from the differential mobility analyzer (DMA) (*D_m* = 10–800 nm) which is not subject to saturation until much higher concentrations because it classifies the aerosol before optical counting. However, the time resolution of the DMA is much slower (74 s) than the CPCs (1 s).

Aerosol volume was determined by the DMA and an external passive cavity aerosol spectrometer probe (0.1–3 μm) (PCASP, PMS Inc., modified by DMT Inc.). The response of the PCASP probe to different diameter particles was calibrated using polystyrene latex spheres (refractive index = 1.58) and this calibration was used for all data analysis. While the PCASP cannot measure particles below 100 nm, it offers the advantage of 1 s time resolution. The PCASP nominally operates at ambient relative humidity while during this flight, because of problems with the Nafion drier, the DMA was operated at relative humidities between 40 and 50%.

2.3.2. Aerosol Mass, Chemistry, and Absorption. Submicrometer aerosol mass and size-resolved chemical composition were measured by an Aerodyne compact time of flight aerosol mass spectrometer (C-ToF-AMS). Submicron water-soluble ions were measured by a particle into liquid sampler - ion chromatograph (PILS-IC, Brechtel Mfg. Inc.). Aerosol optical absorption was measured by a three-wavelength particle soot absorption photometer (PSAP, Radiance Research).

Details concerning the C-ToF-AMS can be found in Drewnick et al. (21). For this airborne deployment the C-ToF-AMS was fitted with a pressure-controlled inlet (22), a 3.5% chopper, the vaporizer was operated at 550 °C, and ion extraction occurred at a rate of ~60 kHz. Detection limits for the instrument, calculated as three times the standard

deviation of the noise for filtered air, are $<0.05 \mu\text{g m}^{-3}$ for all species measured, though, in practice, detection is limited by counting statistics at low aerosol loadings. One important issue concerning C-ToF-AMS data is the collection efficiency of particles within the instrument (23). In this study, all C-ToF-AMS mass loadings were multiplied by a factor of 2 (collection efficiency = 0.5) to attain agreement between the sulfate measurements of the C-ToF-AMS and the PILS-IC during periods where there were no rapid fluctuations in particulate mass loading. A collection efficiency of 0.5 has been observed in numerous other field studies with the AMS (24) and in this study it gives excellent agreement with both the PILS sulfate measurement and DMA derived mass loadings, as described in Section 3.3.

The PILS-IC is described in Sorooshian et al. (25) with specifics related to airborne operation given in Sorooshian et al. (26). For this study, instrument uncertainty was established as $\pm 7\%$. Collected aerosol in solution was delivered to a rotating carousel containing 72 vials, each of which contains material representing a period of ~ 5 min of flight, or alternatively, a distance of 15 km in flight (aircraft speed ~ 50 m/s).

The design of the three wavelength PSAP used in this study is described in Virkkula et al. (27). The PSAP measures cumulative light absorption at 467, 530, and 660 nm as particles are collected onto a filter. All absorption measurements presented in this paper have been corrected for scatter using the methods described in Virkkula et al. (27).

2.3.3. Aerosol Hygroscopic Growth and Cloud Condensation Nuclei Activity. Subsaturation aerosol water uptake was measured by a recently developed instrument, the differential aerosol sizing and hygroscopicity spectrometer probe (DASH-SP; Brechtel Mfg Inc.) while activation of cloud condensation nuclei (CCN) was measured by a flow thermal gradient cloud condensation nuclei counter (CCNc, Droplet Measurement Technologies Inc.) The DASH-SP is described in detail in Sorooshian et al. (28). During this study, the DASH-SP provided simultaneous measurements of growth factor at different relative humidities (RH) for dry DMA-selected particle diameters between $D_m = 150\text{--}200$ nm; the time resolution for this size range inside and outside of the plume was 1–10 s and 10–30 s, respectively. One humidifier was operated dry (RH < 8%), and the other three were at RH settings of 74, 85, and 92%. The uncertainty associated with growth factor measurements is $\pm 4.5\%$, and the uncertainty in the RH measurement is $\pm 1.5\%$. The CCNc is described in detail in Roberts and Nenes (29) and Lance et al. (30). For this study, the instrument was operated at supersaturations between 0.1 and 0.4%.

2.4. Theory for Predicting Subsaturation Hygroscopic Growth. Owing to its simplicity and frequent application, an assumption of independent and additive water uptake by each individual chemical component of a particle was used to predict hygroscopic growth in this study with composition measurements obtained from the C-ToF-AMS (31, 32):

$$\text{GF}_{\text{mixed}}(a_w) = \left(\sum_i \varepsilon_i \text{GF}_i(a_w)^3 \right)^{\frac{1}{3}} \quad (1)$$

where GF_{mixed} is the hygroscopic growth factor of the mixed particle, GF_i is the hygroscopic growth factor of pure compound i , a_w is the activity coefficient of water, and ε_i is the volume fraction of pure compound i in the dry particle. In applying eq 1 we set $a_w = \text{RH}$ (33). Growth factors for the pure inorganic components were obtained from the aerosol inorganics model (34, 35). In the DASH-SP, particles are processed at an RH very near zero before being rehumidified. Since ammonium sulfate does not deliquesce until 79% (33), it is assigned a growth factor of unity at 74% RH. Because C-ToF-AMS results indicate a hydrocarbon-like and presum-

ably hydrophobic organic aerosol component in the ship-exhaust plume, the growth factor for organic material is assumed to be unity at all RH settings.

2.5. Theory for Cloud Condensation Nuclei (CCN) Closure. “CCN closure”, that is, comparison of CCN predictions based on knowledge of particle size and composition with direct measurements of CCN concentrations, is an evaluation of the extent to which CCN behavior can be predicted theoretically using Köhler theory (36). CCN closure calculations within the exhaust plume of the ship were performed at supersaturations ranging from 0.1 to 0.33%. Because the DMA was operated at relative humidities ranging from 40 to 50% during the study, measured aerosol particles contained significant amounts of water, especially in the ship plume where sulfuric acid was the most abundant species. Because prediction of CCN concentrations requires knowledge of the dry size and composition of particles, an algorithm was developed to calculate dry size distributions from the measured humid distributions. First, size-resolved C-ToF-AMS data (averaged over the 74 s scan time of the DMA) were shifted in diameter space until they aligned with the volume distribution from the DMA. Once the mass and volume distributions were aligned, the nonrefractory particle composition of each DMA diameter bin was determined from the C-ToF-AMS data (see Section 3.3 for a discussion of why the dry composition from the C-ToF-AMS, measured versus vacuum aerodynamic diameter, can be aligned with the humid volume distribution from the DMA, measured versus electrical mobility diameter). Next, with knowledge of the composition of each DMA diameter bin, the ISORROPIA program (37) was used to determine the amount of water that the particles in each diameter bin contain at thermodynamic equilibrium at the operating relative humidity of the DMA. Finally the particle volume without water was calculated (assuming volume additivity), particles were rebinned into new smaller size bins, and the average composition of the new diameter bins was calculated. Following this procedure, particle diameters within the ship exhaust plume were found to be between 15 and 28% smaller when dry than when measured by the DMA at $\sim 45\%$ RH. The percentage decrease in diameter was almost exclusively determined by the mass fraction of organic (assumed insoluble) present in a given DMA diameter bin. Data from the CCNc were also averaged to match the time resolution of the scanning DMA meaning one closure calculation can be performed every 74 s except when the CCNc instrument is switching between supersaturations.

Based on C-ToF-AMS and DASH-SP results to be discussed, the aerosol was treated as an internal mixture when predicting CCN concentrations. Because the C-ToF-AMS cannot measure refractory material, black carbon and ash are assumed to be negligible in this closure study (impacts of this assumption are discussed in Section 4.4). Two chemical composition scenarios were considered in the closure: (a) bulk composition, which assumes all particles have the same composition and (b) size-resolved composition, which assigns a specific composition to each particle size. In each of these compositional scenarios, the measured sulfate molar ratio, $\text{SR} = [\text{NH}_4^+]/[\text{SO}_4^{2-}]$, was used to estimate the composition of the inorganic fraction. When $\text{SR} \leq 1$, the sulfate is assumed to be a mixture of NH_4HSO_4 and H_2SO_4 , when $1 < \text{SR} < 2$, the sulfate is assumed to be a mixture of NH_4HSO_4 and $(\text{NH}_4)_2\text{SO}_4$, and when $\text{SR} \geq 2$, the sulfate is considered to be solely $(\text{NH}_4)_2\text{SO}_4$. In the exhaust plume, the sulfate fraction consisted mainly of H_2SO_4 . Because ammonium levels were very low in the ship-exhaust plume ($\text{SR} \sim 0.1$) the size-resolved ammonium measurements from the C-ToF-AMS were too noisy to be used in CCN closure calculations. Instead, the mass ratio of ammonium to sulfate from the bulk composition was assumed at all sizes. Particles



FIGURE 1. Photograph taken of the container ship from the cabin of the CIRPAS Twin Otter (the plane's wing tip is in the foreground) during the study. The exhaust plume is visible traveling with the mean wind at $\sim 10^\circ$ angle to the heading of the ship, which can be inferred by the visible wake.

were assumed to have the surface tension of water and organics were treated as insoluble.

The effective van't Hoff factor, ν_s (which includes an estimate of the osmotic coefficient), is assumed to be 2.5 for ammonium sulfate, obtained from Pitzer activity coefficients (38, 39) for ammonium sulfate CCN with critical supersaturation between 0.2 and 0.6%. Effective van't Hoff factors for sulfuric acid and ammonium bisulfate are assumed to be 2 and 2.5, respectively (38–40). The critical supersaturation, s_c , for each particle with dry diameter d , is calculated from Köhler theory (33),

$$s_c = \left[\frac{256}{27} \left(\frac{M_w \sigma}{RT \rho_w} \right)^3 \left(\frac{M_s}{\rho_s} \right) \left(\frac{\rho_w}{M_w} \right) \frac{d^3}{\epsilon_s \nu_s} \right]^{1/2} \quad (2)$$

where R is the universal gas constant, T is the ambient temperature, σ is the surface tension of the CCN at the point of activation, M_s is the molar mass of the solute, and M_w and ρ_w are the molar mass and density of water, respectively. The volume fraction of solute, ϵ_s , can be calculated as a function of the mass fraction of solute, m_s , and its density, ρ_s ,

$$\epsilon_s = \frac{\frac{m_s}{\rho_s}}{\frac{m_s}{\rho_s} + \frac{1 - m_s}{\rho_i}} \quad (3)$$

where ρ_i is the density of the insoluble organic (assumed to be 1.6 g cm^{-3} , as discussed subsequently). A particle is

counted as a CCN when its calculated s_c is less than or equal to the supersaturation of the CCN. Predicted and measured CCN are then compared to assess closure.

3. Results

3.1. Flight Tracks and Meteorology. Figure 1 is a photo taken from the Twin Otter aircraft during the study; the plume was visible to the naked eye for a considerable distance downwind of the ship. There was a steady $10\text{--}15 \text{ m s}^{-1}$ wind from 311° NW which was blowing at a 10° angle to the ship's path, as can be seen by the different paths of the exhaust plume and ship wake in Figure 1. The flight track for the CIRPAS Twin Otter is shown in Figure 2. Marker size is proportional to sulfate concentration and indicates the relative dilution of the exhaust plume being emitted from the ship. Plume age was estimated from a simple calculation based on the distance between the ship and the aircraft at the time of measurement, knowledge of the ship's velocity (11.3 m s^{-1}) and heading (322° NW), and the average wind speed (11.4 m s^{-1}) and direction (311° NW) during the period between when the exhaust was emitted from the ship and measurement by the aircraft.

The marine boundary layer was well mixed during the 2.5 h period that the Twin Otter probed the ship plume with a temperature of $14.3 \pm 0.4 \text{ }^\circ\text{C}$ ($\theta = 287.9 \pm 0.1$) and a relative humidity of 90–98%. Vertical profiles (Figure S2 in the SI) show an abrupt increase in potential temperature and decrease in relative humidity at approximately 200 m, which is assumed to be the top of the marine boundary layer. Three-

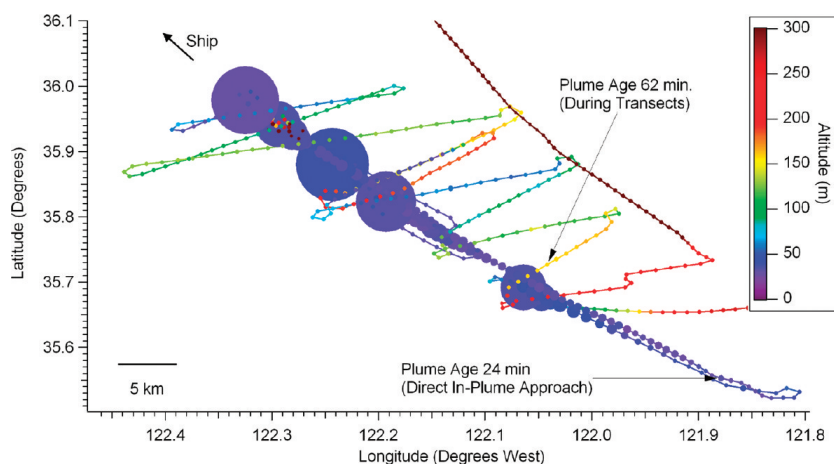


FIGURE 2. Flight track of the CIRPAS Twin Otter during the ship exhaust plume study on July 16, 2007. Marker size is proportional to the mass of sulfate in the particulate phase. The aircraft flew a series of four in-plume approaches to the ship. During the first approach, the estimated exhaust age at the point where the aircraft entered the plume was 24 min. This and each subsequent approach ended when the aircraft reached the stern of the ship, identifiable by the very large sulfate loadings observed there. After finishing the in-plume approaches, a series of 11 downwind transects were flown with the maximum plume age observed during the transects being 62 min. While the location of the 62 min transect may appear closer to the ship than the in-plume observations, it is important to remember that this transect was performed long after the in-plume approaches were finished when the ship had traveled beyond the area shown in the figure.

day Hysplit back trajectories (Figure S3 in the SI) indicate that the air mass present during the study originated in the Pacific Ocean and that there was no direct continental or urban influence on it during the previous 3 days. There is little variation in the back trajectories with altitude, giving further confidence that the measured air was not contaminated by continental outflow (41).

Two different flight strategies were used. In the first half of the flight, four direct approaches were made toward the ship, flying in what was estimated to be the center of the plume. Each approach was initiated at a point that was as far from the ship as possible but where the plume was still clearly distinguishable from background aerosol. In these approaches down the ship plume, it was possible to obtain number, volume, and mass distributions and, importantly, to accurately measure the chemical composition of the ship-exhaust aerosol in a region with very high signal-to-noise. Because negligible differences were observed in any of the measured variables between the four direct approaches in the plume, generally we present data only from the first approach, in which the plume was detected at the farthest distance from the ship. The second half of the flight consisted of a number of plume transects made at progressively farther distances from the ship and at altitudes between 30 and 200 m. In this part of the flight the crosswind and vertical structure of the plume and particle aging at longer time scales were examined.

3.2. In-Stack Composition. Table 2 gives emission factors for all of the gas-phase and mixed (gas and particle) phase species measured from the ship's stack. The data represent the average of triplicate measurements made during the period when the aircraft was probing the exhaust plume; the values are similar to those reported by the engine manufacturer on this vessel. In addition to CO_2 , NO_x , and SO_2 , a wide array of volatile organic compounds were measured, with naphthalene, formaldehyde, acetaldehyde, and acetone being the most abundant.

Table 3 gives the average in-stack emission factors for particulate-phase species. While sulfate is the dominant emission by mass, there is a significant fraction of organic carbon. The cumulative masses of hydrated sulfate, organic carbon, elemental carbon, and estimated ash is about 20% less than the measured particulate mass. The lack of mass

closure is most likely the result of uncertainty in the number of water molecules associated with each sulfate molecule. A ratio of 6.5 H_2O molecules to a H_2SO_4 molecule was used because it represents the lowest energy state for a sulfate-water complex (12, 13). Another reason for poor mass closure is that the organic carbon (OC) has not been converted to organic mass (OM). While this would improve closure, it may not be justified given that previous filter-based measurements of diesel exhaust, where denuders were used to remove gas-phase organics, have shown an overestimation of OC mass of approximately 30% caused by adsorption of gas-phase organics onto the filter (42). Figure 3 shows size-resolved chemical composition measurements of particulate matter within the ship's stack obtained using a micro-orifice uniform deposit impactor (MOUDI, described in Section S1.4 in the SI). The mass ratio of total carbon to hydrated sulfate ($\text{H}_2\text{SO}_4 + 6.5 \text{H}_2\text{O}$) remains relatively constant with size at 0.12 ± 0.02 , but the fraction of unknown mass is much higher at small particle sizes (note that there was too little PM present in size bins above $0.32 \mu\text{m}$ to exceed the detection limit for sulfate measurement and total PM cannot be measured for the smallest size bin as described in Section S1.4 of the SI).

Figure 4 shows a TEM image from the in-stack thermophoretic sampler. Two populations of nanoparticles are observed; one population ranging from 5 to 8 nm and the other ranging from 30 to 100 nm. The 5–8 nm nanoparticles outnumber the larger nanoparticles, a finding that is consistent with airborne measurements with an ultrafine CPC, discussed subsequently, that show significant number of particles between 3 and 10 nm. EDS analysis shows distinctive peaks of sulfur and vanadium from both populations of particles.

3.3. Particle Number, Volume, and Mass in the Airborne Exhaust Plume. Figure 5 shows particle number concentrations during a series of airborne transects made at progressively farther distances from the ship. Data from the three different CPCs and the PCASP are shown. During the first two transects all three CPCs were saturated, consistent with a DMA-measured concentration of 7.8×10^5 particles cm^{-3} near the ship. The relatively low particle number concentrations reported by the PCASP indicate that the vast majority of particles were less than 100 nm in size. On the third transect, the number concentrations recorded by the ultrafine

TABLE 2. Gaseous Stack Emission Factors in g (kWhr)^{-1} by Chemical Class^a

compound	emissions factor	compound	emissions factor
NO _x (as NO ₂)	20.1 ± 0.1	PAHs ^c , alkanes cont'd	
CO	0.29 ± 0.01	Tetradecane	(5.55 ± 0.26) × 10 ⁻⁴
CO ₂	638 ± 4	hexadecane	(4.00 ± 1.32) × 10 ⁻⁴
Calc.SO ₂ ^d	11.9 ± 0.1	octadecane	(3.21 ± 1.13) × 10 ⁻⁴
BTEX^b		nonadecane	(2.00 ± 0.39) × 10 ⁻⁴
1,3 butadiene	(1.3 ± 0.8) × 10 ⁻⁴	fluorene	(2.50 ± 0.74) × 10 ⁻⁴
benzene	(7.0 ± 0.4) × 10 ⁻⁴	phenanthrene	(5.14 ± 2.15) × 10 ⁻⁴
toluene	(4.4 ± 0.9) × 10 ⁻⁴	anthracene	(1.22 ± 0.66) × 10 ⁻⁵
m&p xylene	(3.3 ± 0.5) × 10 ⁻⁴	fluoranthene	(7.48 ± 2.85) × 10 ⁻⁵
ethyl benzene	(1.1 ± 0.3) × 10 ⁻⁴	eicosane	(2.49 ± 0.64) × 10 ⁻⁴
o-xylene	(1.0 ± 0.05) × 10 ⁻⁴	docosane	(6.84 ± 3.63) × 10 ⁻⁴
carbonyls		tetracosane	(9.55 ± 9.06) × 10 ⁻⁴
formaldehyde	(8.32 ± 4.82) × 10 ⁻³	hexacosane	(7.82 ± 7.96) × 10 ⁻⁴
acetaldehyde	(5.21 ± 2.06) × 10 ⁻³	octacosane	(7.37 ± 6.02) × 10 ⁻⁴
acetone	(3.12 ± 2.15) × 10 ⁻³	triacontane	(3.99 ± 2.41) × 10 ⁻⁴
acrolein, propionaldehyde, crotonaldehyde, methyl ethyl ketone, methacrolein, butyraldehyde, benzaldehyde, <i>n</i> -valeraldehyde, <i>m</i> -tolualdehyde, hexaldehyde	<0.53 × 10 ⁻³	pyrene	(4.76 ± 1.48) × 10 ⁻⁵
PAHs ^c and alkanes		benz(a)anthracene	(8.19 ± 1.15) × 10 ⁻⁶
naphthalene	(3.36 ± 1.06) × 10 ⁻²	chrysene	(8.89 ± 0.84) × 10 ⁻⁶
acenaphthylene	(2.35 ± 0.53) × 10 ⁻⁵	benzo(b)fluoranthene	(6.35 ± 1.17) × 10 ⁻⁶
acenaphthene	(1.16 ± 0.63) × 10 ⁻⁴	benzo(k)fluoranthene	(4.73 ± 0.83) × 10 ⁻⁶
dodecane	(2.34 ± 0.19) × 10 ⁻⁴	benzo(a)pyrene	(1.62 ± 0.15) × 10 ⁻⁵
		indeno(1,2,3-cd)pyrene	(4.86 ± 1.04) × 10 ⁻⁶
		dibenzo(a,h)anthracene	(3.64 ± 1.02) × 10 ⁻⁶
		benzo(ghi)perylene	(2.66 ± 1.02) × 10 ⁻⁵

^a Emission factors for PAHs and alkanes are for total (gas and particle phase) emissions. ^b BTEX = benzene, toluene, ethylbenzene, and xylenes. ^c PAH = polycyclic aromatic hydrocarbon. ^d SO₂ gas data is calculated from the sulfur level in the fuel as per ISO 8178 (15).

TABLE 3. Particulate Stack Emission Factors

compound	emissions factor (g/kWhr)
particulate mass (PM) ^a	2.62 ± 0.03
sulfate as H ₂ SO ₄ •6.5H ₂ O	1.87 ± 0.24
sulfate (dry)	0.84 ± 0.11
organic carbon (OC)	0.193 ± 0.004
elemental carbon (EC)	0.007 ± 0.001
ash ^b	0.085

^a Particulate mass measurements were made after filter equilibration at RH = 40% and T = 25 °C (see Section S1.2 of the SI for details) ^b Ash emission factor estimated from the ash content in the fuel.

TSI 3025 CPC dropped below the instrument saturation level of 10⁵ particles cm⁻³. The particle number concentration in the center of the plume during all of the transects exceeded 10⁴ cm⁻³, a level at which the TSI 3010 data are unreliable (7.4% coincidence at 10⁴ particles cm⁻³). On the edges of the plume transects, the ultrafine TSI 3025 detected much higher loadings of particles than either TSI 3010, indicating the presence of significant numbers of particles between 3 and 10 nm (the cutoff points for the TSI 3025 and 3010 CPCs, respectively). The ultrafine particles persist even at the longest plume age observed of 62 min.

Figure 6 shows time series from the C-ToF-AMS, PILS, PCASP, and DMA during the first in-plume approach to the ship. Background aerosol, at loadings typical for marine air in this region, is observed until the plume is first encountered at 21:32 UTC. Following plume identification, the aircraft flew in the plume toward the ship until reaching it at 21:49. The particle volumes measured by the PCASP were much lower than those of the other instruments, indicating that not only the majority of the particle number distribution, but also the majority of the particulate volume and mass distributions were below a diameter of 100 nm.

In Figure 6 and all subsequent figures, the mass loadings shown for the C-ToF-AMS have been multiplied by a factor of 2 to correct for particle bounce off the instrument's vaporizer (see Section 2.3.2). The maximum sulfate loadings determined by the C-ToF-AMS inside the exhaust plume are significantly higher than those determined by the PILS, presumably the result of the longer, 5 min, averaging time for a PILS measurement. To confirm that the higher loadings observed in the C-ToF-AMS were not caused by an increase in collection efficiency related to the high concentrations of sulfuric acid in the exhaust plume (24), C-ToF-AMS results are compared with measurements from the DMA, which has enhanced time resolution (74 s scans) relative to the PILS. Comparing the volume measured by the DMA to the C-ToF-AMS mass measurement requires an estimate of the aerosol density. The C-ToF-AMS measures particle vacuum aerodynamic diameter (D_{va}) while the DMA measures electrical mobility diameter (D_m) allowing determination of particle density (ρ_p) (43). If one assumes that the aerosol consists of an internal mixture of spherical particles, the relationship between the two diameters is $\rho_p = (D_{va}/D_m)\rho_o$, where ρ_o is unit density (1 g cm⁻³).

Figure 7 shows the chemically resolved mass distribution of the in-plume aerosol measured by the C-ToF-AMS along with the number and volume distributions from the DMA. While there is a higher fraction of organic matter in the smaller particles, an assumption of internal mixing appears reasonable in determining an average particle density. Based on the diameter offset between the mass distribution (plotted vs D_{va}) and the volume distribution (plotted vs D_m), the average in-plume particle density is calculated to be 1.4 g cm⁻³.

Because the DMA was run at relative humidities between 40 and 50%, this represents a wet particle density. It may seem inconsistent to use C-ToF-AMS data where particles are essentially dry (a small amount of water is retained by sulfuric acid in the C-ToF-AMS) and DMA data where they

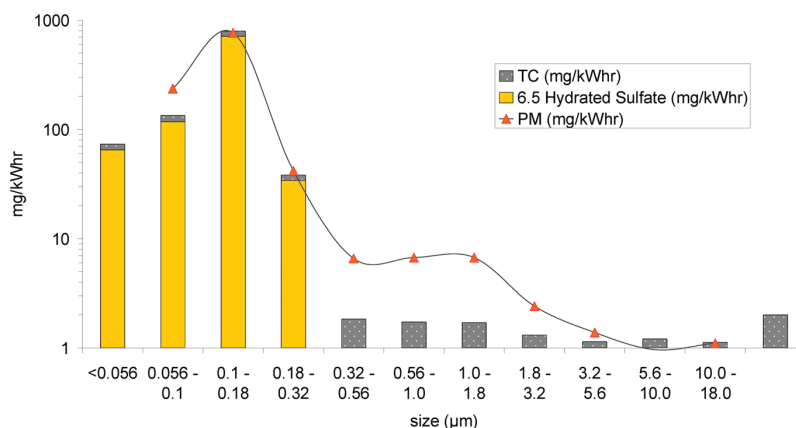


FIGURE 3. Size-resolved particulate chemical composition obtained through the MOUDI/filter setup in the ship's stack. The ratio of total carbon (TC) mass to hydrated sulfur ($\text{H}_2\text{SO}_4 \cdot 6.5\text{H}_2\text{O}$) mass remains relatively constant with size (12% $<0.056\ \mu\text{m}$, 14% $0.056\text{--}0.1\ \mu\text{m}$, 9% $0.1\text{--}0.18\ \mu\text{m}$, and 12% $0.18\text{--}0.32\ \mu\text{m}$).

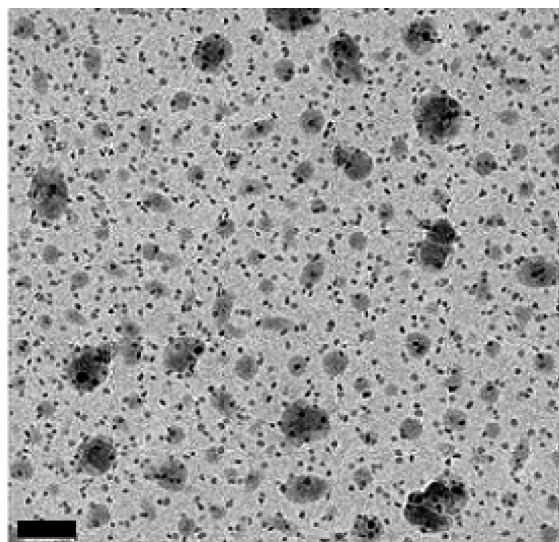


FIGURE 4. TEM image (scale bar in lower left corner = 100 nm) of particles collected with the in-stack thermophoretic sampler. Two classes of particles are observed: (1) nanoparticles in the size range of 5–8 nm and (2) larger particles in a wide size range from 30 to over 100 nm. The nanoparticles outnumber the larger particles. EDS analysis showed distinctive peaks of sulfur and vanadium from both classes of particles.

are wet. However, this is reasonable because of the fortuitous fact that the vacuum aerodynamic diameter of particles composed of sulfuric acid and hydrophobic organic remains virtually unchanged as the particle is dried from 50 to 0% RH. This is because the reduction in size caused by the loss of water is almost exactly compensated for by the increase in density. Using the wet particle density of $1.4\ \text{g cm}^{-3}$, mass loadings can be derived from the DMA volume data. When total particulate mass measured by the C-ToF-AMS is plotted versus the DMA volume multiplied by a wet density of $1.4\ \text{g cm}^{-3}$, the resulting loadings agree within $\pm 10\%$ throughout the plume, except for the point nearest the ship where sufficient time did not exist to complete a full DMA scan. Even at this last point where the highest loading was observed, the two instruments agree to within 20%, with the C-ToF-AMS measuring $470\ \mu\text{g m}^{-3}$ and the DMA, $380\ \mu\text{g m}^{-3}$. The extent of agreement between the mass measured by the PILS, the C-ToF-AMS, and the DMA-derived mass gives confidence

that none of these instruments was subject to obvious saturation issues and that the collection efficiency of the AMS remained constant throughout the flight.

3.4. Airborne Particulate Composition. Table 4 gives the mass fractions of organic, ammonium, sulfate, and nitrate in the particles directly behind the ship and during successive downwind transects of the exhaust plume. Also given are the contributions of $m/z\ 44$ (CO_2^+ , higher fractions indicate more oxidation) and 57 (C_4H_9^+ , higher fraction indicate less oxidation) (44) to the organic mass, the ammonium-to-sulfate molar ratio, and the fraction of the organic mass (measured by the C-ToF-AMS) accounted for by oxalate and other organic acids (measured by the PILS). Organic acid concentrations in the final transect represent primarily background aerosol because the plume transect itself lasted for a few seconds while a PILS vial represents average particle concentrations for a five-minute period. Measurements from the PSAP instrument of aerosol light absorption are an indirect measure of particulate black carbon concentration.

Organics comprise 31% of the aerosol mass immediately aft of the ship. This fraction does not change significantly with age, remaining at 28% after the plume has aged for over an hour. The nonorganic aerosol mass appears to be almost entirely sulfuric acid, given the very low mass fractions of either ammonium or nitrate within the plume. The low mass fraction of organic acids in the plume and the large contribution of $m/z\ 57$ relative to $m/z\ 44$ indicate that the organic is not well oxidized or readily water soluble (45, 46). The estimated O:C atomic ratio for the plume organic aerosol is 0.20 versus 0.74 for the background aerosol (O:C estimates based on eq 4 and discussed in Section 4.1) (47). Figure 8 shows aerosol mass spectra taken in the fresh ship exhaust, in the exhaust plume after it had aged for 62 min, and in the background marine boundary layer. Also shown in Figure 8 is a reference Aerodyne AMS mass spectrum from the exhaust of a diesel bus (48). While the relative magnitude of the major peaks is slightly different in the diesel bus and ship exhaust particulate mass spectra, the major peaks themselves are the same. These are the same major peaks observed by Phinney et al. (49) during previous observations of particulate ship exhaust with an Aerodyne AMS and they indicate particles composed of saturated and unsaturated hydrocarbons (alkanes, $m/z\ 29, 43, 57, 71, 85, \dots$; alkenes and cycloalkanes, $m/z\ 27, 41, 55, 69, 83, \dots$; dienes, alkynes, and cycloalkenes, $m/z\ 67, 81, 95, \dots$; phenylalkanes, $m/z\ 77, 91, 105, 119, \dots$) (50). Peaks known to be associated with PAHs were also observed in the C-ToF-AMS mass spectrum at m/z values above 200. Also evident in Figure 8 is an increase in

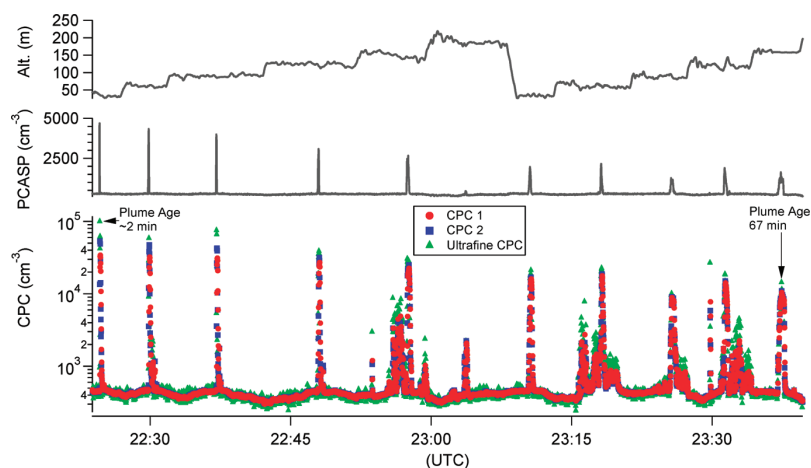


FIGURE 5. Time series of the aerosol number concentration measurements from the TSI 3010 and 3025 CPCs showing significant ultrafine particle concentrations at plume ages up to 1 h. The low PCASP concentrations indicate that the vast majority of particles in the ship exhaust plume are less than 100 nm in diameter. Plume passes were made at several different altitudes.

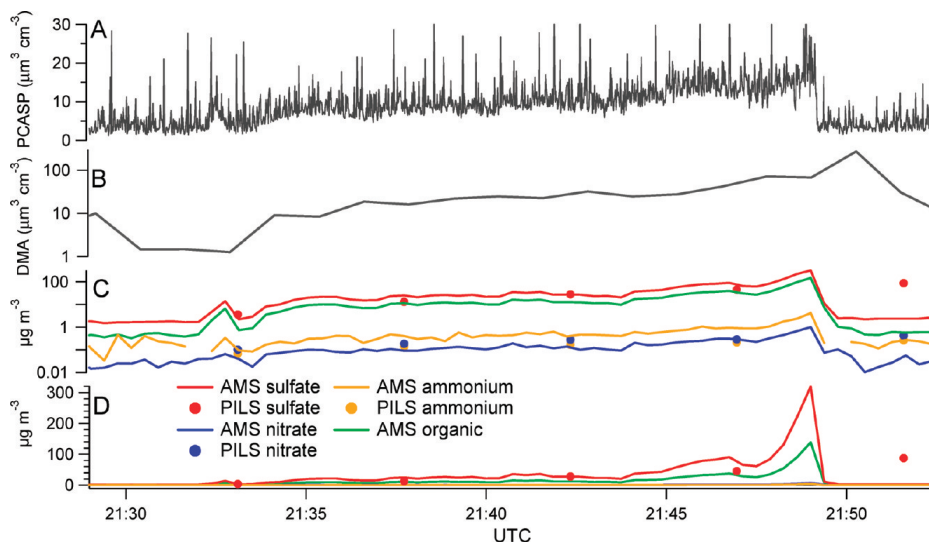


FIGURE 6. Time series of all instruments measuring aerosol mass or volume during the first in-plume approach to the ship. (A) PCASP particle volume (B) DMA particle volume (C and D) AMS and PILS measurements of particle chemistry shown on a log and linear axis, respectively. The plane first enters the exhaust plume at 21:32 UTC, at which point the plume has aged for ~24 min since being emitted from the ship. The plane reaches the stern of the ship at 21:49, though the response of the DMA and the PILS is delayed because of averaging time within the instruments.

the mass fraction of $m/z44$ and a decrease in the mass fraction $m/z57$ in the more aged spectra, though this is thought to be primarily caused by the influence of the more highly oxidized background aerosol mixing in when the plume dilutes, as will be subsequently discussed.

3.5. Aerosol Hygroscopicity. Figure 9 shows the particle hygroscopic growth factors measured by the DASH-SP and predicted by eq 1 with compositional inputs obtained from the C-ToF-AMS. Average growth factors are given for “in plume”, defined as regions where particulate sulfate mass and CN number were more than double those of the background aerosol, and “out of plume”, classified as all nonplume measurements made at similar altitudes to the in-plume measurements. The sulfate molar ratio, $SR = [NH_4^+]/[SO_4^{2-}]$, was used to determine the composition of the inorganic fraction. The same scheme (described in Section 2.5) was used to define the relative amounts of sulfuric acid, ammonium bisulfate, and ammonium sulfate in both sub-saturated hygroscopic growth and CCN calculations. Pre-

dicted particle growth factors were calculated using bulk composition (the average composition of all submicrometer particles). While the DASH-SP measures particles with mobility diameters between 150 and 200 nm, bulk composition was used because the improvement in signal-to-noise was judged to be more important than the rather negligible difference (typically <5%) between bulk composition and the composition of particles in this size range. Organics were assumed to be hydrophobic and assigned a growth factor of unity when calculating hygroscopic growth factors, both in the ship exhaust plume and in the background air.

Because eq 1 requires volume fractions of individual chemical species in the aerosol and the C-ToF-AMS measures mass fractions, it is necessary to estimate the density of each individual chemical component within the particle. Using the techniques described in Section 3.3, the average particle density (at ~45% RH) was determined to be 1.4 g cm^{-3} in the ship-exhaust plume and 1.55 g cm^{-3} outside of the plume. Given the average particle density, the density of the organic

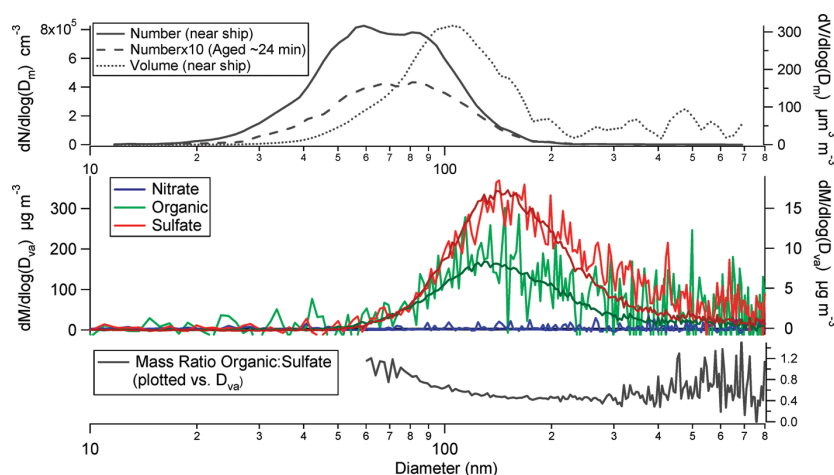


FIGURE 7. Top Panel: Particle number and volume distributions measured by the DMA (at $\sim 45\%$ RH) at different plume ages during the first in-plume approach to the ship. While there is a dramatic reduction in particle number as the plume is diluted, the peak position of the number distribution changes relatively little with plume age. Middle Panel: Chemically resolved mass distribution during the first in-plume approach to the ship. The noisy distributions (right axis) correspond to measurements made after the plume had aged for ~ 24 min while the much smoother distributions (left axis) were obtained in the fresh plume immediately behind the ship. Again, there is little change other than a decrease in particle mass. Bottom Panel: The organic:sulfate mass ratio vs measured by the C-ToF-AMS in the ship exhaust plume.

TABLE 4. Summary of Absorption Coefficient and Nonrefractory (n.r.) Dry Particulate Composition in the Ship Exhaust Plume at Various Plume Ages

est. plume age (min)	0	24	62	out of plume
altitude (m)	30	30	55	35–220
sulfate (% n.r. dry mass)	68	67	70	73
organic mass (% n.r. dry mass)	31	31	28	18
nitrate (% n.r. dry mass)	<1	<1	<1	1
NH ₄ :SO ₄ (mol ratio)	0.1	0.1	0.1	0.5
<i>m/z</i> 57:org (% n.r. dry mass)	4	3	2	0.6
<i>m/z</i> 44:org (% n.r. dry mass)	3	5	8	17
oxalate:org (% n.r. dry mass)	1	1	2	9
org acids:org (% n.r. dry mass)	2	1	2	9
CN:SO ₄ (10 ¹⁵ g ⁻¹)	2.6	2.5	2.3	0.25
B _{ABS} :SO ₄ (Mm ⁻¹ g ⁻¹) ^a	2.4×10^5	2.8×10^5		

^a Measured at 532 nm by the PSAP.

fraction can be estimated using the mass fraction of organic and inorganic species from the C-ToF-AMS, the mass fraction of water from ISORROPIA, assuming volume additivity, and assuming dry densities of 1.83 g cm^{-3} for sulfuric acid, 1.79 g cm^{-3} for ammonium bisulfate, and 1.77 g cm^{-3} for ammonium sulfate. For the purpose of calculating the organic density, all in-plume sulfate was assumed to be sulfuric acid and all out-of-plume sulfate was assumed to be in the form of ammonium sulfate. Organics were found to have a density of $\sim 1.6 \text{ g cm}^{-3}$ in the exhaust plume while outside of the exhaust plume there was high variability in the calculated organic density and a typical organic density of 1.4 g cm^{-3} was assumed. It is important to note that changing the organic density from 1.4 to 1.6 g cm^{-3} results in an $\sim 1\%$ change in predicted growth factor.

Hygroscopic growth factors of in-plume aerosol are suppressed relative to those measured in the background

aerosol. In-plume aerosol has a higher fraction of organic mass (0.28 ± 0.02 vs 0.20 ± 0.15 out of plume), but also has more acidic sulfate (see Table 4). Based on measured composition and the assumptions noted above, both in- and out-of-plume hygroscopic growth factors are overpredicted by eq 1, and the overprediction within the plume is more substantial. The color bar in Figure 9 shows the hygroscopic growth factor of the organic fraction that would need to be assumed to achieve closure between the predicted and measured growth factors. While physically unrealistic, organic growth factors less than 1 indicate that observed growth factors are less than those predicted based on water uptake by the inorganic fraction alone. The presence of negative organic growth factors indicates that the measured growth factors are substantially less than predicted. Using size-resolved chemistry from the C-ToF-AMS in eq 1 would result in a slightly lower mass fraction of organics, eliminating the possibility that a high organic mass fraction was masked by averaging across particle sizes. None of the wet number distributions from the DASH-SP (74, 85, and 92% RH) shows signs of a bimodal distribution, making it improbable that an externally mixed, hydrophobic mode existed to explain the overpredicted particle hygroscopic growth factors. Potential explanations for the suppressed growth factors observed will be discussed subsequently.

3.6. CCN Activity. Figure 10 shows predicted and measured CCN concentrations for a number of points within the ship exhaust plume. These particular in-plume points were chosen because the particle concentrations were relatively stable during an entire scan of the DMA. Again, the sulfate molar ratio, $SR = [\text{NH}_4^+]/[\text{SO}_4^{2-}]$, was used to determine the composition of the inorganic fraction (see Section 2.5). As noted earlier, the low SR suggests that the aerosol sulfate was present mostly as H_2SO_4 in the exhaust plume, while out of plume the particulate sulfate was partially neutralized. All predictions shown are based on eqs 2 and 3, but with different inputs for particulate chemical composition. Before CCN prediction calculations were performed, the dry particle size distribution was estimated based on the measured humid DMA size distribution and C-ToF-AMS measured composition as described in Section 2.5. Because the particulate composition in the ship exhaust plume did not change significantly with distance from the ship, the dry size

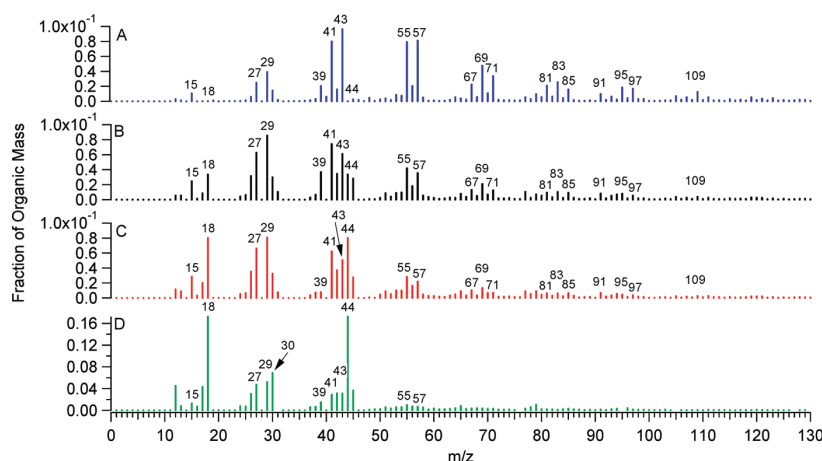


FIGURE 8. (A) Reference AMS organic mass spectrum from the diesel bus chase study of Canagaratna et al. (48). C-ToF-AMS organic mass spectra from (B) the ship exhaust plume a few hundred meters behind the stack, (C) the ship exhaust plume after it had aged for ~62 min, (D) background aerosol in the marine boundary layer outside of the ship exhaust plume. Signal at m/z 39 (typically indicative of potassium and not included in organic spectra) is shown because, based on peak location in the raw spectra (not shown), it does not appear to be potassium. Both spectra (A) and (B) strongly resemble the ship-exhaust organic AMS spectra observed by Phinney et al. (49).

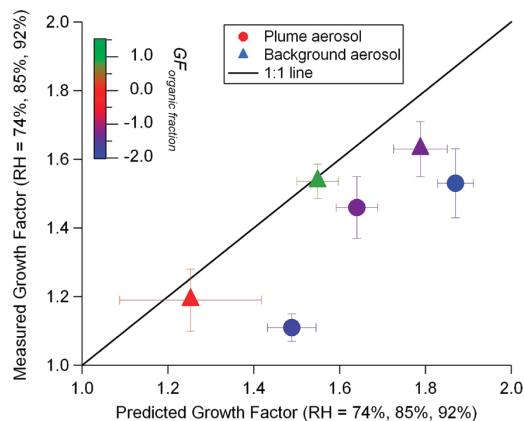


FIGURE 9. Hygroscopic growth factors for particles measured by the DASH-SP and predicted using the volume-weighted mixing rule using bulk chemical composition from the C-ToF-AMS and the assumption that organics have a growth factor of unity. Growth factors are smaller within the exhaust plume than in the background aerosol. Growth factors are suppressed relative to predictions in both the background and the plume aerosol, but the suppression is significantly more dramatic within the exhaust plume. The organic mass fraction is 0.28 ± 0.02 within the plume and 0.20 ± 0.15 outside of the plume. The color scale gives the growth factor that the organic fraction would be required to have to achieve closure between measurements and observations.

distribution was consistently between 15 and 28% smaller than the humid distributions shown in Figure 7. Organics were treated as hydrophobic (based on AMS spectra and DASH-SP results) with a density of 1.6 g cm^{-3} and were assumed to have no effect on surface tension. Assuming an internal mixture and using bulk composition results in an overprediction of CCN number by an average of $23 \pm 6\%$ (Figure 10, top). Using size-resolved composition improves the closure slightly, resulting in an average overprediction of $16 \pm 6\%$ (Figure 10, bottom). The slight improvement in closure using size resolved chemistry occurs because at the higher supersaturations (above $\sim 0.25\%$) the CCN activation

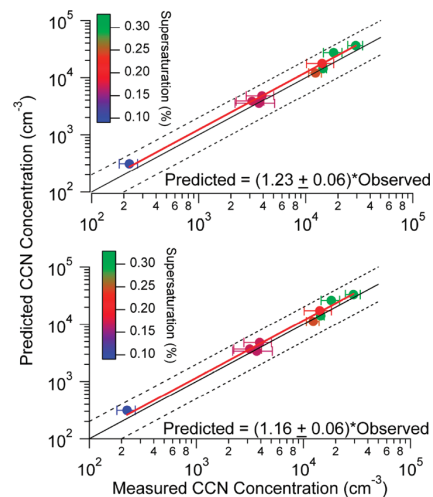


FIGURE 10. CCN droplet closure within the exhaust plume. Top Panel: Results obtained using bulk (size-averaged) chemistry. Bottom Panel: Results obtained when size-resolved chemistry is used in the calculations. Size-resolved chemistry slightly improves the closure. The color of the markers corresponds to the CCNc instrument operating supersaturation during the measurement. Dashed lines indicate values that are twice and one-half of the 1:1 line, whereas the red lines indicate the least-squares best fit. The slopes of the least-squares fits are given in the predicted vs observed equations at the bottom of each panel.

diameter moves toward smaller particles, which have a higher mass fraction of hydrophobic organics and are less CCN active.

Figure 11, which will be referred to as a growth kinetics plot, shows the average diameter achieved by activated particles when exiting the CCNc growth chamber as a function of the instrument supersaturation. Because the aerosol introduced into the CCNc is polydisperse, the particles leaving the activation columns will always exhibit a range of final sizes (this occurs even if the particles are pure ammonium sulfate, because initially larger particles will grow to correspondingly larger sizes). The smallest size that an ammonium sulfate particle can reach is that attained by a particle

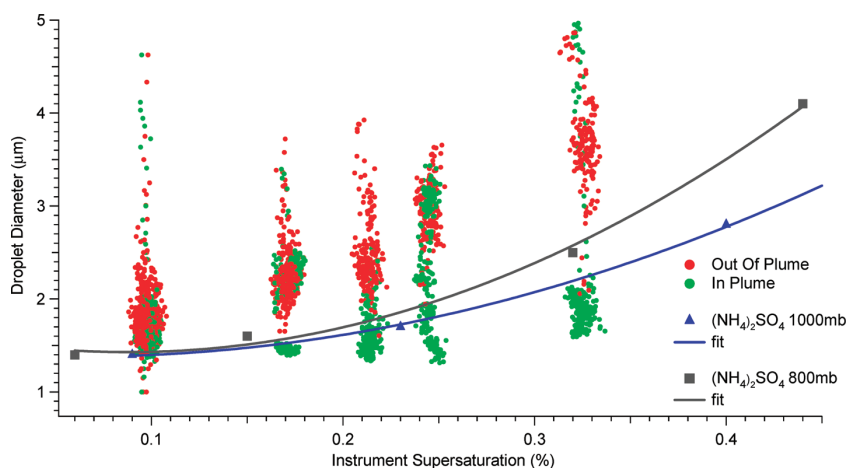


FIGURE 11. Growth kinetics plot for aerosol in and out of the ship exhaust plume. All measurements were made between 845 and 900 mbar, near the middle of the pressure range defined by the two ammonium sulfate calibrations shown in the figure. The calibration lines represent the final diameter achieved by ammonium sulfate particles with the minimum diameter required for activation at the given supersaturation. The vast majority of background particles grow to diameters greater than the minimum defined by the calibrations while the rate of growth of particles within the exhaust plume appears to be suppressed relative to that of ammonium sulfate.

of the minimum diameter required for activation at the operating supersaturation of the instrument; the lines shown in the figure represent this minimum size for ammonium sulfate particles. Any particles attaining a final size smaller than this minimum are likely to be subject to mass transfer limitations; that is, water is taken up more slowly such that the particles activate at a later time within the CCNc growth chamber than ammonium sulfate. It is clear that in-plume particles tend to achieve a smaller size within the CCNc growth chamber than the reference ammonium sulfate particles. The effect is not thought to be the result of depleted supersaturation in the column which has been shown not to occur for CCN concentrations $<10^4 \text{ cm}^{-3}$. This suggests that particles with critical supersaturation between 0.1 and 0.35% may have slower water uptake kinetics than ammonium sulfate. On the contrary, the vast majority of particles outside the ship plume do not exhibit slower water vapor uptake kinetics relative to $(\text{NH}_4)_2\text{SO}_4$.

4. Discussion

4.1. Comparison of Ship and Airborne Data. One goal of the present study is to determine the extent to which in-stack measurements of particulate ship emissions reflect particle properties in the airborne exhaust plume. Owing to a lack of measurements of gas-phase tracers of dispersion (e.g., CO_2 or CO), it is not possible to relate the absolute particulate mass measured in the stack to that in the air, but it is possible to assess agreement between composition measurements. In-stack particulate composition data are summarized in Table 3, while the airborne measurements are given in Table 4. The airborne measurements for sulfate are reported without associated water. Accordingly, the 6.5 H_2O molecules assumed to be associated with a sulfate molecule in the stack can be removed to give a dry sulfate emission factor of 0.84 g kWh^{-1} . To relate the shipboard and airborne organic measurements, it is necessary to estimate a conversion from organic carbon (OC), measured in the stack, to organic mass (OM) measured by the airborne C-ToF-AMS.

Aiken et al. (47) used a high resolution Aerodyne aerosol mass spectrometer, capable of unambiguously measuring the oxygen and carbon content of an aerosol, to relate the O:C atomic ratio to the fraction of signal intensity observed at m/z 44 on unit mass resolution AMS instruments. The relationship, derived from several ground-based and airborne

studies, between the fraction of the organic aerosol signal (OA) present at m/z 44 and the atomic ratio of oxygen to carbon (O:C), given with 95% confidence intervals, is ($R^2 = 0.84$):

$$\text{O:C} = (0.0382 \pm 0.0005)(\% \text{ of OA from } m/z 44) + (0.0794 \pm 0.0070) \quad (4)$$

Aiken et al. (47) used an even broader data set, including several chamber studies in addition to the previously mentioned field studies, to derive a relationship between organic mass (OM) and the O:C atomic ratio ($R^2 = 0.997$):

$$\text{OM/OC} = (1.260 \pm 0.002)(\text{O:C}) + (1.180 \pm 0.001) \quad (5)$$

In Table 4, the percentage of the organic mass spectrum represented by signal at m/z 44 for particles within the exhaust plume is 3.5%, which, using eqs 4 and 5, leads to an OM:OC ratio of 1.45. The in-plume percentage of nonrefractory organic mass was measured to be 31% by the C-ToF-AMS which converts to 21% organic carbon using this estimated OM:OC ratio. Based on the arguments above, the estimated ratio of organic carbon to dry sulfate mass ($\text{OC}:\text{SO}_{4\text{dry}}$) measured in the ship's stack is 0.23 ± 0.03 . The estimated airborne measurement of $\text{OM}:\text{SO}_{4\text{dry}} = 0.43 \pm 0.01$, which converts (again assuming an OM:OC ratio of 1.45) to $\text{OC}:\text{SO}_{4\text{dry}} = 0.30 \pm 0.01$. However, this relatively good agreement between airborne and shipboard measurements is a best case scenario given the previously mentioned overestimation of organic carbon mass in the shipboard measurement caused by adsorption of gas-phase organics onto the filter (estimated to be $\sim 30\%$ based on Shah et al. (42)). Because there was no correction for absorption of gas-phase organics in this study, 0.23 represents an upper limit of the organic carbon to dry sulfate mass ratio measured within the ship's stack.

There are several possible explanations for the higher fraction of organic mass measured in the airborne plume. The in-stack measurements were made at a dilution ratio of about 5:1 which is less dilute than the airborne measurements, even close to the stack. However, additional dilution should cause semivolatile organics to revolatilize and cause less organic mass to be present in the airborne plume. Loss of particulate or semivolatile gaseous organics during the transition from the stack to the filter is likely to be a negligible effect because a transfer line was not used in this study. The slightly higher temperature of the collection point for

TABLE 5. Gas and Particulate Emission Factors in g (kg fuel)⁻¹ from This and Previous Studies of Emissions from Ships Burning Heavy Fuel Oil

	this study	Petzold et al. 2004, 2008 (9, 11)	Chen et al. 2005 (54)	Sinha et al. 2003 (3)	Hobbs et al. 2000 (7)
NO _x (as NO ^a)	65.7 ± 0.3 ^d	112 ^c	30 ± 12 ^e	65.5 ± 3.3 ^e	23 ± 5 ^e
CO	1.5 ± 0.1 ^d			3.0 ± 0.2 ^e	
SO ₂	59.7 ± 0.5 ^c	51 ^c	27 ± 4 ^e	52.2 ± 3.7 ^e	62 ± 25 ^e
PM	12.9 ± 0.1 ^d				
EC	0.04 ± 0.01 ^d	0.18 ± 0.02 ^f			
OC	0.98 ± 0.03 ^d , 1.3 ± 0.5 ^e				
Sulfate	4.3 ± 0.5 ^d				
CN 10 ¹⁶	1.3 ± 0.2 ^{e,g}	1.36 ± 0.24 ^{e,g} , 3.43 ± 1.26 ^{f,g}	4.7 ± 1.3 ^e	6.2 ± 0.6 ^e	1.6 ± 0.5 ^e
CN 10 ¹⁵ (0.1–3 μm)	0.6 ± 0.1 ^e	2.3 ± 0.7 ^e		5.1 ± 0.5 ^e	
CCN/CN (0.3% S)	0.24 ± 0.05 ^e			0.18 ± 0.07 ^e	
OM:SO ₄	0.42 ± 0.02 ^e	0.54 ^f , 0.17 ^{b,f}			

^a Form of NO_x not specified in Petzold et al. ^b OC:SO₄ ratio given in Petzold et al. (2004). ^c Calculated based on fuel composition. ^d In-stack measurement. ^e Airborne plume measurement. ^f Test-bed MAN B&W four-stroke marine diesel engine. ^g CN emissions factor reported for CN > 10 nm (reported in the current study because the 3025 CPC gave suspect results in the emissions plume).

the filters (~25 °C) versus the ambient temperature of the marine boundary layer (14.3 ± 0.4 °C) is also judged to be relatively unimportant based on previous studies in which diesel exhaust filters were collected at different temperatures (51). However, it should be noted that the volatilities of the organics in the heavy fuel oil may have quite different temperature dependencies than those of organics in diesel fuels previously tested.

Given that the higher fraction of particulate organic mass observed in the airborne measurements does not appear to be an artifact of the shipboard measurement methods, the organic material must condense from the gas phase into the particle phase between the point where the stack measurements are made (at the bottom of the stack) and the point at which airborne measurements are first made (~100 m behind the ship). Between the two measurement points, the exhaust gas from the stack passes through a heat exchanger designed to use the otherwise waste heat of exhaust (also called a waste heat boiler). The heat exchanger can lower the temperature of exhaust to ~75–100 °C. This temperature decrease occurs without dilution of the exhaust as opposed to the dilution tunnel system used for in-stack measurements where the exhaust was cooled and diluted simultaneously. The hypothesis that organics condense in the upper regions of the stack and in the waste heat boiler is supported by Figures 3 and 7, which show that the fraction of organic mass is constant with particle size in the stack measurements but that organic mass is enriched on smaller airborne particles. This pattern of larger mass fraction on smaller particles, which have more surface area, is consistent with a gas-to-particle condensational process (assuming the condensing organic is nonvolatile enough not to be affected by the higher vapor pressure caused by the increased curvature of the smaller particles).

4.2. Plume Dilution and Aging. Because of the favorable wind and cloudless conditions during the study, it was possible to fly directly in the exhaust plume until it had reached an estimated age of 24 min and to detect the plume in transects up to an estimated age of 62 min. Measurements of plume composition at different ages are given in Table 4. Of significance is the fact that there is essentially no change in the organic:sulfate mass ratio with time. This constant ratio indicates that condensed organics in the particulate phase were not volatile enough to repartition back to the gas phase as the plume diluted and gas-phase organic concentrations decreased. Additionally, while organic matter does appear to condense into the particle phase between the lower stack (where in-stack measurements were made) and the point where airborne measurements were first made (a few

hundred meters behind the ship), no further organic matter condenses into the particle phase as the plume ages after the point of the first airborne measurements.

While the ratio of organic:sulfate mass remains essentially constant, the fraction of the mass spectrum represented by the peak at *m/z* 44 does increase significantly with increasing plume age, indicating an increasingly oxidized aerosol. This appears to be the result of the mixing of plume and background aerosol. As shown in Figure 8 and tabulated in Table 4, the fraction of the organic signal at *m/z* 44 is significantly higher (17%) in the background marine aerosol than it is in the freshly emitted plume (3%). The average mass loading of organic aerosol in the background air is 0.48 μg m⁻³, while closest to the ship it is 148 μg m⁻³. During the transect at a plume age of 62 min, the peak organic mass loading observed was 2.0 μg m⁻³. Accordingly, one can approximate the organic mass spectrum during this transect as a linear combination of 0.48 μg m⁻³ (24%) background aerosol and 1.52 μg m⁻³ (76%) plume aerosol. Assuming the mass spectrum of the plume aerosol remains unchanged after 62 min of aging, this simple linear combination of plume and background aerosol predicts that 6.4% of the organic signal will be present in the peak at *m/z* 44, which is close to the 8% that is observed. From this analysis, it appears that there is little change in the mass spectrum of the particulate organic during the first hour after emission. The conclusion that the increase in signal at *m/z* 44 with plume age is a result primarily of dilution lends further confidence to the hypothesis that the mass fraction and composition of particulate organics are determined soon after the exhaust is emitted from the ship.

4.3. Hygroscopic Growth. Particulate hygroscopic growth is suppressed in the ship exhaust plume relative to the background aerosol. While there is a higher fraction of organic mass inside the plume (31%) relative to the background aerosol (18%), the closure study using the volume-weighted mixing rule shows that when this organic mass is accounted for there is relatively good closure between predicted and measured growth factors outside of the exhaust plume but very poor closure within it. It is worth noting that while the closure outside the exhaust plume is reasonable, it was obtained by assuming that organics have the lowest physically realistic growth factor of unity. It is somewhat surprising that a growth factor of unity would be appropriate for the highly oxidized organics found outside of the exhaust plume, though significant mass fractions of insoluble organics and lower than predicted growth factors have been previously observed in marine aerosols in this region (52).

The fact that the simple volume-weighted mixing rule with compositional inputs from C-ToF-AMS measurements is unable to realistically represent the hygroscopic behavior of the mixture of fresh, hydrocarbon-like organic and sulfuric acid found within the plume could be explained in several ways. First and most probable, the DASH-SP may not be able to fully dry the exhaust-plume particles which contain large amounts of sulfuric acid. If the particles are not fully dried before they are humidified, then the measured growth factor will be underestimated because the particle's dry size is overestimated. A second possibility is that the organic material in the exhaust plume may be slowing uptake of water onto the particles. A simple model of the DASH-SP growth chamber, which has a particle residence time of ~ 4 s, indicates that an accommodation coefficient (α) of $\sim 10^{-4}$ (or equivalently slow mass transfer through the organic layer) is required to simulate the measured growth factors at 85 and 92% RH (an even smaller α ($\sim 10^{-5}$) is required to simulate the measured growth factor at 74% RH, but the sizing of OPC in the DASH-SP is questionable at this lower RH because of uncertainties in the refractive index).

The final possibility is that the volume fraction of organics has been incorrectly estimated. This is possible because the particles that the DASH-SP measures (150–200 nm) are at the edge of the volume/mass distribution where there is relatively poor signal-to-noise. Figure 7 clearly shows that a 200 nm mobility diameter particle is at the tail end of the volume distribution and that the corresponding C-ToF-AMS composition measurements in this region of the mass distribution are rather uncertain. It is also important to remember that the volume distribution given in Figure 7 is given at $\sim 45\%$ RH and would be shifted to smaller sizes (by $\sim 20\%$, see section 2.5) if it were dry. However, there is no obvious indication that the fraction of organics would dramatically increase at larger particle sizes and a brief sensitivity study showed that a 60% reduction in sulfate volume fraction is needed to predict the growth factors measured in the exhaust plume at 85% and 92% RH (an even further reduction of sulfate volume fraction would be needed to simulate the measurements at 74% RH). This type of reduction in sulfate seems improbable.

For completeness, it is important to note that black carbon is not detected by the C-ToF-AMS, though it is clearly present in the exhaust plume as shown by the PSAP measurements. Particles containing significant fractions of black carbon will be assigned erroneously high volume fractions of water-soluble inorganics based on C-ToF-AMS composition measurements. Despite this, the effect of black carbon is estimated to be relatively minor overall given the good agreement between C-ToF-AMS measured particle mass and DMA measured particle volume and given the low ash content in the fuel.

4.4. CCN Closure. Ship emissions are clearly a source of particles in the marine boundary layer, but because these particles typically have a smaller mean diameter and contain more organic than background marine particles, it is uncertain what fraction act as CCN under the relatively low supersaturations of marine stratocumulus clouds. The results of this study imply that, for the size distribution of particles emitted from this ship, knowledge of the size-resolved chemical composition is relatively unimportant for supersaturations below 0.3%. However, if the supersaturation is above 0.3% or if the emitted particles are slightly larger, knowledge of the size-resolved composition becomes critical for accurately predicting CCN because of the high mass fractions of hydrophobic organics, which inhibit CCN formation, observed at smaller particle sizes.

The impact of soot (black carbon) and ash particles on CCN closure was also considered. Because the C-ToF-AMS cannot detect refractory material, the presence of soot or

ash will lead to overprediction of CCN. This overprediction occurs because measurements from the C-ToF-AMS are used to assign chemical compositions to the volume distribution measured by the DMA. If present, soot and ash will be measured by the DMA and assigned an incorrect composition based on the C-ToF-AMS measurements of the nonrefractory aerosol. Because soot and ash tend to be less CCN active than mixed organic/sulfate particles, this leads to an overestimation of CCN number. Based on the PSAP measurements and the estimate based on fuel composition given in Table 3, soot and ash appear to be a relatively minor contributor to aerosol mass and their presence is not expected to be a major for the overestimation of CCN number concentration, though it may partially account for the slight overestimation of CCN calculated for this study.

5. Implications

The ship studied here, with a 2-stroke, slow-speed diesel engine, represents a very common class of vessel. Emission factors from this study and relevant literature studies of ships burning heavy fuel oil are given in Table 5. All emission factors have been normalized to be in units of $(\text{kg fuel})^{-1}$ using the carbon dioxide balance method which was also used, in slightly varying forms, in all of the previous literature cited in Table 5. This method is based on the fact that CO_2 is the principal carbon emission from combustion of HFO (while carbon is also emitted as CO, methane, nonmethane organic compounds (NMOC), and particulate mass, the mass contribution of these species is insignificant relative to CO_2). Assuming complete combustion to CO_2 and a hydrogen to carbon ratio of 1.8 for the fuel (53), 3.2 kg of CO_2 is formed per kg of fuel burned. Because CO_2 was measured in the stack, this conversion factor can be used to convert in-stack emission factors to a $(\text{kg fuel})^{-1}$ basis. Because neither CO_2 nor other gas-phase species were measured on the airborne platform, in-plume particulate measurements were scaled to in-stack CO_2 using particulate sulfate mass measurements (made on both the shipboard and airborne platforms) and assuming that perturbations in sulfate particulate mass above background atmospheric levels were caused solely by the ship exhaust. A potential source of error in this method is that the mass of particulate sulfate could change between the stack measurements and the atmosphere; however, further conversion is unlikely.

The SO_2 emission factors in Table 5 give some confidence that the heavy fuel oil being burned in these different studies was relatively similar, at least in terms of percent sulfur. The NO_x measured in the ship's stack during this study is significantly higher than any of the previous airborne measurements. While it is similar to the Petzold et al. study (11), their numbers were estimated based on fuel composition and knowledge of engine operating conditions. While the CN emission factor varies between studies, all of the data show that the number of CN with diameters above 100 nm is roughly an order of magnitude less than the number of CN with diameters smaller than this. This study represents the second time that an emission factor for CCN has been calculated. The fraction of CN (> 10 nm in diameter) that activate into CCN at 0.3% supersaturation was found to be 0.24, similar to the 0.18 found by Sinha et al. (3). Finally, the airborne organic to sulfate mass ratio from this study (which is significantly higher than the in-stack measurement) agrees well with the most recent test-bed results of Petzold et al. (11); both of these estimates are significantly higher than the previous estimate from Petzold et al. (9) which was used by Eyring et al. (1) to estimate global emissions of 0.134 Tg OC per year; these results suggest that the global annual emissions of organic carbon may be significantly higher than previously estimated.

Acknowledgments

This work was supported by the Office of Naval Research and CARB. S.M.M. and L.T.P. acknowledge support from the NASA Earth and Space Sciences Fellowship. A.N. acknowledges support from the NASA Radiation Science Program and an NSF CAREER. We gratefully acknowledge the NOAA Air Resources Laboratory (ARL) for the provision of the HYSPLIT transport and dispersion model. We are grateful to the ship crew and the shipping company, and the analytical support of Ms. Kathy Cocker, and Ms. Varalakshmi Jayaram.

Note Added after ASAP Publication

The Acknowledgments were modified in the version of this paper that published ASAP February 4, 2009; the corrected version published ASAP February 13, 2009.

Supporting Information Available

Information detailing the methods used for the in-stack measurements presented in this study is given in Section S1. Figure S1 gives a flow diagram of the sampling system used onboard the container ship. Figure S2 gives vertical profiles of relative humidity and potential temperature in and above the marine boundary layer. Figure S3 give 3-day NOAA Hysplit back trajectories for the air mass present during the study. This material is available free of charge via the Internet at <http://pubs.acs.org>.

Literature Cited

- Eyring, V.; Kohler, H. W.; van Aardenne, J.; Lauer, A. Emissions from international shipping: 1. The last 50 years. *J. Geophys. Res.* **2005**, *110*, D17305, doi: 10.1029/2004JD005619.
- Capaldo, K.; Corbett, J. J.; Kasibhatla, P.; Fischbeck, P.; Pandis, S. N. Effects of ship emissions on sulphur cycling and radiative climate forcing over the ocean. *Nature* **1999**, *400* (6746), 743–746.
- Sinha, P.; Hobbs, P. V.; Yokelson, R. J.; Christian, T. J.; Kirchstetter, T. W.; Bruintjes, R. Emissions of trace gases and particles from two ships in the southern Atlantic Ocean. *Atmos. Environ.* **2003**, *37* (15), 2139–2148.
- Corbett, J. J.; Winebrake, J. J.; Green, E. H.; Kasibhatla, P.; Eyring, V.; Lauer, A. Mortality from ship emissions: A global assessment. *Environ. Sci. Technol.* **2007**, *41*, 8512–8518.
- Lauer, A.; Eyring, V.; Hendricks, J.; Jockel, P.; Lohmann, U. Global model simulations of the impact of ocean-going ships on aerosols, clouds, and the radiation budget. *Atmos. Chem. Phys.* **2007**, *7*, 5061–5079.
- Corbett, J. J.; Koehler, H. W. Updated emissions from ocean shipping. *J. Geophys. Res.* **2003**, *108*, D20, doi: 10.1029/2003jd003751.
- Hobbs, P. V.; Garrett, T. J.; Ferek, R. J.; Strader, S. R.; Hegg, D. A.; Frick, G. M.; Hoppel, W. A.; Gasparovic, R. F.; Russell, L. M.; Johnson, D. W.; O'Dowd, C.; Durkee, P. A.; Nielsen, K. E.; Innis, G. Emissions from ships with respect to their effects on clouds. *J. Atmos. Sci.* **2000**, *57* (16), 2570–2590.
- Kasper, A.; Aufdenblatten, S.; Fors, A.; Mohr, M.; Burtscher, H. Particulate emissions from a low-speed marine diesel engine. *Aerosol Sci. Technol.* **2007**, *41* (1), 24–32.
- Petzold, A.; Feldpausch, P.; Fritzsche, L.; Minikin, A.; Lauer, A.; Bauer, H. Particle emissions from ship engines. In *Journal of Aerosol Science Supplement 2*, European Aerosol Conference: Budapest, 2004; 35, S1095–S1096.
- Williams, E.; Lerner, B.; Quinn, P.; Bates, T. Measurements of gas and particle emissions from commercial marine vessels, AGU Fall Meeting Abstracts, 2005.
- Petzold, A.; Hasselbach, J.; Lauer, P.; Baumann, R.; Franke, K.; Gurk, C.; Schlager, H.; Weingartner, E. Experimental studies on particle emissions from cruising ship, their characteristic properties, transformation and atmospheric lifetime in the marine boundary layer. *Atmos. Chem. Phys.* **2008**, *8* (9), 2387–2403.
- Agrawal, H.; Malloy, Q. G. J.; Welch, W. A.; Miller, J. W.; Cocker, D. R. In-use gaseous and particulate matter emissions from a modern ocean going container vessel. *Atmos. Environ.* **2008**, *42* (21), 5504–5510.
- Agrawal, H.; Welch, W. A.; Miller, J. W.; Cocker, D. R. Emission measurements from a crude oil tanker at sea. *Environ. Sci. Technol.* **2008**, *42* (19), 7098–7103.
- Corbett, J. J. New directions: Designing ship emissions and impacts research to inform both science and policy. *Atmos. Environ.* **2003**, *37* (33), 4719–4721.
- ISO 8178-1 Reciprocating Internal Combustion Engines - Exhaust Emission Measurement—Part 1: Test-Bed Measurement of Gaseous Particulate Exhaust Emissions, 1st ed.; International Standards Organization: Geneva, 1996; 8, 150.
- Protection of the environment. In *Code of Federal Regulations*, 40 CFR 86; U.S. Government Printing Office: Washington, DC.
- Shah, S. D.; Ogunyoku, T. A.; Miller, J. W.; Cocker, D. R. On-road emission rates of PAH and n-alkane compounds from heavy-duty diesel vehicles. *Environ. Sci. Technol.* **2004**, *39* (14), 5276–5284.
- Siegl, W. O.; Richert, J. F. O.; Jensen, T. E.; Schuetzle, D.; Swarin, S. J.; Loo, J. F.; Probst, A.; Nagy, D.; Schlenker, A. M. Improved emissions speciation methodology for phase II of the auto/oil air quality improvement research programs hydrocarbons and oxygenates. In *SAE Technical Paper 1993, Series No. 930142, Special Publication sp-1000*; Society of Automotive Engineers: Washington, DC, 1993.
- NIOSH Manual of Analytical Methods; National Institute of Occupational Safety and Health: Cincinnati, OH, 1996.
- Dekati mass monitor (DMM). <http://www.dekati.com/cms/dmm>.
- Drewnick, F.; Hings, S. S.; DeCarlo, P.; Jayne, J. T.; Gonin, M.; Fuhrer, K.; Weimer, S.; Jimenez, J. L.; Demerjian, K. L.; Borrmann, S.; Worsnop, D. R. A new time-of-flight aerosol mass spectrometer (TOF-AMS) - instrument description and first field deployment. *Aerosol Sci. Technol.* **2005**, *39*, 637–658.
- Bahreini, R.; Dunlea, E. J.; Matthew, B. M.; Simons, C.; Docherty, K. S.; DeCarlo, P. F.; Jimenez, J. L.; Brock, C. A.; Middlebrook, A. M. Design and operation of a pressure-controlled inlet for airborne sampling with an aerodynamic aerosol lens. *Aerosol Sci. Technol.* **2008**, *42* (6), 465–471.
- Huffman, J. A.; Jayne, J. T.; Drewnick, F.; Aiken, A. C.; Onasch, T.; Worsnop, D. R.; Jimenez, J. L. Design, modeling, optimization, and experimental tests of a particle beam width probe for the aerodynamic aerosol mass spectrometer. *Aerosol Sci. Technol.* **2005**, *39*, 1143–1163.
- Canagaratna, M. R.; Jayne, J. T.; Jimenez, J. L.; Allan, J. D.; Alfarra, M. R.; Zhang, Q.; Onasch, T. B.; Drewnick, F.; Coe, H.; Middlebrook, A.; Delia, A.; Williams, L. R.; Trimborn, A. M.; Northway, M. J.; DeCarlo, P. F.; Kolb, C. E.; Davidovits, P.; Worsnop, D. R. Chemical and microphysical characterization of ambient aerosols with the aerodynamic aerosol mass spectrometer. *Mass Spectrom. Rev.* **2007**, *26* (2), 185–222.
- Sorooshian, A.; Brechtel, F. J.; Ma, Y. L.; Weber, R. J.; Corless, A.; Flagan, R. C.; Seinfeld, J. H. Modeling and characterization of a particle-into-liquid sampler (PILS). *Aerosol Sci. Technol.* **2006**, *40* (6), 396–409.
- Sorooshian, A.; Chan, A. W. H.; Feingold, G.; Flagan, R. C.; Seinfeld, J. H. Particulate organic acids and overall water-soluble aerosol composition measurements from the 2006 Gulf of Mexico Atmospheric Composition and Climate Study (GoMACCS) *J. Geophys. Res.* **2007**, *112*, D13, D13201, doi: 10.1029/2007JD008537.
- Virkkula, A.; Ahlquist, N. C.; Covert, D. S.; Arnott, W. P.; Sheridan, P. J.; Quinn, P. K.; Coffman, D. J. Modification, calibration and a field test of an instrument for measuring light absorption by particles. *Aerosol Sci. Technol.* **2005**, *39* (1), 68–83.
- Sorooshian, A.; Hersey, S.; Brechtel, F. J.; Corless, A.; Flagan, R. C.; Seinfeld, J. H. Rapid, size-resolved aerosol hygroscopic growth measurements: Differential aerosol sizing and hygroscopicity spectrometer probe (DASH-SP). *Aerosol Sci. Technol.* **2008**, *42* (6), 445–464.
- Roberts, G. C.; Nenes, A. A continuous-flow streamwise thermal-gradient CCN chamber for atmospheric measurements. *Aerosol Sci. Technol.* **2005**, *39* (3), 206–221.
- Lance, S.; Medina, J.; Smith, J. N.; Nenes, A. Mapping the operation of the DMT continuous flow CCN counter. *Aerosol Sci. Technol.* **2006**, *40* (4), 242–254.
- Aklilu, Y.; Mozurkewich, M.; Prenni, A. J.; Kreidenweis, S. M.; Alfarra, M. R.; Allan, J. D.; Anlauf, K.; Brook, J.; Leaitch, W. R.; Sharma, S.; Boudries, H.; Worsnop, D. R. Hygroscopicity of particles at two rural, urban influenced sites during pacific 2001: Comparison with estimates of water uptake from particle composition. *Atmos. Environ.* **2006**, *40*, 2650–2661.
- Gysel, M.; Crosier, J.; Topping, D. O.; Whitehead, J. D.; Bower, K. N.; Cubison, M. J.; Williams, P. I.; Flynn, M. J.; McFiggans, G. B.; Coe, H. Closure study between chemical composition and hygroscopic growth of aerosol particles during TORCH2. *Atmos. Chem. Phys.* **2007**, *7* (24), 6131–6144.

- (33) Seinfeld, J. H.; Pandis, S. N., *Atmospheric Chemistry and Physics: From Air Pollution to Climate Change*, 2nd ed.; Wiley-Interscience: Hoboken, N. J., 2006.
- (34) Clegg, S. L.; Brimblecombe, P.; Wexler, A. S. Thermodynamic model of the system $\text{H}^+ - \text{NH}_4^+ - \text{Na}^+ - \text{SO}_4^{2-} - \text{NO}_3^- - \text{Cl}^- - \text{H}_2\text{O}$ at 298.15 K. *J. Phys. Chem. A* **1998**, *102* (12), 2155–2171.
- (35) Wexler, A. S.; Clegg, S. L.; Brimblecombe, P. On-line aerosol inorganics model. <http://mae.ucdavis.edu/~sclegg/aim.html>.
- (36) Medina, J.; Nenes, A.; Sotiropoulou, R. E. P.; Cottrell, L. D.; Ziemba, L. D.; Beckman, P. J.; Griffin, R. J. Cloud condensation nuclei closure during the International Consortium for Atmospheric Research on Transport and Transformation 2004 campaign: Effects of size-resolved composition. *J. Geophys. Res.* **2007**, *D10S31*, doi: 10.1029/2006jd007588.
- (37) Nenes, A.; Pandis, S. N.; Pilinis, C. Isorropia: A new thermodynamic equilibrium model for multiphase multi-component inorganic aerosols. *Aquat. Geochem.* **1998**, *41*123152, <http://nenes.eas.gatech.edu/ISORROPIA>.
- (38) Brechtel, F. J.; Kreidenweis, S. M. Predicting particle critical supersaturation from hygroscopic growth measurements in the humidified TDMA. Part I: Theory and sensitivity studies. *J. Atmos. Sci.* **2000**, *57* (12), 1854–1871.
- (39) Brechtel, F. J.; Kreidenweis, S. M. Predicting particle critical supersaturation from hygroscopic growth measurements in the humidified TDMA. Part II: Laboratory and ambient studies. *J. Atmos. Sci.* **2000**, *57* (12), 1872–1887.
- (40) Rose, D.; Gunthe, S. S.; Mikhailov, E.; Frank, G. P.; Dusek, U.; Andreae, M. O.; Poschl, U. Calibration and measurement uncertainties of a continuous-flow cloud condensation nuclei counter (DMT-CCNC): CCN activation of ammonium sulfate and sodium chloride aerosol particles in theory and experiment. *Atmos. Chem. Phys.* **2008**, *8* (5), 1153–1179.
- (41) Draxler, R. R.; Rolph, G. D. Hysplit (hybrid single-particle lagrangian integrated trajectory) model access via NOAA ARL ready website. <http://www.arl.noaa.gov/ready/hysplit4.html>.
- (42) Shah, S. D.; Cocker, D. R.; Miller, J. W.; Norbeck, J. M. Emission rates of particulate matter and elemental and organic carbon from in-use diesel engines. *Environ. Sci. Technol.* **2004**, *38* (9), 2544–2550.
- (43) DeCarlo, P. F.; Slowik, J. G.; Worsnop, D. R.; Davidovits, P.; Jimenez, J. L. Particle morphology and density characterization by combined mobility and aerodynamic diameter measurements. Part I: Theory. *Aerosol Sci. Technol.* **2004**, *38* (12), 1185–1205.
- (44) Zhang, Q.; Alfarra, M. R.; Worsnop, D. R.; Allan, J. D.; Coe, H.; Canagaratna, M. R.; Jimenez, J. L. Deconvolution and quantification of hydrocarbon-like and oxygenated organic aerosols based on aerosol mass spectrometry. *Environ. Sci. Technol.* **2005**, *39*, 4938–4952.
- (45) Kondo, Y.; Miyazaki, Y.; Takegawa, N.; Miyakawa, T.; Weber, R. J.; Jimenez, J. L.; Zhang, Q.; Worsnop, D. R. Oxygenated and water-soluble organic aerosols in Tokyo. *J. Geophys. Res.* **2007**, *112*, doi: 10.1029/2006jd007056.
- (46) Takegawa, N.; Miyakawa, T.; Kawamura, K.; Kondo, Y. Contribution of selected dicarboxylic and omega-oxocarboxylic acids in ambient aerosol to the m/z 44 signal of an Aerodyne aerosol mass spectrometer. *Aerosol Sci. Technol.* **2007**, *41*, 418–437.
- (47) Aiken, A. C.; DeCarlo, P. F.; Kroll, J. H.; Worsnop, D. R.; Huffman, J. A.; Docherty, K.; Ulbrich, I. M.; Mohr, C.; Kimmel, J. R.; Sueper, D.; Zhang, Q.; Sun, Y.; Trimborn, A.; Northway, M.; Ziemann, P. J.; Canagaratna, M. R.; Onasch, T. B.; Alfarra, R.; Prevot, A. S. H.; Dommen, J.; Duplissy, J.; Metzger, A.; Baltensperger, U.; Jimenez, J. L. O/C and OM/OC ratios of primary, secondary, and ambient organic aerosols with high resolution time-of-flight aerosol mass spectrometry. *Environ. Sci. Technol.* **2008**, *42* (12), 4478–4485.
- (48) Canagaratna, M. R.; Jayne, J. T.; Ghertner, D. A.; Herndon, S.; Shi, Q.; Jimenez, J. L.; Silva, P. J.; Williams, P.; Lanni, T.; Drewnick, F.; Demerjian, K. L.; Kolb, C. E.; Worsnop, D. R. Chase studies of particulate emissions from in-use New York City vehicles. *Aerosol Sci. Technol.* **2004**, *38* (6), 555–573.
- (49) Phinney, L.; Leaitch, W. R.; Lohmann, U.; Boudries, H.; Worsnop, D. R.; Jayne, J. T.; Toom-Sauntry, D.; Wadleigh, M.; Sharma, S.; Shantz, N. Characterization of the aerosol over the sub-arctic north east Pacific Ocean. *Deep-Sea Res. Part II* **2006**, *53* (20–22), 2410–2433.
- (50) McLafferty, F. W.; Turecek, F., *Interpretation of mass spectra*, 4th ed.; University Science Books: Sausalito, CA, 1993; p 371.
- (51) Cocker, D. R.; Shah, S. D.; Johnson, K. C.; Zhu, X. N.; Miller, J. W.; Norbeck, J. M. Development and application of a mobile laboratory for measuring emissions from diesel engines. 2. Sampling for toxics and particulate matter. *Environ. Sci. Technol.* **2004**, *38* (24), 6809–6816.
- (52) Kaku, K. C.; Hegg, D. A.; Covert, D. S.; Santarpia, J. L.; Jonsson, H.; Buzorius, G.; Collins, D. R. Organics in the northeastern Pacific and their impacts on aerosol hygroscopicity in the subsaturated and supersaturated regimes. *Atmos. Chem. Phys.* **2006**, *6*, 4101–4115.
- (53) Tuttle, K. L. Combustion-generated emissions in marine propulsion systems. In *Environmental Symposium: Ship Design and Operation in Harmony with the Environment*; Society of Naval Architects and Marine Engineers: Jersey City, NJ, 1995; pp 311–323.
- (54) Chen, G.; Huey, L. G.; Trainer, M.; Nicks, D.; Corbett, J.; Ryerson, T.; Parrish, D.; Neuman, J. A.; Nowak, J.; Tanner, D.; Holloway, J.; Brock, C.; Crawford, J.; Olson, J. R.; Sullivan, A.; Weber, R.; Schaffler, S.; Donnelly, S.; Atlas, E.; Roberts, J.; Flocke, F.; Hubler, G.; Fehsenfeld, F. An investigation of the chemistry of ship emission plumes during ITCT 2002. *J. Geophys. Res.* **2005**, *110*, D10.

ES802413J

Appendix C

On the link between ocean biota emissions, aerosol, and maritime clouds: Airborne, ground, and satellite measurements off the coast of California*

*Reproduced with permission from "On the link between ocean biota emissions, aerosol, and maritime clouds: Airborne, ground, and satellite measurements off the coast of California" by Sorooshian, A., Padro, L.T., Nenes, A., Feingold, G., McComiskey, A., Hersey S.P., Gates, H., Jonsson, H., Miller, S.D., Stephens, G.L., Flagan R.C., and Seinfeld, J.H., *Global Biogeochemical Cycles*, 23, doi:10.1029/2009GB003464, 2009. Copyright 2009 by the American Geophysical Union.



On the link between ocean biota emissions, aerosol, and maritime clouds: Airborne, ground, and satellite measurements off the coast of California

Armin Sorooshian,^{1,2,3} Luz T. Padró,⁴ Athanasios Nenes,^{4,5} Graham Feingold,² Allison McComiskey,^{2,6} Scott P. Hersey,⁷ Harmony Gates,⁷ Haflidi H. Jonsson,⁸ Steven D. Miller,¹ Graeme L. Stephens,^{1,9} Richard C. Flagan,⁷ and John H. Seinfeld⁷

Received 14 January 2009; revised 9 June 2009; accepted 24 June 2009; published 14 October 2009.

[1] Surface, airborne, and satellite measurements over the eastern Pacific Ocean off the coast of California during the period between 2005 and 2007 are used to explore the relationship between ocean chlorophyll *a*, aerosol, and marine clouds. Periods of enhanced chlorophyll *a* and wind speed are coincident with increases in particulate diethylamine and methanesulfonate concentrations. The measurements indicate that amines are a source of secondary organic aerosol in the marine atmosphere. Subsaturated aerosol hygroscopic growth measurements indicate that the organic component during periods of high chlorophyll *a* and wind speed exhibit considerable water uptake ability. Increased average cloud condensation nucleus (CCN) activity during periods of increased chlorophyll *a* levels likely results from both size distribution and aerosol composition changes. The available data over the period of measurements indicate that the cloud microphysical response, as represented by either cloud droplet number concentration or cloud droplet effective radius, is likely influenced by a combination of atmospheric dynamics and aerosol perturbations during periods of high chlorophyll *a* concentrations.

Citation: Sorooshian, A., et al. (2009), On the link between ocean biota emissions, aerosol, and maritime clouds: Airborne, ground, and satellite measurements off the coast of California, *Global Biogeochem. Cycles*, 23, GB4007, doi:10.1029/2009GB003464.

1. Introduction

[2] A physical relationship with potentially significant climatic implications that remains poorly understood is that between ocean ecology, aerosol, and clouds. Ocean biota emissions influence cloud condensation nucleus (CCN) properties, which in turn affect clouds through the following two so-called aerosol indirect effects: (1) for a fixed liquid water amount, more numerous subcloud aerosol results in more reflective clouds because of more abundant and

smaller cloud droplets [Twomey, 1977]; and (2) for more numerous and smaller cloud droplets, suppressed droplet collision-coalescence results in less precipitation and clouds with enhanced albedo [Albrecht, 1989]. Marine stratocumulus clouds exert a strong net cooling effect globally owing to their persistent coverage over oceans, their high albedo compared to relatively dark ocean surfaces, and their close proximity to the surface. Stratocumulus clouds are especially abundant in subtropical subsidence regions, such as off the coast of California, where strong inversions exist at the boundary layer top.

[3] Ocean biota emissions influence marine aerosol. Oceans are a source of particulate matter, particularly organic, via the following mechanisms: (1) primary emissions as a result of bubble bursting [Hoffman and Duce, 1976; Gershey, 1983; Blanchard, 1989; Tseng et al., 1992; Middlebrook et al., 1998; Mårtensson et al., 2003; Lewis and Schwartz, 2004; O'Dowd et al., 2004; Keene et al., 2007]; (2) secondary formation via the oxidation of emitted volatile organic compounds (VOCs) followed by condensation onto preexisting particles [O'Dowd and de Leeuw, 2007]; (3) secondary formation by the partitioning of VOCs into cloud droplets, followed by aqueous-phase reactions to produce low-volatility organics that remain in the aerosol phase after droplet evaporation [Warneck, 2003; Crahan et al., 2004; Ervens et al., 2004; Yu et al., 2005; Sorooshian et al., 2006a, 2007a, 2007b]; and

¹Cooperative Institute for Research in the Atmosphere, Colorado State University, Fort Collins, Colorado, USA.

²Earth Systems Research Laboratory, NOAA, Boulder, Colorado, USA.

³Now at Department of Chemical and Environmental Engineering, University of Arizona, Tucson, Arizona, USA.

⁴School of Chemical and Biomolecular Engineering, Georgia Institute of Technology, Atlanta, Georgia, USA.

⁵School of Earth and Atmospheric Sciences, Georgia Institute of Technology, Atlanta, Georgia, USA.

⁶Cooperative Institute for Research in Environmental Science, University of Colorado at Boulder, Boulder, Colorado, USA.

⁷Departments of Environmental Science and Engineering and Chemical Engineering, California Institute of Technology, Pasadena, California, USA.

⁸Center for Interdisciplinary Remotely-Piloted Aircraft Studies, Naval Postgraduate School, Monterey, California, USA.

⁹Department of Atmospheric Sciences, Colorado State University, Fort Collins, Colorado, USA.

(4) new particle formation [Hegg *et al.*, 1990; Covert *et al.*, 1992; Leck and Bigg, 1999; Kazil *et al.*, 2008]. Recent measurements indicate that another pathway for organic aerosol formation is through aqueous-phase processing in deliquesced particles [Liggio *et al.*, 2005; Volkamer *et al.*, 2009; Corrigan *et al.*, 2008; Hennigan *et al.*, 2008].

[4] Perhaps the most documented example of the influence of ocean biota on aerosol involves ocean-emitted dimethylsulfide (DMS) undergoing oxidation to ultimately produce sulfate [Andreae and Raemdonck, 1983; Shaw, 1983; Charlson *et al.*, 1987; Ayers and Caine, 2007, and references therein]. DMS can be emitted by phytoplankton directly, by the decomposition of dimethyl sulfoniopropionate, or by complex physiological and ecological interactions [e.g., Challenger and Simpson, 1948; Lovelock *et al.*, 1972; Andreae, 1990; Leck *et al.*, 1990]. Facchini *et al.* [2008a] have also shown that biogenic emissions are a source of amines, specifically diethylamine (DEA) and dimethylamine (DMA), in marine aerosol via a gas-to-particle conversion mechanism. Meskhidze and Nenes [2006, hereinafter referred to as MN06] proposed a secondary organic aerosol (SOA) formation mechanism via the oxidation of ocean-emitted isoprene. Recent laboratory CCN experiments have shown that 2-methyltetrols, soluble isoprene oxidation products, can increase CCN levels in pristine marine atmospheres that are limited in CCN [Ekstrom *et al.*, 2008]. However, Arnold *et al.* [2008] suggested an oceanic isoprene source is insignificant in modulating marine aerosol abundances.

[5] In addition to ocean-derived VOCs condensing onto preexisting particles, organics can partition into cloud droplets and undergo aqueous-phase oxidation to produce low-volatility organic species such as organic acids and oligomers. This is supported by similar spatial distributions between enhanced glyoxal levels and ocean chlorophyll [Fu *et al.*, 2008]; that study showed that there is a large marine source of dicarbonyls (e.g., glyoxal and methylglyoxal) missing in the GEOS-Chem global chemical transport model, which can be explained by marine biota emissions. Glyoxal, methylglyoxal, and glycolaldehyde, an aqueous-phase precursor to glyoxal [Perri *et al.*, 2008], have been shown in laboratory studies to form low-volatility particulate organics after subsequent aqueous-phase oxidation [Carlton *et al.*, 2007; Altieri *et al.*, 2008; Perri *et al.*, 2008]. The aqueous-phase oxidation process presents another route by which marine biota emissions can influence aerosol properties.

[6] The nature of primary biogenic particles remains poorly understood, owing to their diverse source mechanisms and the difficulty in their quantification [Andreae and Rosenfeld, 2008]. Numerous studies have pointed to the importance of considering organic species in the surface microlayer of the ocean surface that can be lofted to the atmosphere in addition to sea salt [Riley, 1963; Blanchard, 1964]. Primary marine aerosol have been shown to be enriched with organics, especially water-insoluble species, in the submicron size range during periods of enhanced primary productivity [O'Dowd *et al.*, 2004]. The surface-active properties of such species can substantially affect the CCN activity of marine aerosol [e.g., Facchini *et al.*, 1999].

A body of work has specifically shown that ocean waters contain insoluble organic submicrometer particles that are typically joined into chains or aggregated balls, termed "marine microcolloids" [Wells and Goldberg, 1991, 1993; Benner *et al.*, 1992; Wells, 1998; Bigg *et al.*, 2004; Leck and Bigg, 2005a]. The particles are connected by a gel-like material identified as marine exopolymer secretions (EPS) of algae and bacteria [Decho, 1990; Verdugo *et al.*, 2004]. It has been shown that a fraction of the EPS can spontaneously assemble into gels and that these molecules exhibit high surface activity and strongly resist water loss [Chin *et al.*, 1998]. It was shown in the high Arctic that the CCN concentration was not governed by oxidation products of DMS, but by the concentration in the air of the small insoluble organic particles derived from the surface layer via bubble bursting, onto which acidic gases condense [Leck and Bigg, 2005b]. They also showed that similar processes likely occur over all oceans [Leck and Bigg, 2008; Bigg and Leck, 2008]. Although the importance of surface-active organic aerosols for pristine marine clouds has been demonstrated [Lohmann and Leck, 2005], consideration should be given to the complication that the gels of airborne marine aggregates can potentially collapse as a result of ultraviolet light exposure [Orellana and Verdugo, 2003], polymer hydrolysis by bacterial ectoenzymes [Verdugo *et al.*, 2004], or acidification [Chin *et al.*, 1998].

[7] Clearly, significant uncertainty remains concerning the relative abundance of marine particulate matter (specifically organic) originating from biota emissions, the identity, transformation, and fates of those specific species, and the extent to which those species alter the physico-chemical properties of particles. Since ocean emissions have been shown to modulate aerosol properties, it is of interest to evaluate if there are concomitant changes in cloud properties.

[8] Recent work has studied the effect of phytoplankton blooms on cloud properties, via changes in CCN properties, using satellite remote sensing measurements (MN06) [Miller and Yuter, 2008; hereinafter referred to as MY08]. The methodology used in these two studies consisted of comparing cloud droplet effective radius (r_e) with levels of chlorophyll *a* (chl *a*), the photosynthetic pigment in phytoplankton. These studies showed that r_e and chl *a* can be inversely proportional at a specific location and time frame; however, the correlation between r_e and chl *a* is sensitive to the methodology used, including the location studied, the time frame, and the use of threshold chl *a* levels to distinguish between bloom and nonbloom conditions (N. Meskhidze and A. Nenes, unpublished manuscript, 2008).

[9] The goal of our study is to further investigate the relationship between chl *a*, aerosol properties, and cloud microphysics using data from three measurement platforms (ground, aircraft, and satellite). The winds associated with the California current cause upwelling as surface water flows west, allowing nutrient-rich water to upwell, which results in frequent high chl *a* conditions. We investigate ocean-aerosol-cloud interactions in the marine atmosphere adjacent to the California coast. First, the spatial and temporal variation of chl *a* levels are presented off the coast

of California. Then we evaluate whether enhanced chl *a* levels influence aerosol properties, and if so, by how much. Finally, we determine the extent to which cloud properties are affected during high chl *a* periods.

2. Experimental Methods

[10] This study is based on data from three measurement platforms (airborne, ground, satellite) off the coast of California between 2005 and 2007. The spaceborne satellite data are presented for the entire duration of 2005–2007, whereas the aircraft data are from July 2007, and the ground data are from June to September 2005. It is noted that July typically represents the month with the maximum stratocumulus coverage for this area [Warren *et al.*, 1986].

2.1. Airborne Measurements

[11] During July 2007, airborne measurements were made on board the Center for Interdisciplinary Remotely-Piloted Aircraft Studies (CIRPAS) Twin Otter as part of the Marine Stratus/Stratocumulus Experiment (MASE II). We specifically report on measurements between 12 and 31 July off the central coast of California (35.5 N, 37.0 N; 122.0 W, 123.5 W). The description of the instrument payload can be found in Table 1, and for a more detailed explanation of the instruments, the reader is referred to Hersey *et al.* [2009]. Measurements were carried out to characterize aerosol and cloud properties.

[12] Aerosol and cloud droplet size distribution data were obtained by a differential mobility analyzer (DMA) and forward scattering spectrometer probe (FSSP, PMS, Incorporated, modified by DMT, Incorporated), respectively. Submicrometer water-soluble aerosol chemical composition (i.e., inorganics, organic acids, amines) was measured by a particle-into-liquid sampler coupled to ion chromatography (PILS-IC, Brechtel Manufacturing, Incorporated) [Sorooshian *et al.*, 2006b]. A continuous flow thermal gradient cloud condensation nuclei counter (CCNc, Droplet Measurement Technologies, Incorporated) [Roberts and Nenes, 2005; Lance *et al.*, 2006] was used to quantify the number of particles that activate at supersaturations ranging from 0.1% to 0.6%. Subsaturated aerosol hygroscopicity measurements were provided by a differential aerosol sizing and hygroscopicity spectrometer probe (DASH-SP; Brechtel Manufacturing, Incorporated) [Sorooshian *et al.*, 2008b].

2.2. Ground Measurements

[13] McComiskey *et al.* [2009] detail the suite of instruments deployed at the Department of Energy Atmospheric Radiation Measurement (ARM) Mobile Facility at Pt. Reyes, California (38.10 N; 122.96 W) from mid-March through mid-September in 2005. For this study, we present data only between 27 June and 13 September. Table 1 describes the relevant instrumentation at the site. It is noted that r_e was calculated using measurements of liquid water path (LWP) and cloud optical depth (τ_d) with the following equation [Stephens, 1978]:

$$r_e = 1.5(\text{LWP}/\tau_d), \quad (1)$$

where LWP is in g m^{-2} and r_e is in μm . As shown by McComiskey *et al.* [2009], cloud drop number concentration (N_d) was derived from measurements of LWP and τ_d using the adiabatic assumption:

$$N_d = C(T, P)\tau_d^3 \text{LWP}^{-2.5}, \quad (2)$$

where $C(T, P)$ is a known function of cloud base temperature (T) and pressure (P).

[14] In situ aerosol data were obtained from the Aerosol Observation System [Sheridan *et al.*, 2001; Delene and Ogren, 2002], into which air was sampled from a 30 m tower. We use aerosol index (AI), defined as the product of aerosol light scattering and the Ångström exponent (\tilde{a}), as a CCN proxy. The Ångström exponent is related to the shape of the aerosol size distribution and is inversely related to average particle size. AI has been shown to correlate better with cloud properties and columnar aerosol concentrations as compared to aerosol optical depth [Nakajima *et al.*, 2001]. All ground-based data are interpolated to synchronize with the 20 s temporal resolution of the microwave radiometer (MWR), which is the source of the LWP measurement.

2.3. Satellite Remote Sensing Measurements

[15] Table 1 summarizes the satellite data products that were used. Measurements of chl *a* are from the Sea-viewing Wide Field-of-view Sensor (Sea-WiFS) and cloud and aerosol measurements are obtained from the Moderate Resolution Imaging Spectroradiometer (MODIS) on both the AQUA and TERRA satellites. MODIS cloud data are used only when the cloud fraction exceeded 70%. Cloud fraction and r_e data are not inversely correlated, which would have indicated bias in r_e associated with broken clouds [Marshak *et al.*, 2006].

[16] We note that chl *a* is a measurement of phytoplankton biomass and it is not necessarily a proxy for primary production [Meredith *et al.*, 2003]. However, it has been shown that chl *a* and primary production are correlated in certain regions [Meredith *et al.*, 2003; Korb and Whitehouse, 2004; Perry *et al.*, 1989], and numerous other studies have used chl *a* as a proxy for identifying periods of low and high ocean biological activity [e.g., Andreae *et al.*, 1994; O'Dowd *et al.*, 2004; Ware and Thomson, 2005; MN06; Prakash and Ramesh, 2007; MY08; Facchini *et al.*, 2008b]. Therefore, we consider chl *a* as a proxy for phytoplankton biomass and also suggest that it may also represent primary production (i.e., biota emissions), but that caution must be exercised in doing so.

[17] Since recent work by MN06 and MY08 has used MODIS and Sea-WiFS data, it is important to compare the sampling statistics and overall methodology used here as compared to those studies, as these differences may have a bearing on the conclusions (Meskhidze and Nenes, unpublished manuscript, 2008). Meskhidze and Nenes show that an accurate evaluation of the correlation between chl *a* and r_e should include all values of these parameters as opposed to assigning a threshold value for chl *a* to distinguish between bloom and nonbloom conditions. In this study, we use all data available (no thresholds) between 2005 and 2007, which coincides with locations and times

Table 1. Summary of Relevant Instrumentation From Three Measurement Platforms

Platform	Measurement Reported	Instrument
Airborne (CIRPAS Twin Otter); Time span = July 2007; Daily measurement time (UTC) = 1600–2000; Location = off the central California coast	particle concentration ($D_p > 3$ nm) cloud drop size distribution ($D_p = 2–46 \mu\text{m}$) aerosol size distribution ($D_p = 10–800$ nm) cloud liquid water content cloud condensation nucleus (CCN) concentration (supersaturation = 0.29–0.32%) subsaturation hygroscopicity ($D_{p, dry} = 200$ nm, RH = 85%) water-soluble composition ($D_p < 1 \mu\text{m}$)	condensation particle counter (model 3025, TSI, Incorporated) forward scattering spectrometer probe (FSSP, PMS, modified by DMT, Incorporated) scanning differential mobility analyzer Gerber PVM-100 probe CCN counter (DMT, Incorporated; <i>Roberts and Nenes</i> [2005] and <i>Lance et al.</i> [2006]) differential aerosol sizing and hygroscopicity probe (DASH-SP) (Brechtel Manufacturing, Incorporated; <i>Sorooshian et al.</i> [2008b]) particle-into-liquid sampler (PILS) (Brechtel Manufacturing, Incorporated; <i>Sorooshian et al.</i> [2006b]) microwave radiometer (MWR; <i>Turner et al.</i> [2007]) two-channel narrow field-of-view radiometer (2NFOV; <i>Chiu et al.</i> [2006]) 2NFOV/MWR nephelometer (model 3563, TSI, Incorporated)
Ground (ARM Facility); Time span = June–September 2005; Daily measurement time (UTC) = 1500–2400; Location = Pt. Reyes, California	cloud liquid water path cloud optical depth cloud droplet effective radius aerosol index (= total aerosol light scattering \times Angstrom exponent; scattering data are from 550 nm) cloud condensation nucleus (CCN) concentration (supersaturation = 0.55%) cloud drop number concentration chlorophyll <i>a</i> concentration cloud liquid water path, cloud droplet effective radius, aerosol optical thickness	CCN counter (DMT, Incorporated) MWR/2NFOV Sea-viewing Wide Field-of-view Sensor (SeaWiFS) level 3 AQUA/TERRA MODIS level 2 (collection 5)
Space (satellite remote sensing); Time span = 2005–2007; Daily measurement time (UTC) = 18:20–19:50 (TERRA), 20:30–22:00 (AQUA)		

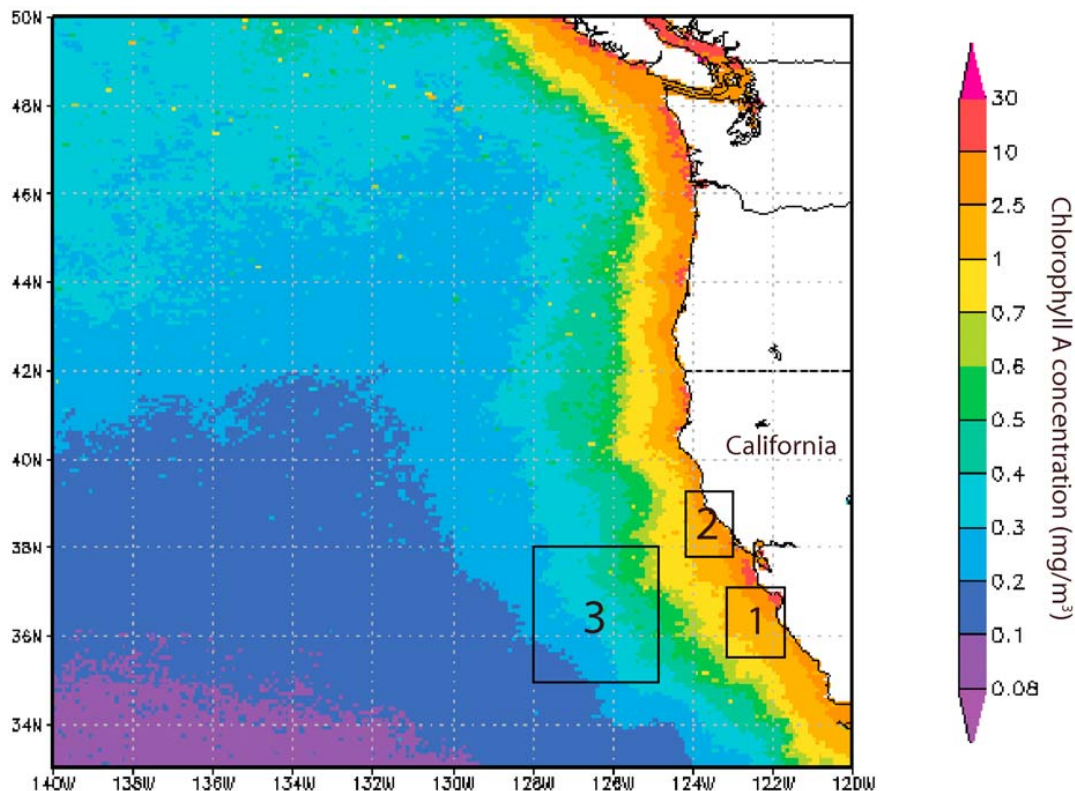


Figure 1. Average SeaWiFS chl *a* concentrations off the western United States coast between 2005 and 2007. Spatial domain 1 corresponds to the vicinity of the aircraft measurements off the central California coast, domain 2 is in the vicinity of the ground-based measurements at Pt. Reyes, and domain 3 represents a low chl *a* area farther west over the Pacific Ocean. Image courtesy of NASA's Giovanni (<http://giovanni.gsfc.nasa.gov>).

when in situ measurements are available off the coast of California. As discussed in section 3.1, we perform this analysis for three regions (Figure 1), two of which coincide with measurement sites, and one farther west over the ocean that is removed from high chl *a* areas. The area of the spatial domains was chosen to be relatively small as compared to those in MN06 and MY08 to allow a close comparison with in situ and surface measurements. Expanding the area of the spatial domains by up to a factor of four was found to have no bearing on the conclusions. The range of chl *a* levels in our regions of study are comparable to those of MN06 and MY08; however, the influence of ocean biota emissions on clouds does not scale linearly with chl *a* (Meskhidze and Nenes, unpublished manuscript, 2008).

[18] Although our choice of location for the remote sensing measurements is restricted by the availability of in situ measurements, it is still important to consider the potential influence from nonbiogenic sources (e.g., anthropogenic pollution and dust) in the region. Daily aerosol optical thickness (AOT) measurements at $0.55 \mu\text{m}$ from MODIS reveal that during the respective year of measurements in the domain of the three regions in Figure 1, average AOT levels were between 0.12 and

0.15 for 2005–2007. As a basis for comparison, globally averaged AOT over cloud-free oceans was determined by Kaufman *et al.* [2005] to be 0.14 using 2 years of MODIS data, with an anthropogenic component amounting to 0.033. They also assumed a baseline level of 0.06 ± 0.01 to represent calm marine conditions. We note that exclusion of MODIS data on the few days with the highest AOT values (0.3–0.5) does not alter the conclusions drawn from the satellite measurements.

3. Results and Discussion

[19] In order to evaluate the effect of ocean chl *a* on aerosol and cloud properties in the area of interest, all measurements during times influenced by fresh anthropogenic pollution have been removed from this analysis; these instances have been identified using back-trajectory data from the NOAA HYSPLIT model (R. R. Draxler and G. D. Rolph, Hybrid Single-Particle Lagrangian Integrated Trajectory (HYSPLIT) model, 2003, accessed via NOAA ARL READY Web site, <http://www.arl.noaa.gov/ready/hysplit4.html>, NOAA Air Resources Laboratory, Silver Spring, Maryland) and particle concentration data during

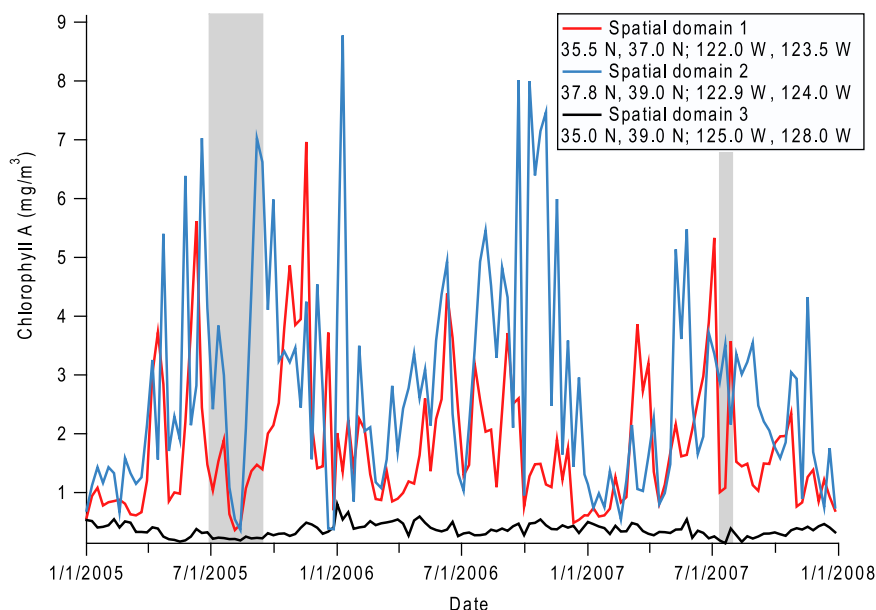


Figure 2. Time series of chl *a* concentration in the three spatial domains shown in Figure 1: (1) within the aircraft measurement spatial domain; (2) near the ground measurements by Pt. Reyes; and (3) in a low chl *a* area farther west over the Pacific Ocean. The shaded areas represent the periods when field measurements were carried out (domain 1, July 2007; domain 2, June–September 2005).

the duration of the field measurements. Our screening procedure to remove dirty air masses from the analysis of the aircraft data resulted in noticeable differences in composition and hygroscopicity [see *Hersey et al.*, 2009]. For example, hygroscopicity was significantly suppressed in dirty air masses and sulfate levels in dirty and clear air masses were $\geq 2 \mu\text{g}/\text{m}^3$ and $\leq 1 \mu\text{g}/\text{m}^3$, respectively. Approximately 10% and 34% of the data are removed for the period of the aircraft campaign (July 2007) and the overall study period (2005–2007), respectively. It is noted, however, that the background marine aerosol composition is still influenced by aged ship emissions in the form of sulfate and organics [e.g., *Capaldo et al.*, 1999]. Our goal is to assess the effects of marine biota emissions on aerosol and clouds on top of the baseline aerosol conditions for the region. All measurements are also removed when there was evidence of a decoupled marine boundary layer, which was identified using vertical profiles of meteorological and particle concentration data. Conditions such as these would not favor an interaction of boundary layer aerosol and clouds, and would therefore obfuscate the analysis.

3.1. Temporal and Spatial Variation in chl *a*

[20] Figure 1 displays the average chl *a* levels between 2005 and 2007 off the U.S. west coast. Labeled boxes correspond to the three spatial domains in which MODIS data are evaluated: (1) aircraft measurement region; (2) surface-based measurement region; and a (3) low chl *a* area farther off the coast. Figure 2 shows chl *a* levels between 2005 and 2007 for these three regions. Significantly higher

chl *a* conditions exist adjacent to the California coast each year as compared to farther west off the coast. In addition, the chl *a* levels show significant variation during the time periods of the two field measurement programs, which allows us to examine the variation of aerosol and cloud measurements as a function of chl *a*.

[21] Aircraft data from July 2007 are divided into three week-long periods in Table 2 that are synchronized with Sea-WiFS measurements. We examine 3-day back-trajectories for the sampled air masses from each flight with respective chl *a* concentrations in those source regions to evaluate the level of aerosol exposure to potential ocean biota emissions prior to sampling. Marine boundary layer aerosol typically have a residence time of a few days prior to their removal primarily by wet deposition. Sampled air from the first week originated farther west over the Pacific Ocean. The second period consisted of air masses that usually originated farther west over the ocean, but with some air masses transported southward along the coast toward the end of that week. Air masses sampled during the final week were transported southward along the coast. Figure 3 shows typical back trajectories for the two scenarios. Chl *a* levels for the region farther west over the ocean were significantly lower and more stable ($0.24 \pm 0.05 \text{ mg}/\text{m}^3$; 32.0 N, 40.0 N; 122.0 W, 140.0 W) than those in the domain of the aircraft measurements (35.5 N, 37.0 N; 121.5 W, 123.5 W) and farther up the coast (35.0 N, 50.0 N; 121.5 W, 127.0 W). Chl *a* concentrations increased each successive week during the time of the aircraft study in the two latter regions (aircraft measurement domain: 1.01, 1.08, 3.58 mg/m^3 ; up the coast: 1.38, 1.69, 2.24 mg/m^3). The wind speed in the aircraft

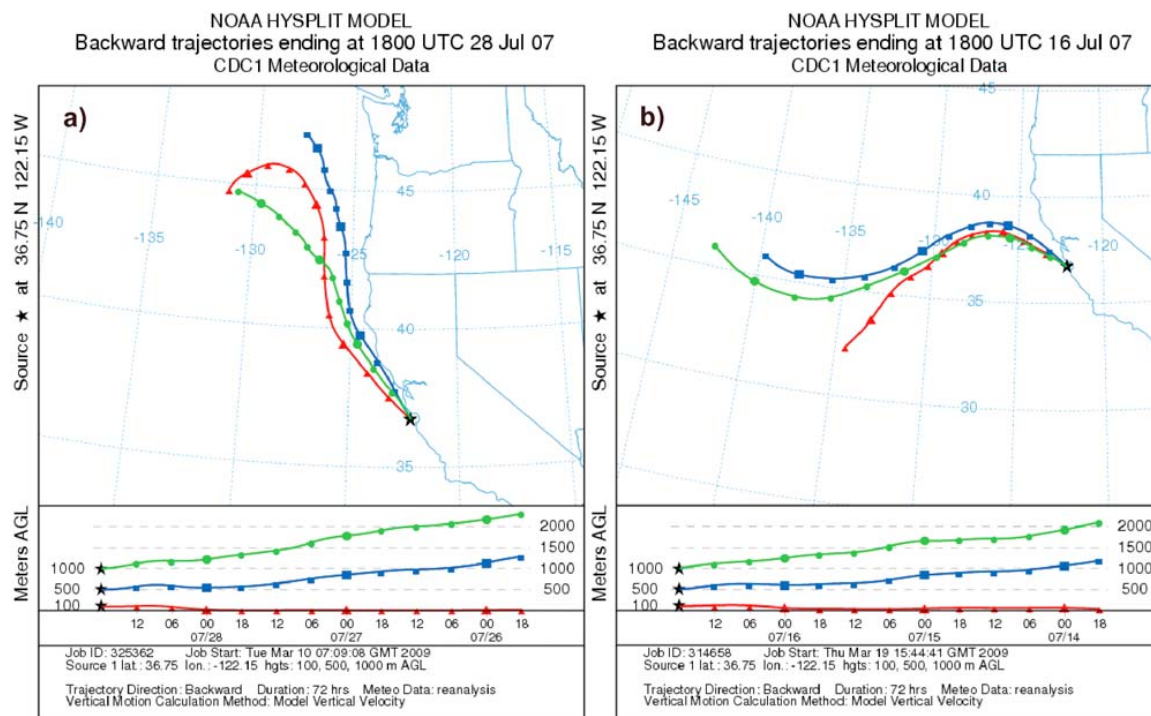


Figure 3. Typical back-trajectories for air masses originating in (a) more chl *a* enriched areas farther north as compared to those that originate (b) farther west over the ocean where there are significantly lower chl *a* levels. The back-trajectory analysis is for altitudes up to 1 km, and the airborne measurements were usually performed below 500 m during the MASE II field study. Produced with HYSPLIT from the NOAA ARL Web site (<http://www.arl.noaa.gov/ready/>).

measurement domain was also highest during the third week, which is consistent with the lowest average sea-surface temperature, indicative of enhanced upwelling. Wind speed (<http://www.ndbc.noaa.gov/>) and upwelling index (<http://www.pfeg.noaa.gov/>), a measure of upwelling strength, were moderately correlated during these three periods ($r^2 = 0.40$); the correlation was similar ($r^2 = 0.42$) during the duration of the Pt. Reyes measurements in the summer of 2005. The data indicate that the air masses probed during the third period of aircraft flights experienced the most exposure to high chl *a* areas, followed in order by the second and first periods.

3.2. Ocean-Derived Biogenic Markers in Marine Aerosol

[22] Aircraft measurements are used to investigate the relationship between ocean emissions and aerosol composition. The average concentrations of methanesulfonate (MSA), an oxidation product of DMS, and diethylamine (DEA) increase as a function of chl *a*, with a significant increase (more than a factor of two) simultaneous with the significant enhancement in chl *a* during the final time period in Table 2. The higher wind speed during the final period may have also resulted in peak concentrations of these species, especially MSA, since DMS levels have been

associated with increased wind speed [e.g., *Andreae et al.*, 1994]. But we note that owing to the relatively long residence time of atmospheric aerosol, local DMS emissions are not necessarily correlated with particulate MSA. DEA and MSA are also not necessarily expected to exhibit a similar temporal trend during periods of high biological activity since MSA production is strongly associated with photochemical activity unlike amines [*Facchini et al.*, 2008a]. Although it has been shown that in specific regions and plankton ecological regimes (chl *a* < 0.25 mg/m³) that DMS concentrations in water exhibit the same trend as chl *a* [*Andreae*, 1985; *Andreae et al.*, 1994], enhanced MSA levels are not expected to be a result of high chl *a* since diatoms (poor DMS emitters) are predominant in upwelling regions. The large standard deviations in MSA concentration on a weekly basis are possibly linked to complex physical and biological interactions that govern the production and breakdown of DMS in water.

[23] Figure 4 shows that MSA and diethylamine are moderately correlated ($r^2 = 0.41$), and when detected simultaneously, MSA was on average 7.1 times more abundant. Both DEA and MSA exhibit their highest concentrations at altitudes less than 100 m over the ocean surface and then decay with increasing altitude in the boundary layer (Figure 4). These two species did not exhibit

Table 2. Aircraft Measurements Over a 3-Week Period During July 2007 off the Central Coast of California^a

Date	Chlorophyll <i>a</i> (ng/m ³)	DEA (ng/m ³)	MSA (ng/m ³)	Organic Acids (ng/m ³)	Sulfate (ng/m ³)	Particle Concentration (number/cm ³)	Size Distribution Modes (nm)	CCN (0.29–0.32%) (number/cm ³)	Growth Factor (RH = 85%)	<i>N_d</i> (number/cm ³)	LWC (g/m ³)	Cloud Depth (m)	σ_v^2	Wind Speed (m/s)
12–19 July	1.01	14 [2]	24 [18]	62 [106]	783 [594]	307 [239]	36 [28], 98 [54]	73 [27]	NA	104 [56]	0.15 [0.07]	205 [35]	0.06 [0.08]	7.3 [1.1]
20–27 July	1.08	17 [5]	27 [22]	46 [55]	533 [358]	275 [230]	47 [4], 166 [16]	116 [73]	1.52 [0.12]	99 [28]	0.15 [0.07]	214 [70]	0.08 [0.07]	9.9 [2.1]
28 July to 4 August	3.58	35 [13]	56 [49]	68 [123]	641 [409]	301 [92]	45 [5], 134 [25]	137 [79]	1.67 [0.05]	130 [47]	0.20 [0.08]	358 [60]	0.16 [0.14]	12.6 [1.5]

^aValues in brackets represent standard deviations. (DEA, diethylamine; MSA, methanesulfonate; SST, sea-surface temperature; *N_d*, cloud droplet number concentration; σ_v^2 , turbulent kinetic energy).

an increase in concentration in polluted air masses, specifically downwind of ships. These results are consistent with those of *Facchini et al.* [2008a] who showed that DEA and MSA are both enhanced in cleaner air masses. Since they measured significantly higher DEA concentrations during a period of high biological activity, this strongly suggests that the third week of our aircraft study was characterized by a higher amount of biota emissions, which is coincident with higher chl *a* levels and enhanced wind speeds. *Facchini et al.* [2008a] concluded that similar to ammonia and other reduced gases like DMS, that DEA may be a microbial turnover end product of labile organic matter [*Gibb et al.*, 1999; *Johnson et al.*, 2007].

[24] Sulfate, ammonium, and organic acids (defined here as the sum of carboxylic acids with C₁–C₉) do not exhibit a noticeable trend with chl *a* (Table 2). Although sulfate is an oxidation product of MSA, the two species are not highly correlated owing to background concentrations of sulfate likely from aged anthropogenic emissions. Organic acids, especially oxalate, tend to be more abundant in and above clouds, as compared to below clouds, because of a cloud processing mechanism, especially in the same sampling location as the current study [*Crahan et al.*, 2004; *Sorooshian et al.*, 2007a]. DEA likely condenses onto preexisting particles partly because the average subcloud particle number concentration was similar during the three time periods (275–307 cm⁻³). These data are consistent with the conclusions drawn by *Facchini et al.* [2008a], who proposed that a gas-to-particle conversion process rather than a bubble bursting mechanism results in amine species partitioning to the aerosol phase. This latter hypothesis is supported by measurements of gaseous amines in the marine atmosphere [*Vanneste et al.*, 1987]. Amines have been shown to form amine salts by acid-base chemistry with either sulfuric or nitric acid, and then condense onto existing particle surfaces [*Murphy et al.*, 2007; *Sorooshian et al.*, 2008a]. As sulfate usually exceeds nitrate by more than an order of magnitude in this region, sulfuric acid is likely the acid reacting with the amine base.

[25] At the peak of the chl *a* levels in July 2007, the cumulative mass concentration of MSA and DEA was approximately 14% that of sulfate. DEA and MSA were the only ocean biota tracers speciated in this study, but this does not preclude the possibility that other ocean-derived particulate components were present; these other species, potentially including primary biogenic emitted species, are hypothesized to have lower water solubility since they could not be speciated using the PILS-IC technique. *O'Dowd et al.* [2004] showed that during bloom periods in North Atlantic waters, the organic fraction contributes ~63% to the submicrometer aerosol mass (~45% is water-insoluble and ~18% is water-soluble). They also showed that the organic fraction of the aerosol decreases to ~15% during periods of low ocean biological activity. Extrapolating their results to our study suggests that MSA and DEA constitute a minor proportion of the ocean-derived organic component and generally represent a conservative estimate of the effect of ocean biota emissions on marine aerosol composition and

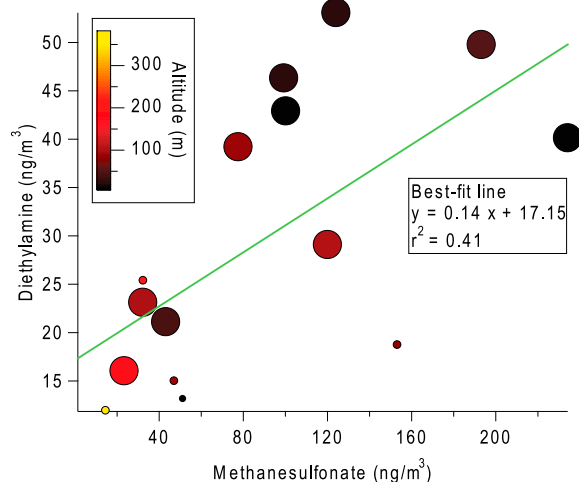


Figure 4. Relationship between particulate diethylamine (DEA) and methanesulfonate (MSA) in the marine boundary layer off the central California coast. Marker sizes are proportional to chl *a* concentration (range = 1.01–3.58 mg m⁻³). The highest concentrations of DEA and MSA exist at lower altitudes near the ocean surface and are coincident with higher chl *a* concentrations.

other associated properties (e.g., aerosol size distribution, CCN activity).

3.3. Does the Modified Composition Influence Aerosol Hygroscopicity?

[26] We examine aerosol hygroscopic subsaturated growth factors ($GF = D_{p,wet}/D_{p,dry}$, where $D_{p,dry} = 0.2 \mu\text{m}$) to determine whether a modification of aerosol composition due to ocean emissions influences water uptake. The selected dry particle diameter of $0.2 \mu\text{m}$ lies within the size range ($0.125\text{--}0.25 \mu\text{m}$) identified in a separate study in the Northern Atlantic where MSA and DEA reached significant mass concentrations [Facchini *et al.*, 2008a]. Table 2 shows an enhancement, from 1.52 ± 0.12 to 1.67 ± 0.05 , in the below-cloud growth factors at $\text{RH}_{\text{wet}} = 85\%$ ($\text{RH}_{\text{dry}} < 8\%$) for the last two time periods (no data are available from the first period). These growth factors and respective standard deviations are comparable to other measurements in the vicinity of clouds in the same geographic area [Hersey *et al.*, 2009]. It is noted that the growth factors ($\text{RH}_{\text{wet}} = 85\%$) for pure ammonium bisulfate and sulfuric acid, which were the two predominant forms of sulfate during these flights, are ~ 1.62 and ~ 1.91 , respectively [Brechtel and Kreidenweis, 2000]. Little variation existed between the second and third periods for the subcloud ammonium-to-sulfate molar ratios (0.70 ± 0.56 to 0.64 ± 0.45).

[27] Using the hygroscopic closure method of Hersey *et al.* [2009] for MASE II measurements provides an estimate of the organic fraction growth factor needed to achieve perfect closure between the composition and

growth factor measurements, assuming additive and independent water uptake by the individual aerosol components. Since the hygroscopic growth factors of organic acids, a class of organics with relatively high water solubility, are considerably less than those of ammonium bisulfate and sulfuric acid at $\text{RH} = 85\%$ [Saxena *et al.*, 1995; Hansson *et al.*, 1998; Li *et al.*, 1998; Ansari and Pandis, 2000; Cruz and Pandis, 2000; Peng *et al.*, 2001; Prenni *et al.*, 2001, 2003; Wise *et al.*, 2003; Sorooshian *et al.*, 2008b], it is expected that any addition of organic matter to acidic sulfate particles should suppress the overall hygroscopicity. For the second and third periods the calculated organic growth factors are 1.45 ± 0.37 and 1.35 ± 0.22 , respectively, which represent relatively high values for organics. Although the overall growth factor increased during the third period, the predicted organic growth factor decreased owing to a reduced organic volume fraction. An enhanced inorganic volume fraction relative to organics during the third period can potentially be explained by MSA producing hygroscopic sulfate components in the aerosol. The results indicate that the organic component of the marine aerosol during periods of high chl *a*, which contains a mixture of organics from ocean emissions and likely aged anthropogenic pollution (i.e., aged ship emissions), exhibits significant hygroscopicity.

3.4. Do Ocean Biota Emissions Enhance CCN Concentrations?

[28] The average CCN concentration at $\sim 0.3\%$ supersaturation tended to increase each successive weeklong period, during which time the average total submicrometer particle number concentration did not change significantly (Table 2). The activated fraction of aerosol (ratio of CCN to total particle concentration) increased each successive period as well (0.24, 0.42, 0.46). Although the average CCN values exhibit an increasing trend as a function of chl *a*, we note that caution must be applied before extrapolating the results of this section owing to the considerable variability in the CCN measurement during the individual weeks. To evaluate the extent to which ocean emissions influence CCN activity, it is necessary to decouple effects associated with aerosol composition and size distribution. The subcloud dry aerosol size distributions exhibited variability on different days. A mode diameter usually existed between 20 and 50 nm and also between 80 and 170 nm (Table 2), the latter being more important with regard to droplet activation. Since the levels of measured biogenic aerosol markers were similar during the first two periods in the vicinity of the aircraft measurements, the increase in CCN concentration during the second week was likely due to size distribution effects. The larger subcloud mode size is significantly larger during the second week ($166 \pm 16 \text{ nm}$ versus $98 \pm 54 \text{ nm}$).

[29] Since the size of the larger mode decreased from the second to third period, the increase in CCN activity during the third period is likely due to chemical effects. This is consistent with the enhancement in the subsaturated hygroscopic growth factor during the third period, which is coincident with higher DEA and MSA levels. Organics originating from ocean emissions can partition to the aerosol phase and influence CCN activity by adding solute

Table 3. Correlation Between chl *a* and Cloud Droplet Effective Radius for Various LWP Bins^a

Time Duration	Spatial Domain	Measurement Platform	LWP Bins (g/m ²)			
			50–75	75–100	100–125	125–150
2005–2007	1 in Figure 1 (aircraft domain)	AQUA	−0.04 (64)	0.01 (104)	−0.21 (87)	−0.08 (85)
		TERRA	−0.12 (139)	−0.14 (165)	−0.13 (129)	−0.11 (71)
	2 in Figure 1 (ground site domain)	AQUA	0.11 (38)	0.1 (86)	−0.17 (101)	0.04 (78)
		TERRA	−0.25 (120)	−0.13 (157)	−0.24 (143)	−0.29 (62)
	3 in Figure 1 (low chl <i>a</i> area)	AQUA	0.25 (41)	0.05 (135)	0.2 (138)	0.27 (93)
		TERRA	0.23 (140)	0.16 (242)	0.12 (205)	0.01 (101)
2005	ground site	surface	0.06 (19)	0.04 (22)	0.29 (21)	−0.08 (22)
2005	ground site	surface (chl <i>a</i> versus N_d)	−0.11 (19)	−0.19 (22)	−0.37 (21)	−0.12 (22)

^aNumber of data points for each correlation (*r*) calculation are shown in parentheses. Note: The bottom row shows the correlation between chl *a* and cloud droplet number concentration (N_d). LWP, liquid water path.

and suppressing surface tension; these effects of organics on CCN activity have been discussed in previous work [Shulman *et al.*, 1996; Li *et al.*, 1998; Facchini *et al.*, 1999; Nenes *et al.*, 2002; Cavalli *et al.*, 2004]. It has been shown that surface tension decreases as a function of water-soluble organic carbon during bloom periods in the North Atlantic [Cavalli *et al.*, 2004]; these authors attributed the surface tension depression to organic species with both polar groups and aliphatic chains. Furthermore, the surface layer of seawater is enriched with surface-active organic matter, including previously mentioned microcolloids, fatty acids, humic substances, alcohols, and lipidic and proteinaceous material that have the potential to alter the surface tension behavior of particles [Lion and Leckie, 1981; Gershey, 1983; Wells and Goldberg, 1991, 1993; Benner *et al.*, 1992, 1997; Chin *et al.*, 1998; Mochida *et al.*, 2002; Bigg *et al.*, 2004; Cavalli *et al.*, 2004; Verdugo *et al.*, 2004; Bigg, 2007; Leck and Bigg, 2005a, 2005b, 2008].

3.5. Are CCN and Cloud Droplet Number Concentrations Correlated?

[30] To evaluate the extent to which a link exists between ocean emissions and cloud properties via a modulation in CCN properties, we examine cloud droplet number concentrations (N_d) while simultaneously considering dynamical effects (Table 2). N_d increased during the third period ($130 \pm 47 \text{ cm}^{-3}$) as compared to the previous two ($104 \pm 56 \text{ cm}^{-3}$ and $99 \pm 28 \text{ cm}^{-3}$). Thus, the average N_d exhibited a noticeable enhancement coincident with the enhanced chl *a* levels during the third period. The third period was, however, also characterized by an overall increase in cloud liquid water content (LWC), cloud depth, wind speed, and turbulent kinetic energy (TKE), as represented by the square of the standard deviation of the cloud base updraft velocity (σ_w^2); the values of these dynamical parameters were similar the first two periods (except wind speed), during which time the average N_d did not change considerably. To evaluate aerosol effects on N_d simultaneously with dynamic effects, we compare concentrations of CCN and N_d for all three periods. Average CCN levels increase each successive time period, while the average N_d increases only in the final week when cloud turbulence was higher. When isolating events with a relatively small range in CCN ($80\text{--}87 \text{ cm}^{-3}$), the correlation between TKE and N_d was $r^2 = 0.95$ ($n = 3$), while the correlation between CCN and N_d for events with a small range in TKE ($0.03\text{--}0.06$) was only $r^2 = 0.41$ ($n = 3$). These results suggest that although enhanced chl *a*, and

presumably enhanced biota emissions, altered aerosol composition (i.e., enhanced DEA) and CCN concentrations, atmospheric dynamics were likely more important in influencing N_d . However, the relative contribution of aerosol effects during periods of enhanced chl *a* and dynamical effects on cloud microphysics is uncertain, especially owing to the large variabilities and limited measurements. These uncertainties motivate the subsequent investigation into the effect of chl *a* on cloud microphysics using remote sensing measurements.

3.6. Do Enhanced Ocean Biota Emissions Affect Cloud Droplet Effective Radius?

[31] Remote sensing measurements of r_e from MODIS within the domain of the aircraft measurements, the surface-based measurements (discussed in detail in section 3.7), and a low chl *a* area are evaluated. In order to isolate effects of an aerosol perturbation on clouds, the r_e data are stratified into LWP bins in accord with Twomey's [1977] approach. Data are only used for LWP between $50\text{--}150 \text{ g/m}^2$ to avoid measurements of thin or broken clouds ($<50 \text{ g/m}^2$) and precipitating clouds ($>150 \text{ g/m}^2$). Since there were relatively few MODIS measurements in each LWP bin during the duration of the field measurements, cumulative data from 2005 to 2007 are used.

[32] Table 3 shows that although the correlation between chl *a* and r_e was typically weak, it was usually negative in the high chl *a* regions and positive in the low chl *a* area. The largest negative correlation was $r = -0.29$ ($n = 62$; LWP = $125\text{--}150 \text{ g/m}^2$) in the vicinity of the surface-based measurements. Further stratification of the r_e data at each LWP bin into additional bins of cloud top pressure does not result in a significant change in the overall correlations. Because the correlation between chl *a* and r_e is usually negative in the high chl *a* regions (although weak), the data do not preclude the possibility that ocean emissions can lead to enhanced N_d and reduced r_e .

3.7. Surface-Based Measurements From Pt. Reyes, California

[33] Finally, we examine the relationship between chl *a*, aerosol, and clouds at the surface-based site at Pt. Reyes. Owing to the closer proximity to clouds, surface-based remote sensing measurements are not prone to some of the measurement challenges of spaceborne data. In addition, the ground site is adjacent to the coastline, which provides a

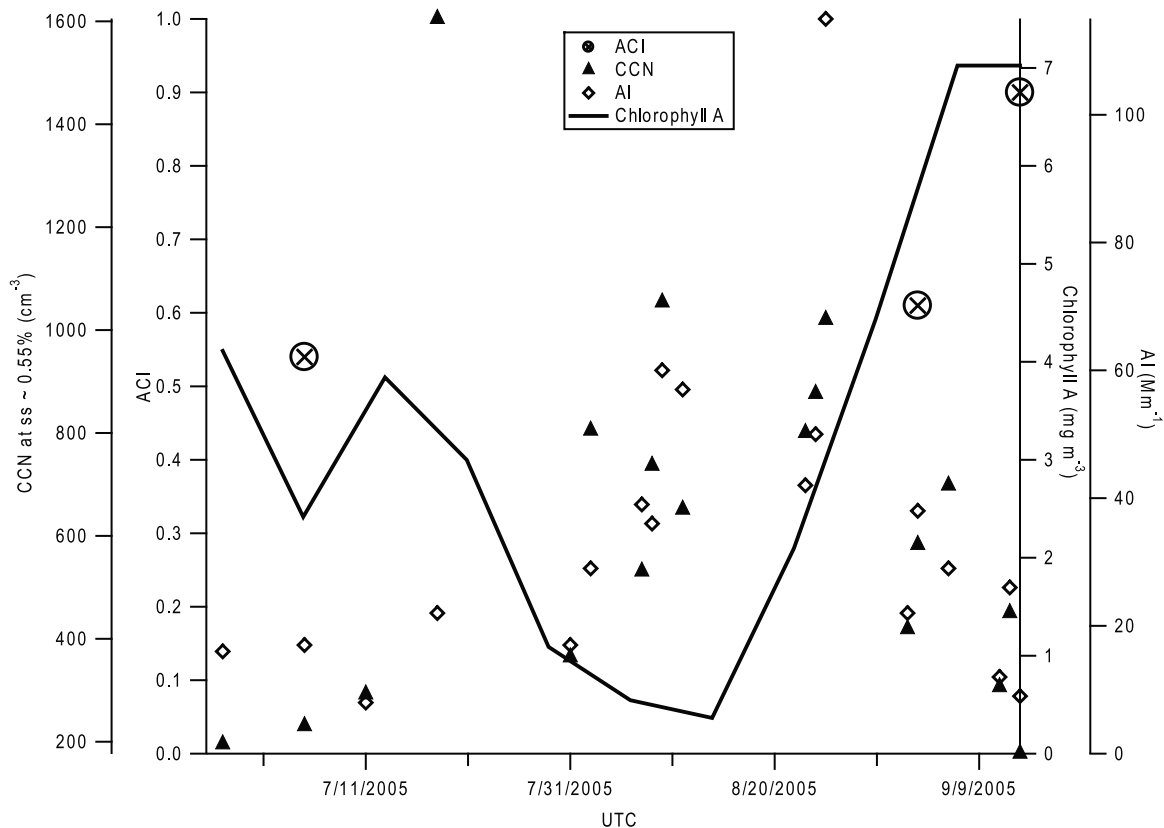


Figure 5. Temporal evolution of surface-based measurements of aerosol-cloud interactions (ACI) (equation (3)), cloud condensation nucleus (CCN) concentration, aerosol index (AI), and chl *a* concentration at Pt. Reyes, California.

different positional perspective compared to airborne measurements performed above the ocean.

[34] In the analysis below, we evaluate how a quantity representing aerosol-cloud interactions varied as a function of time during the period of surface measurements. Using the methodology of *McComiskey et al.* [2009], we quantify aerosol-cloud interactions (ACI) here as

$$\text{ACI} = \frac{d \ln N_d}{d \ln \alpha} (0 < \text{ACI} < 1) \quad (3)$$

[*Feingold et al.*, 2001], where α is an observed proxy for aerosol abundance ($\alpha = \text{CCN}$ in our case). An ACI value of unity indicates that all particles activate into droplets. It has been shown that ACI values are sensitive to variability in various aerosol properties (e.g., concentration, size distribution, chemistry) [*Facchini et al.*, 1999; *Feingold et al.*, 2001; *Nenes et al.*, 2002; *Lance et al.*, 2004; *Dusek et al.*, 2006] and cloud dynamics [*Leitch et al.*, 1996; *Feingold et al.*, 2003; *Kim et al.*, 2008]. With regard to aerosol properties, numerous studies have shown that droplet activation is more sensitive to size distribution rather than composition [*Fitzgerald*, 1974; *Feingold*, 2003; *Ervens et al.*, 2005; *Dusek et al.*, 2006].

[35] Figure 5 displays the temporal evolution of the ACI measurements, other daily averaged aerosol parameters (CCN and AI), and chl *a*. Chl *a* levels ranged between 0.36 and 7.02 mg/m³, consistent with the range measured during the aircraft measurements in July 2007. Chl *a* shows a weak correlation with both CCN concentration ($r^2 = 0.02$) and AI ($r^2 = 0.07$) during the period of the ground measurements. The lack of correlation with AI is consistent with the aircraft measurements, which show that particle concentrations exhibited no significant relationship with chl *a*. The lack of a correlation between chl *a* and CCN concentrations suggests that for the aerosol transported to the ground site, a sufficient change in composition and size distribution did not occur as a function of nearby chl *a* variations to influence the water uptake properties. These results are in contrast to the aircraft measurements, and this may be attributed to how the measurements were performed (airborne over water versus on the ground adjacent to the coastline). It is possible that there was more continental influence near the ground-based site and that volatilization and chemical transformation may have altered the composition and size distribution of air parcels by the time they reached the ground site. The latter hypothesis is supported by the aircraft measurements that showed DEA decaying

rapidly in concentration with increasing altitude above the ocean surface.

[36] The average ACI value for aggregate Pt. Reyes data was found to be 0.48 ($n = 20,996$; $r^2 = 0.14$) [McComiskey *et al.*, 2009]. LWP and ACI were found to be inversely related for $LWP < 150 \text{ g/m}^2$, likely because enhanced droplet collision-coalescence (i.e., reduction in N_d) at higher LWP obscures ACI values associated with droplet activation. For $LWP > 150 \text{ g/m}^2$, ACI was highly variable and sometimes negative owing to the small range of α , presumably resulting from wet scavenging. ACI measurements are reported for only 3 days in this study because of the difficulty in achieving sufficient variability in aerosol abundance on other days to provide a robust calculation of ACI. For this reason, it is significantly more difficult to determine ACI values from satellite and aircraft measurements [McComiskey *et al.*, 2009]. The three ACI values as follows: 0.54 ($n = 1286$, $r^2 = 0.24$, $LWP = 80 \pm 17 \text{ g/m}^2$), 0.61 ($n = 423$, $r^2 = 0.22$, $LWP = 130 \pm 27 \text{ g/m}^2$), and 0.90 ($n = 657$, $r^2 = 0.54$, $LWP = 195 \pm 45 \text{ g/m}^2$). ACI is positively correlated with LWP ($r^2 = 0.93$), and the highest ACI value was coincident with the time period exhibiting the highest chl a concentration ($\sim 7 \text{ mg/m}^3$). Because the ACI analysis is based only on three data points, it is not possible to deduce any general causal links between ACI and ocean emissions with strong confidence, especially since no relationship was observed between chl a and CCN activity.

[37] The correlation between chl a and ground-based measurements of r_e ranges from $r = -0.08$ to $r = 0.29$, and there is less statistical significance for these correlations as compared to the MODIS analysis. The correlation between N_d and chl a was negative for all LWP bins examined ($r = -0.11$ – -0.37). These data are in contrast to the MODIS data and do not provide conclusive evidence of the influence of ocean biota emissions on cloud microphysics, a result that may be at least partly due to a limited data set. The Pt. Reyes measurements however provide a valuable snapshot of how a fixed measurement platform can be used to explore the ocean-aerosol-cloud relationship.

4. Conclusions

[38] Airborne, ground, and satellite measurements have been used to evaluate the relationship between ocean chl a , aerosol, and clouds off the coast of California. A step-by-step analysis has been carried out to address the following: (1) Did enhanced phytoplankton biomass, as identified by chl a concentrations, occur during the time frame of the airborne and ground field measurements?; (2) Do increases in chl a affect aerosol properties (composition, size distribution, hygroscopicity, CCN activity)?; and (3) When holding dynamical parameters constant (e.g., LWP), do modulations in aerosol properties from increased chl a levels influence cloud microphysics?

[39] Chl a data between 2005 and 2007 along the California coast exhibit significant fluctuations and periods of enhanced phytoplankton biomass, and potentially other ecological and physical interactions resulting in marine biota emissions. Furthermore, chl a levels in a spatial domain farther west off the California coast exhibited much

lower concentrations (\sim an order of magnitude), thereby providing a control area. Aircraft measurements provide evidence that increased chl a levels influence aerosol composition. Enhanced chl a levels and wind speeds are coincident with higher particulate concentrations of DEA and MSA, the abundances of which were typically an order of magnitude less than that of sulfate. DEA is likely produced via the reaction of the gaseous amine and acidic sulfates. Subsaturation aerosol hygroscopicity data indicate that the ocean-emitted organics are sufficiently hygroscopic that they do not significantly suppress the overall growth factor of the multicomponent marine aerosol. Average CCN concentrations increased as a function of chl a while total particle concentrations were relatively stable; it is argued that both chemical and size distribution effects led to enhanced CCN levels as a function of chl a . The increase in CCN did not, however, translate to enhanced N_d . The data show that dynamic factors, such as turbulent kinetic energy (σ_w), may be more important in governing N_d . But there are considerable variations and a limited number of CCN and N_d measurements and we cannot confidently quantify the relative contributions of dynamic and aerosol effects on cloud microphysical properties.

[40] Measurements from a coastline ground site at Pt. Reyes exhibit a weak correlation between chl a and several properties including CCN concentration, AI, N_d , and r_e . Cloud r_e data, stratified by LWP, from MODIS on the AQUA and TERRA satellites were compared to chl a levels in the vicinity of the field measurements and a lower chl a area farther west. Although relatively weak, the correlation between chl a and r_e was usually negative in the high chl a areas and positive in the low chl a areas. An inverse relationship at constant LWP suggests that ocean biota activity results in more numerous and smaller cloud drops.

[41] This work shows that cloud microphysical properties off the coast of California may be influenced by both dynamical factors (e.g., turbulence) and the modification of aerosol properties during periods of increased chl a and presumably greater biota emissions. The multiplatform data set presented here does not provide overwhelming evidence for a causal link between ocean biota emissions and cloud microphysics owing to limited data, conflicting results between the ground-based and satellite remote sensing measurements for the relationship between chl a and r_e , and the relatively large variability observed during the period of the aircraft measurements for key parameters such as CCN and N_d . However, the results show that there is a clear link between ocean phytoplankton biomass and aerosol properties, including the presence of particulate DEA, and that the intriguing relationships between ocean emissions, aerosol, and clouds need to be further explored. In addition, future work should investigate the role of primary biogenic emissions such as marine microcolloids [e.g., Decho, 1990; Verdugo *et al.*, 2004; Leck and Bigg, 2008; Bigg and Leck, 2008] in influencing cloud microphysics. To unravel such complexities and the extent to which there is a causal link between ocean biological productivity, aerosol, and maritime clouds, additional multiplatform measurements are desirable. Although attention has been placed here on the influence of marine biota activity on aerosol and

clouds, another important issue to explore is the extent to which clouds influence marine biota activity by way of reflecting sunlight, thereby regulating photosynthesis.

[42] **Acknowledgments.** This work was supported by the Office of Naval Research grant N00014-04-1-0118 and the Atmospheric Radiation Measurement Program of the U.S. Department of Energy under grant DE-AI02-06ER64215. A.S. acknowledges support from the Cooperative Institute for Research in the Atmosphere Postdoctoral Research Program and Colorado State University. G.F. and A.M. acknowledge support from NOAA's Climate Goal. The images and data used in this study were acquired using the GES-DISC Interactive Online Visualization and Analysis Infrastructure (Giovanni) as part of the NASA's Goddard Earth Sciences (GES) Data and Information Services Center (DISC). The authors gratefully acknowledge the NOAA Air Resources Laboratory (ARL) for provision of the HYSPLIT transport and dispersion model.

References

- Albrecht, B. A. (1989), Aerosols, cloud microphysics, and fractional cloudiness, *Science*, **245**, 1227–1230, doi:10.1126/science.245.4923.1227.
- Altieri, K. E., S. P. Seitzinger, A. G. Carlton, B. J. Turpin, G. C. Klein, and A. G. Marshall (2008), Oligomers formed through in-cloud methylglyoxal reactions: Chemical composition, properties, and mechanisms investigated by ultra-high resolution FT-ICR mass spectrometry, *Atmos. Environ.*, **42**, 1476–1490, doi:10.1016/j.atmosenv.2007.11.015.
- Andreae, M. O. (1985), Dimethylsulfide in the water column and the sediment porewaters of the Peru upwelling area, *Limnol. Oceanogr.*, **30**, 1208–1218.
- Andreae, M. O. (1990), Ocean-atmosphere interactions in the global biogeochemical sulfur cycle, *Mar. Chem.*, **30**, 1–29, doi:10.1016/0304-4203(90)90059-L.
- Andreae, M. O., and H. Raemdonck (1983), Dimethyl sulfide in the surface ocean and the marine atmosphere: A global view, *Science*, **221**, 744–747, doi:10.1126/science.221.4612.744.
- Andreae, M. O., and D. Rosenfeld (2008), Aerosol-cloud-precipitation interactions. Part 1: The nature and sources of cloud-active aerosols, *Earth Sci. Rev.*, **89**, 13–41, doi:10.1016/j.earscirev.2008.03.001.
- Andreae, T. W., M. O. Andreae, and G. Schebeske (1994), Biogenic sulfur emissions and aerosols over the tropical South Atlantic: 1. Dimethylsulfide in seawater and in the atmospheric boundary layer, *J. Geophys. Res.*, **99**(D11), 22,819–22,829, doi:10.1029/94JD01837.
- Ansari, A. S., and S. N. Pandis (2000), Water absorption by secondary organic aerosol and its effect on inorganic aerosol behavior, *Environ. Sci. Technol.*, **34**, 71–77, doi:10.1021/es990717q.
- Arnold, S. R., et al. (2008), Evaluation of the global oceanic isoprene source and its impacts on marine organic carbon aerosol, *Atmos. Chem. Phys. Discuss.*, **8**, 16,445–16,471.
- Ayers, G. P., and J. M. Caine (2007), The CLAW hypothesis: A review of the major developments, *Environ. Chem.*, **4**, 366–374, doi:10.1071/EN07080.
- Benner, R., J. D. Padulski, M. McCarthy, J. I. Hedges, and P. G. Hatcher (1992), Bulk chemical characteristics of dissolved organic matter in the ocean, *Science*, **255**, 1561–1564, doi:10.1126/science.255.5051.1561.
- Benner, R., B. Biddanda, B. Black, and M. McCarthy (1997), Abundance, size distribution and stable carbon and nitrogen isotopic compositions of marine organic matter isolated by tangential-flow ultrafiltration, *Mar. Chem.*, **57**, 243–263, doi:10.1016/S0304-4203(97)00013-3.
- Bigg, E. K. (2007), Sources, nature and influence on climate of marine airborne particles, *Environ. Chem.*, **4**, 155–161, doi:10.1071/EN07001.
- Bigg, E. K., and C. Leck (2008), The composition of fragments of bubbles bursting at the ocean surface, *J. Geophys. Res.*, **113**, D11209, doi:10.1029/2007JD009078.
- Bigg, E. K., C. Leck, and L. Tranvik (2004), Particulates of the surface microlayer of open water in the central Arctic Ocean in summer, *Mar. Chem.*, **91**, 131–141, doi:10.1016/j.marchem.2004.06.005.
- Blanchard, D. C. (1964), Sea-to-air transport of surface active material, *Science*, **146**, 396–397, doi:10.1126/science.146.3642.396.
- Blanchard, D. C. (1989), The ejection of drops from the sea and their enrichment with bacteria and other materials: A Review, *Estuaries*, **12**, 127–137, doi:10.2307/1351816.
- Brechtel, F. J., and S. M. Kreidenweis (2000), Predicting particle critical supersaturation from hygroscopic growth measurements in the humidified TDMA. Part I: Theory and sensitivity studies, *J. Atmos. Sci.*, **57**, 1854–1871, doi:10.1175/1520-0469(2000)057<1854:PPCSFH>2.0.CO;2.
- Capaldo, K., J. J. Corbett, P. Kasibhatla, P. Fischbeck, and S. N. Pandis (1999), Effects of ship emissions on sulphur cycling and radiative climate forcing over the ocean, *Nature*, **400**, 743–746, doi:10.1038/23438.
- Carlton, A. G., B. J. Turpin, K. E. Altieri, S. Seitzinger, A. Reff, H. J. Lim, and B. Ervens (2007), Atmospheric oxalic acid and SOA production from glyoxal: Results of aqueous photooxidation experiments, *Atmos. Environ.*, **41**, 7588–7602, doi:10.1016/j.atmosenv.2007.05.035.
- Cavalli, F., et al. (2004), Advances in characterization of size-resolved organic matter in marine aerosol over the North Atlantic, *J. Geophys. Res.*, **109**, D24215, doi:10.1029/2004JD005137.
- Challenger, F., and M. I. Simpson (1948), Studies on biological methylation. Part XII: A precursor of the dimethyl sulphide evolved by *Polysiphonia fastigiata*, Dimethyl-2-carboxy-ethylsulphonium hydroxide and its salts, *J. Chem. Soc.*, **3**, 1591–1597, doi:10.1039/jr9480001591.
- Charlson, R. J., J. E. Lovelock, M. O. Andreae, and S. G. Warren (1987), Oceanic phytoplankton, atmospheric sulfur, cloud albedo and climate, *Nature*, **326**, 655–661, doi:10.1038/326655a0.
- Chin, W. C., M. V. Orellana, and P. Verdugo (1998), Spontaneous assembly of marine dissolved organic matter into polymer gels, *Nature*, **391**, 568–572, doi:10.1038/35345.
- Chiu, J. C., A. Marshak, Y. Knyazikhin, W. J. Wiscombe, H. W. Barker, J. C. Barnard, and Y. Luo (2006), Remote sensing of cloud properties using ground-based measurements of zenith radiance, *J. Geophys. Res.*, **111**, D16201, doi:10.1029/2005JD006843.
- Corrigan, A. L., S. W. Hanley, and D. O. Haan (2008), Uptake of glyoxal by organic and inorganic aerosol, *Environ. Sci. Technol.*, **42**, 4428–4433, doi:10.1021/es7032394.
- Covert, D. S., V. N. Kapustin, P. K. Quinn, and T. S. Bates (1992), New particle formation in the marine boundary layer, *J. Geophys. Res.*, **97**, 20,581–20,589.
- Crahan, K. K., D. Hegg, D. S. Covert, and H. Jonsson (2004), An exploration of aqueous oxalic acid production in the coastal marine atmosphere, *Atmos. Environ.*, **38**, 3757–3764, doi:10.1016/j.atmosenv.2004.04.009.
- Cruz, C. N., and S. N. Pandis (2000), Deliquescence and hygroscopic growth of mixed inorganic-organic atmospheric aerosol, *Environ. Sci. Technol.*, **34**, 4313–4319, doi:10.1021/es9907109.
- Decho, A. W. (1990), Microbial exopolymer secretions in ocean environments: Their role(s) in food webs and marine processes, *Oceanogr. Mar. Biol. Ann. Rev.*, **28**, 73–153.
- Delene, D. J., and J. A. Ogren (2002), Variability of aerosol optical properties at four North American surface monitoring sites, *J. Atmos. Sci.*, **59**, 1135–1150, doi:10.1175/1520-0469(2002)059<1135:VOAOPA>2.0.CO;2.
- Dusek, U., et al. (2006), Size matters more than chemistry for cloud-nucleating ability of aerosol particles, *Science*, **312**, 1375–1378, doi:10.1126/science.1125261.
- Ekstrom, S., B. Noziere, and H. C. Hansson (2008), The cloud condensation nuclei (CCN) properties of 2-methyltetrols and C₃–C₆ polyols from osmolality and surface tension measurements, *Atmos. Chem. Phys. Discuss.*, **8**, 17,237–17,256.
- Ervens, B., G. Feingold, G. J. Frost, and S. M. Kreidenweis (2004), A modeling study of aqueous production of dicarboxylic acids: 1. Chemical pathways and speciated organic mass production, *J. Geophys. Res.*, **109**, D15205, doi:10.1029/2003JD004387.
- Ervens, B., G. Feingold, and S. M. Kreidenweis (2005), Influence of water-soluble organic carbon on cloud drop number concentration, *J. Geophys. Res.*, **110**, D18211, doi:10.1029/2004JD005634.
- Facchini, M. C., M. Mircea, S. Fuzzi, and R. J. Charlson (1999), Cloud albedo enhancement by surface-active organic solutes in growing droplets, *Nature*, **401**, 257–259, doi:10.1038/45758.
- Facchini, M. C., et al. (2008a), Important source of marine secondary organic aerosol from biogenic amines, *Environ. Sci. Technol.*, **42**, 9116–9121, doi:10.1021/es8018385.
- Facchini, M. C., et al. (2008b), Primary submicron marine aerosol dominated by insoluble organic colloids and aggregates, *Geophys. Res. Lett.*, **35**, L17814, doi:10.1029/2008GL034210.
- Feingold, G. (2003), Modeling of the first indirect effect: Analysis of measurement requirements, *Geophys. Res. Lett.*, **30**(19), 1997, doi:10.1029/2003GL017967.
- Feingold, G., L. A. Remer, J. Ramaprasad, and Y. J. Kaufman (2001), Analysis of smoke impact on clouds in Brazilian biomass burning regions: An extension of Twomey's approach, *J. Geophys. Res.*, **106**, 22,907–22,922, doi:10.1029/2001JD000732.
- Feingold, G., W. L. Eberhard, D. E. Veron, and M. Previdi (2003), First measurements of the Twomey indirect effect using ground-based remote sensors, *Geophys. Res. Lett.*, **30**(6), 1287, doi:10.1029/2002GL016633.
- Fitzgerald, J. W. (1974), Effect of aerosol composition on cloud droplet size distribution: Numerical study, *J. Atmos. Sci.*, **31**, 1358–1367, doi:10.1175/1520-0469(1974)031<1358:EOACOC>2.0.CO;2.

- Fu, T. M., D. J. Jacob, F. Wittrock, J. P. Burrows, M. Vrekoussis, and D. K. Henze (2008), Global budgets of atmospheric glyoxal and methylglyoxal, and implications for formation of secondary organic aerosols, *J. Geophys. Res.*, *113*, D15303, doi:10.1029/2007JD009505.
- Gershay, R. M. (1983), Characterization of seawater organic-matter carried by bubble-generated aerosols, *Limnol. Oceanogr.*, *28*, 309–319.
- Gibb, S. W., R. Fauzi, C. Montoura, P. S. Liss, and R. G. Barlow (1999), Distribution and biogeochemistry of methylamines and ammonium in the Arabian Sea, *Deep Sea Res.*, *46*, 593–615, doi:10.1016/S0967-0645(98)00119-2.
- Hansson, H. C., M. J. Rood, S. Koloutsou-Vakakis, K. Hameri, D. Orsini, and A. Wiedensohler (1998), NaCl aerosol particle hygroscopicity dependence on mixing with organic compounds, *J. Atmos. Chem.*, *31*, 321–346, doi:10.1023/A:1006174514022.
- Hegg, D. A., L. F. Radke, and P. V. Hobbs (1990), Particle-production associated with marine clouds, *J. Geophys. Res.*, *95*(D9), 13,917–13,926, doi:10.1029/JD095iD09p13917.
- Hennigan, C. J., M. H. Bergin, J. E. Dibb, and R. J. Weber (2008), Enhanced secondary organic aerosol formation due to water uptake by fine particles, *Geophys. Res. Lett.*, *35*, L18801, doi:10.1029/2008GL035046.
- Hersey, S. P., A. Sorooshian, S. M. Murphy, R. C. Flagan, and J. H. Seinfeld (2009), Aerosol hygroscopicity in the marine atmosphere: A closure study using high-resolution, size-resolved AMS and multiple-RH DASH-SP data, *Atmos. Chem. Phys.*, *9*, 2543–2554.
- Hoffman, E. J., and R. A. Duce (1976), Factors influencing organic-carbon content of marine aerosols: Laboratory study, *J. Geophys. Res.*, *81*, 3667–3670, doi:10.1029/JC081i021p03667.
- Johnson, M., R. Sanders, V. Avgoustidi, M. Lecas, L. Brown, D. Hansell, M. Moore, S. Gibb, P. Liss, and T. Jickells (2007), Ammonium accumulation during a silicate-limited diatom bloom indicates the potential for ammonia emission events, *Mar. Chem.*, *106*, 63–75, doi:10.1016/j.marchem.2006.09.006.
- Kaufman, Y. J., O. Boucher, D. Tanre, M. Chin, L. A. Remer, and T. Takemura (2005), Aerosol anthropogenic component estimated from satellite data, *Geophys. Res. Lett.*, *32*, L17804, doi:10.1029/2005GL023125.
- Kazil, J., R. G. Harrison, and E. R. Lovejoy (2008), Tropospheric new particle formation and the role of ions, *Space Sci. Rev.*, *137*, 241–255, doi:10.1007/s11214-008-9388-2.
- Keene, W. C., et al. (2007), Chemical and physical characteristics of nascent aerosols produced by bursting bubbles at a model air-sea interface, *J. Geophys. Res.*, *112*, D21202, doi:10.1029/2007JD008464.
- Kim, B. G., M. A. Miller, S. E. Schwartz, Y. G. Liu, and Q. L. Min (2008), The role of adiabaticity in the aerosol first indirect effect, *J. Geophys. Res.*, *113*, D05210, doi:10.1029/2007JD008961.
- Korb, R. E., and M. Whitehouse (2004), Contrasting primary production regimes around South Georgia, Southern Ocean: Large blooms versus high nutrient, low chlorophyll waters, *Deep Sea Res., Part I*, *51*, 721–738, doi:10.1016/j.dsr.2004.02.006.
- Lance, S., A. Nenes, and T. A. Rissman (2004), Chemical and dynamical effects on cloud droplet number: Implications for estimates of the aerosol indirect effect, *J. Geophys. Res.*, *109*, D22208, doi:10.1029/2004JD004596.
- Lance, S., J. Medina, J. N. Smith, and A. Nenes (2006), Mapping the operation of the DMT Continuous Flow CCN counter, *Aerosol Sci. Technol.*, *40*, 242–254, doi:10.1080/02786820500543290.
- Leaitch, W. R., C. M. Banic, G. A. Isaac, M. D. Couture, P. S. K. Liu, I. Gultepe, S. M. Li, L. Kleinman, P. H. Daum, and J. I. MacPherson (1996), Physical and chemical observations in marine stratus during the 1993 North Atlantic regional experiment: Factors controlling cloud droplet number concentrations, *J. Geophys. Res.*, *101*, 29,123–29,135, doi:10.1029/96JD01228.
- Leck, C., and E. K. Bigg (1999), Aerosol production over remote marine areas - A new route, *Geophys. Res. Lett.*, *26*, 3577–3580, doi:10.1029/1999GL010807.
- Leck, C., and E. K. Bigg (2005a), Biogenic particles in the surface microlayer and overlying atmosphere in the central Arctic Ocean during summer, *Tellus, Ser. B*, *57*, 305–316, doi:10.1111/j.1600-0889.2005.00148.x.
- Leck, C., and E. K. Bigg (2005b), Source and evolution of the marine aerosol: A new perspective, *Geophys. Res. Lett.*, *32*, L19803, doi:10.1029/2005GL023651.
- Leck, C., and E. K. Bigg (2008), Comparison of sources and nature of the tropical aerosol with the summer high Arctic aerosol, *Tellus, Ser. B*, *60*, 118–126.
- Leck, C., U. Larsson, L. E. Bagander, S. Johansson, and S. Hajdu (1990), Dimethyl sulfide in the Baltic Sea - annual variability in relation to biological-activity, *J. Geophys. Res.*, *95*, 3353–3363, doi:10.1029/JC095iC03p03353.
- Lewis, E. R., and S. E. Schwartz (2004), *Sea salt Aerosol Production: Mechanisms, Methods, Measurements and Models—A Critical Review*, *Geophys. Monogr. Ser.*, vol. 152, 413 pp., AGU, Washington, D. C.
- Li, Z. D., A. L. Williams, and M. J. Rood (1998), Influence of soluble surfactant properties on the activation of aerosol particles containing inorganic solute, *J. Atmos. Sci.*, *55*, 1859–1866, doi:10.1175/1520-0469(1998)055<1859:IOSSPO>2.0.CO;2.
- Liggio, J., S. M. Li, and R. McLaren (2005), Heterogeneous reactions of glyoxal on particulate matter: Identification of acetals and sulfate esters, *Environ. Sci. Technol.*, *39*, 1532–1541, doi:10.1021/es048375y.
- Lion, L. W., and J. O. Leckie (1981), The biogeochemistry of the air-sea interface, *Annu. Rev. Earth Planet. Sci.*, *9*, 449–486, doi:10.1146/annurev.ea.09.050181.002313.
- Lohmann, U., and C. Leck (2005), Importance of submicron surface-active organic aerosols for pristine Arctic clouds, *Tellus, Ser. B*, *57*, 261–268.
- Lovelock, J. E., R. J. Maggs, and R. A. Rasmussen (1972), Atmospheric dimethyl sulfide and natural sulfur cycle, *Nature*, *237*, 452–453, doi:10.1038/237452a0.
- Marshak, A., S. Platnick, T. Varnai, G. Y. Wen, and R. F. Cahalan (2006), Impact of three-dimensional radiative effects on satellite retrievals of cloud droplet sizes, *J. Geophys. Res.*, *111*, D09207, doi:10.1029/2005JD006686.
- Mårtensson, E. M., E. D. Nilsson, G. de Leeuw, L. H. Cohen, and H. C. Hansson (2003), Laboratory simulations and parameterization of the primary marine aerosol production, *J. Geophys. Res.*, *108*(D9), 4297, doi:10.1029/2002JD002263.
- McComiskey, A., G. Feingold, A. S. Frisch, D. D. Turner, M. A. Miller, J. C. Chiu, Q. Min, and J. A. Ogren (2009), An assessment of aerosol-cloud interactions in marine stratus clouds based on surface remote sensing, *J. Geophys. Res.*, *114*, D09203, doi:10.1029/2008JD011006.
- Meredith, M. P., J. L. Watkins, E. J. Murphy, N. J. Cunningham, A. G. Wood, R. Korb, M. J. Whitehouse, S. E. Thorpe, and F. Vivier (2003), An anticyclonic circulation above the Northwest Georgia Rise, Southern Ocean, *Geophys. Res. Lett.*, *30*(20), 2061, doi:10.1029/2003GL018039.
- Meskhidze, N., and A. Nenes (2006), Phytoplankton and cloudiness in the Southern Ocean, *Science*, *314*, 1419–1423, doi:10.1126/science.1131779.
- Middlebrook, A. M., D. M. Murphy, and D. S. Thomson (1998), Observations of organic material in individual marine particles at Cape Grim during the First Aerosol Characterization Experiment (ACE 1), *J. Geophys. Res.*, *103*(D13), 16,475–16,483, doi:10.1029/97JD03719.
- Miller, M. A., and S. E. Yuter (2008), Lack of correlation between chl *a* and cloud droplet effective radius in shallow marine clouds, *Geophys. Res. Lett.*, *35*, L13807, doi:10.1029/2008GL034354.
- Mochida, M., Y. Kitamori, K. Kawamura, Y. Nojiri, and K. Suzuki (2002), Fatty acids in the marine atmosphere: Factors governing their concentrations and evaluation of organic films on sea-salt particles, *J. Geophys. Res.*, *107*(D17), 4325, doi:10.1029/2001JD001278.
- Murphy, S. M., A. Sorooshian, J. H. Kroll, N. L. Ng, P. Chhabra, C. Tong, J. D. Surratt, E. Knipping, R. C. Flagan, and J. H. Seinfeld (2007), Secondary aerosol formation from atmospheric reactions of aliphatic amines, *Atmos. Chem. Phys.*, *7*, 2313–2337.
- Nakajima, T., A. Higurashi, K. Kawamoto, and J. E. Penner (2001), A possible correlation between satellite-derived cloud and aerosol microphysical parameters, *Geophys. Res. Lett.*, *28*, 1171–1174, doi:10.1029/2000GL012186.
- Nenes, A., R. J. Charlson, M. C. Facchini, M. Kulmala, A. Laaksonen, and J. H. Seinfeld (2002), Can chemical effects on cloud droplet number rival the first indirect effect?, *Geophys. Res. Lett.*, *29*(17), 1848, doi:10.1029/2002GL015295.
- O'Dowd, C. D., and G. de Leeuw (2007), Marine aerosol production: A review of the current knowledge, *Philos. Trans. R. Soc. A*, *365*, doi:10.1098/rsta.2007.2043.
- O'Dowd, C. D., M. C. Facchini, F. Cavalli, D. Ceburnis, M. Mircea, S. Decesari, Fuzzi, Y. J. Yoon, and J. P. Putaud (2004), Biogenically driven organic contribution to marine aerosol, *Nature*, *431*, 676–680, doi:10.1038/nature02959.
- Orellana, M. V., and P. Verdugo (2003), Ultraviolet radiation blocks the organic carbon exchange between the dissolved phase and the gel phase in the ocean, *Limnol. Oceanogr.*, *48*, 1618–1623.
- Peng, C., M. N. Chan, and C. K. Chan (2001), The hygroscopic properties of dicarboxylic and multifunctional acids: Measurements and UNIFAC predictions, *Environ. Sci. Technol.*, *35*, 4495–4501, doi:10.1021/es0107531.
- Perri, M. J., S. Seitzinger, and B. J. Turpin (2008), Secondary organic aerosol production from aqueous photooxidation of glycolaldehyde: Laboratory experiments, *Atmos. Environ.*, *43*, 1487–1497, doi:10.1016/j.atmosenv.2008.11.037.

- Perry, M. J., J. P. Bolger, and D. C. English (1989), *Coastal Oceanography of Washington and Oregon*, edited by M. R. Landry and B. M. Hickey, pp. 117–138, Elsevier, Amsterdam.
- Prakash, S., and R. Ramesh (2007), Is the Arabian Sea getting more productive?, *Curr. Sci.*, *92*, 667–671.
- Prenni, A. J., P. J. DeMott, S. M. Kreidenweis, D. E. Sherman, L. M. Russell, and Y. Ming (2001), The effects of low molecular weight dicarboxylic acids on cloud formation, *J. Phys. Chem. A*, *105*, 11,240–11,248, doi:10.1021/jp012427d.
- Prenni, A. J., P. J. De Mott, and S. M. Kreidenweis (2003), Water uptake of internally mixed particles containing ammonium sulfate and dicarboxylic acids, *Atmos. Environ.*, *37*, 4243–4251, doi:10.1016/S1352-2310(03)00559-4.
- Riley, G. A. (1963), Organic aggregates in seawater and the dynamics of their formation and utilization, *Limnol. Oceanogr.*, *8*, 372–381.
- Roberts, G. C., and A. Nenes (2005), A continuous-flow streamwise thermal-gradient CCN chamber for atmospheric measurements, *Aerosol Sci. Technol.*, *39*, 206–221, doi:10.1080/027868290913988.
- Saxena, P., L. M. Hildemann, P. H. McMurry, and J. H. Seinfeld (1995), Organics alter hygroscopic behavior of atmospheric particles, *J. Geophys. Res.*, *100*(D9), 18,755–18,770, doi:10.1029/95JD01835.
- Shaw, G. E. (1983), Bio-controlled thermostatism involving the sulfur cycle, *Clim. Change*, *5*, 297–303, doi:10.1007/BF02423524.
- Sheridan, P. J., D. J. Delene, and J. A. Ogren (2001), Four years of continuous surface aerosol measurements from the Department of Energy's Atmospheric Radiation Measurement Program Southern Great Plains Cloud and Radiation Testbed site, *J. Geophys. Res.*, *106*(D18), 20,735–20,747, doi:10.1029/2001JD000785.
- Shulman, M. L., M. C. Jacobson, R. J. Carlson, R. E. Synovec, and T. E. Young (1996), Dissolution behavior and surface tension effects of organic compounds in nucleating cloud droplets, *Geophys. Res. Lett.*, *23*, 277–280, doi:10.1029/95GL03810.
- Sorooshian, A., et al. (2006a), Oxalic acid in clear and cloudy atmospheres: Analysis of data from International Consortium for Atmospheric Research on Transport and Transformation 2004, *J. Geophys. Res.*, *111*, D23S45, doi:10.1029/2005JD006880.
- Sorooshian, A., F. J. Brechtel, Y. L. Ma, R. J. Weber, A. Corless, R. C. Flagan, and J. H. Seinfeld (2006b), Modeling and characterization of a particle-into-liquid sampler (PILS), *Aerosol Sci. Technol.*, *40*, 396–409, doi:10.1080/02786820600632282.
- Sorooshian, A., M. L. Lu, F. J. Brechtel, H. Jonsson, G. Feingold, R. C. Flagan, and J. H. Seinfeld (2007a), On the source of organic acid aerosol layers above clouds, *Environ. Sci. Technol.*, *41*, 4647–4654, doi:10.1021/es0630442.
- Sorooshian, A., N. L. Ng, A. W. H. Chan, G. Feingold, R. C. Flagan, and J. H. Seinfeld (2007b), Particulate organic acids and overall water-soluble aerosol composition measurements from the 2006 Gulf of Mexico Atmospheric Composition and Climate Study (GoMACCS), *J. Geophys. Res.*, *112*, D13201, doi:10.1029/2007JD008537.
- Sorooshian, A., S. M. Murphy, S. Hersey, H. Gates, L. T. Padró, A. Nenes, F. J. Brechtel, H. Jonsson, R. C. Flagan, and J. H. Seinfeld (2008a), Comprehensive airborne characterization of aerosol from a major bovine source, *Atmos. Chem. Phys.*, *8*, 5489–5520.
- Sorooshian, A., S. Hersey, F. J. Brechtel, A. Corless, R. C. Flagan, and J. H. Seinfeld (2008b), Rapid, size-resolved aerosol hygroscopic growth measurements: Differential aerosol sizing and hygroscopicity spectrometer probe (DASH-SP), *Aerosol Sci. Technol.*, *42*, 445–464, doi:10.1080/02786820802178506.
- Stephens, G. L. (1978), Radiation profiles in extended water clouds. I: Theory, *J. Atmos. Sci.*, *35*, 2111–2122, doi:10.1175/1520-0469(1978)035<2111:RPIEW>2.0.CO;2.
- Tseng, R. S., J. T. Viechnicki, R. A. Skop, and J. W. Brown (1992), Sea-to-air transfer of surface-active organic-compounds by bursting bubbles, *J. Geophys. Res.*, *97*(C4), 5201–5206, doi:10.1029/91JC00954.
- Turner, D. D., S. A. Clough, J. C. Iijegren, E. E. Clothiaux, K. E. Cady-Pereira, and K. L. Gaustad (2007), Retrieving liquid water path and precipitable water vapor from the atmospheric radiation measurement (ARM) microwave radiometers, *IEEE Trans. Geosci. Remote Sens.*, *45*, 3680–3690, doi:10.1109/TGRS.2007.903703.
- Twomey, S. (1977), Influence of pollution on shortwave albedo of clouds, *J. Atmos. Sci.*, *34*, 1149–1152, doi:10.1175/1520-0469(1977)034<1149:TIOPT>2.0.CO;2.
- Vanneste, A., R. A. Duce, and C. Lee (1987), Methylamines in the marine atmosphere, *Geophys. Res. Lett.*, *14*, 711–714, doi:10.1029/GL014i007p00711.
- Verdugo, P., A. L. Alldredge, F. Azam, D. I. Kirchman, U. Passow, and P. H. Santschi (2004), The oceanic gel phase: A bridge in the DOM-POM continuum, *Mar. Chem.*, *92*, 67–85, doi:10.1016/j.marchem.2004.06.017.
- Volkamer, R., P. J. Ziemann, and M. J. Molina (2009), Secondary organic aerosol formation from acetylene (C₂H₂), Seed effect on SOA yields due to organic photochemistry in the aerosol aqueous phase, *Atmos. Chem. Phys.*, *9*, 1907–1928.
- Ware, D., and R. Thomson (2005), Bottom-up ecosystem trophic dynamics determine fish production in the northeast Pacific, *Science*, *308*, 1280–1284, doi:10.1126/science.1109049.
- Warneck, P. (2003), In-cloud chemistry opens pathway to the formation of oxalic acid in the marine atmosphere, *Atmos. Environ.*, *37*, 2423–2427, doi:10.1016/S1352-2310(03)00136-5.
- Warren, S. G., C. J. Hahn, R. M. Chervin, and R. L. Jenne (1986), Global Distribution Of Total Cloud Cover And Cloud Type Amounts Over Land, *NCAR Tech. Note NCAR/TN-273+STR, NTIS DE87-006903*, Natl. Cent. Atmos. Res., Boulder, Colo.
- Wells, M. L. (1998), Marine colloids: A neglected dimension, *Nature*, *391*, 530–531, doi:10.1038/35248.
- Wells, M. L., and E. D. Goldberg (1991), Occurrence of small colloids in sea-water, *Nature*, *353*, 342–344, doi:10.1038/353342a0.
- Wells, M. L., and E. D. Goldberg (1993), Colloid aggregation in seawater, *Mar. Chem.*, *41*, 353–358, doi:10.1016/0304-4203(93)90267-R.
- Wise, M. E., J. D. Surratt, D. B. Curtis, J. E. Shilling, and M. A. Tolbert (2003), Hygroscopic growth of ammonium sulfate/dicarboxylic acids, *J. Geophys. Res.*, *108*(D20), 4638, doi:10.1029/2003JD003775.
- Yu, J. Z., S. F. Huang, J. H. Xu, and M. Hu (2005), When aerosol sulfate goes up, so does oxalate: Implication for the formation mechanisms of oxalate, *Environ. Sci. Technol.*, *39*, 128–133, doi:10.1021/es049559f.

G. Feingold and A. McComiskey, Earth Systems Research Laboratory, NOAA, 325 Broadway, R/CSD2, Boulder, CO 80305, USA.

R. C. Flagan, H. Gates, and J. H. Seinfeld, Department of Chemical Engineering, California Institute of Technology, Mail Code 210-41, Pasadena, CA 92215, USA.

S. P. Hersey, Department of Environmental Science and Engineering, California Institute of Technology, Mail Code 210-41, Pasadena, CA 92215, USA.

H. H. Jonsson, CIRPAS, Hangar 507, 3200 Imjin Road, Marina, CA 93933, USA.

S. D. Miller and G. L. Stephens, CIRA, Colorado State University, 1375 Campus Delivery, Fort Collins, CO 80523, USA.

A. Nenes and L. T. Padró, School of Chemical and Biomolecular Engineering, Georgia Institute of Technology, 311 Ferst Drive, Atlanta, GA 30332, USA.

A. Sorooshian, Department of Chemical and Environmental Engineering, University of Arizona, P.O. Box 210011, Tucson, AZ 85721, USA. (armin@email.arizona.edu)

Appendix D

Chemical Composition of Gas- and Aerosol-Phase Products from the Photooxidation of Naphthalene*

*Reproduced with permission from "Chemical Composition of Gas- and Aerosol-Phase Products from the Photooxidation of Naphthalene" by Kautzman, K.E., Surratt, J.D., Chan, M.N., Chan, A.W.H., Hersey, S.P., Chhabra, P.S., Dalleska, N.F., Wennberg, P.O., Flagan R.C., and Seinfeld, J.H., *Journal of Physical Chemistry A*, 114 (2), 913-934, 2010. Copyright 2010 by the American Chemical Society.

Chemical Composition of Gas- and Aerosol-Phase Products from the Photooxidation of Naphthalene

K. E. Kautzman,[†] J. D. Surratt,[†] M. N. Chan,[‡] A. W. H. Chan,[†] S. P. Hersey,[‡] P. S. Chhabra,[†] N. F. Dalleska,[‡] P. O. Wennberg,^{‡,§} R. C. Flagan,^{†,‡} and J. H. Seinfeld^{*,†,‡}

Division of Chemistry and Chemical Engineering, Division of Engineering and Applied Science, and Division of Geological and Planetary Sciences, California Institute of Technology, Pasadena, CA

Received: September 3, 2009; Revised Manuscript Received: October 15, 2009

The current work focuses on the detailed evolution of the chemical composition of both the gas- and aerosol-phase constituents produced from the OH-initiated photooxidation of naphthalene under low- and high-NO_x conditions. Under high-NO_x conditions ring-opening products are the primary gas-phase products, suggesting that the mechanism involves dissociation of alkoxy radicals (RO) formed through an RO₂ + NO pathway, or a bicyclic peroxy mechanism. In contrast to the high-NO_x chemistry, ring-retaining compounds appear to dominate the low-NO_x gas-phase products owing to the RO₂ + HO₂ pathway. We are able to chemically characterize 53–68% of the secondary organic aerosol (SOA) mass. Atomic oxygen-to-carbon (O/C), hydrogen-to-carbon (H/C), and nitrogen-to-carbon (N/C) ratios measured in bulk samples by high-resolution electrospray ionization time-of-flight mass spectrometry (HR-ESI-TOFMS) are the same as the ratios observed with online high-resolution time-of-flight aerosol mass spectrometry (HR-ToF-AMS), suggesting that the chemical compositions and oxidation levels found in the chemically-characterized fraction of the particle phase are representative of the bulk aerosol. Oligomers, organosulfates (R-OSO₃), and other high-molecular-weight (MW) products are not observed in either the low- or high-NO_x SOA; however, in the presence of neutral ammonium sulfate seed aerosol, an organic sulfonic acid (R-SO₃), characterized as hydroxybenzene sulfonic acid, is observed in naphthalene SOA produced under both high- and low-NO_x conditions. Acidic compounds and organic peroxides are found to account for a large fraction of the chemically characterized high- and low-NO_x SOA. We propose that the major gas- and aerosol-phase products observed are generated through the formation and further reaction of 2-formylcinnamaldehyde or a bicyclic peroxy intermediate. The chemical similarity between the laboratory SOA and ambient aerosol collected from Birmingham, Alabama (AL) and Pasadena, California (CA) confirm the importance of PAH oxidation in the formation of aerosol within the urban atmosphere.

1. Introduction

A large fraction (80–90% in some locations) of atmospheric organic aerosol is secondary in origin.¹ The formation of secondary organic aerosol (SOA) results from the formation of low-vapor-pressure products in the oxidation of volatile organic compounds (VOCs), where the resultant low-vapor-pressure oxidation products partition between the gas and aerosol phases. Many VOCs, such as monoterpenes (e.g., α -pinene) and single-ringed aromatic hydrocarbons (e.g., toluene), are known to produce SOA. However, the mass of SOA observed in many locations cannot be accounted for by known precursor VOC, suggesting that many sources of SOA are not yet identified or well characterized.^{2–4} Recent identification of isoprene oxidation as a significant source of SOA,^{5–12} the role of NO_x in forming SOA from the oxidation of aromatics^{13–15} and other hydrocarbons,^{16–18} the effects of aerosol acidity and heterogeneous chemistry (e.g., oligomer^{19–27} and organosulfate formation^{24,28–32}), and the contribution of glyoxal to SOA formation^{24,33–35} have provided significant insights into potential missing and poorly characterized sources of SOA. Additionally, Robinson et al.³⁶

have shown that primary organic aerosol (POA), previously considered as nonvolatile, contains gas-phase components of intermediate volatility that themselves are sources of SOA.

Although it is traditionally assumed that small volatile aromatic organic compounds, such as toluene and benzene, are the primary precursors for anthropogenic SOA, it has recently been shown that substantial contributions to SOA formation may also come from compounds of lower volatility,³⁶ such as polycyclic aromatic hydrocarbons (PAHs). PAHs account for a significant portion of the semivolatile gas-phase emissions from diesel fuels,³⁷ with substantial emissions also being produced from gasoline engines,³⁸ wood burning,^{39,40} and cooking sources.^{41,42} Photooxidation of PAHs has been shown to produce high-MW, low-vapor-pressure, oxygenated compounds.^{40,43–47} The nitro PAHs, specifically nitronaphthalenes, have been observed in ambient particulate matter⁴⁸ and are of particular importance due to their expected role as carcinogens.^{49–52}

We have previously reported SOA yields, defined as the ratio of mass of SOA formed, ΔM_o , to the mass of hydrocarbon reacted, ΔHC , from the photooxidation of naphthalene, 1-methylnaphthalene (1-MN), 2-methylnaphthalene (2-MN), and 1,2-dimethylnaphthalene (1,2-DMN) as a function of organic mass loading under both high- and low-NO_x conditions.¹⁵ Yields for high-NO_x conditions were observed between 0.19 and 0.30 for

* Author to whom correspondence should be addressed. Phone: (626) 395-4635, Fax: (626) 796-2591, E-mail: seinfeld@caltech.edu.

[†] Division of Chemistry and Chemical Engineering.

[‡] Division of Engineering and Applied Science.

[§] Division of Geological and Planetary Sciences.

TABLE 1: Instruments Employed in Chamber Experiments^a

instrumentation	measurement	time resolution	detection limit/range
hygrometer (capacitance probe)	temperature	online	10–50 °C
Vaisala HMP233	humidity	online	5–95%
chemiluminescent NO _x analyzer	NO, NO ₂ concentrations	online	2 ppb
luminol NO _x analyzer	concentration of NO ₂ separated from PAN by GC	online	5 ppb
O ₃ analyzer	ozone concentration	online	2 ppb
differential mobility analyzer (DMA)	aerosol number concentration, size distribution, and volume concentration	4 min	0.2 μm ³ cm ⁻³ , 15–780 nm
gas chromatography/flame ionization detector (GC/FID)	parent hydrocarbon concentration	12 min	~1 ppb ^b
chemical ionization mass spectrometry (CIMS)	gas-phase oxidation products	~9 min	~0.1 ppb ^b , unit mass resolution
gas chromatography/electron ionization-time-of-flight mass spectrometry (GC/EI-TOFMS)	gas-phase oxidation products, structural identification	semionline, off-line	0.5 ppb ^b , resolution ~7000
ultra performance liquid chromatography/electrospray ionization-time-of-flight mass spectrometry (UPLC/ESI-TOFMS)	particle-phase products, structural identification	off-line	1 ng m ⁻³ ^b , resolution ~12 000
high performance liquid chromatography/electrospray ionization-ion trap mass spectrometry (HPLC/ESI-ITMS)	particle-phase products, structural identification	off-line	1 ng m ⁻³ ^b , unit mass resolution
high-resolution time-of-flight aerosol mass spectrometry (HR-ToF-AMS)	particle-phase composition	online	0.03 μg m ⁻³ , 50–600 nm
particle into liquid sampler-ion chromatography (PILS-IC)	water-soluble aerosol composition	online	~0.1 μg m ⁻³ ^b

^a Instruments employed at the Caltech dual chamber environmental facility. ^b Detection limits dependent on identity of target species.

naphthalene, 0.19 and 0.39 for 1-MN, 0.26 and 0.45 for 2-MN, and constant at 0.31 for 1, 2-DMN, at aerosol mass loadings between 10 and 40 μg m⁻³. Under low-NO_x conditions, yields were found to be 0.73, 0.68, and 0.58, for naphthalene, 1-MN, and 2-MN, respectively. Gas-phase products were tentatively identified, and trends involving ring-opening versus ring-retaining oxidation mechanisms were established. Calculations of SOA formation from these PAHs demonstrated that these precursors may contribute significantly to the amount of urban SOA. The suite of instruments associated with the Caltech dual indoor environmental chamber facility (Table 1), by which the data to be presented were obtained, permits a thorough analysis of the generation of SOA commencing with the oxidation of the gas-phase hydrocarbon to the formation of SOA. Here we describe the detailed evaluation of the chemical composition of both the gas- and aerosol-phase constituents produced from the photooxidation of naphthalene, the most abundant PAH in the urban atmosphere.⁴⁸

2. Experimental Section

2.1. Chamber Experiments. All experiments were carried out in the Caltech dual 28 m³ Teflon chambers. Details of the facilities have been described previously.^{53,54} Before each experiment, the chambers were flushed with dried purified air for >24 h, until the particle number concentration was <100 cm⁻³ and the volume concentration was <0.1 μm³ cm⁻³. In most experiments, ammonium sulfate seed aerosol was used to promote condensation of low volatility oxidation products. The seed aerosol was generated by atomization of a 0.06 M aqueous ammonium sulfate solution. The hydrocarbon was introduced into the chamber by flowing purified air through an FEP tube packed with solid naphthalene at 1 L min⁻¹.

For high-NO_x experiments (NO > 350 ppb initially) nitrous acid (HONO) was used as the OH precursor. HONO was prepared by adding 10 mL of 1 wt % aqueous NaNO₂ dropwise into 20 mL of 10 wt % sulfuric acid in a glass bulb. A stream

of dry air was then passed through the bulb, sending HONO into the chamber. During this process, NO and NO₂ formed as side products and were also introduced into the chamber. NO/NO_x was measured with a commercial chemiluminescence NO_x monitor (Horiba, APNA-360). In some experiments, NO₂ was monitored by a gas chromatograph with luminol detector (University of California, Riverside, CA) in which NO₂ and peroxyacyl nitrate (PAN) were separated by gas chromatography and detected by chemiluminescence of reaction with luminol.⁵⁵ Reaction of HONO with luminol is unlikely, and thus no interference with the NO₂ signal is expected. The NO₂ measurement from the NO_x monitor is higher due to interferences from HONO. The injection of HONO was stopped when the mixing ratio of NO₂ reached about 80 ppb in the chamber as measured by the Riverside NO₂ monitor. Additional NO was added until total NO was about 400 ppb. For all experiments, the concentrations of NO and NO₂ remained approximately constant over the course of photooxidation, and ozone (O₃) concentrations remained insignificant. For low-NO_x experiments, hydrogen peroxide (H₂O₂) was used as the OH precursor. Prior to atomization of the ammonium sulfate seed, H₂O₂ was introduced by bubbling purified air through a 50% aqueous H₂O₂ solution for 2.5 h at 5 L min⁻¹ resulting in a mixing ratio of 2–8 ppm of H₂O₂.

The aerosol number concentrations, size distributions, and volume concentrations were measured by a differential mobility analyzer (DMA, TSI model 3081) coupled with a condensation nuclei counter (TSI, CNC-3760). After allowing for all concentrations to stabilize, irradiation was initiated. The temperature (*T*), relative humidity (RH), and concentrations of O₃, NO, and NO_x were continuously monitored. Table 2 summarizes the experimental conditions for the series of naphthalene oxidation experiments conducted.

2.2. Gas-Phase Measurements.

2.2.1. Gas Chromatography/Flame-Ionization Detection (GC/FID). The concentration of naphthalene was continuously monitored by GC/FID. Chamber air was sampled into a 10 mL

TABLE 2: Experimental Conditions from Chamber Experiments

	initial naphthalene (ppb)	oxidant precursor ^a	initial NO ₂ (ppb)	initial NO (ppb)	initial O ₃ (ppb)	T (°C) ^b	RH (%) ^b	initial seed volume (μm ³ /cm ³)	end volume (μm ³ /cm ³)
1	60	H ₂ O ₂	0	0	6	26	6	14	143
2	25	H ₂ O ₂	0	3	4	26	19	26	50
3	20	H ₂ O ₂	0	2	2	24	10	11	38
4	20	H ₂ O ₂	0	1	1	24	13	11	40
5	48	HONO	166	401	3	28	5	16	65
6	30	HONO	245	455	1	25	7	15	51
7	35	HONO	289	487	3	25	10	15	50
8	30	HONO	260	480	3	26	17	11	n.a.

^a H₂O₂ is used for low-NO_x conditions; HONO is used for high-NO_x conditions. ^b Reported value is averaged over the course of the experiment.

injection loop and injected onto a HP5 15 m × 0.53 mm ID × 1 μm thickness column installed on a 6890N Agilent GC. The GC was temperature-programmed as follows; initial temp 60 °C, hold 1 min, ramp 35 °C min⁻¹ to 140 °C, ramp 20 °C min⁻¹ to 200 °C, hold 2 min. The GC response was calibrated by dissolving a known mass of the naphthalene in dichloromethane, and then vaporizing a known volume of that solution into a 38 L Teflon chamber.

2.2.2. Chemical Ionization Mass Spectrometry (CIMS).

Monitoring of gas-phase oxidation products was carried out in real time by the use of a CIMS instrument. The details of this instrument are described elsewhere.^{17,56,57} Briefly, a 2.5 standard liters per minute (slm) aliquot of air is drawn from the experimental chamber through a 1.6 m long 0.25 in. Teflon tube. 300 standard cubic centimeters per minute (sscm) of this flow is introduced into the CIMS instrument and ionized by a reagent ion. The resultant ions are filtered using a quadrupole mass spectrometer with unit mass resolution. The instrument can operate in both negative mode, using CF₃O⁻ as a reagent ion, and in positive proton transfer reaction (PTR)-MS mode. Negative mode is found to be more selective toward detection of polar molecules, particularly acids, whereas positive mode detects a broader range of organic compounds. Mass scans were performed covering masses 55–450 amu for negative mode, and 56–350 amu for positive mode, with a total scan time of ~9 min. Mass scans were continuously repeated over the course of each experiment.

2.2.3. Gas Chromatography/Electron Impact Time-of-Flight Mass Spectrometry (GC/EI-TOFMS).

The GC/EI-TOFMS instrument (Waters, GCT Premier) is outfitted with a standard 6890N Agilent GC for introduction of volatile samples. The ion source employed here is a traditional 70 eV positive (+)EI source. The ions produced are continuously accelerated across the source to 40 eV and perpendicularly extracted into the TOF mass analyzer at a rate >25 kHz. The ions then pass through a single reflectron with an effective path length of 1.2 m. Ions are subsequently detected by a chevron stack of microchannel plates. The arrival times of the ions are recorded by a time-to-digital converter at a rate of 3.6 GHz, providing high mass accuracy (~7000). All data are acquired and analyzed using MassLynx software version 4.1.

Various components have been added to aid with sample introduction into the GC/EI-TOFMS instrument. A preconcentrator (Entech Instruments, model 7100A) is used to draw, concentrate, and focus gas-phase samples into discrete peaks on the GC column. The preconcentrator extracts air from the environmental chamber and then cryogenically traps and concentrates VOCs in the sample. We have used two different trapping methods with the preconcentrator. The first method, microscale purge and trap (MPT), is a three-stage procedure to efficiently concentrate gas samples. The initial trap, which is

filled with glass beads, is used to remove water vapor from the sample and removes bulk atmospheric gases (e.g., O₂ and N₂). The initial concentration step is then followed by trapping of VOCs with a Tenax adsorbent trap, and the sample is subsequently flushed into the cryofocusing module where the sample is focused and rapidly injected onto the GC column. The second method, cold trap dehydration (CTD), uses only the Tenax trap and cryofocusing modules. Although CTD is less effective at removing moisture from humid samples, it is the preferred method of sample concentration for water-soluble compounds such as aldehydes. This method also provides superior handling of samples with high CO₂ levels. Both the MPT and CTD methods have been found to be effective for sampling volatile and semivolatile compounds, although for the highly oxidized products of interest here, the preconcentrator is believed to be the controlling factor for the ultimate detection limit of these latter products. All modules in the preconcentrator have an upper temperature range of 200 °C. Similarly, the transfer line between the preconcentrator and GC can be heated only to a maximum of 150 °C. The upper temperature limit of the preconcentrator makes detection of low-vapor-pressure oxidized compounds challenging.

The concentrations of naphthalene (<40 ppb) employed in the chamber experiments outlined in Table 2 preclude detection of the gas-phase oxidation products by the GC/EI-TOFMS technique as implemented at Caltech. Thus, additional high-concentration experiments were carried out in a separate 3 m³ Teflon chamber to identify gas-phase products from the photooxidation of naphthalene under high- and low-NO_x conditions using the GC/EI-TOFMS instrument. The initial mixing ratio of the naphthalene in these experiments was ~40 ppm, and the concentration of HONO in high-NO_x experiments was ~10 ppm. For low-NO_x experiments initial mixing ratios of H₂O₂ were ~30–80 ppm. Two methods were used to monitor the formation of gas-phase oxidation products; first, 1000 mL samples were drawn from the 3 m³ Teflon chamber and introduced directly into the three-step preconcentrator. After preconcentration, the sample was injected onto the GC DB-5MS column (30 m × 0.25 mm ID × 0.25 μm thickness) and temperature-programmed as follows: initial temp 40 °C, hold 2 min, ramp 5 °C min⁻¹ to 300 °C. This method has limited time resolution due to the preconcentration and GC steps. In order to improve the time resolution, Tenax tube samples were collected. Air from the 3 m³ Teflon chamber was drawn through Tenax TA glass tubes (Supelco, 6 mm × 11.5 cm) at a rate of 0.455 L min⁻¹ using a critical orifice. Each tube sampled chamber air for 20 min. Subsequently, the tubes were desorbed at 300 °C into the preconcentrator and analyzed as described above. Gas-phase products were identified by NIST library searching the mass spectra,⁵⁸ and authentic standards were used when possible. No

differences were observed between the preconcentrator MPT and CTD methods.

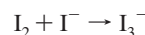
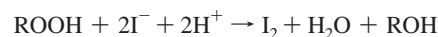
2.3. Particle-Phase Measurements.

2.3.1. Chamber Filter Sample Collection, Extraction, and Off-Line Detailed Chemical Characterization Protocols. A detailed description of the aerosol filter sample collection and extraction protocol has been previously published.⁵⁹ Briefly, aerosol samples are collected on Teflon filters (PALL Life Sciences, 47-mm diameter, 1.0- μm pore size, teflomembrane). Filter samplers employed for aerosol filter sample collection used a front and back-up filter sampling approach, where back-up filters were collected in order to examine if aerosol breakthrough was occurring on the front filter or whether evaporation of semivolatiles from the front filter was occurring during filter sampling. In all experiments outlined in Table 2, no SOA constituents were found on the back-up filters, and as a result, all detailed chemical characterizations are reported only for the front filters. Filter sampling was initiated when the aerosol volume reached its maximum (constant) value, as determined by the DMA. Depending on the total volume concentration of aerosol in the chamber, the duration of filter sampling was 1.8–2.1 h, which resulted in 2.0–2.9 m³ of total chamber air sampled. Teflon filter extraction protocols in high-purity methanol (LC-MS CHROMASOLV-Grade, Sigma-Aldrich) have been described previously.⁵⁹ Additional filter extractions using 5 mL of high-purity acetonitrile (LC-MS CHROMASOLV-Grade, Sigma-Aldrich) were also performed by 45 min of sonication to ensure detection of SOA constituents not soluble in methanol. No additional compounds were recovered using the less-polar acetonitrile solvent. Thus, all results from the off-line ESI-MS measurements are reported only for the methanol filter extractions. The resultant filter extracts were then analyzed by a Waters ACQUITY ultra performance liquid chromatography (UPLC) system, coupled with a Waters LCT Premier TOF mass spectrometer equipped with an ESI source, allowing for accurate mass measurements (i.e., determination of molecular formulas) to be obtained for each observed ion. Operation protocols, including column information and employed chromatographic method, for the UPLC/ESI-TOFMS technique have been described in detail previously.⁵⁹

Selected naphthalene low- and high-NO_x methanol filter extracts were also analyzed by a Thermo Finnigan Surveyor high performance liquid chromatography (HPLC) system (pump and autosampler) coupled to a Thermo Finnigan LCQ ion trap mass spectrometer (ITMS) equipped with an ESI source, allowing for tandem MS measurements (i.e., generation of product ions) to be obtained. The combination of accurate mass and tandem MS measurements significantly aided in detailed structural characterization efforts. Data were acquired and processed using Xcalibur version 1.3 software. A Waters Atlantis T3 column (3 μm particle size; 2.1 \times 150 mm) was employed, which is similar to the Water ACQUITY UPLC HSS column used for the UPLC/ESI-TOFMS analysis. The mobile phases consisted of 0.1% acetic acid in water (A) and 0.1% acetic acid in methanol (B). The applied 45 min gradient elution program was as follows: the concentration of eluent B was kept at 3% for 4 min, then increased to 100% in 21 min, holding at 100% for 10 min, then decreased to 3% in 5 min, and kept at 3% for 5 min. The injection volume and flow rate were 10 μL and 0.2 mL min⁻¹, respectively. The ion trap mass analyzer was operated under the following conditions: sheath gas flow (N₂), 65 arbitrary units; auxiliary gas flow (N₂), 3 arbitrary units; source voltage, -4.5 kV; capillary voltage, -14.5 V; tube lens offset, 7 V; capillary temperature, 200 °C; and maximum ion

injection time, 200 ms. Two scan events were used during each chromatographic run; scan event 1 was the full scan mode in which data were collected from m/z 120 to 600 in the negative ionization mode and scan event 2 was the MS² mode in which product ions were generated from significant base peak ions observed in scan event 1. For MS² experiments, an isolation width of 2.5 m/z units and a normalized collision energy level of 35% were applied. The [M - H]⁻ ion signal optimization was carried out by introducing a 1 mg mL⁻¹ malic acid standard solution. Due to the on-axis ESI source that is characteristic of the LCQ ITMS instrument, a solvent delay time of 3.5 min (which diverted the column effluent from the ESI source to waste) was employed to prevent clogging by nonvolatile salts at the entrance of the capillary.

Measurements of total peroxide content from the extracted filter samples were acquired by the UV-vis iodometric spectroscopy method.¹⁹ Filter samples used for this analysis were extracted and prepared differently from the filter samples used in the UPLC/ESI-TOFMS and HPLC/ESI-ITMS analyses.¹¹ Standard calibration curves were generated using a series of benzoyl peroxide solutions. The structure of the benzoyl peroxide, a peroxy group linking two benzene rings, was judged to be an excellent surrogate for the naphthalene system. Calibrations and measurements were performed on a Hewlett-Packard 8452A diode array spectrophotometer. Peroxides in the form of HOOH, ROOH, and ROOR are quantified by measuring the absorbance at 470 nm of the reaction product I₃⁻ produced under anaerobic, dark, and acidic conditions by the following reaction scheme:



Detection of I₃⁻ at 470 nm is 10 nm to the red from the peak of the characteristic absorbance of I₃⁻ and has been chosen to avoid interferences with other organic compounds absorbing in this region. Extractions from three high-NO_x and three low-NO_x filters were performed to ensure reproducibility across experiments. No contribution of H₂O₂ to this measurement is expected due to the dry conditions employed in the present experiments, as well as owing to previous quality control experiments demonstrating that no H₂O₂ could be measured on filter samples collected from a nonirradiated chamber mixture containing only gaseous H₂O₂, VOC, and ammonium sulfate seed aerosol. These latter quality control filter samples were collected for the same duration as filter samples collected from SOA chamber experiments.

Of particular concern to the UV-vis measurements is the presence of nitronaphthalenes and nitrobenzenes in high-NO_x filter samples, which in solution have a color similar to the I₃⁻ produced from the reaction of I⁻ with the peroxides in solution. 1000 ppm standard solutions of nitronaphthalenes (i.e., 4-nitro-1-naphthol and 2-nitro-1-naphthol), nitrobenzenes (i.e., 2-nitrophenol and 3-hydroxy-4-nitrobenzoic acid), and epoxides (i.e., α -pinene oxide, 2-methyl-2-vinyloxirane, and 2,3-epoxy-1,4-diol) were prepared and tested to confirm that no interferences were present from these compounds in the UV-vis measurement. From the analyses of the 1000 ppm standards, it was found that the nitronaphthalenes and nitrobenzenes were the only classes of compounds to absorb weakly at 470 nm, and as a result, we reanalyzed the nitronaphthalene and nitrobenzene standards at a concentration more relevant to the high-NO_x SOA

Photooxidation of Naphthalene

samples characterized in the current study. Since the highest concentration of the nitronaphthalenes and of the nitrobenzenes was measured at ~ 5 ppm by the UPLC/(–)ESI-TOFMS technique (Tables 2S–4S, Supporting Information), the absorbance of a 5 ppm standard mixture of the nitronaphthalenes (i.e., 4-nitro-1-naphthol and 2-nitro-1-naphthol) and of the nitrobenzenes (i.e., 2-nitrophenol and 3-hydroxy-4-nitrobenzoic acid) was measured by the UV–vis technique. It was found that the absorbance of this standard mixture, which possessed a yellowish color characteristic of nitroaromatics in solution, was insignificant at this SOA-relevant concentration.

Non-nitro containing benzene standards (i.e., phthalic acid and *trans*-cinnamic acid) were also prepared and analyzed. These compounds did not contribute to the absorbance measurement at 470 nm, consistent with the lack of color observed in their respective standard solutions. As a result of these measurements, it was assumed that the absorbance (peroxide) measurements acquired for the high- and low- NO_x SOA samples were not affected by chemical artifacts. Finally, blank Teflon filters were also extracted and prepared in the same manner as the filter samples collected from chamber experiments; these blank filters produced no significant absorbance at 470 nm, indicating that the filter medium did not interfere with the peroxide measurements.

2.3.2. High-Resolution Time-of-Flight Aerosol Mass Spectrometry (HR-ToF-AMS). Real-time aerosol mass spectra were obtained using an Aerodyne HR-ToF-AMS.⁶⁰ The HR-ToF-AMS was operated in both a lower resolution, higher sensitivity “V-mode”, and a high-resolution “W” mode, switching between modes once every minute. The V-mode data were analyzed to extract sulfate, ammonium, and organic spectra.⁶¹ Calculation of the SOA densities were achieved by comparing the particle mass distributions obtained using the particle ToF mode and the volume distributions obtained by the DMA in nucleation (seed-free) experiments.⁶² O/C, N/C, and H/C ratios were determined from W mode data using the APES toolbox and applying the procedures outlined in Aiken et al.^{63,64} The particle-phase signal of CO^+ and the organic contribution to H_xO^+ ions were estimated as described in Aiken et al.⁶⁴

2.3.3. Particle-into-Liquid Sampler/Ion Chromatography (PILS/IC). The PILS/IC instrument is designed to measure aerosol water-soluble ions and is based on the original design of Weber et al.⁶⁵ The current instrument has been modified to utilize syringe pumps to introduce the samples from the impactor into vials for later analysis by IC.⁶⁶ Chamber air, sampled through a 1 mm cut-size impactor, is passed through three denuders (URG and Sunset Laboratories) to remove gas-phase species. The aerosol is mixed with steam in a condensation chamber and grows by condensation of supersaturated water vapor to diameters $>1 \mu\text{m}$. Droplets grow sufficiently large to be collected by impingement on a quartz impactor, are washed to the bottom of the impactor, then collected and stored in airtight vials. Vials are analyzed off-line by IC (ICS-2000 with 25 μL sample loop, Dionex Inc.); columns used in the IC and the chromatographic methods employed have been previously described in detail by Sorooshian et al.⁶⁶ Vials were collected prior to each experiment to establish background levels of individual species, including Na^+ , NH_4^+ , K^+ , Mg^{2+} , Ca^{2+} , SO_4^{2-} , Cl^- , NO_2^- , NO_3^- , oxalate, pyruvate, formate, and phthalate. Chromatographic peaks were identified and quantified using authentic standards; standards used in the current work are: teraphthalic acid, benzoic acid, *trans*-cinnamic acid, 5-hydroxy isophthalic acid, 1,2,4-benzene tricarboxylic acid, 4-formylcinnamic acid, 2-hydroxy isophthalic acid, 3-hydroxy benzoic

acid, 4-hydroxybenzoic acid, 3-formyl benzoic acid, 3-hydroxy-4-nitrobenzoic, 2-nitrophenol, 2-nitro-1-naphthol, 4-nitro-1-naphthol, and salicylic acid. Additionally, the presence of dicarboxylic acids of C_2 (oxalic), C_3 (malonic), C_4 (succinic), C_5 (glutaric), and C_6 (adipic) compounds were investigated using authentic standards.

2.4. Ambient Aerosol Samples: Filter Collection Protocols and Off-Line Chemical Analysis. Selected archived quartz fiber filters collected from Birmingham, AL during the Southeastern Aerosol Research and Characterization (SEARCH) 2004 campaign were reanalyzed by the UPLC/(–)ESI-TOFMS technique, as described above for the naphthalene SOA chamber filters. Details of the SEARCH network, which includes descriptions of each site, aerosol filter sample collection protocols, gas- and particle-phase measurements conducted, can be found elsewhere.^{67,68} Birmingham, AL (denoted as BHM in the SEARCH network) is an urban site consisting of both industrial and residential settings. Quartz fiber filter extractions and sample preparation procedures have been described previously.⁶⁹ However, solid-phase extraction (SPE) was not employed in the current study to avoid possible loss of early eluting naphthalene SOA products.

In addition to the ambient aerosol filters samples collected from Birmingham, AL, quartz fiber filters were also collected in Pasadena, CA, during June and July, 2009 using the same high-volume filter sampling approach as used by the SEARCH network. These samples are a part of the Pasadena Aerosol Characterization Observatory (PACO), an ambient sampling study located on the campus of Caltech. Selected PACO filter samples collected on June 3, June 19, and July 14, 2009, were analyzed by the UPLC/(–)ESI-TOFMS technique as described above. These filters represent 4 h integrated morning (7–11 a.m.) and 4 h integrated afternoon (3–7 p.m.) sampling periods. June 19 and July 14 were chosen for this chemical analysis due to the high total organic mass aerosol loadings as measured by a compact time-of-flight AMS instrument (maximum of 21.12 and 11.72 $\mu\text{g m}^{-3}$, respectively, assuming a collection efficiency of 0.5), O_3 mixing ratios (71 and 56 ppb, respectively), and daytime temperature (29 and 34 $^\circ\text{C}$, respectively). June 3 was chosen as a relatively clean day for comparison with June 19 and July 14, and had a maximum total organic mass aerosol loading of 5.66 $\mu\text{g m}^{-3}$ (assuming a collection efficiency of 0.5), O_3 mixing ratio of 19 ppb, and daytime temperature of 20 $^\circ\text{C}$. Further results and details from the PACO 2009 campaign will be presented in a forthcoming publication. Here, the chemical characterization data obtained from the ambient filters were compared to that of the naphthalene SOA chamber experiments to identify potential ambient SOA tracer compounds that can be used in source apportionment studies.

2.5. Chemicals. Most of the reagents used in this study were purchased from Sigma Aldrich and their stated purities are listed in Table 1S (Supporting Information). Additionally, 2-formylcinnamaldehyde was synthesized by ozonolysis of naphthalene using the technique of Larson et al.,⁷⁰ but was not purified. Identification of both *E*- and *Z*- isomers was confirmed by NMR measurements.

3. Results

3.1. High- NO_x Conditions.

3.1.1. Chemical Characterization of High- NO_x Gas-Phase Oxidation Products. Table 3 lists the gas-phase products detected by the CIMS instrument in positive and negative ion modes and structures identified by the GC/EI-TOFMS technique. These data are compared to aerosol measurements made by the UPLC/ESI-TOFMS technique, thus establishing the connection between the gas and particle phases. When the CIMS is operated

TABLE 3: Summary of Chemically Characterized Gas- and Particle-Phase Products Produced from the Photooxidation of Naphthalene

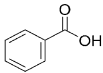
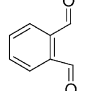
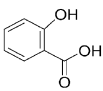
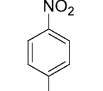
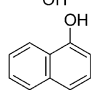
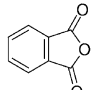
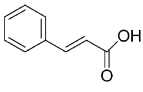
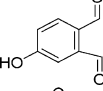
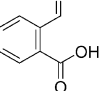
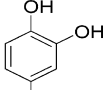
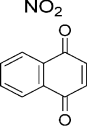
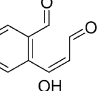
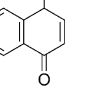
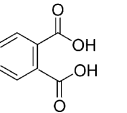
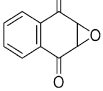
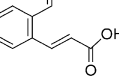
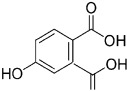
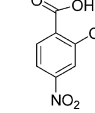
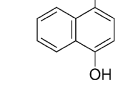
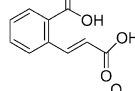
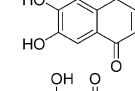
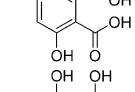
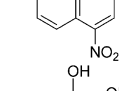
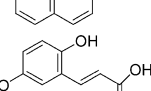
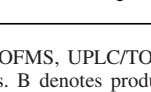
MW	Gas-phase measurements			Particle-phase measurements					proposed structure ^g	
	CIMS detection ^a			GC/EI-TOFMS		UPLC/ESI-TOFMS				
	[M + H] ⁺	[M + F] ⁻	[M + CF ₃ O] ⁻	accurate mass	error (mDa)	accurate mass ^b	avg. error (mDa)	% SOA ^c HNO _x		% SOA ^d LNO _x
122	B	B		122.0368	-0.4	121.0301 121.0293 121.0267	0.3	1.57	2.12	
134	B			134.0390	2.4	135.0444	-0.2	n.q.	n.q.	
138		B	B			137.0253 137.0228 137.0255 137.0222	-0.05	1.64	3.63	
139						138.0225 138.0179 138.0198	1.0	1.13	0	
144	B	B	B			143.0531 143.0536	3.7	n.q.	n.q.	
148	B	B	B							
148						147.0432 147.0473 147.0480	1.6	0.25	0.57	
150						151.0401	0.6	n.q.	n.q.	
50	B	B	B			149.0231 149.0241 149.0239 149.0248	-0.1	1.24	2.8	
155						154.013	2.5	0.94	0	
158	B			158.0387	1.9	159.0453	0.7	n.q.	n.q.	
160	B		B	160.0524	0.40					
160						161.0578	-2.5	n.q.	n.q.	
164						165.0539 165.0545 165.0525	-1.6	n.d.	n.q.	
166	B					165.0181 165.0148	2.3	2.71	4.01	

TABLE 3: Continued

MW	Gas-phase measurements			Particle-phase measurements				proposed structure ^e		
	CIMS detection ^a			GC/EI-TOFMS		UPLC/ESI-TOFMS				
	[M + H] ⁺	[M + F] ⁻	[M + CF ₃ O] ⁻	accurate mass	error (mDa)	accurate mass ^b	avg.error (mDa)		% SOA ^c	% SOA ^d
173				173.0495 173.0477	1.7 1.3					
174	B	B	B	174.0328	1.1					
176	B	B	B			175.0377 175.0375 175.0395 175.0403	0.8	1.46	0.53	
178	B		B			179.069	-1.8	n.q.	n.q.	
180						179.0325 179.0327 179.0341 179.0320	0.6	2.53	4.56	no tentative structure proposed
182						181.0128 181.0146 181.0128	0.3	3.3	9.8	
183						182.0096 182.0072	0.5	0.52	0	
189	H	H		189.0417	-0.9	188.0336 188.0367 188.0310 188.0341 188.0326 188.0357	0.9	0.4	0	
192	B					191.0364 191.0381 191.0345 191.0375	0.0	2.05	1.28	
192						193.0511	1.0	n.q.	n.q.	
198						197.0108	2.2	n.q.	3.5	
205			H			204.0295 204.0281 204.0286	1.0	0.39	0	
207						206.0477 206.0469	2.0	0.07	0	
208	B					207.03020 207.02891 207.02930 207.03070 207.02830	-0.6	2.18	4.54	

^a CIMS does not permit structural identification. All proposed structures are derived from either GC/TOFMS, UPLC/TOFMS, or previously identified structures found in the literature. H denotes products observed only under high-NO_x conditions. B denotes products observed under both NO_x conditions. ^b Accurate masses are determined by [M - H]⁻ or [M + H]⁺ mode. Reported masses are thus 1 H⁺ from the true mass. ^c High-NO_x case (HNO_x). ^d Low-NO_x case (LNO_x). ^e For simplicity only one isomer is shown. Number of observed isomers can be determined by the number of entries in the accurate mass column.

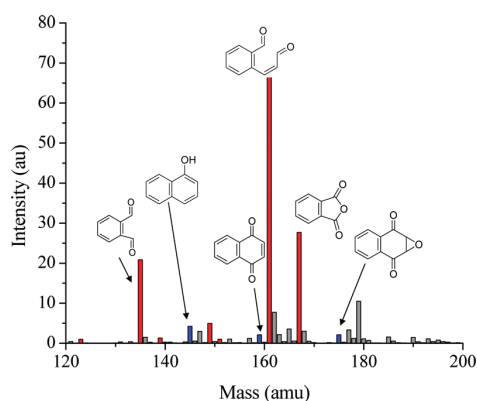


Figure 1. (+)CIMS mass spectrum taken at 70% reacted naphthalene under high- NO_x conditions. Red data indicate ring-opening products. Ring-retaining products are indicated in blue.

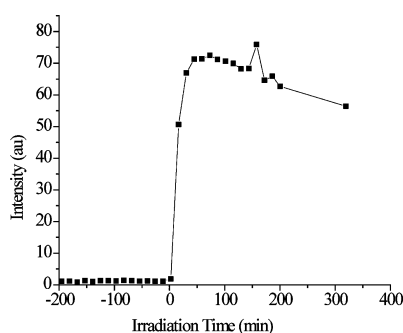


Figure 2. Time trace of 2-formylcinnamaldehyde obtained by the (+)CIMS technique.

in positive mode, compounds with proton affinities higher than that of water extract a proton and are subsequently detected by quadrupole MS; this mode is used for detecting a wide variety of organic compounds. The masses seen in positive mode will generally be detected as $[\text{M} + \text{H}]^+$ ions and are denoted in the CIMS $[\text{M} + \text{H}]^+$ column shown in Table 3. The negative mode of operation is highly selective toward acidic and polar molecules. The analyte clusters with CF_3O^- forming an $[\text{M} + \text{CF}_3\text{O}]^-$ cluster ion, or subsequently loses CF_2O to form the $[\text{M} + \text{F}]^-$ ion. Generally, identification of an $[\text{M} + \text{F}]^-$ ion corresponds with detecting carboxylic acids, while $[\text{M} + \text{CF}_3\text{O}]^-$ ions may also include hydroxy carbonyls. Owing to the unit-mass resolution of the CIMS technique, structural assignments are based on the results from the GC/EI-TOFMS and from previous results on the photooxidation of naphthalene. Products identified, along with suggested structures and accurate mass measurements obtained by the GC/EI-TOFMS technique are presented in Table 3.

The (+)CIMS mass spectrum from a typical high- NO_x experiment is shown in Figure 1. 2-Formylcinnamaldehyde (at m/z 161), phthalaldehyde (at m/z 135), and phthalic anhydride (at m/z 167) represent the largest peaks. We refer to these compounds as “ring-opening” products and indicate their presence in Figure 1 by the red mass spectral peaks. These observed compounds are consistent with those of other studies that report products of naphthalene and will be discussed subsequently. Closed-ring or “ring-retaining” compounds, such as isomeric naphthols (at m/z 145), 1,4-naphthoquinone (at m/z 159), 2,3-epoxy-1,4-naphthoquinone (at m/z 175), and isomeric nitronaphthols (at m/z 190), are also tentatively identified, as indicated by blue mass spectral peaks in Figure 1.

In the CIMS positive mode, the most abundant gas-phase product identified is a compound detected at m/z 161 (Figure 1). This compound is also observed in the GC/EI-TOFMS data and is positively identified as 2-formylcinnamaldehyde based on a mass spectral comparison with a synthesized standard (as shown in Figure 2S, Supporting Information). The present amounts of this compound are significantly less than found in other studies^{71,72} due to losses in the preconcentrator. The time trace for 2-formylcinnamaldehyde under typical high- NO_x conditions in Figure 2 indicates that 2-formylcinnamaldehyde grows rapidly once oxidation is initiated, then decays relatively slowly. From the (–)CIMS measurements, we learn that, after about 2 h of irradiation, all the HONO is consumed; naphthalene concentrations stabilize and generation of 2-formylcinnamaldehyde ends. 2-formylcinnamaldehyde then decays at a rate of 0.06 h^{-1} due to photolysis. After 6 h of irradiation, ~70% of the initially formed 2-formylcinnamaldehyde remains.

Results from the GC/EI-TOFMS technique demonstrate the presence of both the 1- and 2-nitronaphthalene isomers in the gas phase. 1-Nitronaphthalene has been positively identified using an authentic reference standard (Sigma-Aldrich, 99%) in conjunction with NIST library matching. 2-Nitronaphthalene is identified based on NIST library matching, accurate mass measurements, and comparison of the mass spectrum with the 1-nitronaphthalene isomer. Nitronaphthols are also identified based on NIST library matching. The 4-nitro-1-naphthol authentic standard was run for comparison, but did not match the retention time of the assigned peak. We expect that this is another structural isomer of 4-nitro-1-naphthol, most likely either 1-nitro-2-naphthol or 2-nitro-1-naphthol, both of which have been identified in previous studies.^{72,73} Naphthoquinone and 2,3-epoxy-1,4-naphthoquinone are also observed. In addition to these ring-retaining compounds, benzoic acid and phthalaldehyde are also observed by the GC/EI-TOFMS technique. Chromatograms for selected photooxidation products observed by the GC/EI-TOFMS method are shown in Figure 1S (Supporting Information).

The two methods of sample collection described in Section 2.2.3 yield similar results. Directly introducing the sample into the preconcentrator yielded greater intensities for the nitronaphthalene products; however, the gas-phase product of MW 160 (2-formylcinnamaldehyde) was detected with reduced efficiency using this method. Although the second Tenax tube method detected the gas-phase product of MW 160 with greater efficiency, phthalaldehyde was not detected. Detection of all other oxidation products was comparable using these two sampling techniques.

3.1.2. Chemical Characterization of High- NO_x SOA. The chemical composition of naphthalene SOA was probed with the battery of techniques described earlier. HR-ToF-AMS particle-phase data were acquired under a wide range of initial naphthalene mixing ratios. The naphthalene mixing ratios for which aerosol measurements from other instruments were acquired are 20–30 ppb. Hydrocarbon mixing ratios, along with the calculated density and observed aerosol atomic O/C, N/C, and H/C ratios are presented in Table 4. Errors in accuracy associated with AMS compositional ratios are reported as $\pm 30\%$, $\pm 22\%$, and $\pm 10\%$ of the measured O/C, N/C, and H/C ratios, respectively, in accordance with findings from Aiken et al.⁶⁴ Densities of 1.48 g cm^{-3} were found for high- NO_x SOA.

Under high- NO_x conditions, ~53% of the overall SOA mass is chemically characterized by off-line chemical analyses of aerosol filter samples using both the UPLC/(–)ESI-TOFMS and total peroxide content measurement techniques. An UPLC/

TABLE 4: Summary of Experimental Conditions and Results from the HR-ToF-AMS Instrument

[naphthalene] (ppb)	NO _x	seed vol (μm ³ /cm ³)	end vol (μm ³ /cm ³)	density (g/cm ³)	SOA mass (μg/m ³)	O/C ratio	N/C ratio	H/C ratio
5	low	10.64	18.48	1.55	12.15	0.61 ± 0.18	0	0.97 ± 0.1
20	low	10.48	41.48	1.55	48.06	0.72 ± 0.22	0	0.88 ± 0.09
60	low	13	143	1.55	201.5	0.6 ± 0.18	0	0.82 ± 0.08
5	high	12.25	16.23	1.48	6.18	0.55 ± 0.17	0.01 ± 0.02	1.03 ± 0.1
25	high	12.82	39.18	1.48	40.87	0.55 ± 0.17	0.01 ± 0.02	0.90 ± 0.1
30	high	0	26.3	1.48	40.76	0.45 ± 0.15	0.01 ± 0.02	0.90 ± 0.1
40	high	14.67	63.11	1.48	75.08	0.51 ± 0.15	0.01 ± 0.01	0.81 ± 0.08

(−)ESI-TOFMS base peak ion chromatogram (BPC) obtained for a typical high-NO_x naphthalene SOA experiment is shown in Figure 3. Peaks found under both the high- and low-NO_x conditions are denoted in black, while those SOA constituents found only in the high-NO_x case are denoted in green. Due to the use of (NH₄)SO₄ seed aerosol, bisulfate (detected as *m/z* 97) was found to elute first from the reverse-phase C18 column. A complete listing of the high-NO_x SOA constituents identified and quantified by the UPLC/(−)ESI-TOFMS technique is provided in Tables 2S–4S (Supporting Information). As shown in Tables 2S–4S (Supporting Information) and Table 3, ~24–28% of the high-NO_x naphthalene SOA is chemically characterized at the molecular level by the UPLC/(−)ESI-TOFMS technique. These chemical characterizations are further supported by the tandem MS measurements provided by the HPLC/(−)ESI-ITMS technique; major product ions produced for each of the major characterized high-NO_x SOA constituents are also listed in Tables 2S–4S (Supporting Information). All SOA constituents were quantified by calibration with either an authentic or surrogate standard. Dominant contributions to the high-NO_x SOA mass come from phthalic acid and hydroxy benzoic acids. Standard deviations for each UPLC/(−)ESI-TOFMS identified product were calculated across experiments (experiments 2–5 in Table 2). The fraction of SOA mass assigned to each product has a standard deviation of less than 3%, and the average standard deviation for the entire product range was ~2%, indicating the high level of reproducibility of these experiments.

As shown by the time trace in Figure 4, analysis by the PILS/IC technique confirms that phthalic acid is a significant component of the high-NO_x SOA (Retention Time (RT) = 13.88

min), increasing from 0 to 5.23 μg m^{−3} over the course of the experiment (Experiment 7 in Table 2). Figure 5 shows the ion chromatograms for a high-NO_x chamber sample on the bottom panel. The top panel shows a chromatogram from a 2 ppm standard of phthalic acid. The chromatographic peak with RT of 15.27 min also shows trends of increasing concentration with photochemical age and is not present in background vials, suggesting that this peak corresponds to a SOA constituent; however, this compound could not be identified using available standards. No other water-soluble SOA constituents are observed by the PILS/IC technique, indicating that small organic acids do not account for the unidentified fraction of the SOA mass. This is in contrast to data from the photooxidation of single-ringed aromatic compounds, such as benzene, toluene, and *m*-xylene, for which small organic acids comprise a substantial portion of the overall SOA mass (unpublished data). Small organic acids have also been observed in SOA generated from the photooxidation of 1,3,5-trimethylbenzene.⁷⁴

On the basis of results from the UPLC/(−)ESI-TOFMS method, N-containing compounds account for ~3% of the total high-NO_x SOA mass formed. Most of the N-containing compounds were quantified using calibration curves generated by either 2-nitro-1-naphthol or 4-nitro-1-naphthol standards. Using 4-nitro-1-naphthol in the quantification of these products yields concentrations that are an order of magnitude reduced from calibrations utilizing the 2-nitro-1-naphthol isomer. Final quantitative results reported here are determined by use of the more conservative mass concentrations. Quantification of these chemically characterized SOA constituents yields an N/C ratio of 0.04. This ratio should be considered as a lower limit for the N/C ratio, because some of the N-containing compounds that are

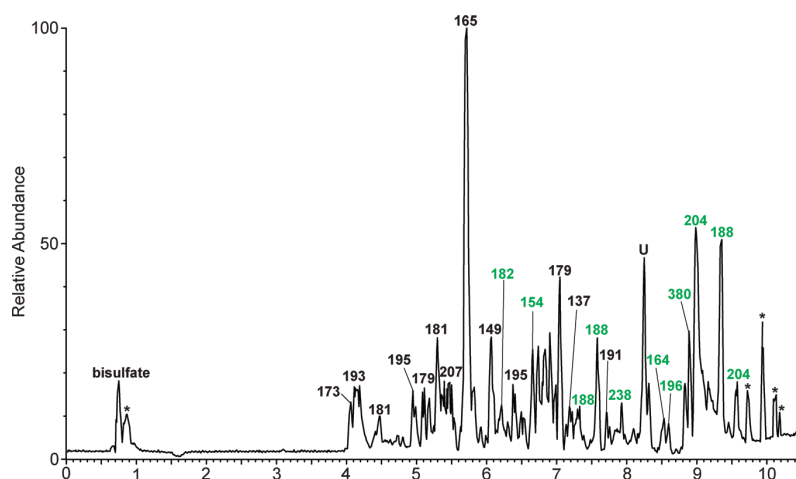


Figure 3. UPLC/(−)ESI-TOFMS base peak ion chromatogram (BPC) of a representative naphthalene high-NO_x SOA sample (Experiment 6). Chromatographic peaks designated with black [M − H][−] ions are also observed in the naphthalene low-NO_x SOA samples. Chromatographic peaks designated with green [M − H][−] ions are only observed in the naphthalene high-NO_x SOA samples. Chromatographic peaks designated with an asterisk, *, were also observed on a blank filter, and they are not considered high-NO_x SOA constituents. Major chromatographic peaks that remain uncharacterized in this study are designated as: U.

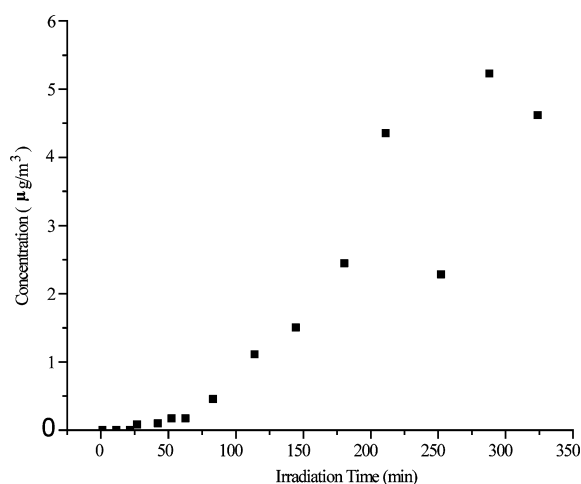


Figure 4. Time trace of phthalic acid acquired from Experiment 6 using the PILS/IC technique.

likely formed are not directly detectable by the UPLC/(−)ESI-TOFMS technique unless the molecule also contains a functional group with an acidic proton that can be abstracted. For example, the UPLC/(−)ESI-TOFMS method detects six isomers of nitronaphthol, as shown in Table 3; however, the 1- and 2-nitronaphthalene compounds identified in the gas phase by the GC/EI-TOFMS technique are not detected, even though the nitronaphthalenes are reported to exist primarily in the particle phase.⁴⁶ Given that the 1- and 2-nitronaphthalene isomers are reported to account for 0.3–7%^{43,45,72} of the gas-phase yield, and may partition into the particle phase,⁴⁶ the detection of these nonacidic nitronaphthalenes in the aerosol phase would likely increase the N/C ratio. We also expect that the formation of PANs, for example from phthaldialdehyde, may play a significant role in SOA formation in the atmosphere. However, owing to the large NO to NO₂ ratio employed in these experiments, and to the difficulty in detecting nonacidic N-containing compounds, PANs are not observed in either the gas- or aerosol-phase.

Bulk HR-ToF-AMS measurements yield measurements of N-containing compounds producing N/C ratios ranging from 0.01–0.044. We place upper and lower bounds on the N/C ratio using calculations with and without the addition of compounds that possess NO⁺ and NO₂⁺ mass spectral peaks, respectively. Under high-NO_x conditions, OH and NO₂ can react to form nitric acid. Nitric acid can then react with ammonium from the ammonium sulfate seed to produce inorganic nitrates. This process should be of minimal importance for the experiments performed here owing to the dry experimental conditions; however, for the lower-limit calculations, we exclude compounds that have contributions from NO⁺ and NO₂⁺ mass spectral peaks from the N/C calculation to prevent biasing the chemical composition calculations with the formation of these inorganic nitrates. These lower-limit calculations include only the measurement of organic nitrate (NO₃) functional groups, yielding an atomic N/C ratio of 0.01. Only one organic nitrate is identified by the UPLC/(−)ESI-TOFMS method, supporting the minimal contribution from this class of compounds. However, inclusion of “NO family” ions with mass spectral peaks corresponding to NO⁺ and NO₂⁺ is necessary to account for the NO₂ groups observed in compounds such as nitronaphthalene, but may introduce artifacts from inorganic nitrates. Inclusion of the NO and NO₂ groups increases the atomic N/C ratio to 0.044, thus providing an upper bound of the N/C ratio. Inclusion of these compounds into the composition calculations also shifts the O/C ratios from 0.51 ± 0.17 (Table 4) to 0.57 ± 0.17. Again, the upper-bound of 0.044 ± 0.01 for the N/C is in good agreement with the lower bound of 0.036 obtained from the UPLC/(−)ESI-TOFMS data as discussed above.

In general, the procedures for compositional analysis determined from high-resolution AMS data are still relatively new, and further studies of the technique are necessary to fully understand the data acquired using this complex instrument. For example, calibrations of compositional ratios performed here are based on AMS data from Aiken et al.,⁶³ which likely possess a different molecular composition than that of the current experiments. To achieve more accurate ratios, the ionization efficiency of each oxidation product by atomizing standards into

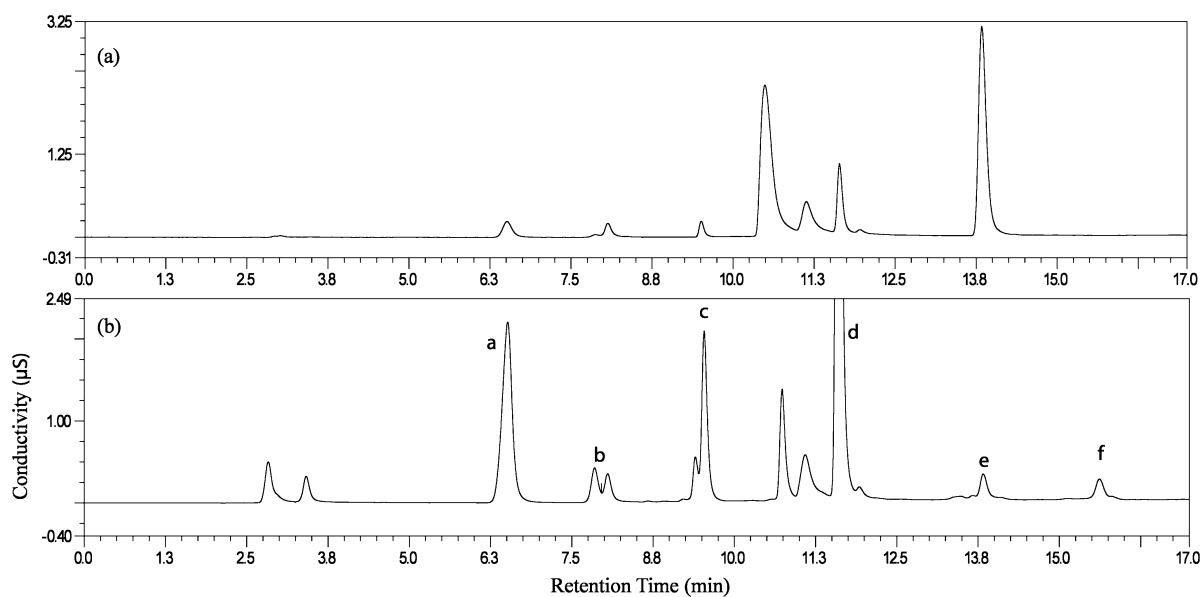


Figure 5. Chromatograms obtained by the PILS/IC technique. The top panel shows a 2 ppm standard of phthalic acid. The bottom panel shows a representative chromatogram of a PILS sample collected under high-NO_x conditions in the presence of ammonium sulfate seed (Experiment 7). Peak assignments are: a-chloride, b-nitrite, c-nitrate, d-sulfate, e-phthalic acid, f-unidentified peak (see text).

Photooxidation of Naphthalene

the AMS instrument need to be investigated or alternatively, a much larger database of structures would need to be assembled. More work needs to be performed to fully characterize the appropriateness of the compositional ratios acquired by this technique, particularly for the N-containing compounds which have received less attention.

The high- NO_x naphthalene SOA chemically characterized through the filter sampling methods exhibits an average atomic O/C ratio of 0.48. This ratio is largely consistent with the measurements from the HR-ToF-AMS technique, from which an overall O/C ratio of 0.51 ± 0.17 is detected. Atomic H/C ratios of 0.83 calculated from the filter data are also in agreement with the HR-ToF-AMS value of 0.9 ± 0.10 , and as stated above, the N/C ratios are also in relative agreement. The implications of the agreement of the O/C, H/C, and N/C ratios between these two analytical techniques is that the 53% of the total SOA mass that has been chemically characterized is an excellent representation of the chemical composition and oxidation level of the entire high- NO_x naphthalene SOA.

The total peroxide measurement based on the iodometric spectroscopic method indicates that under high- NO_x conditions ~28% of the total SOA mass can be attributed to organic peroxides (i.e., ROOH and/or ROOR). Contributions of organic peroxides are calculated by determining the molar concentration of peroxides in the solution. The measured concentration of peroxides obtained by absorption at 470 nm is converted to $\mu\text{g m}^{-3}$ using the known solution volume, molar-weighted average mass, and the volume of chamber air sampled. The molar-weighted average MW is determined by multiplying the MW of each product by the product mole fraction and summing over the individual products. For the high- NO_x system, we have taken a molar-weighted average mass of the chemically characterized SOA constituents listed in Tables 2S–4S (Supporting Information) and assumed this to be the average MW of the unknown organic peroxide structures. The assumption that this average MW would be representative for the unknown organic peroxides is supported by the similar O/C, N/C, and H/C ratios found using both the chemically characterized filter data and the total aerosol HR-ToF-AMS measurements. For the high- NO_x case, the molar-weighted average mass is determined to be 172 amu. As will be discussed subsequently, we believe this is a conservative estimate of the average peroxide mass. If the actual average mass of the peroxides is indeed higher than the assumed mass of 172 amu, then the contribution from peroxides to the total SOA mass would increase. It should be noted that the iodometric spectroscopic method provides no detailed chemical characterization of the quantified organic peroxide content.

3.2. Low- NO_x Conditions.

3.2.1. Chemical Characterization of Low- NO_x Gas-Phase Oxidation Products. A representative (+)CIMS mass spectrum obtained for naphthalene photooxidation under low- NO_x conditions is shown in Figure 6. This mass spectrum was taken at the same fraction of naphthalene reacted as that for the high- NO_x experiment previously shown in Figure 2, and thus the extents of reaction are similar. Whereas the tentatively identified products are the same as those observed under high- NO_x conditions, the relative intensities of the identified compounds are substantially different. In the low- NO_x case, the intensities of the ring-retaining products (e.g., naphthol, naphthoquinone, and epoxyquinone), as denoted by blue mass spectral peaks in Figure 6, are all significantly greater than those found under high- NO_x conditions. Nevertheless, the m/z 161 signal continues to dominate the overall (+)CIMS mass spectrum. When compared with data from both the high- NO_x experiments and

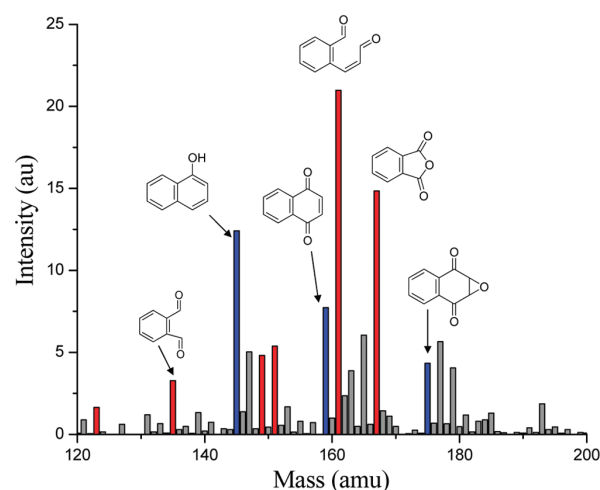


Figure 6. (+)CIMS mass spectrum taken at 70% reacted naphthalene under low- NO_x conditions. Red data indicate ring-opening products. Ring-retaining products are indicated in blue.

from injection of the synthesized standard, it is found that the GC retention times, mass spectra, and exact masses (i.e., chemical formulas) obtained using the GC/EI-TOFMS technique match, thus confirming that the compound observed at m/z 161 in the (+)CIMS mass spectrum under low- NO_x conditions is 2-formylcinnamaldehyde.

3.2.2. Chemical Characterization of Low- NO_x SOA. An UPLC/(–)ESI-TOFMS BPC obtained for a typical low- NO_x naphthalene SOA experiment is shown in Figure 7. Detailed comparison of this chromatogram and the high- NO_x BPC (Figure 3) demonstrates that the aerosol compositions are quite similar. All of the chromatographic peaks are also observed in the naphthalene high- NO_x SOA samples. No N-containing SOA constituents are observed under low- NO_x conditions due to the lack of NO and NO_2 addition reactions. Under low- NO_x conditions, we have been able to chemically characterize ~68% of the SOA mass, as compared to the ~53% identified in the high- NO_x regime. The increase in speciation is the result of a substantial enhancement in the concentration of the acidic species under low- NO_x conditions, with consistent peroxide contributions under both NO_x conditions. As shown in Table 3 and in Supporting Information, the fractions of total SOA mass attributed to phthalic acid and hydroxy phthalic acid, for example, increase by factors of 2 and 3, respectively. Similar increases are observed for benzoic acid, hydroxy benzoic acid, cinnamic acid, and dihydroxy cinnamic acid. The ring-retaining compounds are present in low- NO_x SOA samples, but we cannot remark on their relative abundance compared to the high- NO_x case, owing to the fact that standards are often not available, and these components were not quantified. Detection efficiencies for these nonacidic ring-retaining compounds are lower than those of the acidic ring-opening compounds. Hydroxy cinnamic acid (see Table 3, MW 164) was the only additional compound identified specific to the low- NO_x regime. The atomic O/C compositional ratio from filter sampling methods is 0.50, and the H/C ratio is 0.82. O/C and H/C ratios determined from the HR-ToF-AMS technique are 0.64 ± 0.19 and 0.89 ± 0.1 , respectively.

The total organic peroxide contribution was determined in the same manner as that carried out for the high- NO_x experiments as detailed in Section 3.1.2. The molar-weighted average mass was determined to be slightly higher than that of the high-

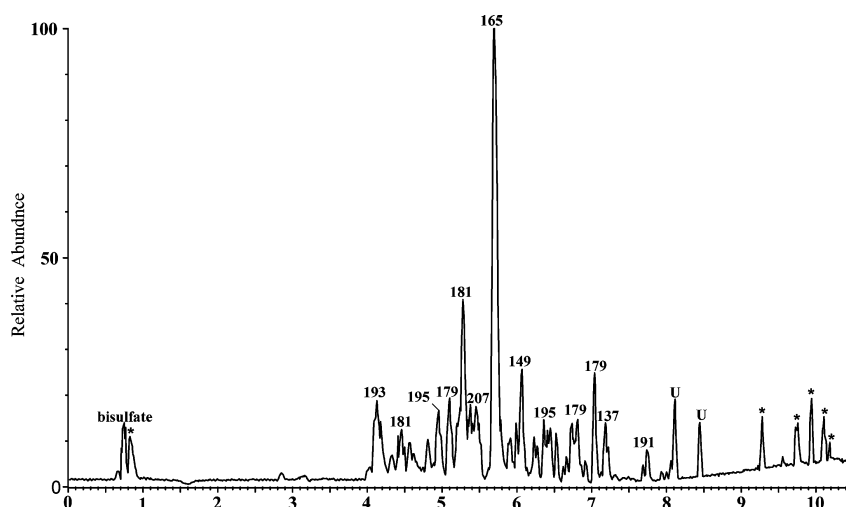


Figure 7. UPLC/(-)ESI-TOFMS base peak ion chromatogram (BPC) of a representative naphthalene low- NO_x SOA sample (Experiment 3). All major chromatographic peaks are marked with their corresponding $[\text{M} - \text{H}]^-$ base peak ions. Chromatographic peaks designated with an asterisk, *, were also observed on a blank filter, and they are not considered high- NO_x SOA constituents. Major chromatographic peaks that remain uncharacterized in this study are designated as: U.

NO_x SOA at 174 amu due to the increased contribution from larger acids, for example, hydroxy phthalic acid (MW 182 and observed by the UPLC/(-)ESI-TOFMS technique at m/z 181). The total peroxide contribution under low- NO_x conditions is calculated to be $\sim 26.2\%$ of the total SOA mass. This is similar to the 28% contribution found in the high- NO_x case. As in the high- NO_x case, we believe this to be a lower limit of the total peroxide contribution to the SOA mass.

4. Discussion

4.1. High- NO_x Conditions.

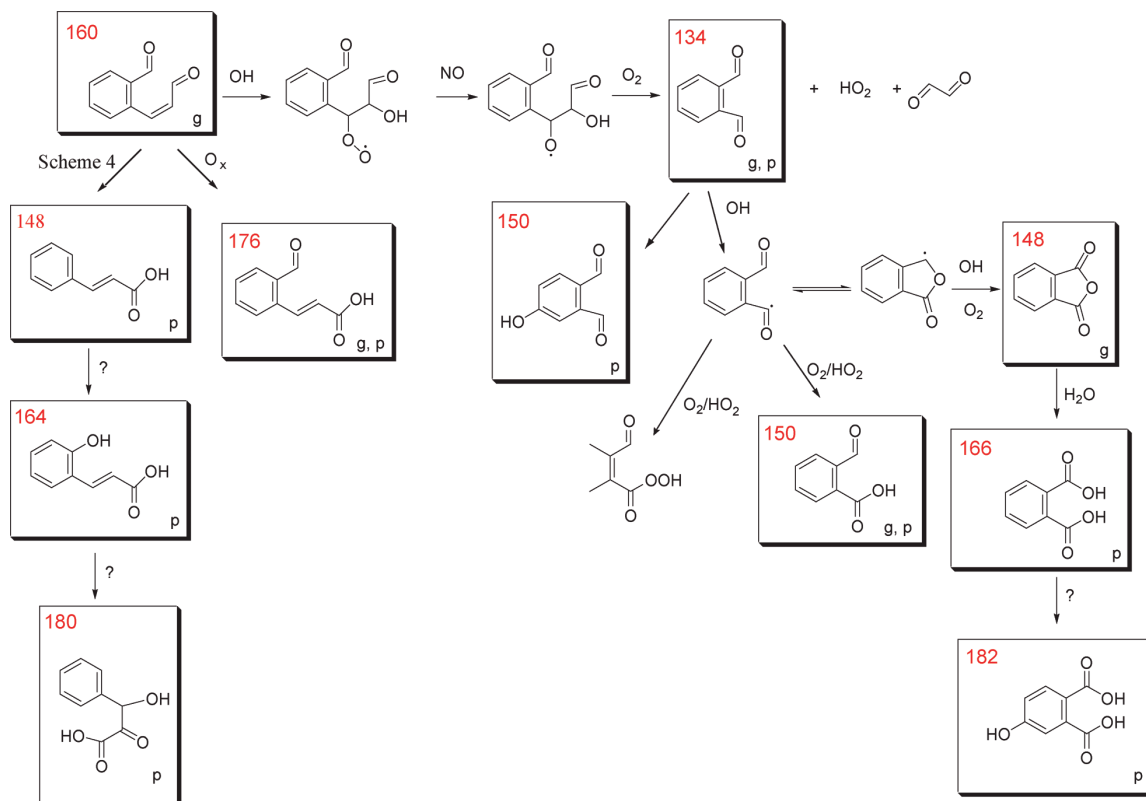
4.1.1. High- NO_x Gas-Phase Chemistry. The gas-phase mechanism of naphthalene photooxidation has been the subject of considerable study. Our present findings can be viewed within the context of this prior work. We concentrate first on the high- NO_x case, an atmospherically interesting situation owing to the coemissions with other anthropogenic sources and the relatively short lifetime of naphthalene in the urban atmosphere.^{43,75–78} Proposed formation mechanisms of the major high- NO_x naphthalene gas-phase products are provided in Scheme 1. The gas-phase photooxidation products detected are boxed, and the MWs of the identified products are highlighted in red. The mechanism presented here does not incorporate all of the chemically characterized products; a complete list of identified products can be found in Tables 2S–4S (Supporting Information). The majority of the gas-phase mechanism has been previously established.^{43,45,47,72,79,80} Qu et al.⁸¹ have performed theoretical calculations exploring the OH oxidation of naphthalene in the presence of O_2 and NO_x , and have detailed much of the gas-phase reaction dynamics. As determined by Wang et al.,⁴⁷ 68% of the OH addition occurs at the C_1 position to form the hydroxycyclohexadienyl radical. The 1-hydroxycyclohexadienyl radical lies 10 kcal mol^{-1} lower in energy than the 2-isomer.⁸¹ The preference for addition at the 1-site is supported by the fact that 2-nitronaphthalene is ~ 2 times more abundant than the 1-nitronaphthalene isomer.⁸⁰ The addition, the 1-site also determines the formation of the epoxide, although 2-formylcinnamaldehyde could be formed from either the 1- or 2-hydroxycyclohexadienyl radical.

The OH-naphthalene adduct reacts with either NO_2 or O_2 . GC/FID data combined with GC/MS-negative ion chemical

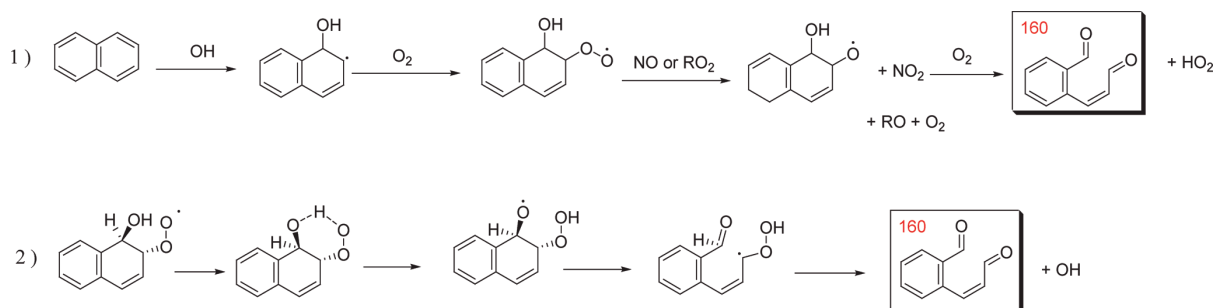
ionization (NCI) data from other chamber studies⁸⁰ suggest that the NO_2 and O_2 reactions with the OH-naphthalene adduct may be of equal importance for NO_2 mixing ratios in the range of 60 ppb. The NO_2 mixing ratio used in the present high- NO_x experiments is ~ 80 ppb, so these pathways should be of roughly equal importance in the present experiments. A detailed description of the importance of the NO/NO_2 in these experiments is previously discussed in Section 3.2.1.

The N-containing compounds (i.e., nitronaphthalenes and nitronaphthols) formed through the NO_2 reaction pathway are of particular interest due to their mutagenic properties.^{50,51} In extensive studies of the nitronaphthalene isomers, along with other nitroarene compounds, Arey and co-workers^{43,48,73,80,82} have found that both 1- and 2-nitronaphthalene isomers form during daytime conditions by OH reaction of naphthalene, but actually concentrations of these compounds reach a maximum at night due to N_2O_5 chemistry.⁴⁸ The major loss process for 1- and 2-nitronaphthalene under atmospheric conditions is photolysis, with photolytic lifetimes on the order of 2 h.⁷³ Photolysis is approximately an order of magnitude more important than OH reaction, for which the reaction rate coefficients are 5.4×10^{-12} $\text{cm}^3 \text{ molecule}^{-1} \text{ s}^{-1}$ and 5.6×10^{-12} $\text{cm}^3 \text{ molecule}^{-1} \text{ s}^{-1}$ for the 1- and 2-nitro isomers, respectively. Arey et al.⁷³ also suggest that 1-nitronaphthalene is the precursor to the 1,4-naphthoquinone product, which is formed through a photolysis pathway, denoted in Scheme 1 by an open arrow. These OH rates are consistent with the work of Bunce et al.⁴⁵ for which lifetimes of 20–34 h against OH reaction for the 1-nitronaphthalene and 2-nitronaphthalene isomers, respectively, were calculated using the same OH concentration, but neglecting the photolysis pathway.

Formation of ring-opening compounds is consistent with decomposition of the alkoxy (RO) radicals formed from the RO_2 + NO pathway,⁷² which leads to 2-formylcinnamaldehyde (MW 160) and observed by the (+)CIMS technique at m/z 161, the precursor to the majority of the ring-opening products found in Scheme 2. 2-formylcinnamaldehyde is detected as both *E*- and *Z*- isomers and is the major gas-phase product observed under high- NO_x conditions.^{45,71,72} Sasaki et al.⁷² suggested a combined yield for the cinnamaldehyde *E*- and *Z*- isomers of 35%. Although two further compounds with MW 160 are identified,

SCHEME 2: Proposed Mechanism for the Formation of Ring-Opening Products from the Further Reaction of 2-Formylcinnamaldehyde^a

^a Observed products are boxed. MWs are shown in red, and the phase of the observed product (gas, g, or particle, p,) is denoted in the lower right corner.

SCHEME 3: Suggested Mechanism for the Formation of 2-Formylcinnamaldehyde^a

^a Mechanism 2 from ref 81 begins with the formation of the peroxide assuming the same initial steps as demonstrated in mechanism 1.

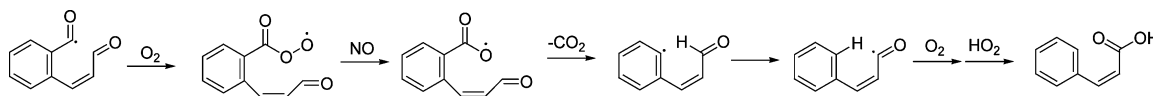
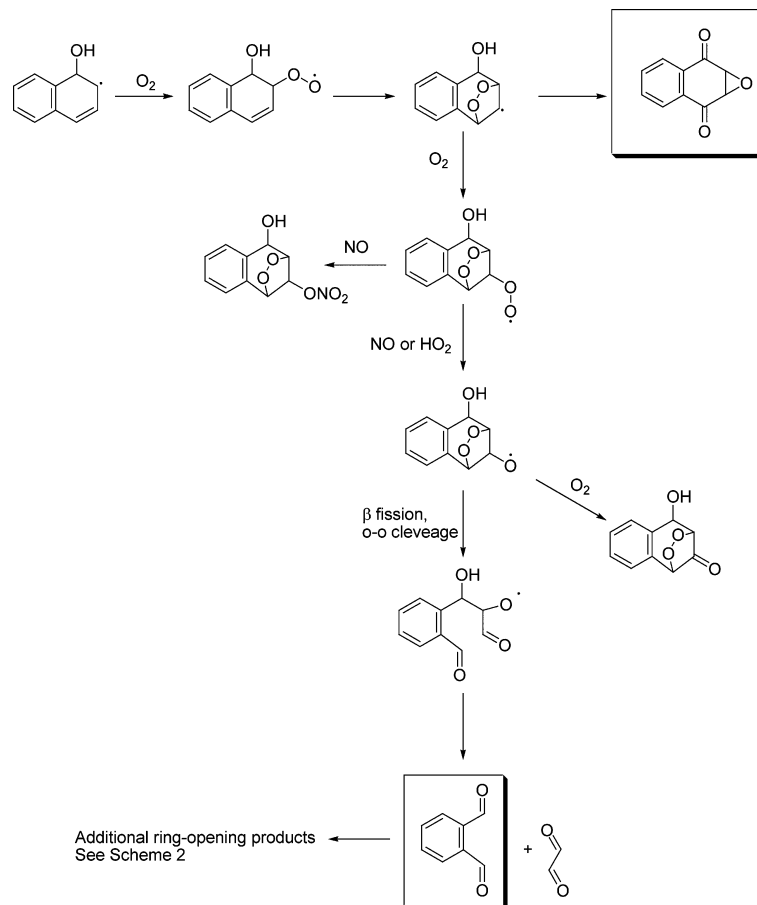
of 58–61% for the combined *E*- and *Z*- isomers of 2-formylcinnamaldehyde with the OH-reaction and photolysis decay pathways being of equal importance under experimental conditions.

In addition to the aforementioned products we have identified a range of C₇ and C₉ compounds (benzoic acid, etc) in low abundance. While some of these compounds have been previously observed,⁴⁵ a mechanism leading to them has not yet been proposed. We suggest two possible mechanisms as minor routes. Photolytic loss of the formyl group from 2-formylcinnamaldehyde followed by a hydride shift to the benzene ring and further oxidation by O₂ and HO₂ seems to be a plausible mechanism for forming compounds in this class.

Alternatively, as shown in Scheme 4, C₇ and C₉ compounds could be formed through O₂ addition to the radical formed on

the formyl group by H-abstraction by OH radical to form a RO₂ radical that subsequently reacts with NO to form an alkoxy radical. Loss of a CO₂ moiety followed by a hydride shift and oxidation of the radical carbonyl to form an acid would generate the observed product with MW 148 denoted in Scheme 2. Similarly, the corresponding peroxyacid would likely be formed in conjunction with the acid (MW 148) during the O₂ addition, and may go on to further react in the aerosol phase.

4.1.2. High-NO_x SOA Chemistry. Two previous studies have addressed the chemical composition of SOA formed from the photooxidation of naphthalene.^{46,84} We present here detailed quantitative analysis on the chemical composition and potential reaction pathways relevant to naphthalene high-NO_x SOA formation. The compounds identified from the UPLC/(–)ESI-TOFMS analysis of filter samples yield atomic O/C, N/C, and

SCHEME 4: Possible Mechanism for the Formation of C7 and C9 Compounds**SCHEME 5: Proposed Reaction Mechanisms for Bicyclic Peroxide Structure**

H/C ratios that are in agreement with bulk measurements from HR-ToF-AMS samples. This indicates that the chemical nature of the characterized SOA constituents is a good representation of the bulk aerosol formed from the photooxidation of naphthalene under high- NO_x conditions. The chemical mechanisms shown in Schemes 1 and 2 demonstrate how the gas-phase oxidation products are likely to evolve by further oxidation to form the components identified in the aerosol phase. The “g” and “p” superscripts associated with each product denote the phase of the component. A minor fraction of the SOA mass is attributed to the N-containing compounds such as nitronaphthols. The chemically characterized portion of the aerosol, which we assume to be representative of the bulk aerosol based on detailed composition measurements, is primarily composed of single-ring (ring-opening) acids (e.g., formylcinnamic acid and further oxidized compounds from phthalic acid).

We have performed calculations determining the average number of carbonyls/molecule for the SOA in order to compare with previous FTIR measurements. Dekermenjian et al.⁸⁴ reported an average of 3.2 carbonyl/molecule based on the assumption that the average molecule possesses a 10 carbon backbone. As shown in Table 3, many of the compounds with

significant yield possess C8 structures, thus calling into question the appropriateness of assuming a 10-carbon backbone. In order to determine the average number of carbonyls/molecule we have counted the number of carbonyl groups on each identified product, and weighted this number by mole fraction, to establish that the average structure possesses ~ 1.25 carbonyls/molecule. We believe the average we report here is an accurate representation of the degree of molecular oxidation, as it is based on identified structures for which the bulk composition is known. In comparison, the chemical composition determined by FTIR will be strongly dependent on the length of the carbon backbone, the accuracy of the composition calibrations, and the form of the carbonyl group (e.g., acidic, aldehydic, or ketone).⁸⁵

Organic peroxides are found to contribute $\sim 28\%$ of the total high- NO_x SOA mass. We propose that a mechanism for the formation of these compounds may occur through the formation of a bicyclic peroxy radical as shown in Scheme 5. Analogous reaction pathways have been examined in single-ringed aromatic hydrocarbons (SAH). For toluene, benzene, and *m*-xylene it was proposed that isomerization of the primary RO_2 radical to form the bridged bicyclic structure is faster than the competing reaction with NO_2 , and a reaction with NO to form the RO

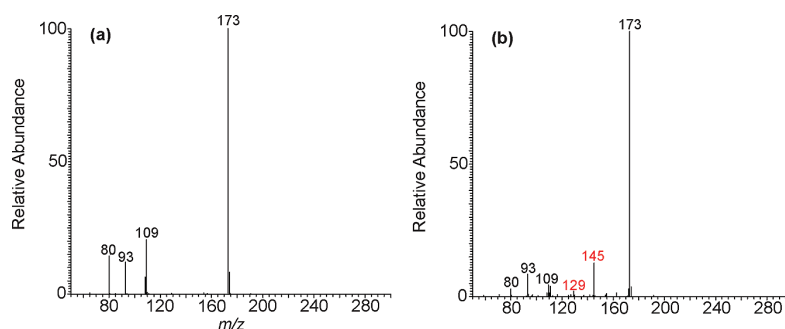


Figure 8. (–)ESI-ITMS MS² of *m/z* 173 collected via direct infusion analysis from (a) a 20 ppm 4-hydroxybenzene sulfonic acid standard and from (b) a naphthalene high-NO_x SOA sample (Experiment 6). Due to the generation of these MS² spectra via direct infusion, isobaric *m/z* 173 ions were analyzed simultaneously from the high-NO_x SOA sample. As a result, red ions highlighted in (b) are not due to the hydroxybenzene sulfonic acid. Product ions observed at *m/z* 93 and 109 are due to neutral losses of SO₂ and SO₃, respectively, which are neutral losses characteristic of aromatic sulfonates. The product ion observed at *m/z* 80 is due to the production of SO₃[–], which is also a characteristic ion of aromatic sulfonates. The hydroxybenzene sulfonic acids lack the presence of a *m/z* 97 ion (i.e., HSO₄[–]) in their MS² spectra, which is a characteristic product ion of organosulfate functional groups (–ROSO₃).

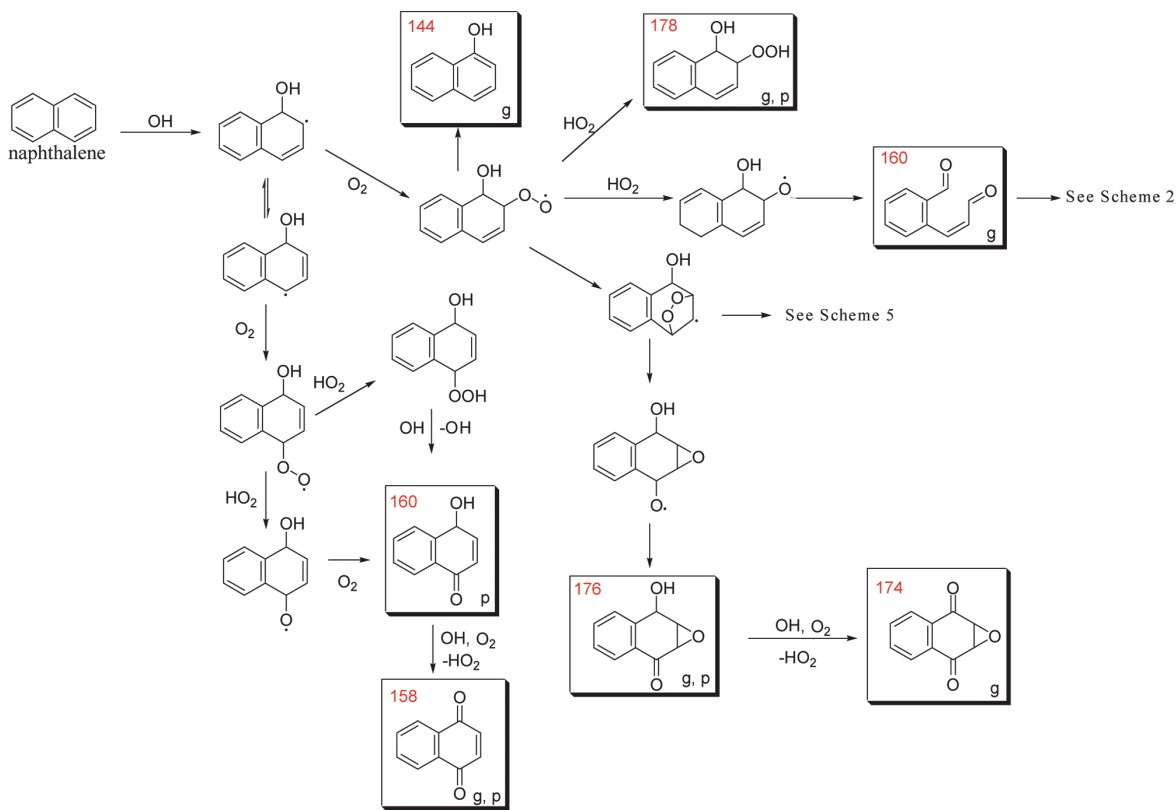
radical may only occur after O₂ addition.⁸⁶ The simplest bicyclic structure from naphthalene, which has molar mass of 192 amu, is shown below in Scheme 5. Thus, structures related to the bicyclic RO₂ radical would yield masses of 192 or higher, and the contributions from peroxides based on the average yield-weighted calculations detailed in Section 3.1.2 would be underestimated. If one uses the single-ringed aromatic compounds as exemplary of the PAH products, then a reasonable mechanism for both peroxides and ring-opening products can be determined as shown in Scheme 5. The initial naphthalene–OH adduct can either undergo hydrogen abstraction through reaction with O₂ to form naphthol or can react with O₂ to form the RO₂ radical. For benzene, master equation calculations suggest that formation of the phenolic compound accounts for 55–65% of the reaction mechanism, and the formation of the bicyclic peroxy radical is the other major pathway.⁸⁷ Resonance fluorescence studies for several aromatic species have also shown that the OH-aromatic adduct reacts preferentially with O₂ over both NO₂ and NO to form either the alcohol or the bicyclic peroxide structure, and reaction with NO can only occur after the initial addition of O₂.⁸⁶ Reactions of the aromatic-peroxy adduct with NO to form the alkoxy radical are found to be of minor importance for the SAH.^{86,88} The bicyclic peroxy radical that forms from the aromatic–OH reaction with O₂ can isomerize to yield an epoxide; however, this route has been suggested based on master equation calculations⁸⁷ for benzene, and based on *ab initio* calculations⁸⁶ for toluene, to be of minor importance in the atmosphere, although the epoxide formed from this type of mechanism has been detected in the experiments reported here. For benzene, the pathway to the bicyclic RO₂ structure has a 10 kcal mol^{–1} barrier and is exothermic by ~69 kcal mol^{–1}. Comparatively, the barrier to epoxide formation is 74 kcal mol^{–1} and the reaction is exothermic by 59 kcal mol^{–1}.⁸⁷ Once the bicyclic RO₂ radical forms, the radical termination steps can lead to a carbonyl, an organic nitrate, or an RO radical, with the latter undergoing β-fission followed by cleavage of the bridge O–O bond to form ring-opening products. For the SAH, the primary fate of the bicyclic radical is isomerization to form the epoxide or reaction with O₂ to lead to ring-opening products. We include the route through reaction of the alkoxy radical with O₂ to form the carbonyl merely for completeness, but this should be a very minor channel.

Both the mechanism through the bicyclic structure (Scheme 5) and the mechanism shown for the formation of phthalaldehyde in Scheme 2 are supported by the observed concu-

rent growth of glyoxal.⁴⁷ However, reaction through the bicyclic mechanism generates phthalaldehyde and glyoxal as first generation products, while further reaction through 2-formylcinnamaldehyde (Scheme 2) leads to second-generation glyoxal and phthalaldehyde. The bicyclic structure to form ring-opened products has been extensively studied for the single-ringed aromatics,⁸⁹ but to the best of our knowledge, has only been suggested in the pathway to epoxide formation for the PAH compounds. Given that about 70% of the 2-formylcinnamaldehyde was found to remain at the completion of the chamber experiments, formation of the ring-opening products through an alternate pathway may be of significance. Further mechanistic studies on the reaction pathways of bicyclic structures related to PAHs could yield important insights into the further gas-phase reactions of this class of compounds.

In addition to the ring-opening and ring-retaining structures previously outlined, an organic sulfonic acid (R–SO₃), which was characterized as hydroxybenzene sulfonic acid using an authentic standard, is observed here in naphthalene SOA produced under both high- and low-NO_x conditions in the presence of neutral ammonium sulfate seed aerosol. Comparisons of these mass spectra are displayed in Figure 8. Product ions observed at *m/z* 93 and 109 are due to neutral losses of SO₂ and SO₃, respectively. These neutral losses are characteristic of aromatic sulfonates.⁹⁰ The product ion observed at *m/z* 80 is due to the production of SO₃[–], which is also a characteristic ion of aromatic sulfonates.^{91,92} The hydroxybenzene sulfonic acids lack the presence of a *m/z* 97 ion (i.e., HSO₄[–]) in their MS² spectra, which is a characteristic product ion of organosulfate functional groups (–ROSO₃).^{29,32,59} The absence of this peak clearly suggests that the product identified cannot be an organosulfate. In combination with the accurate mass measurements and similar retention times, the comparison of these MS² spectra further supports the identification of hydroxybenzene sulfonic acids in naphthalene low- and high-NO_x SOA formed in the presence of ammonium sulfate seed. The formation of this product requires reaction with the ammonium sulfate seed, as the seed is the only source of sulfur in the system; however, the mechanism by which an organic sulfonic acid would be produced remains unclear. Methyl sulfonate has been reported in marine layer aerosol due to the oxidation of dimethyl sulfide.^{93–95} The presence of sulfonate compounds known as of linear alkylbenzene sulfonates (LAS) has been observed in river and seawater⁹⁶ as well. LAS compounds, which are used as surfactants in the manufacturing of cleaning products,⁹⁷ are

SCHEME 6: Proposed Low-NO_x Mechanism for the Formation of Ring-Retaining Products and 2-Formylcinnamaldehyde (MW 160) under Low-NO_x Conditions^a



^a Observed products are boxed. MWs are shown in red, and the phase of the observed product (gas, g, or particle, p) is denoted in the lower right corner.

found in these aquatic systems due to incomplete removal from wastewaters. Most recently, Altieri et al.⁹⁸ have observed the presence of sulfonates in the environment due to pollution sources does not yield insights into the generation of these compounds in our chamber studies. Nevertheless, the photooxidation of PAHs (e.g., naphthalene) in the presence of sulfur-containing aerosols might yield an additional source of sulfonates found in the environment.

4.2. Low-NO_x Conditions.

4.2.1. Low-NO_x Gas-Phase Chemistry. Although the major gas-phase products observed under low-NO_x conditions are similar to those under high-NO_x conditions, the intensities of the resultant compounds differ dramatically. Scheme 6 shows the proposed mechanism for the formation of the identified products under low-NO_x conditions. Under low-NO_x conditions, the ring-opening products can be formed mechanistically through RO₂ + RO₂ or RO₂ + HO₂ pathways. Given the high concentrations of HO₂ prevalent in these chamber studies, the RO₂ + RO₂ route is calculated to be of minor importance compared to RO₂ + HO₂ reactions. A simple kinetic simulation similar to those performed for SAH,¹³ indicates that in order for RO₂ + RO₂ mechanisms to be competitive with RO₂ + HO₂ reactions, RO₂ + RO₂ rate constants would need to be at least a factor of 10 larger than RO₂ + HO₂ rate constants based on relative concentrations of RO₂ and HO₂ found in the chamber. From the master chemical mechanism (MCM) version 3.1 it is found that $k_{(RO_2+HO_2)}$ are generally on the order of 2.0×10^{-11} cm³ molecule⁻¹ s⁻¹, whereas $k_{(RO_2+RO_2)}$ are no more than $1.0 \times$

10^{-12} cm³ molecule⁻¹ s⁻¹, indicating that RO₂ + HO₂ pathways should dominate over RO₂ + RO₂ reactions under our experimental conditions.

We also acknowledge that a different pathway for the 1,4-naphthoquinone product under low-NO_x conditions may be possible. In their study of the OH-initiated photooxidation of naphthalene, Qu et al.⁸¹ predict that the quinone is formed by addition of HO₂ to 1-naphthol followed by reaction with O₂ to form the 1,4-carbonyl peroxy naphthalene intermediate. Two subsequent reactions with HO₂ yield 1,4-naphthoquinone and OH radical. The overall reaction is exothermic by -58.49 kcal/mol. This type of HO₂ mechanism has not been well established, and reaction rates have not been reported, thus determining the atmospheric importance of such a mechanism is not possible, although it is energetically plausible.

4.2.2. Low-NO_x SOA Composition Chemistry. Under low-NO_x conditions ~68% of the SOA mass has been identified, of which 26.2% is associated with organic peroxide compounds, and the remaining 42% is chemically characterized at the molecular level in Table 3 (and Tables 5S–7S) with dominant contributions coming from acids. Under low-NO_x conditions a significant enhancement in the formation of acids is observed. As shown in Table 3, the contribution of hydroxyphthalic acid to the overall SOA mass increases from 3% in high-NO_x condition to 9% for the low-NO_x case. The increase in the concentration of acidic species is expected in the low-NO_x case as RO₂ + HO₂ chemistry dominates over the formation of alkoxy radicals in the absence of NO. However, the formation of alkoxy radicals through an RO₂ + HO₂ route still leads to

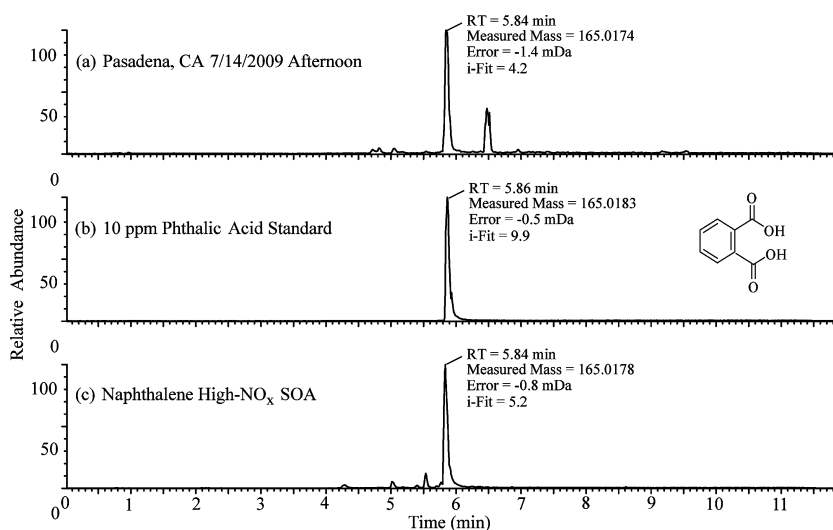


Figure 9. UPLC/(-)ESI-TOFMS EICs of m/z 165 from (a) ambient samples collected in Pasadena, CA, (b) a 10 ppm phthalic acid standard, and (c) naphthalene high- NO_x experiments (Experiment 6).

the presence of ring-opening species, as does the bicyclic mechanism shown in Scheme 5. The 28% of SOA mass attributed to organic peroxides, along with the enhancement of acidic species, indicates the importance of $\text{RO}_2 + \text{HO}_2$ reactions. The further reaction of bicyclic RO_2 radicals may contribute significantly to the generation of ring-opening products, the epoxide, and organic peroxide species. O/C ratios from the filter sampling method are slightly higher than in the high- NO_x data (0.50 vs 0.48, respectively), as is expected given the enhancement of acidic species. AMS data shows that the O/C ratios and H/C ratios are also slightly higher in the low- NO_x experiments, though still within error bars when compared to the high- NO_x experiments. These higher compositional ratios obtained from the AMS technique appear to not only be an effect of increasing acid concentration, but also of aging. Owing to the lower OH concentration achieved in the low- NO_x experiments, longer reaction times are required to reach a constant aerosol volume, thus more oxidation may occur in the aerosol, though the observed affect is small.

4.3. Atmospheric Significance of Naphthalene SOA: Identification of Potential Ambient SOA Tracers in Urban Atmospheres. Urban aerosol filter samples collected in Birmingham, AL and in Pasadena, CA, were examined for the presence of naphthalene SOA constituents chemically characterized in the present study (Table 3). The UPLC/(-)ESI-TOFMS data obtained from the urban aerosol samples are compared to the laboratory-generated high- NO_x naphthalene SOA. Upon detailed comparison of the UPLC/(-)ESI-TOFMS BPCs obtained from both the laboratory-generated and ambient organic aerosol samples, it becomes evident that several of naphthalene high- NO_x SOA constituents characterized in the present study are observed in the urban aerosol samples. Figure 9 shows the UPLC/(-)ESI-TOFMS extracted ion chromatograms (EICs) of m/z 165 obtained from an urban aerosol sample collected from Pasadena, CA, a 10 ppm phthalic acid authentic standard, and a typical naphthalene high- NO_x photooxidation experiment, respectively. The comparison of these 3 EICs suggests that phthalic acid may be a potential ambient naphthalene SOA tracer

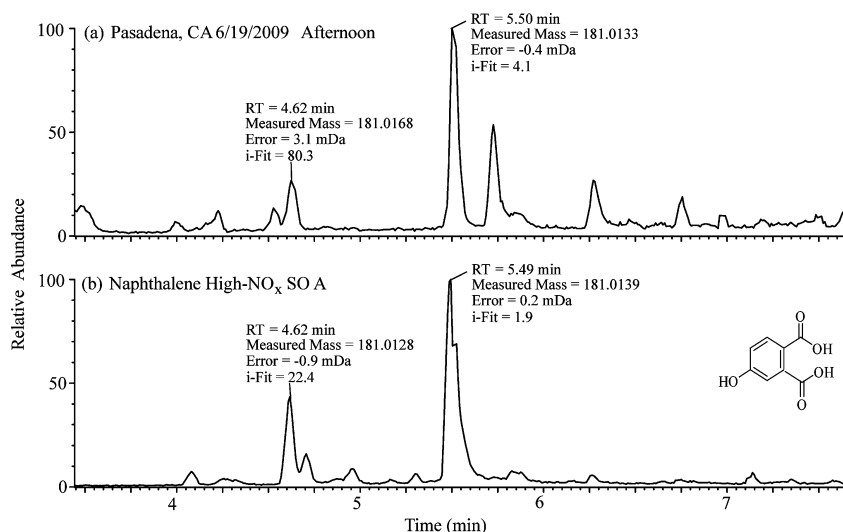


Figure 10. UPLC/(-)ESI-TOFMS EICs of m/z 181 from (a) ambient samples collected in Pasadena, CA and (b) naphthalene high- NO_x experiments (Experiment 6).

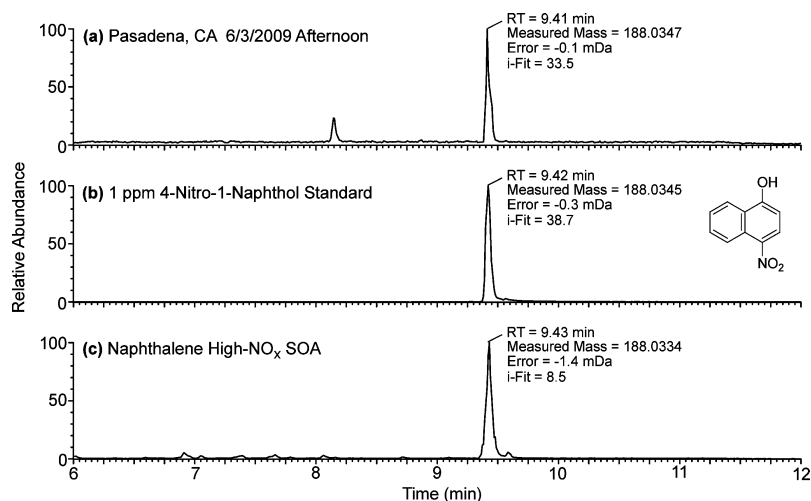


Figure 11. UPLC/(-)ESI-TOFMS EICs of m/z 188 from (a) ambient samples collected in Pasadena, CA, (b) a 1 ppm standard of 4-nitro-1-naphthol, and (c) naphthalene high- NO_x experiments (Experiment 6).

that could be used in a SOA source apportionment methods.^{99,100} Additionally, Figure 3S (Supporting Information) shows the UPLC/(-)ESI-TOFMS EICs of m/z 165 obtained for a typical naphthalene high- NO_x SOA sample, a 10 ppm phthalic acid standard, and an urban aerosol sample collected from Birmingham, AL. The use of phthalic acid as a potential tracer compound for naphthalene photooxidation is tempting due to the large quantities ($\sim 14 \text{ ng m}^{-3}$) found in the ambient aerosol sample collected from Birmingham, AL. In comparison, 2-methyltetrols, which are ambient tracer compounds for isoprene SOA, have been measured between 200 pg m^{-3} and 365 ng m^{-3} during the summer in aerosol samples collected from many forested locations.¹⁰¹ Since isoprene is the most abundant nonmethane hydrocarbon emitted into the atmosphere annually, the mass concentrations of phthalic acid found in urban aerosol samples analyzed in the present study are of some significance. In fact, phthalic acid and other dicarboxylic acids have been previously proposed as tracers.^{102,103} However, because phthalic acid/anhydride is known to be formed from a wide variety of sources including sewage sludge^{104,105} and plastic processing,¹⁰⁶ its use as a tracer is of questionable value.

Figure 10 shows the UPLC/(-)ESI-TOFMS EICs of m/z 181 obtained in a typical naphthalene high- NO_x SOA sample and in an urban aerosol sample collected from Pasadena, CA. The chromatographic peaks eluting at 5.45 min have the same elemental compositions (i.e., molecular formulas) as determined by the accurate mass measurements. This strongly indicates that the hydroxy phthalic acid product characterized in Table 3 can be used as an ambient tracer compound for naphthalene SOA; however, it cannot be ruled out that, as with phthalic acid, other sources may contribute to the formation of hydroxy phthalic acid in ambient aerosol. As a result, we cannot suggest that hydroxy phthalic acid be used solely as an ambient tracer compound for naphthalene SOA.

Another naphthalene high- NO_x SOA constituent found in the urban aerosol samples is 4-nitro-1-naphthol (MW 189). Figure 11 shows the UPLC/(-)ESI-TOFMS EICs of m/z 188 obtained for an urban aerosol sample collected from Pasadena, CA, a 1 ppm 4-nitro-1-naphthol authentic standard, and a typical naphthalene high- NO_x SOA sample. The comparison of these EICs clearly demonstrates the presence of this naphthalene high- NO_x SOA compound in ambient aerosol. Additionally, Figure 4S

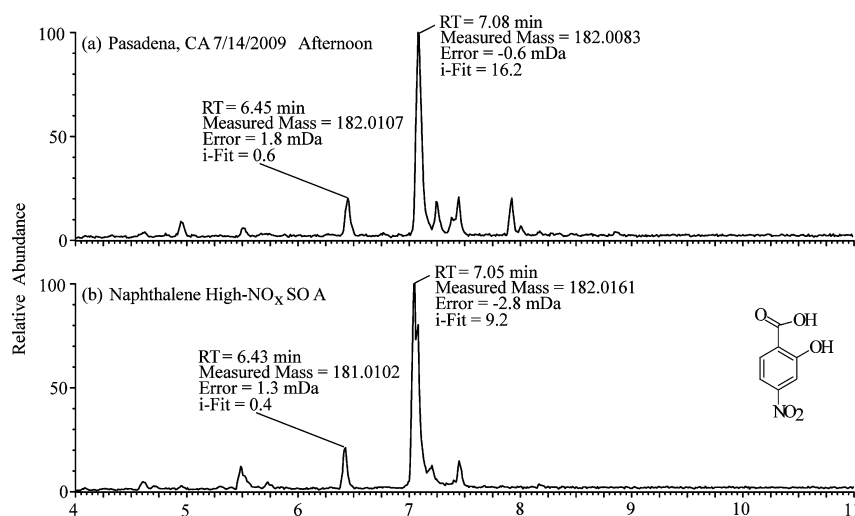


Figure 12. UPLC/(-)ESI-TOFMS EICs of m/z 182 from (a) ambient samples collected in Pasadena, CA and (b) naphthalene high- NO_x experiments (Experiment 6).

(Supporting Information) shows the UPLC/(−)ESI-TOFMS EICs of m/z 188 obtained for a typical naphthalene high- NO_x SOA sample, a 1 ppm 4-nitro-1-naphthol authentic standard, and an urban aerosol sample collected from Birmingham, AL, respectively. Concentrations of 4-nitro-1-naphthol from the Birmingham, AL site were found to be 1.6 ng m^{-3} , and the concentration of 4-nitro-1-naphthol collected from Pasadena, CA during summertime polluted conditions was 228 pg m^{-3} . This compound could prove to be an excellent ambient tracer for anthropogenic PAH chemistry. Apparent from the chamber studies, and Birmingham, AL and Pasadena, CA ambient aerosol samples, this compound, found at concentrations comparable to those of other common tracers (i.e., 2-methyltetrol), appears not to have been reported from alternate biogenic or anthropogenic sources. The added concern of N-containing naphthalene compounds, such as the 4-nitro-1-naphthol found in these ambient aerosol samples, as possible carcinogens makes these compounds of particular interest.

Comparison of the UPLC/(−)ESI-TOFMS EICs of m/z 182 found in Figure 12 demonstrate that the hydroxy nitrobenzoic acid with MW 183 characterized in the naphthalene high- NO_x SOA (Table 3) is also present in aerosol samples collected from Pasadena, CA. We note that this single-ring aromatic SOA constituent may also form in the atmosphere due to the photooxidation of SAHs (e.g., toluene). However, we have verified that naphthalene is a valid precursor to the presence of this compound in SOA. Since other SAHs and PAHs likely contribute to the formation of this compound in urban aerosol, it is likely not reasonable to use this compound solely as a naphthalene SOA tracer.

As a result of our detailed comparison of the laboratory-generated naphthalene high- NO_x SOA and the urban aerosol samples, we recommend that 4-nitro-1-naphthol might serve as a suitable ambient tracer for naphthalene SOA. It is worth mentioning that other compounds not highlighted here in this discussion were also observed in both the laboratory-generated and ambient aerosol, but these were concluded to be unsuitable ambient tracer compounds for naphthalene SOA; these include the following $[\text{M} - \text{H}]^-$ ions identified in Table 3: m/z 137, 149, 154, 179, 193, and 209.

5. Conclusions

We report extensive studies on the gas- and particle-phase constituents produced from the OH-initiated photooxidation of naphthalene under both high- and low- NO_x conditions. These studies provide significant insights into the chemical mechanisms that lead to SOA formation. For the high- NO_x case, 53% of the SOA mass is chemically identified, of which organic peroxides constitute 28%. The comparison of O/C and H/C ratios between the off-line molecularly characterized analyses are in agreement with measurements from online bulk measurements suggesting that the chemically characterized portion of the aerosol is representative of bulk aerosol components. Additionally, hydroxybenzene sulfonic acid is observed in the aerosol phase for both the low- and high- NO_x cases, although a mechanism for the generation of this product is not established. Under low- NO_x conditions, ~68% of the SOA mass has been chemically identified, of which 26.2% is associated with organic peroxides. A significant enhancement in the formation of acids is observed relative to the high- NO_x case.

Naphthalene high- NO_x SOA constituents characterized in the present study are compared with urban aerosol samples collected from Birmingham, AL and Pasadena, CA, confirming the presence of SOA from naphthalene photooxidation in the urban

atmosphere. In particular, phthalic acid, hydroxy phthalic acid, 4-nitro-1-naphthol and hydroxy nitrobenzoic acid are observed in both the laboratory-generated high- NO_x SOA and the urban organic aerosols. Of these compounds, 4-nitro-1-naphthol appears to be a valid ambient organic tracer for naphthalene high- NO_x SOA.

Acknowledgment. This research was funded by the Office of Science (BER), US Department of Energy Grant No. DE-FG02-05ER63983, US Environmental Protection Agency STAR Research Assistance Agreement No. RD-83374901 and US National Science Foundation grant ATM-0432377. The Electronic Power Research Institute provided support for the SEARCH network field samples. The GC/TOF and CIMS instruments used in this study were purchased as part of a major research instrumentation grant from the National Science Foundation (ATM-0619783). Assembly and testing of the CIMS instrument was supported by the Davidow Discovery Fund. The Waters UPLC/(−)ESI-TOFMS (LCT Premier XT TOFMS) was purchased in 2006 with a grant from the National Science Foundation, Chemistry Research Instrumentation and Facilities Program (CHE-0541745). We thank J. Stockdill for synthesis of 2-formylcinnamaldehyde. We would also like to thank E. S. Edgerton of Atmospheric Research & Analysis (ARA), Inc., for providing the high-volume filter sampler, as well as providing detailed information on its operation procedures, used in the sampling of fine aerosols during PACO. This publication has not been formally reviewed by the EPA. The views expressed in this document are solely those of the authors and EPA does not endorse any products mentioned in this publication.

Note Added in Proof. We proposed the formation of ring-opening products by a bicyclic peroxy intermediate in the text and in Scheme 5. After this work was submitted the following paper came to our attention: Nishino, N.; Arey, J.; Atkinson R. *Environ. Sci. Technol.* **2009**, in press. Nishino et al. also suggest the formation of phthalaldehyde and glyoxal by the route in Scheme 5.

Supporting Information Available: Table 1S lists the chemicals employed in this study along with their purities. Tables 2S–7S display identification, quantification and (−)ESI-ITMS MS^2 information for experiments 2–8. EICs for selected photooxidation products observed using the GC/EI-TOFMS technique are shown in Figure 1S. Figure 2S compares mass spectra for 2-formylcinnamaldehyde (MW 160) from injection of the standard and from chamber studies. Figures 3S and 4S compare ambient data collected in Birmingham, AL and samples collected in Pasadena, CA, with authentic standards. This material is available free of charge via the Internet at <http://pubs.acs.org>.

References and Notes

- (1) Kroll, J. H.; Seinfeld, J. H. *Atmos. Environ.* **2008**, *42*.
- (2) Volkamer, R.; Jimenez, J. L.; Martini, F. S.; Dzepina, K.; Zhang, Q.; Salcedo, D.; Molina, L. T.; Worsnop, D. R.; Molina, M. J. *Geophys. Res. Lett.* **2006**, *33*, 4.
- (3) Heald, C. L.; Jacob, D. J.; Park, R. J.; Russell, L. M.; Huebert, B. J.; Seinfeld, J. H.; Liao, H.; Weber, R. J. *Geophys. Res. Lett.* **2005**, *32*, 4.
- (4) de Gouw, J. A.; Middlebrook, A. M.; Warneke, C.; Goldan, P. D.; Kuster, W. C.; Roberts, J. M.; Fehsenfeld, F. C.; Worsnop, D. R.; Canagaratna, M. R.; Pszenny, A. A. P.; Keene, W. C.; Marchewka, M.; Bertman, S. B.; Bates, T. S. *J. Geophys. Res.* **2005**, *110*.
- (5) Claeys, M.; Graham, B.; Vas, G.; Wang, W.; Vermeylen, R.; Pashynska, V.; Cafmeyer, J.; Guyon, P.; Andreae, M. O.; Artaxo, P.; Maenhaut, W. *Science* **2004**, *303*, 1173.

- (6) Claeys, M.; Wang, W.; Ion, A. C.; Kourtchev, I.; Gelencsér, A.; Maenhaut, W. *Atmos. Environ.* **2004**, *38*, 4093.
- (7) Dommen, J.; Metzger, A.; Duplissy, J.; Kalberer, M.; Alfarra, M. R.; Gascho, A.; Weingartner, E.; Prévôt, A. S. H.; Verheggen, B.; Baltensperger, U. *Geophys. Res. Lett.* **2006**, *33*.
- (8) Edney, E. O.; Kleindienst, T. E.; Jaoui, M.; Lewandowski, M.; Offenber, J. H.; Wang, W.; Claeys, M. *Atmos. Environ.* **2005**, *39*, 5281.
- (9) Kroll, J. H.; Ng, N. L.; Murphy, S. M.; Flagan, R. C.; Seinfeld, J. H. *Geophys. Res. Lett.* **2005**, *32*, L18808.
- (10) Kroll, J. H.; Ng, N. L.; Murphy, S. M.; Flagan, R. C.; Seinfeld, J. H. *Environ. Sci. Technol.* **2006**, *40*, 1869.
- (11) Surratt, J. D.; Murphy, S. M.; Kroll, J. H.; Ng, N. L.; Hildebrandt, L.; Sorooshian, A.; Szmigielski, R.; Vermeylen, R.; Maenhaut, W.; Claeys, M.; Flagan, R. C.; Seinfeld, J. H. *J. Phys. Chem. A* **2006**, *110*, 9665.
- (12) Szmigielski, R.; Surratt, J. D.; Vermeylen, R.; Szmigielska, K.; Kroll, J. H.; Ng, N. L.; Murphy, S. M.; Sorooshian, A.; Seinfeld, J. H.; Claeys, M. *J. Mass Spectrom.* **2007**, *42*, 101.
- (13) Ng, N. L.; Kroll, J. H.; Chan, A. W. H.; Chhabra, P. S. *Atmos. Chem. Phys.* **2007**, *7*.
- (14) Song, C.; Na, K. S.; Cocker, D. R. *Environ. Sci. Technol.* **2005**, *39*, 3143.
- (15) Chan, A. W. H.; Kautzman, K. E.; Chhabra, P. S.; Surratt, J. D.; Chan, M. N.; Crouse, J. D.; Kürten, A.; Wennberg, P. O.; Flagan, R. C.; Seinfeld, J. H. *Atmos. Chem. Phys.* **2009**, *9*, 3049.
- (16) Hatakeyama, S.; Izumi, K.; Fukuyama, T.; Akimoto, H.; Washida, N. *J. Geophys. Res.* **1991**, *96*, 947.
- (17) Ng, N. L.; Chhabra, P. S.; Chan, A. W. H.; Surratt, J. D.; Kroll, J. H.; Kwan, A. J.; McCabe, D. C.; Wennberg, P. O.; Sorooshian, A.; Murphy, S. M.; Dalleska, N. F.; Flagan, R. C.; Seinfeld, J. H. *Atmos. Chem. Phys.* **2007**, *7*, 3909.
- (18) Presto, A. A.; Huff Hartz, K. E.; Donahue, N. M. *Environ. Sci. Technol.* **2005**, *39*.
- (19) Docherty, K. S.; Wu, W.; Lim, Y. B.; Ziemann, P. J. *Environ. Sci. Technol.* **2005**, *39*, 4049.
- (20) Gao, S.; Keywood, M.; Ng, N. L.; Surratt, J.; Varutbangkul, V.; Bahreini, R.; Flagan, R. C.; Seinfeld, J. H. *J. Phys. Chem. A* **2004**, *108*, 10147.
- (21) Iinuma, Y.; Böge, O.; Gnauk, T.; Herrmann, H. *Atmos. Environ.* **2004**, *38*, 761.
- (22) Jang, M. S.; Czoschke, N. M.; Lee, S.; Kamens, R. M. *Science* **2002**, *298*, 814.
- (23) Kalberer, M.; Paulsen, D.; Sax, M.; Steinbacher, M.; Dommen, J.; Prevot, A. S. H.; Fisseha, R.; Weingartner, E.; Frankevich, V.; Zenobi, R.; Baltensperger, U. *Science* **2004**, *303*, 1659.
- (24) Liggio, J.; Li, S. M.; McLaren, R. *J. Geophys. Res.* **2005**, *110*.
- (25) Liggio, J.; Li, S. M.; McLaren, R. *Environ. Sci. Technol.* **2005**, *39*, 1532.
- (26) Tobias, H. J.; Ziemann, P. J. *Environ. Sci. Technol.* **2000**, *34*, 2105.
- (27) Tolocka, M. P.; Jang, M.; Ginter, J. M.; Cox, F. J.; Kamens, R. M.; Johnston, M. V. *Environ. Sci. Technol.* **2004**, *38*, 1428.
- (28) Gómez-González, Y.; Surratt, J. D.; Cuyckens, F.; Szmigielski, R.; Vermeylen, R.; Jaoui, M.; Lewandowski, M.; Offenber, J. H.; Kleindienst, T. E.; Edney, E. O.; Blockhuys, F.; Van Alsenoy, C.; Maenhaut, W.; Claeys, M. *J. Mass Spectrom.* **2008**, *43*, 371.
- (29) Iinuma, Y.; Müller, C.; Berndt, T.; Böge, O.; Claeys, M.; Herrmann, H. *Environ. Sci. Technol.* **2007**, *41*, 6678.
- (30) Iinuma, Y.; Müller, C.; Böge, O.; Gnauk, T.; Herrmann, H. *Atmos. Environ.* **2007**, *41*, 5571.
- (31) Surratt, J. D.; Gómez-González, Y.; Chan, A. W. H.; Vermeylen, R.; Shahgholi, M.; Kleindienst, T. E.; Edney, E. O.; Offenber, J. H.; Lewandowski, M.; Jaoui, M.; Maenhaut, W.; Claeys, M.; Flagan, R. C.; Seinfeld, J. H. *J. Phys. Chem. A* **2008**, *112*, 8345.
- (32) Surratt, J. D.; Kroll, J. H.; Kleindienst, T. E.; Edney, E. O.; Claeys, M.; Sorooshian, A.; Ng, N. L.; Offenber, J. H.; Lewandowski, M.; Jaoui, M.; Flagan, R. C.; Seinfeld, J. H. *Environ. Sci. Technol.* **2007**, *41*, 517.
- (33) Galloway, M. M.; Chhabra, P. S.; Chan, A. W. H.; Surratt, J. D.; Flagan, R. C.; Seinfeld, J. H.; Keutsch, F. N. *Atmos. Chem. Phys.* **2009**, *9*, 3331.
- (34) Kroll, J. H.; Ng, N. L.; Murphy, S. M.; Varutbangkul, V.; Flagan, R. C.; Seinfeld, J. H. *J. Geophys. Res.* **2005**, *110*, 10.
- (35) Volkamer, R.; Martini, F. S.; Molina, L. T.; Salcedo, D.; Jimenez, J. L.; Molina, M. J. *Geophys. Res. Lett.* **2007**, *34*.
- (36) Robinson, A. L.; Donahue, N. M.; Shrivastava, M. K.; Weitkamp, E. A.; Sage, A. M.; Grieshop, A. P.; Lane, T. E.; Pierce, J. R.; Pandis, S. N. *Science* **2007**, *315*, 1259.
- (37) Schauer, J. J.; Kleeman, M. J.; Cass, G. R.; Simoneit, B. R. T. *Environ. Sci. Technol.* **1999**, *33*, 1578.
- (38) Schauer, J. J.; Kleeman, M. J.; Cass, G. R.; Simoneit, B. R. T. *Environ. Sci. Technol.* **2002**, *36*, 1169.
- (39) Ravindra, K.; Sokhi, R.; Van Grieken, R. *Atmos. Environ.* **2008**, *42*, 2895.
- (40) Schauer, J. J.; Kleeman, M. J.; Cass, G. R.; Simoneit, B. R. T. *Environ. Sci. Technol.* **2001**, *35*, 1716.
- (41) Schauer, J. J.; Kleeman, M. J.; Cass, G. R.; Simoneit, B. R. T. *Environ. Sci. Technol.* **1999**, *33*, 1566.
- (42) Schauer, J. J.; Kleeman, M. J.; Cass, G. R.; Simoneit, B. R. T. *Environ. Sci. Technol.* **2002**, *36*, 567.
- (43) Atkinson, R.; Arey, J. *Polycycl. Aromatic Compd.* **2007**, *27*, 15.
- (44) Atkinson, R.; Aschmann, S. M.; Arey, J.; Carter, W. P. L. *Int. J. Chem. Kinetics* **1989**, *21*, 801.
- (45) Bunce, N. J.; Liu, L.; Zhu, J.; Lane, D. A. *Environ. Sci. Technol.* **1997**, *31*, 2252.
- (46) Mihele, C. M.; Wiebe, H. A.; Lane, D. A. *Polycycl. Aromatic Compd.* **2002**, *22*, 729.
- (47) Wang, L.; Atkinson, R.; Arey, J. *Environ. Sci. Technol.* **2007**, *41*, 2803.
- (48) Arey, J.; Atkinson, R.; Zielinska, B.; McElroy, P. A. *Environ. Sci. Technol.* **1989**, *23*, 321.
- (49) Gupta, P.; Harger, W. P.; Arey, J. *Atmos. Environ.* **1996**, *30*, 3157.
- (50) Helmig, D.; Arey, J.; Harger, W. P.; Atkinson, R.; Lopezcancio, J. *Environ. Sci. Technol.* **1992**, *26*, 622.
- (51) Helmig, D.; Lopezcancio, J.; Arey, J.; Harger, W. P.; Atkinson, R. *Environ. Sci. Technol.* **1992**, *26*, 2207.
- (52) Groszovsky, A. J.; Sasaki, J. C.; Arey, J.; Eastmond, D. A.; Parks, K. K.; Atkinson, R. *Res. Rep. Health Eff. Inst.* **1999**, *1*.
- (53) Cocker, D. R.; Flagan, R. C.; Seinfeld, J. H. *Environ. Sci. Technol.* **2001**, *35*, 2594.
- (54) Keywood, M. D.; Varutbangkul, V.; Bahreini, R.; Flagan, R. C.; Seinfeld, J. H. *Environ. Sci. Technol.* **2004**, *38*, 4157.
- (55) Burkhardt, M. R.; Maniga, N. I.; Stedman, D. H.; Paur, R. *J. Anal. Chem.* **1988**, *60*, 816.
- (56) Paulot, F.; Crouse, J. D.; Kjaergaard, H. G.; Kroll, J. H.; Seinfeld, J. H.; Wennberg, P. O. *Atmos. Chem. Phys.* **2009**, *9*, 1479.
- (57) Crouse, J. D.; McKinney, K. A.; Kwan, A. J.; Wennberg, P. O. *Anal. Chem.* **2006**, *78*, 6726.
- (58) Stein, S. M. Y.; Tchekhovski, D.; Mallard, G.; Mikaia, A.; Zaikin, V.; Zhu, J.; Clifton, C.; Sparkman, D. *The NIST Mass Spectral Search Program for the NIST/EPA/NIH Mass Spectral Library*, 2005 ed.; 2005.
- (59) Surratt, J. D.; Gómez-González, Y.; Chan, A. W. H.; Vermeylen, R.; Shahgholi, M.; Kleindienst, T. E.; Edney, E. O.; Offenber, J. H.; Lewandowski, M.; Jaoui, M.; Maenhaut, W.; Claeys, M.; Flagan, R. C.; Seinfeld, J. H. *J. Phys. Chem. A* **2008**, *112*, 8345.
- (60) DeCarlo, P. F.; Kimmel, J. R.; Trimborn, A.; Northway, M. J.; Jayne, J. T.; Aiken, A. C.; Gonin, M.; Fuhrer, K.; Horvath, T.; Docherty, K. S.; Worsnop, D. R.; Jimenez, J. L. *Anal. Chem.* **2006**, *78*, 8281.
- (61) Allan, J. D.; Delia, A. E.; Coe, H.; Bower, K. N.; Alfarra, M. R.; Jimenez, J. L.; Middlebrook, A. M.; Drewnick, F.; Onasch, T. B.; Canagaratna, M. R.; Jayne, J. T.; Worsnop, D. R. *J. Aerosol Sci.* **2004**, *35*, 909.
- (62) Bahreini, R.; Keywood, M. D.; Ng, N. L.; Varutbangkul, V.; Gao, S.; Flagan, R. C.; Seinfeld, J. H.; Worsnop, D. R.; Jimenez, J. L. *Environ. Sci. Technol.* **2005**, *39*, 5674.
- (63) Aiken, A. C.; DeCarlo, P. F.; Jimenez, J. L. *Anal. Chem.* **2007**, *79*, 8350.
- (64) Aiken, A. C.; Decarlo, P. F.; Kroll, J. H.; Worsnop, D. R.; Huffman, J. A.; Docherty, K. S.; Ulbrich, I. M.; Mohr, C.; Kimmel, J. R.; Sueper, D.; Sun, Y.; Zhang, Q.; Trimborn, A.; Northway, M.; Ziemann, P. J.; Canagaratna, M. R.; Onasch, T. B.; Alfarra, M. R.; Prevot, A. S. H.; Dommen, J.; Duplissy, J.; Metzger, A.; Baltensperger, U.; Jimenez, J. L. *Environ. Sci. Technol.* **2008**, *42*, 4478.
- (65) Weber, R. J.; Orsini, D.; Daun, Y.; Lee, Y. N.; Klotz, P. J.; Brechtel, F. *Aerosol Sci. Technol.* **2001**, *35*, 718.
- (66) Sorooshian, A.; Brechtel, F. J.; Ma, Y. L.; Weber, R. J.; Corless, A.; Flagan, R. C.; Seinfeld, J. H. *Aerosol Sci. Technol.* **2006**, *40*, 396.
- (67) Edgerton, E. S.; Hartsell, B. E.; Saylor, R. D.; Jansen, J. J.; Hansen, D. A.; Hidy, G. M. *J. Air Waste Manage. Assoc.* **2005**, *55*, 1527.
- (68) Hansen, D. A.; Edgerton, E. S.; Hartsell, B. E.; Jansen, J. J.; Kandasamy, N.; Hidy, G. M.; Blanchard, C. L. *J. Air Waste Manage. Assoc.* **2003**, *53*, 1460.
- (69) Gao, S.; Surratt, J. D.; Knipping, E. M.; Edgerton, E. S.; Shahgholi, M.; Seinfeld, J. H. *J. Geophys. Res.* **2006**, *111*, D14314.
- (70) Larson, R. A.; Garrison, W. J.; Marley, K. A. *Tetrahedron Lett.* **1986**, *27*, 3987.
- (71) Nishino, N.; Arey, J.; Atkinson, R. *Environ. Sci. Technol.* **2009**.
- (72) Sasaki, J.; Aschmann, S. M.; Kwok, E. S. C.; Atkinson, R.; Arey, J. *Environ. Sci. Technol.* **1997**, *31*, 3173.
- (73) Atkinson, R.; Aschmann, S. M.; Arey, J.; Zielinska, B.; Schuetzle, D. *Atmos. Environ.* **1989**, *23*, 2679.
- (74) Fisseha, R.; Dommen, J.; Sax, M.; Paulsen, D.; Kalberer, M.; Maurer, R.; Hoffer, F.; Weingartner, E.; Baltensperger, U. *Anal. Chem.* **2004**, *76*, 6535.
- (75) Lu, R.; Wu, J.; Turco, R. P.; Winer, A. M.; Atkinson, R.; Arey, J.; Paulson, S. E.; Lurmann, F. W.; Miguel, A. H.; Eiguren-Fernandez, A. *Atmos. Environ.* **2005**, *39*, 489.

- (76) Fraser, M. P.; Cass, G. R.; Simoneit, B. R. T. *Environ. Sci. Technol.* **1998**, *32*, 2051.
- (77) Marr, L. C.; Kirchstetter, T. W.; Harley, R. A.; Miguel, A. H.; Hering, S. V.; Hammond, S. K. *Environ. Sci. Technol.* **1999**, *33*, 3091.
- (78) Bunce, N. J. D.; H. G. *Can. J. Chem.* **1992**, *70*, 1966.
- (79) Lane, D. A.; Fielder, S. S.; Townsend, S. J.; Bunce, N. J.; Zhu, J.; Liu, L.; Wiens, B.; Pond, P. *Polycycl. Aromatic Compd.* **1996**, *9*, 53.
- (80) Nishino, N.; Atkinson, R.; Arey, J. *Environ. Sci. Technol.* **2008**, *42*, 9203.
- (81) Qu, X. H.; Zhang, Q. Z.; Wang, W. X. *Chem. Phys. Lett.* **2006**, *429*, 77.
- (82) Atkinson, R.; Arey, J. *Polycycl. Aromatic Compd.* **2007**, *27*, 15.
- (83) Nishino, N. A. J.; Atkinson, R. *Environ. Sci. Technol.* **2009**.
- (84) Dekermenjian, M.; Allen, D. T.; Atkinson, R.; Arey, J. *Aerosol Sci. Technol.* **1999**, *30*, 273.
- (85) Palen, E. J.; Allen, D. T.; Pandis, S. N.; Paulson, S. E.; Seinfeld, J. H.; Flagan, R. C. *Atmos. Environ., Part A* **1992**, *26*, 1239.
- (86) Koch, R.; Knispel, R.; Elend, M.; Siese, M.; Zetzsch, C. *Atmos. Chem. Phys.* **2007**, *7*, 2057.
- (87) Glowacki, D. R.; Wang, L. M.; Pilling, M. J. *J. Phys. Chem. A* **2009**, *113*, 5385.
- (88) Suh, I.; Zhang, R. Y.; Molina, L. T.; Molina, M. J. *J. Am. Chem. Soc.* **2003**, *125*, 12655.
- (89) Calvert, J. G.; Atkinson, R.; Becker, K. H.; Kamens, R. M.; Seinfeld, J. H.; Wallington, T. J.; Yarwood, G. *The Mechanisms of Atmospheric Oxidation of Aromatic Hydrocarbons*; Oxford University Press, Inc.: New York, 2002.
- (90) Reemtsma, T. J. *Chromatogr. A* **2003**, *1000*, 477.
- (91) Rodil, R.; Quintana, J. B.; Lopez-Mahia, P.; Muniategui-Lorenzo, S.; Prada-Rodriguez, D. *Anal. Chem.* **2008**, *80*, 1307.
- (92) Frömel, T.; Peschka, M.; Fichtner, N.; Hierse, W.; Ignatiev, N. V.; Bauer, K. H.; Knepper, T. P. *Rapid Commun. Mass Spectrom.* **2008**, *22*, 3957.
- (93) Barnes, I.; Hjorth, J.; Mihalopoulos, N. *Chem. Rev.* **2006**, *106*, 940.
- (94) Johnson, M. T.; Bell, T. G. *Environ. Chem.* **2008**, *5*, 259.
- (95) Tang, M. J.; Zhu, T. *Sci. China Ser. B-Chem.* **2009**, *52*, 93.
- (96) Lara-Martin, P. A.; Gomez-Parra, A.; Gonzalez-Mazo, E. *Environ. Pollut.* **2008**, *156*, 36.
- (97) Lara-Martin, P. A.; Gomez-Parra, A.; Gonzalez-Mazo, E. *J. Chromatogr. A* **2006**, *1137*, 188.
- (98) Altieri, K. E.; Turpin, B. J.; Seitzinger, S. P. *Atmos. Chem. Phys.* **2009**, *9*, 2533.
- (99) Kleindienst, T. E.; Jaoui, M.; Lewandowski, M.; Offenber, J. H.; Lewis, C. W.; Bhavsar, P. V.; Edney, E. O. *Atmos. Environ.* **2007**, *41*, 8288.
- (100) Offenber, J. H.; Lewis, C. W.; Lewandowski, M.; Jaoui, M.; Kleindienst, T. E.; Edney, E. O. *Environ. Sci. Technol.* **2007**, *41*, 3972.
- (101) Hallquist, M.; Wenger, J. C.; Baltensperger, U.; Rudich, Y.; Simpson, D.; Claeys, M.; Dommen, J.; Donahue, N. M.; George, C.; Goldstein, A. H.; Hamilton, J. F.; Herrmann, H.; Hoffmann, T.; Iinuma, Y.; Jang, M.; Jenkin, M. E.; Jimenez, J. L.; Kiendler-Scharr, A.; Maenhaut, W.; McFiggans, G.; Mentel, T. F.; Monod, A.; Prevot, A. S. H.; Seinfeld, J. H.; Surratt, J. D.; Szmigielski, R.; Wildt, J. *Atmos. Chem. Phys.* **2009**, *9*, 5155.
- (102) Schuetzle, D.; Cronn, D.; Crittenden, A. L.; Charlson, R. J. *Environ. Sci. Technol.* **1975**, *9*, 838.
- (103) Chebbi, A.; Carlier, P. *Atmos. Environ.* **1996**, *30*, 4233.
- (104) Mougin, C.; Dappozze, F.; Brault, A.; Malosse, C.; Schmidt, J. E.; Amellal-Nassr, N.; Patureau, D. *Environ. Chem. Lett.* **2006**, *4*, 201.
- (105) Thiruvenkatachari, R.; Kwon, T. O.; Moon, I. S. *J. Environ. Sci. Health, Part A* **2006**, *41*, 1685.
- (106) Butte, W.; Hostrup, O.; Walker, G. *Gefahrstoffe Reinhaltung Der Luft* **2008**, *68*, 79.

JP908530S

Appendix E

Reactive intermediates revealed in secondary organic aerosol formation from isoprene*

*Reproduced with permission from “Reactive intermediates revealed in secondary organic aerosol formation from isoprene” by Surratt, J.D., Chan, M.N., Chan, A.W.H., Eddingsaas, N.C., Loza, C.L., Kwan, A.J., Hersey, S.P., Flagan R.C., Wennberg, P.O., and Seinfeld, J.H., *Proceedings of the National Academy of Sciences*, 107 (15), 6640–6645, 2010. Copyright 2009 by the National Academy of Sciences.

Reactive intermediates revealed in secondary organic aerosol formation from isoprene

Jason D. Surratt^a, Arthur W. H. Chan^a, Nathan C. Eddingsaas^a, ManNin Chan^b, Christine L. Loza^a, Alan J. Kwan^b, Scott P. Hersey^b, Richard C. Flagan^{a,b}, Paul O. Wennberg^{b,c}, and John H. Seinfeld^{a,b,1}

^aDivision of Chemistry and Chemical Engineering, California Institute of Technology, Pasadena, CA 91125^bDivision of Engineering and Applied Science, California Institute of Technology, Pasadena, CA 91125^cDivision of Geological and Planetary Sciences, California Institute of Technology, Pasadena, CA 91125

Edited by Barbara J. Finlayson-Pitts, University of California, Irvine, Irvine, CA, and approved November 23, 2009 (received for review September 30, 2009)

Isoprene is a significant source of atmospheric organic aerosol; however, the oxidation pathways that lead to secondary organic aerosol (SOA) have remained elusive. Here, we identify the role of two key reactive intermediates, epoxydiols of isoprene (IEPOX = β -IEPOX + δ -IEPOX) and methacryloylperoxynitrate (MPAN), which are formed during isoprene oxidation under low- and high-NO_x conditions, respectively. Isoprene low-NO_x SOA is enhanced in the presence of acidified sulfate seed aerosol (mass yield 28.6%) over that in the presence of neutral aerosol (mass yield 1.3%). Increased uptake of IEPOX by acid-catalyzed particle-phase reactions is shown to explain this enhancement. Under high-NO_x conditions, isoprene SOA formation occurs through oxidation of its second-generation product, MPAN. The similarity of the composition of SOA formed from the photooxidation of MPAN to that formed from isoprene and methacrolein demonstrates the role of MPAN in the formation of isoprene high-NO_x SOA. Reactions of IEPOX and MPAN in the presence of anthropogenic pollutants (i.e., acidic aerosol produced from the oxidation of SO₂ and NO₂, respectively) could be a substantial source of "missing urban SOA" not included in current atmospheric models.

acid-catalyzed particle-phase reactions | epoxides | methacryloylperoxynitrate | organosulfates

Isoprene (2-methyl-1,3-butadiene, C₅H₈) is the most abundant nonmethane hydrocarbon emitted into the Earth's atmosphere, with emissions estimated to be 440–660 TgC yr⁻¹ (1). The atmospheric hydroxyl (OH) radical-initiated oxidation of isoprene, so-called photooxidation, plays a key role in establishing the balance of hydrogen oxide (HO_x = OH + HO₂) radicals in vegetated areas (2, 3) and influences urban ozone formation in populated areas blanketed with biogenic emissions (4). Formation of low-volatility compounds during isoprene oxidation has been estimated to be the single largest source of atmospheric organic aerosol [i.e., secondary organic aerosol (SOA)] (5–8).

The photooxidation of unsaturated volatile organic compounds (VOCs) proceeds through formation of a hydroxy peroxy (RO₂) radical, the fate of which depends on the concentration of nitrogen oxides (NO_x = NO + NO₂). Higher SOA yields from isoprene are observed under low-NO_x (or NO_x-free) conditions; in this regime, RO₂ radicals react primarily with HO₂, a pathway that tends to produce lower-volatility oxidation products than that involving the reaction of RO₂ with NO (9–11). Under high-NO_x conditions, RO₂ radicals react with NO to produce alkoxy (RO) radicals, or as a minor pathway, organic nitrates (RONO₂). For small VOCs (\leq C₁₀), like isoprene, these RO radicals generally fragment into smaller more volatile products, resulting in small amounts of SOA (9–11). Despite the fact that SOA from isoprene has been extensively studied (8), the chemical pathways to its formation under both low- and high-NO_x conditions have remained unclear. In this study we examine the mechanism of isoprene SOA formation in these two limiting regimes.

Results and Discussion

Isoprene SOA Formation under Low-NO_x Conditions: Role of Aerosol Acidity. Formation of SOA from the photooxidation of isoprene under low-NO_x conditions is enhanced in the presence of acidified sulfate seed aerosol over that in the presence of neutral aerosol (12); this is not observed under high-NO_x conditions because the aerosol phase is likely acidic enough due to the formation and presence of nitric acid (HNO₃) (13) and/or organic acids (12). The effect of increasing aerosol acidity on both gas- and aerosol-phase composition provides a critical clue to the chemical mechanism of SOA formation from isoprene under low-NO_x conditions. Enhancement of isoprene SOA mass with increasing aerosol acidity observed in laboratory chamber studies (12, 14, 15), including increased mass concentrations of the 2-methyltetrols (14, 15), organosulfates of isoprene (i.e., hydroxy sulfate esters) (15), and high-molecular weight (MW) SOA constituents (15), has been explained by acid-catalyzed particle-phase reactions. Although a linear correlation between the SOA mass formed and measured aerosol acidity (i.e., nmol H⁺ m⁻³) has been found under dry conditions [approximately 30% relative humidity (RH)] (15), the actual acid-catalyzed particle-phase reactions responsible for these observed enhancements in isoprene SOA formation remain unclear, especially because previously proposed reactions, like that of organosulfate formation by alcohol sulfate esterification (16–18), appear to be kinetically unfavorable at atmospheric conditions (19).

Shown in Fig. 1A–F are the chemical ionization mass spectrometry (CIMS) (see *Materials and Methods*) time traces for selected ions corresponding to the important gas-phase products formed from the photooxidation of 49 and 40 ppb of isoprene in the presence of neutral and highly acidified sulfate seed aerosol, respectively. The SOA mass yields from isoprene were 1.3 and 28.6% for the neutral and highly acidified sulfate seed aerosol experiments, respectively. Under the conditions of these experiments, the RO₂ radicals formed react primarily with HO₂. In addition to the formation of hydroxycarbonyls, methyl-butenediols, hydroxyhydroperoxides (ISOPOOH), methacrolein (MACR), and methyl vinyl ketone (MVK), all of which are first-generation gas-phase oxidation products (Fig. 1A–D), we also observe the formation of second-generation epoxydiols of isoprene (IEPOX), as indicated in Fig. 1F (i.e., 9 and 0.6 ppb of IEPOX was measured in the neutral and acidic cases, respectively). Although the 2-methyltetrols (Fig. 1E) can be produced from RO₂ radical-cross reactions, their formation through this route is of minor

Author contributions: J.D.S., A.W.H.C., N.C.E., R.C.F., P.O.W., and J.H.S. designed research; J.D.S., A.W.H.C., N.C.E., M.N.C., C.L.L., A.J.K., and S.P.H. performed research; J.D.S., A.W.H.C., and N.C.E. analyzed data; and J.D.S., A.W.H.C., N.C.E., P.O.W., and J.H.S. wrote the paper.

The authors declare no conflict of interest.

This article is a PNAS Direct Submission.

¹To whom correspondence should be addressed. E-mail: seinfeld@caltech.edu

This article contains supporting information online at www.pnas.org/cgi/content/full/091114107/DCSupplemental.

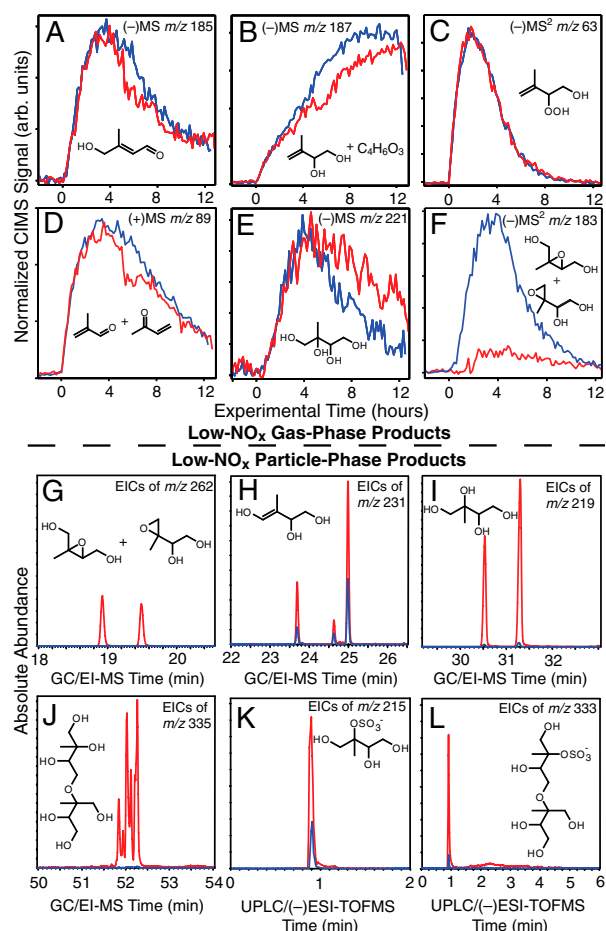


Fig. 1. Comparison of important gas- and particle-phase products produced from isoprene under low- NO_x conditions in the presence of either neutral (blue lines) or highly acidified (red lines) sulfate seed aerosol. In most cases, only one structural isomer is shown.

significance (approximately 0.2 ppb) in these experiments owing to the dominant $\text{RO}_2 + \text{HO}_2$ pathway. The hydroxycarbonyls (approximately 0.8 ppb) and methyl-butenediols (approximately 0.8 ppb) are first-generation products also formed from RO_2 radical-cross reactions; however, part of the CIMS signal associated with the methyl-butenediols (Fig. 1B) arises from later-generation oxidation products with the elemental composition $\text{C}_4\text{H}_6\text{O}_3$, likely a C_4 -hydroxydicarbonyl and/or C_4 -acid. Hydroxynitrates of isoprene were also observed (<0.1 ppb). Their formation results from background NO in the chamber. Thus a fraction of the MACR and MVK produced results from $\text{RO}_2 + \text{NO}$ reactions (approximately 3% of RO_2 radicals reacted with NO).

IEPOX (i.e., δ -IEPOX) was proposed to form from the photooxidation of isoprene under low- NO_x conditions in order to tentatively explain the formation of chemically characterized SOA constituents (12, 20). Gas-phase IEPOX (β -IEPOX and δ -IEPOX) was recently shown to form in substantial yields (upward of 75%) from the further oxidation of ISOPOOH (approximately 12 ppb measured in both the neutral and acidic cases in Fig. 1C) by OH under low- NO_x conditions (3). The substantial reduction of gas-phase IEPOX in the presence of highly acidified sulfate seed aerosol (Fig. 1F) confirms the role of IEPOX in the enhancement of isoprene SOA mass under low- NO_x conditions at increased aerosol acidity.

Isoprene low- NO_x SOA was analyzed offline by gas chromatography/electron ionization–quadrupole mass spectrometry (GC/EI-MS) with prior trimethylsilylation and ultra performance liquid chromatography/electrospray ionization–time-of-flight mass spectrometry operated in the negative ion mode [UPLC/(–)ESI-TOFMS] (see *Methods and Materials*). Particle-phase IEPOX is characterized here using GC/EI-MS. The GC/EI-MS mass spectra of the trimethylsilyl (TMS)-derivatives of IEPOX associated with the two chromatographic peaks in Fig. 1G are shown in Fig. S1. Extracted ion chromatograms (EICs) of selected ions corresponding to particle-phase IEPOX, as well as the previously characterized C_5 -alkene triols (20), 2-methyltetrols (5), hemiacetal dimers (12), organosulfate derivatives of the 2-methyltetrols (16, 17), and organosulfate derivatives of the hemiacetal dimers (18) are shown in Fig. 1G–L, respectively. Mass spectra in the present study for the previously characterized low- NO_x SOA constituents shown in Fig. 1H–L correspond to those collected in prior work (5, 12, 16, 20), and are shown in Fig. S1 and S2. The abundances of all low- NO_x SOA constituents shown in Fig. 1G–L are enhanced significantly in the presence of acidified sulfate seed aerosol. Using a suitable surrogate standard (i.e., *meso*-erythritol to quantify the 2-methyltetrols), we estimate that the mass concentrations of these compounds increased from $0.1 \mu\text{g m}^{-3}$ for the neutral case to $5.1 \mu\text{g m}^{-3}$ for the highly acidic case, corresponding to approximately 10 to 20%, respectively, of the total SOA mass formed.

Identification of IEPOX as the Intermediate Responsible for Acid-Enhanced Isoprene SOA. We hypothesize that particle-phase reactions of IEPOX play a significant role in the formation of the other major low- NO_x SOA constituents shown in Fig. 1H–L, as well as in the enhancement of total SOA mass. To test this hypothesis, we synthesized 2,3-epoxy-1,4-butanediol (BEPOX) (see *Materials and Methods*), which is the butadiene derivative of IEPOX, and conducted reactive uptake experiments in the presence of both neutral and highly acidified sulfate seed aerosol. BEPOX is used in these experiments instead of IEPOX because precursors for IEPOX are not commercially available. In these dark and dry ($<10\%$ RH) experiments, no OH precursor (e.g., H_2O_2) or NO_x was present; thus, only reactive uptake of BEPOX onto seed aerosol occurred. Two variations of these reactive uptake experiments were carried out: (i) BEPOX was added first, followed by the injection of seed aerosol; or (ii) seed aerosol was added first, followed by the injection of BEPOX. CIMS time traces corresponding to version (i) of the BEPOX reactive uptake experiments are shown in Fig. 2A. The only parameter varied was the acidity of the sulfate seed aerosol. BEPOX is rapidly removed from the gas phase within the first hour after the acidified sulfate seed aerosol is injected into the well-mixed chamber. Upon the injection of neutral sulfate seed aerosol, BEPOX disappears from

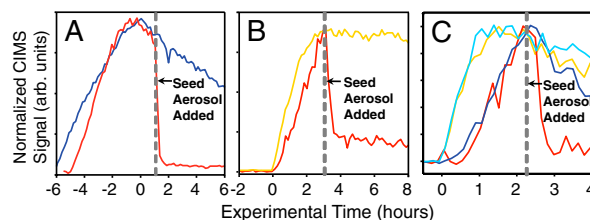


Fig. 2. CIMS time traces: (A) Reactive uptake of gas-phase BEPOX in the presence of either neutral (blue line) or highly acidified (red line) sulfate seed aerosol under dark conditions. (B) Hydroxy hydroperoxide (orange line) and BEPOX (red line) produced from butadiene under low- NO_x conditions. (C) ISOPOOH (neutral seed = light blue line; highly acidic seed = orange line) and IEPOX (neutral seed = blue line; highly acidic seed = red line) produced from isoprene under low- NO_x conditions. Signals of the IEPOX are normalized to that of the ISOPOOH when lights are turned off.

wall loss only and not reactive uptake. Once the injection of gas-phase BEPOX ended (indicated at time zero in Fig. 2A), it decayed at similar rates before either the neutral or highly acidified sulfate seed aerosol was injected. The clear conclusion is that BEPOX loss to the highly acidic seed aerosol results from acid-catalyzed particle-phase reactions.

SOA formed in the acidified BEPOX reactive uptake experiments shown in Fig. 2A was collected for offline chemical analyses by GC/EI-MS and UPLC/(–)ESI-TOFMS (Fig. S3). In addition to sharing similar retention times (RTs), the mass spectrum of the TMS-derivative of the particle-phase BEPOX (Fig. S3) corresponds exactly to that of the synthesized BEPOX standard (Fig. S4). The major chromatographic peak observed in the EIC of m/z 248 (Fig. S3) is attributable to particle-phase BEPOX, whereas the two later-eluting minor peaks represent BEPOX isomers. The other major SOA constituents characterized from the reactive uptake of BEPOX are also exact analogues of isoprene SOA formed under low- NO_x conditions (i.e., differing by a mass of 14 Da, which corresponds to a CH_2 group); these include: C_4 -alkene triols, tetrols (i.e., threitol and erythritol), dimers, organosulfate derivatives of the tetrols, and organosulfate derivatives of the dimers (Fig. S3). Equivalent to the low- NO_x isoprene SOA (Fig. 1G–L), these BEPOX SOA constituents were significantly enhanced under increased seed aerosol acidity, consistent with the rapid removal of gas-phase BEPOX onto the highly acidified sulfate seed aerosol. The tetrols (i.e., threitol and erythritol) were quantified by GC/EI-MS and their summed mass was found to increase from 43 ng m^{-3} to $1.0 \text{ } \mu\text{g m}^{-3}$ from neutral to highly acidic conditions.

In version (ii) of the BEPOX reactive uptake experiments, within the first hour after the addition of BEPOX, the sulfate aerosol mass concentration decayed more rapidly (by approximately 58% of its initial loading) in the highly acidic case than that which could be explained by wall loss alone, indicating depletion of the inorganic sulfate through chemical reaction with BEPOX (Fig. S5). A similar observation made in isoprene SOA formation (16) is consistent with the reactive uptake of IEPOX forming organosulfates of isoprene. The SOA mass generated after the injection of gas-phase BEPOX increased from 0.9 to $15.8 \text{ } \mu\text{g m}^{-3}$ from neutral to acidified sulfate seed aerosol. Importantly, organosulfates of BEPOX (i.e., organosulfate

derivatives of the tetrols and dimers, as well as higher order organosulfates shown in Fig. S6) were also characterized in these experiments (Fig. S3). We conclude from these observations that conversion of inorganic sulfate into organosulfates occurs by the acid-catalyzed ring opening of the epoxydiols followed by the subsequent nucleophilic addition of inorganic sulfate.

Reactive uptake onto acidified sulfate seed aerosol also occurs when BEPOX and IEPOX are formed from butadiene and isoprene photooxidation, respectively. 100 ppb of butadiene and 50 ppb of isoprene were initially irradiated in the absence of seed aerosol (Fig. 2B and C, respectively). Once sufficient gas-phase levels of both BEPOX and IEPOX formed, seed aerosol was injected. For the butadiene experiment (Fig. 2B), only highly acidified sulfate seed aerosol was injected. Because hydroxyhydroperoxides and BEPOX, gas-phase oxidation products of butadiene, are isomers both detected by the CIMS technique at m/z 189, characteristic daughter ions produced from m/z 189 were used to differentiate between these two compounds. The daughter ions at m/z 63 and 169 are uniquely characteristic of the hydroxyhydroperoxide and BEPOX, respectively (3). Upon the injection of acidified sulfate seed aerosol, BEPOX was the only oxidation product rapidly removed from the gas-phase mixture (decayed by approximately 75% within the first hour after seed aerosol was injected). The SOA constituents from butadiene shown in Fig. 2B are precisely those shown in Fig. S3. In the case of isoprene photooxidation (Fig. 2C), as observed for the BEPOX reactive uptake and butadiene photooxidation (Fig. 2A and B, respectively), gas-phase IEPOX disappeared significantly only in the presence of acidified sulfate seed aerosol (Fig. 2C). Moreover, the constituents characterized in the SOA formed from the latter experiment are precisely those shown in Fig. 1G–L.

Mechanism of Isoprene SOA Formation Under Low- NO_x Conditions.

An updated chemical mechanism for SOA formation from isoprene under low- NO_x conditions is shown in Fig. 3. The gas-phase formation of IEPOX has been fully characterized by Paulot et al. (3). Here we have established that the reactive uptake of IEPOX occurs by the acid-catalyzed ring opening of this epoxydiol, followed by the subsequent addition of the following nucleophiles: (i) H_2O , (ii) inorganic sulfate, (iii) a 2-methyltetrol

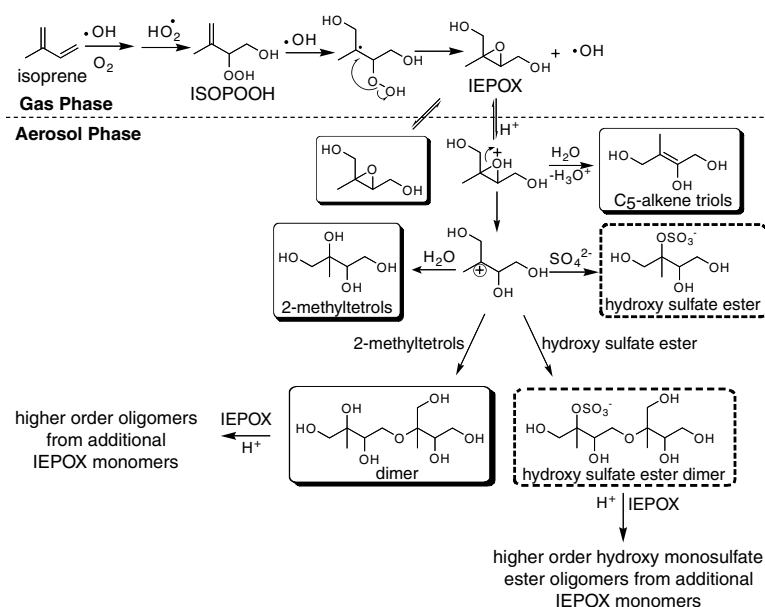


Fig. 3. Mechanism for the enhancement of SOA formation from isoprene under lower- NO_x conditions due to increased aerosol acidity. SOA constituents in shaded and dashed boxes are observed by GC/MS and UPLC/(–)ESI-TOFMS, respectively. Only the β -IEPOX is considered here, but this also applies to δ -IEPOX.

already formed in the aerosol, and (iv) a hydroxy sulfate ester already present in the aerosol. Unreacted particle-phase IEPOX observed in the isoprene SOA is likely a result of equilibrium gas-to-particle partitioning. Although the formation of 2-methyltetrols has been detected from the further oxidation of methyl-butenediols under conditions in which $\text{RO}_2 + \text{RO}_2$ reactions dominate (at large isoprene mixing ratios, i.e., 8–12 ppm C) (21), the atmospheric formation of the 2-methyltetrols will occur primarily via the further reaction of IEPOX as shown in Fig. 3, because the HO_2 concentration exceeds that of all RO_2 radicals (22) and because rate coefficients of $\text{RO}_2 + \text{RO}_2$ reactions are usually smaller than those for $\text{RO}_2 + \text{HO}_2$ reactions (23). The organosulfates of isoprene are shown conclusively to form from the reactive uptake of IEPOX, rather than by the previously proposed alcohol sulfate esterification mechanism (18). This conclusion is consistent with recent work by Iinuma et al. (24), who showed organosulfates of α - and β -pinene form through the reactive uptake of α - and β -pinene oxides only in the presence of acidified sulfate seed aerosol. Additionally, recent work has shown that organosulfate formation is kinetically favorable only for epoxides and not for alcohols at atmospherically relevant conditions (19).

Although the C_5 -alkene triols were observed in these experiments, their exact formation mechanism remains unclear. We cannot rule out the possibility that these compounds are produced from the trimethylsilylation step prior to GC/EI-MS analysis because a TMS-derivative of the synthesized BEPOX standard was found to have a contribution from C_4 -alkene triols. Preliminary results suggest that these compounds are more abundant than the tetrols under high RH conditions. Enhanced C_5 -alkene triol concentrations have been observed when transitioning from the dry to wet seasons in the Amazon (20). Finally, the dimers previously observed in both laboratory-generated isoprene SOA and organic aerosol collected from the Amazon are likely not a result of hemiacetal formation (12); rather, these dimers are shown to form from polymerization of IEPOX by acid-catalyzed ring opening of IEPOX.

Isoprene SOA Formation under High- NO_x Conditions: Role of MPAN. The majority of the high- NO_x SOA yield from isoprene has previously been traced to the oxidation of a major [25% yield (25)] first-generation oxidation product of isoprene, MACR (9, 12). Providing further evidence of the role of MACR, the chemical composition of the SOA produced in the oxidation of MACR is similar to that found in studies of the oxidation of isoprene, especially 2-methylglyceric acid (2-MG), a C_4 -dihydroxycarboxylic acid, which undergoes esterification to produce low-volatility oligoesters (12, 26). Both 2-MG and its corresponding diester have been observed in ambient aerosol samples (7).

The preservation of the four-carbon backbone in the SOA produced following the oxidation of MACR provides significant constraints on the gas-phase mechanism that yields the SOA precursor. Oxidation of MACR by OH proceeds both via addition to the double bond (approximately 55%) and abstraction of the aldehydic hydrogen (45%) (27, 28). Preservation of the carbon backbone generally precludes formation of RO radicals because they rapidly decompose to form hydroxyacetone (via OH addition) and methylvinyl radicals (via aldehydic abstraction) (28). This suggests that, following abstraction of the aldehydic hydrogen by OH, formation of MPAN is likely key to SOA production. MPAN is formed from MACR with a maximum yield of approximately 45% (27, 29). Following addition of OH to the double bond, the only known gas-phase mechanism that prevents C-C fragmentation in the presence of NO_x is the channel leading to the formation of a hydroxynitrate (7, 27, 30). Thus, to oxidize both the double bond and the aldehydic hydrogen, one route to C_4 preservation leads to the formation of the hydroxynitrate of MPAN. Alternatively, the addition of OH to MPAN might lead

to the formation of bridged oxygen compounds if the alkyl radical (or subsequent RO_2 or RO radicals) rearrange unimolecularly and decompose by breaking off the weak peroxyxynitrate moiety forming peroxy or epoxy carbonyls.

To test the hypothesis that the formation of MPAN is key for SOA formation, 277 ppb MACR was oxidized by OH (formed via HONO photolysis) in the presence of a very high concentration of NO (>500 ppb). Under these conditions, the peroxyacyl radical formed following H-abstraction (and addition of O_2) reacts primarily with NO to form formaldehyde, CO, and CO_2 rather than with NO_2 to form MPAN (27, 29). Although formation of hydroxynitrate was observed from the addition channel (approximately 10–15% of hydroxyacetone), little SOA was produced (mass yield <2%). SOA yields (2.9% from 257 ppb MACR) were higher when 290 ppb of NO was added, and highest (5.1% from 285 ppb MACR) when 350 ppb of additional NO_2 (instead of NO) was injected. As shown in Fig. S7, the relative aerosol-phase concentrations of oligoesters are also enhanced under higher $[\text{NO}_2]/[\text{NO}]$ ratios, consistent with the trends observed in SOA yields from MACR photooxidation. The RTs and molecular formulas match those of the oligoester products formed in isoprene high- NO_x SOA. NO levels remained above 120 ppb during the course of all the experiments, and thus $\text{RO}_2 + \text{HO}_2$ and $\text{RO}_2 + \text{RO}_2$ reactions are not competitive. HONO levels, as measured by CIMS, were within 15% among these experiments. The observed increase in SOA at higher NO_2 levels is also unlikely to be a result of condensation of nitric acid from OH + NO_2 reactions because addition of gas-phase nitric acid did not lead to additional aerosol growth. The observed effect of $[\text{NO}_2]/[\text{NO}]$ ratio on oligoester formation and overall aerosol yields in MACR photooxidation suggests the importance of peroxyxynitrate formation via an $\text{RO}_2 + \text{NO}_2$ pathway. In the chamber, the lifetime of MPAN against thermal decomposition is about 100 min (31) and can be effectively much longer under higher $[\text{NO}_2]/[\text{NO}]$ ratios because the peroxyacyl radicals formed following thermal decomposition react preferentially with NO_2 reforming MPAN.

Identification of MPAN as Key Intermediate in Formation of SOA from Isoprene and MACR. To verify the hypothesis that the route to high- NO_x SOA formation from isoprene goes through MPAN, experiments were carried out with synthesized MPAN (see *Materials and Methods*). When MPAN was injected into the chamber in the presence solely of ammonium sulfate seed, SOA was not observed. Significant aerosol growth was observed only upon photooxidation of MPAN (with photolysis of HONO used as the OH source). Moreover, as shown in Fig. 4, the composition of SOA formed from MPAN oxidation was similar to that from high- NO_x photooxidation of MACR and isoprene. In particular, 2-MG and its corresponding oligoesters are identified in all three aerosol samples using both GC/EI-MS and UPLC/(–)ESI-TOFMS. Detailed chemical characterization of 2-MG and its corresponding oligoesters (12, 26) and similar analysis of the current samples confirm the presence of these products in aerosol formed from MPAN oxidation (Fig. 4 and Table S1). Other aerosol components found in isoprene SOA, such as compounds with a C_5 -hydroxynitrate backbone, are not found in MACR or MPAN SOA, but their contribution to total aerosol mass is likely small, and their formation mechanisms have been tentatively established (18). We confirmed that 2-MG and its corresponding oligoesters are formed as a result of MPAN oxidation and not an impurity (i.e., methacrylic acid) (SI Text).

Additional experiments provide insight into the mechanism by which 2-MG is formed from the OH reaction of MPAN. Oxidation of 2-methyl-3-buten-2-ol (MBO), structurally similar to isoprene but lacking the second double bond, leads to no aerosol formation. This suggests that formation of 2-MG requires OH reaction with the double bond of MPAN. OH addition to the MPAN double bond, followed by addition of O_2 , leads to forma-

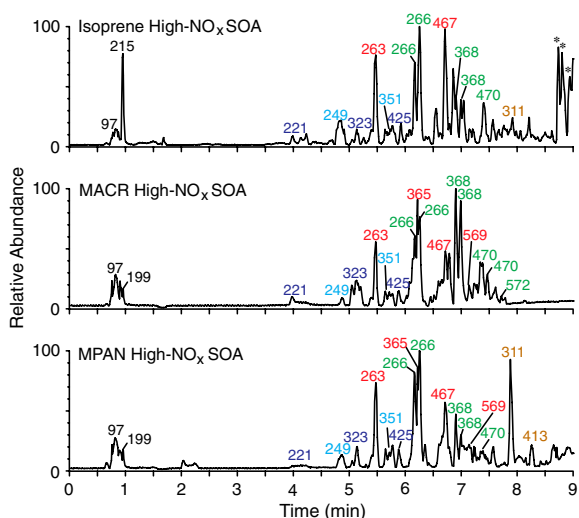


Fig. 4. UPLC(-)ESI-TOFMS BPCs. The numbers listed above each peak correspond to the respective $[M-H]^-$ base peak ions. Similar-colored $[M-H]^-$ ions are of the same oligoester series (Table S1). m/z 97, 199, and 215 correspond to sulfate, an organosulfate of 2-MG (16), and an organosulfate of 2-methyltetrols (15, 16), respectively.

tion of an RO_2 radical; under the chamber conditions, reaction with NO is most likely, leading to formation of either an RO radical or a C_4 -hydroxynitrate peroxyacetyl nitrate (PAN). Owing to the 2-position of the alkoxy group, this C_4 -alkoxy radical is unlikely to undergo traditional H-atom transfer isomerization and therefore decomposes rapidly to break the C_4 -backbone. One possibility is that 2-MG is formed through the C_4 -hydroxynitrate-PAN channel (see Fig. 5). Dommen et al. (32) observed lower-volatility isoprene SOA (which is consistent with the formation of oligomers) to form under dry rather than humid conditions, which is consistent with a mechanism that involves decomposition of the C_4 -hydroxynitrate-PAN into 2-MG and allows for subsequent esterification of 2-MG into the observed oligoesters. We do not, however, have conclusive chemical evidence to support the hypothesis that the C_4 -hydroxynitrate-PAN is the main precursor to the isoprene high- NO_x SOA. Indeed, there is some evidence that this is not the route. A signal, comparable

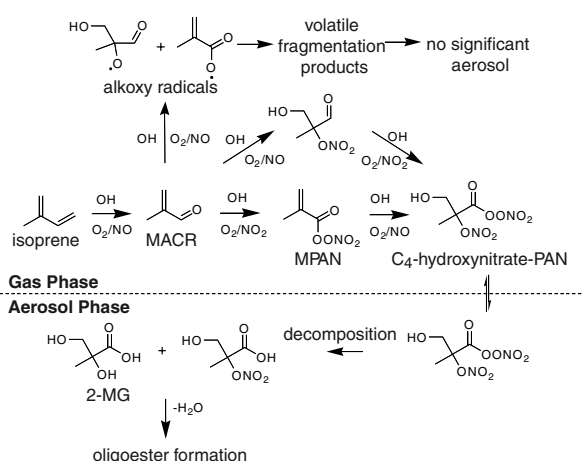


Fig. 5. Possible chemical mechanism for the formation of isoprene SOA under high- NO_x conditions. Detailed chemical structures of the high- NO_x SOA constituents resulting from the oligoester formation can be found in Table S1.

in magnitude to the hydroxynitrate of MACR (at m/z 234) and highly correlated to the time trace of SOA formation, is observed at m/z 311: a mass consistent with the cluster of CF_3O^- with the C_4 -hydroxynitrate-PAN. Assuming the same CIMS response factor as glycolaldehyde, the signal at m/z 311 is consistent with all of the C_4 -hydroxynitrate-PAN being accounted for in the gas phase (assuming the yield of the C_4 -hydroxynitrate from MPAN is comparable to the yield of the hydroxynitrate from MACR), and as a result, this compound could not be the SOA precursor. Thus, it is possible that some unknown C_4 -preserving chemical reaction is occurring when MPAN is oxidized by OH (e.g., similar to the formation of IEPOX under low- NO_x conditions, the OH-MPAN radical adduct intramolecularly rearranges into a highly strained epoxide before O_2 adds).

The OH reaction rate constants of saturated PANs are sufficiently small ($<1 \times 10^{-13} \text{ cm}^3 \text{ mol}^{-1} \text{ s}^{-1}$) that the major sink for these compounds in the atmosphere is thermal decomposition to the peroxyacyl radical followed by reaction with NO and subsequent decomposition to CO_2 . By contrast, the OH reaction of MPAN is competitive with thermal decomposition (28). Here we confirm that MPAN is the key intermediate in the isoprene and MACR systems in the formation of 2-MG and its corresponding low-volatility oligoesters in the aerosol phase. If a PAN-type compound is involved in the formation of aerosol-phase products, the aerosol yields should depend on the $[NO_2]/[NO]$ ratio because this ratio determines whether the peroxyacyl radicals produced via thermal decomposition reform PANs or react with NO and decompose. With urban $[NO_2]/[NO]$ ratios typically around 7, SOA mass yields from isoprene and MACR previously measured at $[NO_2]/[NO]$ ratios around 1 could be underestimated (8). Experimentally, such high $[NO_2]/[NO]$ ratios are not achieved using HONO as an OH source, because NO is produced from both the synthesis of HONO and photolysis of HONO with UV irradiation.

Atmospheric Implications. The importance of IEPOX and MPAN in forming isoprene SOA under low- and high- NO_x conditions, respectively, provides significant insights into heretofore-unidentified aerosol precursors. In the presence of anthropogenic pollutants, such as NO_2 and acidic aerosol produced from the oxidation of SO_2 , SOA mass yields from isoprene under high- and low- NO_x conditions, respectively, increase substantially. Because isoprene is estimated to be the largest single contributor to global SOA, these results may help to resolve two existing dilemmas in atmospheric chemistry: (i) Radiocarbon (^{14}C) data consistently indicate that well over half of the ambient SOA is of modern (biogenic) origin (7, 33), whereas correlations between water-soluble organic carbon and anthropogenic tracers, such as CO, suggest that much of the SOA is actually of anthropogenic origin (34, 35); and (ii) comparisons between measured and predicted SOA based on known precursors suggest that there is a substantial amount of “missing urban SOA” not included in current models (35–37). Revising the chemistry of isoprene in regional and global SOA models could lead to a decrease in this discrepancy; however, the measurement and parameterization of aerosol acidity requires additional work.

Materials and Methods

Experimental Details. The experiments were carried out in the Caltech dual 28- m^3 fluorinated ethylene propylene Teflon chambers (38). Seed aerosol is generated using a constant rate atomizer. Dilute solutions (concentrations of 0.06 M or lower) of ammonium sulfate and magnesium sulfate with sulfuric acid are used for neutral and highly acidic seed aerosol, respectively. The particle number and volume concentrations are corrected for particle wall loss using size-dependent coefficients determined from loss of inert particles. Isoprene, MACR, or MBO is added to the chamber by vaporizing a known volume of the hydrocarbon in a glass bulb. In the reactive uptake experiments (Table S2 and SI Text), BEPOX is injected into the chamber by vaporizing a small (approximately 30 mg) amount of the solid at approximately 60 °C

in a small glass vial and introducing the vapor into the chamber in a stream of N_2 . The amount injected into the chamber is estimated by measuring the mass loss of BEPOX after injection. MPAN is injected in a similar manner in a -10°C ice-salt bath. At -10°C , dodecane has a negligible vapor pressure, and as a result, is not expected to be introduced into the chambers. In low- NO_x photooxidation experiments (Table S2 and SI Text), the photolysis of H_2O_2 is used to generate OH radicals. In order to prevent partitioning of H_2O_2 into the seed aerosol, all low- NO_x experiments were conducted under dry conditions ($<10\%$ RH). At the relatively high mixing ratios of H_2O_2 , significant HO_2 radical levels are produced by the $\text{OH} + \text{H}_2\text{O}_2$ reaction, which is favored at the slow chamber photolysis rate of H_2O_2 . In high- NO_x photooxidation experiments, the photolysis of nitrous acid (HONO) is used as the OH precursor (see Table S3 and SI Text).

Gas-Phase Measurements. The concentrations of isoprene, MACR and MBO are monitored by a gas chromatograph equipped with a flame ionization detector (GC/FID, Agilent 6890N). NO/NO_x and O_3 are monitored by commercial chemiluminescence monitors (Horiba, APNA 360 and APOA 360, respectively). A custom-modified Varian 1200 CIMS was used to continuously monitor gas-phase species (3) (SI Text).

Aerosol-Phase Measurements. Aerosol size distributions and volume concentrations are measured using a differential mobility analyzer (TSI, Inc., 3081) with a condensation nuclei counter (TSI, Inc., 3760). Aerosol samples are collected onto Teflon filters for offline chemical characterization by both GC/EIMS with prior trimethylsilylation and UPLC/ESI-TOFMS. Filter handling and extraction protocols in high-purity methanol have been described previously for aerosol samples analyzed by the UPLC/(-)ESI-TOFMS technique (18). De-

tails of the sample preparation and operation protocols for the GC/EI-MS technique can be found in the SI Text. Selected SOA samples formed from the reactive uptake of BEPOX on either neutral or acidified sulfate seed aerosol were continuously sampled by a particle-into-liquid sampler with subsequent offline analysis by ion chromatography (39).

Materials

Isoprene (Aldrich, 99%), MACR (Aldrich, 95%), and MBO (Aldrich, 98%) are obtained from commercial sources. BEPOX is synthesized following the procedure derived by Skinner et al. (40) (SI Text). MPAN is synthesized from methacrylic anhydride (Aldrich, 94%) in dodecane (Sigma-Aldrich, 99 + %, anhydrous) based on the method of Nouaime et al. (41) with a few modifications (SI Text). The purity of the product is confirmed by gas-phase FTIR spectroscopy (SI Text).

ACKNOWLEDGMENTS. This work was supported by the Office of Science (Biological and Environmental Research), Electric Power Research Institute, U.S. Department of Energy Grant DE-FG02-05ER63983, and U.S. Environmental Protection Agency (EPA) STAR agreement RD-833749. The CIMS instrument was purchased as part of a major research instrumentation grant from the National Science Foundation (Grant ATM-0619783); assembly and testing was supported by the Davidow Discovery Fund. We thank Andreas Kürten for assembling the CIMS instrument and John D. Crouse for synthesizing and characterizing (with H-NMR) the BEPOX. The Waters UPLC-LCT Premier XT time-of-flight mass spectrometer was purchased in 2006 with a grant from the National Science Foundation, Chemistry Research Instrumentation and Facilities Program (Grant CHE-0541745). N.C.E. was supported by the Camille and Henry Dreyfus Postdoctoral Program in Environmental Chemistry. We also thank Magda Claeys for useful discussions.

- Guenther A, et al. (2006) Estimates of global terrestrial isoprene emissions using MEGAN (model of emissions of gases and aerosols from nature). *Atmos Chem Phys*, 6:3181–3210.
- Lelieveld J, et al. (2008) Atmospheric oxidation capacity sustained by a tropical forest. *Nature*, 452:737–740.
- Paulot F, et al. (2009) Unexpected epoxide formation in the gas-phase photooxidation of isoprene. *Science*, 325:730–733.
- Chameides WL, Lindsay RW, Richardson J, Kiang CS (1988) The role of biogenic hydrocarbons in urban photochemical smog: Atlanta as a case study. *Science*, 241:1473–1475.
- Claeys M, et al. (2004) Formation of secondary organic aerosols through photooxidation of isoprene. *Science*, 303:1173–1176.
- Henze DK, et al. (2008) Global modeling of secondary organic aerosol formation from aromatic hydrocarbons: High- vs. low-yield pathways. *Atmos Chem Phys*, 8:2405–2420.
- Hallquist M, et al. (2009) The formation, properties and impact of secondary organic aerosol: Current and emerging issues. *Atmos Chem Phys*, 9:5155–5236.
- Carlton AG, Wiedinmyer C, Kroll JH (2009) A review of secondary organic aerosol (SOA) formation from isoprene. *Atmos Chem Phys*, 9:4987–5005.
- Kroll JH, Ng NL, Murphy SM, Flagan RC, Seinfeld JH (2006) Secondary organic aerosol formation from isoprene photooxidation. *Environ Sci Technol*, 40:1869–1877.
- Presto AA, Hartz KEH, Donahue NM (2005) Secondary organic aerosol production from terpene ozonolysis 2. Effect of NO_x concentration. *Environ Sci Technol*, 39:7046–7054.
- Kroll JH, Seinfeld JH (2008) Chemistry of secondary organic aerosol: Formation and evolution of low-volatility organics in the atmosphere. *Atmos Environ*, 42:3593–3624.
- Surratt JD, et al. (2006) Chemical composition of secondary organic aerosol formed from the photooxidation of isoprene. *J Phys Chem A*, 110:9665–9690.
- Lim YB, Ziemann PJ (2009) Chemistry of secondary organic aerosol formation from OH radical-initiated reactions of linear, branched, and cyclic alkanes in the presence of NO_x . *Aerosol Sci Technol*, 43:604–619.
- Edney EO, et al. (2005) Formation of 2-methyl tetrols and 2-methylglyceric acid in secondary organic aerosol from laboratory irradiated isoprene/ NO_x / SO_2 /air mixtures and their detection in ambient $\text{PM}_{2.5}$ samples collected in the eastern United States. *Atmos Environ*, 39:5281–5289.
- Surratt JD, et al. (2007) Effect of acidity on secondary organic aerosol formation from isoprene. *Environ Sci Technol*, 41:5363–5369.
- Surratt JD, et al. (2007) Evidence for organosulfates in secondary organic aerosol. *Environ Sci Technol*, 41:517–527.
- Gómez-González Y, et al. (2008) Characterization of organosulfates from the photooxidation of isoprene and unsaturated fatty acids in ambient aerosol using liquid chromatography/(-)electrospray ionization mass spectrometry. *J Mass Spectrom*, 43:371–383.
- Surratt JD, et al. (2008) Organosulfate formation in biogenic secondary organic aerosol. *J Phys Chem A*, 112:8345–8378.
- Minerath EC, Elrod MJ (2009) Assessing the potential for diol and hydroxy sulfate ester formation from the reaction of epoxides in tropospheric aerosols. *Environ Sci Technol*, 43:1386–1392.
- Wang W, et al. (2005) Characterization of oxygenated derivatives of isoprene related to 2-methyltetrols in Amazonian aerosols using trimethylsilylation and gas chromatography/ion trap mass spectrometry. *Rapid Commun Mass Spectrom*, 19:1343–1351.
- Kleindienst TE, Lewandowski M, Offenberg JH, Jaoui M, Edney EO (2009) The formation of secondary organic aerosol from the isoprene +OH reaction in the absence of NO_x . *Atmos Chem Phys*, 9:6541–6558.
- Ren XR, et al. (2003) Intercomparison of peroxy radical measurements at a rural site using laser-induced fluorescence and Peroxy Radical Chemical Ionization Mass Spectrometer (PerCIMS) techniques. *J Geophys Res*, 108(D19):4605.
- Atkinson R, et al. (2006) Evaluated kinetic and photochemical data for atmospheric chemistry: Volume II—Gas phase reactions of organic species. *Atmos Chem Phys*, 6:3625–4055.
- linuma Y, Böge O, Kahnt A, Herrmann H (2009) Laboratory chamber studies on the formation of organosulfates from reactive uptake of monoterpene oxides. *Phys Chem Chem Phys*, 11:7985–7997.
- Tuazon EC, Atkinson R (1990) A product study of the gas-phase reaction of isoprene with OH radical in the presence of NO_x . *Int J Chem Kinet*, 22:1221–1236.
- Szmigielski R, et al. (2007) Characterization of 2-methylglyceric acid oligomers in secondary organic aerosol formed from the photooxidation of isoprene using trimethylsilylation and gas chromatography/ion trap mass spectrometry. *J Mass Spectrom*, 42:101–116.
- Tuazon EC, Atkinson R (1990) A product study of the gas-phase reaction of methacrolein with the OH radical in the presence of NO_x . *Int J Chem Kinet*, 22:591–602.
- Orlando JJ, Tyndall GS, Paulson SE (1999) Mechanism of the OH-initiated oxidation of methacrolein. *Geophys Res Lett*, 26:2191–2194.
- Bertman SB, Roberts JM (1991) A PAN analog from isoprene photooxidation. *Geophys Res Lett*, 18:1461–1464.
- Paulot F, et al. (2009) Isoprene photooxidation: New insights into the production of acids and organic nitrates. *Atmos Chem Phys*, 9:1479–1501.
- Roberts JM, Bertman SB (1992) The thermal decomposition of peroxyacetic nitric anhydride (PAN) and peroxyacetic nitric anhydride (MPAN). *Int J Chem Kinet*, 24:297–307.
- Dommen J, et al. (2006) Laboratory observation of oligomers in the aerosol from isoprene/ NO_x photooxidation. *Geophys Res Lett*, 33:L13805.
- Schichtel BA, et al. (2008) Fossil and contemporary fine particulate carbon fractions at 12 rural and urban sites in the United States. *J Geophys Res*, 113:D02311.
- Weber RJ, et al. (2007) A study of secondary organic aerosol formation in the anthropogenic-influenced southeastern United States. *J Geophys Res*, 112:D13302.
- de Gouw JA, et al. (2005) Budget of organic carbon in a polluted atmosphere: Results from the New England Air Quality Study in 2002. *J Geophys Res*, 110:D16305.
- Heald CL, et al. (2005) A large organic aerosol source in the free troposphere missing from current models. *Geophys Res Lett*, 32:L18809.
- Volkamer R, et al. (2006) Secondary organic aerosol formation from anthropogenic air pollution: Rapid and higher than expected. *Geophys Res Lett*, 33:L17811.
- Keywood MD, Varutbangkul V, Bahreini R, Flagan RC, Seinfeld JH (2004) Secondary organic aerosol formation from the ozonolysis of cycloalkenes and related compounds. *Environ Sci Technol*, 38:4157–4164.
- Sorooshian A, et al. (2006) Modeling and characterization of a particle-into-liquid sampler (PILS). *Aerosol Sci Technol*, 40:396–409.
- Skinner JR, Wilcoxon CH, Carlson GJ (1958) Production of epoxides. *United States Patent Office* 2,833,788.
- Nouaime G, et al. (1998) Sequential oxidation products from tropospheric isoprene chemistry: MACR and MPAN at a NO_x -rich forest environment in the southeastern United States. *J Geophys Res*, 103(D17):22463–22471.

Appendix F

Constraining the contribution of organic acids and AMS m/z 44 to the organic aerosol budget: On the importance of meteorology, aerosol hygroscopicity, and region*

*Reproduced with permission from “Constraining the contribution of organic acids and AMS m/z 44 to the organic aerosol budget: On the importance of meteorology, aerosol hygroscopicity, and region” by Sorooshian, A., Murphy, S.M., Hersey S.P., Bahreini, R., Jonsson, H., Flagan R.C., and Seinfeld, J.H., *Geophysical Research Letters*, 37 (21), doi:10.1029/2010GL044951, 2010. Copyright 2010 by the American Geophysical Union.

Constraining the contribution of organic acids and AMS m/z 44 to the organic aerosol budget: On the importance of meteorology, aerosol hygroscopicity, and region

Armin Sorooshian,^{1,2} Shane M. Murphy,³ Scott Hersey,⁴ Roya Bahreini,³ Hafliði Jonsson,⁵ Richard C. Flagan,⁴ and John H. Seinfeld⁴

Received 8 August 2010; revised 14 September 2010; accepted 21 September 2010; published 4 November 2010.

[1] Airborne measurements in regions of varying meteorology and pollution are used to quantify the contribution of organic acids and a mass spectral marker for oxygenated aerosols, m/z 44, to the total organic aerosol budget. Organic acids and m/z 44 separately are shown to exhibit their highest organic mass fractions in the vicinity of clouds. The contribution of such oxygenated species is shown to increase as a function of relative humidity, aerosol hygroscopicity (and decreasing organic mass fraction), and is typically greater off the California coast versus the continental atmospheres studied. Reasons include more efficient chemistry and partitioning of organic acid precursors with increasing water in the reaction medium, and high aqueous-phase processing times in boundary layers with higher cloud volume fractions. These results highlight the importance of secondary organic aerosol formation in both wet aerosols and cloud droplets.

Citation: Sorooshian, A., S. M. Murphy, S. Hersey, R. Bahreini, H. Jonsson, R. C. Flagan, and J. H. Seinfeld (2010), Constraining the contribution of organic acids and AMS m/z 44 to the organic aerosol budget: On the importance of meteorology, aerosol hygroscopicity, and region, *Geophys. Res. Lett.*, 37, L21807, doi:10.1029/2010GL044951.

1. Introduction

[2] The chemical complexity of atmospheric aerosols poses a challenge for accurate modeling of their interactions with water vapor, radiation, and clouds. It is now well established that the organic fraction of atmospheric aerosols becomes increasingly oxidized with age, leading to species that are both less volatile and more hygroscopic [Jimenez *et al.*, 2009]. Water-soluble organic species, especially organic acids, are of interest owing to their hygroscopic properties [Hallquist *et al.*, 2009]. Oxidized organic compounds can be generated in cloud droplets as well as moist

aerosols [Volkamer *et al.*, 2009; Lim *et al.*, 2010; Ervens and Volkamer, 2010], and increased partitioning of water-soluble organic compounds (WSOC) with increasing sub-saturated relative humidity (RH) is observed [Hennigan *et al.*, 2008, 2009]. While the concentrations of organic acids are documented in different regions [Sorooshian *et al.*, 2007a, and references therein], the extent to which such water-soluble oxygenated acids contribute to total organic aerosol levels is not well established in a variety of atmospheres [Takegawa *et al.*, 2007; Kondo *et al.*, 2007].

[3] We present an analysis of datasets from four aircraft field studies that addresses the following questions: (1) What is the contribution of organic acids and the mass spectral peak m/z 44 to total organic aerosol mass in a variety of clear and cloudy atmospheres?; and (2) How does the relative abundance depend on meteorology, background aerosol physicochemical properties, and reaction medium (i.e., wet aerosols versus dilute droplets)?

2. Measurements

[4] Airborne measurements were carried out with the Center for Interdisciplinary Remotely-Piloted Aircraft Studies (CIRPAS) Twin Otter during the following campaigns: International Consortium for Atmospheric Research on Transport and Transformation (ICARTT, August 2004; Ohio River Valley), Marine Stratus/Stratocumulus Experiments (MASE I and II, in July 2005 and 2007, respectively; off the central California coast), and the Gulf of Mexico Atmospheric Composition and Climate Study (GoMACCS, August–September 2006; Southeastern Texas). Three aircraft inlets were utilized: (i) a forward-facing inlet outside of clouds [Hegg *et al.*, 2005]; (ii) a counterflow virtual impactor (CVI) inlet in clouds to isolate droplet residual particles [Sorooshian *et al.*, 2006b]; and (iii) a reverse-facing inlet in clouds to isolate interstitial aerosol particles (used only during MASE II).

[5] Particulate organic acid measurements were carried out with a particle-into-liquid sampler (PILS; Brechtel Mfg Inc.) coupled to an ion chromatograph [Sorooshian *et al.*, 2006a]. Data are presented for a suite of organic acids ions (saturated dicarboxylic acids C_2 – C_9 , acetic, formic, pyruvic, glyoxylic, maleic, malic, and methanesulfonic acids). Independent measurements of inorganic mass (sulfate, nitrate, ammonium) and total non-refractory organic mass were obtained with a quadrupole Aerosol Mass Spectrometer (Aerodyne AMS) [Jayne *et al.*, 2000; Bahreini *et al.*, 2003] during the first experiment (ICARTT) and with a compact Time of Flight Aerosol Mass Spectrometer

¹Department of Chemical and Environmental Engineering, University of Arizona, Tucson, Arizona, USA.

²Department of Atmospheric Sciences, University of Arizona, Tucson, Arizona, USA.

³Earth Systems Research Laboratory, NOAA, Boulder, Colorado, USA.

⁴Departments of Environmental Science and Engineering and Chemical Engineering, California Institute of Technology, Pasadena, California, USA.

⁵Center for Interdisciplinary Remotely-Piloted Aircraft Studies, Naval Postgraduate School, Monterey, California, USA.

Table 1. Statistical Summary of Various Ratios Between Organic Aerosol Markers in Different Regions

	Pacific Coast ^a				Continental ^b			
	Average	STD	Slope	r ²	Average	STD	Slope	r ²
Oxalate: Organic	0.04	0.04	0.02	0.34	0.03	0.02	0.02	0.42
Organic Acid: Organic	0.06	0.06	0.02	0.32	0.04	0.04	0.02	0.45
Oxalate: <i>m/z</i> 44	0.27	0.23	0.17	0.45	0.18	0.15	0.16	0.47
Organic Acid: <i>m/z</i> 44	0.39	0.33	0.19	0.43	0.23	0.22	0.18	0.50
<i>m/z</i> 44: Organic	0.18	0.10	0.11	0.77	0.15	0.05	0.14	0.92
Oxalate: <i>m/z</i> 57	2.47	2.96	0.09	0.12	2.82	2.34	1.90	0.25
Organic Acid: <i>m/z</i> 57	2.72	3.37	0.10	0.08	3.17	2.64	2.00	0.24

^a“Pacific Coast” corresponds to MASE I/II data ($n = 586$).

^b“Continental” represents ICARTT/GoMACCS data ($n = 384$).

(Aerodyne C-ToF-AMS) [Drewnick *et al.*, 2005; Murphy *et al.*, 2009] during MASE I, MASE II, and GoMACCS. Other AMS data discussed include the organic mass represented by *m/z* 44 (higher fractions relative to total organic mass suggest more oxidation) and 57 (higher fractions suggest more hydrocarbon-like organics) [Zhang *et al.*, 2005; Aiken *et al.*, 2008]. As an example of the measurement agreement between the AMS and PILS, the sulfate concentrations for the data set in this study exhibit an overall correlation of $r^2 = 0.90$ ($n = 970$) and an AMS:PILS ratio of 0.98. No significant relationship was observed between the AMS:PILS sulfate ratio and variables of interest in this study including ambient RH and organic mass fraction.

[6] Sub-saturated aerosol hygroscopicity measurements were provided by a differential aerosol sizing and hygroscopicity spectrometer probe (DASH-SP; Brechtel Mfg Inc.) [Sorooshian *et al.*, 2008]. DASH-SP data are only reported for the MASE II campaign, corresponding to particles with dry diameters of either 150, 175, or 200 nm, and humidified to RHs of either 74%, 85%, or 92%.

3. Cumulative Results

[7] Cumulative statistics associated with ratios of various oxygenated organic markers relative to the total organic mass are given in Table 1, with the data categorized into “Pacific Coast” (MASE I and MASE II) and “Continental” conditions (ICARTT and GoMACCS). Note that background marine conditions often do not exist off the central coast of California owing to aged ship and continental emissions [Murphy *et al.*, 2009]. Conversely, air masses during GoMACCS (southeastern Texas) may have been marine-influenced. The term “organic acids” will henceforth refer to the sum of the species quantified by the PILS as listed above. Particular attention is placed on oxalate as it was the dominant organic acid in these field studies and has been shown to be produced in clouds [Sorooshian *et al.*, 2006b, 2007a/2007b].

[8] Total organic mass and the organic mass associated with *m/z* 44 are highly correlated ($r^2 = 0.77$ – 0.92), suggesting that organic aerosol production in the studied regions was linked to the formation of oxidized organic aerosol species. The average mass ratios of oxalate:organic, organic acid:organic, oxalate:*m/z* 44, organic acid:*m/z* 44, and *m/z* 44:organic are highest in the Pacific Coast atmosphere, indicative of a more oxidized average organic component. This is thought to be partly a result of the greater fraction of the marine boundary layer volume occupied by clouds relative to the continental atmospheres studied, allowing for longer aqueous-phase processing times

[Feingold *et al.*, 1998]. Oxalate and the cumulative organic acids accounted for a maximum of 21% and 44% of the marine organic mass, respectively. The organic acids are weakly correlated with *m/z* 57, suggesting that there is not a strong non-oxidized emissions source of organic acids (such as emissions from ships [Murphy *et al.*, 2009]). The correlations are higher for the organic acids versus *m/z* 44 as compared to organic acids versus total organics, demonstrating that *m/z* 44 is more closely linked to oxygenated organic acid species. As a basis for comparison, Takegawa *et al.* [2007] observed higher correlations between selected carboxylic acids and *m/z* 44 ($r^2 = 0.85$ – 0.94), and showed that the acids contributed $14 \pm 5\%$ to the *m/z* 44 mass concentration. The differences in those values may be linked to the varying measurement methods and region (those organic acid measurements involved ground-based filters in Tokyo).

[9] The relatively large standard deviations in Table 1 indicate that the ratios exhibit dependence on conditions other than region. Figure 1 summarizes the variation of chemical ratios in Table 1 as a function of location below altitudes of 5 km (“clear air” away from clouds, “below cloud”, “droplet residual particles” in cloud, “interstitial aerosol” in cloud, and “above cloud”). The various ratios usually exhibit the lowest values in “clear air” and the highest values and correlation coefficients (between ratio components) in cloud droplet residual particles, owing to the effectiveness of in-cloud formation [Sorooshian *et al.*, 2006b, 2007a/2007b]. As higher values are observed in cloud droplet residual particles versus interstitial aerosols, this likely reflects some combination of more efficient chemistry and partitioning of WSOC precursors as a function of increasing volume of liquid water. This result is consistent with prior measurements of enhanced partitioning of water-soluble organic species in cloud and fog droplets relative to interstitial aerosols [Facchini *et al.*, 1999; Blando and Turpin, 2000; Limbeck and Puxbaum, 2000; Collett *et al.*, 2008].

4. Relative Humidity Effect

[10] Figure 2 shows the relationship between RH and the same organic ratios examined in Figure 1. The ratios remain relatively constant until an RH near 70%, above which the ratios increase, behavior that is remarkably similar to measurements that showed maximum partitioning of WSOC to the particle phase for $RH > 70\%$ in the Atlanta atmosphere during the summertime [Hennigan *et al.*, 2008]. There is a much wider dynamic range in the organic acid:*m/z* 44 ratios (Figure 2a: 0.10–0.63 from 0 to 100% RH) as compared to

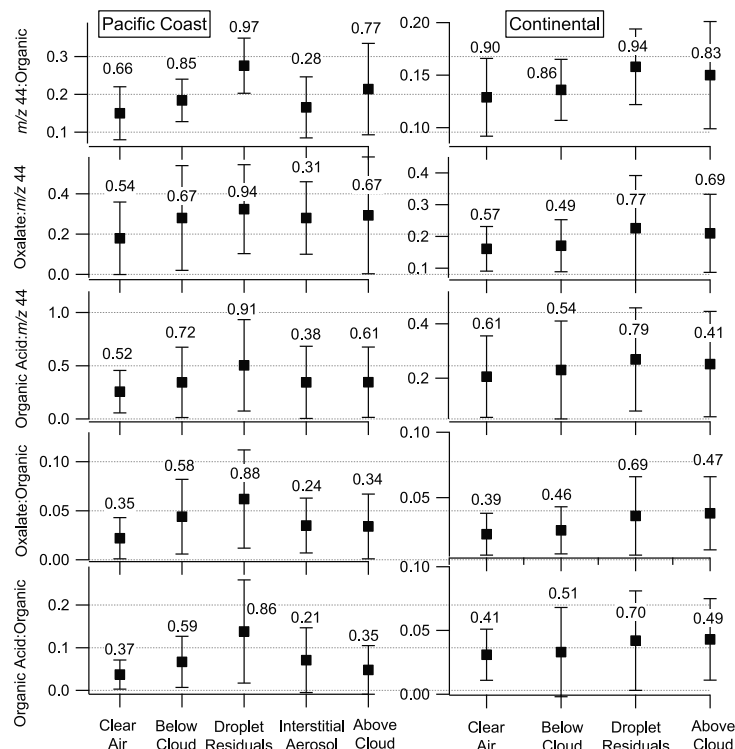


Figure 1. Relationship between ratios of organic aerosol markers and location with respect to clouds. Numbers next to markers indicate the correlation (r^2) between the two components of the ratios examined.

organic acid:organic ratios (Figure 2b: 0.02–0.08 from 0 to 100% RH), pointing to the more vigorous enrichment of organic acids relative to the oxygenated aerosol fraction represented by m/z 44. Although not shown, the organic ratios in Figure 2 exhibit the same RH-dependent qualitative behavior in each region examined, and are typically higher for the Pacific Coast across the entire RH range.

5. Aerosol Hygroscopicity Effect

[11] To further examine the role of liquid water in influencing the ratios of organic acids and oxygenated organics to the total organic mass, the relationship between aerosol hygroscopicity and these ratios is investigated in bins of ambient RH. This analysis can most directly be performed for the MASE II mission when hygroscopicity was measured. To control for the effect of ambient RH and to still do the analysis with a sufficient amount of data, the m/z 44: organic ratio is examined for measurements between RHs of 60–95%. Figure 3d shows that this ratio tends to increase as a function of the hygroscopic growth factor ($GF = D_{p,wet}/D_{p,dry}$) at the three pre-selected DASH-SP RHs (74%, 85%, 92%). This indicates that for the RH range examined, particles with a greater tendency to take up water will have an organic component that is more enriched with oxygenated species.

[12] Since hygroscopicity was not directly quantified in the other three field studies (ICARTT, GoMACCS, MASE I), the organic mass fraction of aerosols (= AMS organic mass/AMS total mass = 1–inorganic fraction) will be used as a

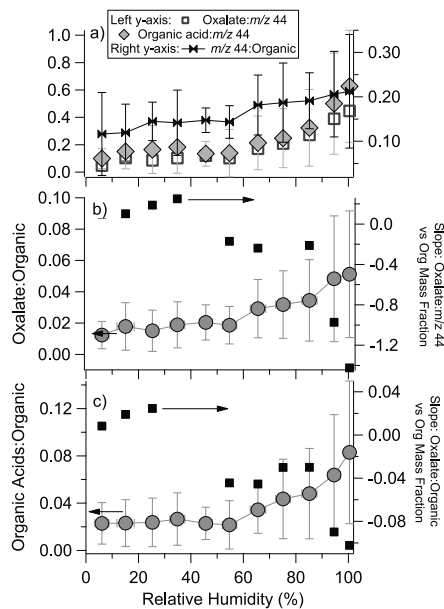


Figure 2. (a) Dependence of numerous organic ratios on RH. Data are grouped in RH bins (10% increments). (b, c) The right y-axes correspond to the slopes of “oxalate: m/z 44 vs organic mass fraction” and “oxalate:organic vs organic mass fraction” in each RH bin, where the organic mass fraction is used as a proxy for aerosol hygroscopicity. Only statistically significant slopes at 95% confidence are shown.

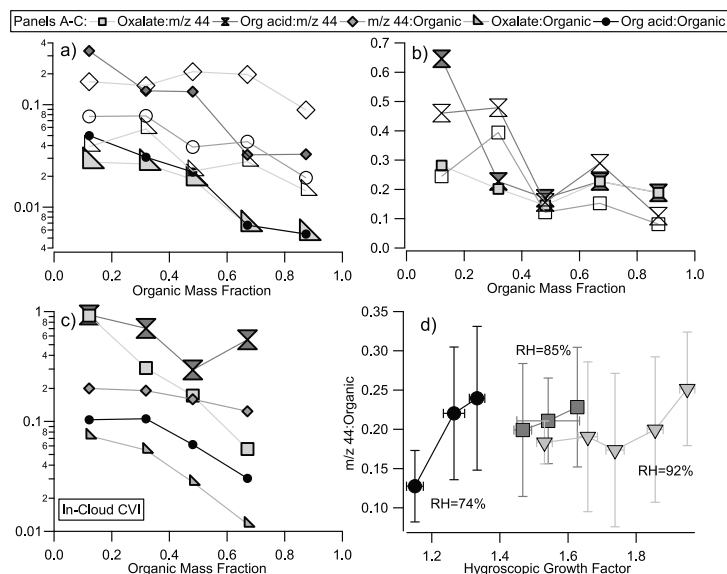


Figure 3. (a–c) Dependence of numerous organic ratios on organic mass fraction for ambient RHs between 60–95%. Data are grouped in organic mass fraction bins (0.2 increments). Open markers in Figures 3a and 3b correspond to low total aerosol mass concentrations ($1\text{--}5\ \mu\text{g m}^{-3}$) and filled markers correspond to higher total aerosol mass concentrations ($5\text{--}50\ \mu\text{g m}^{-3}$). (d) m/z 44:organic ratio as a function of hygroscopic growth factor at three pre-selected DASH-SP RHs (74%, 85%, 92%) for a dry diameter of 200 nm during MASE II for ambient RHs between 60–95%.

hygroscopicity proxy. At least for the MASE II region, hygroscopicity expectedly increases with decreasing organic mass fraction, as shown by Hersey *et al.* [2009], with the effect more pronounced at higher RHs. It is shown in Figures 2b and 2c that in the highest RH bins ($> 50\%$), the enrichment of organic acids and oxalate is most pronounced at lower organic mass fractions. This is more clearly illustrated in Figures 3a and 3b where it is shown that the contribution of organic acids and m/z 44 to the total organic mass typically increases as a function of decreasing organic mass fraction for in-cloud droplet residual particles and for wet aerosols between ambient RHs of 60 to 95%. These results agree with those of MASE II in that higher aerosol hygroscopicity will result in more aerosol-laden water, and therefore the enrichment of organic acids and other oxygenated organics relative to the total organic mass.

[13] Since the amount of liquid water in particles increases as a function of higher hygroscopic aerosol mass concentrations, the effect of aerosol mass on the various ratios of organic acid and oxygenated organics to total organic mass is also examined. Out-of-cloud data are examined in Figures 3a and 3b in bins of “low” and “high” aerosol mass concentrations. It is difficult to see any enhancement in the organic acids or m/z 44 at the higher mass concentrations, except in conditions of very low organic mass fractions (< 0.2). When binning the field data by m/z 44 mass concentration, the ratios in Figures 3a and 3b still were not greater at the higher m/z 44 levels. These measurements do not exhibit as clear a signal as recent studies showing a linear relationship between SOA production and aerosol seed concentration (and water mass) [Ervens and Volkamer, 2010], and greater WSOC aerosol/gas partitioning ratios as a function of increasing particulate WSOC concentration

[Hennigan *et al.*, 2009]. This may be owing to the enrichment of species other than organic acids in the regions studied.

6. Conclusions

[14] From several airborne field missions, a highly water-soluble class of organics, specifically organic acids, and also a larger body of oxygenated species indicated by the m/z 44 mass spectral peak, are found to contribute to the total organic aerosol fraction, with the absolute contribution increasing as a function of RH and aerosol hygroscopicity (and decreasing organic mass fraction). The contribution of organic acids is highest in cloud droplet residuals and is larger for the Pacific Coast (up to more than 44% of the organic mass) relative to the continental atmospheres examined. The high fraction of such species in the former region is thought to be at least partly due to longer aerosol residence times in the aqueous phase owing to higher cloud volume fractions in the boundary layer. These results highlight the important dual role of both ambient RH and hygroscopicity in leading to an enrichment of oxygenated organics, especially organic acids, in ambient aerosols. More liquid water associated with aerosol particles facilitates the dissolution of organic acid precursors, such as glyoxal, and also conversion of such species to the eventual organic acids [Blando and Turpin, 2000].

[15] This work shows that the relative amount of organic acids (especially oxalate) to other aerosol components (e.g., organic mass, m/z 44) can be used as tracers for air parcels that have undergone aqueous-phase processing. This work strengthens a growing consensus among modeling, laboratory chamber, and ground-based field studies that liquid water content plays a key role in organic aerosol formation.

[16] **Acknowledgments.** AS acknowledges support from an Office of Naval Research YIP award (N00014-10-1-0811). SMM acknowledges a NASA Earth and Space Sciences Fellowship and a NRC Postdoctoral Fellowship. The aircraft measurements were supported by NOAA grant NA06OAR4310082, ONR grant N00014-04-1-0118, and NSF grant ATM-0340832. The authors acknowledge Barbara Ervens for helpful discussions.

References

- Aiken, A. C., et al. (2008), O/C and OM/OC ratios of primary, secondary, and ambient organic aerosols with high resolution time-of-flight aerosol mass spectrometry, *Environ. Sci. Technol.*, *42*, 4478–4485, doi:10.1021/es703009q.
- Bahreini, R., J. L. Jimenez, J. Wang, R. C. Flagan, J. H. Seinfeld, J. T. Jayne, and D. R. Worsnop (2003), Aircraft-based aerosol size and composition measurements during ACE-Asia using an Aerodyne aerosol mass spectrometer, *J. Geophys. Res.*, *108*(D23), 8645, doi:10.1029/2002JD003226.
- Blando, J. D., and B. J. Turpin (2000), Secondary organic aerosol formation in cloud and fog droplets: A literature evaluation of plausibility, *Atmos. Environ.*, *34*, 1623–1632, doi:10.1016/S1352-2310(99)00392-1.
- Collett, J. L., P. Herckes, S. Youngster, and T. Lee (2008), Processing of atmospheric organic matter by California radiation fogs, *Atmos. Res.*, *87*, 232–241, doi:10.1016/j.atmosres.2007.11.005.
- Drewnick, F., et al. (2005), A new time-of-flight aerosol mass spectrometer (TOF-AMS): Instrument description and first field deployment, *Aerosol Sci. Technol.*, *39*, 637–658, doi:10.1080/02786820500182040.
- Ervens, B., and R. Volkamer (2010), Glyoxal processing outside clouds: Towards a kinetic modeling framework of secondary organic aerosol formation in aqueous particles, *Atmos. Chem. Phys.*, *10*, 8219–8244, doi:10.5194/acp-10-8219-2010.
- Ervens, B., G. Feingold, G. J. Frost, and S. M. Kreidenweis (2004), A modeling study of aqueous production of dicarboxylic acids: 1. Chemical pathways and speciated organic mass production, *J. Geophys. Res.*, *109*, D15205, doi:10.1029/2003JD004387.
- Facchini, M. C., et al. (1999), Partitioning of the organic aerosol component between fog droplets and interstitial air, *J. Geophys. Res.*, *104*, 26,821–26,832, doi:10.1029/1999JD900349.
- Feingold, G., S. M. Kreidenweis, and Y. Zhang (1998), Stratocumulus processing of gases and cloud condensation nuclei: 1. Trajectory ensemble model, *J. Geophys. Res.*, *103*, 19,527–19,542, doi:10.1029/98JD01750.
- Hallquist, M., et al. (2009), The formation, properties and impact of secondary organic aerosol: current and emerging issues, *Atmos. Chem. Phys.*, *9*, 5155–5236, doi:10.5194/acp-9-5155-2009.
- Hegg, D. A., D. S. Covert, P. A. Covert, and H. Jonsson (2005), Determination of the efficiency of an aircraft aerosol inlet, *Aerosol Sci. Technol.*, *39*, 966–971, doi:10.1080/02786820500377814.
- Hennigan, C. J., M. H. Bergin, J. E. Dibb, and R. J. Weber (2008), Enhanced secondary organic aerosol formation due to water uptake by fine particles, *Geophys. Res. Lett.*, *35*, L18801, doi:10.1029/2008GL035046.
- Hennigan, C. J., M. H. Bergin, A. G. Russell, A. Nenes, and R. J. Weber (2009), Gas/particle partitioning of water-soluble organic aerosol in Atlanta, *Atmos. Chem. Phys.*, *9*, 3613–3628, doi:10.5194/acp-9-3613-2009.
- Hersey, S. P., A. Sorooshian, S. M. Murphy, R. C. Flagan, and J. H. Seinfeld (2009), Aerosol hygroscopicity in the marine atmosphere: A closure study using high-resolution, size-resolved AMS and multiple-RH DASH-SP data, *Atmos. Chem. Phys.*, *9*, 2543–2554, doi:10.5194/acp-9-2543-2009.
- Jayne, J. T., D. C. Leard, X. F. Zhang, P. Davidovits, K. A. Smith, C. E. Kolb, and D. R. Worsnop (2000), Development of an aerosol mass spectrometer for size and composition analysis of submicron particles, *Aerosol Sci. Technol.*, *33*, 49–70, doi:10.1080/027868200410840.
- Jimenez, J. L., et al. (2009), Evolution of organic aerosols in the atmosphere, *Science*, *326*, 1525–1529, doi:10.1126/science.1180353.
- Kondo, Y., Y. Miyazaki, N. Takegawa, T. Miyakawa, R. J. Weber, J. L. Jimenez, Q. Zhang, and D. R. Worsnop (2007), Oxygenated and water-soluble organic aerosols in Tokyo, *J. Geophys. Res.*, *112*, D01203, doi:10.1029/2006JD007056.
- Lim, H. J., Y. Tan, M. J. Perri, S. P. Seitzinger, and B. J. Turpin (2010), Aqueous chemistry and its role in secondary organic aerosol (SOA) formation, *Atmos. Chem. Phys. Discuss.*, *10*, 14,161–14,207, doi:10.5194/acpd-10-14161-2010.
- Limbeck, A., and H. Puxbaum (2000), Dependence of in-cloud scavenging of polar organic aerosol compounds on the water solubility, *J. Geophys. Res.*, *105*, 19,857–19,867, doi:10.1029/2000JD900123.
- Murphy, S. M., et al. (2009), Comprehensive simultaneous shipboard and airborne characterization of exhaust from a modern container ship at sea, *Environ. Sci. Technol.*, *43*, 4626–4640, doi:10.1021/es802413j.
- Sorooshian, A., et al. (2006a), Modeling and characterization of a particle-into-liquid sampler (PILS), *Aerosol Sci. Technol.*, *40*, 396–409, doi:10.1080/02786820600632282.
- Sorooshian, A., et al. (2006b), Oxalic acid in clear and cloudy atmospheres: Analysis of data from International Consortium for Atmospheric Research on Transport and Transformation 2004, *J. Geophys. Res.*, *111*, D23S45, doi:10.1029/2005JD006880.
- Sorooshian, A., N. L. Ng, A. W. H. Chan, G. Feingold, R. C. Flagan, and J. H. Seinfeld (2007a), Particulate organic acids and overall water-soluble aerosol composition measurements from the 2006 Gulf of Mexico Atmospheric Composition and Climate Study (GoMACCS), *J. Geophys. Res.*, *112*, D13201, doi:10.1029/2007JD008537.
- Sorooshian, A., et al. (2007b), On the source of organic acid aerosol layers above clouds, *Environ. Sci. Technol.*, *41*, 4647–4654, doi:10.1021/es0630442.
- Sorooshian, A., S. Hersey, F. J. Brechtel, A. Corless, R. C. Flagan, and J. H. Seinfeld (2008), Rapid, size-resolved aerosol hygroscopic growth measurements: Differential aerosol sizing and hygroscopicity spectrometer probe (DASH-SP), *Aerosol Sci. Technol.*, *42*, 445–464, doi:10.1080/02786820802178506.
- Takegawa, N., T. Miyakawa, K. Kawamura, and Y. Kondo (2007), Contribution of selected dicarboxylic and omega-oxocarboxylic acids in ambient aerosol to the m/z 44 signal of an aerodyne aerosol mass spectrometer, *Aerosol Sci. Technol.*, *41*, 418–437, doi:10.1080/02786820701203215.
- Volkamer, R., P. J. Ziemann, and M. J. Molina (2009), Secondary organic aerosol formation from acetylene (C₂H₂): Seed effect on SOA yields due to organic photochemistry in the aerosol aqueous phase, *Atmos. Chem. Phys.*, *9*, 1907–1928, doi:10.5194/acp-9-1907-2009.
- Zhang, Q., et al. (2005), Deconvolution and quantification of hydrocarbon-like and oxygenated organic aerosols based on aerosol mass spectrometry, *Environ. Sci. Technol.*, *39*, 4938–4952, doi:10.1021/es048568l.

R. Bahreini and S. M. Murphy, Earth Systems Research Laboratory, NOAA, 325 Broadway, Boulder, CO 80305, USA.

R. C. Flagan, S. Hersey, and J. H. Seinfeld, Departments of Environmental Science and Engineering and Chemical Engineering, California Institute of Technology, 1200 E. California Blvd., Pasadena, CA 91125, USA.

H. Jonsson, Center for Interdisciplinary Remotely-Piloted Aircraft Studies, Naval Postgraduate School, PO Box 550, Monterey, CA 93933, USA.

A. Sorooshian, Department of Chemical and Environmental Engineering, University of Arizona, PO Box 210011, Tucson, AZ 85721, USA. (armin@email.arizona.edu)